

# **Piping System Response to Detonations.**

**Results of ES1, TS1 and SS1 Testing.**

**J. E. Shepherd and R. Akbar**

Graduate Aeronautical Laboratories  
California Institute of Technology  
Pasadena, CA 91125

Explosion Dynamics Laboratory Report FM2009.001

April 30, 2009

Revision of August 22, 2010

Prime Sponsor: US Department of Energy, Office of River Protection, Hanford, WA.  
Sponsor: Project Assistance Corporation, contract ORP-CAL001.

## Abstract

We report on a series of 61 tests carried out in the Explosion Dynamics Laboratory, California Institute of Technology, on the structural response of piping and support systems to internal detonations in hydrogen-nitrous oxide mixtures. This work was carried out for the US Department of Energy, Office of River Protection at Richland, Wa in support of the Hydrogen in Piping and Ancillary Vessels (HPAV) program that is developing criteria and methods for evaluating hydrogen hazards in the Waste Treatment Plant (WTP) under construction at the Hanford Site.

The piping systems were fabricated using 304 stainless steel, 2-in (50 mm) diameter, schedule 40 commercial pipe with a nominal wall thickness of 3.8 mm (0.15 in) and welded construction to ASME B31.3 standards. The piping was supported using custom brackets or cantilever beams fastened to steel plates bolted and epoxied to the reinforced concrete walls of the laboratory. For most tests, we used nearly-ideal detonations in a 30/70 H<sub>2</sub>-N<sub>2</sub>O mixture at 1 atm initial pressure and 300 K. The detonation speed were close (within 1%) to the Chapman-Jouguet velocity and detonation cell sizes much smaller than the tube diameter. Pressure, hoop and longitudinal strain, displacement, acceleration, and support strains were measured using a high-speed (1 MHz recording speed) digital data acquisition system and calibrated signal conditioners for all instruments. The testing was carried out under a Quality Assurance plan based on ANSI/ASQ Z1.13-1999 which was determined by the DOE after surveillance visits to meet the requirements of the ASME standard NQA-1, Subpart 4.2 and the data was approved by the DOE for use in supporting development of methods and criteria by which HPAV is evaluated. The digital data and documentation of the tests are available on the CIT Explosion Dynamics Laboratory web site <http://www.galcit.caltech.edu/EDL/data-hanford/>.

The piping systems contained bends, tees, and multi-dimensional direction changes. The tests provided fundamental data on longitudinal and hoop strains, junction forces for bends and tees, the interaction with the detonations with water-filled sections, and the loads on cantilever beam supports. The deformations were all within the elastic range in the present series of tests. The peak strains are reported for each case and compared with static estimates based on CJ and reflected CJ pressures in order to define bounds on the dynamic load factors. Wave speeds were computed from time-of-arrival data and replica testing was carried out for all conditions in order to provide confidence in the experimental results. Modeling of the piping systems and finite-element simulations of selected tests were carried out by Dominion Engineering Inc. (DEI) and Bechtel National, Inc. (BNI) to develop and validate detonation propagation and bend force models.

The 35 ES1 tests used a piping specimen consisting of a straight horizontal section about 3 m long (12-ft), a 3.8D (200 mm) radius bend, and a straight vertical section about 1.8 m (6 ft) high. Tests in ES1 examined the force created when the detonation passed through the bend, the effect of DDT, reflection of a detonation and propagation of shock waves in a water-filled vertical section, and forces on cantilever beam supports mounted to the piping system and end flange. The 16 TS1 tests used a specimen with a single "tee" component connecting three pipe segments approximately 1.5 m (60 in) long, supported by either anchors fixed to the plates or cantilever beams. Tests were carried out with detonation propagation in both directions (branch and run) of the tee to determine the effective force on the tee. The 10

SS1 tests used a complex piping system that consisted of five individual segments (including ES1 and TS1) bolted together with 300-lb slip-on flanges welded at the end of each piping segment. The flanges were not gasketed but had metal-to-metal contact to transmit forces and were machined to accept O-rings for sealing. SS1 formed a three-dimensional network mounted on three walls of the facility with a maximum end-to-end length of about 20.5 m (67.5 ft) containing 10 bends (all nominally identical), seven cantilever supports, a tee, and three dead ends. Tests were performed with two sets of instrumentation locations and ignition from two of the three ends.

# Contents

<b>List of Figures</b>	<b>6</b>
<b>List of Tables</b>	<b>17</b>
<b>1 Introduction</b>	<b>19</b>
1.1 Testing Summary . . . . .	20
1.2 Online Information and Companion Reports . . . . .	21
<b>2 Test Facility</b>	<b>22</b>
2.1 Support system anchoring . . . . .	22
2.2 Piping specimens . . . . .	23
2.3 Cantilever Beam Supports . . . . .	25
2.4 Fixed End Brackets . . . . .	26
2.5 Initial gas conditions . . . . .	27
2.6 Ignition System . . . . .	27
2.7 Gas Fill System . . . . .	28
<b>3 Instrumentation</b>	<b>29</b>
3.1 Strain . . . . .	29
3.2 Pressure . . . . .	30
3.3 Temperature . . . . .	31
3.4 Displacement . . . . .	31
3.5 Acceleration and forces . . . . .	33
3.6 Data Acquisition System . . . . .	33
3.7 Quality Assurance . . . . .	35
<b>4 Test Procedures</b>	<b>37</b>
4.1 Facility Evacuation . . . . .	37
4.2 Gas Handling . . . . .	37
4.3 Mixing Within the Facility . . . . .	39
4.4 Post Shot Purge and Cold-Trap Use . . . . .	39
4.5 Data Validation and Reduction . . . . .	39
<b>5 ES1 Test Series</b>	<b>42</b>
5.1 Shot List . . . . .	45
5.2 Detailed description . . . . .	47
5.2.1 Shots 1-6 . . . . .	47
5.2.2 Shots 7-14 . . . . .	47
5.2.3 Shots 15-21 . . . . .	48
5.2.4 Shots 22-24 . . . . .	49
5.2.5 Shots 25-27 . . . . .	49
5.2.6 Shots 28-33 . . . . .	50
5.2.7 Shots 34-35 . . . . .	51
5.3 Key results . . . . .	51

5.3.1	Pressure and Strain Histories . . . . .	51
5.3.2	Repeatability: Wave speeds, pressures, and strains . . . . .	54
5.3.3	Analysis of Hoop and Axial Strains . . . . .	59
5.3.4	DDT Pressures and Strains . . . . .	81
5.3.5	Bend, Cantilever, and Reflecting End forces . . . . .	89
5.3.6	Detonation Wave Interaction with a Water-Filled Section . . . . .	97
<b>6</b>	<b>TS1 Test Series</b>	<b>104</b>
6.1	Shot List . . . . .	104
6.2	Detailed description . . . . .	109
6.2.1	Shots 36-41 . . . . .	109
6.2.2	Shots 42-45 . . . . .	110
6.2.3	Shots 46-49 . . . . .	110
6.2.4	Shots 50 and 51 . . . . .	111
6.3	Key Results . . . . .	111
6.3.1	Pressure and Strain Histories . . . . .	112
6.3.2	Peak Strain and Pressure . . . . .	112
6.3.3	Wave Speeds . . . . .	116
6.3.4	Repeatability and Symmetry . . . . .	117
6.4	Effect of Support Variations . . . . .	120
6.5	Bending, axial, and support strains . . . . .	123
6.5.1	Support Strain Analysis . . . . .	127
6.6	Comparison with Finite-Element Simulations . . . . .	129
6.7	Summary . . . . .	133
<b>7</b>	<b>SS1 Test Series</b>	<b>134</b>
7.1	Test Program . . . . .	140
7.2	Detonation Wave Speeds . . . . .	142
7.3	Peak Pressures and Strains . . . . .	146
7.4	Finite Element Simulations . . . . .	153
7.4.1	Displacement Gage Analysis Issues . . . . .	164
7.5	Summary . . . . .	167
<b>8</b>	<b>Summary</b>	<b>169</b>
8.1	Issues and Suggestions for Future Studies . . . . .	169
<b>9</b>	<b>Acknowledgments</b>	<b>171</b>
	<b>Bibliography</b>	<b>172</b>
<b>A</b>	<b>Properties of CJ wave in H<sub>2</sub>-N<sub>2</sub>O</b>	<b>176</b>
<b>B</b>	<b>Properties of Schedule 40 pipe</b>	<b>177</b>
<b>C</b>	<b>Room 19 Plate Mounting Arrangement</b>	<b>179</b>

<b>D</b>	<b>Check List</b>	<b>184</b>
<b>E</b>	<b>ES1 Engineering Drawings</b>	<b>188</b>
<b>F</b>	<b>ES1 thickness measurements</b>	<b>204</b>
<b>G</b>	<b>Cantilever Beam Supports</b>	<b>205</b>
	G.1 Engineering Drawings . . . . .	205
	G.2 Instrumentation and Calibration . . . . .	209
	G.2.1 Single Gage in a Quarter-Bridge Circuit . . . . .	209
	G.2.2 Two Gages in a Half-Bridge Circuit . . . . .	210
	G.2.3 Two Gages Connected Independently . . . . .	211
	G.2.4 Three-gage Rosettes . . . . .	211
	G.2.5 Static Calibration . . . . .	212
<b>H</b>	<b>Anchor Brackets</b>	<b>217</b>
<b>I</b>	<b>ES1 Sensor Locations</b>	<b>226</b>
<b>J</b>	<b>ES1 Data Plots</b>	<b>239</b>
<b>K</b>	<b>TS1 Engineering Drawings</b>	<b>293</b>
<b>L</b>	<b>TS1 Sensor Locations</b>	<b>302</b>
<b>M</b>	<b>TS1 Data Plots</b>	<b>304</b>
<b>N</b>	<b>SS1 Engineering Drawings</b>	<b>346</b>
<b>O</b>	<b>SS1 Data Plots</b>	<b>361</b>
	O.1 Sensor Locations . . . . .	361
	O.2 Shot 53 . . . . .	366
	O.3 Shot 54 . . . . .	370
	O.4 Shot 55 . . . . .	375
	O.5 Shot 56 . . . . .	380
	O.6 Shot 58 . . . . .	385
	O.7 Shot 59 . . . . .	390
	O.8 Shot 60 . . . . .	395
	O.9 Shot 61 . . . . .	400
<b>P</b>	<b>Quality Assurance Plan</b>	<b>405</b>
<b>Q</b>	<b>PVP Conference Paper</b>	<b>416</b>

# List of Figures

1	Control room portion of room 19 showing data acquisition system in rack panel and control system on the wall. . . . .	22
2	a) mounting plate b) south wall c) north wall d) west wall. . . . .	23
3	a) SAE J1926 9/16-18 fitting (the fitting is 0.82 in long) and adapter. b, c) located on pipe. d) adapter after welding to pipe. . . . .	24
4	Slip-on flange welds for ES1. . . . .	25
5	Cantilever support U1 with a single 3-gage strain rosette and typical attachment to the piping specimen with a 3/8 u-bolt. . . . .	25
6	Gas handling flanges and fixed end brackets. a) ES1 Upper flange plumbing b) ES1 lower flange plumbing c) Mounting holes for nylon insert d) Spark plug mounted and connected . . . . .	26
7	Spark plug electrodes showing a) clean and b) contaminated conditions. . . . .	27
8	Shchelkin spiral and mounting pins. . . . .	28
9	Circuit of custom spark generation unit used to ignite the mixtures. . . . .	29
10	Strain gages mounted onto a piping section. a) Single gage Vishay model CEA-06-250UN-350. b) Tee rosette, Vishay model CEA-06-125UT-350. . . . .	30
11	PCB pressure gage mounted in SAE fitting. Gage front has not been coated with RTV yet. . . . .	32
12	Thermocouple junction with exposed bead mounted in SAE fitting. . . . .	32
13	Displacement gages installations. a) Micro-Epsilon 1401 located at position D3. b) Keyence LKG-407 located at position D4. A mirror is used to rotate the beam path by 90° to measure vertical motion. . . . .	33
14	a) Accelerometer mounting for tests 22-23; b) 3-gage rosette mounted on U1; c) 3-gage rosette mounted on U2; d) single gage (one of four) mounted on U3. . . . .	34
15	Schematic of the data acquisition system and sensors. . . . .	35
16	Plumbing schematics for the three versions (ES1, TS1, SS1 from top to bottom) of the facility. . . . .	38
17	ES1 specimen layout showing mounting locations (both ends anchored) and wall plates. . . . .	42
18	ES1 overall dimensions showing reference plane for instrument locations. . . . .	43
19	ES1 sensor layout for standard pressure and strain arrangement. Pressure sensors were moved in some tests, see App. N. . . . .	43
20	ES1 as installed for tests with both ends anchored. . . . .	44
21	ES1 test (shot 3) results for near-CJ detonation propagation from W to E. a) Sensor layout for the majority of ES1 tests with W-to-E detonation propagation. b) pressure c) and d) strains. . . . .	52
22	ES1 test (shot 3) results for a long duration with high frequency components removed. a) Pressure. b) selected strains gages in the vertical leg of the system. Red lines are exponential functions approximating mean strain. . . . .	53
23	Details of ES1 test results for near-CJ detonation propagation from W to E. . . . .	55
24	Comparison of shots 3 and 4 a) pressure b) strain c) strain d) pressure arrival time. . . . .	56

25	Comparison of peak a) strain and b) pressure for reference tests 3–6, and reverse propagation tests 22, 23, 24. The reference pressures and strains ( $\Phi = 1$ ) are discussed in Section 4.5. . . . .	58
26	Stress and strain analysis of strain gages 4 (hoop) and 5 (axial) for shot 3. . . . .	60
27	Spectral analysis of strain gages S4 (a, b) and S5 (c, d) for shot 3. . . . .	61
28	Hoop (black) and axial (red) strain gages S4 and S5. Data has been filtered at 50 kHz to remove noise and the time axis shifted so that $t = 0$ corresponds to the interpolated detonation arrival time. . . . .	62
29	Stress analysis showing bounding von Mises ellipse with $\sigma_{vM} = 45$ MPa for strain gages 4 and 5, shot 3. . . . .	63
30	Stress analysis showing bounding von Mises ellipse with $\sigma_{vM} = 65$ MPa and principle stresses determined by analyzing the rosette strain gages S8, S9, S10 in shot 35. . . . .	64
31	Axi-symmetric deformations of a pipe. The coordinate system $(x, y, z)$ is a local construction with $z$ parallel to the radial direction, $x$ to the axial direction, and $y$ the circumferential ( $\theta$ ) direction. The mean radius of the pipe is $R$ , the distance $z$ is measured from the midplane surface shown as the dashed line and the local radii of curvature of the midplane surface, $R_y$ and $R_x$ , are positive as shown. The axial wavelength of the flexural oscillation is $\lambda$ . . . . .	65
32	Comparison (Ligon, 2009a) of FEM (ANSYS) simulation of ES1 shot 3 and experimental data for a) strain gage S4 (hoop) and b) S5 (axial) as well as c) S13 (hoop) and d) S14 (axial). . . . .	70
33	Simulation of 2-in pipe tests (ES1, TS1, SS1). Individual contributions to membrane stretching and bending to axial and hoop strains at outer fibers based on steady-state shock wave approximation including shear deformation and rotational inertia. . . . .	76
34	Simulation of 2-in pipe tests (ES1, TS1, SS1). Based on steady-state shock wave approximation including shear deformation and rotational inertia. a) hoop and axial strain. b) hoop and axial stress. . . . .	77
35	Hoop and axial strain gages S5 and S7 for shot 1, tube 4 from Karnesky (2010). The red line is the hoop stress scaled with Eq. 44 . . . . .	78
36	Simulation of the test shown in Fig. 35. Individual contributions to membrane stretching and bending to axial and hoop strains at outer fibers based on steady-state shock wave approximation including shear deformation and rotational inertia. . . . .	79
37	Simulation of the test shown in Fig. 35. a) hoop and axial strain b) hoop and axial stress. . . . .	80
38	Comparison of bracketing values for transition from deflagration to detonation with previous data of Bollinger et al. (1962). . . . .	82
39	Comparison of peak a) strain and b) pressure for reference test 3 and all tests involving a DDT event without water present. The reference pressures and strains ( $\Phi = 1, 30/70$ H <sub>2</sub> /N <sub>2</sub> O) are discussed in Section 4.5. . . . .	85
40	Pressure traces for two DDT tests. a) shot 9 and b) shot 8. . . . .	86
41	Close-up of strains in vertical leg of ES1 during shot 9. Data has been filtered to remove high frequency noise. . . . .	87

42	Pressure and strains measured during the deflagration observed in ES1 shot 14. Data has been filtered to remove high frequency noise. . . . .	88
43	Forces on ES1 piping system created by internal detonation propagation. . .	89
44	Axial strains predicted by the control volume force model and bar wave transmission compared to measured strains in shot 3. a) upstream of bend b) downstream of bend. (Shepherd and Akbar, 2009) . . . . .	91
45	Axial strains predicted by the ANSYS (Ligon, 2009a) and bend pressure distribution force model (Shepherd and Akbar, 2009) compared to measured strains in shot 3. a) & c) upstream of bend S3; b) & d) downstream of bend S15. Experimental data is filtered in c) and d) with a 20 kHz low-pass filter to remove hoop oscillations visible in a) and b). . . . .	92
46	Comparison of axial strains measured in shot 3 with those predicted by the ANSYS (Ligon, 2009a) and ME101 (Lynch, 2009). . . . .	93
47	Force link fixture. a) exploded view. b) looking North c) looking East d) detail of dog screws and captive pin. . . . .	94
48	Forces and strains at reflecting end. a) Forces on east end as predicted by ANSYS (Ligon, 2009a) b) Cantilever bending strains predicted by ANSYS and compared to the strains measured in the force link fixture. . . . .	95
49	Placement of U-Bolt Supports in shots 25–27 and 34-35. . . . .	95
50	ES1 Shot 35, 50 kHz low-pass data. a) Cantilever vertical bending comparison with shot 26. c) Out of plane deflection of bend measured with Keyence laser gage. . . . .	96
51	a) Sensor placement and water free surface location for ES1 Shots 15-21. b) Pressure trace for shot 15. . . . .	98
52	ES1 Shots 15-21 with water in vertical leg compared to shot 3 without water. a) peak strain, b) peak pressure. . . . .	101
53	ES1 Shot 18 with water in vertical leg compared to shot 3 without water. a) Comparison of strains S13 (hoop) and S14 (axial) with the pressure at P7. Pressure data time shifted to interpolated arrival time at strain gage location. b) Comparison of S13 and S14 for shots 13 and 14, time shifted so that onset of hoop deformation approximately coincides for both shots. . . . .	102
54	TS1 mounted on south wall of Room 19. a) configuration for shots 46-49. b) configuration for shots 42-45. . . . .	104
55	Locations of sensors used on TS1. . . . .	105
56	Configuration of TS1 with top anchored and cantilevers on bottom ends. Tests 36-41. . . . .	106
57	Configuration of TS1 with top free and cantilevers on bottom ends. Tests 42-45.	106
58	Configuration of TS1 with top free and anchors on bottom ends. Tests 46-49.	107
59	Configuration of TS1 with all three ends anchored. Tests 50-51. . . . .	107
60	a) Keyence measurement unit with turning mirror. b) U-bolt with teflon pad on vertical leg c) cantilever support on E end c) Cantilever support on W end.	111
61	Pressure signals from two cases. a) Top ignition, shot 38. b) East ignition, shot 40. . . . .	113
62	TS1 measured peak pressures for a) top ignition, b) east side ignition. . . . .	114
63	TS1 measured peak strains for a) top ignition, b) east side ignition. . . . .	115

64	TS1 pressure arrival time pair difference frequency compared to normal distribution. . . . .	117
65	TS1 Shot 38 comparisons. Pressure, and cantilever strain gage signals. 10 ms raw data. a) and b) shot 38 vs. 36. c) and d) shot 38 vs. 37. . . . .	118
66	TS1 Shot 37. Check of pressure and cantilever beam symmetry. 10 ms raw data. . . . .	119
67	TS1 comparison of end conditions. a) Shot 51 (all ends anchored) vs. shot 39 (top anchored and bottom ends on cantilevers). a) Shot 45 (top free) vs. shot 41 (top anchored). . . . .	121
68	TS1 comparison of end conditions for a long time. Shot 51 (all ends anchored) vs. shot 39 (top anchored and bottom ends on cantilevers). . . . .	122
69	TS1 Shot 39 strain analysis. . . . .	124
70	TS1 Shot 39 spectral analysis of selected strain signals. a) and b) hoop strain from gage S11. c) and d) beam bending strain from the difference signal S12-S13. . . . .	125
71	TS1 Shot 39 spectral analysis of selected strain signals. a) S26 cantilever bending strain in vertical direction b) S27 cantilever bending strain in horizontal direction. c) and d) axial and membrane bending strain from the sum signal S12+S13. . . . .	126
72	TS1 key dimensions. Components considered in vibration analysis are shown filled in with gray shading. . . . .	127
73	TS1 Shot 43 comparison of filtered data with ANSYS simulations. Reproduced from p. 22 of Ligon (2009c). . . . .	130
74	TS1 Shot 43 comparison of raw data with ANSYS simulations. Reproduced from p. 26 of Ligon (2009c). . . . .	131
75	TS1 Shot 43 comparison of cantilever support data with ANSYS simulations. Reproduced from p. 27 of Ligon (2009c). . . . .	132
76	SS1 perspective view. . . . .	134
77	SS1 layout in test cell. a) north wall b) transition from north to west wall. . . . .	136
78	SS1 layout in test cell showing west wall. . . . .	137
79	SS1 layout in test cell showing transition from west to south wall. . . . .	138
80	SS1 layout in test cell showing south wall. . . . .	139
81	Pressure data, P1-P8 for shot 53. . . . .	143
82	Pressure data, P10-P18 for shot 53. . . . .	144
83	Pressure data, P19-P20 for shot 53. . . . .	145
84	Linear regression fit to detonation arrival time data for shot 53. . . . .	146
85	SS1 tests peak pressure rise values averaged for each data set. . . . .	150
86	SS1 tests peak strain values averaged for each data set. . . . .	151
87	Comparison of simulations with strain data for longitudinal strain gages S1, S2, S3, S4 for shot 58. Reproduced from p. 33 and 34 of Ligon (2009e). . . . .	155
88	Comparison of simulations with strain data for longitudinal strain gages S13, S14, S15, S16, S17 for shot 60. Reproduced from p. 36 and 37 of Ligon (2009e). . . . .	156
89	Comparison of simulations with strain data for longitudinal strain gages S24, S25, S26, S34, S35 for shot 58. Reproduced from p. 38 of Ligon (2009e). . . . .	157

90	Comparison of simulations with strain data over 100 ms for longitudinal gages S1, S2 for shot 58 and S16, S17 for shot 60. Reproduced from p. 42 and 43 of <a href="#">Ligon (2009e)</a> . . . . .	158
91	Spectral analysis of SS1 strain data for longitudinal for shot 58. a) S2. b) S4. c) S16. d) S17. . . . .	159
92	Spectral analysis of SS1 strain data for longitudinal for shot 58. a) S16, region of hoop resonance. b) S34, region of hoop resonance. c) S34, high-frequency content. d) S34, frequencies less than 5 kHz. . . . .	160
93	Comparison of simulations with strain data for longitudinal strain gages S36, S37, S38, S39 for shot 58. These gages are mounted on the cantilever supports SU1 (S36, S37) and SU4 (S38, S39). Reproduced from p. 40 and 41 of <a href="#">Ligon (2009e)</a> . . . . .	161
94	Processed strain data for longitudinal strain gages S36, S37, S38, S39 for shot 60. These gages are mounted on the cantilever supports SU1 (S36, S37) and SU4 (S38, S39). Sum signals isolate the axial strain (along the cantilever beam, perpendicular to the wall), difference signals isolate the bending strain (perpendicular the cantilever and pipe axis). . . . .	162
95	Comparison of simulations with strain data for displacement gages D1, D2, D3, D4 for shot 58. Reproduced from p. 41 and 42 of <a href="#">Ligon (2009e)</a> . . . . .	163
96	Krohn-Hite low pass filter analysis. . . . .	165
97	Comparison of displacements measured in shot 58 with results of ANSYS simulations, Fig. 26 of <a href="#">Ligon (2009e)</a> , shifted in time to compensate for the filter phase shift. . . . .	166
98	Comparison of peak strains from simulation with measured peak strains for shots 53 and 58. Reproduced from p. 32 of <a href="#">Ligon (2009e)</a> . . . . .	168
99	Nominal dimensions of Room 19 experiment area. . . . .	179
100	Engineering dimensions of anchor plate. . . . .	180
101	Plate layout on North wall. . . . .	181
102	Plate layout on South wall. . . . .	182
103	Plate layout on West wall. . . . .	183
104	Engineering drawing of ES1 assembly. Front view. . . . .	188
105	Engineering drawing of ES1 assembly. Side view. . . . .	189
106	Engineering drawing showing assembly of the SAE boss onto the pipe. . . . .	190
107	Engineering drawing of SAE boss. . . . .	191
108	Perspective view of ES1 assembly mounted on the North wall. . . . .	192
109	Engineering drawing of ES1 300 lb class blind flange. . . . .	193
110	Engineering drawing of ES1 slip-on flange modification. . . . .	194
111	Engineering drawing of original ES1 slip-on flange. . . . .	195
112	Engineering specifications of SAE1926 port. . . . .	196
113	Engineering specification of SAE hex head plugs. . . . .	197
114	Engineering drawing of spring used for Shchelkin spiral. . . . .	198
115	Orientation of ES1 as mounted on North wall. . . . .	199
116	Orientation of ES1 as mounted on North wall. . . . .	200
117	As built dimensions of ES1. Note bend radius is measured to pipe wall in this drawing. . . . .	201

118	Overall dimensions of ES1. Note bend radius is measured to centerline in this drawing. . . . .	202
119	ES1 bend photograph annotated with measured dimensions used to create as-built specifications. . . . .	203
120	Thickness measurements on ES1 specimen. . . . .	204
121	Engineering drawing of cantilever beam - basic outline. . . . .	205
122	Engineering drawing of cantilever beam - hole locations. . . . .	206
123	Strain gage locations on cantilever beams. . . . .	207
124	Dimensions of U-bolts used to fasten pipe to cantilever beams. . . . .	208
125	Quarter bridge configuration: a) Strain gage located on beam; b) bridge circuit.	209
126	Half bridge configuration: a) Strain gages located on top and bottom of beam; b) bridge circuit. . . . .	211
127	Calibration of support beams a) Fixture for creating bending simulation pipe pushing down on the lever b) fixture for simulating pipe pushing up on U-bolt.	213
128	Calibration results using central gage (number 2) of rosette. a) U1 b) U2. . .	214
129	Calibration results for half-bridge configuration on U3. a) AB pair b) CD pair.	215
130	Calibration results for half-bridge configuration on U4. . . . .	216
131	Perspective view of solid model for fixed end anchors. . . . .	217
132	Engineering drawing of anchor base. . . . .	218
133	Engineering drawing of anchor front. . . . .	219
134	Engineering drawing of anchor side. . . . .	220
135	Engineering drawing of gas handling flange. . . . .	221
136	Engineering drawing of nylon spark plug insert. . . . .	222
137	Engineering drawing of backing ring for nylon spark plug insert. . . . .	223
138	Engineering drawing of plug used to fill spark plug insert opening. A pressure transducer (PCB) was mounted in these plugs. . . . .	224
139	Dimensions of cut-away of assembled pipe, gas handling flange, end bracket, and insert plug. . . . .	225
140	Location of sensors on ES1 for all tests except 22 and 23. . . . .	226
141	Location of sensors on ES1 for tests 15-21 with water in vertical leg. . . . .	228
142	Location of sensors on ES1 for tests 22-24. . . . .	230
143	Location of U-bolts in tests 25-27 and 34-35. . . . .	233
144	Arrangement of strain gages for cantilevers in shots 34-35. . . . .	235
145	ES1 Shot 1. Pressure and strain gage signals. . . . .	240
146	ES1 Shot 2. Pressure and strain gage signals. . . . .	241
147	ES1 Shot 3. Pressure and strain gage signals. . . . .	242
148	ES1 Shot 4. Pressure and strain gage signals. . . . .	243
149	ES1 Shot 5. Pressure and strain gage signals. . . . .	244
150	ES1 Shot 6. Pressure and strain gage signals. . . . .	245
151	ES1 Shot 7. Pressure and strain gage signals. . . . .	246
152	ES1 Shot 8. Pressure and strain gage signals. . . . .	247
153	ES1 Shot 9. Pressure and strain gage signals. . . . .	248
154	ES1 Shot 10. Pressure and strain gage signals. . . . .	249
155	ES1 Shot 11. Pressure and strain gage signals. . . . .	250
156	ES1 Shot 12. Pressure and strain gage signals. . . . .	251

157	ES1 Shot 13. Pressure and strain gage signals. . . . .	252
158	ES1 Shot 15. Pressure and strain gage signals. . . . .	253
159	ES1 Shot 16. Pressure and strain gage signals. . . . .	254
160	ES1 Shot 17. Pressure and strain gage signals. . . . .	255
161	ES1 Shot 18. Pressure and strain gage signals. . . . .	256
162	ES1 Shot 19. Pressure and strain gage signals. . . . .	257
163	ES1 Shot 20. Pressure and strain gage signals. . . . .	258
164	ES1 Shot 21. Pressure and strain gage signals. . . . .	259
165	ES1 Shot 22. Pressure and strain gage signals. . . . .	260
166	ES1 Shot 23. Pressure and strain gage signals. 10 ms, unfiltered. . . . .	261
167	ES1 Shot 23. Pressure and strain gage signals. 40 ms, unfiltered. . . . .	262
168	ES1 Shot 23. Pressure and strain gage signals. 10 ms, 20 kHz low-pass filter. . . . .	263
169	ES1 Shot 24. Pressure, strain gage, and accelerometer signals. 10 ms, 50 kHz low-pass filter. . . . .	264
170	ES1 Shot 24 vs 23. Pressure and strain gage signal comparisons, 10 ms. . . . .	265
171	ES1 Shot 25. Pressure, strain gage, and accelerometer signals. 10 ms raw data. . . . .	266
172	ES1 Shot 25. Pressure, strain gage, and accelerometer signals. 10 ms, 50 kHz low-pass filter. . . . .	267
173	ES1 Shot 26. Pressure, strain gage, and accelerometer signals. 10 ms raw data. . . . .	268
174	ES1 Shot 26. Pressure, strain gage, and accelerometer signals. 10 ms, 50 kHz low-pass filter. . . . .	269
175	ES1 Shot 27. Pressure, strain gage, and accelerometer signals. 10 ms raw data. . . . .	270
176	ES1 Shot 27. Pressure, strain gage, and accelerometer signals. 10 ms, 50 kHz low-pass filter. . . . .	271
177	ES1 Shot 27 vs 26. Pressure, strain gage, and accelerometer signals. 10 ms, 50 kHz low-pass filter. . . . .	272
178	ES1 Shot 27 vs 25. Pressure, strain gage, and accelerometer signals. 10 ms, 50 kHz low-pass filter. . . . .	273
179	ES1 Shot 28. Pressure, strain gage, and accelerometer signals. 10 ms raw data. . . . .	274
180	ES1 Shot 28. Pressure, strain gage, and accelerometer signals. 10 ms, 50 kHz low-pass filter. . . . .	275
181	ES1 Shot 29. Pressure, strain gage, and accelerometer signals. 10 ms raw data. . . . .	276
182	ES1 Shot 29. Pressure, strain gage, and accelerometer signals. 40 ms, 50 kHz low-pass filter. . . . .	277
183	ES1 Shot 31. Pressure, strain gage, and accelerometer signals. 10 ms raw data. . . . .	278
184	ES1 Shot 31. Pressure, strain gage, and accelerometer signals. 100 ms raw data. . . . .	279
185	ES1 Shot 32. Pressure, strain gage, accelerometer signals. 10 ms raw data. . . . .	280
186	ES1 Shot 32. Pressure, strain gage, accelerometer, and displacement signals. 100 ms raw data. . . . .	281
187	ES1 Shot 32 vs 33. Pressure, strain gage, and displacement signals. 10 ms raw data. . . . .	282
188	ES1 Shot 33. Pressure, strain gage, accelerometer signals. 10 ms raw data. . . . .	283
189	ES1 Shot 33. Pressure, strain gage, accelerometer, and displacement signals. 100 ms raw data. . . . .	284

190	ES1 Shot 33 vs 3. Pressure, strain gage, and displacement signals. 10 ms raw data. . . . .	285
191	ES1 Shot 33 vs 28. Pressure, strain gage, and displacement signals. 10 ms, 50 kHz low-pass filtered data. . . . .	286
192	ES1 Shot 34. Pressure, strain gage, accelerometer signals. 10 ms raw data. . . . .	287
193	ES1 Shot 34. Pressure, strain gage, accelerometer, and displacement signals. 100 ms raw data. . . . .	288
194	ES1 Shot 35. Pressure, strain gage, accelerometer signals. 10 ms raw data. . . . .	289
195	ES1 Shot 35. Pressure, strain gage, accelerometer signals. 100 ms of 50 kHz low-pass filtered data. . . . .	290
196	ES1 Shot 34 vs 35. Pressure, strain gage, accelerometer signals. 10 ms raw data. . . . .	291
197	ES1 Shot 35 vs 3. Pressure, strain gage, accelerometer signals. 30 ms of 50 kHz low-pass filtered data. . . . .	292
198	Engineering drawing of TS1 assembly. Front, top, and side views. . . . .	293
199	Engineering drawing of TS1 assembly. Side view. . . . .	294
200	Engineering drawing of TS1 assembly. Instrument port locations on tee run pipe segment. . . . .	295
201	Engineering drawing of TS1 assembly. Instrument port locations on tee branch pipe segment. . . . .	296
202	Engineering drawing of TS1 SAE port adapter boss. . . . .	297
203	Engineering drawing of SAE port assembly to piping. . . . .	298
204	Engineering drawing of tee component used in TS1. . . . .	299
205	Engineering drawing of slip-on flange used in TS1. . . . .	300
206	Dimensions of key features of TS1. . . . .	301
207	Arrangement of strain gages for cantilevers in shots 36-45. . . . .	303
208	TS1 Shot 36. Pressure and cantilever strain gage signals. 10 ms raw data. . . . .	304
209	TS1 Shot 36. Pressure and cantilever strain gage signals. 10 ms raw data. . . . .	305
210	TS1 Shot 36. Check of pressure and cantilever beam symmetry. 10 ms raw data. . . . .	306
211	TS1 Shot 37. Pressure and cantilever strain gage signals. 10 ms raw data. . . . .	307
212	TS1 Shot 38. Pressure, strain gage, and cantilever strain gage signals. 10 ms raw data. . . . .	308
213	TS1 Shot 38. Pressure, strain gage, and cantilever strain gage signals. 100 ms raw data. . . . .	309
214	TS1 Shot 38. Check of pressure symmetry. 10 ms raw data. . . . .	310
215	TS1 Shot 39. Pressure, strain gage, and cantilever strain gage signals. 10 ms raw data. . . . .	311
216	TS1 Shot 39. Pressure, strain gage, and cantilever strain gage signals. 100 ms raw data. . . . .	312
217	TS1 Shot 39. Check of pressure symmetry. 10 ms raw data. . . . .	313
218	TS1 Shot 39 vs 38 comparisons. Pressure, and cantilever strain gage signals. 10 ms raw data. . . . .	314
219	TS1 Shot 40. Pressure, strain gage, and cantilever strain gage signals. 10 ms raw data. . . . .	315

220	TS1 Shot 41. Pressure, strain gage, and cantilever strain gage signals. 10 ms raw data. . . . .	316
221	TS1 Shot 41 vs 40. Pressure, strain gage, and cantilever strain gage signals. 10 ms raw data. . . . .	317
222	TS1 Shot 42. Pressure, strain gage, cantilever strain gage, displacement, and accelerometer signals. 10 ms raw data. . . . .	318
223	TS1 Shot 42. Pressure, strain gage, cantilever strain gage, displacement, and accelerometer signals. 100 ms raw data. . . . .	319
224	TS1 Shot 43. Pressure, strain gage, cantilever strain gage, displacement, and accelerometer signals. 10 ms raw data. . . . .	320
225	TS1 Shot 43. Pressure, strain gage, cantilever strain gage, displacement, and accelerometer signals. 100 ms raw data. . . . .	321
226	TS1 Shot 43 vs 39 . Pressure, strain gage, cantilever strain gage signals. 10 ms raw data. . . . .	322
227	TS1 Shot 43 vs 42. Pressure, strain gage, cantilever strain gage, displacement, and accelerometer signals. 10 ms raw data. . . . .	323
228	TS1 Shot 44. Pressure, strain gage, cantilever strain gage, displacement, and accelerometer signals. 10 ms raw data. . . . .	324
229	TS1 Shot 44. Pressure, strain gage, cantilever strain gage, displacement, and accelerometer signals. 100 ms raw data. . . . .	325
230	TS1 Shot 45. Pressure, strain gage, cantilever strain gage, displacement, and accelerometer signals. 10 ms raw data. . . . .	326
231	TS1 Shot 45 vs 44. Pressure, strain gage, cantilever strain gage, displacement, and accelerometer signals. 10 ms raw data. . . . .	327
232	TS1 Shot 45 vs 41. Pressure, strain gage, and cantilever strain gage signals. 10 ms raw data. . . . .	328
233	TS1 Shot 46. Pressure, strain gage, displacement, and accelerometer signals. 10 ms raw data. . . . .	329
234	TS1 Shot 47. Pressure, strain gage, displacement, and accelerometer signals. 10 ms raw data. . . . .	330
235	TS1 Shot 47. Pressure, strain gage, displacement, and accelerometer signals. 100 ms raw data. . . . .	331
236	TS1 Shot 47 vs 46. Pressure, strain gage, displacement, and accelerometer signals. 10 ms raw data. . . . .	332
237	TS1 Shot 47 vs 45. Pressure, strain gage, displacement, and accelerometer signals. 10 ms raw data. . . . .	333
238	TS1 Shot 48. Pressure, strain gage, displacement, and accelerometer signals. 10 ms raw data. . . . .	334
239	TS1 Shot 48. Pressure, strain gage, displacement, and accelerometer signals. 100 ms raw data. . . . .	335
240	TS1 Shot 49. Pressure, strain gage, displacement, and accelerometer signals. 10 ms raw data. . . . .	336
241	TS1 Shot 49. Pressure, strain gage, displacement, and accelerometer signals. 100 ms raw data. . . . .	337

242	TS1 Shot 49 vs 48. Pressure, strain gage, displacement, and accelerometer signals. 10 ms raw data. . . . .	338
243	TS1 Shot 50. Pressure, strain gage, displacement, and accelerometer signals. 10 ms raw data. . . . .	339
244	TS1 Shot 50. Pressure, strain gage, displacement, and accelerometer signals. 100 ms raw data. . . . .	340
245	TS1 Shot 51. Pressure, strain gage, displacement, and accelerometer signals. 10 ms raw data. . . . .	341
246	TS1 Shot 51. Pressure, strain gage, displacement, and accelerometer signals. 100 ms raw data. . . . .	342
247	TS1 Shot 51 vs 50. Pressure, strain gage, displacement, and accelerometer signals. 10 ms raw data. . . . .	343
248	TS1 Shot 51 vs 49. Pressure, strain gage, displacement, and accelerometer signals. 10 ms raw data. . . . .	344
249	TS1 Shot 51 vs 39. Pressure, strain gage, displacement, and accelerometer signals. 10 ms raw data. . . . .	345
250	Engineering drawing of SS1 assembly. . . . .	346
251	Engineering drawing of SS1 assembly. . . . .	347
252	Engineering drawing of SS1 assembly. . . . .	348
253	Engineering drawing of SS1 assembly. . . . .	349
254	Engineering drawing of SS1 assembly. . . . .	350
255	Engineering drawing of SS1 assembly. . . . .	351
256	Engineering drawing of SS1 assembly. . . . .	352
257	Engineering drawing of SS1 assembly. . . . .	353
258	Engineering drawing of SS1 assembly. . . . .	354
259	Engineering drawing of SS1 assembly. . . . .	355
260	Engineering drawing of SS1 assembly. . . . .	356
261	SS1 North wall port locations. . . . .	357
262	SS1 West wall port locations. . . . .	358
263	SS1 South wall port locations. . . . .	359
264	SS1NW corner port locations, overhead view. . . . .	360
265	SS1 North wall sensor locations. Pressure transducer locations correct only for shots 53, 54, 58, and 59; some changes were made for other shots. . . . .	361
266	SS1 West wall sensor locations. Pressure transducer locations correct only for shots 53, 54, 58, and 59; some changes were made for other shots. . . . .	362
267	SS1 South wall sensor locations. Pressure transducer locations correct only for shots 53, 54, 58, and 59; some changes were made for other shots. . . . .	363
268	SS1 Shot 53. Pressure gage signals. 10 ms raw data. . . . .	366
269	SS1 Shot 53. Pressure and strain gage signals. 10 ms raw data. . . . .	367
270	SS1 Shot 53. Strain gage signals. 10 ms raw data. . . . .	368
271	SS1 Shot 53. Strain gage, cantilever strain gage, and displacement signals. 10 ms raw data. . . . .	369
272	SS1 Shot 54. Pressure gage signals. 10 ms raw data. . . . .	370
273	SS1 Shot 54. Pressure and strain gage signals. 10 ms raw data. . . . .	371
274	SS1 Shot 54. Strain gage signals. 10 ms raw data. . . . .	372

275	SS1 Shot 54. Pipe strain and cantilever strain gage signals. 10 ms and 100 ms raw data. . . . .	373
276	SS1 Shot 54. Displacement gage signals. 100 ms raw data. . . . .	374
277	SS1 Shot 55. Pressure gage signals. 10 ms raw data. . . . .	375
278	SS1 Shot 55. Pressure and strain gage signals. 10 ms raw data. . . . .	376
279	SS1 Shot 55. Strain gage signals. 10 ms raw data. . . . .	377
280	SS1 Shot 55. Pipe strain and cantilever strain gage signals. 10 ms and 100 ms raw data. . . . .	378
281	SS1 Shot 55. Displacement gage signals. 100 ms raw data. . . . .	379
282	SS1 Shot 56. Pressure gage signals. 10 ms raw data. . . . .	380
283	SS1 Shot 56. Pressure and strain gage signals. 10 ms raw data. . . . .	381
284	SS1 Shot 56. Strain gage signals. 10 ms raw data. . . . .	382
285	SS1 Shot 56. Pipe strain and cantilever strain gage signals. 10 ms and 100 ms raw data. . . . .	383
286	SS1 Shot 56. Displacement gage signals. 100 ms raw data. . . . .	384
287	SS1 Shot 58. Pressure gage signals. 10 ms raw data. . . . .	385
288	SS1 Shot 58. Pressure and strain gage signals. 10 ms raw data. . . . .	386
289	SS1 Shot 58. Strain gage signals. 10 ms raw data. . . . .	387
290	SS1 Shot 58. Pipe strain and cantilever strain gage signals. 10 ms and 100 ms raw data. . . . .	388
291	SS1 Shot 58. Displacement gage signals. 100 ms raw data. . . . .	389
292	SS1 Shot 59. Pressure gage signals. 10 ms raw data. . . . .	390
293	SS1 Shot 59. Pressure and strain gage signals. 10 ms raw data. . . . .	391
294	SS1 Shot 59. Strain gage signals. 10 ms raw data. . . . .	392
295	SS1 Shot 59. Pipe strain and cantilever strain gage signals. 10 ms and 100 ms raw data. . . . .	393
296	SS1 Shot 59. Displacement gage signals. 100 ms raw data. . . . .	394
297	SS1 Shot 60. Pressure gage signals. 10 ms raw data. . . . .	395
298	SS1 Shot 60. Pressure and strain gage signals. 10 ms raw data. . . . .	396
299	SS1 Shot 60. Strain gage signals. 10 ms raw data. . . . .	397
300	SS1 Shot 60. Cantilever strain gage signals. 100 ms raw and processed data. . . . .	398
301	SS1 Shot 60. Displacement gage signals. 100 ms raw data. . . . .	399
302	SS1 Shot 61. Pressure gage signals. 10 ms raw data. . . . .	400
303	SS1 Shot 61. Pressure and strain gage signals. 10 ms raw data. . . . .	401
304	SS1 Shot 61. Strain gage signals. 10 ms raw data. . . . .	402
305	SS1 Shot 61. Cantilever strain gage signals. 100 ms raw and processed data. . . . .	403
306	SS1 Shot 61. Displacement gage signals. 100 ms raw data. . . . .	404

# List of Tables

1	Piezoelectric pressure sensor specifications. S in the gage type number indicates a stainless steel diaphragm which was used after gages with carbon steel diaphragms were ruined in earlier testing due to acid corrosion. . . . .	31
2	Displacement gage specifications. . . . .	32
3	Cantilever beam instrumentation. . . . .	34
4	Approximate Facility volumes and time for which the recirculation pump is operated. . . . .	39
5	Computed CJ velocity and pressure, reflected shock pressure as a function of initial conditions. . . . .	40
6	Peak strains ( $\Phi = 1$ ) in 2-in Schedule 40 pipe for various combustion modes in 1 atm 30/70 H <sub>2</sub> /N <sub>2</sub> O mixtures. . . . .	41
7	List of shots and conditions carried out with ES1 specimen . . . . .	45
8	List of shots and conditions carried out with ES1 specimen (continued) . . . . .	46
9	Measured ES1 wave speeds and peak pressures (not including the reflected pressure) compared against CJ values. . . . .	57
10	Parameters for the thin-shell model of structural response to a moving load simulating a detonation for two cases. Parameters were computed using the solution including shear deformation and rotary inertia. . . . .	73
11	Computed detonation properties of lean H <sub>2</sub> -N <sub>2</sub> O mixtures and observed distances $L_{DDT}$ for the onset of detonation. The cell widths $\lambda$ are estimates based on extrapolating the existing data Pfahl et al. (1998) using reaction zone length scaling. . . . .	82
12	Estimates of peak forces for ES1 piping system. . . . .	90
13	Free surface location (from igniter) and shock wave speeds in water-filled piping. . . . .	103
14	List of shots and conditions carried out with TS1 specimen . . . . .	108
15	Wave speeds obtained from regression analysis of pressure wave time-of-arrival data. . . . .	116
16	First three axial vibration frequencies of half tee-flange system. . . . .	129
17	List of test conditions for all shots in series SS1 . . . . .	141
18	Detonation wave speeds in the SS1 tests. The nominal CJ speed is 2088 m/s. . . . .	147
19	Detonation CJ wave speeds computed as a function of composition for $T_o = 300.15$ K and $P_o = 101.352$ kPa. . . . .	147
20	Detonation peak pressure rise for SS1 tests 53-56 with E3 ignition. The nominal CJ pressure rise is 2.51 MPa and the reflected CJ pressure rise is 6.4 MPa. . . . .	148
21	Detonation peak pressure rise for SS1 tests 57-61 with E1 ignition. The nominal CJ pressure rise is 2.51 MPa and the reflected CJ pressure rise is 6.4 MPa. . . . .	149
22	SS1 peak strains ( $\mu$ strain) and standard deviations for each gage, averaged over tests with the same ignition location. . . . .	152
23	Properties of CJ detonation in standard (0.3/0.7) H <sub>2</sub> -N <sub>2</sub> O mixture as computed with the Shock and Detonation Toolbox Browne et al. (2004). for nominal initial conditions of the present tests. . . . .	176

24	2-in Schedule 40 Stainless Steel pipe, nominal properties. . . . .	177
25	2-in Schedule 40 Stainless Steel pipe elastic properties. . . . .	177
26	Calibration constants for support beams . . . . .	212
27	ES1 gage locations for tests 1-14. . . . .	227
28	ES1 gage locations for tests 15-21. . . . .	229
29	ES1 gage locations for tests 22-23. . . . .	231
30	ES1 gage locations for test 24. . . . .	232
31	ES1 gages for shots 25-28. Except for the accelerometers, locations are also valid for shots 26 and 27. In shot 28, U2 was moved to the force link location. . . . .	236
32	ES1 gage locations for shots 32-33. Cantilever U3 was mounted in the force link at the bottom of the east flange. Gage D4 was Keyence measurement of out-of-plane motion of the bend. . . . .	237
33	ES1 gage locations for shots 34-35. Cantilevers U3 and U4 mounted in same locations as U2 and U1 in tests 26 and 27. . . . .	238
34	TS1 sensor location. . . . .	302
35	SS1 tests 53-56, location of gages and key features as a distance from the ignition source at E3. . . . .	364
36	SS1 tests 57-61, location of gages and key features as a distance from the ignition source at E1. . . . .	365

# 1 Introduction

This report documents experimental testing carried out at the Explosion Dynamics Laboratory, California Institute of Technology from November 2007 to April 2009. These tests address a number of open issues that have been identified by the Hydrogen in Pipes and Ancillary Vessels (HPAV) Program now in progress for the Waste Treatment Plant (WTP) under construction at the Hanford site. The HPAV program is analyzing potential explosion hazards that may arise due to the accumulation of gases containing hydrogen and oxidizers, such as oxygen or nitrous oxide.

The purpose of these tests is to provide basic data on structural response of a piping system representative of those used at the WTP. The data can be used to improve models of junction forces in bends and tees, validation of finite-element models of piping system dynamics, and the evaluation of fluid-structure interaction in piping systems partially filled with water.

The test program is designed to address the following issues:

1. Validation of structural response modeling of piping systems. EDL will provide test data that can be used to validate models for forces and structural response predictions by Finite Element Models (FEM) and Bechtels structural response code ME101. This will include measurement of structural response of segments containing elbow, tee and closed- end elements. Structural response would include forces on the supports, pressure in the pipes, and hoop and longitudinal strain at selected locations in the pipes. The combustion modes would be both prompt detonation and deflagration.

Some key validation questions for ME101 include:

- (a) Can simple asymmetry factors and point loads be used to model the internal loads created by propagating detonations and Deflagration-to- Detonation Transition (DDT) events?
  - (b) . Can hoop oscillations and beam bending oscillations be decoupled for the purpose of structural response simulations? Estimates of the vibration modes for typical WTP piping indicates that the principal beam bending modes have frequencies on the order of 10 Hz while hoop oscillations have frequencies of 20 kHz. For reasonable damping rates, this suggests that the hoop oscillations may be ignored at time scales long compared to the hoop period and short compared to the beam bending period. However, test data obtained at Caltech with simple piping systems containing tees and bends indicates significant overlap between hoop and bending mode stresses for short sections of tubing.
  - (c) Can structural response due to detonations in a complex piping system be adequately predicted using ME101 and simple rules for applying equivalent point loads to simulate detonation internal loads?
2. Evaluation of hazards that are difficult to model or estimate. EDL will provide fundamental test data on peak forces and strains for high-speed deflagrations and transition from deflagration-to-detonation. We will examine the effect of run-up distance on

structural response due to DDT near closed ends, tees, and bends. Previous work on detonation propagation through these elements would be extended to use much longer pipes and less sensitive mixtures to address the issue of how structural response scales with run up length. Two key issues are:

- (a) How do the pressure profiles and strain response scale with detonation propagation distance and DDT location?
  - (b) Will high-speed deflagrations (200-1000 m/s) excite resonant responses in the piping system? If the sequence of forces created by the combustion wave propagating through the bends and tees has temporal intervals comparable to the beam bending periods, a resonant response with high strain amplitudes may be excited. This is predicted by preliminary computations (DEI Calculation C-6908-00-30) but the modeling of highspeed deflagration pressure loading has not been validated.
3. Evaluate fluid-structure interactions. EDL will provide fundamental data on the propagation of shock waves in tubes partially filled with liquid and liquid-solid suspensions. We will test the interaction of a detonation wave with a liquid-filled section or a liquid-solid suspension filled section. The propagation of stress waves in the pipe and liquid would be tracked using pressure and strain gages. Key issues include:
- (a) What is the magnitude of the stress waves created when a detonation reflects from a liquid filled section?
  - (b) What is the decay rate of stress waves produced in the liquid?

## 1.1 Testing Summary

The test series were divided into three sets corresponding to the three main configurations of testing.

1. ES1 These tests were carried out with single welded piping segment containing one 90-degree bend with a radius of approximately 3 pipe diameters (3D). The piping system was in one plane and attached to the North wall of the facility. A total of 35 tests were carried out to examine structural response due to detonations, deflagration-to-detonation transitions, response of water filled section, measurement of cantilever support forces. Many of the tests were carried out with anchored ends to isolate the piping system from the reaction forces created by the detonation initiation and reflection. Selected tests were carried out with unsupported ends and cantilever beams with U-bolts.
2. TS1 These tests were carried out on a single welded piping segment containing a 90-degree tee junction. The piping system was in one plane and attached to the South wall of the facility. A total of 16 tests were carried out with detonations initiated in the branch or the run of the tee. A combination of cantilever and fixed end conditions was used. The cantilevers were clamped to the piping with U-bolts in selected tests.

3. SS1 These tests were carried out with a combination of five segments of welded construction that were fastened with bolted flanges (no gaskets) to make a serpentine piping system that covered the North, West, and South walls. The system incorporated the two specimens used for TS1 and ES1 with three additional specimens fabricated to create the three-dimensional system which incorporated a combination of three fixed ends, ten bends, and seven cantilever supports. Although all of the bends were of the same 90-degree 3D construction, three of the bends connected piping segments in the out-of-plane direction at the corners of the room. The cantilevers were attached to the piping with U-bolts but teflon slipper pads were used and a small clearance gap was left so that the pipe could move in the axial direction. A total of 10 tests were performed with two different ignition locations.

The piping segments were instrumented with piezoelectric pressure transducers, bonded strain gages, and accelerometers with signals recorded by a high-speed (1 MHz) data acquisition system.

## 1.2 Online Information and Companion Reports

The present report is a summary only of the testing activities. This report documents the test facility, test procedures, test specimens, test configurations, and summarizes the data obtained from each series of tests. Data plots for each test, detailed engineering design information for the specimens, and facility specifications are given in the Appendices.

Extensive additional documentation and the actual data files can be accessed at the Caltech HPAV web site <http://www.galcit.caltech.edu/EDL/data-hanford/>. Access to the website is currently restricted, please contact [Joe Shepherd](#) for information about using the online data archive.

A review of the general issues for structural loading due to detonation in piping is given in [Shepherd \(2009\)](#). Detailed analysis of data from selected ES1 tests and theoretical models of forces created by detonations propagating in bends is presented in a companion report by [Shepherd and Akbar \(2009\)](#). The data from tests carried out with water-filled segments of ES1 is analyzed and results compared to numerical simulations in [Shepherd et al. \(2009\)](#).

Extensive comparisons of selected data from all three test series to finite-element simulations and development of models for junction forces (bend and tee response) has been carried out by Dominion Engineering Inc and Bechtel National Inc. These results are documented in the following reports.

- a. [Ligon \(2009a\)](#) ES1 bend asymmetry factor analysis. DEI Calculation No. C-6916-00-02.
- b. [DEI \(2009\)](#) Gas-Liquid Reflected Detonation Structural System Response
- c. [Ligon \(2009c\)](#) TS1 Tee Asymmetry Factor Analysis.
- d. [Ligon \(2009e\)](#) SS1 System Response Analysis.

## 2 Test Facility

The test facility consist of a fixed structure, piping supports, piping, instrumentation, gas filling and mixing system, ignition system, and a data acquisition system. The basic facility, safety features and control system have been used in a number of previous test programs, for example [Liang and Shepherd \(2007\)](#), [Shepherd et al. \(2008\)](#), [Liang et al. \(2008\)](#).

The reinforced walls of the blast chamber room of room 19 Guggenheim are used to mount the piping system and instrumentation. Room 19 (Fig. 1) has existing instrumentation, gas supply, vacuum, and a safety interlock system. The longest straight pipe segments possible in room 19 are 13 ft horizontal and 7 ft vertical. A serpentine piping system of total length up to 70 ft can be readily accommodated within the lab.



Figure 1: Control room portion of room 19 showing data acquisition system in rack panel and control system on the wall.

### 2.1 Support system anchoring.

In order to get reliable data, the piping supports are anchored to steel plates on the walls of Room 19, Fig 2. The walls of Room 19 are steel-reinforced concrete masonry units constructed to TM 5-1300 (Structures to Resist the Effects of Accidental Explosions) or the steel-reinforced poured-concrete outer support walls of the building. Holes for the mounting plates (18 x 18 in x 1.5 in steel) were laid out and drilled in the concrete using a precision template. There are a total of 33 plates, each fastened with four Hilti HIT-TZ 3/4-in anchor rods that are bonded into the concrete using Hilti HY 150 MAX epoxy. The concrete behind

the plates was cleaned with a needle scaler so that the plates can be bonded with epoxy to the concrete.



Figure 2: a) mounting plate b) south wall c) north wall d) west wall.

The 33 anchor plates were cleaned, shimmed and given final alignment using piano wire and a laser transit. Alignment of the plates is to within 1/16 in or better in the vertical and horizontal plane. The nuts were tightened to 40 ft-lb torque prior to epoxy filling. The edges of the plates were sealed to the walls with tape and quick-set epoxy. Filling ports were attached to the sides and the space between the plates and the concrete walls were filled with Simpson ETI-LV crack repair injection epoxy. The epoxy was cured for 2 weeks before use. A final preload corresponding to 70 ft-lbs of torque was applied to each bolt to provide adequate stiffness and connection to the wall. The nominal room configuration, engineering drawings of the plates, and the layout of the plates on the walls are given in Appendix C.

## 2.2 Piping specimens

The piping specimens were constructed of 304/304L, (2" nominal ID Schedule 40 seamless stainless steel ASTM 312 pipe with 300-lb class slip-on flanges that were machined for O-ring grooves. The nominal properties and dimensions of the piping specimen are given in Appendix B.

The instrumentation mounts (Fig. 3) for the piping specimens are bosses welded to the tubes and machined to accept a SAE J1926 straight-thread O-ring seal plug (9/16-18). The plugs were commodity items (Swagelok) that were machined to mount the the pressure transducers, thermocouple probes, and attachment points for the Shchelkin spiral. Swagelok SilverGoop thread lubricant was used to prevent the plugs from seizing up in the adapter fittings. Blank plugs were installed if gages were not used at that location. Engineering drawings of the piping specimens and details on the components are given in Appendices E, K, and N.

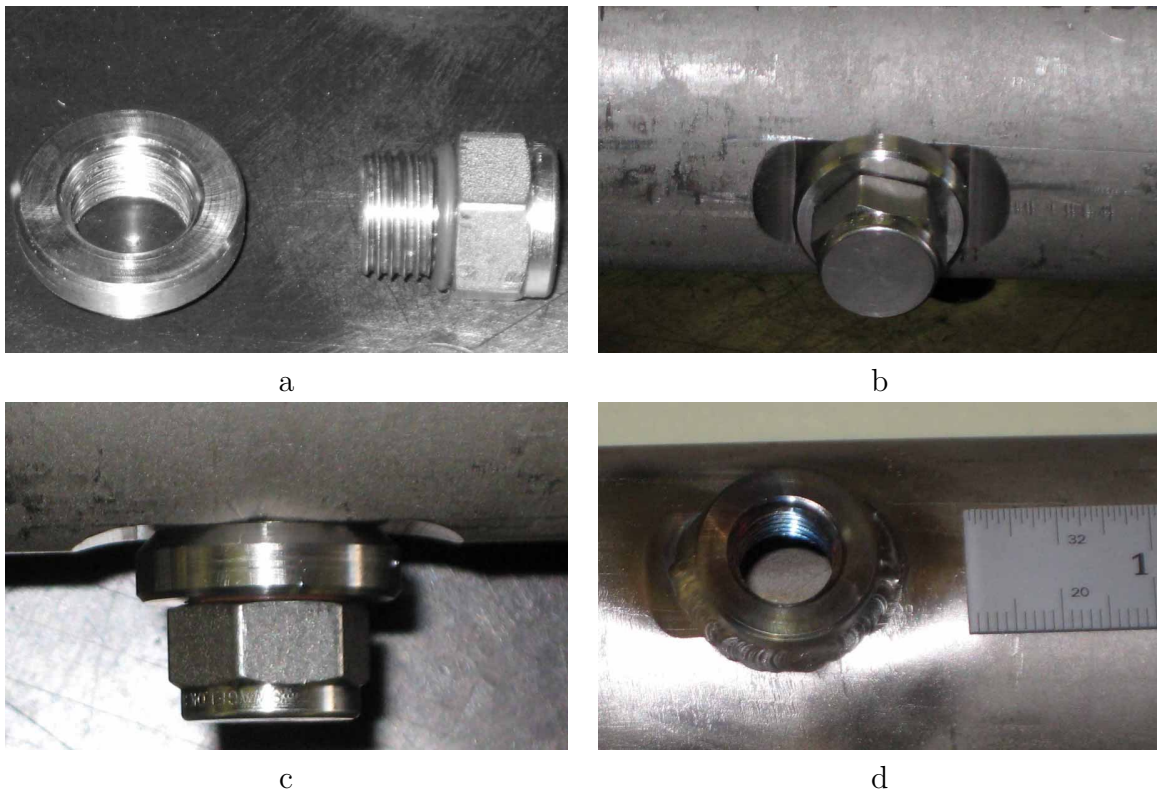


Figure 3: a) SAE J1926 9/16-18 fitting (the fitting is 0.82 in long) and adapter. b, c) located on pipe. d) adapter after welding to pipe.

The piping was welded (Fig. 4) per ASME B31.3 process piping standard using the AWS Standard Welding Procedure AWS B2.1-8-212.2001 and documented per ASME BPV Code Section IX, Article 4 Standard Welding Procedure Specifications. Mike Evarts of DOE confirmed that this is acceptable (His e-mail of March 26, 2008) for satisfying the requirements of AMSE BPVC Section IX as long the implementation conditions of Article V of Section IX are followed. The welds were visually inspected and copies of all documentation related to certification and inspection were provided to Caltech. The piping was pneumatically pressure tested and also vacuum leak checked after delivery to Caltech.



Figure 4: Slip-on flange welds for ES1.

### 2.3 Cantilever Beam Supports

The pipe supports consists of a steel cantilever with a U-bolt attachment to the pipe or tube to simulate actual supports used in the waste treatment plant. The cantilevers were (except for U2 which had the base welded to the lever) machined from a single piece of mild steel. The lever arm was 1.25 in high, 1 in wide and the distance from the bottom of the base to the centerline of the pipe was 5.5 in. The base was 1 in thick and  $4 \times 4$  in with 4 slots made oversize to attach the supports to the mounting plates with 1/2-20 cap screws. In some cases, the cantilevers were instrumented with strain gages in order to measure reaction forces. Calibration data and analysis of force measurement with the cantilevers is discussed in [Shepherd and Akbar \(2009\)](#). The engineering drawings of the cantilevers and U-bolts are given in Appendix G.

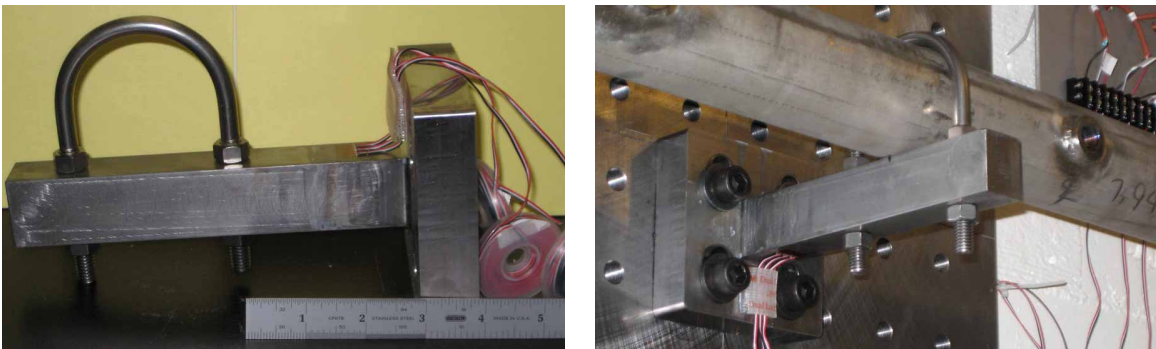


Figure 5: Cantilever support U1 with a single 3-gage strain rosette and typical attachment to the piping specimen with a 3/8 u-bolt.

## 2.4 Fixed End Brackets

For simulating vessel nozzles or rigid attachment points, the slip-on flange welded to the end of the pipe specimen was bolted to an adapter and a reinforced bracket that was bolted to the wall mounting plates. The bracket (see Appendix H for engineering drawings and Fig. 6) was fabricated from 1-in steel plate with angle reinforcements and bolted construction to minimize the compliance. The static deflection of these brackets is discussed in [Shepherd and Akbar \(2009\)](#).

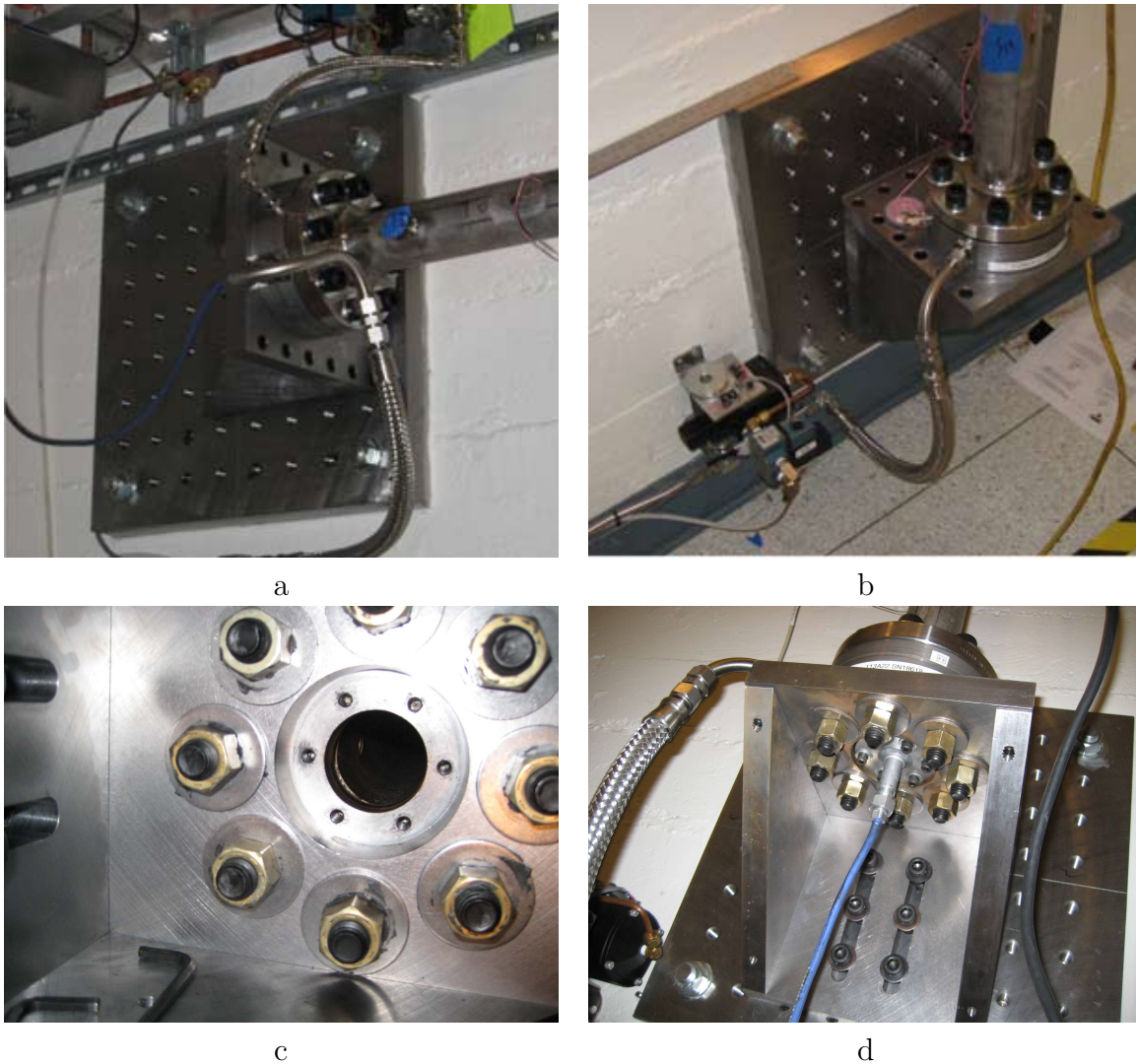


Figure 6: Gas handling flanges and fixed end brackets. a) ES1 Upper flange plumbing b) ES1 lower flange plumbing c) Mounting holes for nylon insert d) Spark plug mounted and connected

## 2.5 Initial gas conditions

We used room temperature (usually between 26 and 27°C) mixtures of hydrogen and nitrous oxide prepared by the method of partial pressures after evacuating the piping system. The total pressure was as close to 760 Torr ( $\pm 1$  Torr) as possible in all cases. The gas was mixed by circulating the mixture through the piping with a bellows pump and then isolating the piping system, allowing sufficient time before ignition so that the gas is stationary. Except for selected experiments on transition to detonation, the testing was carried out with 30% H<sub>2</sub> and 70% N<sub>2</sub>O. Computed detonation and reflected shock properties are given in Appendix A. For the nominal initial conditions in these tests, the detonation velocity is 2088 m/s, the CJ pressure is 2.62 MPa, the reflected shock pressure is 6.50 MPa, and the detonation cell width is approximately 3.3 mm (Akbar et al., 1997).

## 2.6 Ignition System

The ignition system is short-duration ( $< 10 \mu\text{s}$ ) spark discharge across a modified aircraft spark plug (Champion Model REJ38). The "J" electrode was removed so that the discharge was over a distance of about 5 mm. The spark plug is mounted in a nylon plug (to reduce electrical interference) using a brass insert with O-ring and RTV sealant. This nylon insert has a gland seal and is bolted to the plumbing flange adapter with 1/4-20 cap screws and an aluminum backing ring. See Appendix H for engineering drawings and photographs. The spark plug had to be periodically cleaned with grit blasting due to a build-up of combustion products from H<sub>2</sub>-N<sub>2</sub>O mixtures, Fig. 7.

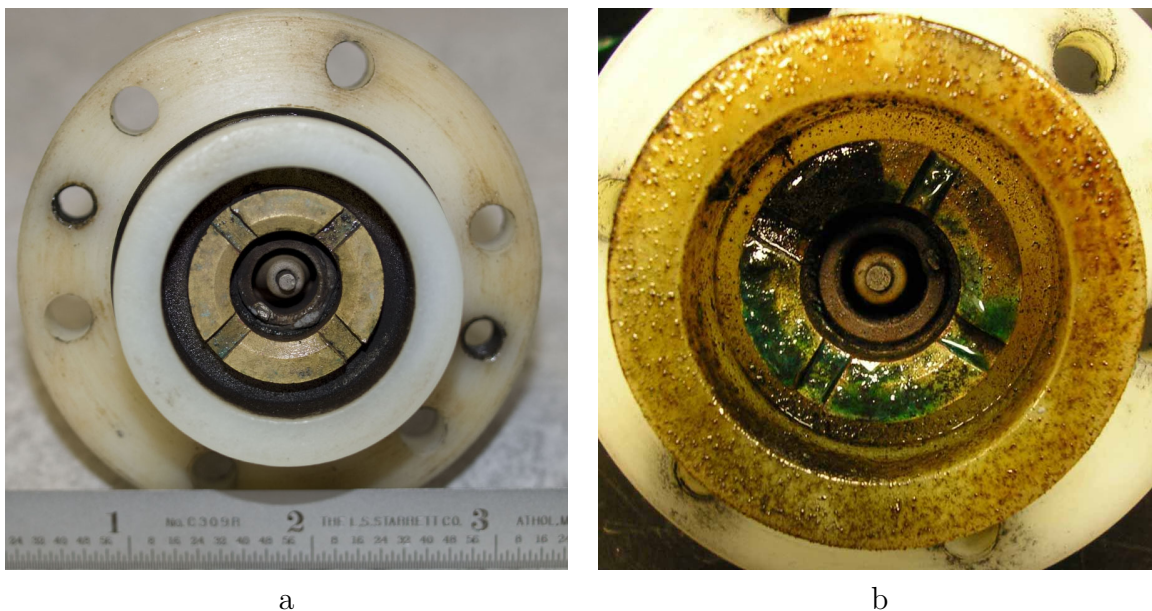


Figure 7: Spark plug electrodes showing a) clean and b) contaminated conditions.

The spark initiates a flame and a Shchelkin spiral (Fig. 8) was used just downstream of the spark plug to generate turbulence and promote transition to detonation. The spiral

consisted of a 12-in length of commercial spring (see Appendix E). The spring is held fixed inside the tube by a mounting pin that passes through the opening created in the spring by heating and deforming the coils. The pin fits into blind holes in the two SAE J1926 plugs that screw into a pair of diametrically located ports on the tube.



Figure 8: Shchelkin spiral and mounting pins.

The spark discharge is generated by using a custom circuit (Fig. 9) to charge a capacitor which is then discharged through a Perkin-Elmer (formerly EG&G) TR-2012 step-up transformer (163:1 secondary:primary ratio) to create the high voltage pulse. The energy stored in the capacitor is on the order of 350 mJ so that the spark discharge energy is much higher than ignition limits for all but the most insensitive mixtures. This ensures prompt ignition even at low pressure and minimizes the chances of misfires.

A number of safety features are incorporated into the discharge circuit to prevent accidental ignition. High voltage cannot be discharged from the capacitor until a sequence of three events has occurred. First, AC power must be applied from the control system by the operator. Second, the capacitor must be charged by applying an arming signal. Third, the capacitor must be discharged by applying a firing signal. The AC power, arming, and firing functions are interlocked to the valve control system, gas leak detectors, room ventilation, and door to the experimental area. In addition to these engineering safety features, a checklist is used to carry out and document the steps in the test procedure (see Appendix D). Arming and firing signals are transmitted through opto-isolators to prevent ground loops.

## 2.7 Gas Fill System

A gas-fill system previously installed in the room was used to precisely control the mixtures that were put into the apparatus. It consisted of a combination of hand and electro-pneumatic valves to control the flow of pressurized gases from storage bottles to the apparatus. The electro-pneumatic valves were operated by a set of switches and relays on the control panel. The valves inside the test area have position sensors that can be read on the control panel.



which provides the necessary bridge balancing, amplification and filtering (the wideband setting was used during all experiments). The signal conditioners have front panel controls for balance, gain, bandwidth, excitation and indicator lights. Cabling or gage faults cause the warning light indicators to illuminate. General purpose strain gages design for mild steel were used because having thermally-matched response was not critical in these dynamic tests. The gages were bonded to the specimen tube using the materials and procedures recommended by the manufacturer.

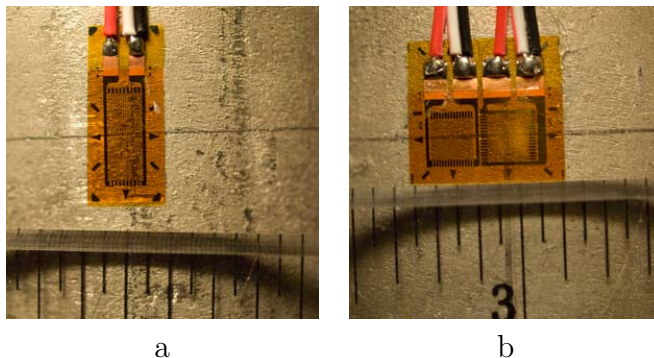


Figure 10: Strain gages mounted onto a piping section. a) Single gage Vishay model CEA-06-250UN-350. b) Tee rosette, Vishay model CEA-06-125UT-350.

There are a number of issues with using strain gages to make measurements in dynamic loading situations; these are discussed at some length in [Shepherd et al. \(2008\)](#). In that study, it was concluded that if sufficient care is taken, that the strain gages can provide useful results for detonation loading. A comparison of strain gages with an optical interferometer demonstrated reasonable agreement but a number of artifacts were observed in strain gage signals under certain conditions.

### 3.2 Pressure

Two types of pressure measurements were made:

1. Static These were made in order to prepare the test mixture using the method of partial pressures. We used a high-accuracy capacitance manometer manufactured by MKS Instruments Inc., Model 121AA (gage P-3 in the schematics in the next sections) with a full scale of 1000 Torr. This gage is accurate to 0.5% of full scale. Vessel evacuation was verified by a thermocouple gage (gage P-2) with typical final evacuation pressures less than 50 milliTorr.
2. Dynamic. Transient pressures were measured by piezoelectric pressure sensors that are designed for high-frequency response and shock waves measurement. We used PCB113A models manufactured by Piezotronics. All of these gages had an identical body and external dimensions and were installed in an identical fashion according to manufacturer's specifications (torque). The five different types of gages had essentially three different performance characteristics as summarized in Table 1. No significant

differences were noticed between the pressure histories recorded for the various sensors, even though the last gage has very different characteristics. The signals pass through a signal conditioning unit (PCB 481) and are digitized by the high-speed data acquisition system. The gages are calibrated and certified by the factory. We added a thin ( $< 1$  mm) layer of silicon rubber (Dow Corning RTV 3145, gray) to the front surface of the gages to reduce the thermal response and protect the sensitive elements from the acidic combustion products. The gages were periodically inspected, RTV coatings replaced when degraded, and the in some cases, the gages were exchanged if cracking of the diaphragms or degraded signals were observed.

Table 1: Piezoelectric pressure sensor specifications. S in the gage type number indicates a stainless steel diaphragm which was used after gages with carbon steel diaphragms were ruined in earlier testing due to acid corrosion.

PCB Model	sensitivity (mv/psi)	Rise Time ( $\mu$ s)	Range (kpsi)	Useful overrange (kpsi)	Non-linearity (% full scale)	Resonant frequency (kHz)
113A24	5	$\leq 1.0$	1	2	$\leq 1$	$\geq 500$
113A22	1	$\leq 1.0$	5	10	$\leq 1$	$\geq 500$
S113B24	5	$\leq 1.0$	1	2	$\leq 1$	$\geq 500$
S113B22	1	$\leq 1.0$	5	10	$\leq 1$	$\geq 500$
S111A24	5	$\leq 1.5$	1	2	$\leq 2$	$\geq 400$

### 3.3 Temperature

Gas temperature was measured using a thermocouple (K-type) gage (Fig. 12) and digital readout display (OMEGA). The readout was calibrated using a NIST-traceable standard voltage source. The bead on the thermocouple was too large to respond during the combustion transient but was sufficient to obtain initial conditions and observe the cooling of the combustion products.

### 3.4 Displacement

Motion of the specimens relative to the test cell walls was monitored by laser-imaging displacement sensors. These image a laser spot or line and infer displacement normal to the laser beam producing the spot, from changes in image and simple triangulation. The three different gages used and their relevant parameters are noted in the table below. The higher frequency gage was a Keyence unit, which had a longer beam path. This was folded in order to use it at the T position on specimen TS1. The nominal calibration of the gages was verified against a precision height gage.

The Micro-Epsilon signals were susceptible to ambient noise and were low-pass pre-filtered (pre-filtering meaning prior to digitization) to alleviate this. The module used for this was a

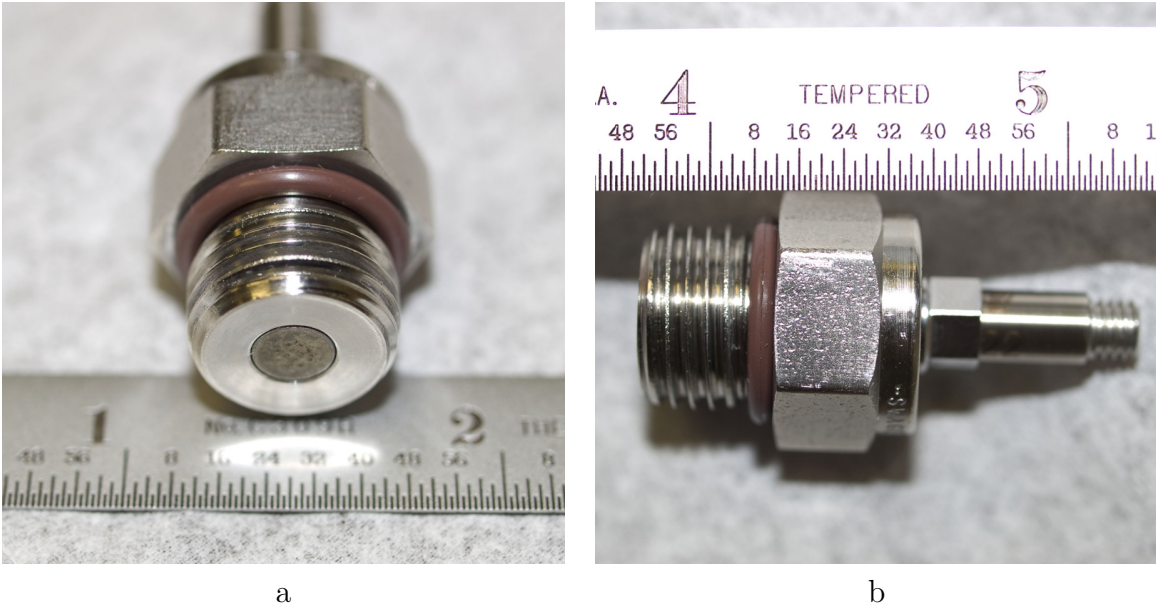


Figure 11: PCB pressure gage mounted in SAE fitting. Gage front has not been coated with RTV yet.

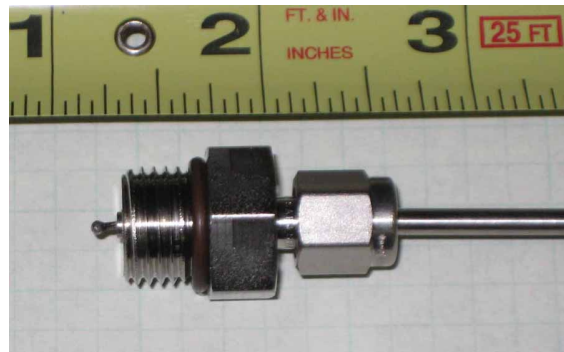


Figure 12: Thermocouple junction with exposed bead mounted in SAE fitting.

Table 2: Displacement gage specifications.

	Micro-Epsilon 1300	Micro-Epsilon 1402	Keyence LKG-407
Frequency Response (Hz)	500	1000	50,000
Range (mm)	±25	± 25 mm	± 100 mm
Resolution ( $\mu\text{m}$ )	25	25	2
Zero origin (mm)	70	70	400

Krohn-Hite 3380 Tunable Active Filter with a 48 db/Octave roll-off. All three Micro-Epsilon modules were low-pass filtered at 250 Hz and AC coupled.

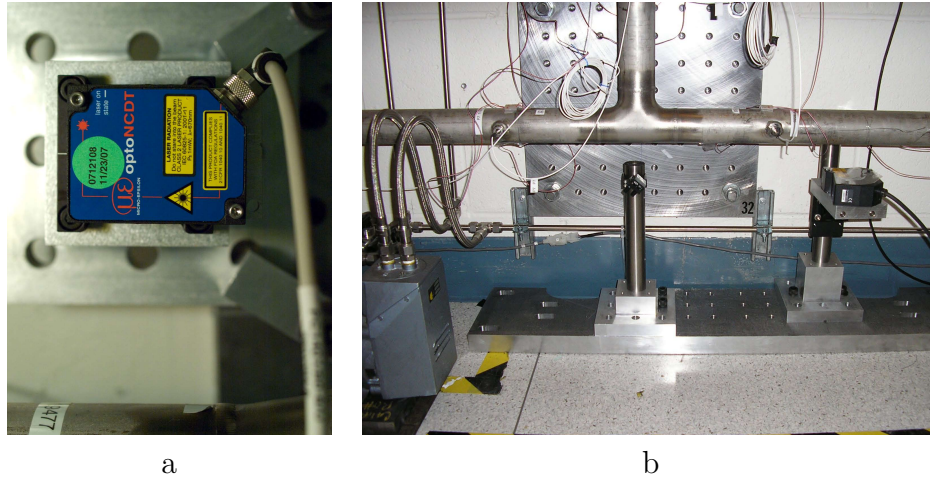


Figure 13: Displacement gages installations. a) Micro-Epsilon 1401 located at position D3. b) Keyence LKG-407 located at position D4. A mirror is used to rotate the beam path by 90° to measure vertical motion.

### 3.5 Acceleration and forces

Piezoelectric accelerometers were used on selected components (Fig. 14a) and locations. PCB model 352A21 piezoelectric transducers with a full scale range of  $\pm 500$  g ( $\pm 4900$  m · s<sup>-1</sup>) and a frequency response of 1 to 10<sup>4</sup> Hz were mounted on selected components using "Petro" wax supplied by PCB Piezotronics. Forces were not directly measured but the support cantilevers (Table 3 and Appendix G) were instrumented in order to infer forces. Different configurations (Fig. 14b-d) of strain gages were used on the beams depending on the test series.

Beams U1 and U2 were made as part of the initial phase of the project and discontinued after Shot 28. The half-bridge configuration and the calibration of the beam is described in Appendix C of Shepherd and Akbar (2009). The pair A-B refers to the cantilever bending strain perpendicular to the axis of the pipe while C-D refers to the cantilever bending in the direction of the pipe axis. The half-bridge configuration was wired to cancel the component of strain along the axis of the cantilevers perpendicular to the mounting plate; this was used in the ES1 and TS1 testing. For the SS1 tests (52-61), the gages were recorded individually so that both the bending and axial strain in the cantilevers could be obtained by the difference and sum of the signals.

### 3.6 Data Acquisition System

In order to have sufficient capacity to simultaneously record all instruments for the largest piping system, a 96-channel data acquisition system was used to record the high-speed data.

Table 3: Cantilever beam instrumentation.

Beam	Strain gage	Testing usage	Notes
U1	Single 3-gage rosette CEA-06-125UR-350/P2	24-28	Prototype
U2	Single 3-gage rosette CEA-06-125UR-350/P2	24-28	Lever welded to base
U3	Four single gages CEA-06-250UN-350/P2	29-35, 36-45	Half-bridge pairs A-B, C-D
U4	Four single gages CEA-06-250UN-350/P2	29-35, 36-45	Half-bridge pairs A-B, C-D
U3	Two single gages CEA-06-250UN-350/P2	52-61	A and B individually
U4	Two single gages CEA-06-250UN-350/P2	52-61	A and B individually

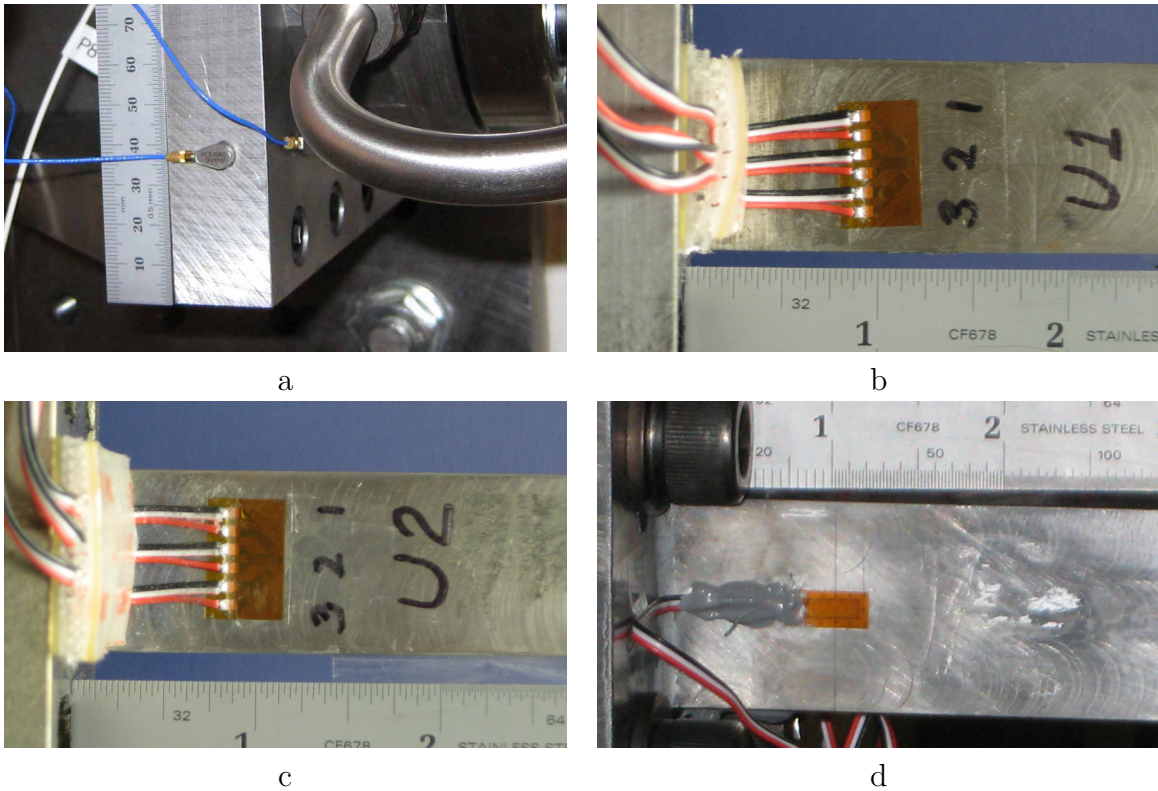


Figure 14: a) Accelerometer mounting for tests 22-23; b) 3-gage rosette mounted on U1; c) 3-gage rosette mounted on U2; d) single gage (one of four) mounted on U3.

The central component of the data acquisition system were a set of high-speed digitizer modules (National Instruments PXI-6133 card with 32Mbyte of on-board memory) used to record 0.5 seconds of data at a rate of  $1 \times 10^6$  samples per second. However the entire memory was not used because as the number of channels increases, the data acquisition program (see below) has trouble manipulating the records in its memory. The digitizers had a specified resolution of 14 bits.

A PXI-Bus chassis (National Instruments PXIe 1065) was used to house the digitizer cards and enabled them to be independently programmed by communicating with a dedi-

cated data acquisition computer (National Instruments 8353) running National Instruments Signal Express software. The computer was equipped with a fast Redundant Array of Independent Drives (RAID) storage system (HDD-8264). Each channel of the acquisition card was programmed with parameters such as sampling rate and voltage range and the triggering of the card were directly set in the menu-based software, without any communication commands or protocol. Each channel received signals from a signal conditioner, which was dependent on the type of gage (see figure below). The entire set of channels, across multiple cards, was triggered by a TTL signal sent out from the firing button to one channel input. This also, simultaneously triggered the spark-discharge that initiated combustion.

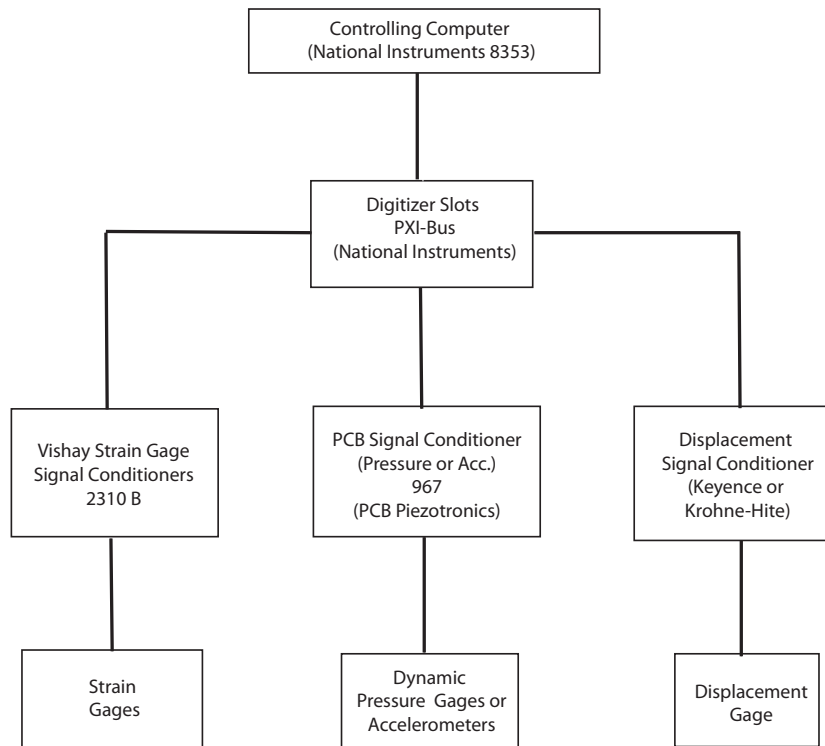


Figure 15: Schematic of the data acquisition system and sensors.

### 3.7 Quality Assurance

The test facility development and testing were all carried out under an approved quality assurance plan given in Appendix P. ANSI/ASQ Z1.13 was used as the QA standard in our research. The QA plan was accepted on March 19, 2008 after review by Bill Smoot of Project Assistance Corp (PAC) who determined that our implementation would also satisfy the requirements of ASME NQA-1 Subpart 4.2.

Certifications were obtained for all specimen materials, the construction of the specimens was carried out by professional machinists and certified welders, and the finished product was inspected by a trained inspector. For all critical measurements, the instruments and

gages used in this project were factory calibrated with standards traceable to the NIST or calibrated in our laboratory using certified precision test equipment. All certifications and procedures were documented according to the approved QA plan and are on file in the Explosion Dynamics Laboratory.

Surveillance of the Caltech QA program was carried out on June 16, 2008 by Bill Smoot of the Project Assistance Corporation (PAC), on January 26 and 27th, and again in April 2009 by Albert Hu and Greg Jones of the U.S. Department of Energy (DOE), Office of River Protection (ORP). There were no findings of deficiency during these visits and on the basis of our successful QA program, the DOE has directed that our data may be used in supporting development of methods and criteria by which HPAV is evaluated. The letter of authorization is reproduced at the end of Appendix P.

## 4 Test Procedures

A detailed checklist (see the example in Appendix D) was used for every combustion test. This serves as an administrative control for safety and provides a permanent record of the operations in each shot. The test procedure was carried out using the remote control system and engineering safety features that were designed into the original facility.

The basic test procedure was to evacuate the specimen and filling tubing, check for leaks, fill the tube using the method of partial pressures, mix the contents using a bellows pump, and then ignite the mixture using the spark plug. The data acquisition system was triggered from the same TTL signal as used to trigger the spark discharge. After the data was recorded and stored, the combustion products in the tube were removed and the tube evacuated to prepare for the next test. The data integrity and quality would be checked through plotting and engineering analysis. Replica tests of each condition were carried out in almost all cases in order to judge the repeatability of measurements.

### 4.1 Facility Evacuation

Each combustion test involves the preparation of mixtures by method of partial pressures which in turn requires that the facility and associated gas handling plumbing be adequately evacuated. This is done at the beginning and during filling operations, as well as after the test to evacuate the products. A Sargent-Welch vacuum pump (Type 1397), with typical pumping rates of 500 liter/min at 1 atm, was used. Referring to Fig. 16, the pump was used to evacuate a 3-in PVC vacuum line which was connected to the gas handling manifold by the main 1-in ball valve V5. For SS1 tests, a second 1-in ball valve (V12) was used to directly connect the test specimen to the vacuum line within the blast room. Typical pumping times varied due to humidity or moisture in the lines, but were of the order of a few hours after each shot. A maximum pressure of 40 mTorr on the thermocouple-type pressure gage (P2) was used reached before the tube was considered evacuated.

### 4.2 Gas Handling

The control panel pressure gages and valve controls are used to manually fill the test channel to the desired pressure with an accuracy of 0.1 kPa. The vacuum pump was used to evacuate the apparatus prior to filling and also the fill lines were evacuated when switching gases. The schematics of the plumbing systems used in the three tests were all slightly different and are shown in Fig. 16.

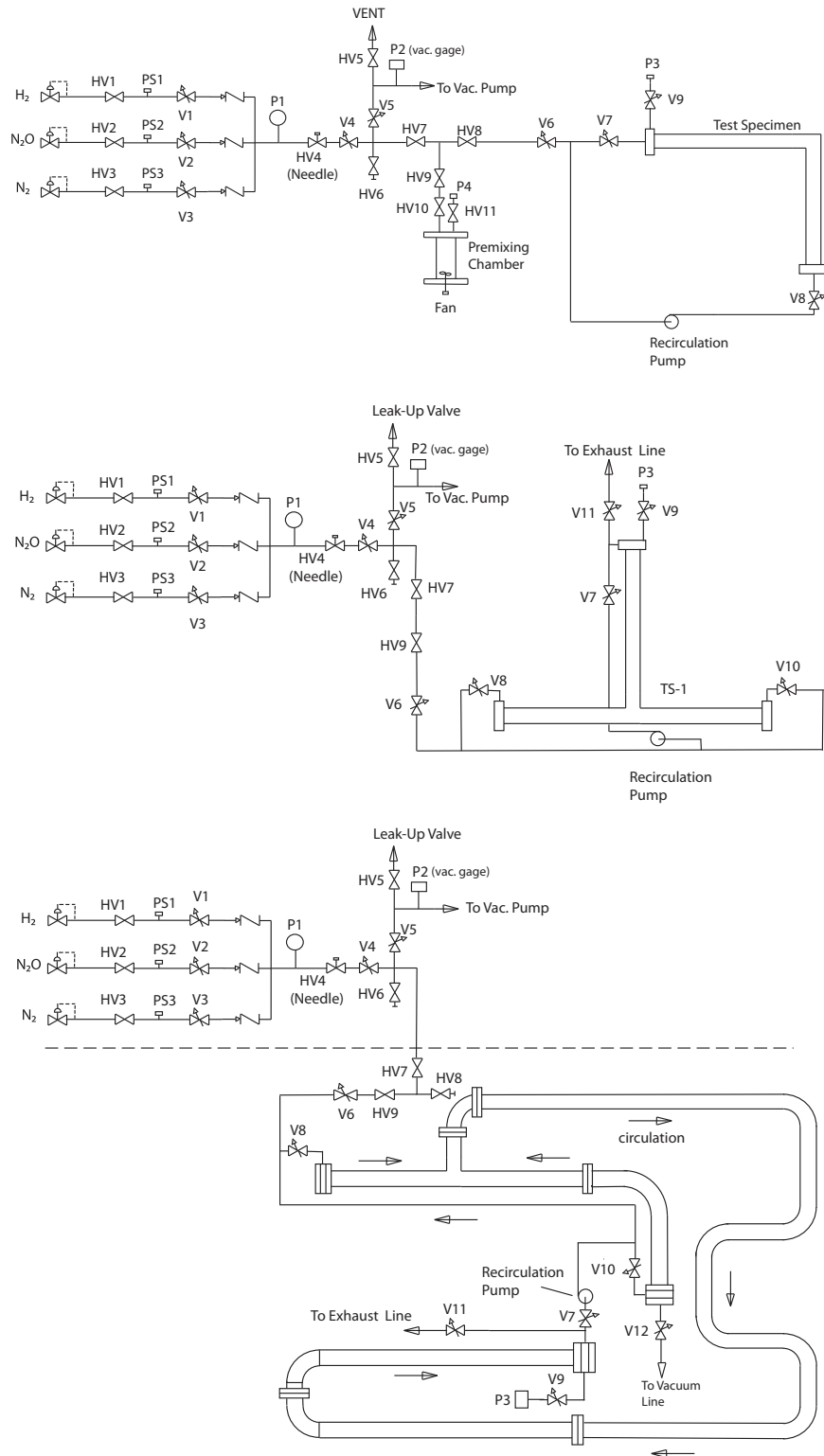


Figure 16: Plumbing schematics for the three versions (ES1, TS1, SS1 from top to bottom) of the facility.

### 4.3 Mixing Within the Facility

All three specimens used a bellows pump and recirculation to mix the gases once they had been added using the method of partial pressures. This was done with a metal bellows pump (MB-32) which is rated to provide about 50 liter/min flow at 1 atm. Typical durations for recirculating the mixture are given in the Table 4. Mixtures were circulated the equivalent of 15 specimen volumes.

Table 4: Approximate Facility volumes and time for which the recirculation pump is operated.

	Volume (liter)	Recirculation Duration (min)
ES1	12	5
TS1	10	5
SS1 (including ES1 and TS1)	50	15 to 20

No attempt was made to optimize the duration of mixing. Instead, we monitored the detonation speed and compared this to the computed Chapman-Jouguet speed. The deficit is the difference between the observed and computed values and is typically less than 1% if the mixture was adequately mixed, the detonation was initiated promptly, and the detonation cell width is much smaller than the tube diameter. These are all conditions needed for an ideal detonation.

### 4.4 Post Shot Purge and Cold-Trap Use

Shots performed at the beginning of the test program (ES1 and TS1 series) showed that the facility was susceptible to the exhaust products which were acidic. In particular, the acidic combustion products were degrading the vacuum pump oil and seals. Even with frequent flushing of the pump oil, the pumps failed after about 30 shots and had to be replaced or refurbished. In order to limit the exposure of the facility to these corrosive vapors, the facility was first purged with nitrogen (exhausted directly into the air vent duct) before evacuating through a liquid nitrogen trap. The liquid nitrogen trap removed most of the remaining moisture and acidic products.

### 4.5 Data Validation and Reduction

The recorded data were validated through the quality assurance procedures outlined in Appendix P. The instrumentation, procedures, data recording and analysis were all controlled under the quality assurance plan. Past experience and extensive replication studies discussed in [Liang et al. \(2008\)](#), [Shepherd et al. \(2008\)](#) were one basis for judging the quality of the data. Comparisons between replica tests and quantitative analysis of the signals (discussed below) formed another basis for judging the data quality. Finally, comparison with analytical

models (Shepherd and Akbar, 2009) and finite-element modeling Shepherd et al. (2009) was used to study the results of these tests and provided a close check on the reliable.

Pressure gage data for detonation testing can be used to compute time of arrival ( $x-t$ ) plots from which velocities can be obtained by least-squares or linear regression analysis. The inverse slope of the space-time regression line is the detonation speed, which can be compared with the ideal computed value. This is a sensitive test of the gas mixture and initiation system. For prompt initiation, the detonation velocity obtained from regression of the time of arrival plot is within 1% of the computed Chapman-Jouguet (CJ) detonation speed. The peak pressures can also be compared to the ideal pressures. Results for individual test series are given in subsequent sections on each configuration.

The ideal detonation properties of the standard gas mixture were computed by the Shock and Detonation ToolBox (Browne et al., 2004). The results for our nominal laboratory initial conditions of 100.325 kPa and 27°C are given in Table 23 of Appendix A. Variations in the initial conditions of pressure, temperature and composition will make cause changes in the ideal CJ parameters. To examine this, the computations were repeated using slightly different input parameters to construct a matrix of values (Table 5) that show the sensitivity of detonation velocity and pressure to these variations. Variations of temperature of 5°C and pressure of 1 kPa result in detonation velocity variations of less than 0.1% and pressure variations up to 2%. The largest variations will occur due to composition changes with a 1% variation in hydrogen fraction resulting in a 0.7% change in detonation velocity.

Table 5: Computed CJ velocity and pressure, reflected shock pressure as a function of initial conditions.

$X_{H_2}$	$P_o$ (kPa)	$T_o$ (K)	$U_{CJ}$ (m/s)	$P_{CJ}$ (MPa)	$P_R$ (MPa)
0.30	101.325	300.15	2087.9	2.621	6.503
0.30	101.325	295.15	2088.4	2.672	6.642
0.30	101.325	305.15	2087.4	2.578	6.389
0.30	100.000	300.15	2087.6	2.586	6.412
0.30	102.000	300.15	2088.1	2.639	6.544
0.29	101.325	300.15	2074.3	2.623	6.510
0.31	101.325	300.15	2101.6	2.621	6.503

Peak strain signals can be compared with the results of single-degree-of-freedom (SDOF) model estimates for hoop (axisymmetric radial vibrations) oscillations of the pipe. The basis of this is described in the monograph by Smith and Hetherington (1994) and specific application to the present situation is described by (Shepherd, 2009) and (Shepherd and Pintgen, 2007). The standard estimate for peak hoop strain is based on the static membrane estimate for the hoop stress

$$\sigma_{\theta,max} \approx \Delta P \frac{R}{h}, \quad (1)$$

where  $\Delta P$  is the characteristic peak applied pressure,  $R$  is the mid-radius of the pipe and  $h$  is the pipe thickness. The peak strain is computed by multiplying the corresponding static

strain by a dynamic load factor  $\Phi$  that is appropriate for the loading regime of interest

$$\epsilon_{\theta,max} \approx \Phi \frac{\Delta P R}{E h}, \quad (2)$$

where  $E$  is Young's modulus. For propagation detonations or shock waves above the critical wave speed  $V_{c0}$  in Appendix B (see also [Beltman and Shepherd \(2002\)](#)),  $\Phi \approx 2$ ; this value is also appropriate for suddenly applied loads [Shepherd and Pintgen \(2007\)](#) where the rise time is faster than oscillation period ( $34 \mu\text{s}$ ) of the hoop oscillation. Using the computed pressure ratios for various combustion modes (see Appendix A) and the pipe dimensions, we obtain the predicted values of peak strain given in Table 6.

Table 6: Peak strains ( $\Phi = 1$ ) in 2-in Schedule 40 pipe for various combustion modes in 1 atm 30/70  $\text{H}_2/\text{N}_2\text{O}$  mixtures.

Mode	$\Delta P$ (MPa)	$\epsilon_{\theta,max}$ ( $\mu\text{strain}$ )
Constant-volume (CV)	1.23	46
Chapman-Jouguet (CJ)	2.52	94
Reflected Chapman-Jouguet (CJ, R)	6.40	239

Based on these estimates, the peak strains that we would expect to observe would be 478  $\mu\text{strain}$  near the point of detonation reflection ( $\Phi = 2$ ). Larger peak values may be recorded if deflagration-to-detonation transition takes place near the measuring location.

## 5 ES1 Test Series

These tests were carried out with single welded piping specimen containing one 90-degree bend with a radius of approximately 3 pipe diameters (3D). The specimen consists of a straight horizontal section about 12-ft long, the 3D radius bend (it is actually about 7.6 in in radius to the centerline as shown in Fig. 119), and a straight vertical section about 6 ft high. The specimen was mounted at each end by stiff anchors to the plates that were described in Section 2. The layout of the specimen on the wall is shown in Fig. 17.

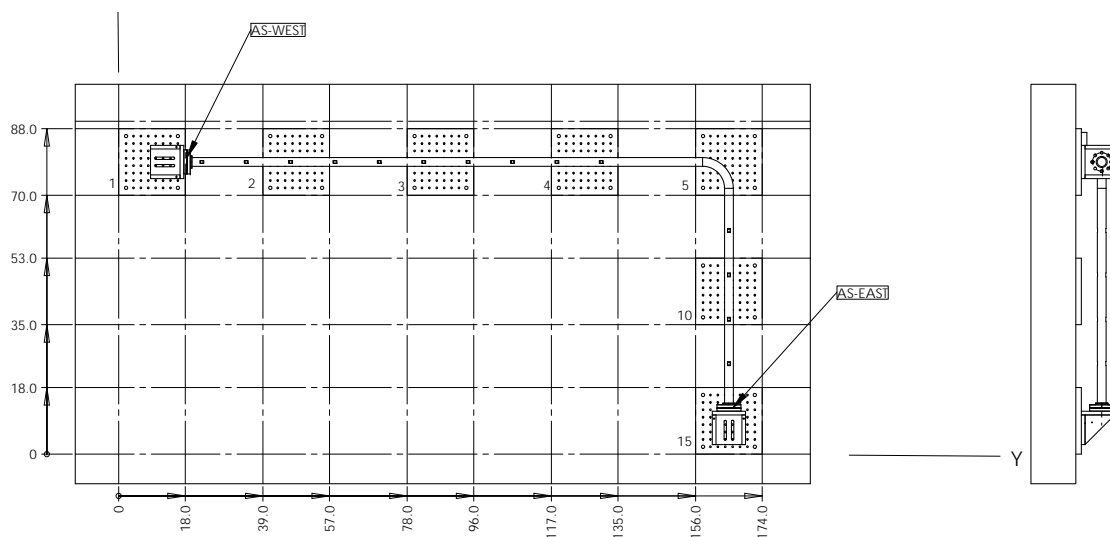


Figure 17: ES1 specimen layout showing mounting locations (both ends anchored) and wall plates.

Engineering drawings are given in Appendix E and an outline with key overall dimensions is shown in Fig. 18. The piping system was in one plane and attached to the North wall of the facility, details of the anchoring system are given in Appendix H. A total of 35 tests were carried out to examine structural response due to detonations, deflagration-to-detonation transitions, response of water filled section, measurement of cantilever support forces. Many of the tests were carried out with anchored ends to isolate the piping system from the reaction forces created by the detonation initiation and reflection. Selected tests as described in the next section were carried out with unsupported ends and cantilever beams with U-bolts. Data plots from each test are given in Appendix J.

Both ends of the specimen were attached to the anchor brackets. The tube is instrumented with 8 piezoelectric pressure transducers, 17 strain gages, and 2 accelerometers in some tests. Nominal sensor locations are shown in Fig. 19 and details for each series of shots are given in Appendix I. The first 10 ms data from the pressure and strain gages have been converted to engineering units and are available as ASCII files for download from the project web site. The data columns and units are identified within the files. The first column is time, the data were sampled at 1 microsecond intervals and the first 100 points were taken before the ignition event.

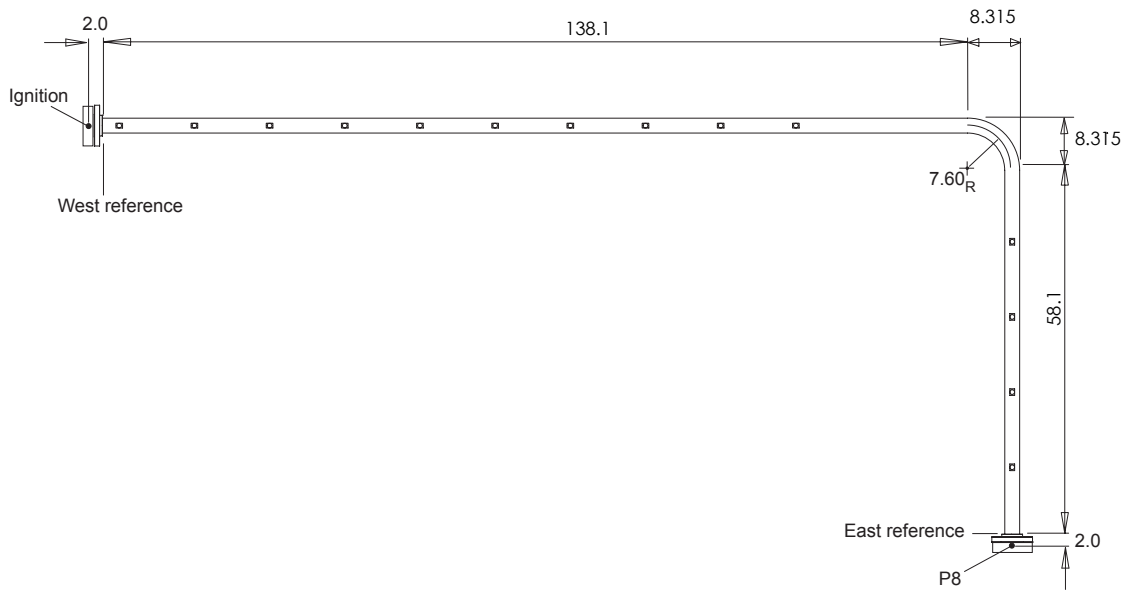


Figure 18: ES1 overall dimensions showing reference plane for instrument locations.

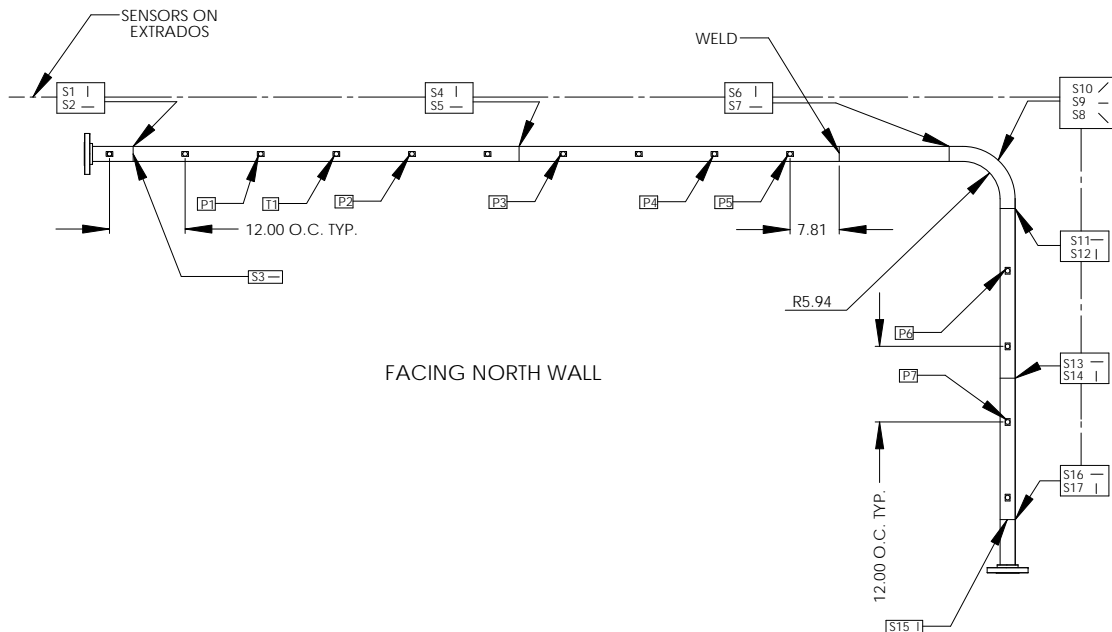


Figure 19: ES1 sensor layout for standard pressure and strain arrangement. Pressure sensors were moved in some tests, see App. N.

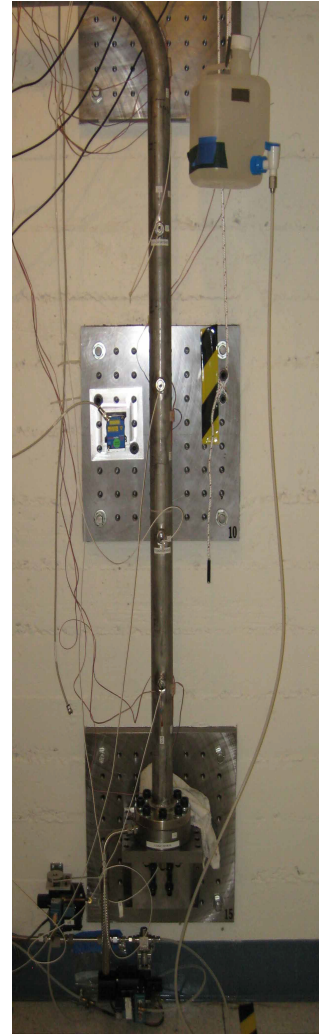
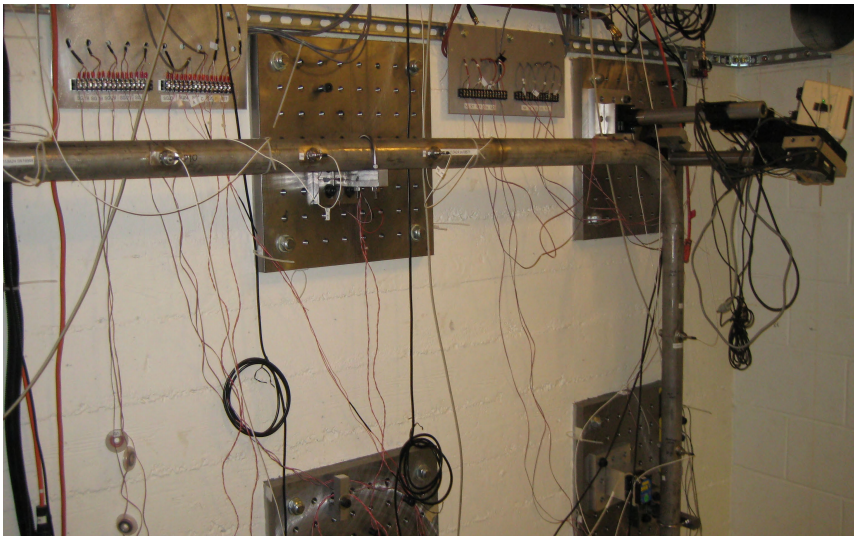


Figure 20: ES1 as installed for tests with both ends anchored.

## 5.1 Shot List

Table 7: List of shots and conditions carried out with ES1 specimen

Shot	$T_o$ (°C)	$P_o$ (kPa)	H <sub>2</sub>	N <sub>2</sub> O	$U_{CJ}$ (m/s)	$P_{CJ}$ (MPa)	Date& Time	Ignition Location	Spiral	Notes
1	27.0	101.325	0.3	0.7	2087.5	2.62	07172008_07:06_PM	West	None	DDT (P1-P2)
2	27.0	101.325	0.3	0.7	2087.5	2.62	07212008_11:00_AM	West	None	Replica of 1, DDT (P2-P3)
3	27.0	101.325	0.3	0.7	2087.5	2.62	07212008_04:30_PM	West	1 ft	Prompt
4	27.0	101.325	0.3	0.7	2087.5	2.62	07222008_02:50_PM	West	1 ft	Replica of 3, Prompt
5	27.0	101.325	0.3	0.7	2087.5	2.62	07222008_06:21_PM	West	2 ft	Prompt
6	27.0	101.325	0.3	0.7	2087.5	2.62	07232008_12:29_PM	West	2 ft	Replica of 5, Prompt
7	27.0	101.325	0.25	0.75	2021.1	2.61	08162008_03:33_PM	West	none	DDT (P2-P3)
8	27.0	101.325	0.2	0.8	1956.0	2.587	08162008_05:41_PM	West	none	DDT (P4-P5)
9	27.0	101.325	0.15	0.85	1891.9	2.56	08162008_08:00_PM	West	none	DDT (P7-P8)
10	27.0	101.325	0.1	0.9	1827.7	2.51	08162008_10:00_PM	West	none	flame only
11	26.0	101.325	0.25	0.75	2021.1	2.61	08272008_5:29_PM	West	none	Replica of 7, DDT (P2-P3)
12	27.0	101.325	0.2	0.8	1956.0	2.587	08282008_6:30_PM	West	none	Replica of 8, DDT (P3-P4)
13	27.0	101.325	0.15	0.85	1891.9	2.56	08292008_05:17_PM	West	none	Replica of 9, DDT (P5-P6)
14	27.0	101.325	0.1	0.9	1827.7	2.51	08302008_06:16_AM	West	2 ft	Replica of 10, flame only
15	25.6	101.325	0.3	0.7	2087.5	2.62	09052008_08:41_PM	West	1 ft	Prompt, 2250 cc water, added gages 9 and 10
16	26.9	101.325	0.3	0.7	2087.5	2.62	09082008_05:35_PM	West	1 ft	Replica of 16. Prompt deto- nation - 2250 cc water
17	26.0	101.325	0.3	0.7	2087.5	2.62	09072008_05:32_PM	West	1 ft	Prompt, 3750 cc water
18	27.1	101.3649967	0.3	0.7	2087.5	2.62	09262008_01:27_PM	West	1 ft	Replica of 17. Prompt, 3750 cc water

Table 8: List of shots and conditions carried out with ES1 specimen (continued)

Shot	$T_o$ (°C)	$P_o$ (kPa)	H <sub>2</sub>	N <sub>2</sub> O	$U_{CJ}$ (m/s)	$P_{CJ}$ (MPa)	Date& Time	Ignition Location	Spiral	Notes
19	26.9	101.3116678	0.17	0.83	1917.5	2.57	09292008_05:29_PM	West	None	DDT, 3750 cc water, 30 Mpa peak
20	25.2	101.3383322	0.15	0.85	1891.9	2.56	10012008_09:54_AM	West	None	Flame only, 3750 cc water
21	26.5	101.3916612	0.17	0.83	1917.5	2.57	10022008_12:45_PM	West	None	High speed flame (?), 3750 cc water
22	26.5	101.4049934	0.3	0.7	2087.5	2.62	10102008_03:03_PM	East	1 ft	Prompt, E to W
23	26.5	101.3916612	0.3	0.7	2087.5	2.62	10122008_08:30_PM	East	1 ft	Replica of 22, Prompt, E to W
24	26.8	101.2183421	0.3	0.7	2087.5	2.62	10152008_05:47_PM	East	1 ft	Replica of 22, Prompt, E to W
25	26.5	101.2316743	0.3	0.7	2087.5	2.62	10212008_01:07_PM	West	1 ft	Prompt, W to E, cantilever supports
26	26.9	101.2316743	0.3	0.7	2087.5	2.62	10212008_10:32_PM	West	1 ft	Prompt
27	26.1	101.2583388	0.3	0.7	2087.5	2.62	10242008_01:25_AM	West	1 ft	Prompt, replica of 26
28	26.6	101.2716711	0.3	0.7	2087.5	2.62	10242008_9:05_PM	West	1 ft	Prompt, force link at east end, removed E cantilever
29	24.9	101.3916612	0.3	0.7	2087.5	2.62	11162008_7:23_PM	West	1 ft	Prompt, removed W cantilever
30	25.0	101	0.3	0.7	2087.5	2.62	11172008_7:23_PM	West	1 ft	Replica of 29, lost data.
31	25.7	101.4316579	0.3	0.7	2087.5	2.62	11192008_6:44_PM	West	1 ft	Replica of 30, force link data invalid
32	26.1	101.3916612	0.3	0.7	2087.5	2.62	11212008_2:56_PM	West	1 ft	Replica of 31. force link data valid
33	25.2	101.2983355	0.3	0.7	2087.5	2.62	11242008_12:32_PM	West	1 ft	Replica of 32
34	26.6	101.2583388	0.3	0.7	2087.5	2.62	12062008_4:38_PM	West	1 ft	Removed force link, added cantilever supports
35	26.3	101.2450066	0.3	0.7	2087.5	2.62	12082008_6:08_PM	West	1 ft	Replica of 34

## 5.2 Detailed description

### 5.2.1 Shots 1-6

Shots 1-6 were carried out to determine the best mechanism for ignition. One key results was that the 1-ft spiral was determined to be adequate for direct initiation and was used for all tests other than the DDT shots. The other key results were a demonstration of the repeatability of the testing (through comparison of data from replicas) and obtaining baseline pressure and strain histories (Shot 3) for the standard configuration. Both ends of the tube were attached to plates with the stiff anchors for tests 1-24.

Shot 1 No spiral, spark plug only at the West end of the specimen. 30/70 H<sub>2</sub>/N<sub>2</sub>O mixture at 1 atm and 26°C nominal initial conditions. DDT occurred between P2 and P3, which is between 1.3 and 2 m from the ignition location.

Shot 2 Replica of shot 1. DDT occurred between P2 and P3, which is between 1.3 and 2 m from the ignition location.

Shot 3 1-ft spiral with spark plug at West end of the specimen. 30/70 H<sub>2</sub>/N<sub>2</sub>O mixture at 1 atm and 26°C nominal initial conditions. A near-CJ wave was produced by the time it reached P2, 1.3 m from the ignition point.

Shot 4 Replica of shot 3. Overlay plots of shot 3 and 4 showed that the test results were replicated in detail for both strain and pressure measurements.

Shot 5 2-ft spiral with spark plug at West end of the specimen. 30/70 H<sub>2</sub>/N<sub>2</sub>O mixture at 1 atm and 26°C nominal initial conditions. Very similar results to tests 3 and 4. No significant differences in the pressure or strain data were observed when using

Shot 6 Replica of shot 5. Overlay plots with shot 5 demonstrated excellent repeatability and overlay plots with shots 3 or 4 showed that there was no significant difference in the data with the longer spiral.

### 5.2.2 Shots 7-14

Shots 7-13 were DDT tests with no spiral and ignition at the west end of the specimen. Different amounts of hydrogen were used to vary the location of DDT. The specimen mounting and all instrument locations were the same as in shots 1-6. Shot 14 was carried out with the 2-ft spiral to see if this would cause DDT for 10% H<sub>2</sub> - it did not. The peak pressures and strains created by the DDT events were key data obtained from these tests.

Shot 7 25% H<sub>2</sub>. DDT occurred between transducers P2 and P3, which is between 1.3 and 2 m from the ignition location.

Shot 8 20% H<sub>2</sub>. DDT occurred between transducers P3 and P4, which is between 2 and 2.5 m from the ignition location.

Shot 9 15% H<sub>2</sub> DDT occurred between transducers P6 and P7, which is between 4.1 and 4.7 m from the ignition location.

Shot 10 10% H<sub>2</sub>. Flame only.

Shot 11 25% H<sub>2</sub>, replica of shot 7. DDT occurred between transducers P2 and P3, which is between 1.3 and 2 m from the ignition location.

Shot 12 20% H<sub>2</sub>, replica of Shot 8. DDT occurred between transducers P3 and P4, which is between 2 and 2.5 m from the ignition location.

Shot 13 15% H<sub>2</sub>, replica of Shot 9. DDT occurred between transducers P5 and P6, which is between 2.8 and 4.1 m from the ignition location.

Shot 14 10% H<sub>2</sub>, 2-ft spiral. Flame only.

### 5.2.3 Shots 15-21

Tests 15-21 were carried out with partial water filling in the vertical leg of the specimen. The goal of these tests was to determine the transmission and reflection of a detonation at the free surface of the water. The magnitude of reflected and transmitted pressure waves as well as the strains in the water filled section of the tube were key data obtained from these tests.

We filled the lower portion of the vertical leg of the specimen with about 2250 cc of water in shots 15 and 16 or 3750 cc in shots 17-21 as shown on Fig. 51a. The water was introduced from the bottom of the specimen using an additional valve (V10) to connect a 1 gallon plastic carboy that was elevated above the final water free surface to compensate for the difference in final pressure inside (760 Torr) and outside (737 Torr) the specimen. The procedure was to first evacuate the specimen, then fill the specimen with gas mixture (30/70 H<sub>2</sub>/N<sub>2</sub>O) using the method of partial pressures to reach a total pressure of about 617 Torr for shots 15-16 and 536 Torr for shots 17-21. The gas pressure is chosen so that after the water is filled to the desired level, the final pressure inside the water-filled specimen will be 760 Torr. The data from pressure transducers in the gas and the water-filled section were used to estimate the time of reflection and therefore the location of the water free surface in the tube.

Shots 15-16 Vertical leg filled with water (2250 cc) to just above P9. W end ignition, 1-ft spiral, 30/70 H<sub>2</sub>/N<sub>2</sub>O mixture, two additional pressure transducers (P9 and P10) added in water-filled section. Gage S17 failed in both tests. The nominal water level was intended to be about 6 in below pressure gage P6 but was about 4 in lower due to underestimating the dead volume between the valve and bottom of the tube.

Shots 17-18 Vertical leg filled with water to bend (3750 cc). 1-ft spiral, W end ignition, 30/70 H<sub>2</sub>/N<sub>2</sub>O mixture, Same instrumentation as 15-16.

Shots 19-21 Vertical leg filled with water to bend (3750 cc). DDT tests, no spiral, W end ignition. Same instrumentation as 15-16.

#### 5.2.4 Shots 22-24

Tests 22 to 24 were carried out with reverse propagation tests (ignition on East end, wave moving toward west), the goal of these tests was to determine if there was systematic effect of the ignition location on the strain waves produced by the detonation propagation through the bend. Some pressure gages failed on shots 22 and 23 and were replaced. Accelerometers were used to anchors and U-bolts to determine how much vibration from the initiation was transmitted to the mounting fixtures through the walls.

Shot 22 Ignition moved to E end, P8 to W end. Short (1 ft) spiral, 30/70 mix. Before shot 22, removed and reinstalled the east end o-ring and checked all fittings. Replaced vacuum pump. Installed accelerometers on W anchor support.

Shot 23 Replica of 22. Sensor P5 is failing on shot 22, replaced between shots 22-23.

Shot 24 Replica of 22 with accelerometers on U- bolts. U-bolts on plates near final position but not attached to the tube. Replaced P1 (damaged diaphragm), P2, P4, P9 (incipient damage on diaphragms), transducer P10 moved between P3 and P4 before the shot.

Ignition was moved back to the east end and used with the 1-ft spiral for the remainder of the testing in ES1. Tests 25-27 and 34-35 used two cantilever supports with the east end free (except for 25) and the west end anchored. The goal of these tests was to measure the support loads on the cantilevers. Tests 27-33 used one cantilever, the west end anchors and a special fixture to support the east end with cantilever to measure forces on the east end of the specimen.

#### 5.2.5 Shots 25-27

Shots 25-27 were carried out with ignition on West end, short (1 ft) spiral, 30/70 H<sub>2</sub>/N<sub>2</sub>O mixture. The goal of these tests was to measure the strains in the cantilever beams with the east end of the tube freed from the anchor. The cantilever support U1 was mounted to the specimen on plate 4 and U2 to the specimen on plate 10; the cantilevers were fastened with U-bolts directly to the piping (nuts on top and bottom of cantilever) with no play or shims between the cantilever or U-bolts and the pipe specimen. The deflection on the cantilevers was measured using 3-gage rosettes on U1 and U2. The cantilevers were statically calibrated using hanging weights to load that cantilevers at the location corresponding to the center of the pipe. The calibrations were based on using a series of masses and fitting the force-strain relation with linear regression. Only the central gages of the rosettes respond to forces along the central plane of the cantilever although all three gages were recorded. The calibrations were: U1 central gage (S19) 10.2 N/microstrain; U2 central gage (S22), 9.86 N/microstrain. These tests are preliminary and were repeated with better cantilever instrumentation in shots 34-35 (see below). The details of the cantilever construction and calibration are given in [Shepherd and Akbar \(2009\)](#).

Shot 25 Moved P10 to between P3 and P4. Prompt detonation. Added 5/16 spacer to W anchor to shim tube to correct distance from plates at cantilever locations. U bolt supports mounted to plates 4 and 10 but pipe remained anchored to the east fixture

for this test. The goal was to determine how the east end anchor fixture influenced the amount of force transferred to the cantilevers by comparison with shots 26 and 27.

Shot 26 Tube removed from E end anchor support, supported by U bolt supports mounted to plates 4 and 10 and west anchor. Accelerometers on tips of U-bolt supports.

Shot 27 Replica of 26, readjusted the E U-bolt support to be square with tube. Accelerometers on E end flange, in transverse directions. P8 data showed spikes, replaced following this shot.

### 5.2.6 Shots 28-33

Shots 28-33 were carried out with ignition on West end, short (1 ft) spiral, 30/70 H<sub>2</sub>/N<sub>2</sub>O mixture. The cantilever on the vertical leg of the specimen was removed and used as the measuring element in a force link attached between the bottom of the specimen and plate 15 (east end flange). The goal of these tests was to directly measure the force on the east end of the tube. A detailed description of these tests, the fixtures and analysis of the forces is given in the companion report [Shepherd and Akbar \(2009\)](#). Shots 28 to 31 had various issues with the force link dues to mechanical problems or issues with data acquisition system. The only valid data for the forces link was shots 32 and 33.

Shot 28 - U2 removed from plate 10 and used as cantilever beam in force link mounted to east flange to measure vertical force. U1 U-bolt support on plate 4 left in place attached to the tube. Using 3-gage rosettes on U1 and U2.

Shots 29 -33 used U3 support with two half bridges as cantilever beam in force link. Cantilever beam U-bolt support on west leg detached from the tube. U3 calibration of AB (1.25 in beam) direction: static proportionality constant = 10.05 N/microstrain. U3 calibration of CD (1.00 in beam) direction: static proportionality constant = 8.078 N/microstrain

Shot 29 First effort with force link - some play in dog bolts in both directions - force link can slip on cantilever. Data valid for pressure and strain gages but not on force link. Data not distributed or analyzed.

Shot 30 Repeat of Shot 29 with Keyence to detect out of plane motion at bend. Data recorded but file not saved due to DAS memory overflow. Data not available.

Shot 31 Repeat of Shot 30. Data on force link shows dog screws had excessive play. Data valid for pressure and strain gages but not force link. Data not distributed.

Shot 32 Repeat of Shot 30 with dog screws tightened on force link. Data valid for all instruments.

Shot 33 replica of Shot 32. Data valid for all instruments.

### 5.2.7 Shots 34-35

Repeat of shots 26 and 27 with new U-bolt supports using twin half-bridge strain instrumentation, see [Shepherd and Akbar \(2009\)](#). The Keyence displacement gage (D4) used to measure out-of-plane motion of bend. U-bolts supports U3 (plate 10) and U4 (plate 4) were clamped firmly to tube, the east end was free. The goal of these tests was to obtain better measurements of cantilever forces and determine if out of plane motion was playing a significant role in the pipe specimen vibration.

The strain gage direction assignments are:

S24 U3 A-B direction, tension (+strain) when tube moves perpendicular to axis toward east.

S25 U3 C-D direction, tension (+strain) when tube along axis away from floor (toward bend).

S26 U4 A-B direction, tension (+strain) when tube moves perpendicular to axis toward floor.

S27 U4 C-D direction, tension (+strain) when tube moves along axis toward east (toward bend).

Shot 34 Removed force link - east end free. U-bolt supports clamped to pipe U3 (plate 10), U4 (plate 4).

Shot 35 Replica of 34.

## 5.3 Key results

Key results from the ES1 test include: demonstrating the repeatability of the measurements; the magnitude of the pressures, hoop and longitudinal strains in the various configurations, including DDT; demonstration of the generation of axial (bar) waves due to the detonation propagation through the pipe bend and interaction of these waves with the detonation-induced strains; interaction of detonation waves with a water-filled section; measure of forces by cantilever beams.

### 5.3.1 Pressure and Strain Histories

A number tests were replicas of the same conditions and many of the instruments were in the same locations, Fig. 21a.

The main features observed on the pressure gages are the sharp jumps in pressure that correspond to the incident detonation and reflected shock wave, highlighted for gage P7 on Fig. 21b, that are generated with the detonation reaches the end of the pipe. The incident detonation is always observed first and the reflected shock is later following a delay that corresponds to the detonation wave propagation between the gage location and the end of the pipe plus the shock wave propagation back to the gage. Oscillations superimposed on the main signal are a combination of actual pressure fluctuations due to transverse waves and artifacts caused by coupling of piping vibrations into modes of transducer vibration that are not compensated for acceleration. The reverberating shock waves generated by the detonation die down after 10-20 ms and the pressure becomes spatially uniform, decaying in

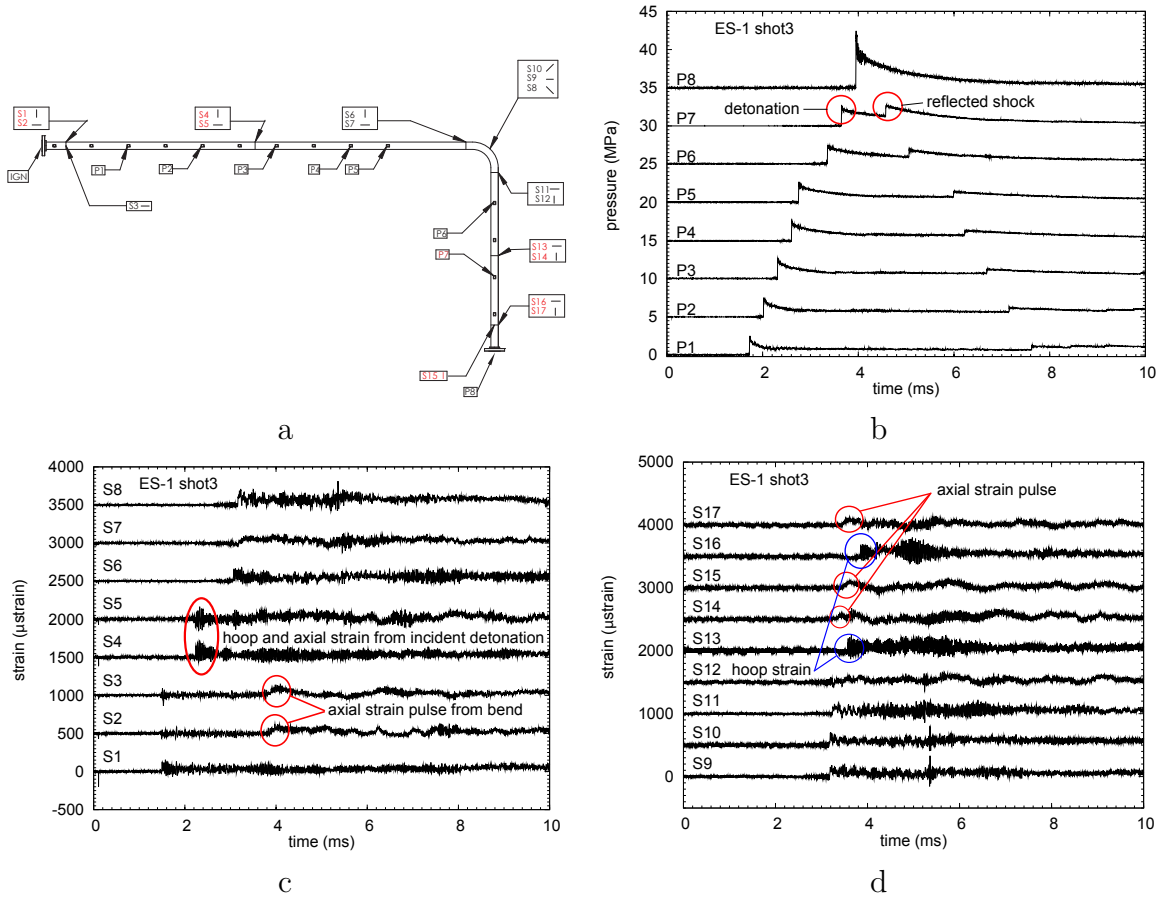


Figure 21: ES1 test (shot 3) results for near-CJ detonation propagation from W to E. a) Sensor layout for the majority of ES1 tests with W-to-E detonation propagation. b) pressure c) and d) strains.

time due to heat transfer into the wall, Fig. 22a. Although the transducers were thermally protected by a thin layer ( $< 1$  mm) of RTV sealant, the pressure signal results should be used cautiously after 10 ms due to thermal artifacts and the intrinsic time-constant of piezoelectric gages. The strain and pressure signals were of good quality, some high-frequency noise (greater than 50 kHz) was present and in some cases was removed by low-pass filtering before plotting the data.

The main features on the strain gages are the oscillations induced by the detonation and shock waves, highlighted for gages S4 and S5 on Fig. 21c, and the axial strain pulses produced by the detonation propagating around the bend, highlighted on gages S2, S3 as well as for S14, S15, and S16 on Fig. 21d. The detonation-induced signals are characterized by an onset coincident with the detonation arrival and oscillations at a frequency of 29 kHz due to the hoop (breathing) mode of pipe vibration. The oscillation is not a simple sine wave because multiple modes are excited and interference effects are significant between these modes as well as flexural waves. Low-frequency oscillations (see the discussion in Shepherd and Akbar (2009)) corresponding to various bending and ovalization modes of the piping system can be

observed on the longitudinal gages over long times (100 ms), Fig. 22b.

In addition to low-frequency (10-1000 Hz) vibrations that are visible, a monotonic rise in hoop and longitudinal strain can be observed in all gages. The smooth red line in Fig. 22b corresponds to an exponential function with a strain increase of 60–100  $\mu$  strain depending on the gage and a time constant of 7 ms. The measured strain at 100 ms ranged between 35 and 100  $\mu$ strain depending on the gage with the highest strains being measured on the bend and the hoop strains were generally but not always higher than the longitudinal strain at the same location.

This is due to a combination of the static pressurization and thermal expansion caused by the transfer of energy from the hot detonation product to the cold tube wall. The maximum hoop strain due to the static pressurization (Table 6) is about 46  $\mu$ strain; the maximum strain due to axial extension (without accounting for bending) will be one-half of this value or 23  $\mu$ strain. A significant fraction of the strain observed at 100 ms is due to thermal stress effects as discussed in detail by [Shepherd and Pintgen \(2007\)](#). Although the peak bulk temperature rise in the tube is only about 2°C if all the energy in the gas (5.3 MJ/kg for adiabatic cooling to room temperature) is transferred to the pipe, the thermal expansion due to this energy transfer will result in 68  $\mu$ strain for the hoop deformation and 34  $\mu$ strain for the axial component (see [Shepherd and Pintgen 2007](#) for details of the calculation). The thermal diffusion time through the pipe thickness is about 4 s but as discussed in [Shepherd and Pintgen \(2007\)](#), thermal stresses due to rapid heat transfer will heat a thin layer of the pipe material next to the hot gas within milliseconds and this will be manifested as a strain on the surface of the pipe due to the thru-wall thermoelastic response.

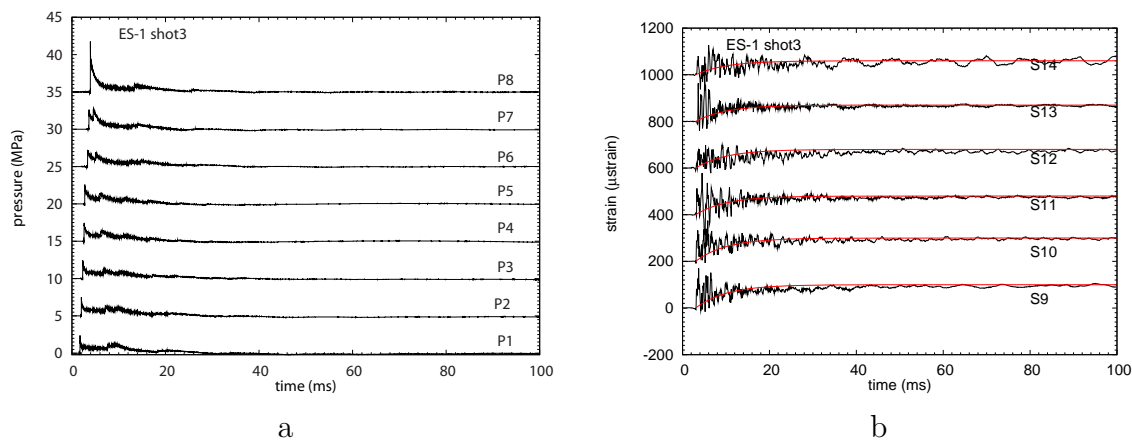


Figure 22: ES1 test (shot 3) results for a long duration with high frequency components removed. a) Pressure. b) selected strains gages in the vertical leg of the system. Red lines are exponential functions approximating mean strain.

The longitudinal strain signals for the strain gages on the spine of the pipe (S2, S5, S7, S12, S14, S17) respond to the superposition of in-plane bending and bar modes of the tube vibration while the longitudinal gages S3, and S15 respond only to the bar waves and out-of-plane bending. The out-of-plane bending was designed to be minimal in these tests by making sure the piping specimen was mounted parallel to the support wall so that the

gages S3 and S15 respond primarily to the bar waves. Bar waves are strain pulses created by detonation changes in direction; when the ends of the ES1 piping are anchored, as in this example, bar waves are created by the detonation moving through the bend. The anchors and wall support system are extremely effective at transmitting the load to the building and minimizing the motion of the piping due to initiation or reflection of the detonation.

Before the detonation reaches the bend, the longitudinal and hoop strains are strictly due to the detonation propagation, illustrated by Fig. 23a. The 29 kHz oscillation in the hoop response (S4) clearly starts when the pressure front arrives and a corresponding oscillation in the longitudinal response (S5) is simultaneously created due to the Poisson coupling between hoop and longitudinal deformation (Shepherd and Inaba, 2010) as well as bending stresses due to the periodic radial deformation. After the detonation reaches the bend, the bar wave (traveling at approximately 4900 m/s, see Table 25) created by the reaction force from the change in detonation direction runs ahead of the detonation moving at about 2088 m/s. The creation of the bar waves at the bend and detailed analysis of the magnitude is discussed in Shepherd and Akbar (2009). The bar wave can be observed as a distinct pulse in front of the detonation-induced strains as shown on S14 Fig. 23b. The axial motion does not produce a strong hoop response but a small amount of compression can be observed on S13. Once the detonation arrives at S13, hoop oscillations similar to those observed on S4 are generated and the signal on S14 is a superposition of the oscillations created by the Poisson effect, bending, and the displacement of the bar wave, Fig. 23c.

The bend-generated bar wave has a finite duration, about 100–200  $\mu\text{s}$ , associated with the time it takes the detonation to pass through the bend (Shepherd and Akbar, 2009). This bar wave will propagate to the anchor supports, reflect and propagate through the pipe in the reverse direction. The superposition of the reflected bar wave increases the axial strain so that the oscillations on gage S14 immediately after the detonation arrives at 3.55 ms are all in the positive direction while those on S3 are alternating in sign.

The strains associated with the bar waves will reverberate within the piping system and contribute to the vibration observed in the first 10-20 ms on Fig. 22. The bar waves propagation can be clearly seen if the longitudinal strain signals are filtered to minimize the hoop oscillation and other high-frequency noise. The waves from S15 and S17 are more distinct but clear evidence of the initial bar wave can also be seen starting at 4.5 ms on gages S2 and S3, Fig. 23d. Close to the bend, the strain signals from the detonation and bend overlap which is why the gages farthest from the bend are shown as an example. The strain gages (S8, S9, S10) mounted on the extrados of the bend show a more complex response although a there is distinct front when the detonation arrives.

### 5.3.2 Repeatability: Wave speeds, pressures, and strains

The results from these tests can be compared to judge the repeatability of the testing with promptly initiated detonations. Tests 3,4, 5,6, 25, 26, 27, 28, 29, 31, 32, 33, 34, and 35 were carried out with nominally the same initial conditions and prompt detonation initiation propagating from the west toward the east end of the specimen. The pressure signals and strain signals can be compared in detail (time history) for these tests, an example is shown in Fig. 24 where the pressure and strain traces are overplotted for shots 3 and 4. The data for shot 4 is shifted by 75  $\mu\text{s}$  as determined from the time-of-arrival of the pressure signals,

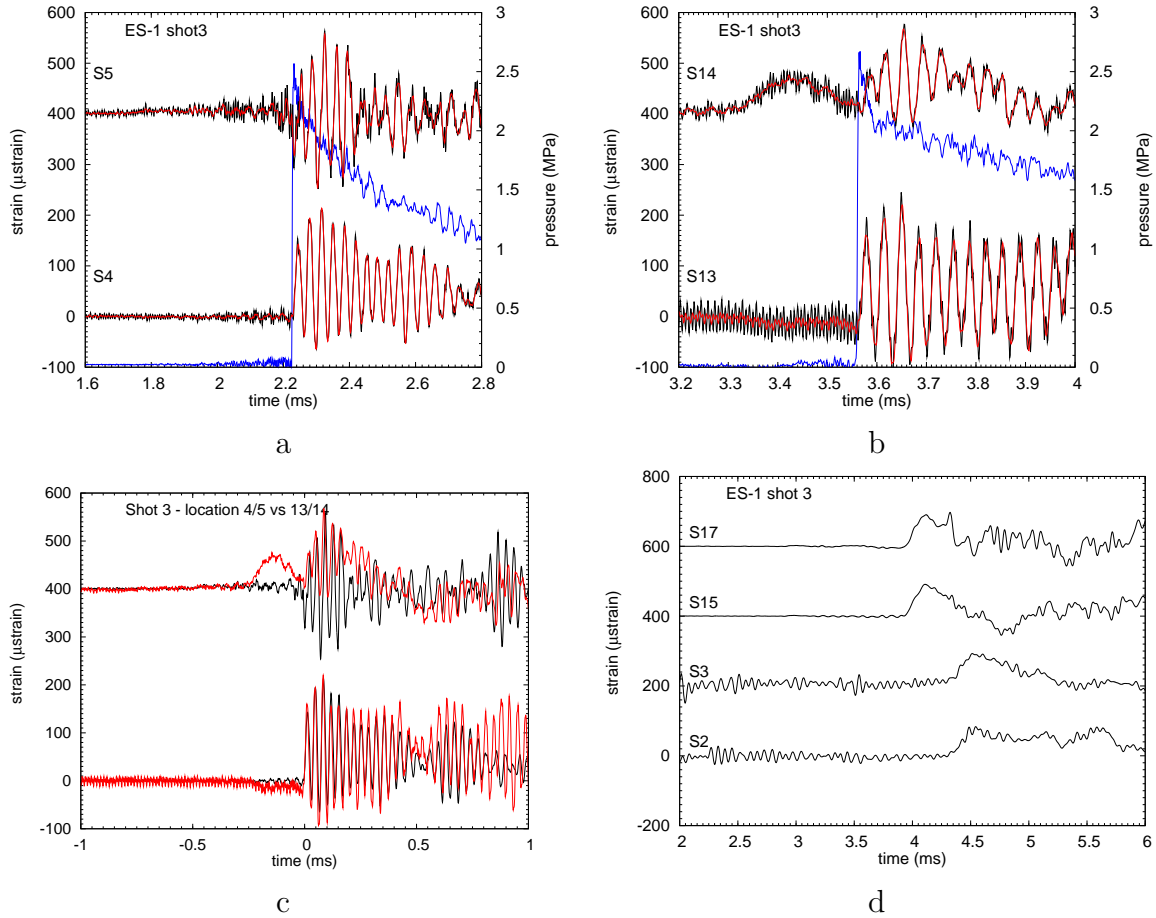


Figure 23: Details of ES1 test results for near-CJ detonation propagation from W to E. a) Incident detonation pressure superimposed on strain signals for hoop (S4) and longitudinal (S5) directions, downstream (after) of the bend. b) Incident detonation pressure superimposed on strain signals for hoop (S13) and longitudinal (S14) directions, before bend. Red lines are signals after low pass filtering to remove frequencies about 50 kHz. c) Strain histories overlaid and time-shifted so that zero corresponds to detonation arrival time. d) Bar wave observed both upstream (S2, S3) and downstream (S15, S17) of the bend, the signal have been low-pass filtered at 20 kHz to reduce interference with the hoop oscillation signal.

Fig. 24d. This shift is due to the intrinsic variability of DDT initiation.

The velocity of incident detonation was determined by linear regression of the initial jump in pressure arrival time data as shown by the two lines in Fig. 24d. The data are extremely consistent with a linear correlation (the regression coefficient is at least 0.9999) and the standard error in the velocity is typically less than 3 m/s. As expected, the wave speeds are slightly lower than the CJ speed (nominally 2088 m/s) and the pressures are slightly higher than the CJ pressure (nominally 2.62 MPa). The lower speed is due to the effects of the boundary layer created by the flow behind the detonation, and the expansion wave interaction with the detonation front. The higher pressures are due to the presence of

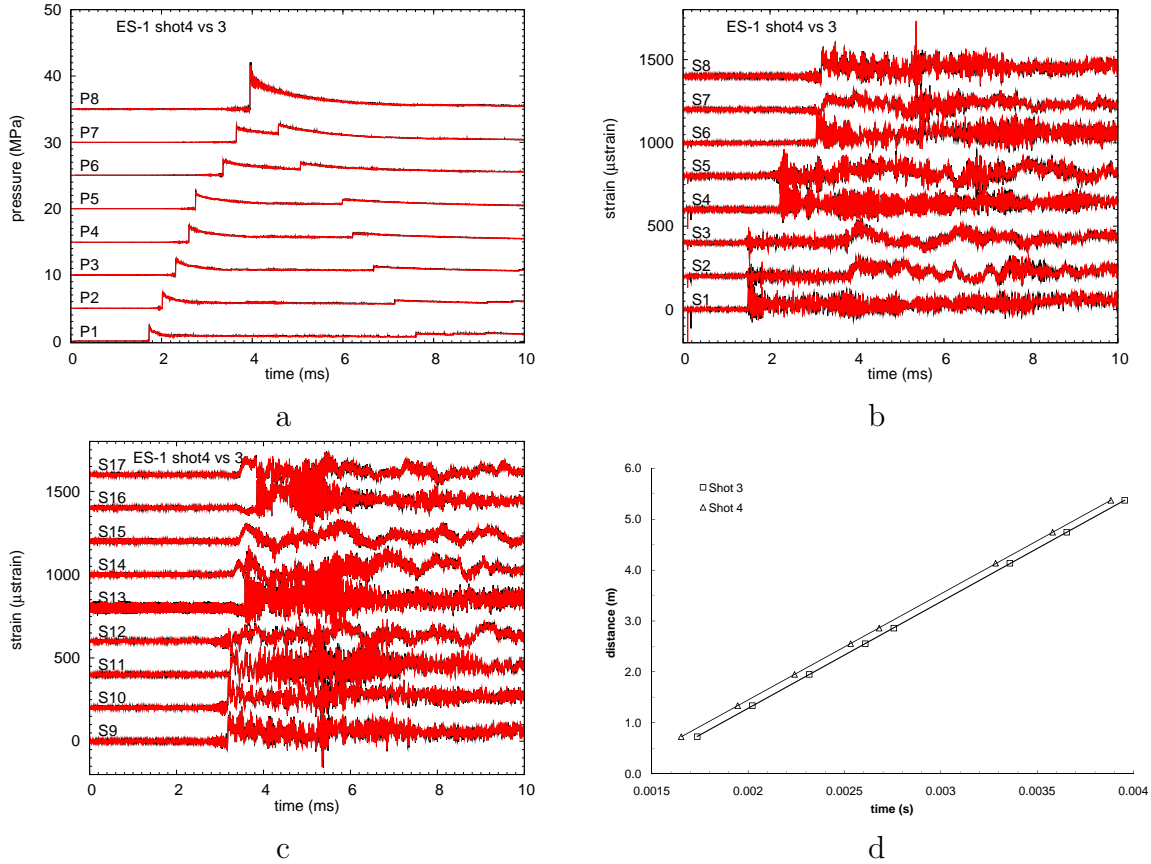


Figure 24: Comparison of shots 3 and 4 a) pressure b) strain c) strain d) pressure arrival time.

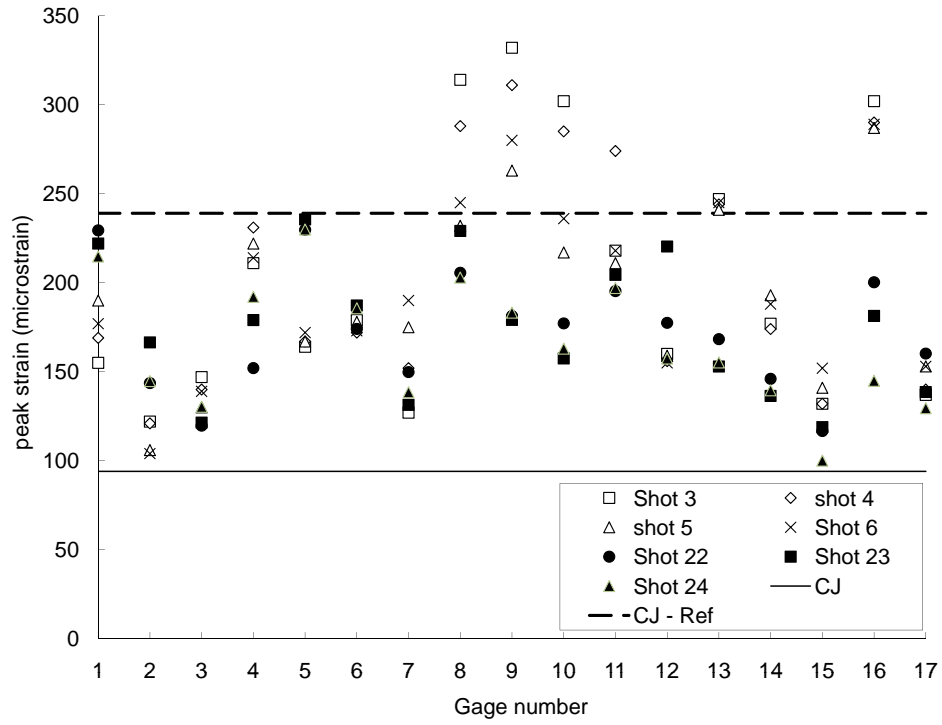
the high pressure in the reaction zone and/or transverse waves; the pressure gauges average over the 5.5 mm diameter sensitive element of the gage while the cell width is about 3 mm and the nominal CJ reaction zone thickness is about 0.08 mm. Due to the very thin structure of the detonation in comparison to the gauge width, the measured pressure is only slightly higher than CJ although the pressures in the reaction zone zone and behind the transverse waves can be up to a factor of two higher than the CJ pressure.

Three tests 22, 23, and 24 were carried out with the same conditions as the other tests in the series but with the ignition moved to the east end of the facility to examine possible systematic effects on detonation propagation. The motivation to look at these "reverse propagation" cases was observations in asymmetry in the measurements of the bar waves generated by the detonation propagation around the bend. The peak strains and pressures from the reference tests 3–6 with "forward" are compared with the "reverse" propagation tests 22–24 in Figs. 25. These plots verify the repeatability of the results but do show that there is an effect of the length of detonation propagation prior to entering the bend. The reflected pressures for the reverse propagation cases are slightly higher than for the forward propagation cases but the peak strains in the bend are substantially lower. With the exception of the bend strains S8-S10 and hoop strains S16 near the reflecting end,

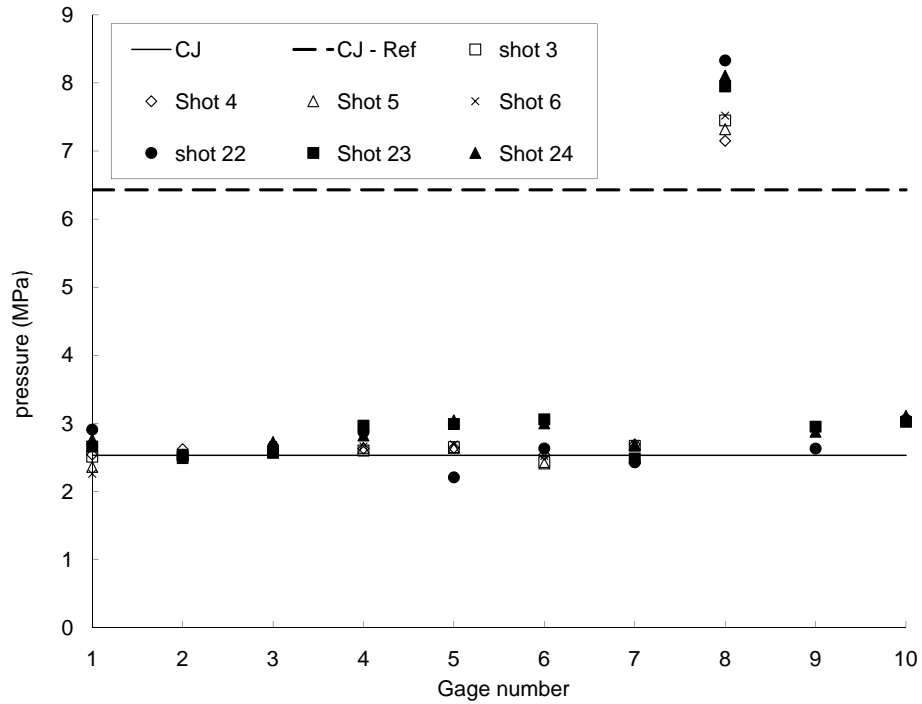
the strains are bounded by  $240 \mu\text{strain}$  which corresponds to the SDOF model for hoop oscillations loaded with the reflected CJ pressure but with a dynamic load factor  $\Phi = 1$ . The strains are all bounded by the SDOF model (2) with the reflected CJ pressure and  $\Phi = 2$ , which is consistent with previous studies (Shepherd, 2009) on detonation tubes with nearly ideal detonation waves. Away from the bends and the end of the tube, the peak strains consistently fall within a band of  $100 \leq \epsilon \leq 250 \mu\text{strain}$ .

Table 9: Measured ES1 wave speeds and peak pressures (not including the reflected pressure) compared against CJ values.

Shot	$U$ (m/s)	$\Delta U/U_{CJ}$ (%)	$P_{max}$ (Mpa)	$\Delta P_{max}/P_{CJ}$ (%)
3	2093.6	0.27	2.567	-2.02
4	2086.1	-0.09	2.606	-0.55
5	2089.0	0.05	2.553	-2.56
6	2088.4	0.02	2.567	-2.02
22	2071.8	-0.77	2.653	1.24
23	2079.5	-0.40	2.804	7.02
24	2079.1	-0.42	2.804	7.02
25	2088.4	0.02	2.768	5.64
26	2088.2	0.01	2.785	6.28
27	2076.4	-0.55	2.795	6.68
28	2084.5	-0.16	2.810	7.25
29	2088.6	0.03	2.804	7.01
31	2078.9	-0.43	2.793	6.60
32	2083.4	-0.22	2.746	4.79
33	2088.9	0.05	2.822	7.70
34	2089.4	0.07	2.802	6.95
35	2087.5	-0.02	2.805	7.05



a.



b.

Figure 25: Comparison of peak a) strain and b) pressure for reference tests 3–6, and reverse propagation tests 22, 23, 24. The reference pressures and strains ( $\Phi = 1$ ) are discussed in Section 4.5.

### 5.3.3 Analysis of Hoop and Axial Strains

A typical set of hoop and axial strains induced by a propagating detonation is shown in Fig. 26a. This pair of signals was obtained for gages S4 (hoop) and S5 (axial) which are located about 1.8 m from the igniter on the horizontal leg of ES1. On the surface of the pipe, the out-of-plane stress  $\sigma_z$  vanishes and the in-plane strains can be analyzed using the formulas of plane stress to convert strain to stress.

$$\sigma_x = \frac{E}{1 - \nu^2} (\epsilon_x + \nu\epsilon_\theta) \quad (3)$$

$$\sigma_\theta = \frac{E}{1 - \nu^2} (\epsilon_\theta + \nu\epsilon_x) \quad (4)$$

The results are shown in Fig. 26b. The maximum stress range is  $-40 \leq \sigma \leq +50$  MPa. The peak hoop strain and stress both occurs within a few cycles of oscillation after the arrival of the detonation wave. The stresses and strains for the axial and circumferential directions are plotted parametrically in Figs. 26c and d for the time period 0-100 ms. Although the axial and hoop strains appear to be uncorrelated, there is a positive correlation between hoop and axial stress. As discussed subsequently, this correlation is apparently due to axisymmetric axial bending stresses induced by the hoop oscillations. This is not due to the Poisson effect associated with membrane stretching, since we would expect a strong negative correlation between axial and hoop strains in that case.

**Frequency Content** Both hoop and axial strain signals show a strong spectral component (Fig. 27) at frequencies close to the primary breathing mode frequency of 29 kHz. The hoop oscillation at this frequency is expected since this is the fundamental mode of the radial motion predicted by all models of the pipe vibration. The axial oscillation at this frequency is expected due to Poisson coupling of the hoop and axial modes and, as pointed out in the next section, the axisymmetric bending motions associated with the hoop oscillation. The hoop signal show modest amount of vibration energy in modes at frequencies of about 10 and 3 kHz and a broad peak below 500 Hz. A similar broad peak at low frequencies is observed in the axial strain as well as substantial energy at discrete frequencies up to 4500 Hz. As discussed in (Shepherd and Akbar, 2009, Section 2), the frequencies less than 500 Hz correspond to various bending modes or coupled radial-axial modes. The frequencies between 500 and 5000 Hz correspond to axial and torsion modes. All of these modes will be coupled due to the bend and end conditions. The very lowest frequency modes (less than 20 Hz) are associated with out-of-plane beam bending, as discussed in Appendix D of Shepherd and Akbar (2009).

**Magnitude and Phase Relationship** The hoop strain is mainly positive (tension) with a maximum value of approximately 211  $\mu$ strain and a minimum of -60  $\mu$ strain; the maximum value is about 10% higher than the SDOF estimate of 190  $\mu$ strain (Table 6) using a dynamic load factor of 2. The axial strain oscillates with approximately equal negative and positive peaks with a maximum amplitude of  $\pm 160$   $\mu$ strain. The large positive excursions are unexpected and inconsistent with membrane stretching in both amplitude and sign. The

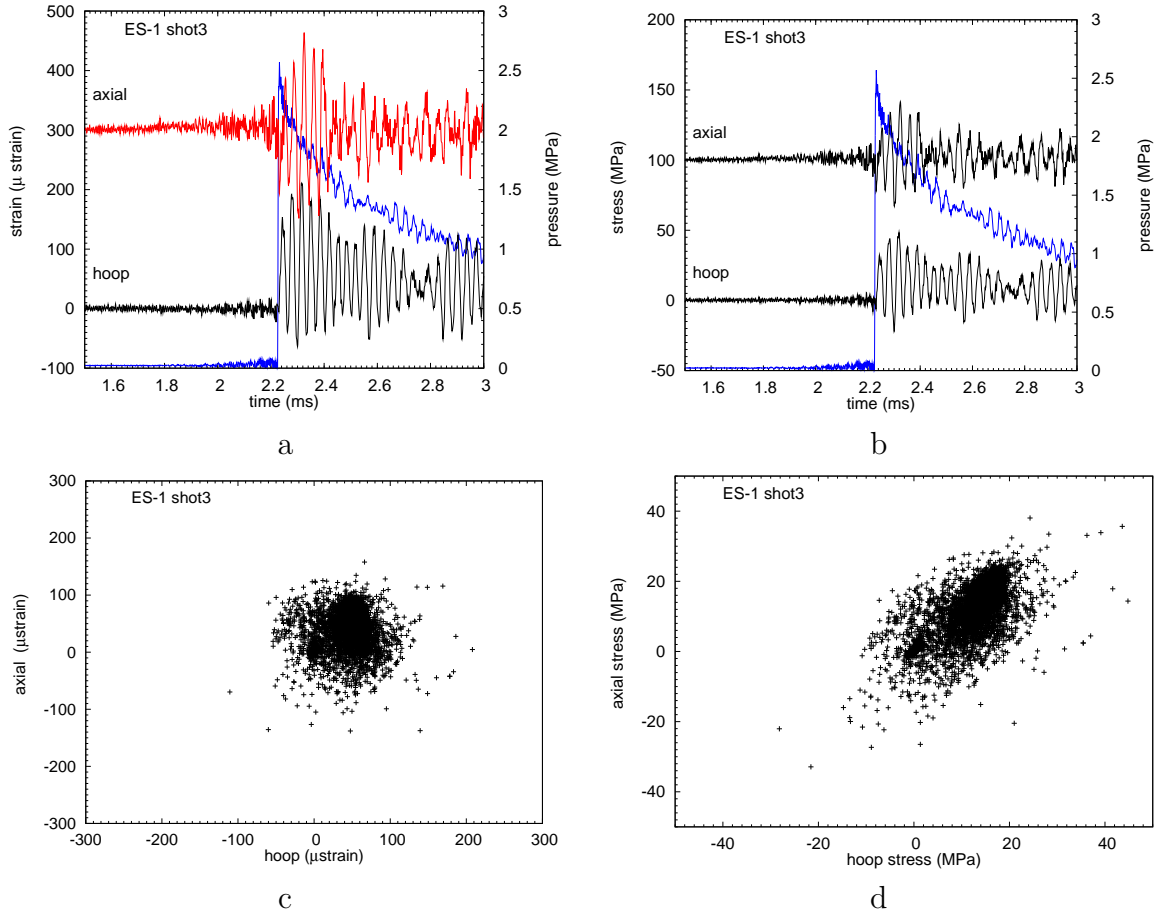


Figure 26: Stress and strain analysis of strain gages 4 (hoop) and 5 (axial) for shot 3.

maximum amplitude of membrane stretching strain in the axial direction based on the Poisson effect is expected (see discussion below) to be about  $-60 \mu\text{strain}$  and the values would be mainly negative (tension). The measured axial strains appear to have a substantial in-phase components (Fig. 28) rather than being out-of-phase with the radial motion as expected from the Poisson effect and membrane stretching alone.<sup>1</sup> This suggests that axi-symmetric bending appears to be making important contributions to the axial strain, an idea which is examined in-depth subsequently.

The phasing of the axial strains relative to the hoop strain and the magnitude of the axial strains are at variance with both the membrane theory and with data from thin-wall tubes. In addition, as discussed further below, the ANSYS simulations fail to properly reproduce the high-frequency axial strains. These peculiarities and discrepancies indicate that our understanding of how to model the pipe response to detonation is still incomplete.

<sup>1</sup>Thanks to Tom Ligon and David Gross of DEI as well as John Minichiello of BNI for pointing out this peculiarity of the data and implications for the importance of axi-symmetric bending for the high-frequency axial strain oscillations.

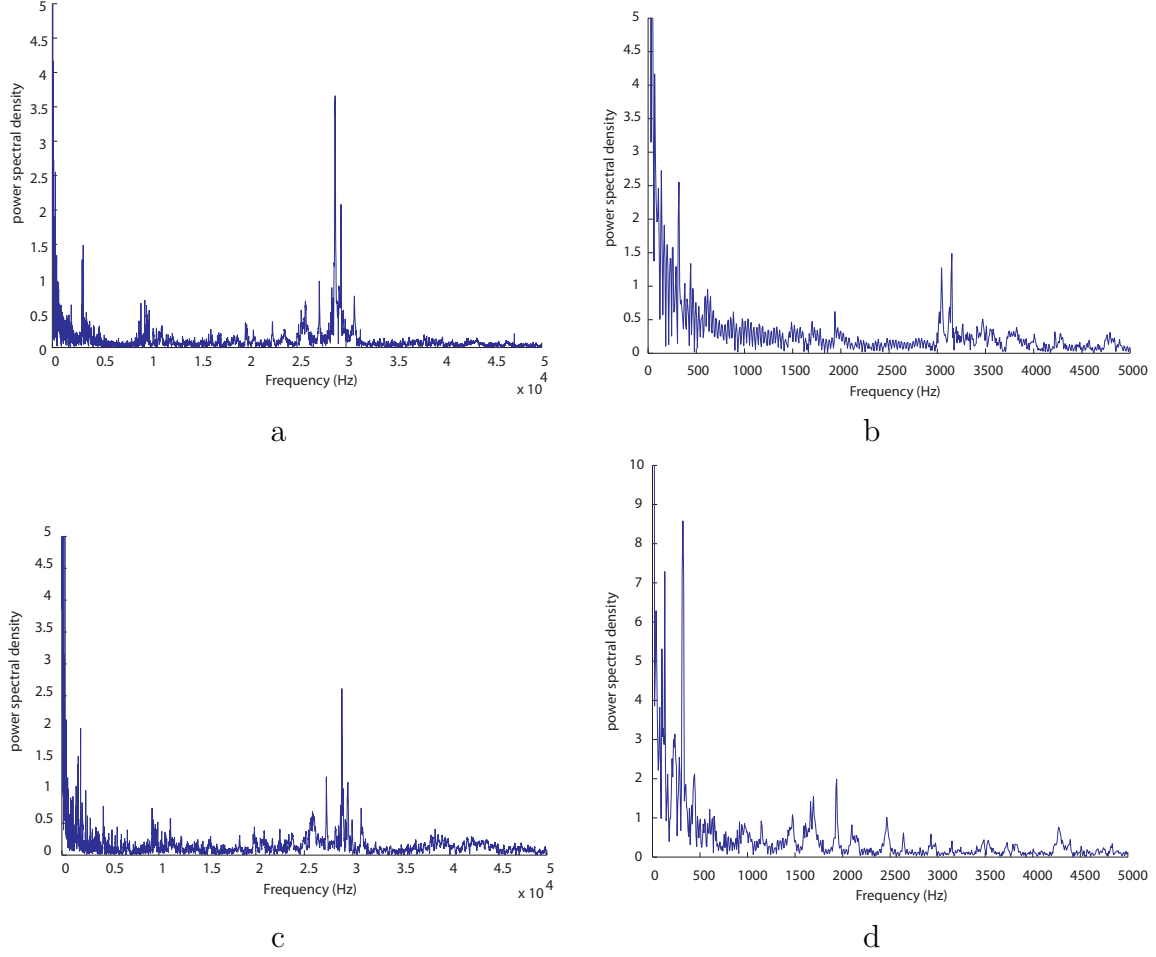


Figure 27: Spectral analysis of strain gages S4 (a, b) and S5 (c, d) for shot 3.

**von Mises Stress** The stresses can be analyzed in term of the *equivalent tensile stress*, also known as the *von Mises stress*, which is defined in terms of the principal stresses  $\sigma_1$ ,  $\sigma_2$ , and  $\sigma_3$  as

$$\sigma_{vM} = \frac{1}{\sqrt{2}} [(\sigma_1 - \sigma_2)^2 + (\sigma_2 - \sigma_3)^2 + (\sigma_3 - \sigma_1)^2]^{1/2} . \quad (5)$$

For the axisymmetric deformation of a cylinder, the principal stresses will be in the hoop and axial direction with a small component in the radial direction

$$\sigma_1 = \sigma_x , \quad (6)$$

$$\sigma_2 = \sigma_\theta , \quad (7)$$

$$\sigma_3 = \sigma_r \approx 0 . \quad (8)$$

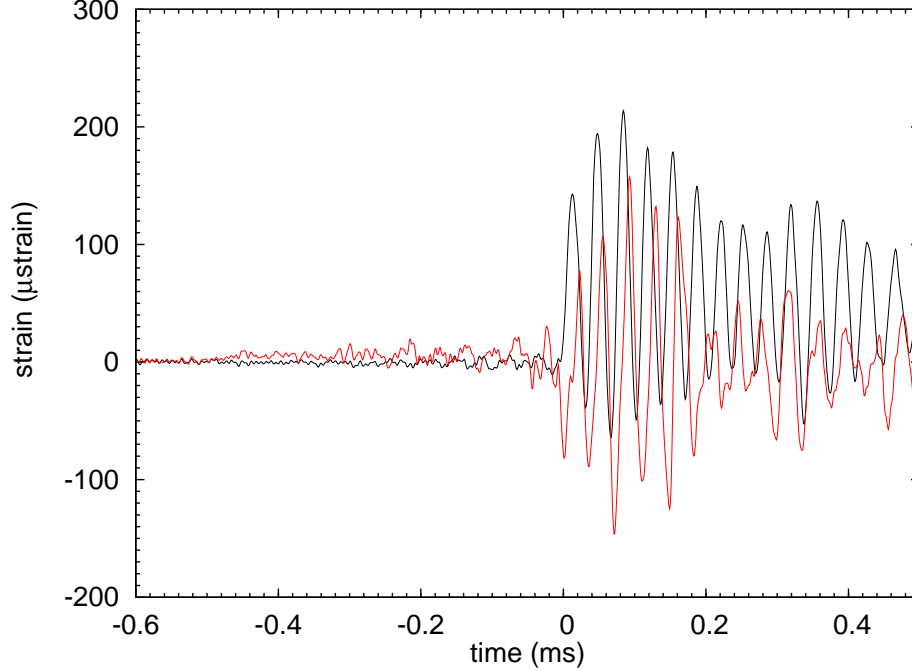


Figure 28: Hoop (black) and axial (red) strain gages S4 and S5. Data has been filtered at 50 kHz to remove noise and the time axis shifted so that  $t = 0$  corresponds to the interpolated detonation arrival time.

The neglect of the radial stress can be justified by recognizing that the equilibrium radial stress distribution is approximately linear across the thickness for a thin shell,

$$\sigma_r = -P_i + (P_i - P_o) \frac{(r - r_i)}{h}, \quad (9)$$

and has a maximum value of  $-P_i$ , the pressure on the interior surface  $r = r_i$  and a minimum value of  $-P_o$  the pressure on exterior surface  $r = r_o$  of the shell. The maximum hoop and axial stresses are on the order of  $R/h$  larger than the maximum radial stress, which justifies the assumption of  $\sigma_3 \approx 0$ . This is equivalent to the assumption of plane stress used to analyze the strains. Under this assumption, the von Mises stress can be written as

$$\sigma_{vM} = \frac{1}{\sqrt{2}} [(\sigma_1 - \sigma_2)^2 + \sigma_2^2 + \sigma_1^2]^{1/2}. \quad (10)$$

A constant value of the von Mises stress defines an ellipse in the  $(\sigma_1, \sigma_2)$  plane. This ellipse can be parametrically defined for  $0 < \phi < 2\pi$  as

$$\sigma_1 = \sigma_{vM} \left( \cos \phi - \frac{1}{2} \sin \phi \right) , \quad (11)$$

$$\sigma_2 = \sigma_{vM} \left( \cos \phi + \frac{1}{2} \sin \phi \right) . \quad (12)$$

For the S4/S5 data, a maximum value of  $\sigma_{vM} = 45$  MPa defines the ellipse shown in Fig. 29. This ellipse bounds all the data points, indicating that the value of 45 MPa is an upper bound on the von Mises stress at this location. A maximum value of the von Mises stress equal to the yield stress  $\sigma_{yp}$  is standard approach for determining the onset of plastic deformation in metals. For type 304 stainless steel, a nominal low-strain rate yield value is typically taken to be  $\sigma_{yp} = 200$  MPa (the ASME piping code minimum value is 172 MPa) so that at the location S4/S5 in ES1 shot 3, the maximum von Mises stress is about 25% of the nominal static yield value. This further corroborates the elastic nature of the present experiments which was inferred from the peak strains, which are substantially less (10%) than the 2000  $\mu$ strain conventionally associated with the onset of plastic deformation in uniaxial strain.

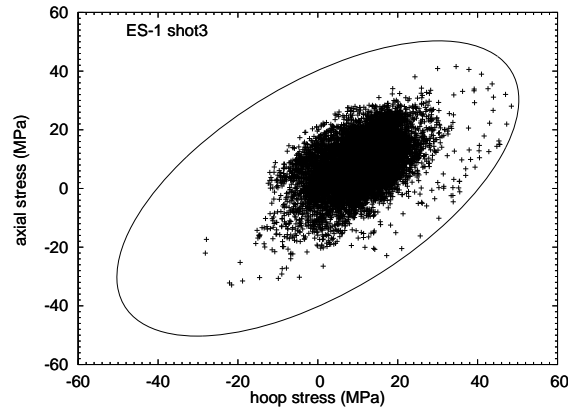


Figure 29: Stress analysis showing bounding von Mises ellipse with  $\sigma_{vM} = 45$  MPa for strain gages 4 and 5, shot 3.

A similar analysis can be carried out for the rosette strain gages mounted on the extrados of the 90-deg bend. The raw strain signals indicate that this is where the highest peak strains are observed, gages S8, S9, S10 in Fig. 25. The extrados of the bend is also where the pipe is thinnest due to the hydraulic forming process. However, the deleterious effects of reducing the wall thickness are partially offset by the work hardening effect of the hydraulic forming process. In order to compute the principle strains, the rosette data was analyzed using the methods outlined in Vishay TN515 (2010). The results are shown in Fig. 30 for one representative test, shot 35. As expected, the stresses are higher than on the straight section of the pipe and the bounding von Mises stress is 65 MPa , about 45% higher than the value of 45 MPa found for gages S4/S5 as discussed previously and presented in Fig. 29.

This analysis can only describe the stress and strain field on the pipe surface. In order to

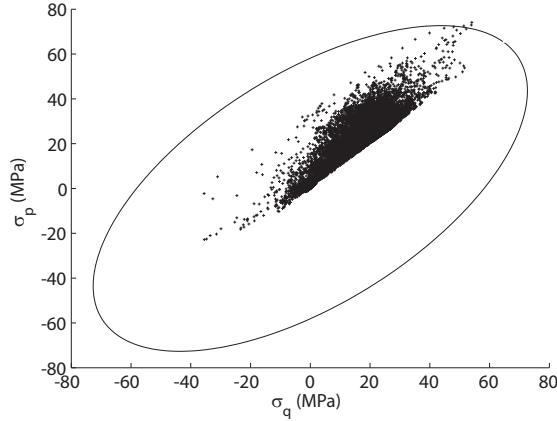


Figure 30: Stress analysis showing bounding von Mises ellipse with  $\sigma_{vM} = 65$  MPa and principle stresses determined by analyzing the rosette strain gages S8, S9, S10 in shot 35.

extrapolate into the interior it is necessary to separate the deformation and stress field into bending and membrane components as well as include the small but nonzero  $\sigma_r$  component. However, since the radial stress is at most 2.5 MPa, neglecting this in comparison to the maximum stress of 50 MPa in the other two components will at most result in a 10% error in  $\sigma_{vM}$ . Since the bending stress will vary linearly through the thickness and is antisymmetric about the middle surface while the membrane stress is independent of radial distance, we expect that the von Mises stress will be a maximum near the inner and outer surfaces of the pipe.

**Membrane and Bending Strains in Shells** The deformation of a thin shell can be approximately described as a superposition of membrane (in-plane stretching) deformations and bending (out-of-plane curvature) deformations, see Chap. 10, [Timoshenko and Gere \(1961\)](#) and Chap. 2, [Calladine \(1983\)](#). We consider the purely axi-symmetric deformations, shown in Fig. 31, which will be induced by the motion of an idealized planar detonation front along the axis of the tube. An approximate representation of the stress-strain field in the pipe wall can be obtained by using thin-shell theory and neglecting the radial stress distribution, which is a reasonable approximation as long as  $\sigma_z \ll \sigma_x$  or  $\sigma_\theta$ . As shown in Fig. 26, this is true for much of the oscillation cycle so we will assume plane stress  $\sigma_z = 0$  in what follows. The in-plane membrane strains along the  $(x, y)$  directions are denoted  $(\epsilon_1, \epsilon_2)$ , are independent of the distance  $z$  within the shell, and are related to the stress resultants  $N_x$  and  $N_y$  through Hooke's law for the membrane,

$$N_x = \frac{Eh}{1 - \nu^2} (\epsilon_1 + \nu\epsilon_2) , \quad (13)$$

$$N_y = \frac{Eh}{1 - \nu^2} (\epsilon_2 + \nu\epsilon_1) . \quad (14)$$

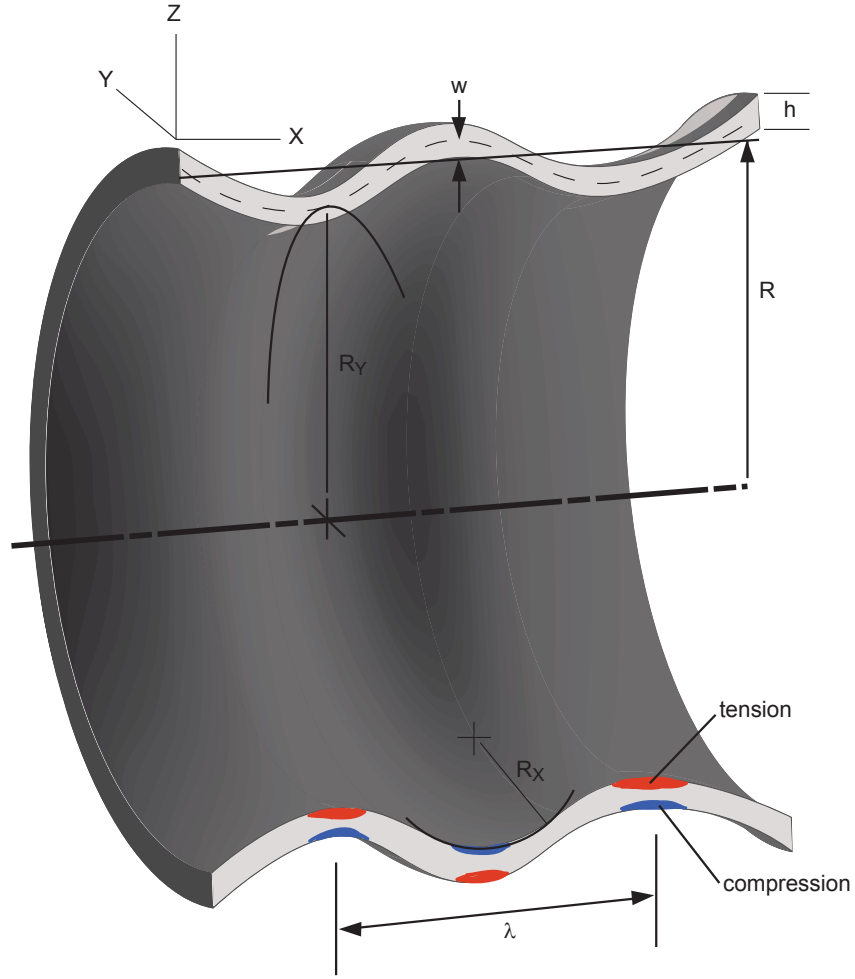


Figure 31: Axi-symmetric deformations of a pipe. The coordinate system  $(x, y, z)$  is a local construction with  $z$  parallel to the radial direction,  $x$  to the axial direction, and  $y$  the circumferential ( $\theta$ ) direction. The mean radius of the pipe is  $R$ , the distance  $z$  is measured from the midplane surface shown as the dashed line and the local radii of curvature of the midplane surface,  $R_y$  and  $R_x$ , are positive as shown. The axial wavelength of the flexural oscillation is  $\lambda$ .

The resulting membrane stresses  $\sigma'$  are

$$\sigma'_x = \frac{N_x}{h}, \quad (15)$$

$$\sigma'_y = \frac{N_y}{h}. \quad (16)$$

For axi-symmetric deformations of a cylinder, the circumferential membrane strain is

$$\epsilon_2 = \frac{w}{R}, \quad (17)$$

and if there is no axial prestress, then the axial membrane strain is due only to the Poisson effect

$$\epsilon_1 = -\nu\epsilon_2 . \quad (18)$$

The strains due to axi-symmetric bending vary through the shell and are zero at the middle surface ( $z = 0$ ), increase linearly with distance  $z$  from the middle surface, and are proportional to the *change* in curvature of the shell. In the present case, there are two principle curvatures  $\kappa_1$  and  $\kappa_2$  along the directions  $(x, y)$  and the changes in curvature due to bending deformations are denoted  $(\chi_1, \chi_2)$ . The changes in curvature  $\chi$  and the membrane stiffness  $D = Eh^3/(12(1 - \nu^2))$  result in axisymmetric moments  $M_x$  and  $M_y$  that create through-wall bending stress and strains. Note that these are distinct from the pipe beam bending mode that results due to the asymmetric moments at the end of the pipe. Beam bending will be manifested as in-plane stretching that varies linearly with distance from the pipe centerline. Shell bending is manifested as bending stains that vary linearly from the mid-surface of the pipe shell. The shell bending moments are related to changes in shell curvature by

$$M_x = \frac{Eh^3}{12(1 - \nu^2)} (\chi_1 + \nu\chi_2) , \quad (19)$$

$$M_y = \frac{Eh^3}{12(1 - \nu^2)} (\chi_2 + \nu\chi_1) . \quad (20)$$

Applying Kirchhoff's assumption that material lines remain straight and normal to the mid-plane, the stresses  $\sigma''$  created by the moments  $M$  are

$$\sigma_x'' = z \frac{E}{1 - \nu^2} (\chi_1 + \nu\chi_2) , \quad (21)$$

$$\sigma_y'' = z \frac{E}{1 - \nu^2} (\chi_2 + \nu\chi_1) . \quad (22)$$

The extreme values of bending stress occurs at the outer fibers  $z = \pm h/2$  and are given by

$$\sigma_{x,max}'' = \pm \frac{6M_x}{h^2} , \quad (23)$$

$$\sigma_{y,max}'' = \pm \frac{6M_y}{h^2} . \quad (24)$$

Superposing the stresses  $\sigma'$  from stretching and  $\sigma''$  from bending, we have the total stress field within the pipe due to axisymmetric deformation

$$\sigma_x = \frac{E}{1 - \nu^2} [\epsilon_1 + \nu\epsilon_2 + z (\chi_1 + \nu\chi_2)] , \quad (25)$$

$$\sigma_y = \frac{E}{1 - \nu^2} [\epsilon_2 + \nu\epsilon_1 + z (\chi_2 + \nu\chi_1)] . \quad (26)$$

At the outermost fibers of the cylinder,  $z = \pm h/2$ , we find the extreme value of the bending stress contribution. Focusing on the outside surface where the measurements were made in the present tests, we have

$$\sigma_x = \frac{E}{1 - \nu^2} \left[ \epsilon_1 + \frac{h}{2} \chi_1 + \nu \left( \epsilon_2 + \frac{h}{2} \chi_2 \right) \right], \quad (27)$$

$$\sigma_y = \frac{E}{1 - \nu^2} \left[ \epsilon_2 + \frac{h}{2} \chi_2 + \nu \left( \epsilon_1 + \frac{h}{2} \chi_1 \right) \right]. \quad (28)$$

Comparing this with Hooke's law evaluated at the outer surface under the plane stress approximation, (3) and (4), we find that the strains measured on the surface are made up of the sum of the membrane and bending strains

$$\epsilon_x = \epsilon_1 + \frac{h}{2} \chi_1, \quad (29)$$

$$\epsilon_\theta = \epsilon_2 + \frac{h}{2} \chi_2. \quad (30)$$

The changes in curvature can be computed from the geometry of axi-symmetric deformation. The principal directions are  $(x, y)$  and we can compute the corresponding principal curvatures  $\kappa$  as the reciprocal of radius of curvature of the curves formed by the intersection of the pipe mid-surface with the coordinate planes as shown in Fig. 31. Initially the pipe is flat in the  $x$  (axial) direction so that the curvature change is just the curvature associated with the deformation  $w(x, t)$

$$\chi_1 = -\frac{\partial^2 w}{\partial x^2} \bigg/ \left[ 1 + \left( \frac{\partial w}{\partial x} \right)^2 \right]^{3/2}, \quad (31)$$

which is by the usual approximation

$$\chi_1 \approx -\frac{\partial^2 w}{\partial x^2}. \quad (32)$$

The initial radius of curvature in the  $y$  (circumferential) direction is  $R$  and under deformation that changes to  $R + w$  so that the change in curvature in the  $y$  direction is

$$\chi_2 = \frac{1}{R + w} - \frac{1}{R} \quad (33)$$

$$\approx -\frac{w}{R^2} \quad (34)$$

The change in curvature  $\chi_2$  is usually neglected since it is much smaller than  $\chi_1$  for practical piping systems.

The final result is that for an axi-symmetric deformation  $w(x)$ , the surface strains are

given in terms of the deformation function as

$$\epsilon_x = -\nu \frac{w}{R} + \frac{h}{2} \left( -\frac{\partial^2 w}{\partial x^2} \right), \quad (35)$$

$$\epsilon_\theta = \frac{w}{R} + \frac{h}{2} \left( -\frac{w}{R^2} \right). \quad (36)$$

If the deformations are spatially periodic  $w(x) = w_o \cos(kx)$  (this is the case for models of detonation-induced deformation, see subsequent discussion), then the ratio of axial to hoop strains will be

$$\frac{\epsilon_x}{\epsilon_\theta} = \frac{\frac{1}{2}hRk^2 - \nu}{1 - \frac{h}{2R}}, \quad (37)$$

and the first term in the denominator can be written in terms of the shell bending length  $\ell_b$  and wavelength  $\lambda = 2\pi/k$

$$= \frac{2\pi^2 \sqrt{3(1-\nu^2)} \frac{\ell_b^2}{\lambda^2} - \nu}{1 - \frac{h}{2R}}. \quad (38)$$

The shows that the contribution of bending to axial strain is proportional to  $\lambda^{-2}$  so we would expect the higher frequency (shorter wavelength) deformations to have much greater contributions to axial strain than the lower frequency (longer wavelength) deformations. Assuming that  $h/2R \ll 1$ , the axial strains will the same size as the hoop strains when

$$\lambda = \left[ \frac{2\pi^2 \sqrt{3(1-\nu^2)}}{1+\nu} \right]^{1/2} \ell_b. \quad (39)$$

For  $\nu = 0.3$ , this occurs when  $\lambda \approx 4.4\ell_b$ . For 2-in Schedule 40 pipe,  $h/2R = .07$  and  $\ell_b = 8.2$  mm (Table 24) so that the bending strain is comparable to the hoop strain when the flexural wavelength is  $\lambda \sim 35$  mm. As discussed subsequently, the flexural disturbance wavelength is about 74 mm behind the detonation front and 18 mm ahead of the front. So we would expect high (relative to the hoop) amplitude axial strains just of the wavefront except that those frequencies are probably too high to be measured with the instrumentation used in the present testing. The axial strains behind the wavefront should also be significant but not as large in relative amplitude. If there are interference effects that reduce the effective wavelength, then we would expect to observe large amplitude axial strains. This would clearly be possible near bends, tees, and reflecting ends and perhaps even for propagating detonations due to stress wave propagation within the pipe wall.

**Measurements vs. FEM Simulations of Strains** The finite element method (FEM) simulations of Ligon (2009a) using the ANSYS code are compared with the experimental for the initial detonation arrival at gage location S4/S5 and S13/S14 in see Fig. 32. The signals downstream of the bend (S13/S14) contain strain components (mainly axial) that are generated by propagation through the bend. At long times, the signals are a superposition of incident detonation and reflected shock signals as well as the bending and axial strains created by the detonation and shock propagation through the bend. For this reason, we focus on the early portion of the S4/S5 signal which should be due only to detonation propagation.

The FEM simulations upstream of the bend do not appear to correctly capture either the qualitative or quantitative behavior of the high-frequency components of the axial signal S5. Ahead of the detonation front, the simulations of S5 show a compressive precursor step load and after the detonation front show a high frequency oscillatory axial strain which is all negative. The precursor is not visible in the measurements and the signal just after the front is alternating positive and negative and with a much higher peak strain than the simulations. The low frequency behavior of the axial strains appears to be much more appropriately simulated, with both qualitative and quantitative agreement.

The hoop strains S4 have the correct quantitative high and low frequency behavior but the simulation peak magnitude is about 25% lower than the measured values. The agreement between simulation and measurement for axial strains is better at the location S13/S14 downstream of the bend. However, at this location, the axial strain has significant components other than induced by the detonation.

We conclude that for hoop strains and low frequency axial strains, the FEM model used in Ligon (2009a) gives reasonable results but the peak hoop strains are under-predicted by about 25%. There are substantial qualitative and quantitative differences in the high-frequency components of axial strain between the FEM results and measurements. Possible explanations include insufficient spatial resolution in the axial direction or the use of a single shell element in the FEM. The shell elements were about 17.8 mm (0.7 in) in length, which can be compared with the shell bending length of 8.2 mm or the flexural wavelength of 72 mm. Based on these dimensions, the elements were not long enough to resolve the bending response and the flexural waves were rather coarsely resolved. Previous experience (Chao, 2004, Karnesky, 2010) in our laboratory indicates the much higher resolution in both the radial and axial directions is needed to properly resolve the motion induced in thin-wall tubes to detonations. The strain gages used in the experiment have a finite spatial extent (4-6 mm) and average over an axial distance that is a substantial fraction of the pipe wall bending length. Although the measurement system recorded data at very high frequencies, the strain gage signal conditioners limited the frequency response to less than 150 kHz so that the high-frequency axial precursor signals (discussed below) were completely attenuated.

High-frequency, large amplitude oscillations of longitudinal strain were also observed in the SwRI testing as discussed in Section 6.2.2.3 of Lachmann and Minichiello (2010). These strains are attributed to through-wall bending stress (Appendix C Lachmann and Minichiello, 2010). In some cases, these strains, as well as the hoop strains, significantly exceed 0.002 with alternating tension/compression cycles, indicating that fatigue may be of concern. It is argued (Section 6.4.3 Lachmann and Minichiello, 2010) that “Shakedown” (Section 3.7 Suresh, 1998) occurs with localized residual stresses developing to prevent net plastic deformation. This would explain the lack of net strain offset although the testing

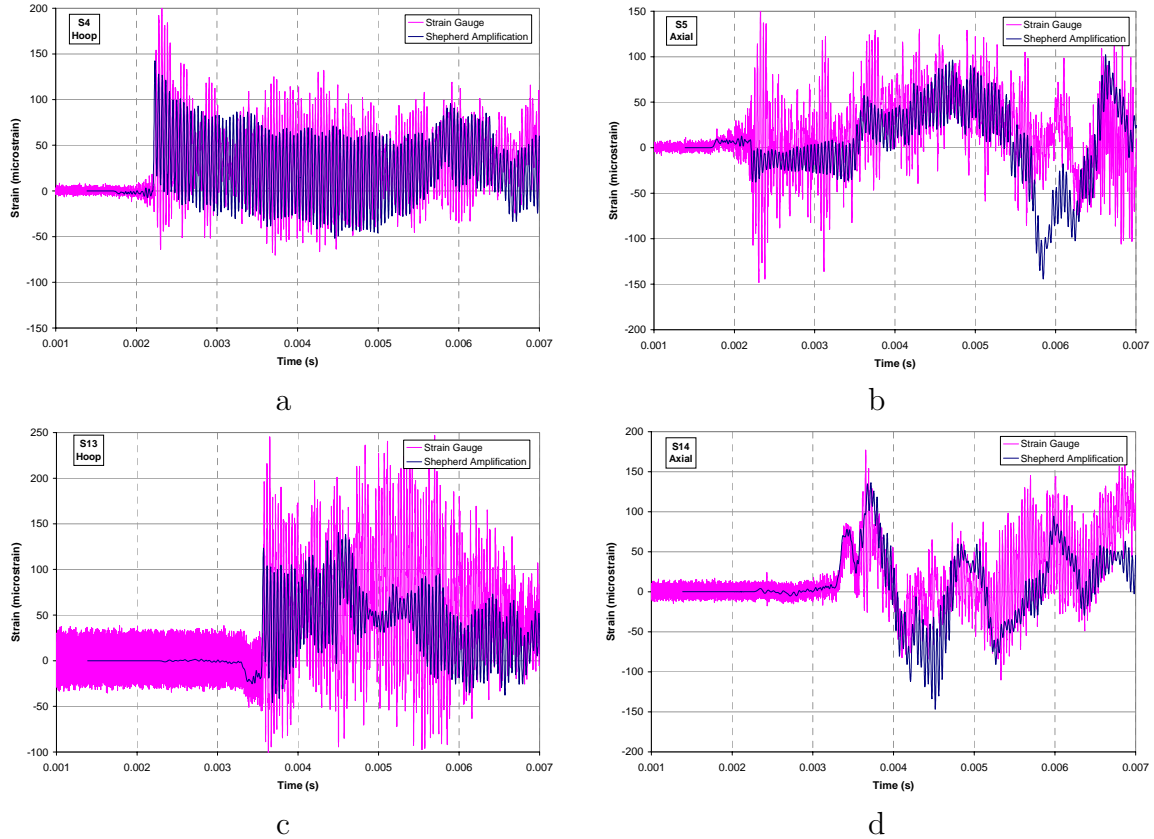


Figure 32: Comparison (Ligon, 2009a) of FEM (ANSYS) simulation of ES1 shot 3 and experimental data for a) strain gage S4 (hoop) and b) S5 (axial) as well as c) S13 (hoop) and d) S14 (axial).

shows peak axial strains as high as 0.005. An analytical solution of static shell response to a localized ring loading is presented in Appendix C of Lachmann and Minichiello (2010) as motivation for how these high bending stresses and resulting axial strains can come about. Although these explanations are plausible, they are clearly identified as speculative. At this time, we have an incomplete understanding and inability to quantitatively model the high-frequency axial strains and estimate the consequences in terms of fatigue.

**Shell Model and Estimate of Bending Strains** The simplest model of detonation-induced vibration is the infinite-tube modeled as a thin shell without rotatory inertia or transverse shear effects (Chapter 4 of Part I Beltman and Shepherd, 1998). The model discriminates between solution regimes depending on the magnitude of the detonation (or shock) speed relative to the possible wave speeds in the shell. The solution of interest in the present case is for detonations propagating faster than the first critical speed  $V_{c0} = 1421$  m/s but slower than the modified shear wave speed  $V_{c1} = 2763$  m/s, Table 25. The solution is divided into two portions, one ahead of the detonation front and one behind. For the present purposes of just comparing signals near the detonation front, we can neglect the

decay of the pressure due to the expansion and treat the load as a jump in pressure (ideal shock wave with no decay) moving with speed  $V$  and located at  $x = Vt$ . In that case, the solution (Beltman and Shepherd, 1998) for radial deformation  $w$  is given by

$$w = \frac{\Delta PR^2}{Eh} \left\{ 1 + \frac{m_2^2}{m_1^2 - m_2^2} \cos \left[ m_1 \frac{\sqrt{12}}{h} (x - Vt) \right] \right\} \quad x < Vt \quad (40)$$

behind the wave front and

$$w = \frac{\Delta PR^2}{Eh} \left\{ \frac{m_1^2}{m_1^2 - m_2^2} \cos \left[ m_2 \frac{\sqrt{12}}{h} (x - Vt) \right] \right\} \quad x > Vt, \quad (41)$$

ahead of the wave front. The quantities  $m_1$  and  $m_2$  are solutions of the dispersion relation. If we neglect shear deformation and rotary inertia, the solution can be obtained analytically.

$$m_2 = \frac{1}{2} \left[ \sqrt{\left(\frac{V}{V_{c3}}\right)^2 + \left(\frac{V_{c0}}{V_{c3}}\right)^2} \mp \sqrt{\left(\frac{V}{V_{c3}}\right)^2 - \left(\frac{V_{c0}}{V_{c3}}\right)^2} \right]. \quad (42)$$

If shear deformation and rotary inertia are included, the dispersion relation solution is not so simply expressed but the roots can be obtained by the straightforward solution of a quadratic equation (Chapter 5 of Part I Beltman and Shepherd, 1998). The smaller of the two roots is essentially unchanged but the larger root is substantially different since inertia effects and shear are significant at high frequency. The dynamic load factor is

$$\Phi = 1 + \frac{m_2^2}{m_2^2 - m_1^2}, \quad (43)$$

and the axial membrane strain is

$$\frac{\partial u}{\partial x} = -\frac{\nu}{1 - (V/V_{c3})^2} \frac{w}{R}. \quad (44)$$

The result is close to but not identical to the static relationship  $\epsilon_1 = -\nu w/R$  given above. The modification accounts for the axial wave dynamics and reduces to the static result in the limit of an incompressible shell  $V_{c3} \gg V$ . The theory does include a bending contribution to the force balance but the contribution of bending to measured axial strain does not appear to have been discussed in previous examinations of this model. We can include the effects of bending by computing the strains using the full shell theory results (29) and (30) with the deformation  $w$  described by this approximate solution.

The solution including shear deformation and rotary inertia based on the Timoshenko formulation includes an additional contribution to the radial displacement and includes as an independent variable the rotation  $\psi_x$  of the material lines originally perpendicular to the shell axis. The dispersion relation and computation of the shear and bending contributions is described in Chapter 5, Part I of Beltman and Shepherd (1998). The strain at the outer

fibers of the pipe due to hoop and axial stretching as well as hoop bending is computed as described previously using the radial deformation  $w(x)$ . The contribution of axial bending to the axial strain at the outer fibers of the pipe is computed from the spatial gradient of the rotation as  $h/2\partial\psi_x/\partial x$  instead of from the change in curvature as in the last term of (29). The dynamic load factor is close to but not identical to the simplest theory since there are additional contributions of bending to the radial deflection.

The solutions for the shell models are traveling waves with wave number  $k$  and angular frequency  $\omega$ , moving with phase velocity  $V = \omega/k$ , the speed of the loading wave. Writing the argument of the cosine as  $kx - \omega t$  we have

$$k_i = m_i \frac{\sqrt{12}}{h}, \quad (45)$$

and the corresponding wavelength is

$$\lambda_i = \frac{2\pi}{k_i}, \quad (46)$$

$$= \frac{2\pi h}{m_i \sqrt{12}}. \quad (47)$$

The angular frequency and period are

$$\omega_i = V k_i, \quad (48)$$

$$f_i = \frac{\omega_i}{2\pi}, \quad (49)$$

$$T_i = \frac{\lambda_i}{V}. \quad (50)$$

The parameters of the model including shear deformation and rotary inertia have been evaluated for the present tests as well as the thin-tube results of Karnesky (2010) and are given in Table 10.

Note that the frequency of oscillations  $f_2$  behind the front are close to the breathing mode frequency  $f_{hoop}$  computed for a cylindrical ring (see Appendix B) and that the wavelength  $\lambda_2 \approx V/f_1$ . The frequencies and wavelengths ahead of the detonation front are substantially higher than behind the front but the amplitudes of the radial deformations are substantially smaller. In the case of the 2-in pipe, the frequency of the precursor oscillations is almost 200 kHz and the wavelength (10 mm) is comparable to length of the strain gages (3–6 mm) so that the axial precursor strains cannot be resolved in the present experiments.

The strains on the outer surface of the pipe can be computed using the solutions (41) and (40) with the shell expressions (35 and (35. Behind the wave front ( $x < Vt$ ) we have

$$w = R\epsilon_s [1 + (\Phi - 1) \cos(kx - \omega t)], \quad (51)$$

Table 10: Parameters for the thin-shell model of structural response to a moving load simulating a detonation for two cases. Parameters were computed using the solution including shear deformation and rotary inertia.

2-in Schedule 40 SS pipe, this study		
$m_1$	0.09505	
$m_2$	0.6652	
$f_1$	28.0	kHz
$f_2$	196.	kHz
$\lambda_1$	74.6	mm
$\lambda_2$	10.7	mm
$\Phi$	1.9055	
$\epsilon_s$	94.1	$\mu$ strain
$\sigma_{vM}$	34	(MPa)
Thin-wall steel tubing, Karnesky		
$m_1$	0.0147	
$m_2$	0.808	
$f_1$	12.7	kHz
$f_2$	69.6	kHz
$\lambda_1$	185	mm
$\lambda_2$	3.36	mm
$\Phi$	1.9776	
$\epsilon_s$	314	$\mu$ strain
$\sigma_{vM}$	132	(MPa)

where the effective static hoop strain for the ring model is

$$\epsilon_s = \frac{\Delta PR}{Eh} . \quad (52)$$

and the bending contribution to the axial strain is

$$-\frac{h}{2} \frac{\partial^2 w}{\partial x^2} = \frac{R h k^2}{2} \epsilon_s (\Phi - 1) \cos(kx - \omega t) . \quad (53)$$

The strain components are

$$\epsilon_\theta = \epsilon_s [1 + (\Phi - 1) \cos(kx - \omega t)] \left(1 - \frac{h}{2R}\right) , \quad (54)$$

and

$$\epsilon_x = \frac{Rhk^2}{2}\epsilon_s(\Phi - 1)\cos(kx - \omega t) - \nu\epsilon_s[1 + (\Phi - 1)\cos(kx - \omega t)] . \quad (55)$$

The wave number  $k$  and frequency  $\omega$  are computed using the root  $m_1$  behind the front.

Ahead<sup>2</sup> of the wave front ( $x > Vt$ ) we have

$$w = R\epsilon_s(\Phi - 2)\cos(kx - \omega t) , \quad (56)$$

and the bending contribution to the axial strain is

$$-\frac{h}{2}\frac{\partial^2 w}{\partial x^2} = \frac{Rhk^2}{2}\epsilon_s(\Phi - 2)\cos(kx - \omega t) . \quad (57)$$

The strain components are

$$\epsilon_\theta = \epsilon_s(\Phi - 2)\cos(kx - \omega t)\left(1 - \frac{h}{2R}\right) , \quad (58)$$

and

$$\epsilon_x = \epsilon_s\left(\frac{Rhk^2}{2} - \nu\right)(\Phi - 2)\cos(kx - \omega t) . \quad (59)$$

The wave number  $k$  and frequency  $\omega$  are computed using the root  $m_2$  ahead of the front. Since  $\Phi$  is only slightly higher than 2 for  $V$  sufficiently higher than  $V_{c0}$  (see Table 10), the case in the present study, the disturbances ahead of the wave front are substantially smaller than those behind, which is observed in the experiment. Only close to the critical speed  $V \sim V_{c0}$  are significant amplitudes of the precursor waves observed, see [Beltman and Shepherd \(2002\)](#).

The expressions can be simplified for the deformations behind the wave front by using the approximate relationship for the frequency  $f_2 \approx f_{hoop}$

$$f_{hoop} = \frac{1}{2\pi R}\sqrt{\frac{E}{\rho(1 - \nu^2)}} , \quad (60)$$

---

<sup>2</sup>From a physical viewpoint, there will be no disturbance in front of the bar wave signal ( $x < V_{c3}t$ ) but mathematically there is no restriction in the model solution since this is for wave propagation over a long (effectively infinite) distance and time.

and wavelength  $\lambda = V/f_{hoop}$  to compute the wavenumber as

$$k = \frac{2\pi}{\lambda}, \quad (61)$$

$$\approx \frac{1}{RV} \sqrt{\frac{E}{\rho(1-\nu^2)}}, \quad (62)$$

$$= \frac{V_{c3}}{RV}. \quad (63)$$

Using a value of  $\Phi = 2$ , the ratio of the maximum value of the axial bending to hoop strain components is

$$\frac{\epsilon_{x,bend}}{\epsilon_{\theta,hoop}} \approx \frac{h}{4R} \left( \frac{V_{c3}}{V} \right)^2 \quad (64)$$

which is 0.18 for 2-in schedule 40 pipe and hydrogen/nitrous oxide detonations. As discussed below, this is not quantitatively correct but does predict that the thicker the shell and the slower the detonation, the greater the contribution of bending to axial strain relative to hoop strain.

The predictions of the shell model for the hydrogen/nitrous oxide detonations in 2-in pipe used in the present tests are shown Fig. 33 and 34. The inclusion of bending is quite significant for axial strain prediction. Since the magnitude of the axial bending and Poisson effects are comparable and out of phase, the oscillations in axial strain almost exactly cancel so that the net result is a constant compressional strain behind the detonation front. Comparison with the experimental results such as Fig. 26 shows that the axial predictions are clearly at variance with the observations that show very large amplitude oscillations. On the other hand, the hoop predictions are very reasonable and agree quantitatively and qualitatively with the observations. The peak von Mises stress is predicted to be about 34 MPa, smaller than the observed bounding value of 45 MPa. The difference can be attributed to the large-amplitude axial strains that occur just behind the detonation front.

The reason for the discrepancies between model results for axial strain and measurement may be due to the very simplified nature of the shell model, which is not an exact solution for the deformations of the pipe. A number of approximations have been introduced in order to solve the problem analytically, most importantly assuming the motion is axi-symmetric, using beam models of the shell motion, and neglecting the transient development that occurs in the physical problem. Previous studies (Beltman and Shepherd, 2002) have shown that in order to get reasonable comparisons for radial strains in thick tubes it is important carry out transient finite element solutions, however, axial strains were not examined critically by Beltman and Shepherd (2002). Note that although the predictions ahead of the wave front are substantially affected by including shear deformation and rotary inertia, the predictions for axial and hoop strains behind the wave front do not depend strongly on these effects. Comparisons (not shown here) indicate that Timoshenko model does not appear to be significantly more accurate for the region behind the detonation front than the Euler-Bernoulli model.

Any phase shift and amplitude differences between the axial and radial deformations will reduce or eliminate the cancelation of the bending and Poisson effects. Examination of Fig. 28 reveals that there are phase differences between the measured hoop and axial strains. Such effects may exist in the full elastic solution to the deformation, which would include radial, axial and shear waves, transient development and potentially, nonlinear geometrical effects. To model these effects would require going beyond the previous simulations (Beltman and Shepherd, 2002) that have been based on linear elasticity and low-frequency approximations to the equations of motion. This will require using explicit, Lagrangian methods with highly resolved meshing such as used by Karnesky (2010) and Chao (2004). Another possibility is that the motion is not axisymmetric so that higher-order modes of the radial motion with circumferential variation may play a role. This would require a much more detailed model of the detonation initiation and stress wave development process than is possible with the diagnostic data available from the present testing.

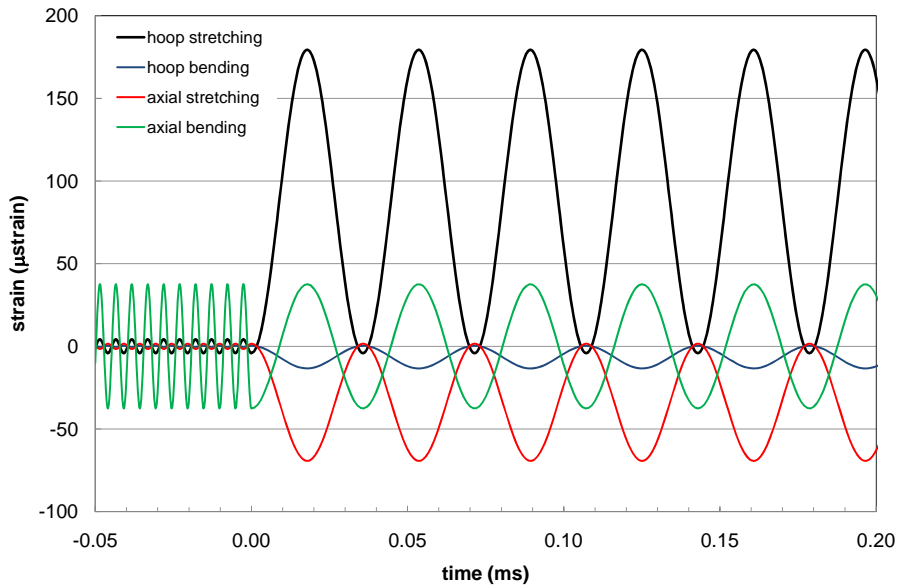
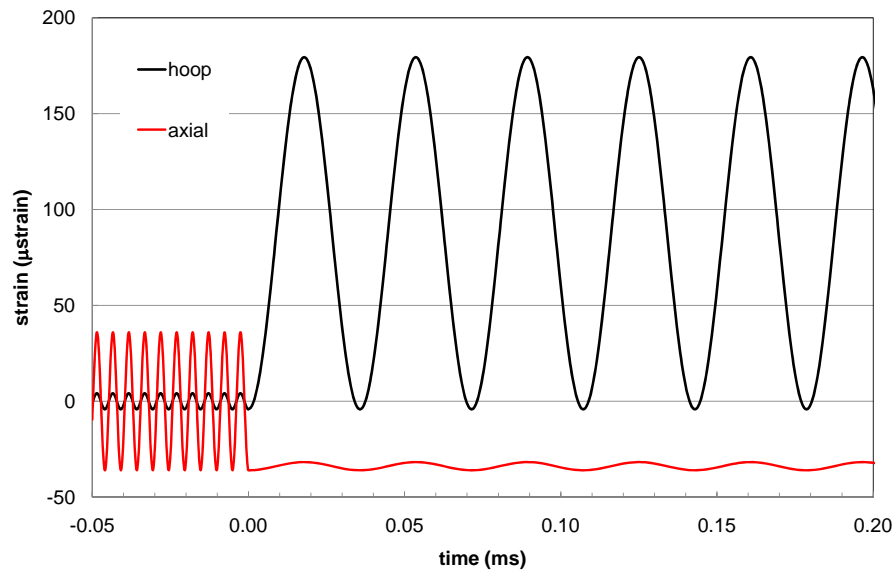
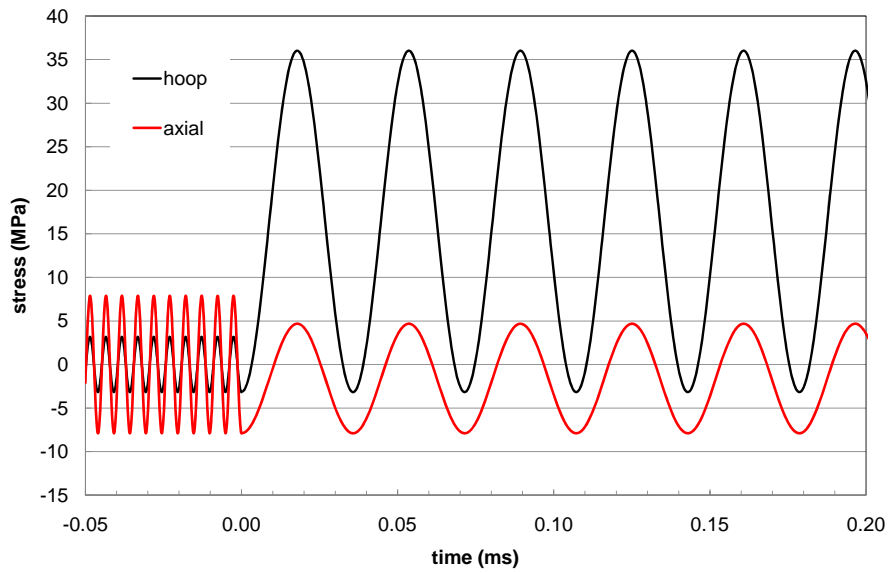


Figure 33: Simulation of 2-in pipe tests (ES1, TS1, SS1). Individual contributions to membrane stretching and bending to axial and hoop strains at outer fibers based on steady-state shock wave approximation including shear deformation and rotational inertia.



(a)



(b)

Figure 34: Simulation of 2-in pipe tests (ES1, TS1, SS1). Based on steady-state shock wave approximation including shear deformation and rotational inertia. a) hoop and axial strain. b) hoop and axial stress.

**Thin-tube results** The shell model results can be compared with the experiments by Karnesky (2010) with a thin-wall tube ( $R/h = 63.5/1.5 = 42.3$ ) for which bending stresses should be negligible. Fig. 35 shows the hoop and axial strain in a test with purely elastic motion. The measuring station is far enough from the reflecting end that the the first three cycles of the initial strain signal (until to 5.7 ms) is entirely due to the incident detonation wave propagation. As shown by the red line, after the arrival of the detonation (5.45 ms), the axial signal is consistent with the predictions of the membrane theory (Eq. 44) both qualitatively and quantitatively. Using the parameters for this tube, the relationship (44) between hoop and axial strain that has been used in this comparison is

$$\epsilon_{axial} = -0.36\epsilon_{hoop}$$

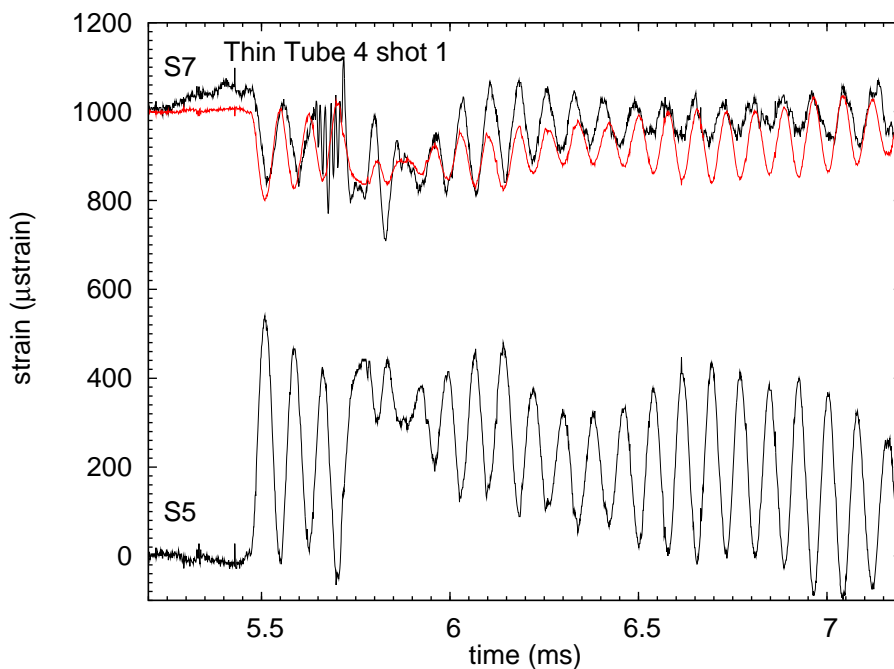


Figure 35: Hoop and axial strain gauges S5 and S7 for shot 1, tube 4 from Karnesky (2010). The red line is the hoop stress scaled with Eq. 44

The shell model (41 and 40) can be evaluated to give the contributions to the strains, Fig. 36. The hoop and axial strains as well as the hoop and axial stress are shown in Fig. 37. As anticipated, the contributions of bending to axial strain are small relative to the Poisson effect and the thin-shell model predictions are in excellent agreement (for the first three cycles) with the experimental results for both hoop and axial strains.

**Summary** Estimates of axial strains induced by axi-symmetric bending indicate that they will be significant for short wavelength motions induced by detonation propagation in thick-wall tubes or pipes. Detailed comparisons with experimental measurements in 2-in schedule

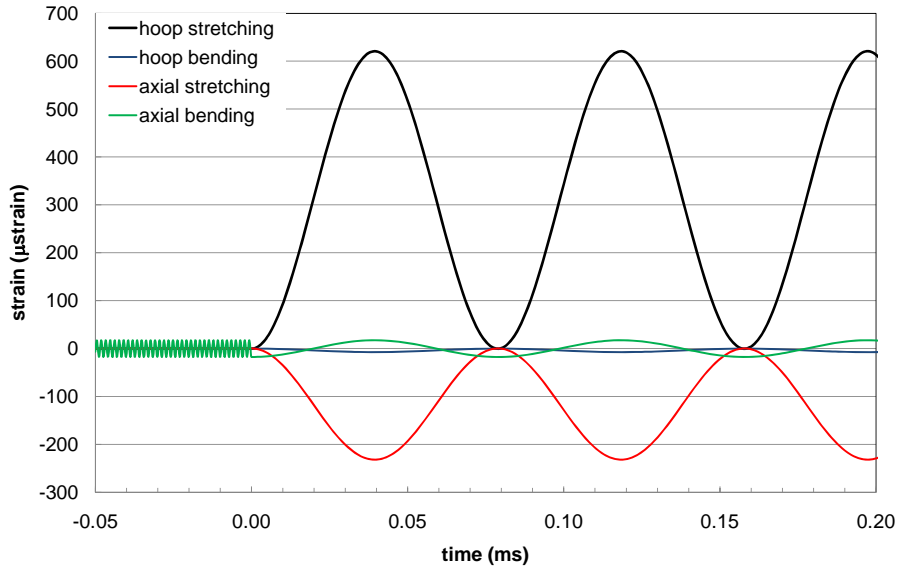
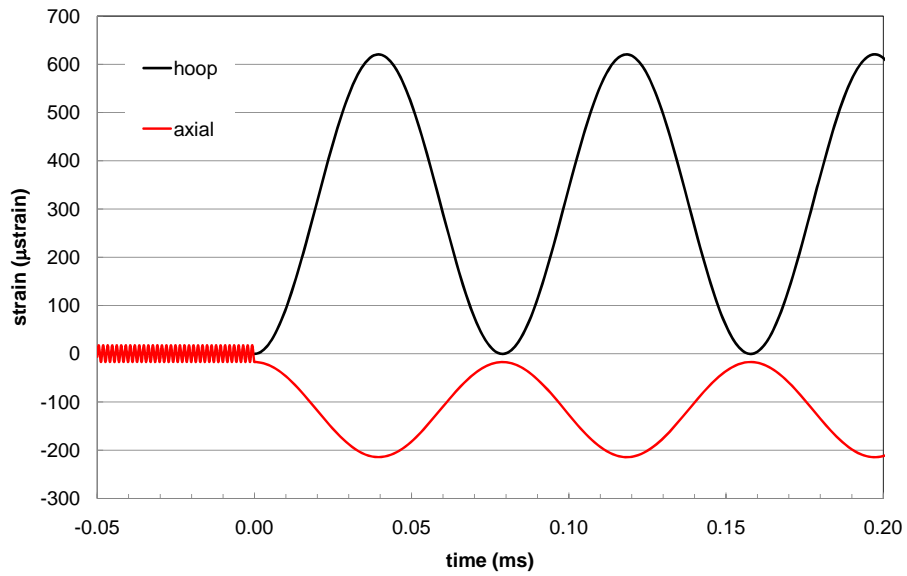
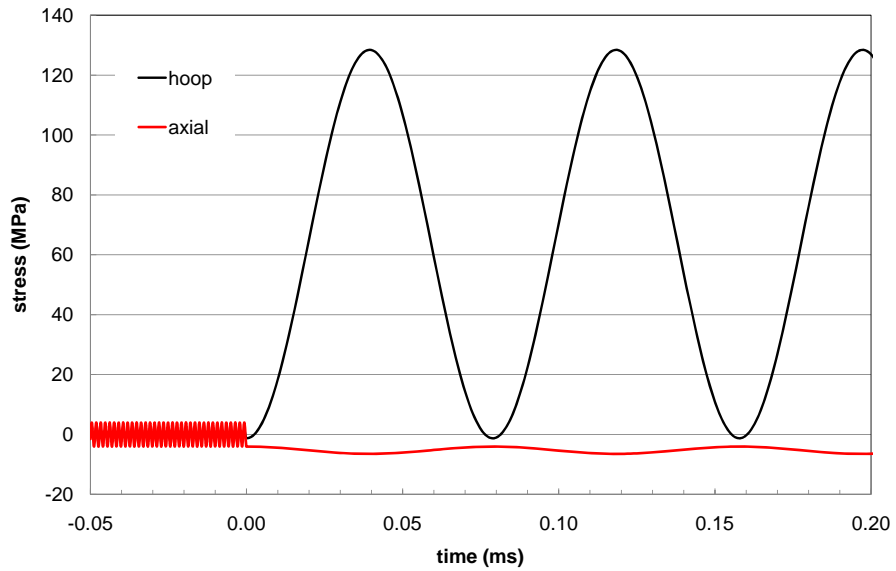


Figure 36: Simulation of the test shown in Fig. 35. Individual contributions to membrane stretching and bending to axial and hoop strains at outer fibers based on steady-state shock wave approximation including shear deformation and rotational inertia.

40 pipe show that the shell models of detonation response give quantitatively correct predictions for hoop strain but are qualitatively and quantitatively incorrect for axial strains near the detonation front. Comparisons with experimental measurements in a thin-wall tube show that the results of the shell model are accurate for both hoop and axial strains. We conclude that the shell approximations to stretching and bending are adequate for the thin tube with  $R/h \sim 43$  but not for the pipe with  $R/h \sim 7$ . The shell approximations for deformation through the thickness of the pipe appear to be the source of the discrepancies in modeling the Schedule 40 pipe. Higher-fidelity numerical simulations will be necessary in order to resolve this issue.



(a)



(b)

Figure 37: Simulation of the test shown in Fig. 35. a) hoop and axial strain b) hoop and axial stress.

### 5.3.4 DDT Pressures and Strains

Ten tests were carried out without a flame accelerating spiral at hydrogen concentrations between 10 and 30% to examine the structural effects of deflagration-to-detonation transition after a period of flame acceleration. The goals of these tests were to determine the transition distances, peak pressures, and strains created by the DDT event. Previous testing (Liang et al., 2006, Akbar et al., 1997, Pfahl et al., 1998, Kaneshige et al., 2000) with these mixtures was carried out in two other facilities located in our laboratory. Detonation initiation and propagation experiments were performed in the Galcit detonation tube or GDT (280 mm diameter, 7.3 m long) with a high-energy gaseous detonation initiator. Tests by Akbar et al. (1997), Pfahl et al. (1998), Kaneshige et al. (2000) were used to measure detonation cell widths but no structural measurements were carried out. Deflagration-to-detonation transitions studies by Liang et al. (2006) made structural measurements inside a 120 mm diameter, 1.2 m long thick-walled tube. The studies in the GDT demonstrated that detonations were possible with a hydrogen concentration as low as 5.7% in a sufficiently large-diameter tube with gaseous detonation initiation. However, the cell width measurements (Pfahl et al., 1998), imply that the detonation cell width  $\lambda$  increases rapidly with decreasing hydrogen concentration, and exceeds 50 mm for less than 10% hydrogen. Since it is difficult to initiate through DDT (Ciccarelli and Dorofeev, 2008) detonations with  $\lambda > D$ , the pipe inner diameter, we did not expect to be able to detonate mixtures with less than 10% in the present series of tests and even the 10% mixture would be marginal. For this reason, the present testing was limiting to the range 10 to 30% hydrogen. Over this range, the CJ detonation speed varies by 10% and the CJ pressure by less than 5% (see Table 11) so all structural effects can be attributed to the pressurization during the deflagration-to-detonation process (Ciccarelli and Dorofeev, 2008, Shepherd, 1992).

The distance  $L_{DDT}$  from the ignition location to the onset of detonation was bracketed by examining the pressure histories and is report in Table 11. Before transition, the pressure shows a series of small shock waves or a relatively smooth increase with a maximum pressure less than 1 MPa. Immediately after transition, the pressure shows a sharp front (rise time of 1–3  $\mu$ s) and a peak pressure of  $\geq 5$  MPa. Note that there is a substantial range of uncertainty ( 2 m) in the transition distance for the leanest mixture (15% H<sub>2</sub>) in which transition to detonation was observed. This is typical of transition distance data in smooth tubes for insensitive mixtures, which show substantial shot-to-shot fluctuations in transition distance. This variability is a consequence of the importance of natural instabilities in the turbulence generation in the flame acceleration and transition process. Without deliberate roughness on the tube walls, fluid dynamic and combustion instabilities are the key processes for generating the enhancement in flame area and burning rate. These processes are known to be subject to large fluctuations with experimental outcomes that are best described statistically. We don't have enough data to provided anything other than the bounds on the transition distances for the present experiments. Our observations of transition distance are consistent (Fig. 38) with those of the SwRI (SwRI, 2009) testing as analyzed in Ligon (2009b) and the study by Bollinger et al. (1962).

Comparison of peak strains and pressures with the reference shot 3 are shown in Fig. 39. Away from the reflecting end, the measured peak pressures are on the order of the reflected detonation pressure. Since the detonation waves resulting from DDT are overdriven, the

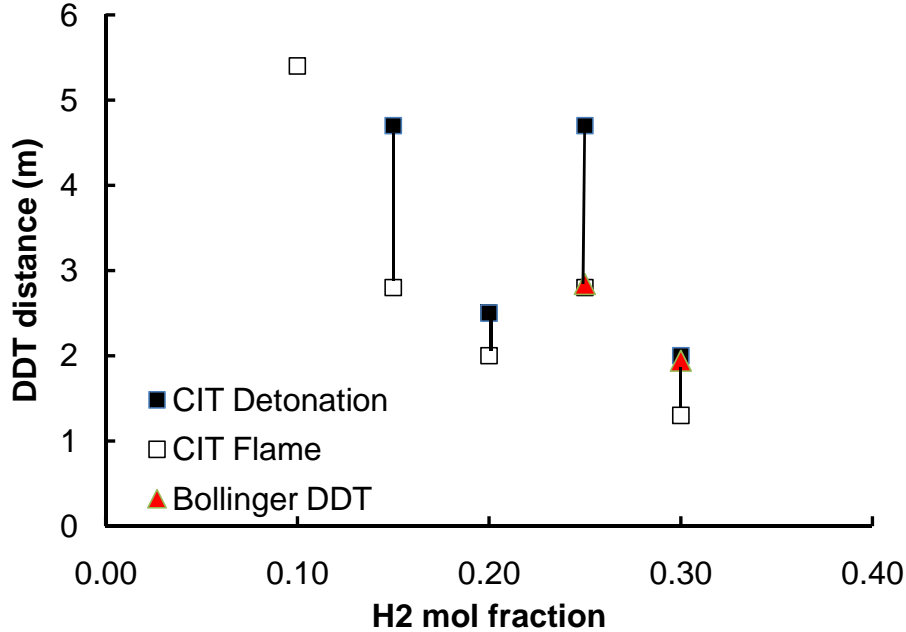


Figure 38: Comparison of bracketing values for transition from deflagration to detonation with previous data of [Bollinger et al. \(1962\)](#).

Table 11: Computed detonation properties of lean  $H_2-N_2O$  mixtures and observed distances  $L_{DDT}$  for the onset of detonation. The cell widths  $\lambda$  are estimates based on extrapolating the existing data [Pfahl et al. \(1998\)](#) using reaction zone length scaling.

Shots	$X_{H_2}$	$U_{CJ}$ (m/s)	$P_{CJ}$ (MPa)	$\Delta_i$ ( $\mu\text{m}$ )	$\lambda$ (mm)	$L_{DDT}$ (m)
ES1						
1, 2	0.30	2088.2	2.62	78.7	3 – 5	1.3–2
7, 11	0.25	2021.1	2.61	100.	4 – 6	1.3–2
8, 12	0.20	1956.0	2.59	140	6 – 9	2–2.5
9, 13	0.15	1891.9	2.56	220	9 – 13.5	2.8–4.7
10, 14	0.10	1827.7	2.51	755	32 – 48	>5.4

peak pressures due to detonation reflection are about a factor of two higher than the CJ case except for shot 9, which has a peak pressure of 32 MPa or about 5 times the CJ pressure. The mechanism for creating such high pressures is the “pressure-piling” effect of the compression associated with deflagration phase of DDT, discussed in [Shepherd \(1992\)](#) and the basis for the estimation method described as the PRC-DDT loading function by [Ahnert \(2006\)](#), [Ligon \(2009b\)](#). The peak strains for almost all cases except shot 9 are on the order of 500  $\mu\text{strain}$  or about twice the  $\Phi = 1$  value associated with reflected detonation. Shot 9 has a peak strain of about 1000  $\mu\text{strain}$  or about 4 times the reflected CJ value. Peak pressures and strains measured in these tests are consistent with earlier tests [Liang et al. \(2006\)](#) in a shorter tube. More recent results in longer tubes [Ligon \(2009b\)](#) show that even higher pressures and strains

can be obtained with longer run-up distances for the DDT event.

Examination of the pressure traces (Appendix J) for these tests shows that, as expected, decreasing the hydrogen concentration results in delaying transition. Two cases are shown in Fig. 40. Shot 9, 15% H<sub>2</sub>, is shown with an expanded vertical scale so that the peak pressure on the reflecting end gage is fully resolved. In shot 9, an overdriven detonation is observed at P7 after a series of weak pressure waves have traveled past P1-P6. The reflection of this overdriven detonation results in the very high value of the peak pressure on P8. The peak strains are observed on S16 (630  $\mu$ strain) and S13 (946  $\mu$ strain), hoop gages that are located closest to the reflecting end of the tube. The peak strain occurs near the start of the detonation wave induced hoop motion at 5.01 ms for gage S13 and 5.05 ms for gage S16, as shown in Fig. 41. This indicates that the mechanism of creating these high strain levels is the excitation of hoop modes by the overdriven detonation. Wave interference effects between the oscillations induced by the incident detonation and reflected shock are clearly seen on S16 but in this test, the peak strain is also close to the onset of oscillation with comparable but slightly lower peak values observed at later times.

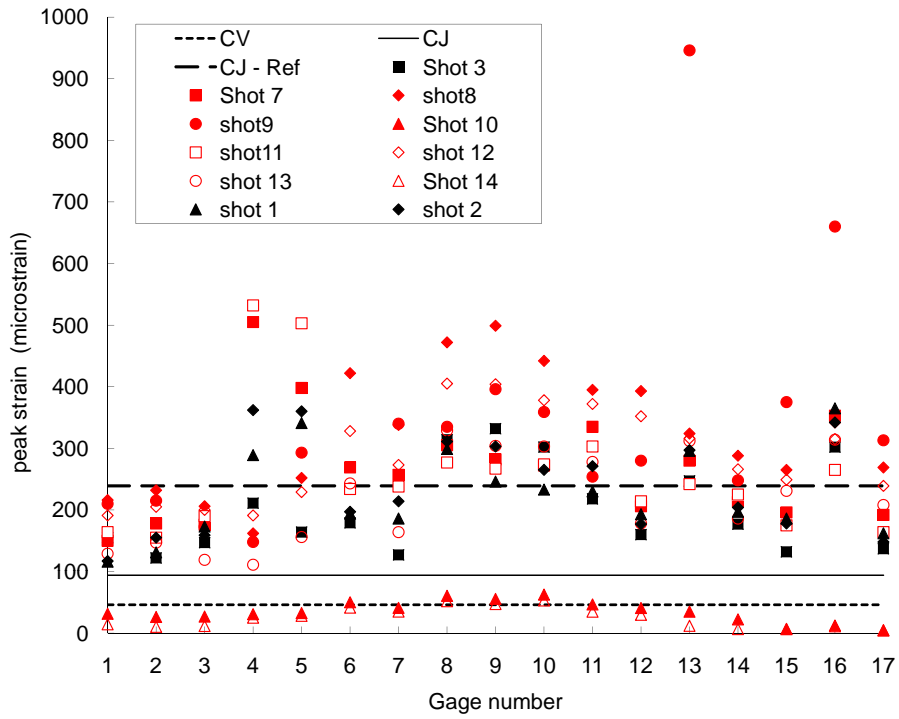
In shot 8, 20% H<sub>2</sub>, the transition event occurs closer to the ignition than in shot 9. Based on the pressure traces, the event occurs near P4, and the overdriven detonation resulting from DDT has decayed sufficiently that the peak reflected pressure on P8 is only about 10 MPa, one-third of the value observed in shot 9. On gages P1, P2 and P3, a series of weak compression waves characteristic of a deflagration are observed. The peak strains are observed at the bend on gages S8 (472  $\mu$ strain) and S9 (499  $\mu$ strain) and near the point of transition on gage S6 (422  $\mu$ strain). The values are only about 1/2 of those in shot 9 due to the smaller amount of deflagration-induced compression prior to DDT. As in shot 9, the peak strains occur when the hoop oscillations are first induced, which is at about 14.5-15 ms for shot 8, indicating that the overdriven detonation waves are the mechanism of creating these high strains.

**Deflagration** No detonation occurs in cases 10 and 14, this is consistent with previous observations showing that as the cell width approaches the tube diameter, transition is inhibited. Our results are also consistent with tests (Ligon, 2010) at SwRI with 2-in piping up to 150 ft long, transition to detonation was not observed for hydrogen concentrations less than 12%. The measured peak pressure rises (maximum of 0.3 MPa) are about 30% of the CV pressure rise of 1.1 MPa. The reduction of peak pressure from ideal value is due to heat transfer from the combustion products to the pipe. Experiments in a  $\sim$ 400 liter vessel (Krok and Shepherd, 1993) with spark ignition of a 10/90 H<sub>2</sub>/N<sub>2</sub>O mixture at an initial pressure of 0.05 MPa resulted in a propagating flame with a 360 ms rise to a peak pressure of 0.57 MPa, 90% of the computed peak pressure of 0.64 MPa. Note that the peak pressure in a deflagration scales linearly with the initial pressure and the 1993 tests were done with reduced initial pressure due to limitations of the apparatus. Increasing the initial pressure by a factor of two will result in a decrease in the flame thickness and a modest effect on the flame speed but ratio of peak pressure to the ideal thermodynamic value is relatively unaffected for most mixtures, for examples see Karnesky et al. (2004).

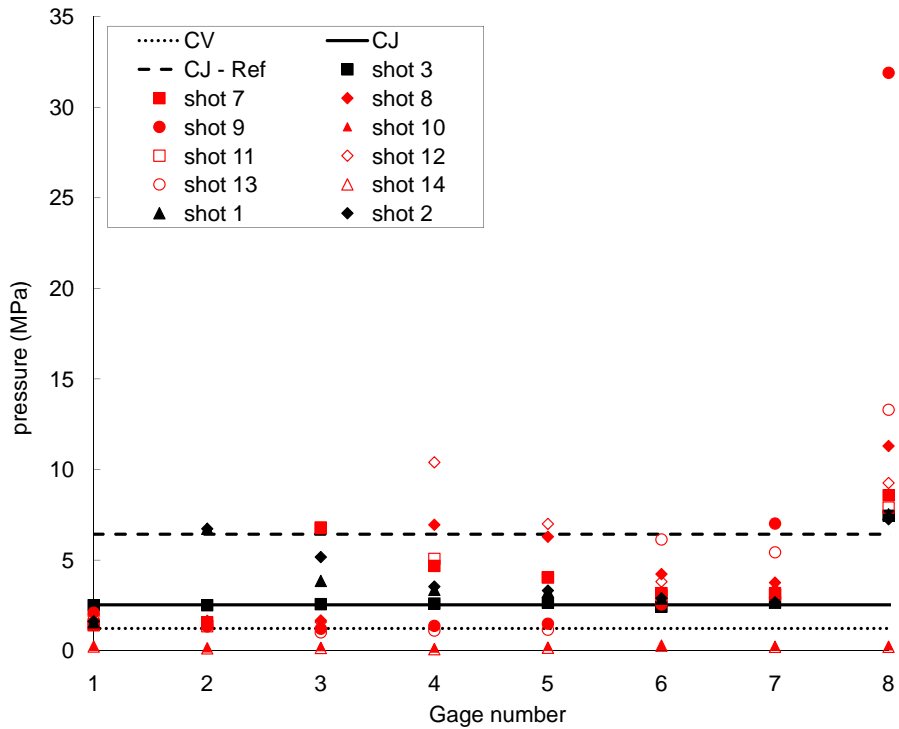
The pressure signals in shot 10 show a broad maximum between 250 and 450 ms although these signals appear to be contain substantial thermal artifacts (negative pressures).

Detonation at 10% H<sub>2</sub> has been observed in larger diameter tubes with stronger initiation sources (Akbar et al., 1997, Pfahl et al., 1998). To see if we could create a detonation at this condition, we installed the two-foot spiral downstream of the spark plug in shot 14. The initial stages of flame propagation in shot 14 were more rapid than in shot 10 with a broad maximum in pressure between 0 and 200 ms with thermal effects obviously setting in after 200 ms. A sharp pressure wave (shock) can be observed at the beginning of the pressure rise, Fig. 42 and reflections of this shock wave can be observed reverberating in the pipe, superimposed on the broad pressure rise associated with the accumulation of very small acoustic waves created by the deflagration process. Similar pressure rise characteristics were observed in the testing at SwRI (Ligon, 2010). The leading pressure wave is a shock with an amplitude of about 40 kPa, which corresponds to a Mach number of 1.16. Based on the ideal solution (Krok, 1991) of a planar steady flame in duct and an expansion ratio between 9 and 11, this corresponds to a flame speed of 100 m/s and a turbulent burning speed of 9-11 m/s. The existing data (Rodriguez, 2008) on laminar burning speeds for this mixture indicate that the laminar burning speeds are the order of 0.2 to 0.4 m/s. The maximum experimentally observed turbulent burning speeds are on the order of 10 times the laminar burning speed (Cicarelli and Dorofeev, 2008), suggesting that the laminar burning speed for the mixture in test 14 may be more on the order of 1 m/s.

The peak strains (50–60  $\mu$ strain) are on the order of or slightly larger than that predicted by the simple static estimate, 45  $\mu$ strain although a substantial portion of this is due to thermal stresses as discussed in Section 5.3.1. The peak strains are a maximum near the bend and decrease significantly as the anchored ends are approached, Fig. 42. The strains are devoid of any significant high frequency oscillations and rise slowly over the 500 ms recording time with peak values at the end of this period. Strain oscillations with a period of 100 Hz are observed which correspond to a higher-order bending mode or a radial-axial mode (Shepherd and Akbar, 2009, Table 1 and Appendix D). The time scale and distribution of the strain suggest that they are primarily due to thermal expansion-induced deformation of the bend.

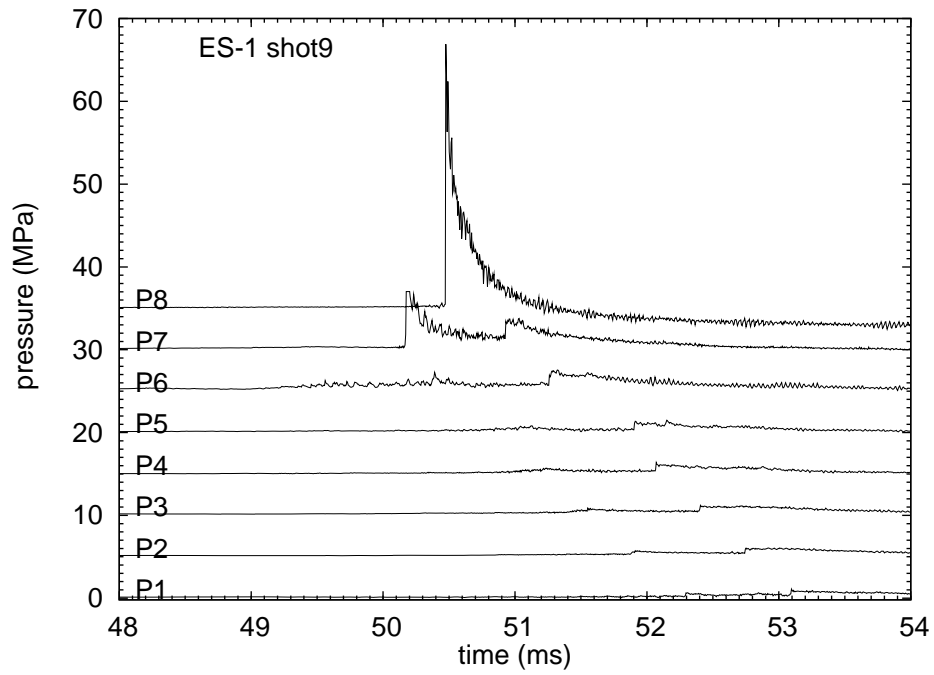


a

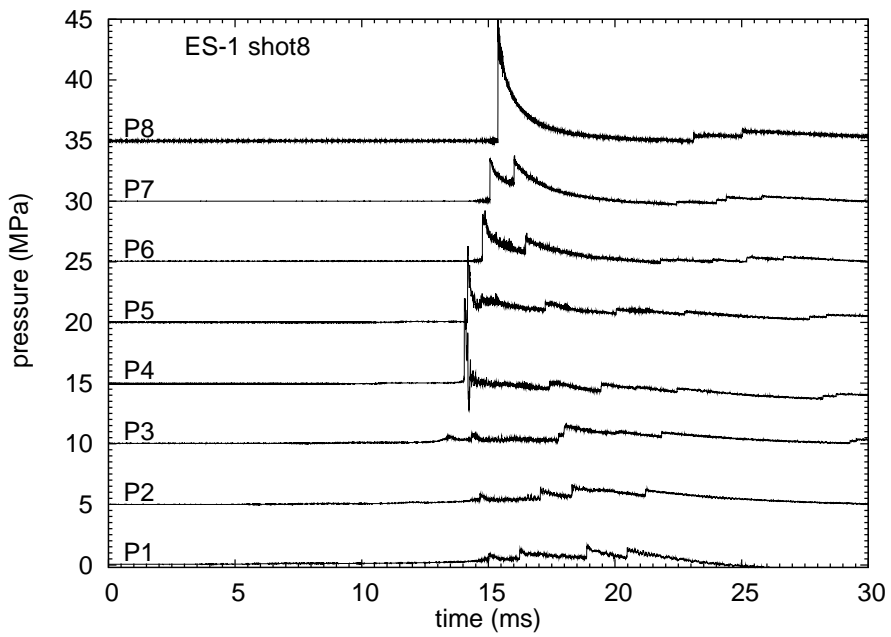


b

Figure 39: Comparison of peak a) strain and b) pressure for reference test 3 and all tests involving a DDT event without water present. The reference pressures and strains ( $\Phi = 1$ , 30/70  $H_2/N_2O$ ) are discussed in Section 4.5.



a



b

Figure 40: Pressure traces for two DDT tests. a) shot 9 and b) shot 8.

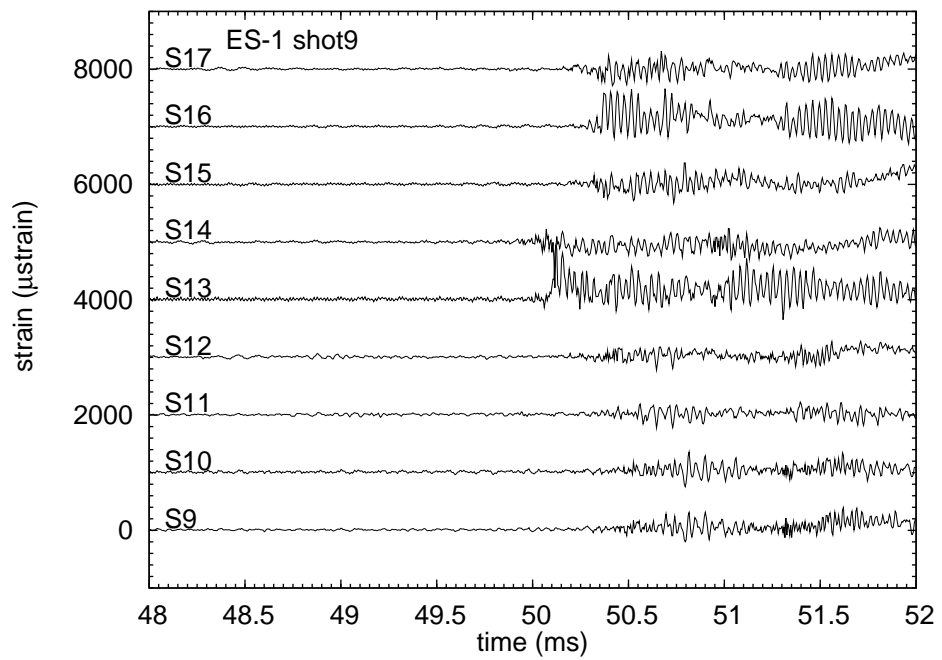


Figure 41: Close-up of strains in vertical leg of ES1 during shot 9. Data has been filtered to remove high frequency noise.

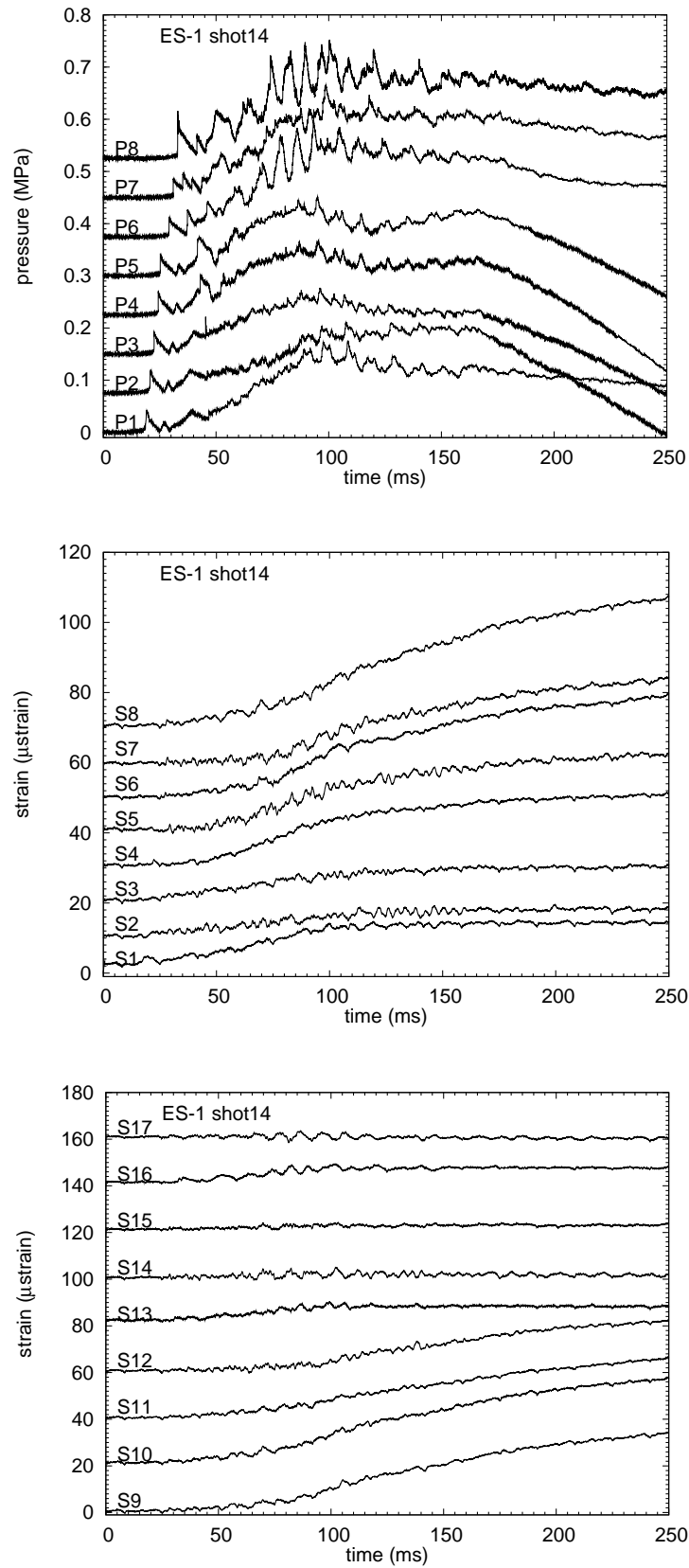


Figure 42: Pressure and strains measured during the deflagration observed in ES1 shot 14. Data has been filtered to remove high frequency noise.

### 5.3.5 Bend, Cantilever, and Reflecting End forces

Several sets of experiments (shots 25-35) were carried out with the goal of measuring the forces on the piping system and supports due to detonation propagation around the bend and reflecting from the closed end of the tube, Fig. 43. Although instructive, these efforts did not provide direct force measurements. Fortunately, the force on the 90-degree bend of ES1 created bar waves that could be detected by the longitudinal strain gages and as discussed in the introduction to this Section and Fig. 23. The bar waves are a unique signature of the forces generated by detonation waves propagating around a bend and can be used as a diagnostic for inferring forces in experiments as well as for validating pressure and force models used in finite element simulations. In this sense, all of the ES1 tests produced useful data on the bend forces although tests 3,4, 23, and 24 were most extensively analyzed in terms of the bar wave propagation.

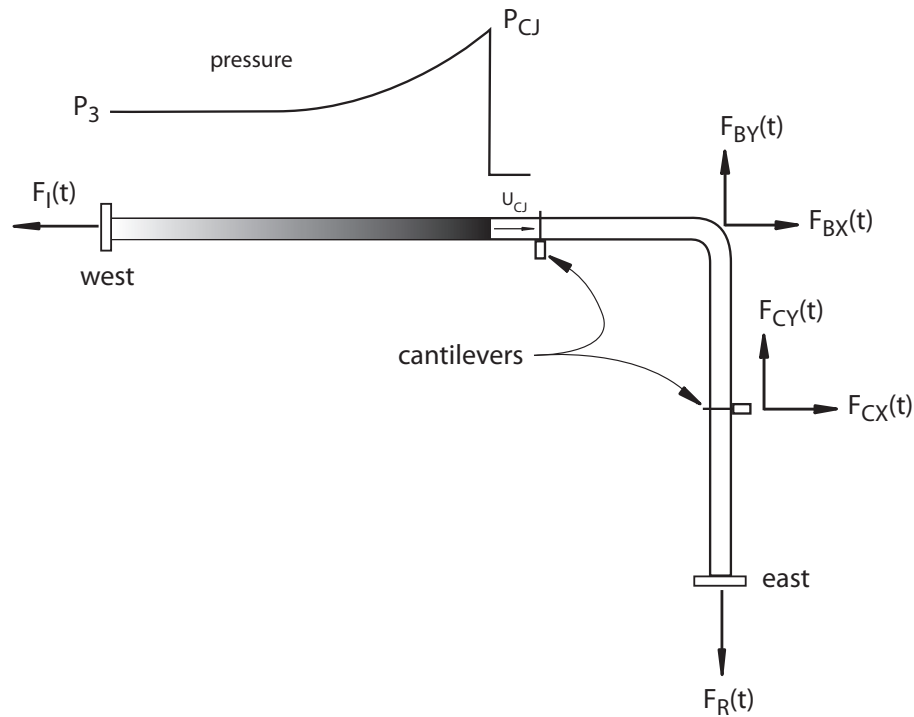


Figure 43: Forces on ES1 piping system created by internal detonation propagation.

Not all forces shown in Fig. 43 were measured or influenced the tube mechanical response in each ES1 test. For example, the cantilever support beams were not present in many tests and in the standard conditions similar to shot 3, the anchor supports at the piping ends provided canceling reaction forces to prevent deflection and the loads were transmitted into the wall through the anchors and plate system. In those cases, the forces  $F_I$ ,  $F_R$  and  $F_C$  do not influence the mechanical motion of the piping system and the strain signals will only reflect the influence of the propagating detonation and the bend forces.

The forces are all functions of time since the loading created by the detonation wave is time dependent. There is a sudden onset of the force when the detonation is initiated  $F_I$  or

arrives at the bend  $F_B$  or reflects from the closed end  $F_R$ . The forces on the cantilevers are also time dependent but more complex than the end forces since the motion of the piping at the cantilever location depends on the propagation of bending motion and bar waves from the location of force application (bend or closed end) to the cantilever location. The peak magnitude of the force can be estimated from the computed peak pressure  $P_3$  or  $P_{R,CJ}$  and pipe cross-section area in the case of  $F_I$  and  $F_R$ , respectively. In the case of the bend forces, control volume considerations of the momentum change through the bend can be used to estimate the force, see [Shepherd and Akbar \(2009\)](#). The estimates of the peak forces are based on the thermochemical computations of pressures in [Appendix A](#) and the cross-section area is based on the nominal internal radius of 26.25 mm for schedule 40, 2-in pipe as given in [Appendix B](#).

Table 12: Estimates of peak forces for ES1 piping system.

Force	Peak Estimate	Magnitude	
		(kN)	(lb <sub>f</sub> )
$F_I$	$A\Delta P_3$	1.84	413
$F_{Bx}$ or $F_{By}$	$2A\Delta P_{CJ}$	11.0	2470
$F_R$	$A\Delta P_R$	14.0	3120

**Bend Force** A detailed discussion of bend forces, analytical models, and comparison with the data was reported in the companion report [Shepherd and Akbar \(2009\)](#). The bend force model and comparison of selected data with finite element simulations is given in [Ligon \(2009a\)](#) and with the Bechtel ME101 piping code in [Lynch \(2009\)](#).

The conclusions of the studies on bend force are:

1. A time-dependent force is generated when a detonation passes through a bend. The force is directed from the intrados toward the extrados along a line that is approximately coincident with the bisector of the bend angle ([Shepherd and Akbar, 2009](#)).
2. The origin of the bend force can either be visualized as due to the change in the momentum of the flow behind the detonation wave or the distribution of pressure inside the bend as the wave front and flow change direction within the pipe ([Shepherd and Akbar, 2009](#)).
3. The time-dependent force generates a longitudinal stress wave in the piping that can be observed on the strain gages aligned with the pipe axis. This can be observed on gages S2, S3 and S15, S17 of all ES1 tests and selected gages on the SS1 [Ligon \(2009e\)](#) tests as well as the SwRI tests ([SwRI, 2009](#)) which were analyzed by [Ligon \(2009d\)](#).
4. The peak magnitude of the bend force is approximately twice that due to the pressure alone since the peak momentum flux of the flow behind the detonation front is comparable to the pressure in the front, ([Shepherd and Akbar, 2009](#), [Ligon, 2009a](#)). Models of the forces using control volume concepts and uniaxial stress wave propagation match the timing and peak values of the longitudinal strain waves [Fig. 44](#).

5. A simple model of the bend force is to use a multiplier (Asymmetry Factor) on the difference between the peak pressure and the pressure in the “tail” of the expansion wave. An factor of 2.0 was first proposed [Gross and Minchello \(2007\)](#) on the basis of analyzing CFD simulations and subsequently validated [Ligon \(2009a\)](#), [Lynch \(2009\)](#) against experimental data. Simulations results are found to be reasonable (within 10%) predictions of measured axial strains if careful account of overlapping flexural wave and bending stresses are accounted for. Comparison is shown in Fig. 45 of the ANSYS results ([Ligon, 2009a](#)) using the pressure distribution discussed in [Shepherd and Akbar \(2009\)](#). Gages S3 and S15 are used for this comparison since these are located on the neutral axis and will be much less sensitive to bending than S2 and S17 and will therefore reflect primarily the axial strain pulses. Further comparisons of selected axial strains are shown in Fig. 46.

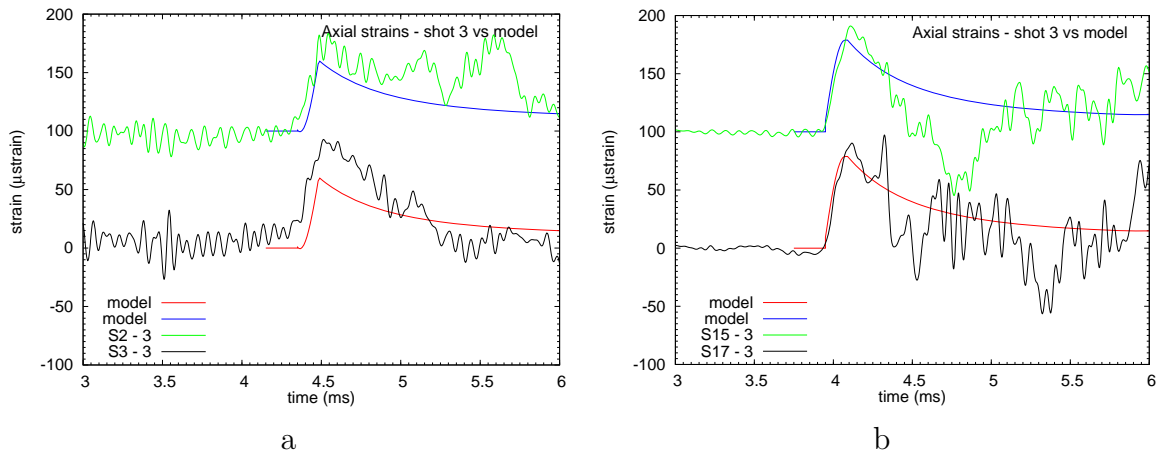


Figure 44: Axial strains predicted by the control volume force model and bar wave transmission compared to measured strains in shot 3. a) upstream of bend b) downstream of bend. ([Shepherd and Akbar, 2009](#))

**Reflecting-end Forces** When the detonation reflects from the closed end of the pipe, the resulting pressure transient creates a force on the pipe directed along the axis and opposite to the direction of initiation wave propagation. The force per unit area on the end is the pressure on gage P8 in Fig. 21. The peak value is approximately 2.4 times the CJ pressure in the propagating wave ([Shepherd et al., 1991](#)) and decays in time as the reflected shock wave propagates back toward the ignition source ([Karnesky, 2010](#)). For a detonation in 30%  $\text{H}_2$ , the ideal peak pressure is about 6.5 MPa, which will result in a peak axial force of 14 kN, see Table 12.

An effort to measure the combination of bend and reflected wave forces, the east end of the pipe was supported by an instrumented cantilever beam as described in Section 6.2 of [Shepherd and Akbar \(2009\)](#). The cantilever beam was held captive in a fixture bolted to the bottom of the end flange, Fig. 47, using three dog screws with hardened tips and a hardened steel pin held captive in a recess. The fixture consisted of two steel blocks, a yoke and a

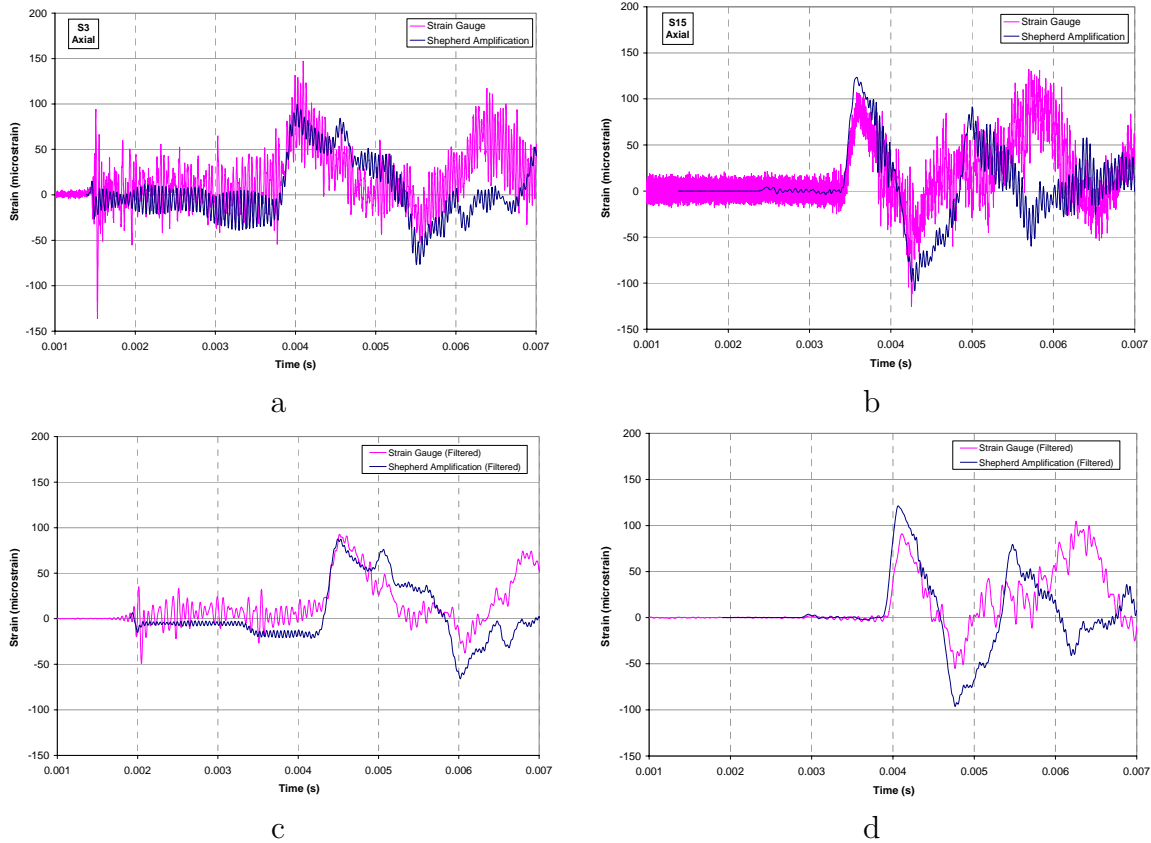


Figure 45: Axial strains predicted by the ANSYS (Ligon, 2009a) and bend pressure distribution force model (Shepherd and Akbar, 2009) compared to measured strains in shot 3. a) & c) upstream of bend S3; b) & d) downstream of bend S15. Experimental data is filtered in c) and d) with a 20 kHz low-pass filter to remove hoop oscillations visible in a) and b).

cap. The yoke was machined from a single billet to form a piece 7 in  $\times$  5 in  $\times$  2.5 in with a cutout to accept the cantilever and a recess to clear the cable for the pressure transducer. The yoke was bolted to the pipe with two cap screws extending through pipe flange and end plate. The cap was a machined from a billet to form a piece 7 in  $\times$  1 in  $\times$  2.5 in and held to the yoke with 8 1/4-20 cap screws. The dimensions were chosen to maximize the stiffness of the fixture but this also increased the mass attached to the end of the pipe. The mass of the yoke and cap together with the screws was 7.25 kg and the mass of the flange, end plate, bolts and ignition components attached to the bottom of the pipe was 10.4 kg. The pipe, end flange fixture, and cantilever beam formed a spring-mass system that make it impossible to interpret the cantilever strains directly as forces due to reflection alone. Methods of analyzing the data are discussed in Shepherd and Akbar (2009).

The force on the east end of the tube is predicted, see Ligon (2009a) and Fig. 48a, to be initially upward due to the bend force transmitted as a bar wave along the vertical leg of the pipe. Once the detonation arrives, the force is predicted to be downward due to the high pressure created when the detonation reflects from the closed end of the pipe. Note that the magnitude of the forces from the bend and reflection are comparable and opposite in sense,

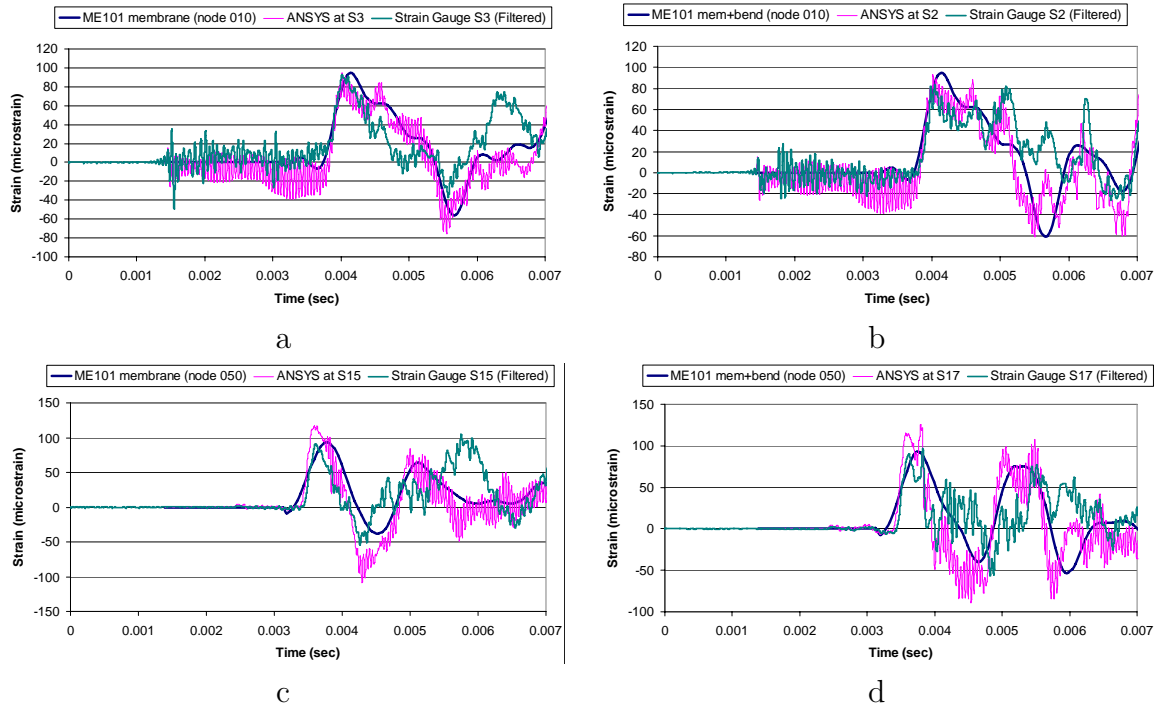


Figure 46: Comparison of axial strains measured in shot 3 with those predicted by the ANSYS (Ligon, 2009a) and ME101 (Lynch, 2009).

as expected from the simple predictions of Table 12.

In addition to a vertical force, the simulations (Ligon, 2009a) predict a smaller lateral force and moment due to the bend force component in the  $X$  direction (horizontal). The measurements of bending strain in the cantilever beam connected to the yoke are compared with the predicted strain in Fig. 48b. The measured and predicted strain history is in qualitative agreement for the first several ms but the peak values are substantially over predicted. This is most likely due to the lack of a detailed geometrical model in the simulation for the cantilever and connection to the force link. As discussed in (Shepherd and Akbar, 2009, Section 6.2), the stiffness of the cantilever beam and inertia of the fixture play a essential role in interpreting the force link data. With a simple single-degree-of-freedom model of the cantilever-fixture assembly and judicious choice of the parameters, it is possible to obtain a reasonable values (12-14 kN) of the peak force, (Shepherd and Akbar, 2009, see Fig. 24).

**Cantilever Beam Support Forces** Shots 25–27 and 34-35 were carried out with the east end of the piping system released from the anchor and cantilever beams supports clamped with U-bolts to the pipe, Fig. 143. The goal was to measure the loads on the supports using the strain at the root of the cantilevers. The cantilever design and calibration is discussed in Appendix G and Shepherd and Akbar (2009). In tests 25–27, a preliminary instrumentation design using single rosette gage was used to measure cantilever bending deflection perpendicular to the pipe axis. This cantilever design is susceptible to errors due

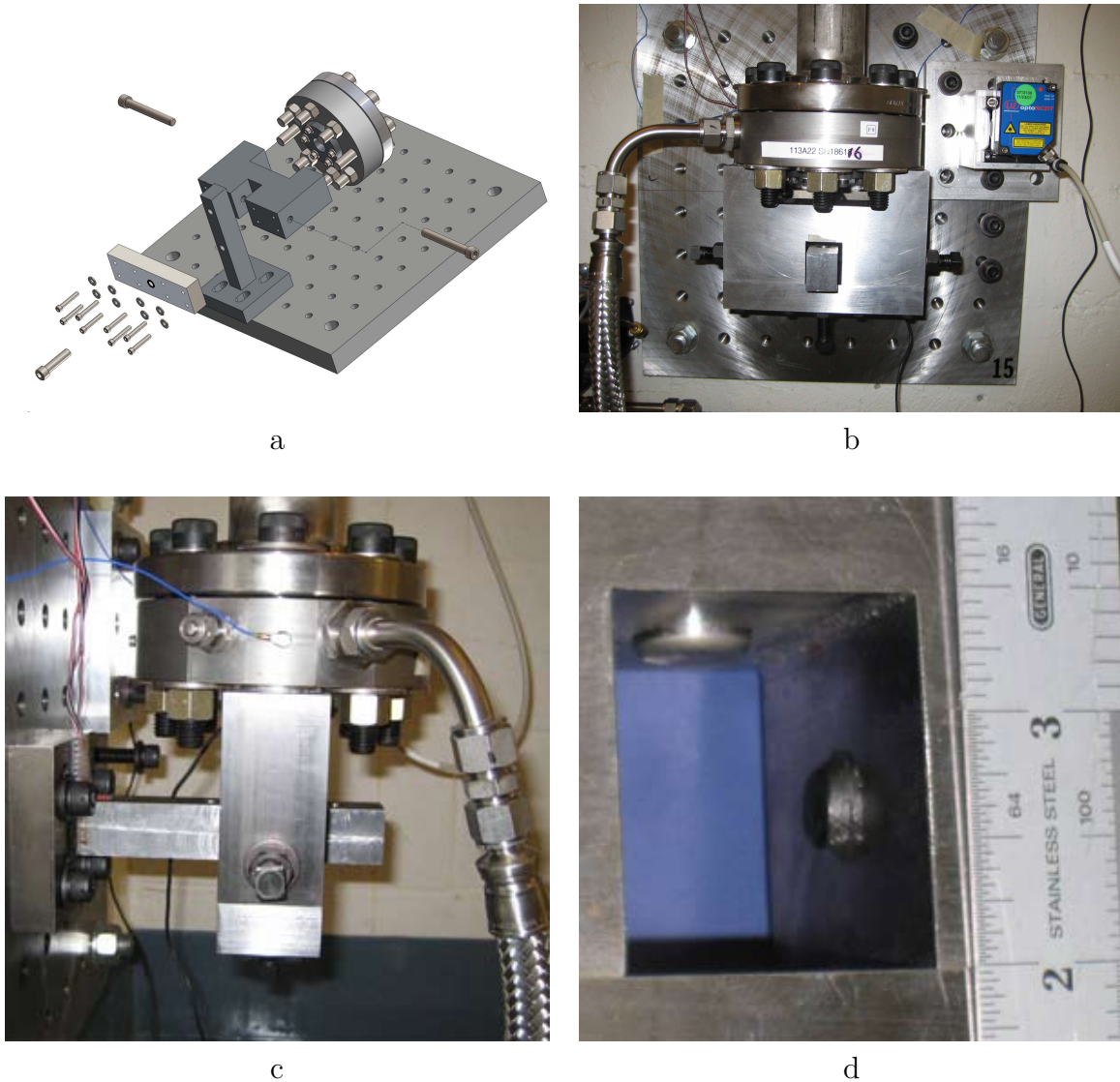


Figure 47: Force link fixture. a) exploded view. b) looking North c) looking East d) detail of dog screws and captive pin.

to torsion and axial loading which can make the data difficult to interpret. An improved design with a pair of half-bridges (Shepherd and Akbar, 2009, see Appendix C) was used in shots 34-35.

Data from the cantilever strain gages is given in Appendix J. By clamping the U-bolts to the pipe specimen, repeatable data was obtained (Fig. 50a) but the ANSYS models were unable to provide either qualitative or quantitative predictions of the cantilever strains. Oscillations in the 100-500 Hz range are apparent, these are characteristic of the piping system as discussed in (Shepherd and Akbar, 2009, Appendix D). Out of plane motion of the bend was monitored by the Keyence displacement gage, Fig. 50b. A modest amount of motion, 0.2 mm peak deflection, was observed and the frequency content was very low as expected since the lowest modes of the out-of-plane motion of the specimen are predicted to

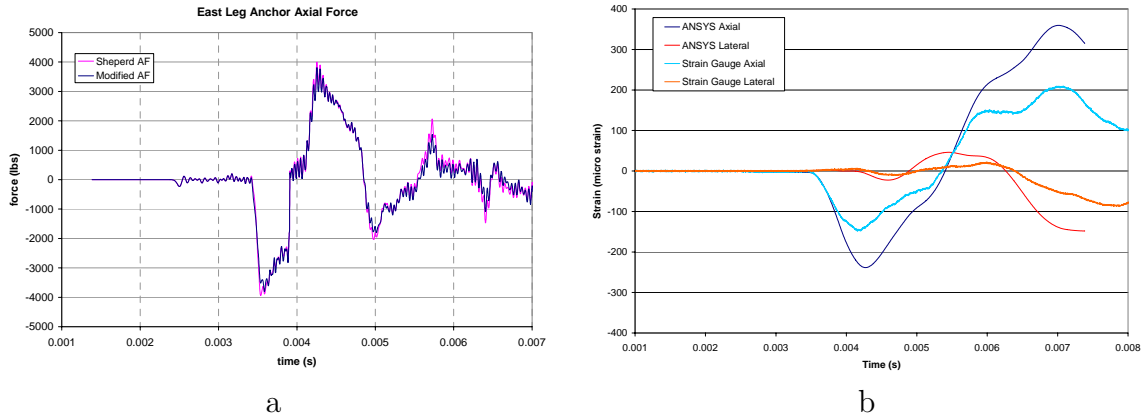


Figure 48: Forces and strains at reflecting end. a) Forces on east end as predicted by ANSYS (Ligon, 2009a) b) Cantilever bending strains predicted by ANSYS and compared to the strains measured in the force link fixture.

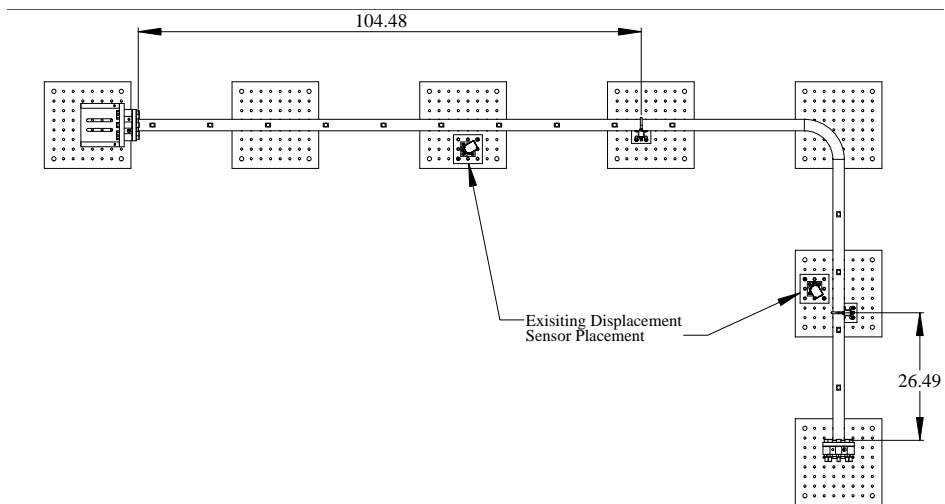
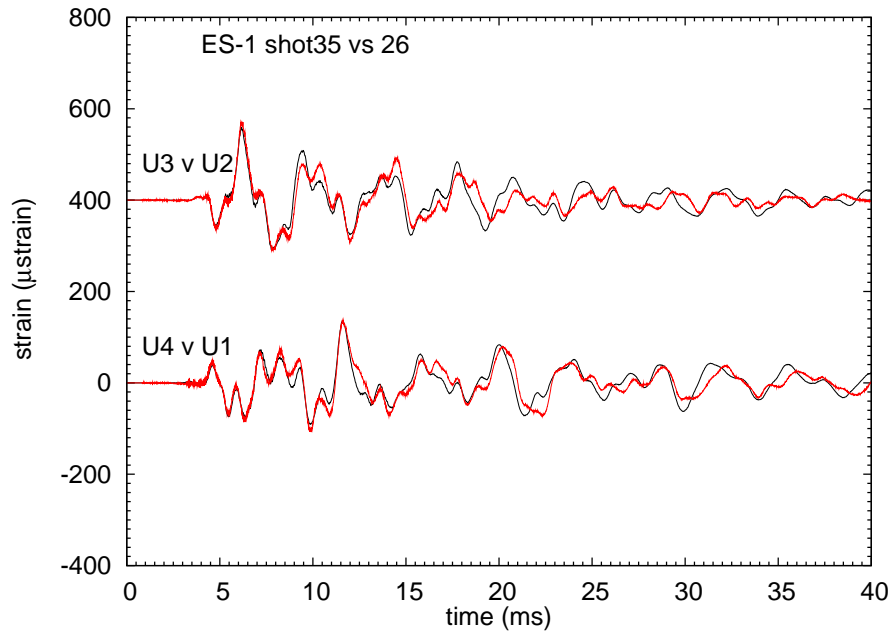
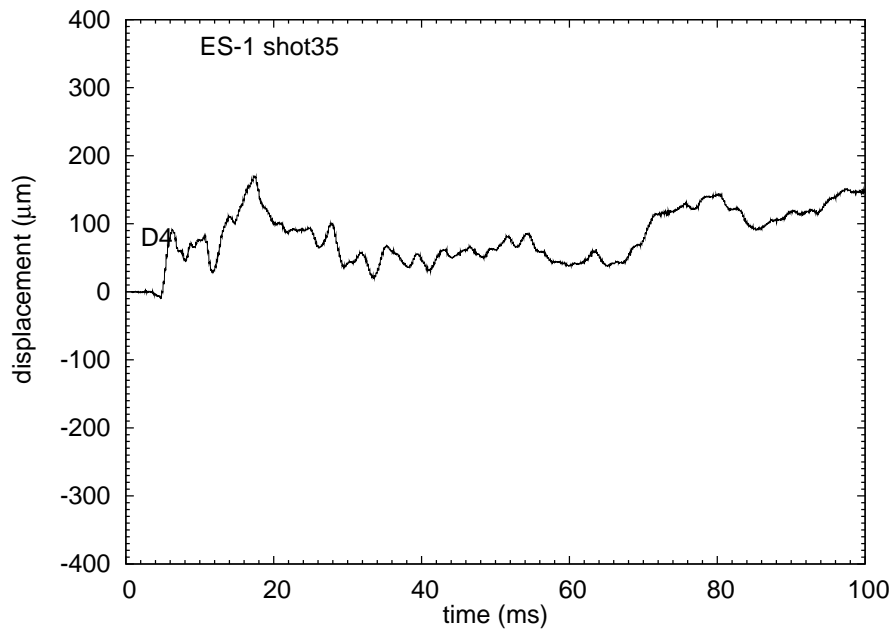


Figure 49: Placement of U-Bolt Supports in shots 25–27 and 34–35.

have a very long period, on the order of 100–200 ms.



a)



b)

Figure 50: ES1 Shot 35, 50 kHz low-pass data. a) Cantilever vertical bending comparison with shot 26. c) Out of plane deflection of bend measured with Keyence laser gage.

**Summary of Attempts to Directly Measure Forces** The efforts to measure and model support forces were instructive but largely unsuccessful. The key results are:

1. High quality strain histories were obtained with instrumented cantilever beams, replica experiments with the east end free demonstrated repeatability.
2. The cantilever U-bolts were tightened onto the piping specimen in order to avoid “chattering” due to play between the pipe and fixture. Although not representative of the actual support installation, this appears to be essential to getting reliable data.
3. Simulation of the cantilever tests with simplified models of the cantilevers was unsuccessful in either qualitative or quantitative prediction of the bending strains.
4. High quality strain histories were obtained from an instrumented cantilever beam and a force link at the bottom of the east end of the specimen. Interpretation of the data was complicated by the mass of the fixture and need to model the details of the cantilever beam.
5. Finite-element models of the force fixture with a simplified beam representation gave qualitatively similar early time prediction but were quantitatively inaccurate. Inverse analysis of the data using a single-degree-of-freedom model gave better agreement for the peak magnitudes of the forces but has substantial uncertainties in the parameters.

### 5.3.6 Detonation Wave Interaction with a Water-Filled Section

A set of 7 experiments, shots 15–21, were carried out with water in the vertical leg of ES1, Fig. 51. The purpose was to determine the pressures and strains transmitted from a gaseous detonation into the a water-filled (simulating the waste slurry in the WTP) section of piping. Two sets of water levels were used with prompt detonation in tests 15 and 16 (2250 cc water) and 17 and 18 (3750 cc water) as well as one test (19) with DDT and two tests (20 and 21) with deflagrations. Results from these tests and analysis using a multi-material simulation were reported in [Shepherd et al. \(2009\)](#), reproduced in Appendix Q. Modeling of these tests with a finite element simulation using a traveling pressure load is presented in [DEI \(2009\)](#).

The pressure data, Fig. 51b and Appendix J, show a transmitted shock wave in the water and a reflected shock wave in the gas. The peak pressures of the incident waves in the gas (2.7 MPa vs. a CJ pressure of 2.5) and water (6 MPa) are consistent with standard detonation wave-free surface interaction analysis ([Meyers, 1994](#), see) predicts a peak pressure in the water (6.35 MPa) that is almost identical to the peak pressure (6.4 MPa) obtained in reflecting the detonation from a hard surface. The propagation speed of the detonation is within 0.5% of the CJ velocity and the propagation of the lead shock wave in the water is about 1310 m/s for shot 15. The propagation of the shock wave in the water is slower than the sound speed of water (1500 m/s) due to the coupling of the pressure wave in the water with the stress waves in the pipe, see the subsequent discussion.

The amplitude of the shock wave in the water does not appreciably attenuate in the  $\sim 1$  m of travel between the free surface and the bottom of the tube although there is an expansion wave following the shock. The shock wave in the water reflects from the bottom and the peak amplitude (10.7 MPa) is slightly lower than double the incident wave. This

is consistent with transmission of a wave into the steel supporting structure at the bottom of the tube. Although this structure is very stiff, it is not completely rigid and in addition to the standard wave interaction processes at the water-steel interface, the reflected shock wave rapidly attenuates as it moves through the pressure drop in the expansion wave.

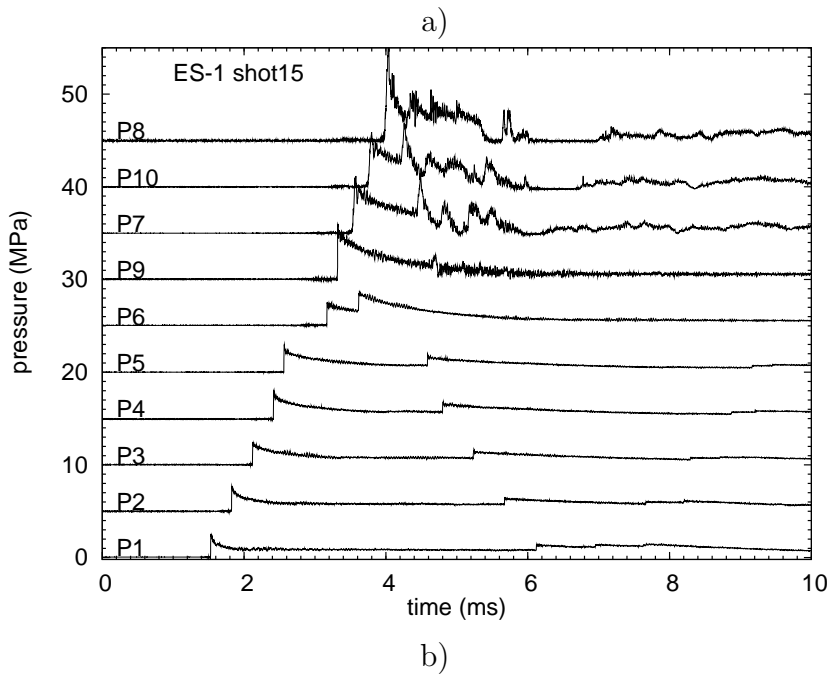
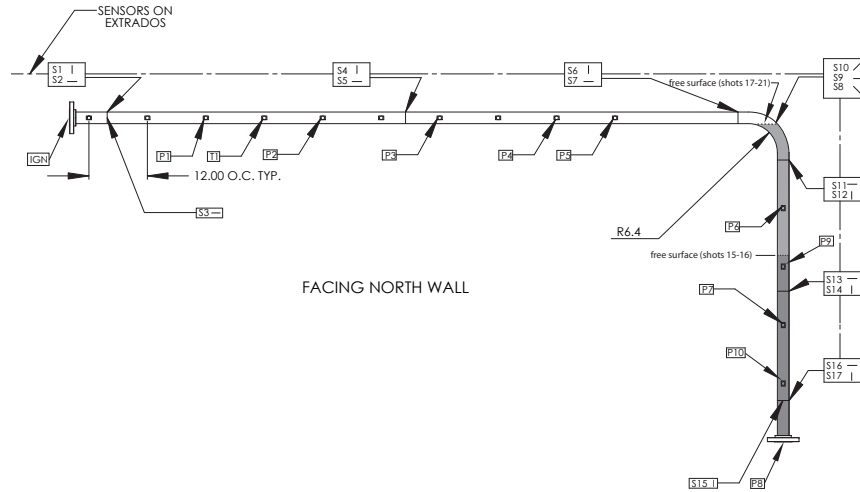


Figure 51: a) Sensor placement and water free surface location for ES1 Shots 15-21. b) Pressure trace for shot 15.

After the reflected shock reaches the free surface of the water, it reflects with a change in sign and creates a tension wave that propagates back to the bottom on the tube. The amplitude of the tension wave increases on reflection from the bottom and causes cavitation of the water. The presence of cavitation is signaled by the portions of the pressure signal

that are flat and close to or below zero in gages P8, P10, and P7 between 5.8 and 7 ms. Since the pressure measured by the gages is relative to the initial pressure in the tube (101 kPa), a level less than -0.1 MPa corresponds to tension in the water. The greatest tension was observed on gage 10 of shot 15, for which the average gage pressure between 6.2 and 6.6 ms is approximately -0.23 MPa for an absolute tension of -120 kPa. The lowest pressures observed on the other gages ranged from +20 to + 70 kPa. By comparison, the vapor pressure of water is 3 kPa at 297°C.

The location of the free surface of the water was not directly measured but we can use the  $x-t$  diagrams to extrapolate the wave trajectories to estimate the location of the free surface from the intersection of the trajectories. The trajectories were estimated using a linear least squares fit of the arrival time-distance data. The free surface was slightly above gage P9 for tests 15 and 16. There is some uncertainty in this value but from the appearance of the pressure signals, it is clear that gage P9 was submerged in the water. For tests 17-21, the location of the free surface was just below the bend; the best estimates of the locations are given in Table 13 and the nominal locations are shown in Fig. 51a.

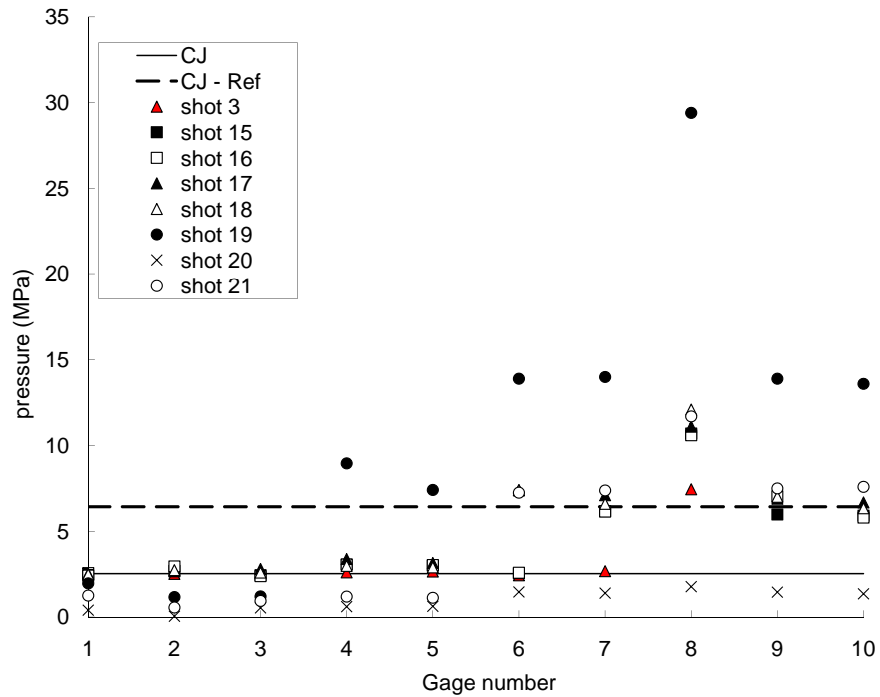
The strain gage records (S13-S16) in the water-filled section are similar in overall appearance (see plots in Appendix J) to the corresponding gages in the gas-only tests. The strains are slightly lower in peak amplitude and the high frequency oscillations are significantly damped in comparison to the tests without water (see data for shot 3 and 4). The longitudinal strain wave precursor on S15 and S14 (gage S17 failed on shots 15 and 16) is almost identical in magnitude and shape to the precursor in the gas only tests, confirming that this signal is associated with the detonation wave propagating through the bend.

The results for two axial gages in shots 18 and 3 are shown in Fig. 53. Since the shock wave in the water travels more slowly than the detonation, the bar wave generated from the bend force (observed on S14 between 3.2 and 3.5 ms) is farther ahead of the pressure and hoop strain signals in shot 18 than in shot 3 at the S13/14 location. In fact, a secondary axial pulse can be seen with a peak at 3.6 ms leading the pressure and hoop signals. This secondary wave is the reflection of the bar wave from the east anchor. Since the bar waves travel at about 5100 m/s, it only takes about 0.3 ms to travel from S13/14 location to the east end anchor and back. Since the anchor is relatively rigid, the bar wave reflects without a change in sign. In shot 3, the reflected bar wave is also present but since the detonation is faster than the water shock, the axial strain signal due to the reflected bar wave is superimposed on the axial signal associated with the hoop-axial coupling and the main pressure disturbance. Despite these differences in the signal history, the peak hoop and axial strains are within 10% for the tests with and without water. The strain signals in the water-filled section are consistent with those observed in separate tests carried out at CIT using impact to generate stress waves in water-filled tubes (Inaba and Shepherd, 2010).

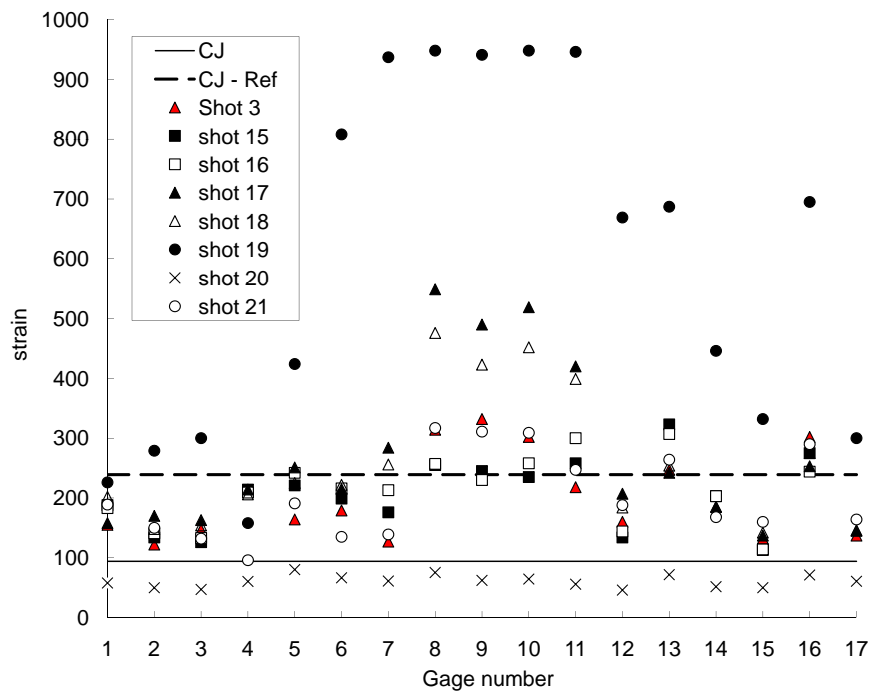
The wave speeds in the water were determined by linear regression of the pressure wave arrival times. Four points were used for tests 15 and 16, five points were used for tests 17 and 18. The results are given in Table 13. These speeds can be compared with the theory of water hammer (Shepherd and Inaba, 2010) which gives the result that the primary stress wave in the water and the pipe wall should propagate at the Korteweg speed

$$c = \frac{c_f}{\sqrt{1 + \beta}} \quad \beta = \frac{DE}{hK} \quad (65)$$

where  $E$  = Young's modulus of pipe material,  $K$  = bulk modulus of water,  $D$  = mean diameter of pipe,  $h$  = pipe wall thickness. Using the piping properties in Appendix B and the properties of water at 27°C,  $\rho = 996.5 \text{ kg/m}^3$  and  $c_f = 1502.2 \text{ m/s}$ , we obtain  $\beta = 0.168$  and  $c = 1390 \text{ m/s}$ . The wave speed for shots 15 and 16 is significantly lower than the Korteweg speed but there is greater uncertainty in the regression fit, probably due to the short length of the water-filled section for these cases. The measured wave speed is within one standard error of the Korteweg speed for shots 17 and 18, which is probably a consequence of the larger distance, 1.76 vs 0.98 m, that the wave has to develop and the larger number, 5 vs. 4, of measuring locations in shots 16-17 vs. 15-16. Extensive measurements in thin-wall steel tubes (Inaba and Shepherd, 2010) have shown excellent agreement (maximum discrepancy of 2%) between the Korteweg theory and the main pressure/hoop strain wave propagation speeds for impact generated shock waves.

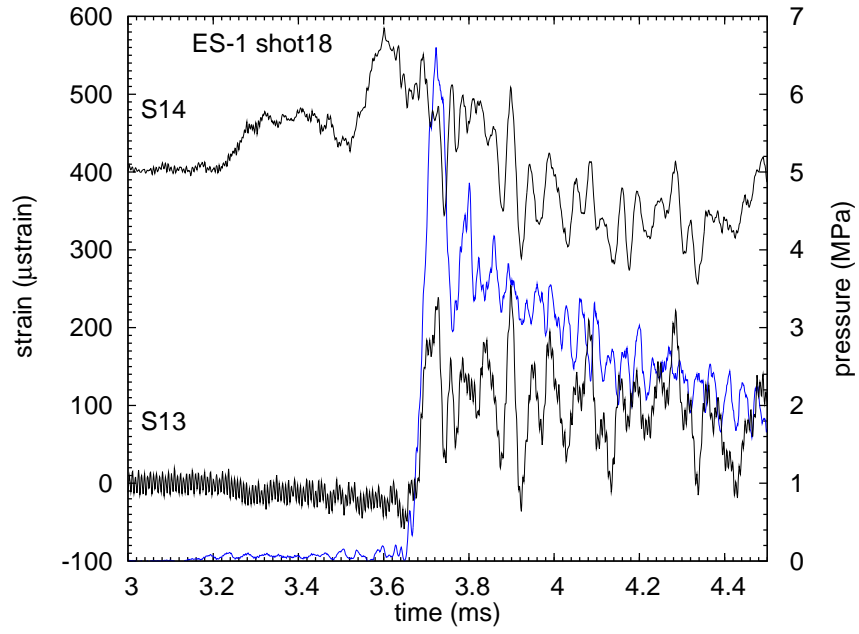


a)

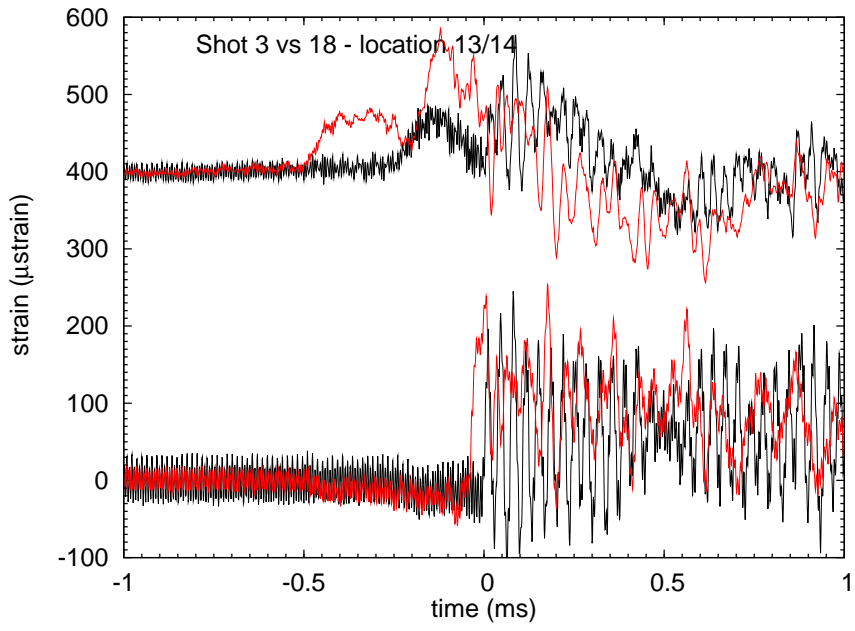


b)

Figure 52: ES1 Shots 15-21 with water in vertical leg compared to shot 3 without water. a) peak strain, b) peak pressure.



a)



b)

Figure 53: ES1 Shot 18 with water in vertical leg compared to shot 3 without water. a) Comparison of strains S13 (hoop) and S14 (axial) with the pressure at P7. Pressure data time shifted to interpolated arrival time at strain gage location. b) Comparison of S13 and S14 for shots 13 and 14, time shifted so that onset of hoop deformation approximately coincides for both shots.

Table 13: Free surface location (from igniter) and shock wave speeds in water-filled piping.

Shot	Free surface (m)	Shock speed (m/s)
15	4.414	$1310 \pm 28$
16	4.385	$1311 \pm 20$
17	3.603	$1380 \pm 9$
18	3.611	$1370 \pm 16$

**Summary of water-filled tube results** The key results from the tests with water-filled sections are:

1. For a CJ detonation, the reflected and transmitted pressures agree with the classical one-dimensional theory of wave interaction.
2. The values of the peak reflected pressure are close to those that would be obtained considering the water as a perfectly reflecting boundary.
3. The transmitted wave propagates at a speed consistent with the Korteweg speed of classical water hammer theory and little to no attenuation in amplitude over  $\sim 1.5$  m. For the case of an incident CJ wave, the speed in the water was between 1310 and 1370 m/s.
4. The amplitude (Fig. 52a) of the transmitted wave is equal to that of the reflected shock wave. When the pressure wave reflects at the closed end of a water-filled section, the peak pressure is approximately twice that of the incident wave.
5. In one DDT event, peak pressures up to 11 times the CJ pressure were observed (Fig. 52a) at the end of the water-filled section.
6. The peak strains (Fig. 52b) induced by a CJ detonation reflecting from the water-filled section of the pipe are comparable to those obtained with a CJ detonation propagating through the entire piping specimen.

## 6 TS1 Test Series

These tests were carried out on a single welded piping system containing a three straight segments of 2-in schedule 40 stainless pipe from the same lot as for the ES1 specimen. The vertical segment was about 60-in long and joined by a 90-degree tee junction to two horizontal segments about 50-in long, see Appendix K for the engineering drawings. The flanges at the end of segment and instrumentation ports were identical in construction method to the ES1 specimen. The piping system supports were shimmed to minimize pre-stress and ensure that the specimen was in a vertical plane when attached to the South wall of the facility as shown in Fig. 54. A total of 16 tests were carried out with detonations initiated in the branch or the run of the tee. A combination of cantilever and fixed end conditions was used as shown in Figs. 56–59. The cantilevers were clamped to the piping with U-bolts in selected tests. Data plots from each test are given in Appendix M.

A total of nine pressure transducers and thirteen strain gages were used on most tests. Instrumentation locations for all tests are shown in Fig. 55 and Table 34 of Appendix L. The Keyence displacement gage described in Section 3.4 can be seen beneath the specimen on Fig. 54b and was used to measure the vertical motion of the bottom of tee on selected tests as discussed in the detailed description of each series. The optical path of the gage had to be rotated 90° by a mirror (seen directly under the tee) in order to accommodate the path length and measure vertical motion. One of the piezoelectric accelerometers was attached to the ignition flange in some shots.



Figure 54: TS1 mounted on south wall of Room 19. a) configuration for shots 46-49. b) configuration for shots 42-45.

### 6.1 Shot List

The tests carried out in TS1 are summarized in Table 14. For all of these tests, the following conditions applied:

1. All tests used a nominal 0.3 H<sub>2</sub>, 0.7 N<sub>2</sub>O mixture at 760 Torr and 25-27°C.

2. Support conditions U3 and U4 are using cantilever beams mounted 3-in in-board from the flange reference surface.
3. Anchor support condition is using angle brackets to connect end flanges to wall plates.
4. Free support condition is leaving flange unsupported except for flex tubing connections to plumbing system through flange adapter.
5. Four different data file column sets were used to accommodate the different sensor configuration, see Table 34. The locations of each transducer are given in Fig. 55 and Table 34.

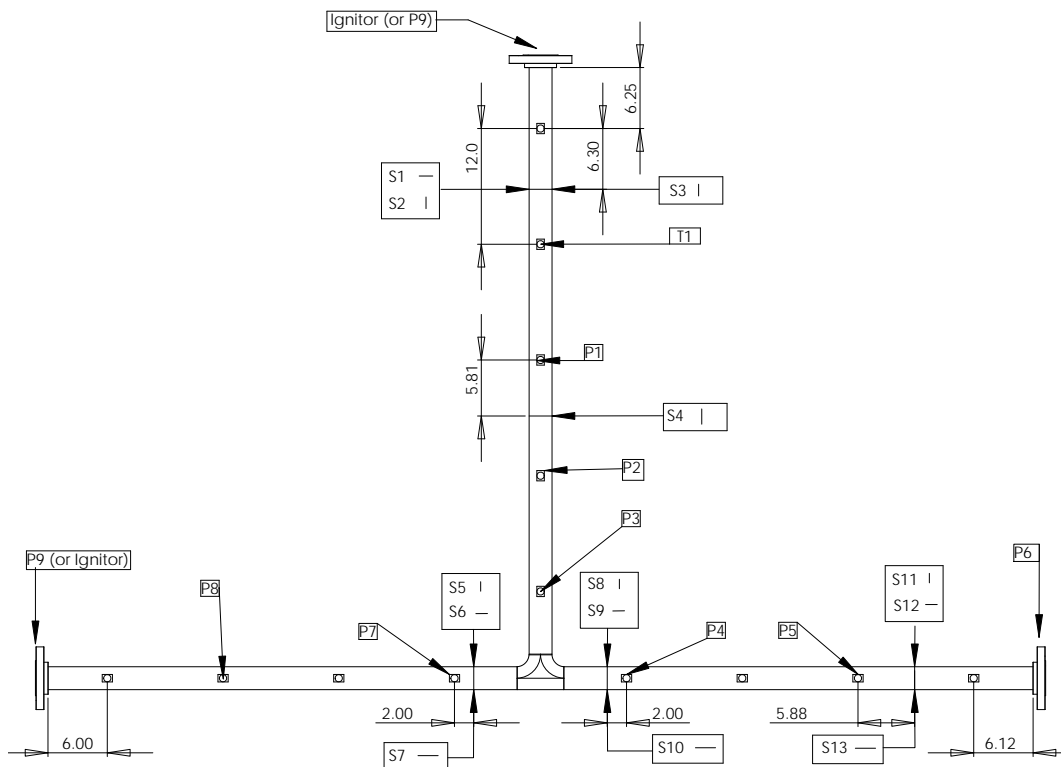


Figure 55: Locations of sensors used on TS1.

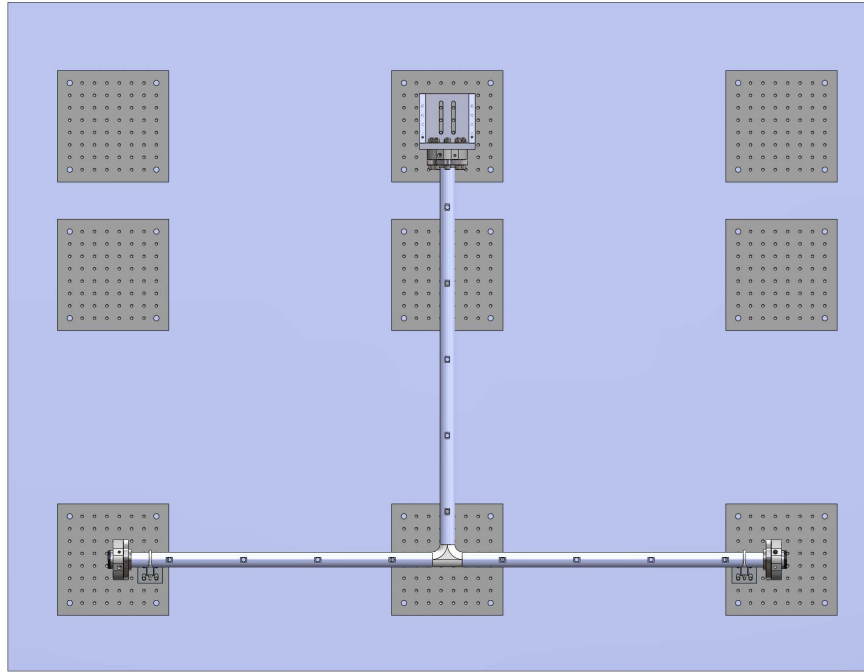


Figure 56: Configuration of TS1 with top anchored and cantilevers on bottom ends. Tests 36-41.

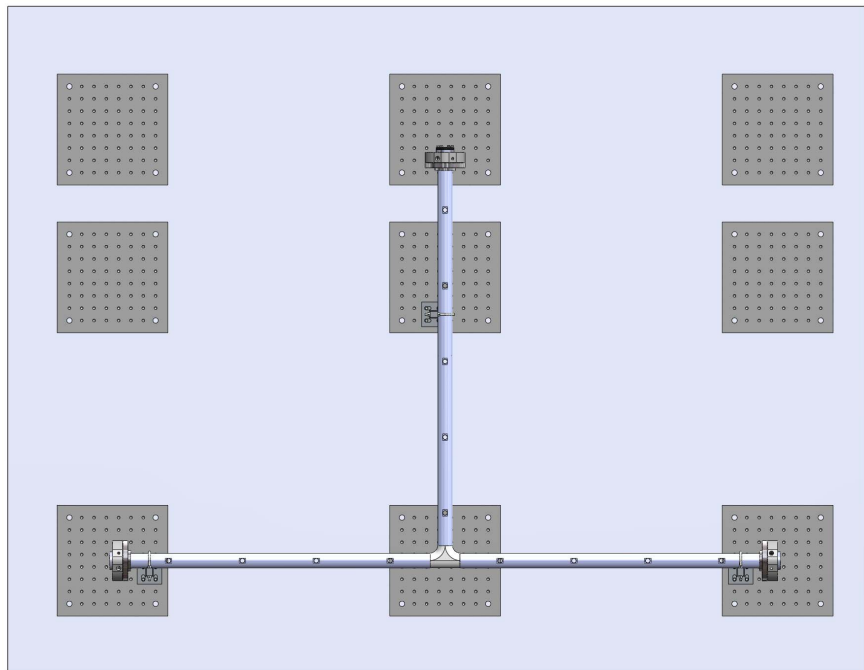


Figure 57: Configuration of TS1 with top free and cantilevers on bottom ends. Tests 42-45.

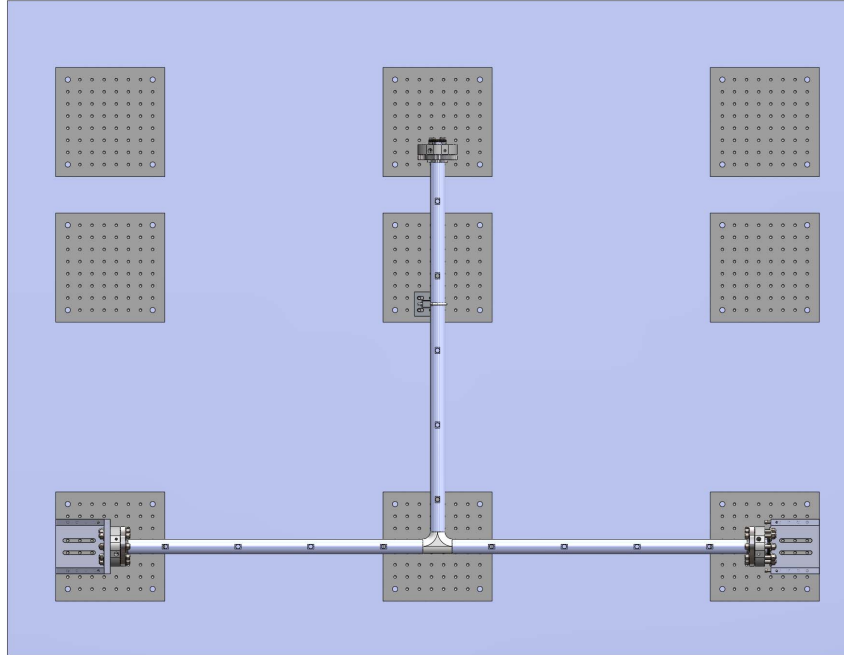


Figure 58: Configuration of TS1 with top free and anchors on bottom ends. Tests 46-49.

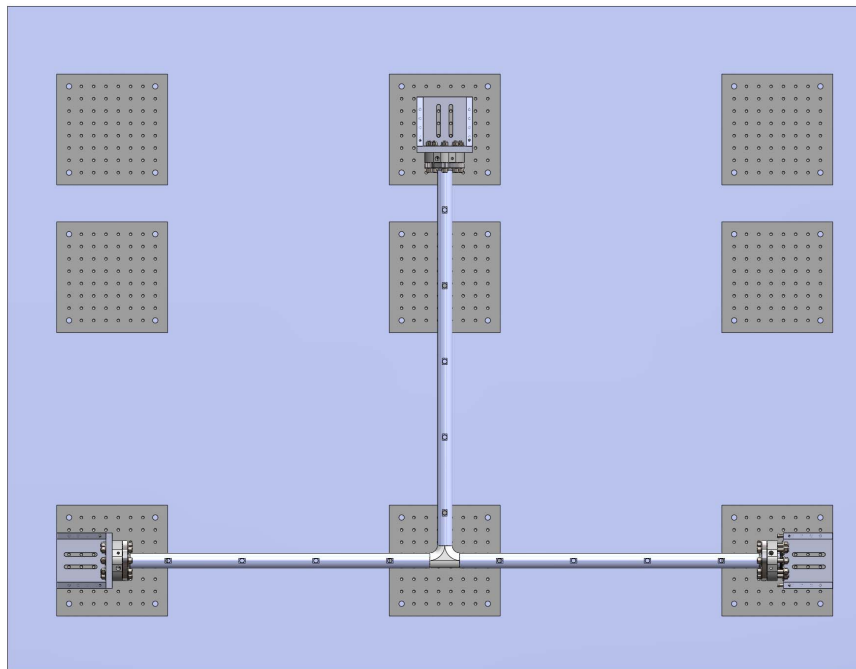


Figure 59: Configuration of TS1 with all three ends anchored. Tests 50-51.

Table 14: List of shots and conditions carried out with TS1 specimen

Shot	$T_o$ (°C)	$P_o$ (Torr)	Date	Ignition	.5 Piping Top	End Conditions		Notes
						West	East	
36	26.0	758.4	17-Dec-08	Top	Anchor	U4	U3	Shakedown with only PCBs and strains on supports, P1-P8, S24-S27 only in data file
37	25.9	759.2	17-Dec-08	Top	Anchor	U4	U3	Replica of 37, P1-P8, S24-S27 only
38	25.3	759.0	04-Jan-09	Top	Anchor	U4	U3	Shakedown with strain gages, added S1-S13 to data file
39	26.5	759.1	04-Jan-09	Top	Anchor	U4	U3	Replica of 38
40	26.2	758.4	07-Jan-09	East	Anchor	U4	U3	Ignition Switched to side
41	26.2	758.9	08-Jan-09	East	Anchor	U4	U3	Replica of 40
42	26.8	758.4	25-Jan-09	Top	Free	U4	U3	Top Freed (but U-bolt installed to limit movement), added D4, ACC3 but data in separate files
43	26.7	758.0	26-Jan-09	Top	Free	U4	U3	Replica of 42, D4, ACC3 added to main data file
44	26.4	758.8	28-Jan-09	East	Free	U4	U3	Top Freed (but U-bolt installed to limit movement)
45	26.6	759.0	28-Jan-09	East	Free	U4	U3	Top Freed (but U-bolt installed to limit movement)
46	25.7	759.3	03-Feb-09	East	Free	Anchor	Anchor	Top Free but with side Anchors (but U-bolt installed to limit movement)
47	26.7	759.0	04-Feb-09	East	Free	Anchor	Anchor	Top Free but with side Anchors (but U-bolt installed to limit movement)
48	27.1	759.3	06-Feb-09	Top	Free	Anchor	Anchor	Top Free with side Anchors (but U-bolt installed to limit movement)
49	26.2	758.5	09-Feb-09	Top	Free	Anchor	Anchor	Top Free with side Anchors (but U-bolt installed to limit movement)
50	26.2	758.5	09-Feb-09	Top	Anchor	Anchor	Anchor	Top Fixed with side Anchors
51	26.4	758.7	09-Feb-09	Top	Anchor	Anchor	Anchor	Top Fixed with side Anchors

## 6.2 Detailed description

The test conditions are summarized in Table 14 and discussed in detail below for each test.

### 6.2.1 Shots 36-41

Tests 36-41 had the same configuration of supports with the top end of pipe restrained by an anchor fixture and the lower E and W ends mounted on cantilever beams as shown in Fig. 56. These tests were designed to provide baseline data on the performance of the tee specimen and loads on the cantilever beams. Since the specimen is nominally symmetric and the ignition was in the center of the vertical leg of the tee, comparing the response of the E and W legs of the tee gives a measure of how symmetric the loading will be when the detonation has to negotiate the tee. Detonation initiation was with the 1-ft Shchelkin spiral in all cases and the loads for these shots are transmitted to the wall through the anchor so that we can clearly separate initiation effects from the structural response due to diffraction through the tee and reflection from E and W ends.

Shot 36 This is a shakedown test with only pressure data and cantilever beam strains recorded. The top is anchored and the horizontal leg is supported by cantilever beams 3-in inboard from flanges. Ignition at top with 1-ft Shchelkin spiral. 30/70 H<sub>2</sub>/N<sub>2</sub>O mixture at 1 atm and 26 C nominal initial conditions.

Shot 37 Replica of shot 36. This is a shakedown test with only pressure data and cantilever beam strains recorded. The top is anchored and the horizontal leg is supported by cantilever beams 3-in inboard from flanges. Ignition at top with 1-ft Shchelkin spiral. 30/70 H<sub>2</sub>/N<sub>2</sub>O mixture at 1 atm and 26 C nominal initial conditions. The data file columns were changed after shots 36 and 37 since more gages were added.

Shot 38 Repeat of shot 37 with addition of 13 strain gages on piping system. The top is anchored and the horizontal leg is supported by cantilever beams 3-in inboard from flanges. Ignition at top with 1-ft Shchelkin spiral. 30/70 H<sub>2</sub>/N<sub>2</sub>O mixture at 1 atm and 26 C nominal initial conditions.

Shot 39 Repeat of shot 38. The top is anchored and the horizontal leg is supported by cantilever beams 3-in inboard from flanges. Ignition at top with 1-ft Shchelkin spiral. 30/70 H<sub>2</sub>/N<sub>2</sub>O mixture at 1 atm and 26 C nominal initial conditions.

Shot 40 Moved ignition location to lower east end and gage P9 to top. The top is anchored and the horizontal leg is supported by cantilever beams 3-in inboard from flanges. Ignition using spark with 1-ft Shchelkin spiral. 30/70 H<sub>2</sub>/N<sub>2</sub>O mixture at 1 atm and 26 C nominal initial conditions.

Shot 41 Replica of shot 41. The top is anchored and the horizontal leg is supported by cantilever beams 3-in inboard from flanges. Ignition at using spark with 1-ft Shchelkin spiral. 30/70 H<sub>2</sub>/N<sub>2</sub>O mixture at 1 atm and 26 C nominal initial conditions.

### 6.2.2 Shots 42-45

Shots 42-45 had the top released from the anchor but a U-bolt guide (teflon sleeve on pipe, U-bolt not tightened) on vertical leg near top, see Fig. 57 and Fig. 60. The lower ends of the specimen remained mounted on cantilevers as in previous testing. Displacement measurement of tee vertical deflection and acceleration of top flange was added to sensor suite. The columns in data set were changed since D4 and ACC3 (on the ignition flange) were added after shot 42. The purpose of these tests was to examine the additional motion and strains that produced by freeing the vertical leg from the fixed support.

Shot 42 Ignition at top. The top is removed from the anchor and the horizontal leg is supported by cantilever beams 3-in inboard from flanges. Ignition at using spark with 1-ft Shchelkin spiral. 30/70 H<sub>2</sub>/N<sub>2</sub>O mixture at 1 atm and 26 C nominal initial conditions.

Shot 43 Replica of 42. Ignition at top. The top is free and the horizontal leg is supported by cantilever beams 3-in inboard from flanges. Ignition at using spark with 1-ft Shchelkin spiral. 30/70 H<sub>2</sub>/N<sub>2</sub>O mixture at 1 atm and 26 C nominal initial conditions.

Shot 44 Ignition at moved to lower east end. The top is free and the horizontal leg is supported by cantilever beams 3-in inboard from flanges. Ignition using spark with 1-ft Shchelkin spiral. 30/70 H<sub>2</sub>/N<sub>2</sub>O mixture at 1 atm and 26 C nominal initial conditions.

Shot 45 Replica of 44. Ignition at lower east end. The top is free and the horizontal leg is supported by cantilever beams 3-in inboard from flanges. Ignition using spark with 1-ft Shchelkin spiral. 30/70 H<sub>2</sub>/N<sub>2</sub>O mixture at 1 atm and 26 C nominal initial conditions.

### 6.2.3 Shots 46-49

In Shots 46-49, the cantilevers were removed and the lower ends restrained on anchor fixtures; the top remained unrestrained, see Fig. 58. The columns in data file were changed since S24, S25, S26, S27 were removed from data set.

Shot 46 Ignition at lower east end. P9 located on top. The top is free and the horizontal segment ends are fixed with anchors. Ignition using spark with 1-ft Shchelkin spiral. 30/70 H<sub>2</sub>/N<sub>2</sub>O mixture at 1 atm and 26 C nominal initial conditions.

Shot 47 Replica of 46. Ignition at lower east end. The top is free and the horizontal segment ends are fixed with anchors. Ignition using spark with 1-ft Shchelkin spiral. 30/70 H<sub>2</sub>/N<sub>2</sub>O mixture at 1 atm and 26 C nominal initial conditions.

Shot 48 Ignition at top. The top is free and the horizontal segment ends are fixed with anchors. Ignition using spark with 1-ft Shchelkin spiral. 30/70 H<sub>2</sub>/N<sub>2</sub>O mixture at 1 atm and 26 C nominal initial conditions.

Shot 49 Replica of 48. Ignition at top. The top is free and the horizontal segment ends are fixed with anchors. Ignition using spark with 1-ft Shchelkin spiral. 30/70 H<sub>2</sub>/N<sub>2</sub>O mixture at 1 atm and 26 C nominal initial conditions.

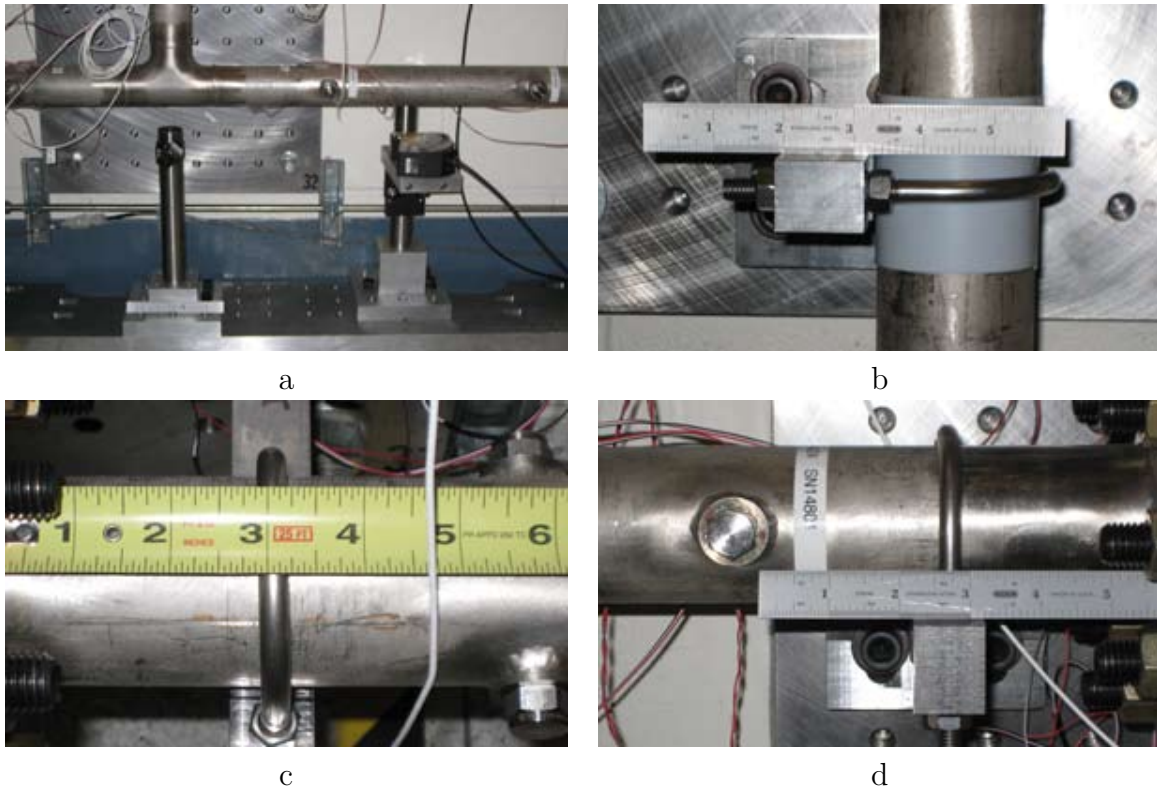


Figure 60: a) Keyence measurement unit with turning mirror. b) U-bolt with teflon pad on vertical leg c) cantilever support on E end c) Cantilever support on W end.

#### 6.2.4 Shots 50 and 51

Shots 50 and 51 had all three ends of the pipe restrained on the anchor fixtures, see Fig. 59; ignition was at the top.

Shot 50 Ignition at top. The top and the horizontal segment ends are fixed with anchors. Ignition using spark with 1-ft Shchelkin spiral. 30/70 H<sub>2</sub>/N<sub>2</sub>O mixture at 1 atm and 26 C nominal initial conditions.

Shot 51 Replica of 50. Ignition at top. The top and the horizontal segment ends are fixed with anchors. Ignition using spark with 1-ft Shchelkin spiral. 30/70 H<sub>2</sub>/N<sub>2</sub>O mixture at 1 atm and 26 C nominal initial conditions.

### 6.3 Key Results

There were two basic configurations in the tee experiments: 1) ignition from the top of the specimen which resulted in symmetric loading of the tee junction and the arms of the tee; 2) ignition from the east end which resulted in an symmetric loading of the fixture. In addition, the ends of piping specimen had one of three conditions: 1) free to move; 2) constrained by U-bolts to cantilever supports; 3) attached to the wall through anchor supports. The

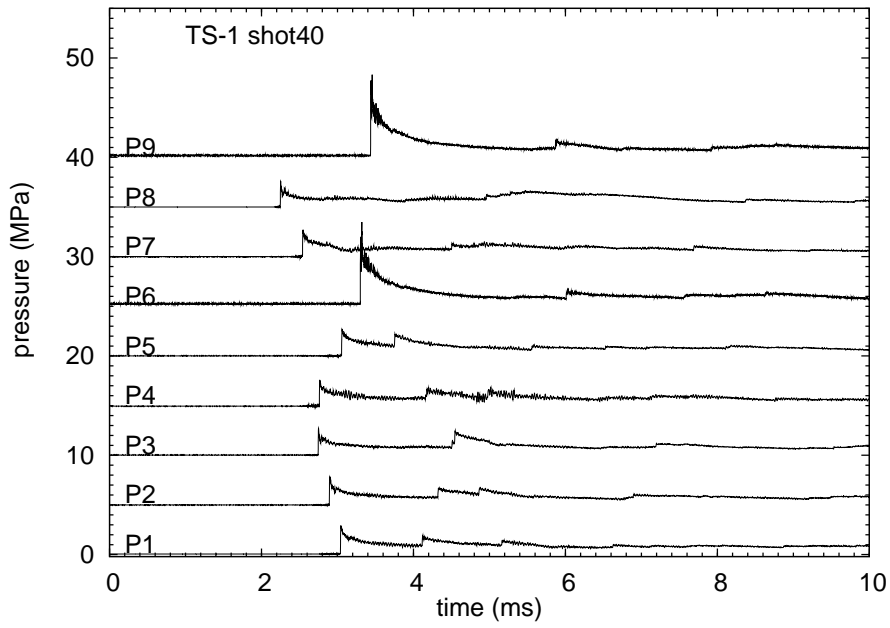
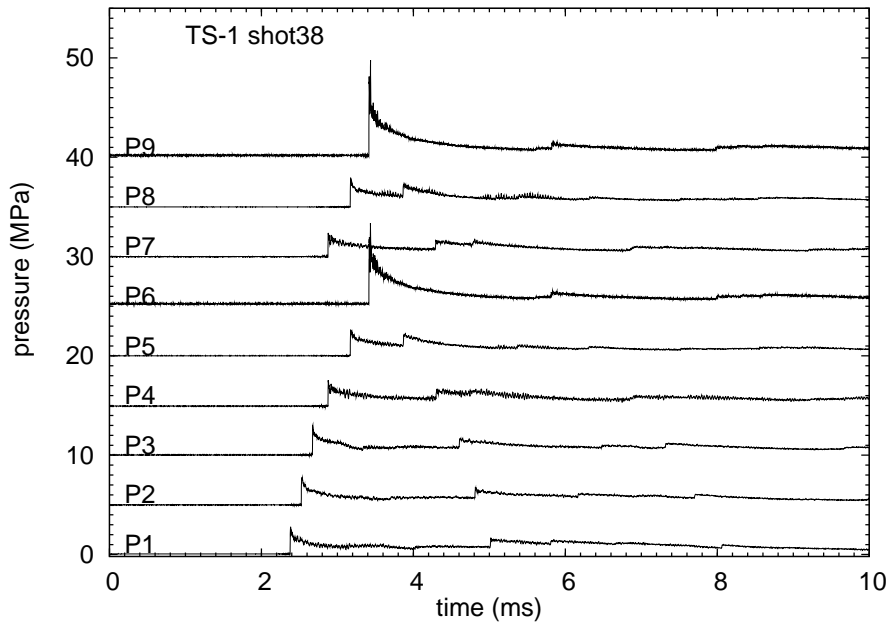
pressure histories are not affected by the end conditions but the strains and displacement histories show significant dependence on how the ends are treated.

### 6.3.1 Pressure and Strain Histories

Example pressure histories for the two ignition cases are shown in Fig. 61. Referring to Fig. 55, transducers P1, P2, and P3 are on the vertical leg and transducers P4, P5 and P6 are on the W leg, while P7, P8 and P9 are on the E leg (except for E ignition when, P9 was move to the top of the vertical leg.). The trace in Fig. 61a is representative of top ignition (shots 38,39, 42, 43, 48, 49, 50 and 51) and the traces on P1, P2, P3 show the incident detonation while the transmitted detonation downstream of the tee are shown on P4-P7, P5-P8, and P6-P9 which are W-E pairs equidistant from the tee junction. The trace in Fig. 61b is representative of east ignition (shots 40, 41, 44, 45, 46, 47) with the incident detonation shown on P8, P7, P4, P5, P6 and the traces on P1, P2, P3, P9 show the transmitted detonation.

### 6.3.2 Peak Strain and Pressure

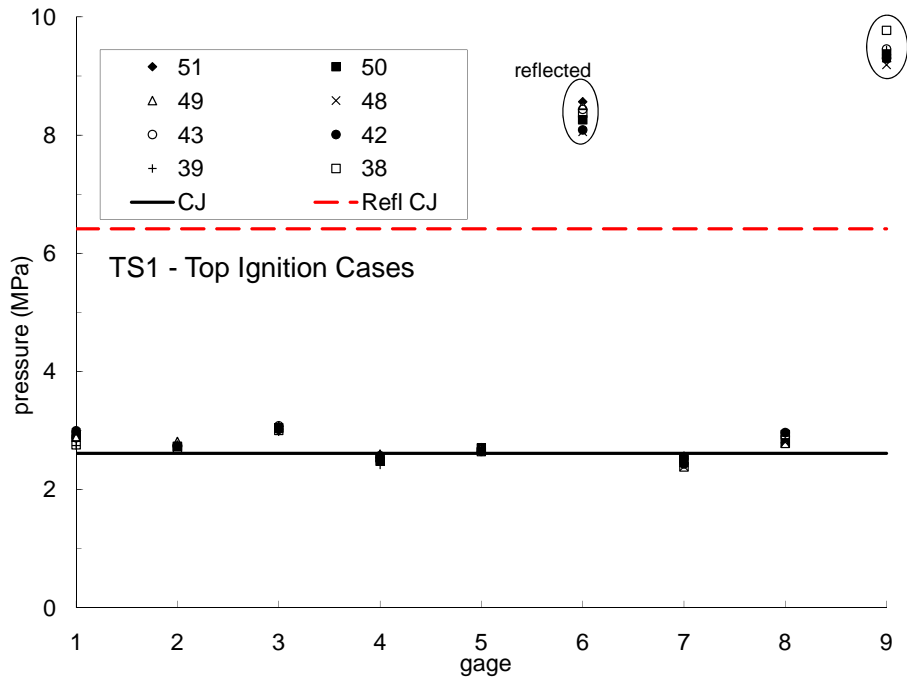
The peak strains and pressures were compared with estimated values based on the CJ and reflected CJ pressures and SDOF structural response with a dynamic load factor of 1. The results are given in Figures 62 and 63. For the propagating detonations, the peak pressure compares very well with the CJ value. The reflected detonation pressures are higher than the ideal CJ value for the same reasons as discussed for ES1 in Section 5.3.2. The peak strains lie between the CJ and reflected CJ values which consistent with the ES1 results and to be expected based on the SDOF model of structural response. In general, both peak pressures and strains are consistent from test-to-test in the TS1 series and the peak values are consistent with the measurements for the promptly initiated detonation cases of ES1 (except for the strains on the ES1 bend which are expected to be exceptional). Strains are bounded in all cases by the value estimated for the reflected CJ SDOF ( $\Phi = 1$ ) model but it is important to note that the details near the tee are not resolved and the tee is forged with a greater wall thickness than the pipe.



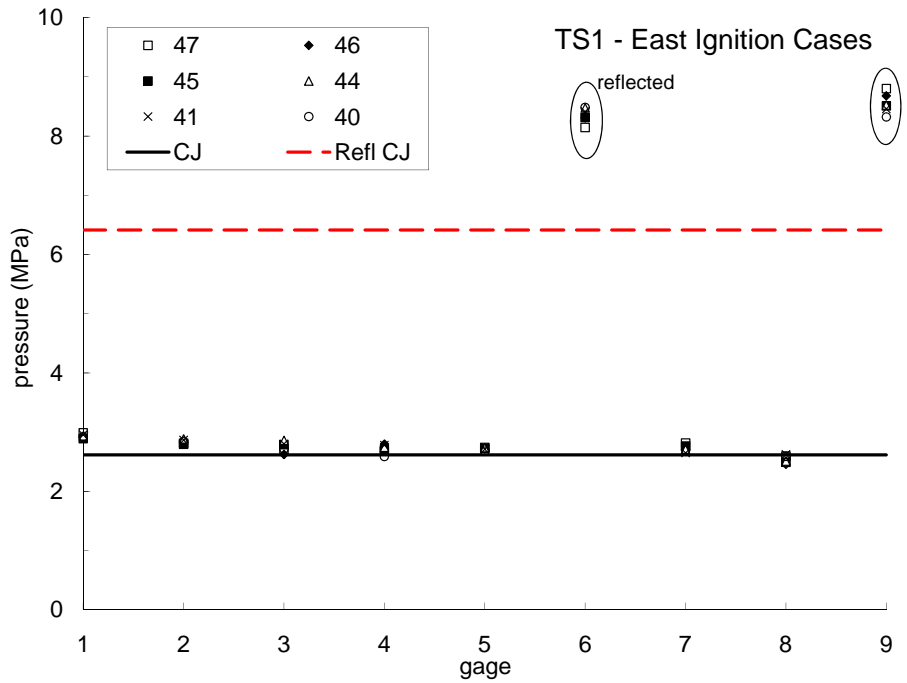
a.)

b.)

Figure 61: Pressure signals from two cases. a) Top ignition, shot 38. b) East ignition, shot 40.

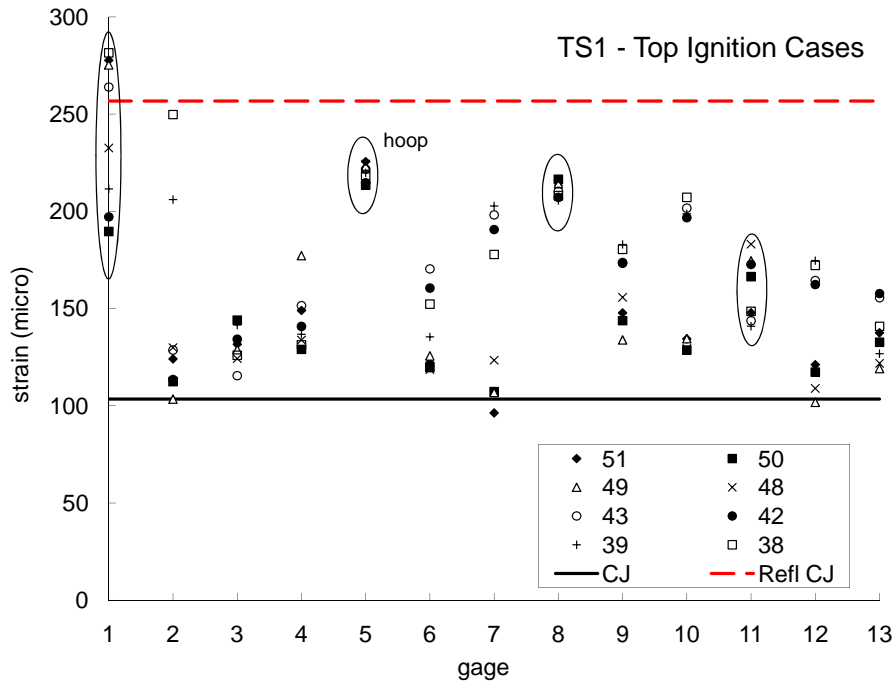


a

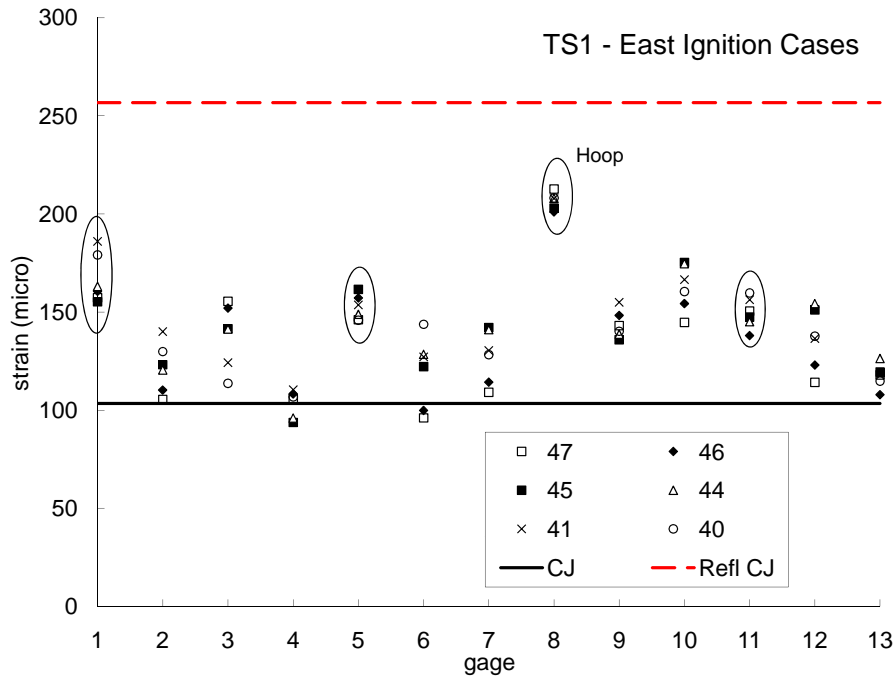


b

Figure 62: TS1 measured peak pressures for a) top ignition, b) east side ignition.



a.



b.

Figure 63: TS1 measured peak strains for a) top ignition, b) east side ignition.

### 6.3.3 Wave Speeds

The wave speeds were analyzed using linear regression to fit the arrival times determined from the pressure gages. In doing so, it was found that there was a significant difference between the wave speed in the initiation section as compared to the branches of the tee. This is not unexpected since diffraction of the detonation through the tee is expected to cause significant disturbance to the wave front. Tilting of the wave front and momentary separation of the reaction zone from the leading shock are expected to be manifested in a decrease of the wave speed. The analysis shows that waves initiated at the top of the tee propagated with a near-CJ velocity (about 1% deficit) but after diffracting the velocity dropped and the average velocity in the branches was about 2015-2020 m/s, a deficit of 3%. Waves initiated on the east branch presumably initially propagated with a velocity that was close to the CJ value. However, after passing through the tee, the speed decreased and the average speed of propagation from the east to the west was about 2058-2061 m/s, a deficit of about 1.3%. The speed on the branch was, with one exception, similar with values of 2050-2066 m/s. The wave speeds were judged to be sufficiently close to the CJ value that the experiments could be analyzed assuming that the waves were ideal.

Table 15: Wave speeds obtained from regression analysis of pressure wave time-of-arrival data.

Shot	Detonation Speed (m/s)	
	Ignition	Branch(es)
	Top ignition	
36	2072	2017
37	2072	2019
38	2080	2015
39	2080	2019
42	2073	2013
43	2072	2017
48	2066	2024
49	2073	2023
50	2073	2015
51	2065	2023
	East ignition	
40	2058	2058
41	2059	2065
44	2059	2065
45	2060	2066
46	2059	2080
47	2061	2059

### 6.3.4 Repeatability and Symmetry

Two examples of repeatability checking are shown in Fig. 65. Additional comparisons of this type can be found in Appendix M. One question that arose with the tee was if the construction was sufficiently symmetric so that the two arms of the tee responded identically. We examined this by looking at the symmetry of the pressure signals and the cantilever strains. In addition, a thorough statistical analysis was carried out of the time-of-arrival of the pressure signals when the tee was symmetrically initiated. An example of a symmetry test is shown in Fig. 66. The pressure signals from the left hand leg have been superimposed on the corresponding traces from the right-hand leg of the tee. The cantilever beam signals have been superimposed by the sign of the horizontal signal was inverted since the vertical deflection with be symmetry about the central leg of the tee but the horizontal deflection will be anti-symmetric.

It is clear from examining these comparison plots that there are no gross asymmetries in any of the data which would indicate a serious problem with dimensions or repeatability of the test procedures. However, since the tee was constructed of commodity components and fabricated by welding, there were concerns that some small variations in dimensions or alignment might be present.

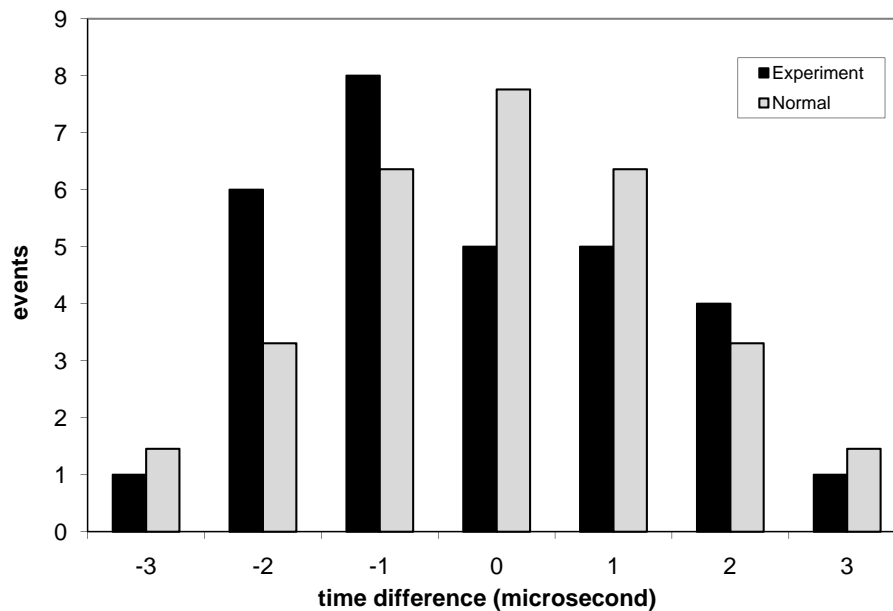


Figure 64: TS1 pressure arrival time pair difference frequency compared to normal distribution.

To examine the possibility of asymmetry further, we took all 30 pairs of arrival time data from the 10 centrally ignited shots and tested the hypothesis that the mean value was different than zero. To do this we compared the frequency distribution of paired arrival time differences to the normal distribution. The arrival times were sorted into  $1 \mu\text{s}$  bins (intervals). The basic descriptive statistics were mean pair difference of  $0.23 \mu\text{s}$  and a standard deviation of  $1.5 \mu\text{s}$ . The normality of the distribution was tested using the goodness-of-fit chi-square

test (Lindgren et al., 1978, p. 246) and a value of  $\chi^2 = 4.32$  was obtained for 29 degrees of freedom. The critical value of  $\chi^2 = 41.4$  at the 95% confidence level so the hypothesis that the distribution is non-normal can be safely rejected. The comparison between the arrival time pair differences and a normal distribution are shown in Fig. 64.

The hypothesis that the mean was nonzero was tested using Student's  $t$ -distribution (Lindgren et al., 1978, p. 180) and a 95% confidence level. The  $t$ -score was  $-0.826$ , well inside the critical regions  $>2.045$  or  $<-2.045$ . Based on these two tests, we concluded that no systematic errors appeared to present in either the construction, test procedure, or data analysis. Note that an arrival time difference of  $1 \mu\text{s}$  corresponds to a distance error of  $\approx 2$  mm.

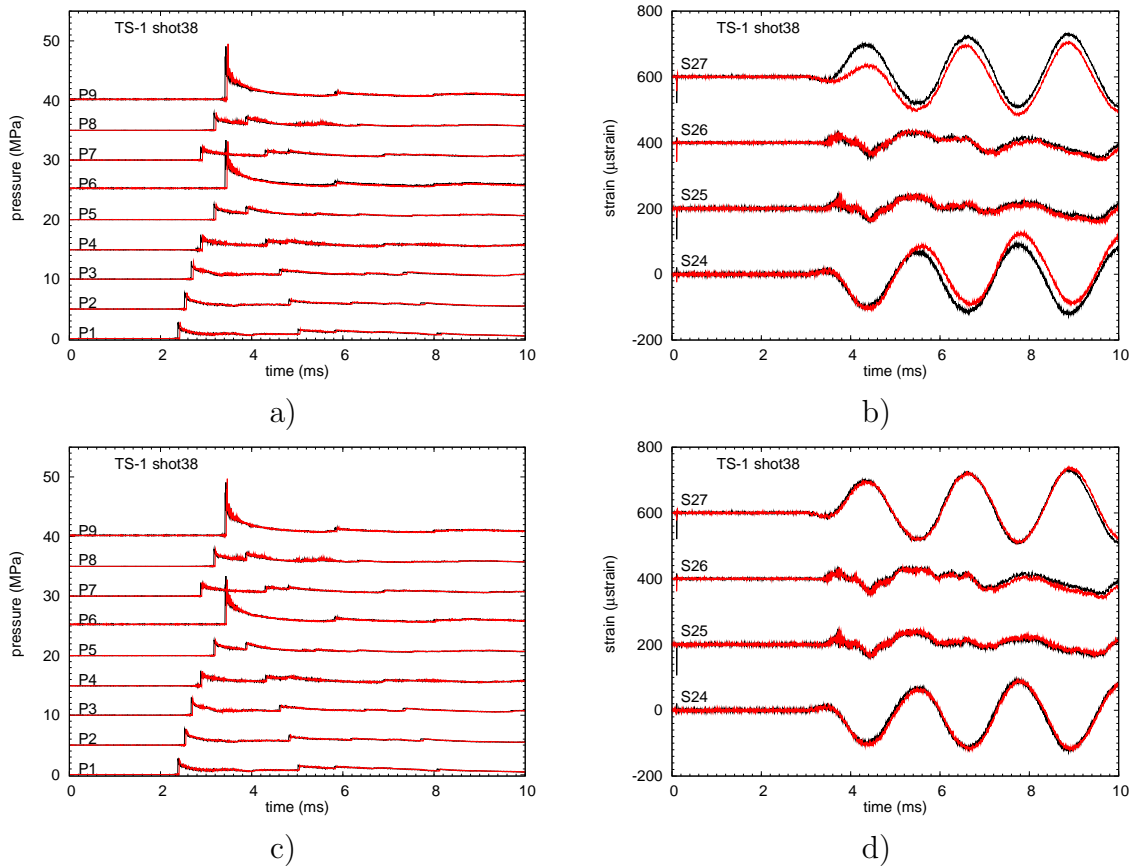
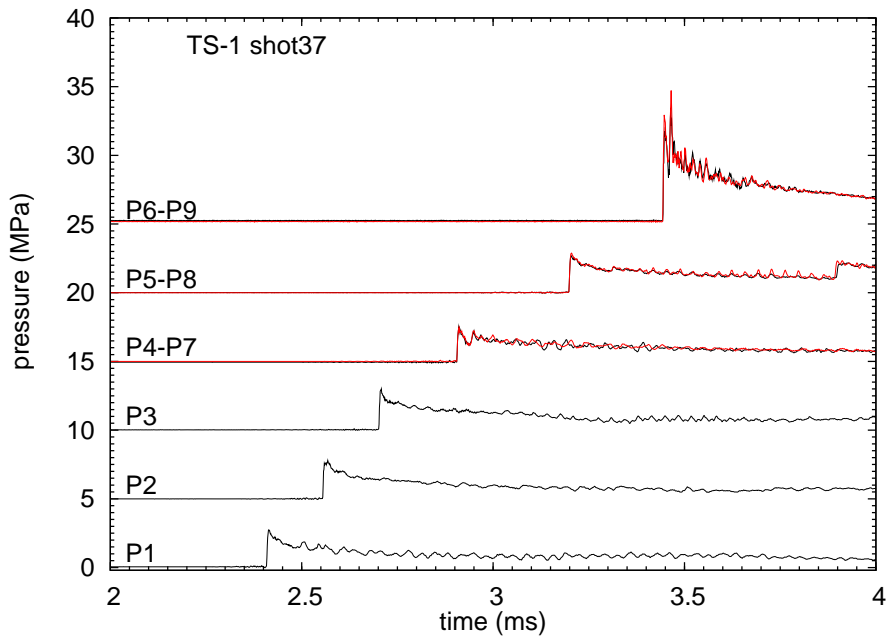
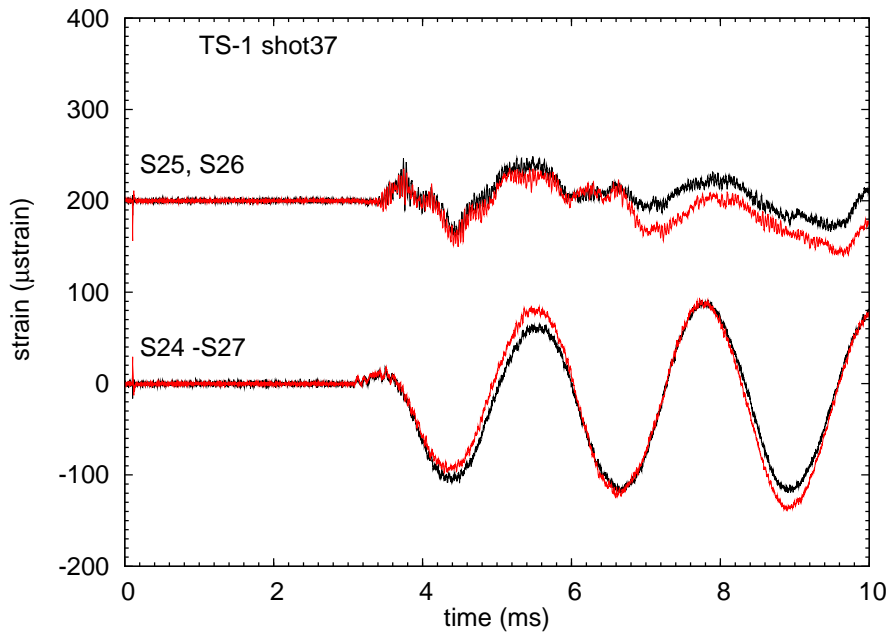


Figure 65: TS1 Shot 38 comparisons. Pressure, and cantilever strain gage signals. 10 ms raw data. a) and b) shot 38 vs. 36. c) and d) shot 38 vs. 37.



a)



b)

Figure 66: TS1 Shot 37. Check of pressure and cantilever beam symmetry. 10 ms raw data.

## 6.4 Effect of Support Variations

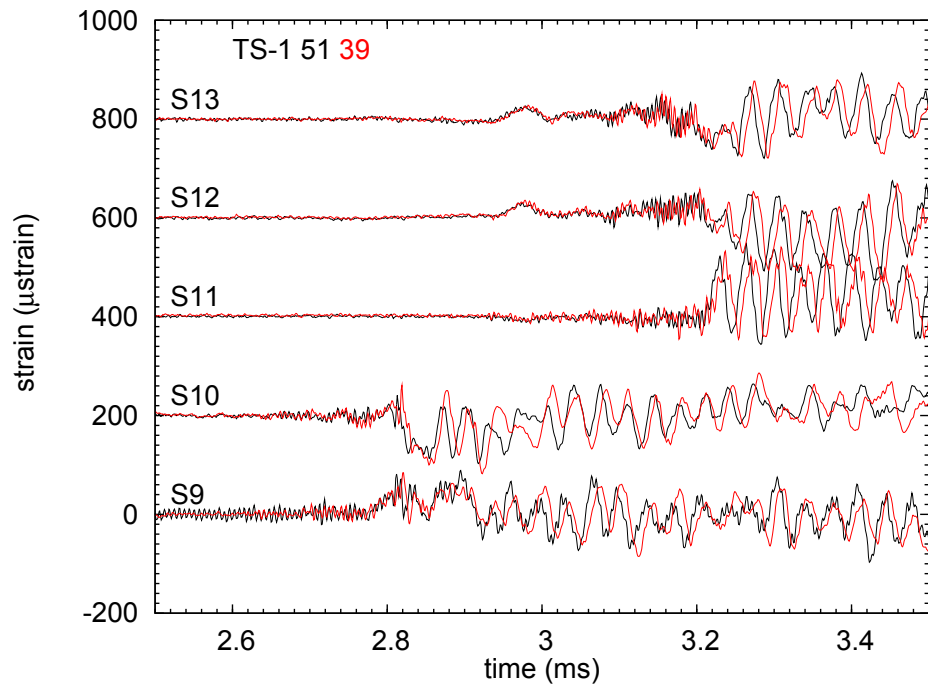
There were four arrangements for the piping end supports. When the ends are either free or supported by cantilever, we expect to see large axial strains in the direction of the piping due to motion induced by the initiation or reflection of the detonation from the end flange. When the ends are fixed by anchors, we expect that the motion is suppressed by transmitting the forces through the anchors into the mounting plates and walls of the test facility.

However, these effects will only appear over a long time scale since the relatively massive flanges (about 10 kg) move relatively slowly compared to the elastic wave propagation processes. As discussed in the next section, the period of the axial vibration of flanges resulting from the axial spring action of pipe is about 2.2 ms whereas the time for the bar wave to propagate the 1.27 m of the horizontal section is 0.25 ms, or 10 times faster. We expect for the fast time dynamics to be dominated by the wave mechanics within the pipe and the support conditions to have relatively little influence.

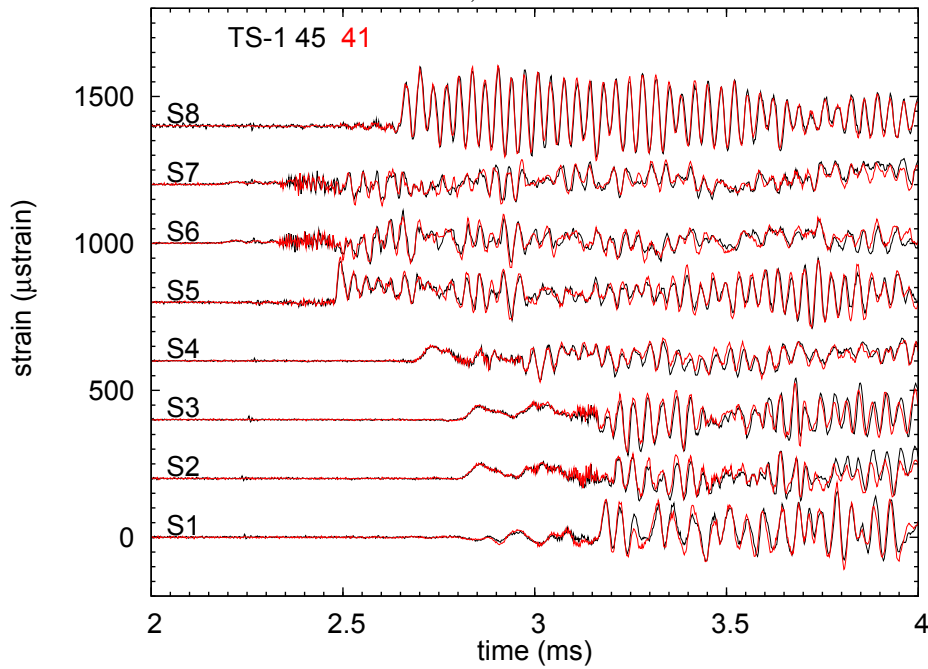
In comparing conditions at the horizontal ends, we have used two top ignition cases, shots 39 and 51, and just examined the strain gages on the west leg in Fig. 67a. The time origin for shot 39 has been adjusted by about  $50 \mu\text{s}$  to align the pressure traces for these two shots. For the first 3.5 ms, the strain signals for these gages are essentially identical which supports the notion that the strain in the pipe is essentially independent of the boundary conditions at early times.

To examine the influence of the top boundary condition, we have used two tests, 45 (top anchored) and 41 (top free), with east ignition. Both test have the horizontal ends supported on cantilevers. The east ignition location is used for this comparison since the reflected detonation loading is much more reproducible and larger in amplitude than the DDT ignition transient with the Shchelkin spiral. The time origin for shot 41 has been adjusted by  $35 \mu\text{s}$  to align the pressure traces for these two shots. For the first 3.5 ms, these strains signals are essentially identical, confirming the previous results that the early time pipe strains are essentially independent of the boundary conditions.

At long time, the boundary conditions clearly do make a difference. In Fig. 68, strain histories on the west horizontal segment are compared for shots 39 (cantilevers) and shot 51 (anchors). Two key differences can be noted. First, in shot 39, the 450 Hz oscillations in axial strain on S9, S10, S12 and S13 are much larger in amplitude and persist for a much longer period in time than for shot 51. Second, there the offset in strain at 100 ms is about three times as larger for shot 39 as for shot 51, except for the hoop strain S11, which has no offset or long-time oscillations in either shot. Both of these features of the axial strain histories are pretty clear-cut consequences of having anchors at the end of the horizontal segments in shot 51 while the ends are free to move in shot 39. The offsets are probably associated with the thermal expansion of the pipe, which is inhibited when the anchors are used.



a)



b)

Figure 67: TS1 comparison of end conditions. a) Shot 51 (all ends anchored) vs. shot 39 (top anchored and bottom ends on cantilevers). a) Shot 45 (top free) vs. shot 41 (top anchored).

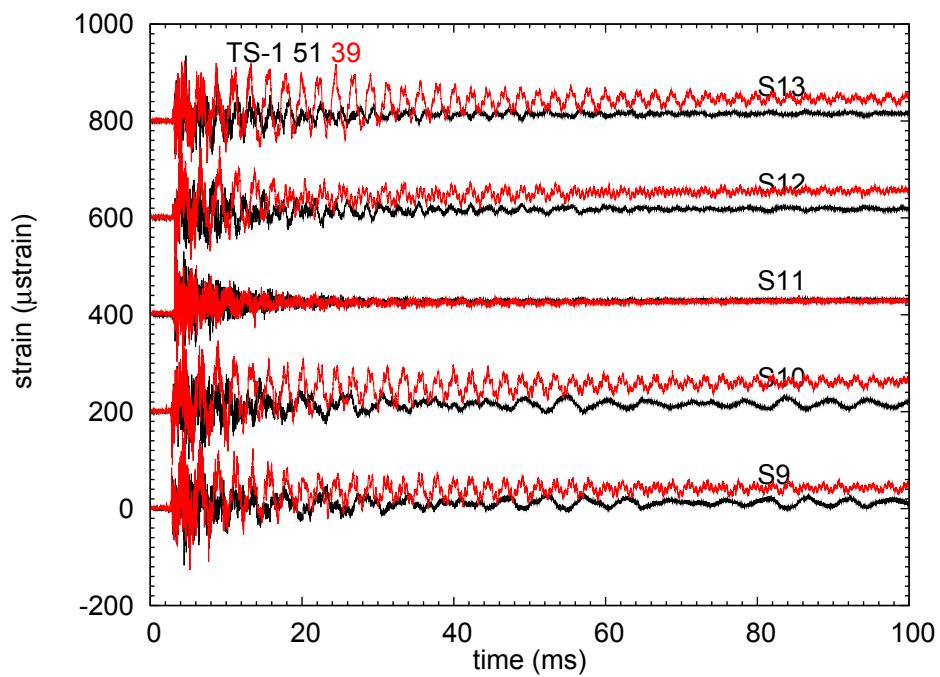


Figure 68: TS1 comparison of end conditions for a long time. Shot 51 (all ends anchored) vs. shot 39 (top anchored and bottom ends on cantilevers).

## 6.5 Bending, axial, and support strains

All except one of the strain gages (S4) were arranged in triples to measure separately hoop strain and longitudinal strains on the opposite sides of the pipe as shown in Fig. 55. Gages S9-S10 and S6-S7 are located 481 mm from the center equidistant from the tee fitting on the W and E horizontal legs, respectively. Gages S12-S13 are located 308 mm inboard of the flange on the W end of the horizontal leg of the tee. Gages S2-S3 are located 463 mm below the top flange on the vertical leg of the tee.

The longitudinal gages measure a combination of axial membrane and beam bending strains. Considering a pair (1, 2) of gages on opposite sides of the pipe, we can decompose the strains into axial membrane (*a*) and beam bending (*b*) components as follows.

$$\epsilon_1 = \epsilon_a + \epsilon_b \quad (66)$$

$$\epsilon_2 = \epsilon_a - \epsilon_b \quad (67)$$

Considering the pipe as a beam, added the strains from the top and bottom gages will cancel the beam bending contribution and subtracting the strains will cancel the axial membrane contribution.

$$\epsilon_a = \frac{1}{2}(\epsilon_1 + \epsilon_2) \quad (68)$$

$$\epsilon_b = \frac{1}{2}(\epsilon_1 - \epsilon_2) \quad (69)$$

We have analyzed the strains from shot 39 using this idea and show the results in Fig. 69. The signals labeled as sum or difference have actually been divided by two so that they correspond to axial and bending strains. Note that this data has been low-pass filtered to remove high (> 50 kHz) noise using the Savitsky-Golay method<sup>3</sup> and had the baselines adjusted to zero in order to better show the features of interest. In addition to the processed signals, the original signals and the hoop strain at that location are shown in the plots. All of the hoop gages are dominated by the characteristic ringing that is associated with the fundamental radial oscillation that is initiated when the detonation passes by that location. The axial membrane strains also contain energy at this frequency since the symmetric periodic deformation of the pipe caused by the hoop oscillation will create through-wall beam bending and the Poisson coupling also creates an axial strain oscillation at this frequency. The results from processing pairs S6& S7 (Fig. 69b) and S9 & S10 (Fig. 69c) are essentially identical as can be expected from the symmetry of the gage locations and the highly symmetrical loading discussed in the previous section. The results for pair S2 & S3 are not considered further since these gages are just downstream of the initiation spiral and subject to an uncharacterized pressure transient.

The analysis of signal pair S12 & S13 gives the most interesting result. A axial strain pulse (3.1 to 3.3 ms on on the sum signal S12+S13) can be clearly observed propagating ahead of the detonation-induced axial strains at 3.3 ms that are coincident with hoop strain onset on S11. This signal is not present in at all in the bending strain (S12-S13) signal. The

---

<sup>3</sup>The `sgolayfilt` function in MATLAB (MathWorks) with  $k = 3$  and  $F = 15$  was used for this purpose.

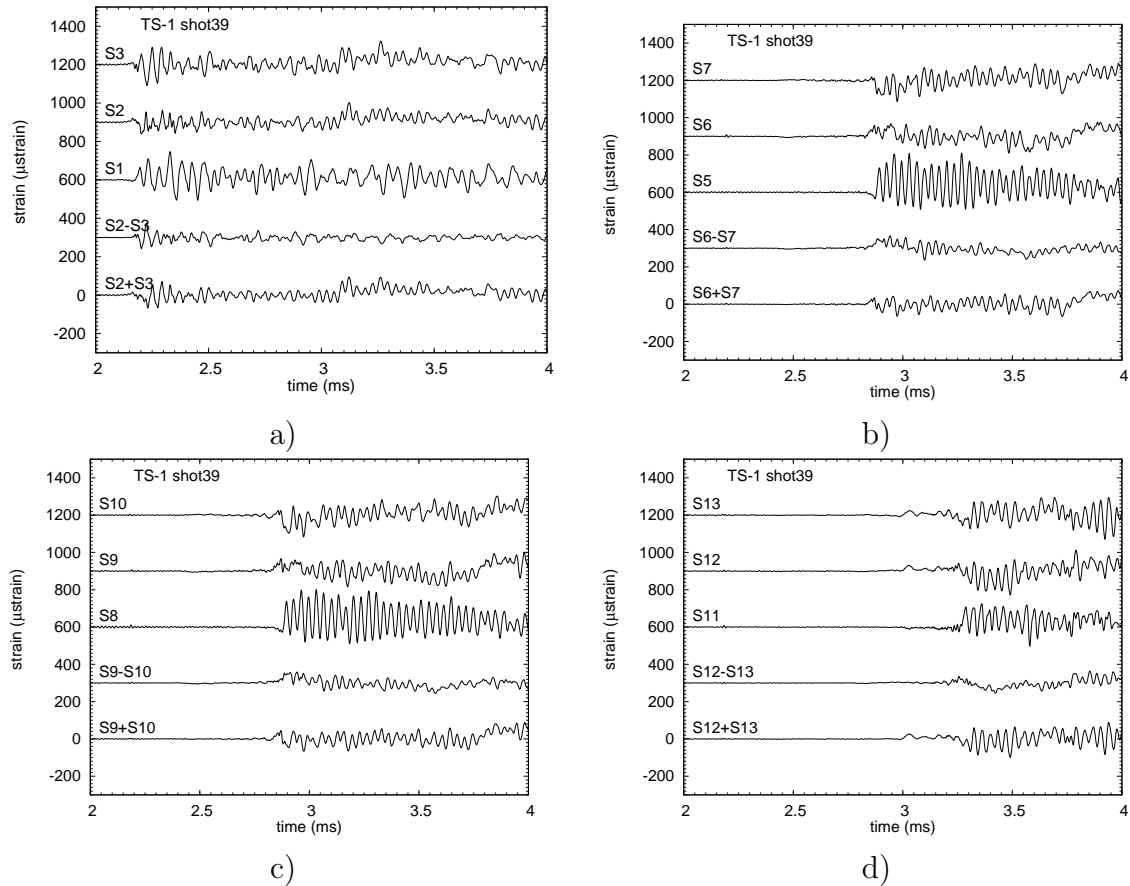


Figure 69: TS1 Shot 39 strain analysis.

arrival time and duration of the axial precursor is consistent with a wave that originates at the tee and propagates at the thin-shell speed of 4900 m/s ahead of the detonation and main flexural waves. Using the ideal wave speeds, we estimate that the axial strain wave takes about  $210 \mu\text{s}$  to propagate from the tee to the S12 gage location and will lead the detonation arrival by about  $355 \mu\text{s}$ .

The frequency content reflects the various vibration modes that are possible in this system. In some cases, the modes are coupled so that common frequencies are observed in gages that measure strains in different components or orientations. In other cases, modes appear to be uncoupled. Examples of frequency power spectra, displayed as single-side amplitude spectrum, computed using a discrete Fourier transform (FFT) in [MathWorks](#), are shown in Figs. 70 and 71. In the hoop strain (Fig. 70a and b), the fundamental hoop breathing mode at about 29 kHz is dominant at high frequencies but there are peaks with similar magnitude at much lower frequencies of 427, 450, 1968, and 3044 Hz. There are actually a number of frequency peaks near 29 kHz, the largest of these is at 28.58 kHz, and the next largest at 29.5 kHz.

The beam bending strains (Fig. 70c and d), show a number of peaks less than 5 kHz with the largest amplitudes being at frequencies of 359, 427, 450, 1152, and 3044 Hz. One possibility is that these modes represent combined ovalization and beam bending (referred to

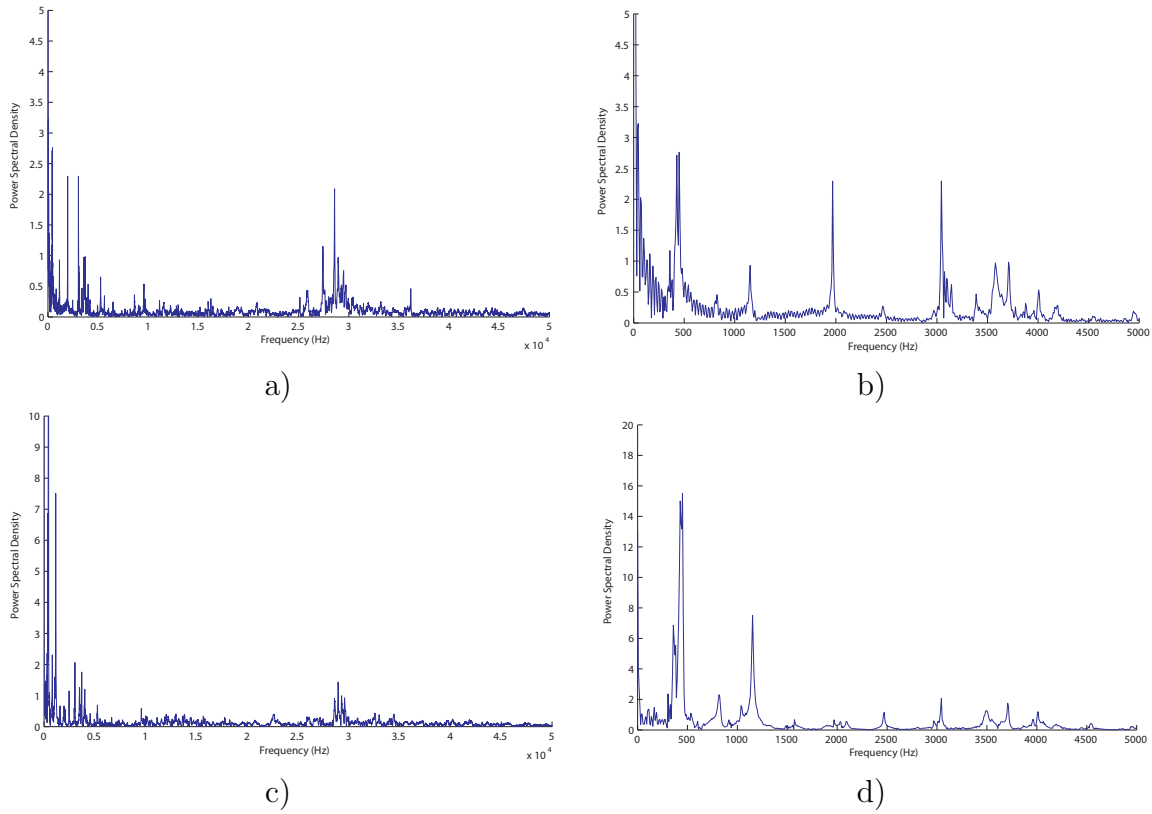


Figure 70: TS1 Shot 39 spectral analysis of selected strain signals. a) and b) hoop strain from gage S11. c) and d) beam bending strain from the difference signal S12-S13.

as radial-axial modes), which would create coupled strains in the hoop and axial directions. The coincidence of the peaks for selected frequencies supports this speculation.

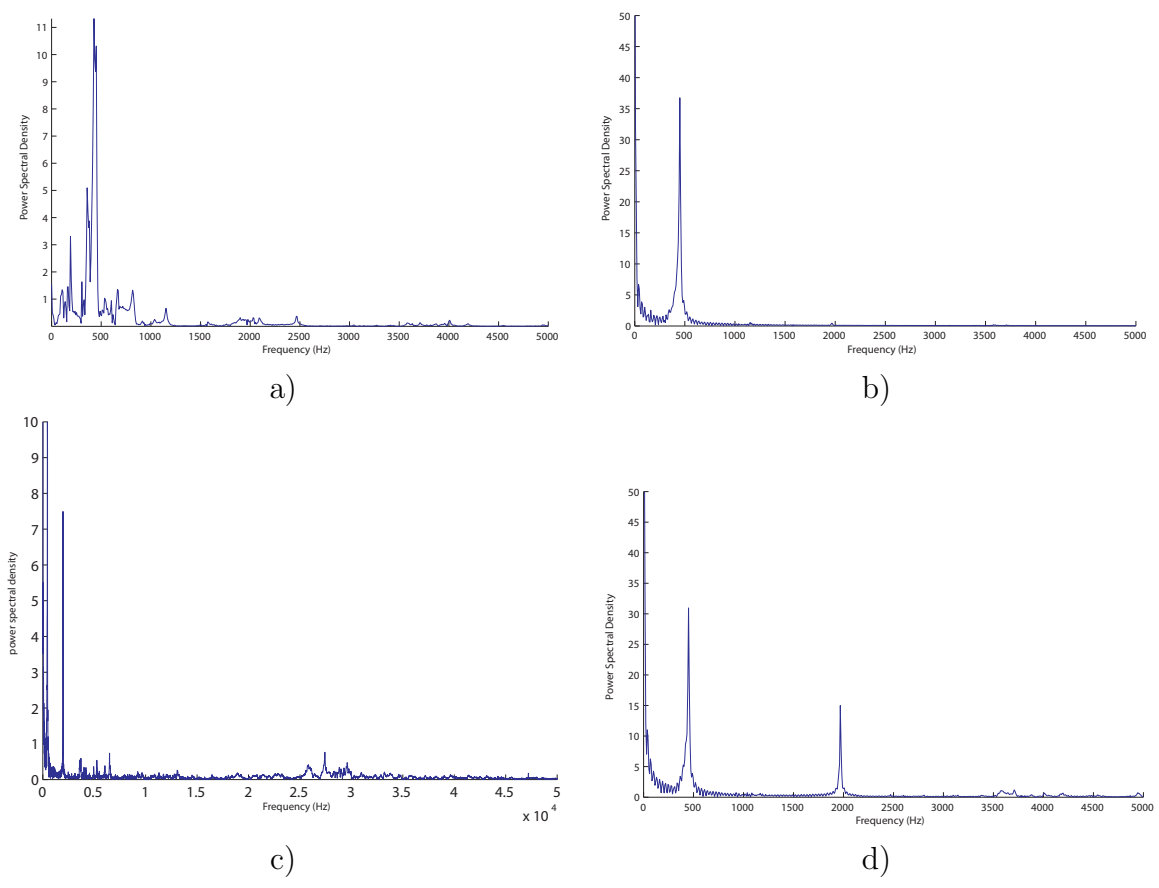


Figure 71: TS1 Shot 39 spectral analysis of selected strain signals. a) S26 cantilever bending strain in vertical direction b) S27 cantilever bending strain in horizontal direction. c) and d) axial and membrane bending strain from the sum signal S12+S13.

### 6.5.1 Support Strain Analysis

The support strains (Fig. 65b, d and 66b) show a very clear periodic signal and corresponding major spectral peak at 450 Hz in the horizontal motion of the cantilever (Fig. 71b) and the axial strain of the pipe (Fig. 71d). There is an additional peak at 1968 Hz in the axial strain.

The prominent vibration at 450 Hz can be explained by considering the mechanics of the motion in the horizontal direction of the horizontal leg of the pipe between the tee and the closed end. Since the excitation and the piping system are symmetric about the centerline of the vertical pipe, it is only necessary to consider the motion of one-half of the horizontal section. We can model this as a spring-mass system that is excited by the reflection of the detonation from the closed end. Consider the western half of the bottom of the tee, shown in Fig. 72. The reflection of the detonation from the closed west end will create an oscillation

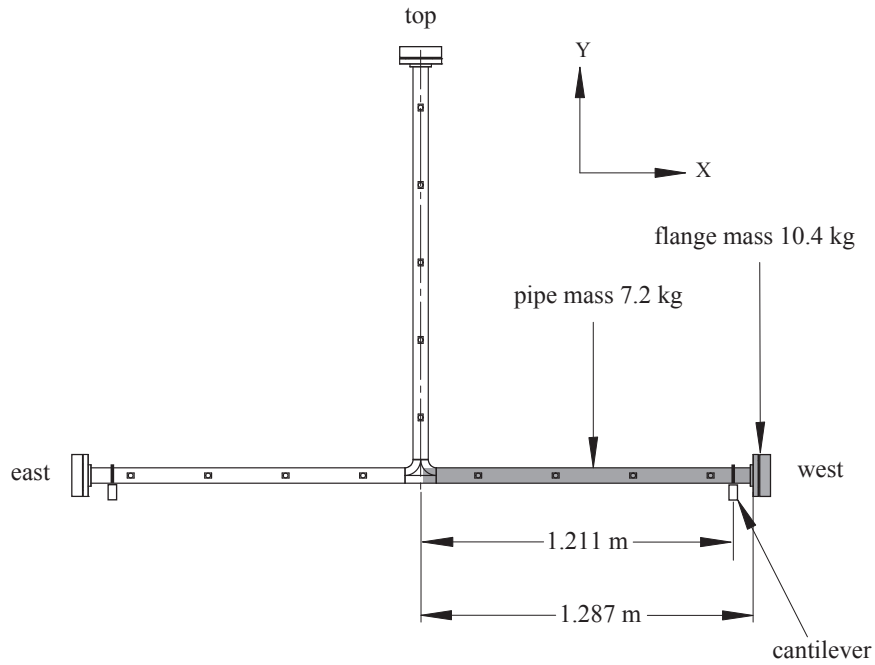


Figure 72: TS1 key dimensions. Components considered in vibration analysis are shown filled in with gray shading.

in the  $X$ -direction. The restoring force is due predominantly to the elastic axial motion of the pipe, which has an effective spring constant in the  $x$ -direction of

$$k_{p,x} = \frac{EA}{L} , \quad (70)$$

$$= 1.04 \times 10^8 \text{ N/m} \quad (71)$$

The cantilever  $x$  spring constant is an order of magnitude smaller (p. 69 [Shepherd and Akbar, 2009](#))

$$k_{c,x} = 1.85 \times 10^7 \text{ N/m} , \quad (72)$$

so we can neglect the bending resistance of the cantilever in the  $x$ -direction. Since this is a relatively low frequency oscillation, the pipe can be treated as a beam-like spring with a distributed mass  $M_p$  attached to the flange assembly treated as a rigid mass  $M_f$ . The longitudinal oscillation frequencies of a beam fixed at one end and with a rigid mass at the other is (See Table 8-16 of [Blevins, 2001](#))

$$f = \frac{\lambda_i}{2\pi L} \sqrt{\frac{E}{\rho}} , \quad (73)$$

where the eigenvalues  $\lambda_i$  are determined by the solution of

$$\cot \lambda_i = \frac{M_f}{M_p} \lambda_i . \quad (74)$$

Using the dimensions for schedule 40 pipe (Table 24) the cross-sectional area is

$$A = \pi(R_o^2 - R_i^2) , \quad (75)$$

$$= 6.92 \times 10^{-4} \text{ m}^2 . \quad (76)$$

Using the length from the center of the tee to the flange as the beam length  $L = 1.287$  m, the mass of the pipe is

$$M_p = \rho AL , \quad (77)$$

$$= 7.169 \text{ kg} . \quad (78)$$

The mass of the flange assembly is 10.4 kg so that

$$M_f/M_p = 1.45 . \quad (79)$$

The roots and associated frequencies of the three lowest modes are given in Table 16. The lowest frequency (mode 1) is within 0.3% of the measured frequency of 450.1 Hz principal peak observed in Fig. 71b and d. The frequency of mode 2 is within 1% of the measured frequency of 1968 Hz next largest peak observed in Fig. 71d. There is a much smaller and broader peak between 3500-3700 Hz that overlaps the third mode location. The  $x$  motion of the cantilever is driven by the beam since they are connected by the U-bolt but only the lowest mode can be observed since the other modes are above the resonant frequency of the cantilever (670–830 Hz) and strongly damped.

Two dominant spectral peaks are observed at 450.1 and 427 Hz, as well as a number of smaller peaks are present between 100-1200 Hz in the spectrum (Fig. 71a) of the cantilever

Table 16: First three axial vibration frequencies of half tee-flange system.

$i$	$\lambda_i$	$f_i$ (Hz)
1	0.7461	451.7
2	3.345	2025.4
3	6.039	3656.7

bending strain in the vertical direction. A number of these frequencies are in common with the beam bending spectrum, 70a and b. This is reasonable since the beam bending modes are expected to be strongly coupled to vertical motion of the cantilever support due to the U-bolt.

The vertical motions are more difficult to create a simple model for than the horizontal motions. The axial stiffness of the vertical leg of the tee, the pipe bending in beam motion, the vertical motion of the cantilever support as well as the vertical oscillations of the flange mass at the free ends will all contribute to determining the modes and frequencies. The cantilever is about 100 times stiffer than the horizontal pipe segment in beam bending so one approximation is to ignore the bending stiffness of the horizontal segments of the pipe and only consider the cantilever vertical motion with a combination of a fraction of the pipe mass and the flange mass. The axial stiffness of the vertical leg of the pipe is about 4 times higher than that of the cantilever so any realistic model needs to include vertical deflection and restoring action on the tee. Rather than attempt to create a simplified representation of TS1 to model the vertical motion, resolving the mode structure and resonant frequencies is left for future work that is probably best performed by finite element analysis.

## 6.6 Comparison with Finite-Element Simulations

Numerical simulations using ANSYS and a detailed finite element model of TS1 were reported in Ligon (2009c). Selected results from these comparisons are shown in Figs. 73-75 for shot 43. Using a very simple model of the interaction of the detonation with the tee, good agreement is obtained for both the qualitative and quantitative features of axial and hoop strains.

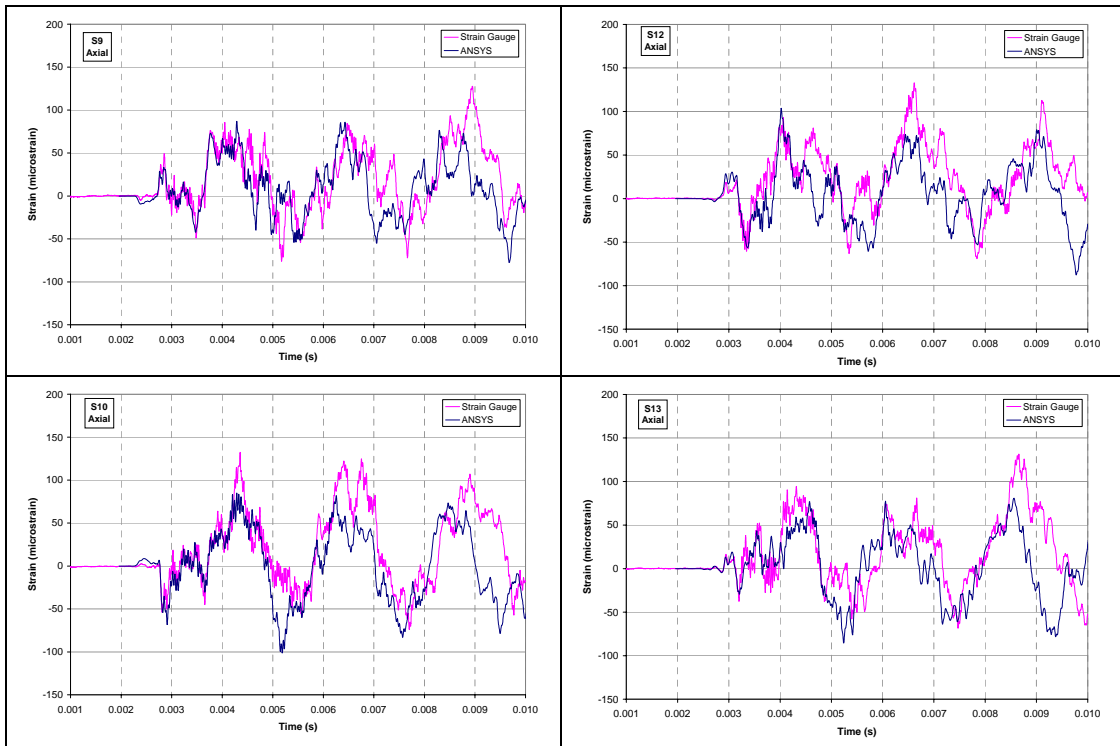


Figure 73: TS1 Shot 43 comparison of filtered data with ANSYS simulations. Reproduced from p. 22 of Ligon (2009c).

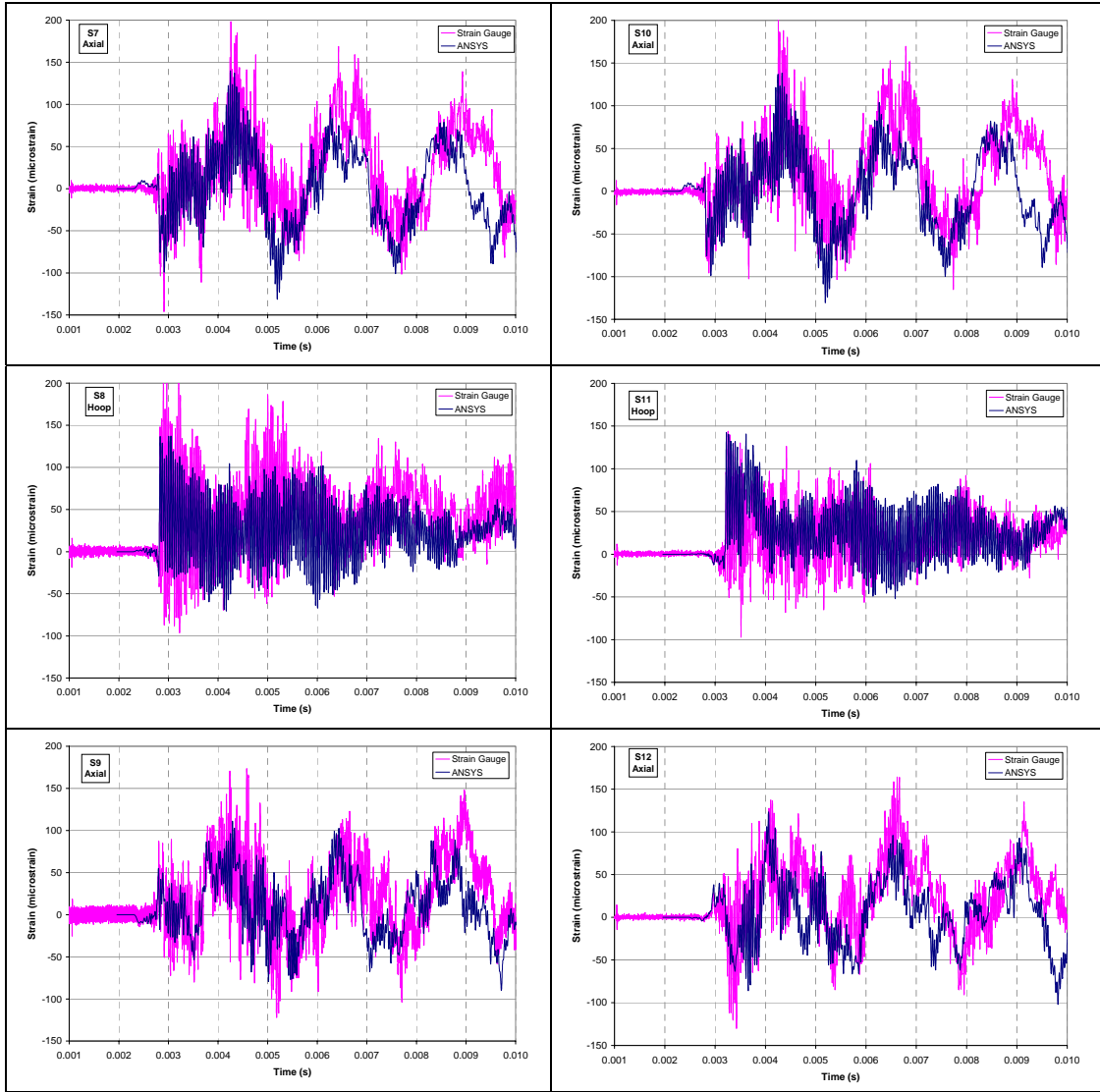


Figure 74: TS1 Shot 43 comparison of raw data with ANSYS simulations. Reproduced from p. 26 of Ligon (2009c).

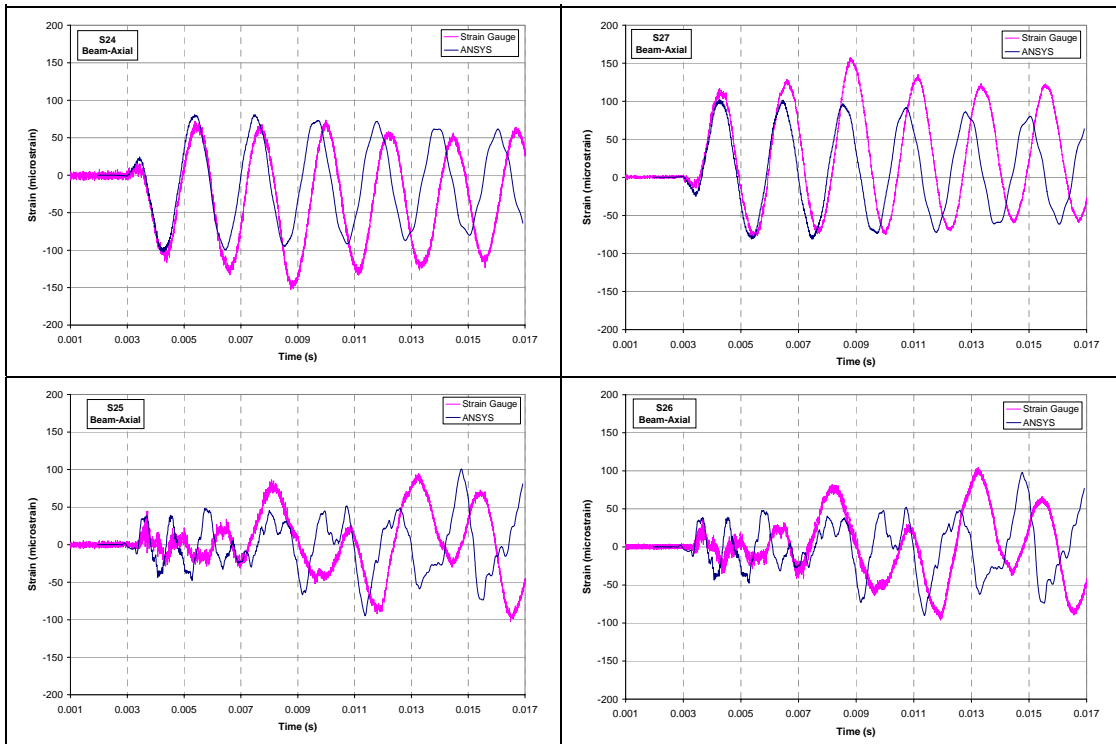


Figure 75: TS1 Shot 43 comparison of cantilever support data with ANSYS simulations. Reproduced from p. 27 of [Ligon \(2009c\)](#).

## 6.7 Summary

1. 30/70 H<sub>2</sub>/N<sub>2</sub>O detonations propagate through a 90-degree Tee with relatively little disturbance in either direction.
2. A reflection factor of 2 is appropriate for computing the detonation force when normally incident on the tee.
3. Using cantilever beams that were clamped to the pipe, the deflections of the cantilevers and the strains (axial and hoop) in the pipe could be adequately predicted by finite element simulations.
4. The support loads are adequately predicted in the case of TS1.
5. At early times,  $< 4$  ms, the boundary condition (cantilevers vs anchors) on the pipe ends does not play a role in determining the pipe axial strain.
6. At long times,  $\sim 100$  ms, the boundary condition on the pipe has a very strong influence on the axial strain history including the characteristic frequencies of oscillations, amplitudes, and offset.
7. The pipe strains are bounded by estimates based  $P_{CJ,ref}$  with  $\Phi = 1$ .

## 7 SS1 Test Series

These tests were carried out with a combination of five segments of welded construction that were fastened with bolted flanges (no gaskets) to make a serpentine piping system that covered the North, West, and South walls. The system incorporated the two specimens used for TS1 and ES1 with three additional specimens fabricated to create the three-dimensional system which incorporated a combination of three fixed ends, ten bends, and seven cantilever supports. An overview of the system is shown in Fig. 76 and engineering drawings of the specimens are given in Appendix N. The construction method (certified welding) and materials (2-in Schedule 40 304/316L seamless pipe) were the same as used for TS1 and ES1. Each piping segment was terminated with slip-on flange that was welded on using interior and exterior fillet welded as discussed in Section 2.

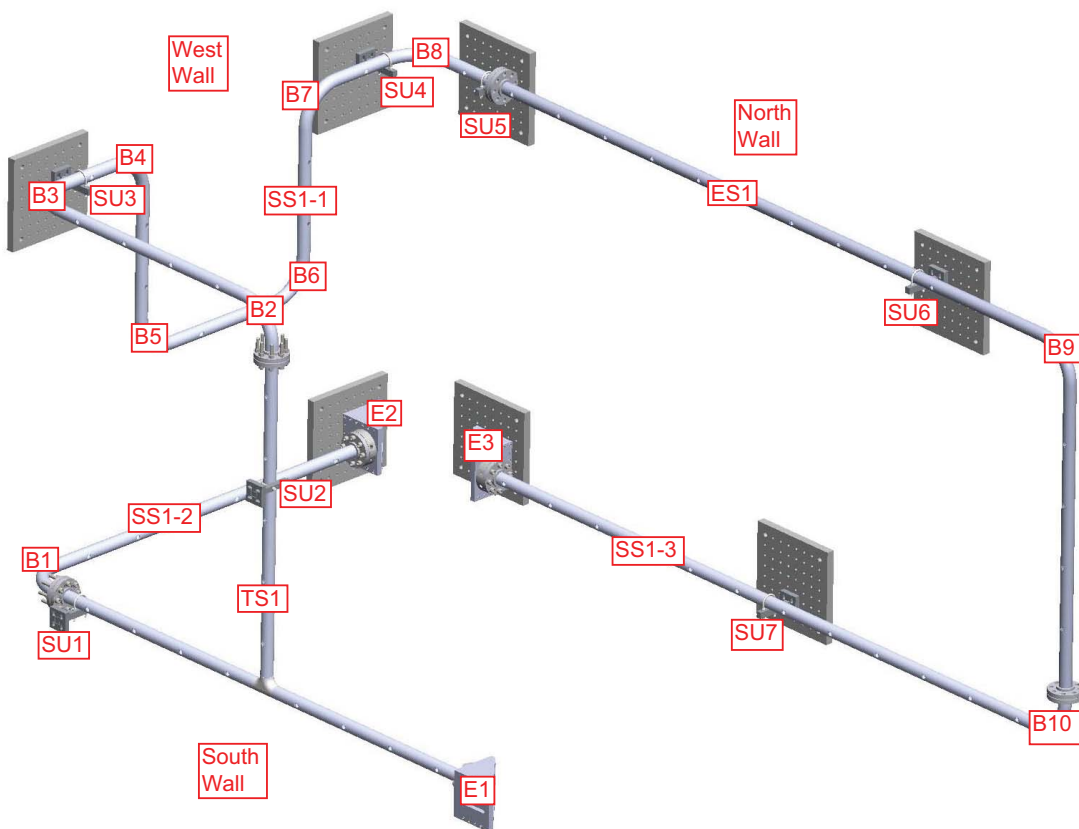


Figure 76: SS1 perspective view.

**Bends** There were ten 90-degree bends that were welded to straight sections. The bends were created by hydraulic forming and were similar to that used in ES1. Three of the bends (B1, B3, and B8) connected piping segments in the out-of-plane direction at the corners of the room, the other eight bends connected pipe segments that were in the same plane. The radius of the bend measured to the intrados of the pipe is 6.40 in and the radius of the centerline is 7.60 in. The nominal wall thickness of the pipe is about 0.149 in but due to

the hydraulic forming process, the pipe is thinner on the extrados (as thin as 0.138 in) and thicker on the intrados (as much as 0.164 in).

**Strain and Pressure gages** Only longitudinal strain gages were used in these tests. Additional strain gages were added in order to determine in plane, out-of-plane and separate axial strains from bending. The locations of the strain and pressure gages are shown in the sensor layout schematics on Figs. 265–267.

**Supports** The piping system was supported by three fixed anchors, E1, E2, and E3, described in Section H, and seven additional beam cantilevers supports (SU1–SU7) that were attached to the piping with U-bolts as described in Section G. A thin sheet of Teflon was glued to the pipe and the cantilever. The U-bolts were not tightened but a small (0.005–0.010 in) clearance gap was left so that the pipe could move in the axial direction. Only two strain gages (in the vertical or A–B locations as shown in Fig. 123) were recorded for two supports. The strain gages were not connected in a half-bridge as in the ES1 testing (see Shepherd and Akbar (2009)) but recorded separately to determine the in-plane and out-of-plane forces by digitally processing the signals.

**Ignition** All tests were carried out with a 1-ft Shchelkin spiral and the standard spark ignition source as used in the previous tests and described in Section 2.6. One shakedown test (52) and four full tests (53-56) were carried out using ignition at location E3 ((NW corner of SS1-1), and four full tests (58-61) were carried out using ignition at location E1 (SE corner of TS1). All tests resulted in prompt detonation (within 1-2 ft from the spiral) and analysis of the pressure wave arrival time data showed that the detonation speeds were within 1% of the computed CJ velocity.

**Layout** Photographs of the layout of the piping system in the test cell are shown in Fig. 77-80.



a



b

Figure 77: SS1 layout in test cell. a) north wall b) transition from north to west wall.



Figure 78: SS1 layout in test cell showing west wall.



Figure 79: SS1 layout in test cell showing transition from west to south wall.

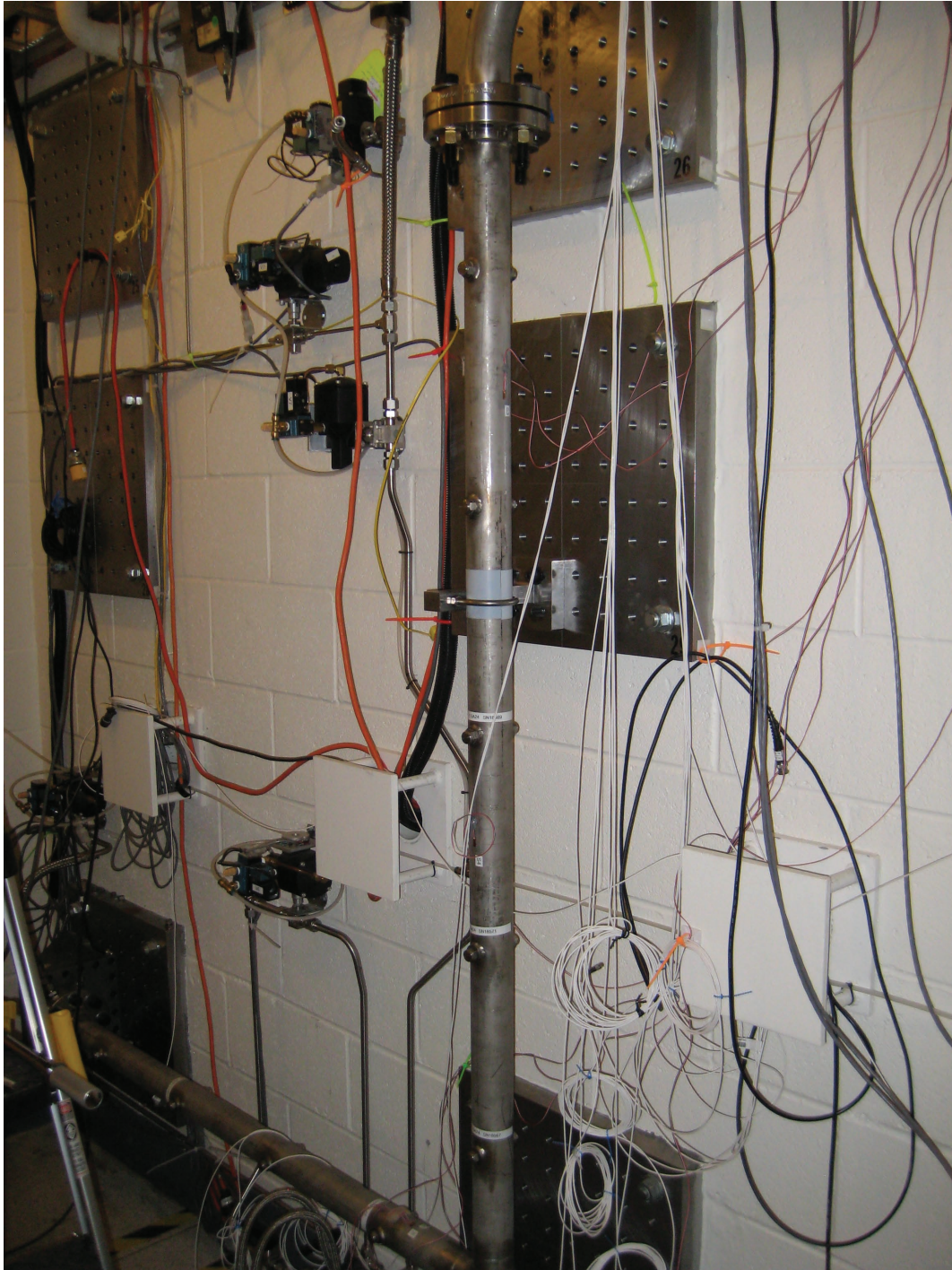


Figure 80: SS1 layout in test cell showing south wall.

## 7.1 Test Program

A total of 10 tests were performed with two different ignition locations. The mixture was nominally a 30:70 H<sub>2</sub>:N<sub>2</sub>O mixture at 1 atm and 26-27°C for all tests. Data plots and sensor locations are given in Appendix O. The tests are described briefly below and in Table 17.

Shot 52 Ignition location E3, signal set 0, pressure transducers only. This tests was used to only to check the operability of the SS1 test assembly.

Shot 53 Ignition at E3, signal set 1, pressure transducers, strain gages, and displacement gages.

Shot 54 Replica of shot 53 with the same signal set.

Shot 55 Replica of shot 53 with signal set 2.

Shot 56 Replica of shot 55 with signal set 2.

Shot 57 DAS did not trigger and no data was collected.

Shot 58 Ignition at E1, signal set 1. Replaced gage P13. Moved location of gages P18 and P12.

Shot 59 Replica of 58.

Shot 60 Replica of 58 with signal set 3.

Shot 61 Replica of 60.

There were 4 sets of signal combinations. Due to a failure in the data acquisition system, we were unable to record as many channels as we had originally planned so that we had to carry out repeat tests with signals swapped in order to cover all the strain gages that were of interest. The signal sets are described below and in the tables in Appendix O.

Signal set 0 Shot 52 only. Pressure transducers P1–P15 only.

Signal set 1 Shots 53, 54, 58, and 59. Pressure transducers P1–P20, longitudinal stain gages on the piping S1–S27, longitudinal strain gages S36–S37 on support SU2 mounted on the vertical leg of TS1, and strain gages S38–S39 mounted on support SU4 on SS1-1, displacement gages D1, D2, D3, and D4.

Signal set 2 Shots 55, and 56. Pressure transducers P1–P20, longitudinal strain gages on the piping S1–S11, S20–S35, strain gages S36–S37 on support SU2 mounted on the vertical leg of TS1, and strain gages S38–S39 mounted on support SU4 on SS1-1, displacement gages D1, D2, D3, and D4.

Signal set 3 Shots 60, and 61. Pressure transducers P5–P17, P19, P20, longitudinal strain gages on the piping S4–S35, strain gages S36–S37 on support SU2 mounted on the vertical leg of TS1, and strain gages S38–S39 mounted on support SU4 on SS1-1, displacement gages D1, D2, D3, and D4.

Table 17: List of test conditions for all shots in series SS1

Shot	Mixture	$P$ Torr	$T$ °C	Ignition Location	Signal Set	Date	Time	Notes
52	H2:30 N2O:70	760.4	26.8	E3	0	4-Mar-09	6:15	Shakedown test, pressure data only 15 gages.
53	H2:30 N2O:70	760.7	26.8	E3	1	2-Apr-09	6:09	D1= 1401 s/n 712108, D3 1300 s/n 711028
54	H2:30 N2O:70	760.4	26.6	E3	1	5-Apr-09	23:41	replica of 53, D1= 1401 s/n 712108, D3 1300 s/n 711028
55	H2:30 N2O:70	760.6	27.1	E3	2	8-Apr-09	13:50	Signal set changed, D1 and D3 units swapped; same for all subsequent tests
56	H2:30 N2O:70	760.8	26.6	E3	2	8-Apr-09	22:19	Replica of 55
57	H2:30 N2O:70	-	-	E1	1	-	-	Early trigger and data was lost.
58	H2:30 N2O:70	760.7	27.1	E1	1	10-Apr-09	18:45	Ignition location change, replaced P13, P18, and P12 moved.
59	H2:30 N2O:70	760.6	27.1	E1	1	11-Apr-09	4:47	replica of 58.
60	H2:30 N2O:70	760.7	27.0	E1	3	12-Apr-09	1:15	Changed signal set to 3
61	H2:30 N2O:70	760.9	26.9	E1	3	12-Apr-09	22:29	Replica of 60

## 7.2 Detonation Wave Speeds

Detonation speeds were determined by carrying out linear regression on the arrival times of the leading front of the detonation wave from the pressure gage signals. A typical set of signals for shot 53 are shown in Fig. 81, 82, and 83.

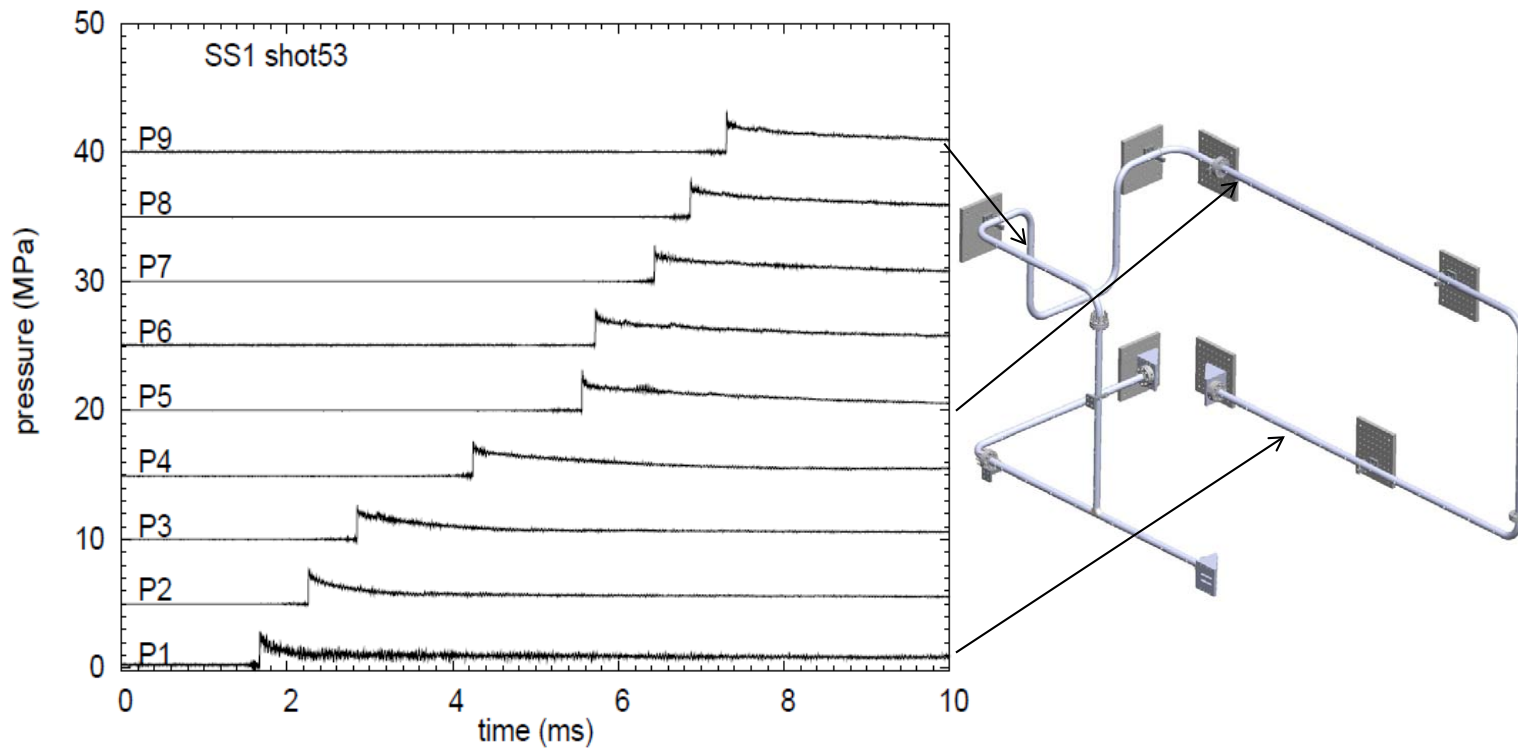


Figure 81: Pressure data, P1-P8 for shot 53.

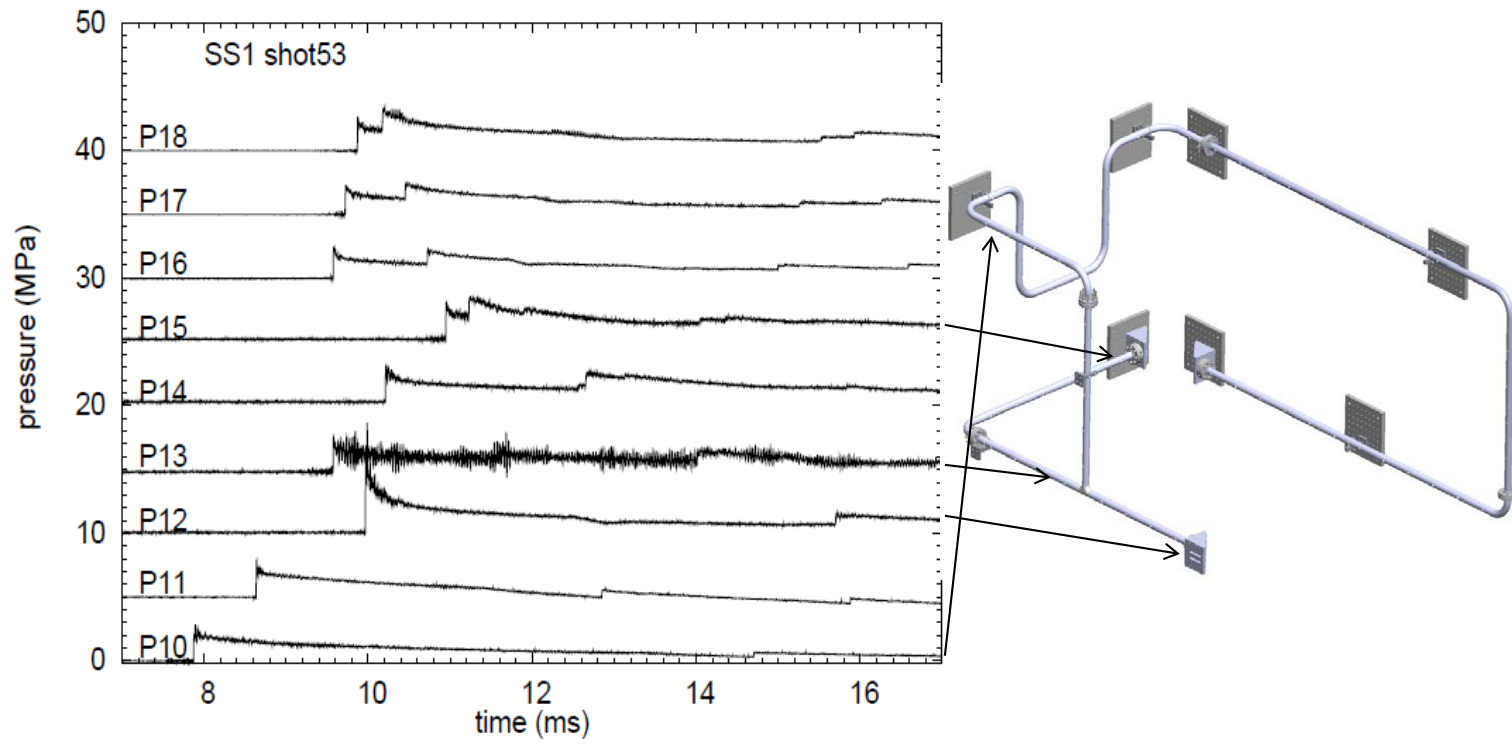


Figure 82: Pressure data, P10-P18 for shot 53.

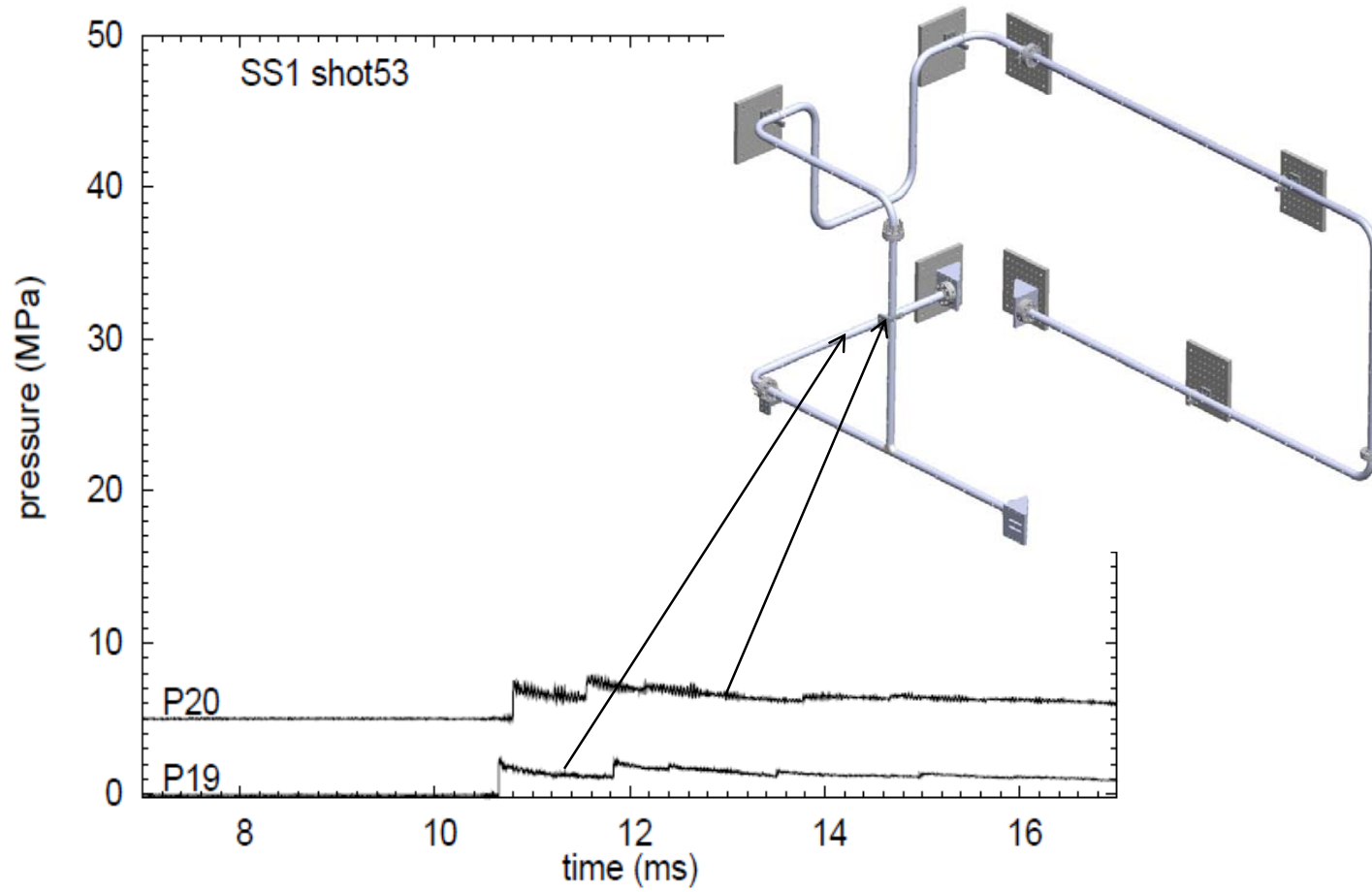


Figure 83: Pressure data, P19-P20 for shot 53.

The transducer locations were computed as the axial distance (along the pipe centerline) from the ignition point to the gage location as determined by the as-built (measured) dimensions on the installed piping system. In all cases, an excellent fit was obtained between the arrival times and gage locations, an example is shown for shot 53 in Fig. 84.

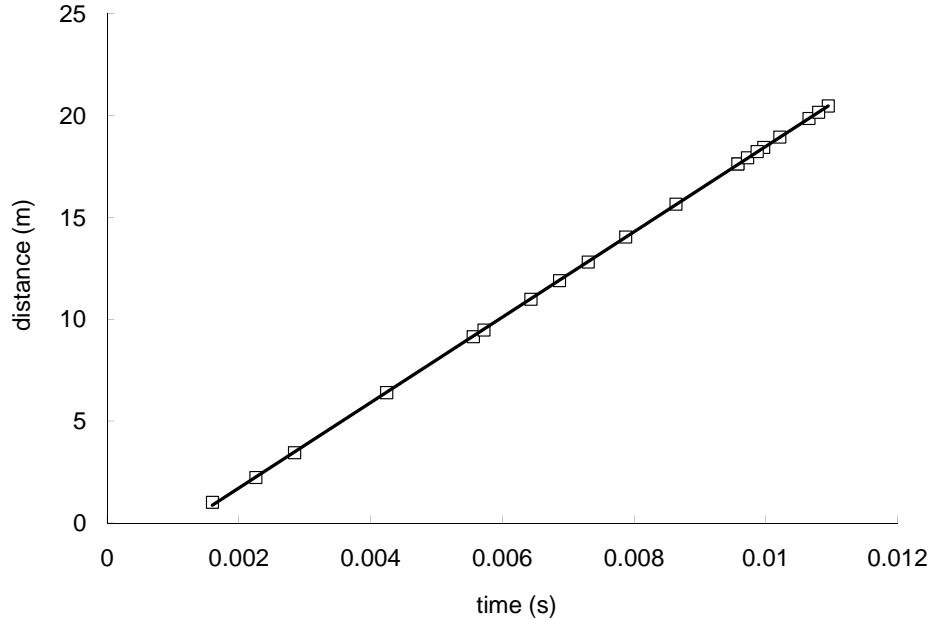


Figure 84: Linear regression fit to detonation arrival time data for shot 53.

A pressure rise threshold of between 0.5 and 1 MPa was used to determine the arrival time. All recorded pressure transducers were used in the determination of wave speed for each test. The measured wave speed was very consistent but in all cases was more than one- $\sigma$  from the nominal CJ speed of 2088.0 m/s. There are two possible reasons: 1) due to large number of bends and three-dimensional construction, the location of the transducer ports was subject to some uncertainty and the errors stacked up since increment measurements were used to determine the locations. 2) small variations in the initial composition can result in observed variation in the CJ wave speed, see Table 19.

### 7.3 Peak Pressures and Strains

In all tests except for 52, 20 pressure sensors were used. Table 20 gives the locations used in tests 53-56 with ignition in location E3. Table 21 gives the locations used in test tests 58-61 with ignition in location E1. The distances shown are different because the measurement is from the ignition location although almost all transducers were in the same ports in the two series of tests. The values of peak pressure rise and the associated standard deviation were computed from the pressure signals for both data sets. Peak pressures are substantially higher than the CJ values or in case of P12, the reflected CJ value. This is typical for peak pressures measured from unfiltered data. The structure of the detonation wave leads to these localized high pressures due to the cellular structure (instability or transverse waves) on the

Table 18: Detonation wave speeds in the SS1 tests. The nominal CJ speed is 2088 m/s.

shot	$U$ (m/s)	$\sigma_U$ (m/s)
52	2091.4	2.1
53	2097.3	3.2
54	2093.4	2.7
55	2093.7	3.4
56	2097.6	3.3
58	2099.9	1.9
59	2102.5	2.5
60	2100.9	3.6
61	2102.9	4.3

Table 19: Detonation CJ wave speeds computed as a function of composition for  $T_o = 300.15$  K and  $P_o = 101.352$  kPa.

$X_{H_2}$	$U_{CJ}$ (m/s)
0.28	2060.8
0.29	2074.3
0.30	2087.9
0.31	2101.6
0.32	2115.5

front. If the data is filtered to remove the high frequency content but not so much that the shock wave is obscured, the peak values will be closer to or slightly less than the CJ values.

Table 20: Detonation peak pressure rise for SS1 tests 53-56 with E3 ignition. The nominal CJ pressure rise is 2.51 MPa and the reflected CJ pressure rise is 6.4 MPa.

Sensor	Average (Mpa)	Stdev (Mpa)	Distance (m)	Section	Port
1	2.89	0.07	1.011	SS1-3	4
2	2.70	0.02	2.230	SS1-3	8
3	2.57	0.08	3.449	SS1-3	12
4	2.56	0.04	6.398	ES1	17
5	3.18	0.07	9.141	ES1	26
6	2.74	0.07	9.474	SS1-1	27
7	2.71	0.03	10.982	SS1-1	30
8	2.79	0.04	11.897	SS1-1	32
9	3.11	0.03	12.811	SS1-1	34
10	2.84	0.02	14.037	SS1-1	36
11	2.89	0.02	15.650	TS1	40
12	8.57	0.14	18.439	TS1	E1
13	3.34	0.30	17.625	SS1-2	50
14	3.15	0.04	18.949	SS1-2	53
15	3.52	0.06	20.473	SS1-2	58
16	2.47	0.02	17.625	TS1	47
17	2.45	0.04	17.930	TS1	46
18	3.22	0.06	18.235	TS1	45
19	2.33	0.01	19.863	SS1-2	56
20	2.86	0.03	20.168	SS1-2	57

Table 21: Detonation peak pressure rise for SS1 tests 57-61 with E1 ignition. The nominal CJ pressure rise is 2.51 MPa and the reflected CJ pressure rise is 6.4 MPa.

Sensor	Average (Mpa)	Stdev (Mpa)	Distance (m)	Section	Port
1	3.77	0.49	17.428	SS1-3	4
2	2.72	0.03	16.209	SS1-3	8
3	2.29	0.04	14.990	SS1-3	12
4	2.84	0.03	12.041	ES1	17
5	3.00	0.02	9.298	ES1	26
6	2.89	0.02	8.965	SS1-1	27
7	2.82	0.08	7.457	SS1-1	30
8	2.70	0.04	6.543	SS1-1	32
9	2.95	0.01	5.628	SS1-1	34
10	2.58	0.05	4.403	SS1-1	36
11	3.18	0.03	2.789	TS1	40
12	8.65	0.04	18.439	SS1-1	E3
13	2.85	0.02	1.884	SS1-2	50
14	3.14	0.02	3.207	SS1-2	53
15	3.62	0.03	4.731	SS1-2	58
16	2.38	0.05	0.814	TS1	47
17	2.02	0.02	0.509	TS1	46
18	4.09	0.07	18.343	SS1-3	1
19	2.36	0.05	4.122	SS1-2	56
20	2.72	0.03	4.427	SS1-2	57

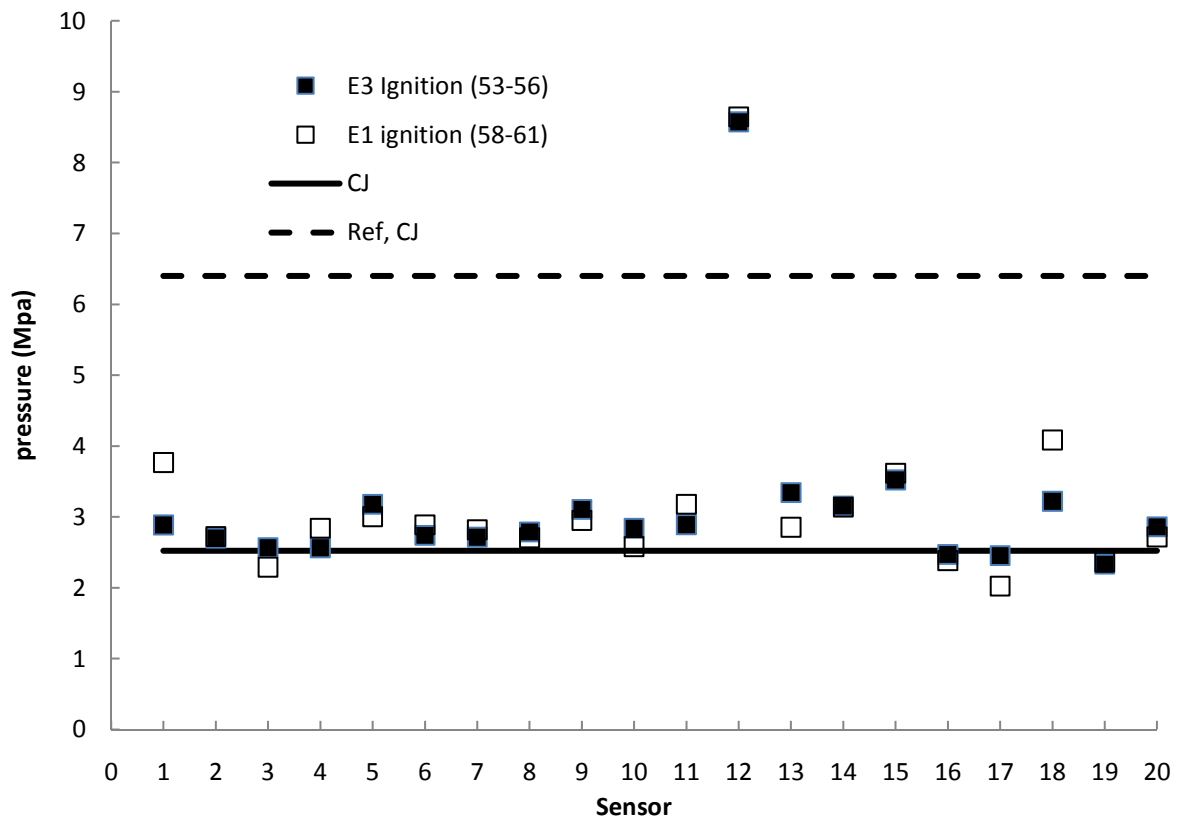


Figure 85: SS1 tests peak pressure rise values averaged for each data set.

The peak strains were determined for each gage and all tests. Grouping the data into two sets, the average peak strain and standard deviation were determined and are reported in Table 22. The location of each set of strain gages is given in Tables 36 and 35. The average peak strain was 166  $\mu$ strain for the tests with E3 ignition and 150  $\mu$ strain for tests with E1 ignition. All of these gages were oriented in the axial (longitudinal) direction. The values are similar to those observed in the other tests. The maximum and minimum values are bounded, see Fig. 86, by the reference strains of Table 6 computed for CJ detonations and reflected shocks created by CJ detonations. The bounding values for SS1 peak strains are consistent with the CJ detonation measurements for ES1, Fig. 25, and TS1, Fig. 63. Slightly higher strains are measured on the elbow and near the reflecting end of ES1 but otherwise all other gages in all tests fall within the same limits,  $90 \leq \epsilon \leq 250 \mu$ strain.

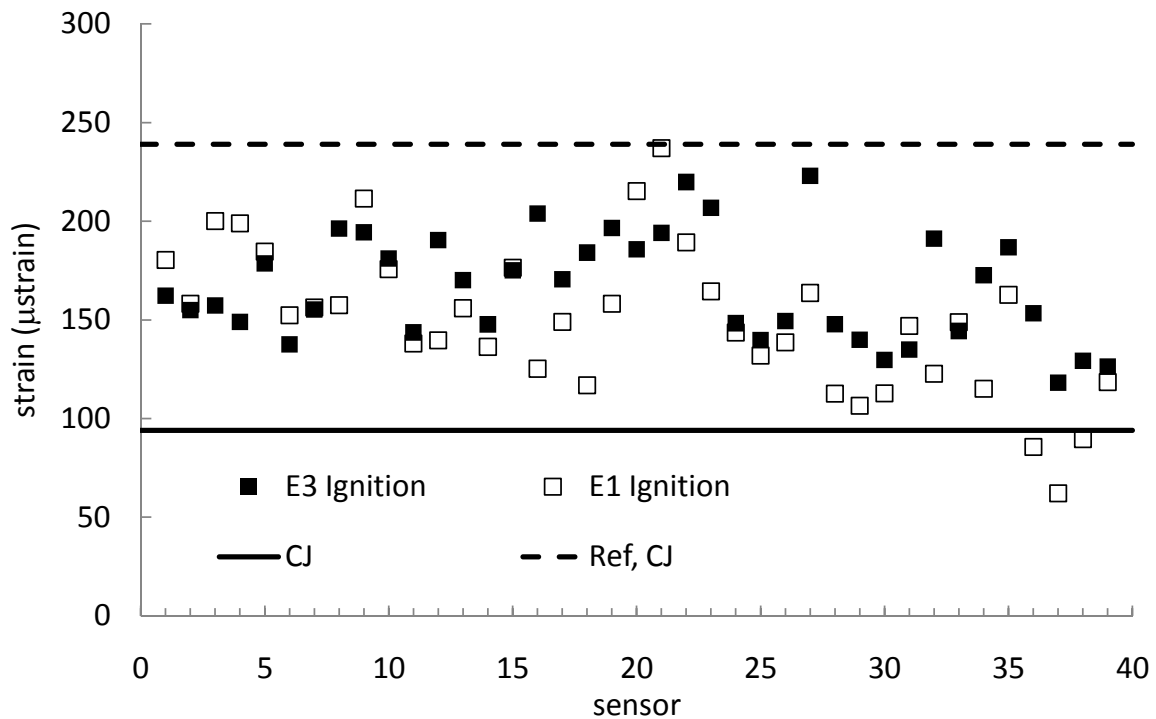


Figure 86: SS1 tests peak strain values averaged for each data set.

Table 22: SS1 peak strains ( $\mu$ strain) and standard deviations for each gage, averaged over tests with the same ignition location.

Gage	E3 Ignition Tests 52-56		E1 Ignition Tests 58-61	
	Average	Std Dev	Average	Std Dev
1	162.3	2.0	180.4	4.7
2	155.0	14.2	158.2	2.8
3	157.4	10.1	200.1	2.6
4	149.1	3.7	198.9	4.8
5	178.6	10.2	184.6	5.8
6	137.6	6.9	152.4	6.4
7	155.3	3.5	156.3	5.9
8	196.3	20.3	157.5	9.7
9	194.4	11.5	211.4	2.0
10	181.1	6.0	175.8	5.0
11	143.7	14.6	138.0	1.2
12	190.4	5.6	139.6	7.5
13	170.1	1.8	155.9	15.0
14	147.8	2.8	136.4	0.4
15	175.1	4.3	176.5	4.3
16	204.0	14.4	125.3	3.8
17	170.7	10.3	149.0	11.2
18	184.1	3.0	116.8	5.7
19	196.6	4.3	158.2	7.5
20	185.8	5.4	215.3	3.8
21	194.2	11.6	237.0	22.2
22	219.9	14.6	189.3	3.3
23	206.9	5.1	164.4	5.2
24	148.3	7.6	143.6	3.2
25	139.8	5.2	131.9	2.7
26	149.4	4.7	138.7	2.8
27	223.0	58.0	163.7	3.2
28	147.8	15.4	112.6	31.9
29	139.9	41.6	106.6	48.3
30	129.7	48.5	112.8	28.9
31	135.0	62.1	147.0	37.0
32	191.3	5.9	122.8	6.9
33	144.4	3.1	148.9	4.5
34	172.6	3.0	115.1	5.3
35	186.8	6.2	162.7	5.3
36	153.4	0.4	85.6	1.3
37	118.2	0.7	62.1	2.4
38	129.3	1.8	89.6	0.1
39	126.4	1.2	118.4	1.0

## 7.4 Finite Element Simulations

Several tests were simulated by Dominion Engineering (Ligon, 2009e) using a ideal CJ pressure profile and a detailed finite-element model of the piping and support system. The results of these simulations have been compared with data from selected shots in the following figures.

The strain signals comparisons for shot 58 and 60 (both with ignition at E1) are shown in Figs. 87-93. For the first 12 ms of the test, the simulation and experiment appear to be in very reasonable quantitative and qualitative agreement. There is clearly a higher frequency content in the measurements than in the simulations but that is to be expected based on the spatial and temporal resolution used in the simulations.

For the gages farthest from the ignition source, shown in Fig. 87, several distinct axial waves are clearly visible ahead of the high-frequency signal that indicates the arrival of the detonation front. These waves are generated by the detonation propagating around the bends between the ignition source and the measurement location as discussed in Section 5 and Shepherd and Akbar (2009).

Very substantial oscillations are excited in the u-shaped segment of SS1-1, as observed on S16 and S17 in Fig. 88. In general, the strain signals in Fig. 88-89 have a much richer frequency content than that of ES1 or TS1, a consequence of much larger number of modes available for excitation and the few constraints, which enable coupling of the detonation induced vibration into a much larger number of modes. Spectral analysis of 100 ms records for representative strain signals is shown in Fig. 91 and 92. For S16, the main peaks in the power spectra are at 38, 76, 221 and 618 Hz with a number of smaller peaks visible between 0-5000 Hz. For S17, the main peaks are observed at 38, 100, 251, and 816 Hz. There is also a significant amount of energy in vibration close to the hoop vibration frequency of 29.04 kHz, however, there is not a single isolated peak but a number (5-10) of peaks because of the coupling between radial and axial modes, (Blevins, 2001, Section 12.2.3). Over 100 ms, Fig. 90, there is an offset of the strain of about 100  $\mu$ strain which is not reproduced by the simulations. This rise is due to the thermal expansion of the piping system, an effect that is discussed at length in Ligon (2009d). A heat transfer model was not included in the simulations reported in Ligon (2009e) because these effects were secondary to the main goal of validating the mechanical models of structural loading.

Two of the cantilever beam supports were instrumented with strain gages, data for shot 58 are given in Fig. 93. The location of the strain gages is as described in Appendix G but only the AB pairs were used for cantilevers U3 and U4. Each gage was connected in a quarter-bridge configuration and the signal recorded separately. The sum of the two signals will give the axial loading in the direction perpendicular to the mounting wall and pipe axis. The difference of the two signals will give the bending in the direction parallel to the wall and perpendicular to the pipe axis. As shown in Fig. 94, the axial strains are quite small in comparison to the bending strains, which is not surprising since the beams are quite stiff in the axial direction.

As shown on the photographs in Fig. 93, a teflon sheet was glued to the pipe and the U-bolt was adjusted so that the pipe could slide axially. This was done to attempt to mimic the mounting configuration in commercial systems, in which an air gap of about 1/16-inch is maintained between the U-bolt and the pipe. In our installation, we tried to avoid a

gap since that creates “chattering” and contact forces as the pipe rattles around inside the U-bolt/support constraint. Unfortunately, it was difficult to maintain contact since each U-bolt has to be individually checked and readjusted after each shot. It is evident from the data that gaps were present for most tests. The rattling motion and contact are difficult to simulate accurately and prevent meaningful comparisons of the results of the cantilever strain measurements with simulations. In addition, the teflon sheet is very compliant and absorbs energy through inelastic deformation, altering the shape and magnitude of resulting strain from the expected values that assume the connection between the support and pipe is rigid. For these reasons, there is a relatively poor comparison in Fig. 93 between the simulated and measured cantilever strains after the first 100-200  $\mu s$ . It is clear that the teflon sheet mounting method is the source of the difficulty in these tests since in the TS1 tests with supports, excellent comparison with simulations was obtained (Fig. 75) when the sheets were omitted and the U-bolts tightened to secure the pipe to the support.

The displacement gage signals are shown in Fig. 95. Gages 1-3 were of a different design than 4 and the data required special filtering. As a consequence, a phase delay was introduced into the displacement relative to the other signals. The magnitude of the phase delay and the correction for that are discussed in the subsequent section. The corrected signals are in reasonable agreement at early times but not at longer time. Although the peak amplitude of the displacement is reasonably predicted at all times, there are high-frequency features in the simulated displacements that are not observed in the measurements. It is not clear if this is related to the filtering operation or the non-ideal U-bolt support conditions.

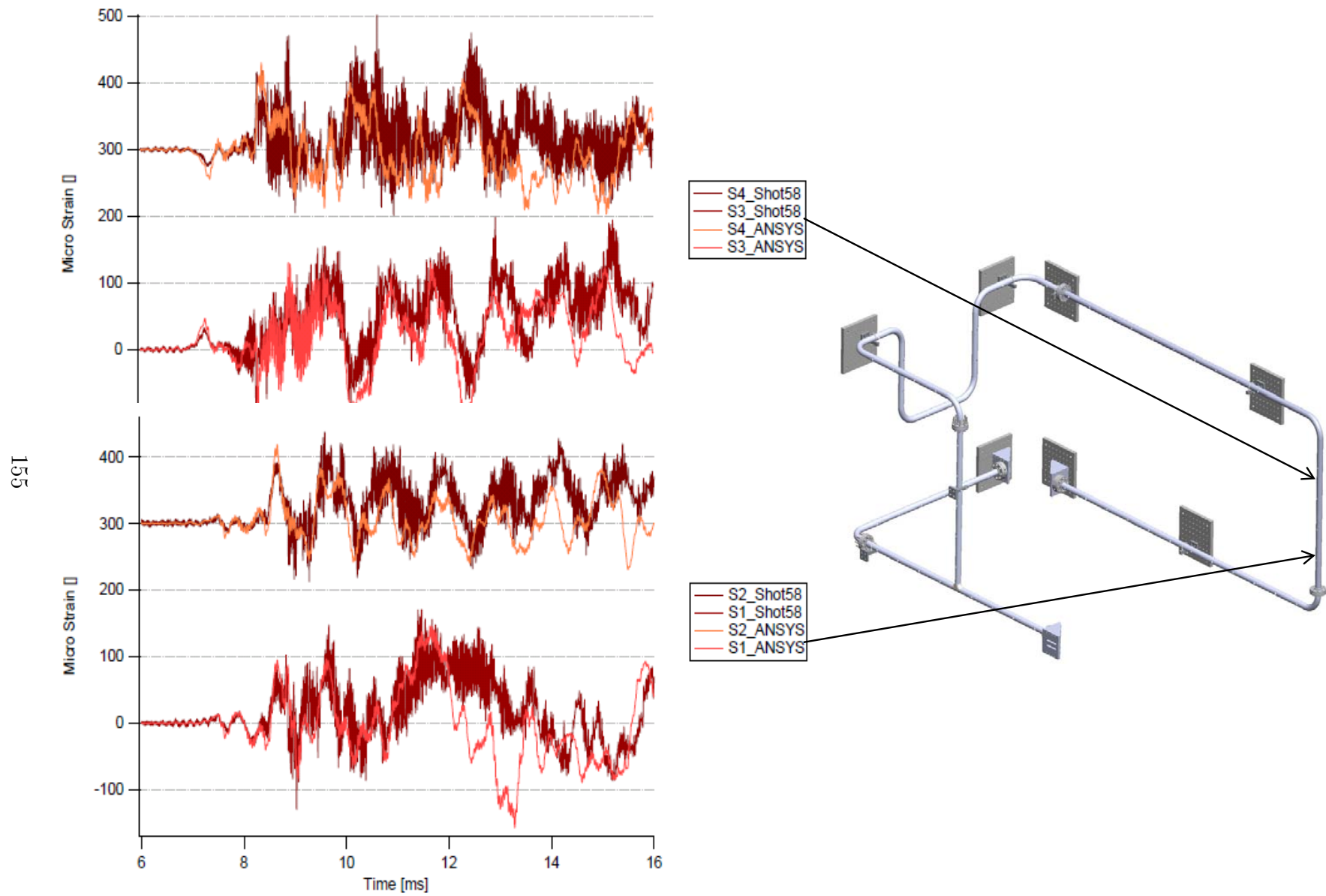


Figure 87: Comparison of simulations with strain data for longitudinal strain gages S1, S2, S3, S4 for shot 58. Reproduced from p. 33 and 34 of [Ligon \(2009e\)](#).

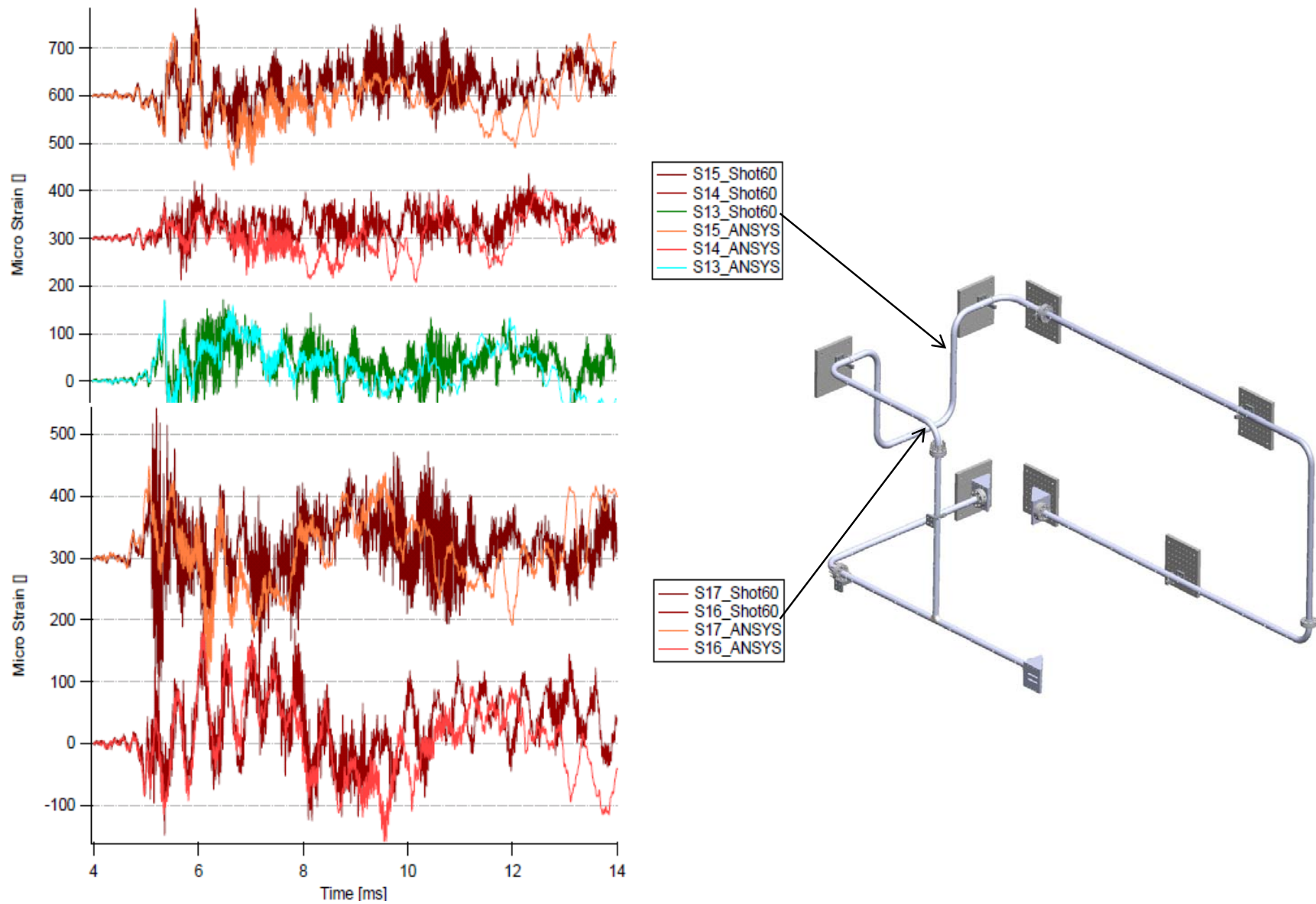
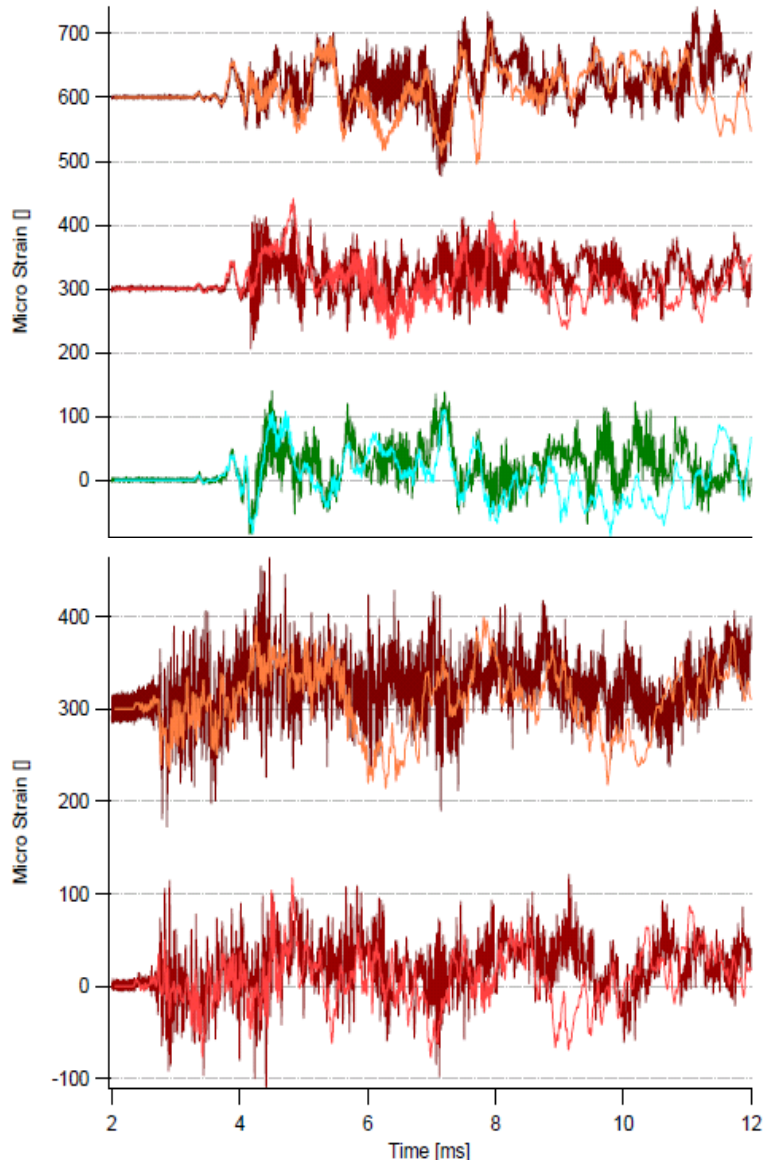


Figure 88: Comparison of simulations with strain data for longitudinal strain gages S13, S14, S15, S16, S17 for shot 60. Reproduced from p. 36 and 37 of [Ligon \(2009e\)](#).



— S26\_Shot58  
 — S25\_Shot58  
 — S24\_Shot58  
 — S26\_ANSYS  
 — S25\_ANSYS  
 — S24\_ANSYS

— S35\_Shot58  
 — S34\_Shot58  
 — S35\_ANSYS  
 — S34\_ANSYS

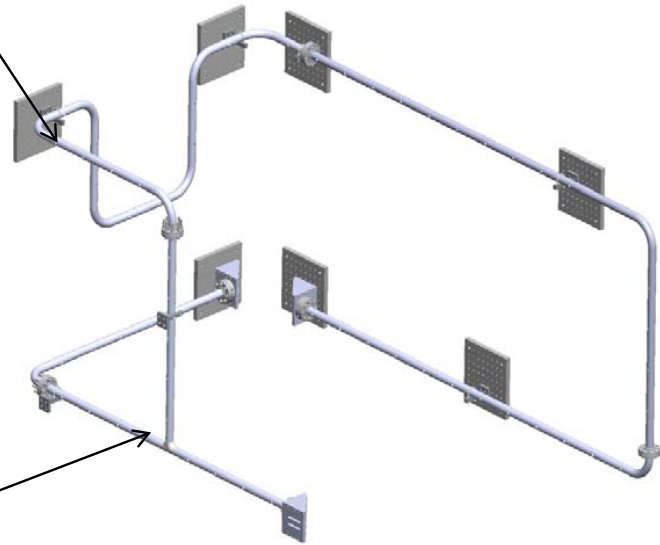


Figure 89: Comparison of simulations with strain data for longitudinal strain gages S24, S25, S26, S34, S35 for shot 58. Reproduced from p. 38 of Ligon (2009e).

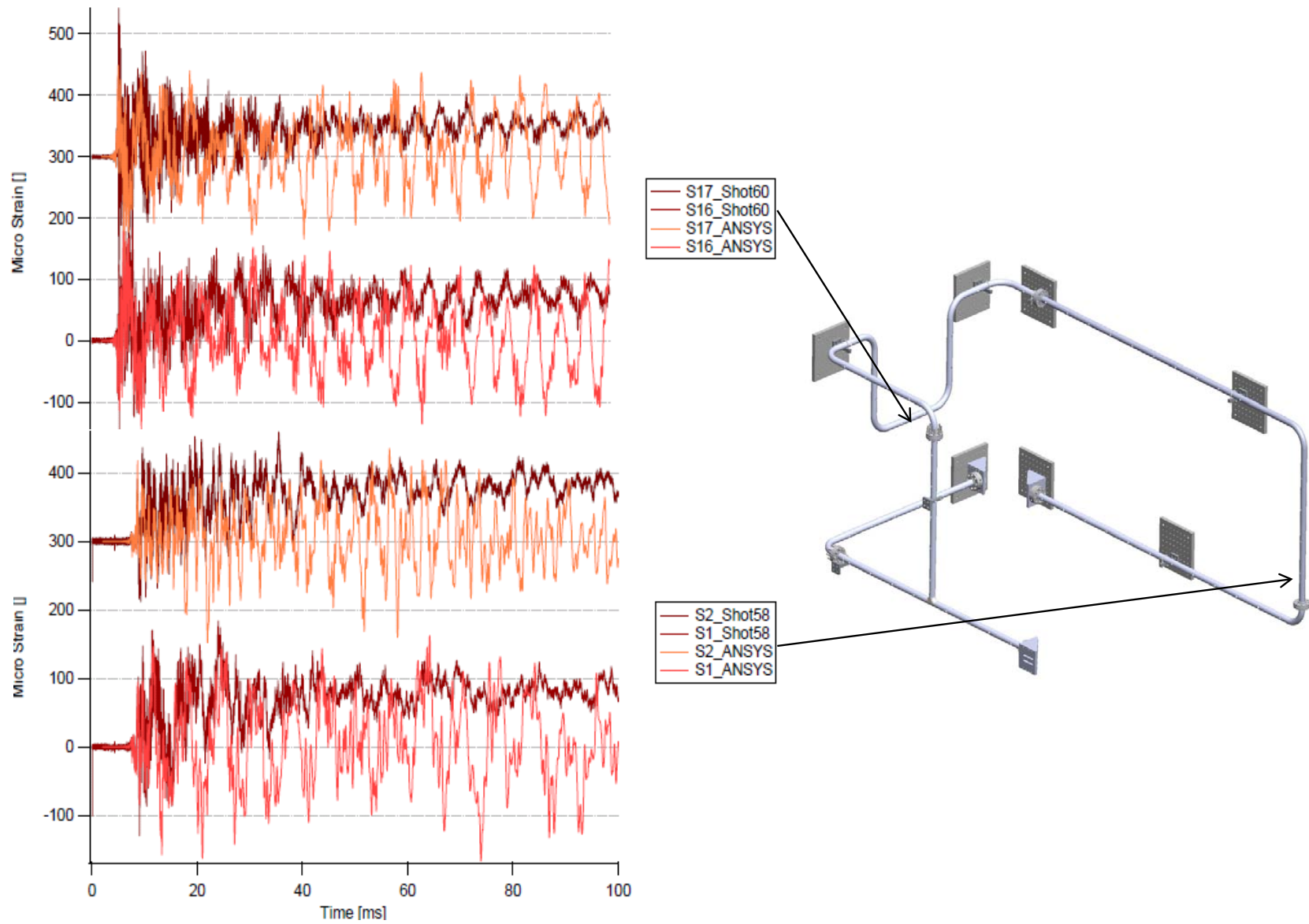
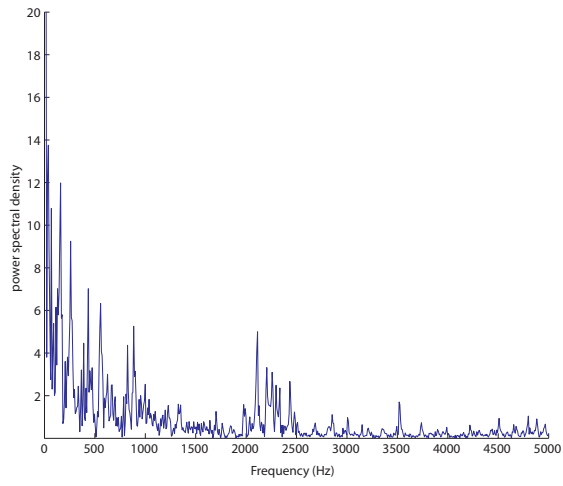
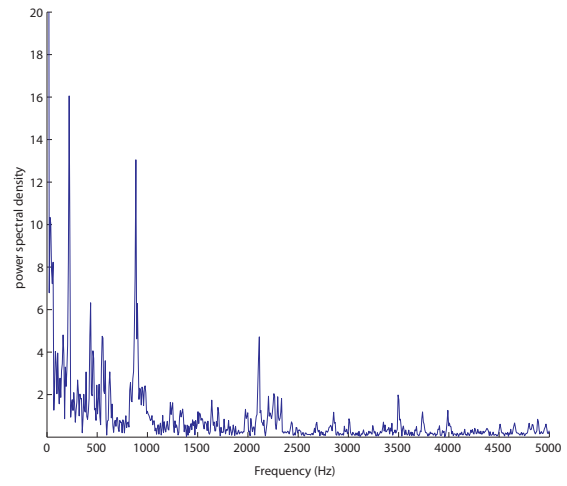


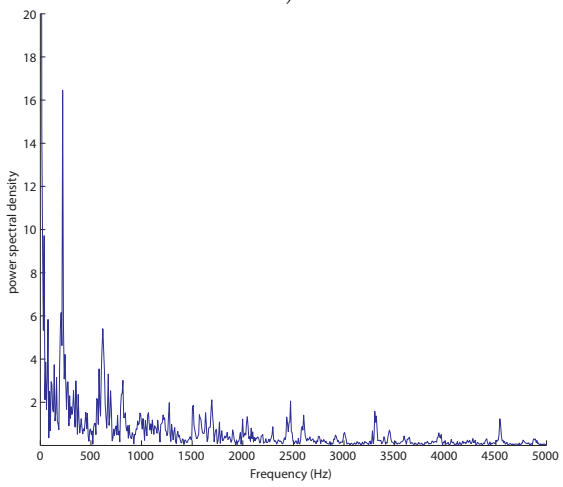
Figure 90: Comparison of simulations with strain data over 100 ms for longitudinal gages S1, S2 for shot 58 and S16, S17 for shot 60. Reproduced from p. 42 and 43 of [Ligon \(2009e\)](#).



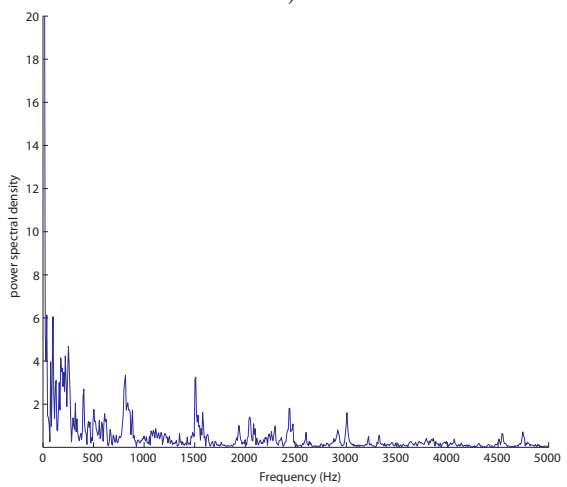
a)



b)

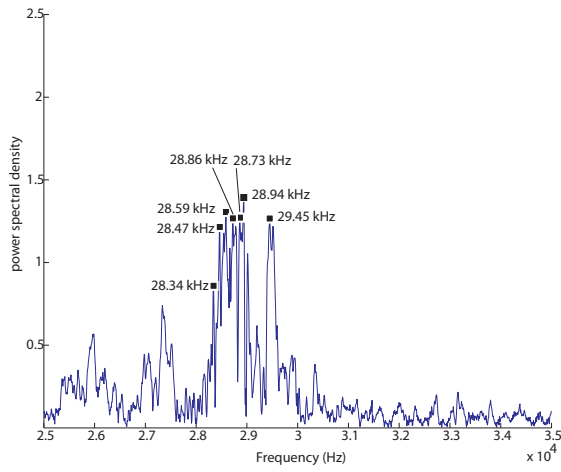


c)

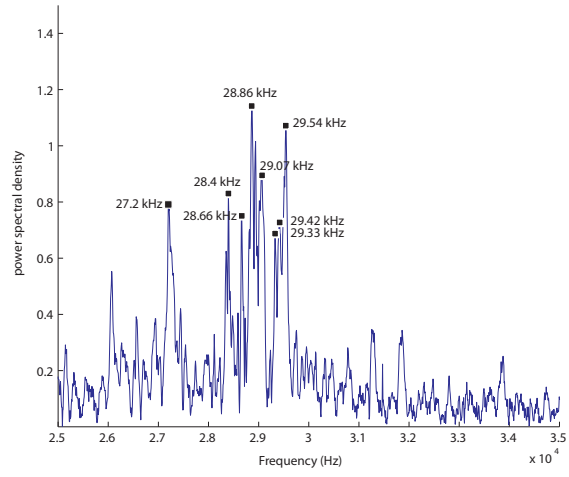


d)

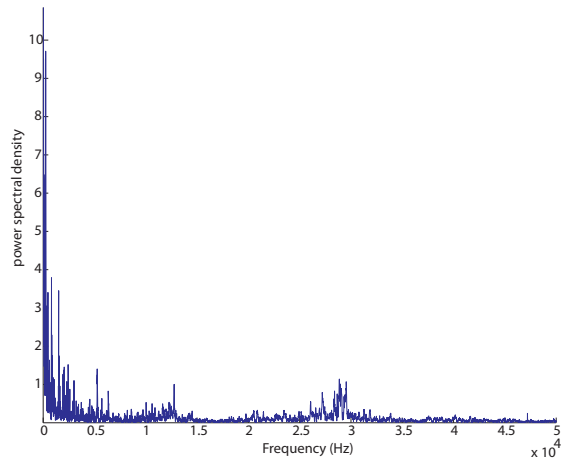
Figure 91: Spectral analysis of SS1 strain data for longitudinal for shot 58. a) S2. b) S4. c) S16. d) S17.



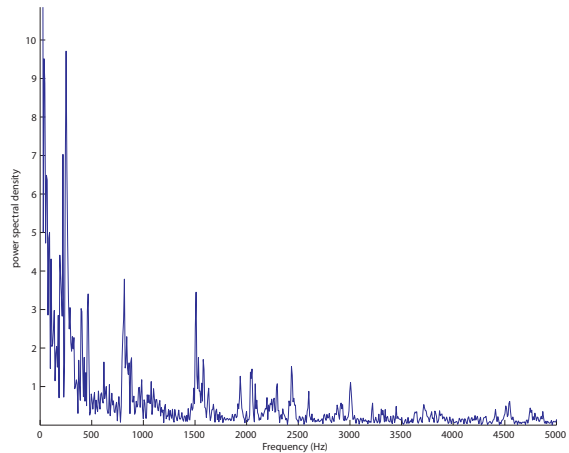
a)



b)



c)



d)

Figure 92: Spectral analysis of SS1 strain data for longitudinal for shot 58. a) S16, region of hoop resonance. b) S34, region of hoop resonance. c) S34, high-frequency content. d) S34, frequencies less than 5 kHz.

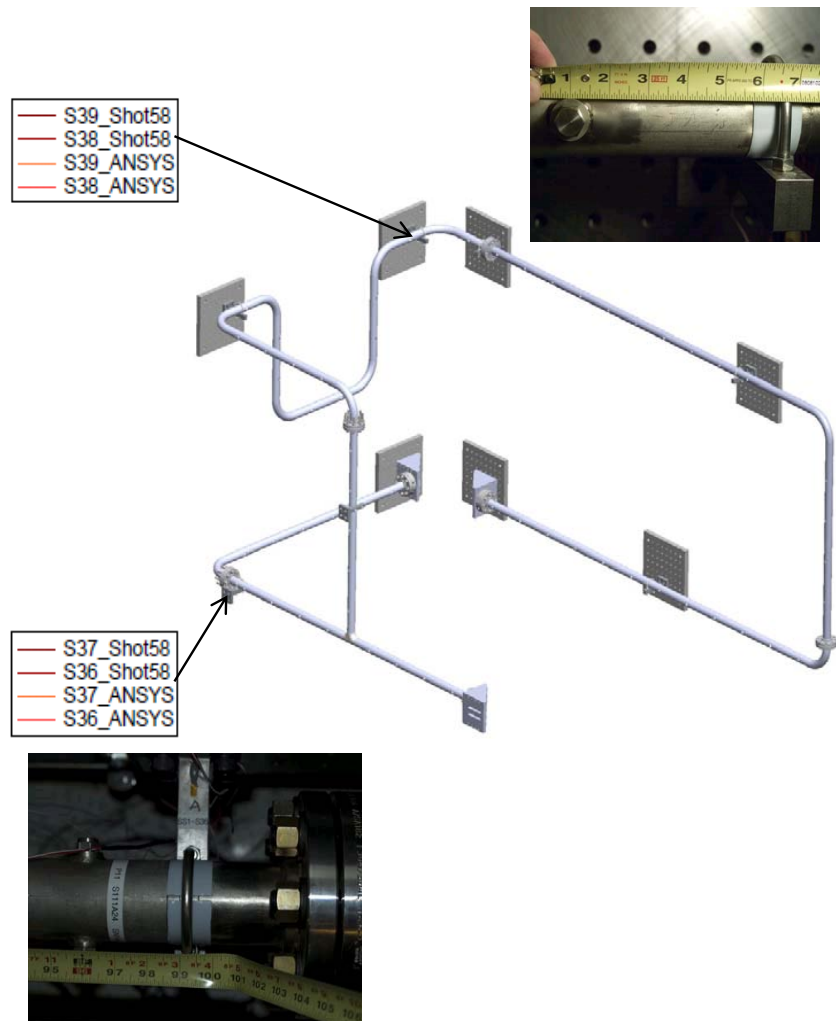
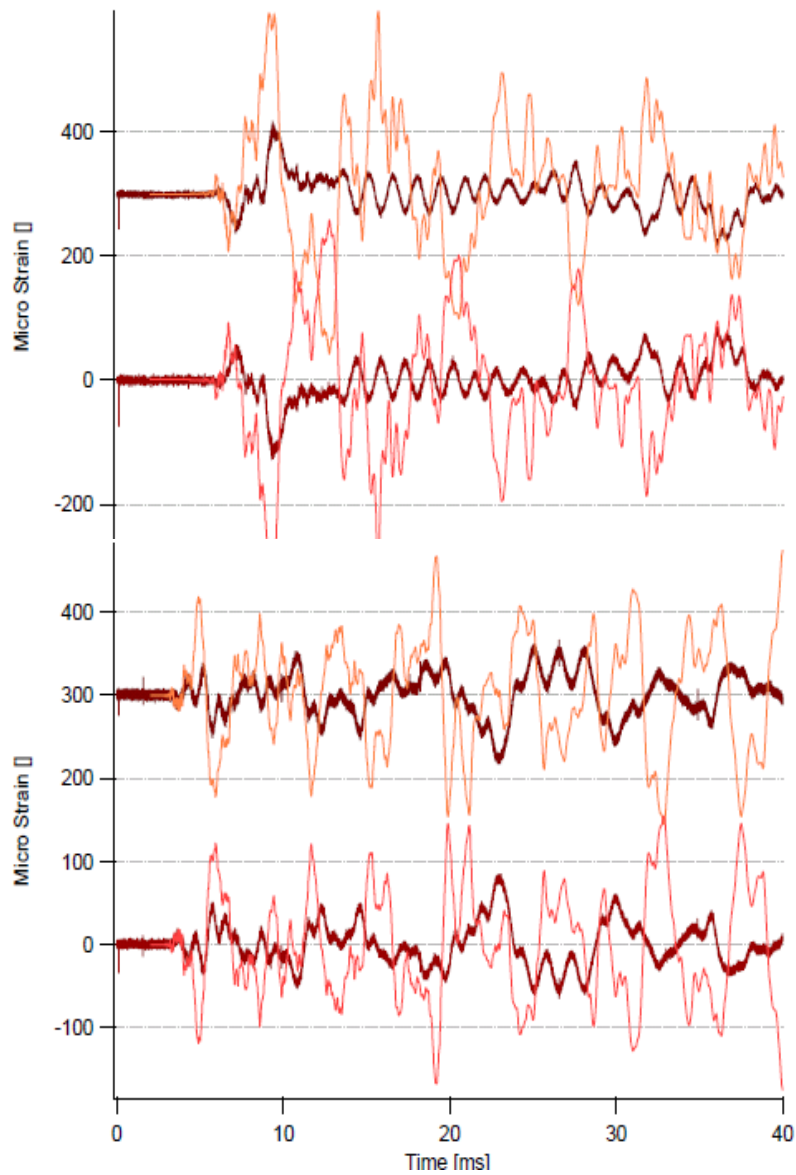


Figure 93: Comparison of simulations with strain data for longitudinal strain gages S36, S37, S38, S39 for shot 58. These gages are mounted on the cantilever supports SU1 (S36, S37) and SU4 (S38, S39). Reproduced from p. 40 and 41 of [Ligon \(2009e\)](#).

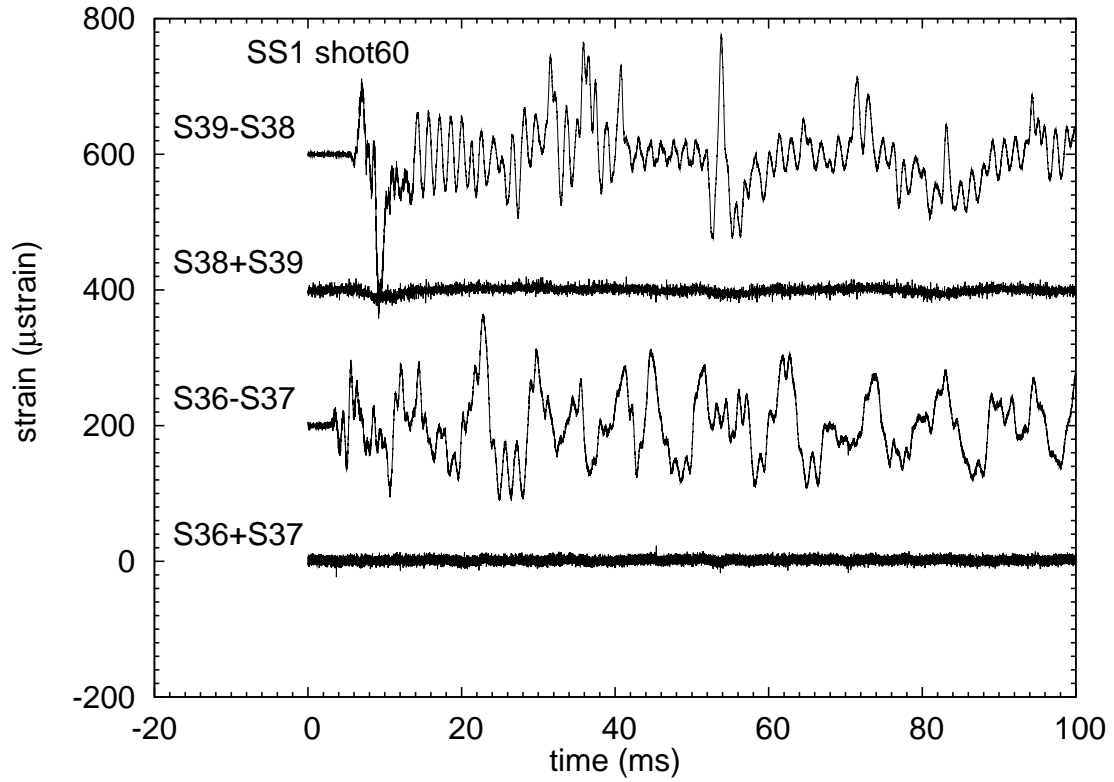


Figure 94: Processed strain data for longitudinal strain gages S36, S37, S38, S39 for shot 60. These gages are mounted on the cantilever supports SU1 (S36, S37) and SU4 (S38, S39). Sum signals isolate the axial strain (along the cantilever beam, perpendicular to the wall), difference signals isolate the bending strain (perpendicular the cantilever and pipe axis).

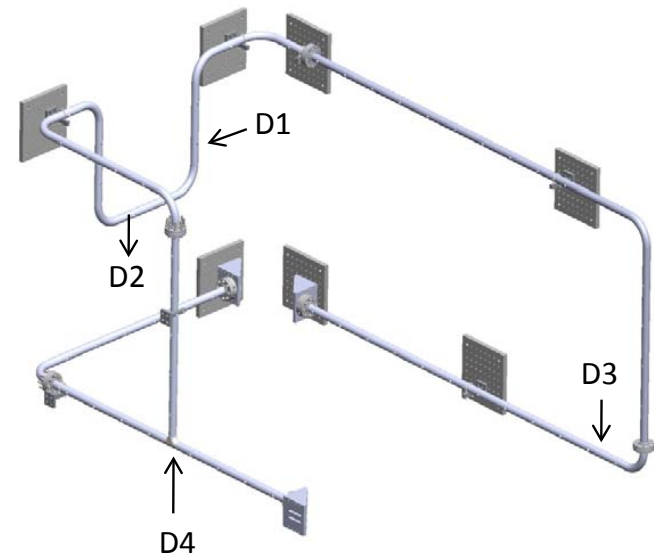
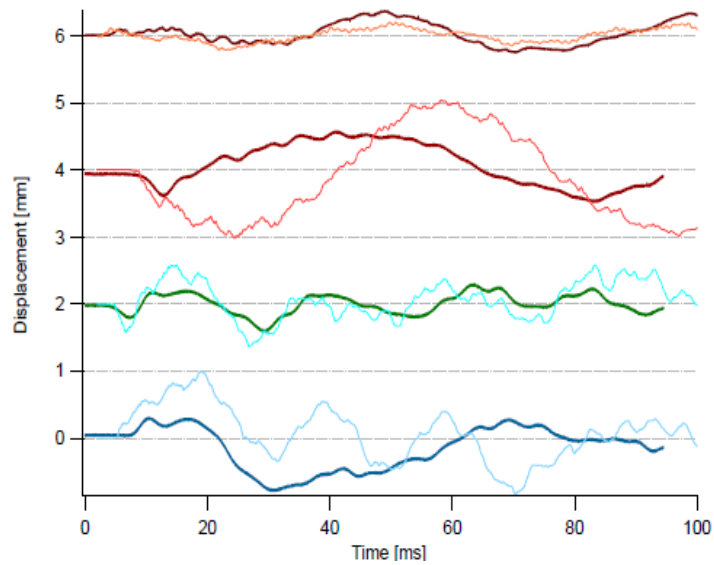
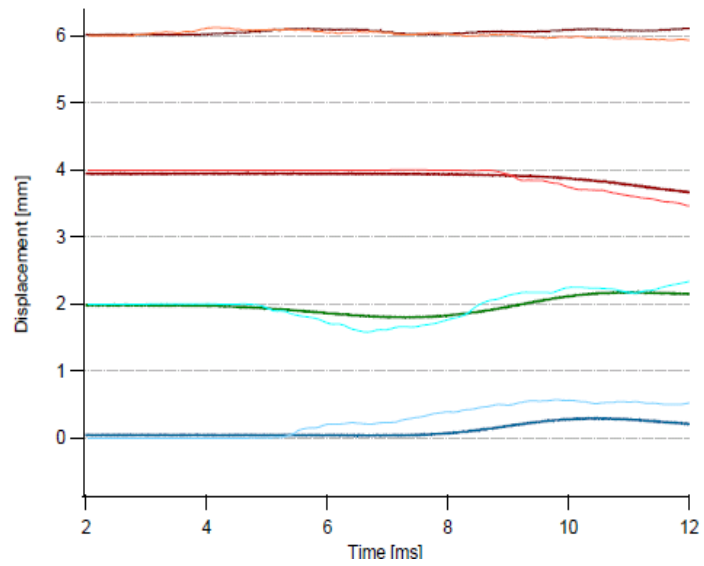


Figure 95: Comparison of simulations with strain data for displacement gages D1, D2, D3, D4 for shot 58. Reproduced from p. 41 and 42 of Ligon (2009e).

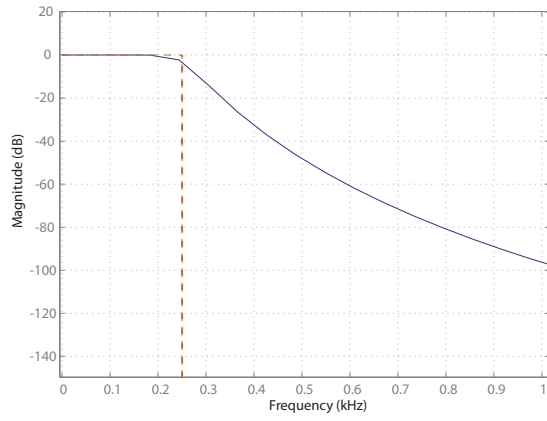
### 7.4.1 Displacement Gage Analysis Issues

The displacement gage signals (for the micro epsilon gages only- D1,D2 and D3) were put through a Krohn-Hite Model 3284 tunable active filter using a 250Hz (3-db point) cutoff and low-pass, Butterworth setting (8th order) and ac-coupling (0.16 Hz). This was done in order to improve signal to noise ratio because there was significant noise contamination affecting the signals from these micro-epsilon gages, under the test conditions. The filter has a very flat amplitude response, but it does also have some initial ringing and effective phase delay. This is a precision, calibrated instrument and for our operating condition can be modeled analytically as a 8-pole Low-Pass Butterworth filter with a 250 Hz 3dB cut-off point. Measurements using a frequency generator and oscilloscope confirmed that the analytical model was quite accurate.

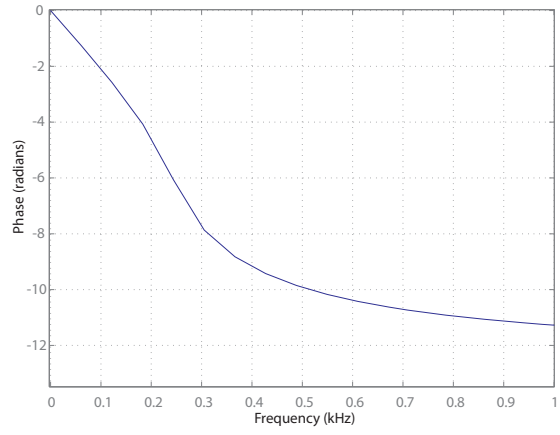
The effect of the filter was simulated [MathWorks](#) using a model waveform

$$d(t) = (1 - \exp(-t/\tau)) \sin(2\pi ft) \quad (80)$$

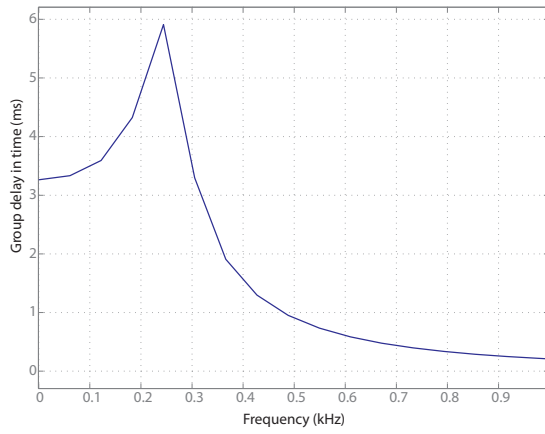
with a 50 Hz frequency  $f$  and an initial exponential amplitude growth time constant  $\tau = 10$  ms. The results are shown in Fig. 96. The filter amplitude response is quite flat (Fig. 96a) until the cutoff frequency is reached and then the response rolls off sharply as per the advertised rate of 48 db per octave. This effectively eliminates all noise that has higher (even slightly) frequency content than the cut-off frequency but does modify the signal history because the filter introduces a significant phase shift (Fig. 96b)  $\phi$  that depends strongly on frequency  $f$ ; this is an unavoidable consequence of any time-domain filtering operation. The phase shift is manifested as a time-delay that can be quantified in terms of the group delay ( $-d\phi/df$ ) which is the average time delay of the signal introduced by the filter as a function of frequency, (Fig. 96c). Note that even at  $f = 0$ , the group delay is nonzero and equal to about 3.3 ms and rising to about 6 ms at the cutoff frequency. For the model signal, this results in the time delay of about 3.3 to 3.5 ms in the filter output as compared to the input, Fig. 96d. This delay was first noticed in comparing the simulated and filtered data ([Ligon, 2009e](#)) and observing that the displacement gage signals appeared quite a bit later in time than expected based on the strain and pressure signals. Once the origin of this delay was confirmed at being due to the filtering process, the time origin of the displacement signals were adjusted by about 3.4 ms when comparing predicted and measured displacements, see Fig. 97 taken from [Ligon \(2009e\)](#).



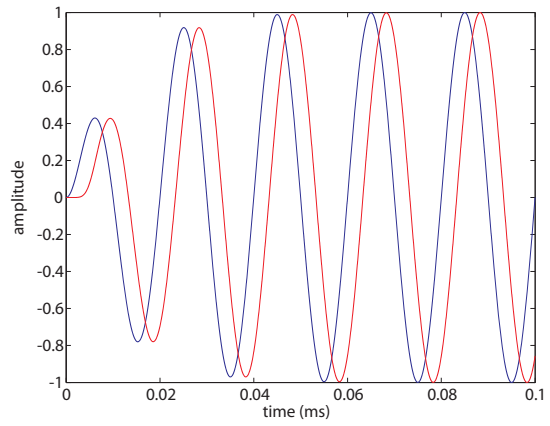
a)



b)



c)



d)

Figure 96: Krohn-Hite low pass filter analysis.

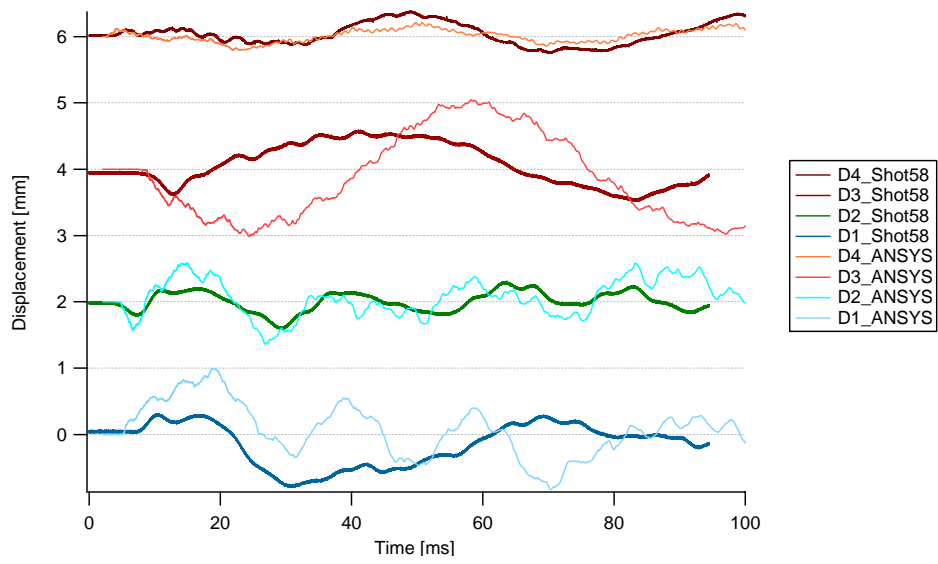


Figure 97: Comparison of displacements measured in shot 58 with results of ANSYS simulations, Fig. 26 of [Ligon \(2009e\)](#), shifted in time to compensate for the filter phase shift.

## 7.5 Summary

A set of ten tests were carried out in a complex piping system that contained ten in-plane and out-of-plane bends, a tee, and two dead ends. The piping specimens had hydraulically-formed bends and welded construction like that found in the WTP except for the flanges used to join the five individual segments that made up the piping system. Instrumentation included 20 piezo-electric pressure transducers, 30 strain gages, and four displacement gages. The piping was supported on seven cantilevers, with U-bolts restraining the piping with teflon slipper pads. Two of the cantilevers were instrumented to measure bending and axial strain in two perpendicular axes. The key results were:

1. Detonations in 30/70  $\text{H}_2\text{N}_2\text{O}$  mixtures propagated through the entire length (67.5 ft or 20.6 m) within 1% of the CJ velocity in all cases.
2. The peak pressures and strains were consistent with the tests in two simple geometries of the single bend (ES1) and single tee (TS1).
3. Detonation propagation inside the piping system was modeled with a finite element simulations (Ligon, 2009e) using previously developed models for the detonation propagation through a system containing bends and tees. The finite element representation used a combination of shell, pipe, beam, and mass elements to represent that piping system and supports. The results were:
  - (a) The simulated pressure, strain, and displacement histories were qualitatively in excellent agreement with the observed signals and quantitative agreement was very good in most cases.
  - (b) Peak axial strains are on average under-predicted by about 13%.
  - (c) Filtering the axial strains to remove high frequency oscillations improved the agreement between measured and simulated strains so that the simulations predicted the peak values within predicted within  $\pm 30\%$  (Fig. 98) with an average under-prediction of only 6%.
  - (d) Predicted strains on the U-bolt cantilever beam supports were in reasonable agreement with measurement at early (0-10 ms) to intermediate (10-40 ms) times but substantially off at long times (40-100 ms). In part, this is due on not clamping the supports securely to the piping but having a small gap with a teflon slipper pad between the U-bolt and beam.
  - (e) Predicted pipe displacements were qualitatively and quantitatively reasonable at early times (0-10 ms) but large (up 300%) over-predictions were observed at the three locations away from the tee. Results at the tee were within 25-45% of the data.
4. For the purposes of code validation, future work should be done without the teflon slipper pads and clamping the pipe securely to the supports.
5. The filter introduced a frequency-dependent phase-shift that is manifested as a displacement of the filtered signal in time from the raw value. This has to be accounted

for in comparing the experimental data with the simulation. Testing and simulations was carried out to determine the effect of the filtering process.

6. Alternate methods of displacement measurement or data processing should be explored to eliminate the need for low-pass filtering that induces such severe phase shifts in the data.

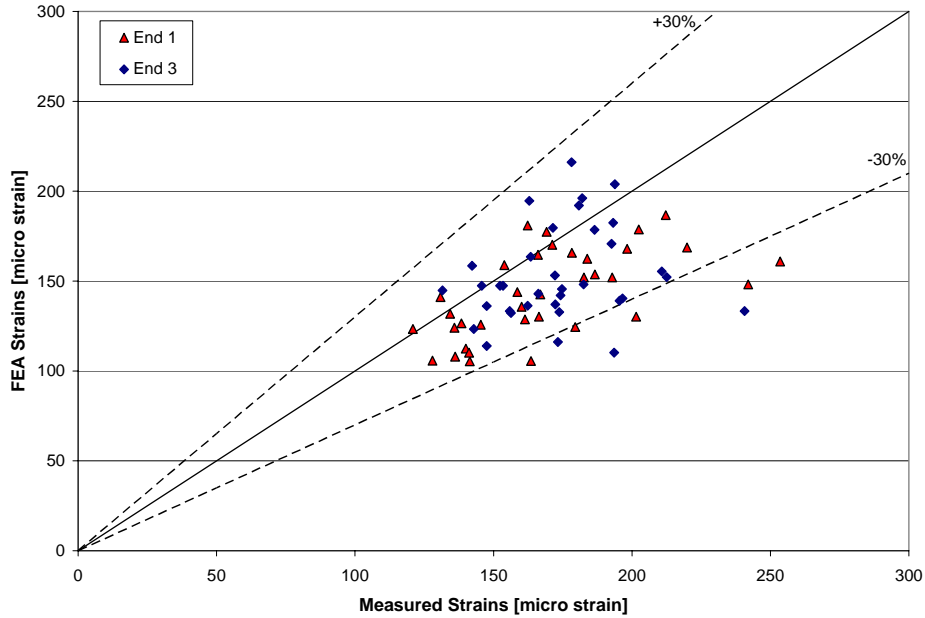


Figure 98: Comparison of peak strains from simulation with measured peak strains for shots 53 and 58. Reproduced from p. 32 of [Ligon \(2009e\)](#).

Overall, the SS1 testing provided high-quality data that was used to validate the finite-element simulation modeling for detonation propagation through a complex piping system. The modeling relied on previously developed methods based on the SS1 and TS1 as well as the SwRI testing for the effective structural loading by the detonation as well as the mathematical representation of the piping and supports. These models were not adjusted in carrying out this comparison so it gives a fair comparison of the ability to model the structural response of a complex piping system to a detonation.

## 8 Summary

A set of 61 tests were carried out with H<sub>2</sub>/N<sub>2</sub>O detonation inside three configurations of piping. Data on pressure, strain, acceleration, and displacement were obtained for variations on each configuration. Instrumented cantilever beams were used to simulate supports and infer forces. The results from these tests are available in electronic form for analysis and validation of simulations of detonation propagation inside piping systems.

The results were used at CIT and DEI to develop and validate structural loading models for use in FEM simulations. These included:

1. Hoop and axial strains due to detonation propagation
2. Forces due to detonation propagation through bends
3. Reflection of detonation wave and propagation of shock waves in water-filled sections
4. Forces due to detonation propagations through a tee
5. Forces on cantilever supports
6. Complete piping system with multiple bends, supports, a tee, and dead ends.

High-quality data was obtained as evidenced by the repeatability of replica testing, low noise levels, comparisons with computed detonation properties and simplified structural models. The data were of sufficiently high-quality to be used in validating FEM models, identifying, and resolving issues with modeling assumptions. Overall, the original test objectives were met and the HPAV project was able to make significant progress on the issues that were

### 8.1 Issues and Suggestions for Future Studies

There were some issues with the fixture design and instrumentation that limited the value of certain data. Displacement and support strains were the two main groups of data that were affected. There were also some issues with the instrumentation to measure force and various facility-related problems that we struggled with.

1. The U-bolt supports in the SS1 testing were not securely clamped to the piping but had a slip fit on teflon pads. This resulted in chatter in the cantilever strain signals which possibly propagated into tube strain and displacement measurements. Future work should use either clamped U-bolts without the pads, which was successfully used in TS1 and some ES1 tests, or better slip fixtures that can be easily modeled.
2. 3-gage rosettes were only used on the ES1 bend so we were not able to define principal stresses and directions. More 3-gage rosettes should be used and tests with different pipe wall thicknesses are needed to characterize and determine the origin of the high-frequency axial strains.

3. Bending and membrane strains were inferred from paired gages in selected cases in TS1 and SS1 but not SS1. More use should be made of this technique to separate the contributions to the piping axial strains.
4. Lower noise, higher-sensitivity displacement gages that will not require such extensive filtering are necessary in order to prevent large time shifts in filtered data.
5. Tests with other fuel-oxidizer systems such as  $\text{H}_2\text{-O}_2$  and  $\text{CH}_4\text{-O}_2$  are desirable for several reasons. First, this should be done to make sure that the results are sufficiently general to apply to a broad range of applications. Second, if the testing could be done with other fuels that have more benign combustion products, this would also reduce the cost and time spent maintaining the plumbing and vacuum system. We had to have vacuum pumps rebuilt a number of times despite finally installing liquid nitrogen traps. The combustion products of  $\text{H}_2\text{N}_2\text{O}$  leave an acidic residue in the piping and quickly ruin the vacuum pump oil.
6. Direct measurement of loads at the initiation and reflecting end of the piping were not successful. The substantial mass of the fixtures and stiffness of the attached piping system made these measurements difficult to interpret. Other techniques such as Hopkinson bar-type methods and/or high-speed load cells should be explored in order to better quantify these loads.
7. The water-hammer testing should be repeated using suspensions with rheology similar to that of the waste in order to determine the influence of viscoelastic effects on structural response.

## 9 Acknowledgments

The prime sponsor of this work was the US Department of Energy, Office of River Protection (ORP) and funding sponsor was the Project Assistance Corporation (PAC) of Richland, WA. The work was funded under DOE Contract DE-AB27-03-RVI14546 through PAC Contract ORP-CAL001. The contract monitor at the ORP was Lew Miller from November 2007 to February 2008, Greg Jones from February 2008 to April 2009, with Albert Hu participating from January to April 2009. David Gross and Tom Ligon of DEI, Ed Rodriguez of GNNA, John Minichiello and Mike Wentink of BNI were key members of the HPAV team that we have been working with on this program. They have all made substantial contributions to the development of the CIT testing program and analysis of the test data.

We thank Silas Hilliard for his work on design and computer model generation of many components as well as assistance with the testing. The Bertin Brothers Construction Company came up with many innovative solutions to locating and mounting the plates on the test cell walls. We note with sadness the passing of Dale Giese of Centerline Welding who helped substantially with the development of welding and machining procedures for the piping specimens. Royal Welding, Hales Manufacturing, and the staff of the Aeronautics and Physics machine shops contributed to fabricating the specimens and many fixtures used in these tests. Expert Swagelok plumbing and mounting of fixtures was provided by Steve Ballard. Gayle Lund of CIT Sponsored Research patiently worked through the nearly infinite iterations required to negotiate this contract and the special conditions needed to accommodate the Quality Assurance program. Russell Shepherd had very useful insights into the interpretation of the statistical tests for the arrival time data. Ravi Ravichandran provided substantial advice about the analysis of stress and strain. Finally, thanks to Alexandra Katsas for carrying out the very substantial amount of ordering, straightening out the tax situation with purchasing, and helping administer the QA program.

## Bibliography

- S. Ahnert. DDT pulse shape elastic validation. DEI Calculation No. C-6908-00-27, June 2006. [82](#)
- R. Akbar, M. Kaneshige, E. Schultz, and J.E. Shepherd. Detonations in H<sub>2</sub>-N<sub>2</sub>O-CH<sub>4</sub>-NH<sub>3</sub>-O<sub>2</sub>-N<sub>2</sub> mixtures. Technical Report FM97-3, GALCIT, July 1997. [27](#), [81](#), [84](#)
- W. Beltman and J.E. Shepherd. Linear elastic response of tubes to internal detonation loading. *Journal of Sound and Vibration*, 252(4), 2002. [41](#), [74](#), [75](#), [76](#), [177](#)
- W.M. Beltman and J.E. Shepherd. Structural response of shells to shock and detonation loading. Technical Report FM98-3, GALCIT, April 1998. [70](#), [71](#)
- R. D. Blevins. *Formulas for Natural Frequency and Mode Shape*. Krieger, 2001. [128](#), [153](#)
- L. E. Bollinger, J. A. Laughrey, and R. Edse. Experimental detonation velocities and induction distances in hydrogen-nitrous oxide mixtures. *American Rocket Society Journal*, 32: 81–82, January 1962. [7](#), [81](#), [82](#)
- A. Bray, G. Barbato, and R. Levi. *Theory and practice of Force Measurement*. Academic Press, 1990. [209](#)
- S. Browne, J. Ziegler, and J. E. Shepherd. Numerical solution methods for shock and detonation jump conditions. Technical Report FM2006.006, GALCIT, 2004. [17](#), [40](#), [176](#)
- C. R. Calladine. *Theory of Shell Structures*. Cambridge University Press, 1983. [64](#)
- Tong Wa Chao. *Gaseous Detonation-Driven Fracture of Tubes*. PhD thesis, California Institute of Technology, Pasadena, California, March 2004. [69](#), [76](#)
- G. Ciccarelli and S. Dorofeev. Flame acceleration and transition to detonation in ducts. *Progress Energy Combust Sci*, 2008. doi:10.1016/j.pecs.2007.11.002. [81](#), [84](#)
- DEI. Gas-liquid reflected detonation structural system response. DEI Calculation No. C-6916-00-07, December 2009. [21](#), [97](#)
- D. J. Gross and J. C. Minchello. DOE questions regarding HPAV inputs to piping system response models. DEI Memo M-6908-00-36, April 2007. [91](#)
- Kazuaki Inaba and Joseph E. Shepherd. Flexural waves in fluid-filled tubes subject to axial impact. *J. Pressure Vessel Technol.*, 132:021302, April 2010. [99](#), [100](#)
- M.J. Kaneshige, E. Schultz, U.J. Pfahl, J.E. Shepherd, and R. Akbar. Detonations in mixtures containing nitrous oxide. In G. Ball, R. Hillier, and G. Roberts, editors, *Proceedings of the 22nd International Symposium on Shock Waves*, volume 1, pages 251–256, 2000. [81](#)
- J. Karnesky, E. Koos, and J. E. Shepherd. Transmission of hexane-air explosions. Explosion Dynamics Laboratory Report FM2004.003, California Institute of Technology, August 2004. [83](#)

- James A. Karnesky. *Detonation Induced Strain in Tubes*. PhD thesis, California Institute of Technology, 2010. [7](#), [69](#), [72](#), [76](#), [78](#), [91](#)
- H. Kolsky. *Stress Waves in Solids*. Dover, 1963. [177](#)
- J. Chris Krok. One-dimensional flame propagation mechanisms. Unpublished notes on the solution of ideal steady high-speed flames. RPI, Troy, NY, July 1991. [84](#)
- J.C. Krok and JE Shepherd. Electrical and frictional ignition of N<sub>2</sub>O-H<sub>2</sub>-N<sub>2</sub>-Air mixtures. Technical report, Rensselaer Polytechnic Institute, June 1993. Explosion Dynamics Laboratory Report for Los Alamos National Laboratories. [83](#)
- S. Lachmann and J. Minichiello. Hpav engineering analysis methods and criteria. Technical Report 24590-WTP-RPT-ENG-07-011, Rev 3, Bechtel River Protect Project, Waste Treatment Plant, April 2010. [69](#), [70](#)
- Z. Liang and J.E. Shepherd. Explosion testing of the nested can containment system. part I: Planar gap. part II. thick-walled tube. part III. 3013 outer can. Technical Report FM2007-001, Graduate Aeronautical Laboratory, California Institute of Technology, May 2007. [22](#)
- Z. Liang, J. Karnesky, and J.E. Shepherd. Structural response to reflected detonations and deflagration-to-detonation transition in H<sub>2</sub>-N<sub>2</sub>O mixtures. Technical Report FM2006-003, Graduate Aeronautical Laboratory, California Institute of Technology, August 2006. [81](#), [82](#)
- Z. Liang, T. Curran, and J. E. Shepherd. Structural response of piping components to detonation loading. Technical Report FM2006.008, Graduate Aeronautical Laboratories, California Institute of Technology, August 2008. [22](#), [39](#)
- T. Ligon. ES1 bend asymmetry factor analysis. DEI Calculation No. C-6916-00-02, February 2009a. [7](#), [8](#), [21](#), [69](#), [70](#), [90](#), [91](#), [92](#), [93](#), [95](#)
- T. Ligon. The idealized PRC-DDT pulse shape validation. DEI Calculation No. C-6916-00-04, In revision, March 2010, February 2009b. [81](#), [82](#)
- T. Ligon. TS1 tee asymmetry factor analysis. DEI Calculation No. C-6916-00-08, April 2009c. [9](#), [21](#), [129](#), [130](#), [131](#), [132](#)
- T. Ligon. Structural system response pipe element validation. DEI Calculation No. C-6916-00-09 R0, June 2009d. [90](#), [153](#)
- T. Ligon. SS1 system response analysis. DEI Calculation No. C-6916-00-10, August 2009e. [9](#), [10](#), [21](#), [90](#), [153](#), [155](#), [156](#), [157](#), [158](#), [161](#), [163](#), [164](#), [166](#), [167](#), [168](#)
- T. Ligon. Deflagration structural response. DEI Calculation No. C-6916-00-13, Draft D, March 2010. [83](#), [84](#)
- B. W. Lindgren, G. W. McElrath, and D. A. Berry. *Introduction to Probability and Statistics*. McMillan, fourth edition, 1978. [118](#)

- K. Lynch. Pipe stress - comparison of ME101 detonation analysis results to ANSYS for CIT ES-1 model. Bechtel Calculation No. 24590-WTP-P6C-P40T-00020, April 2009. 8, 90, 91, 93
- The MathWorks. MatLab: The language of technical computing. version 7.3.0.267 (R2006b). See documentation on `sgolay` function at <http://www.mathworks.com>. 123, 124, 164
- M. A. Meyers. *Dynamic behavior of materials*. John Wiley & Sons, 1994. 97, 177
- C. C. Perry. Measurement of force, torque, and other mechanical variables with strain gages. Measurements Group technical note downloaded November 2008 from <http://www.davidson.com.au/products/strain/mg/technology/technotes.asp>, 2008. 209, 210
- U. Pfahl, E. Schultz, and J.E. Shepherd. Detonation cell width measurements for H<sub>2</sub>-N<sub>2</sub>O-O<sub>2</sub>-CH<sub>4</sub>-NH<sub>3</sub> mixtures. Technical Report FM98-5, GALCIT, April 1998. 17, 81, 82, 84
- E. A. Rodriguez. Pressure-time history for design of HPAV vessel and piping subjected to gaseous H<sub>2</sub>-N<sub>2</sub>O deflagrations. Technical Report GNNA-0-039, Gobal Nuclear Networks, LLC, December 2008. 84
- J. E. Shepherd. Pressure loads and structural response of the BNL high-temperature detonation tube. Technical Report A-3991, Brookhaven National Laboratory, January 1992. Revised September 24, 1992. 81, 82
- J. E. Shepherd. Structural response of piping to internal gas detonation. *Journal of Pressure Vessel Technology*, 131(3), 2009. 21, 40, 57
- J. E. Shepherd and R. Akbar. Forces due to detonation propagation in a bend. Technical Report FM2008-002, Graduate Aeronautical Laboratories California Institute of Technology, February 2009. 8, 21, 25, 26, 33, 40, 49, 50, 51, 52, 54, 59, 84, 90, 91, 92, 93, 94, 128, 135, 153, 212
- J. E. Shepherd and K. Inaba. Shock loading and failure of fluid-filled tubular structures. In A. Shukla, G. Ravichandran, and Y. Rajapakse, editors, *Dynamic Failure of Materials and Structures*, pages 153–190. Springer, 2010. 54, 99
- J. E. Shepherd and F. Pintgen. Elastic and plastic structural response of tubes to deflagration-to-detonation transition. Technical Report FM2006-005, Graduate Aeronautical Laboratories California Institute of Technology, January 2007. 40, 41, 53
- J. E. Shepherd, J. Karnesky, F. Pintgen, and J. C. Krok. Experimental measurements of strains and blast waves resulting from detonations in tubes. Technical Report FM2006.010, Graduate Aeronautical Laboratories, California Institute of Technology, 2008. 22, 30, 39
- J. E. Shepherd, R. Akbar, and E. A. Rodriguez. Gaseous detonation in piping systems partially filled with liquid. In *ASME Pressure Vessels and Piping Conference*. ASME, 2009. PVP2009-77734, July 26-30 2009, Prague, Czech Republic. 21, 40, 97

- J.E. Shepherd, A. Teodorczyk, R. Knystautas, and J.H. Lee. Shock waves produced by reflected detonations. *Progress in Astronautics and Aeronautics*, 134:244–264, 1991. 91
- P.D. Smith and J.G. Hetherington. *Blast and Ballistic Loading of Structures*. Butterworth/Heinemann, 1994. 40
- S. Suresh. *Fatigue of materials*. Cambridge University Press, 2nd edition, 1998. 69
- SwRI. HPAV gaseous deflagration, detonation, and deflagration-to-detonation (DDT) test program. Technical Report SwRI Project 18-14165, Engineering Dynamics Department, Southwest Research Institute, 6220 Culebra Road, San Antonio, TX 78228-0510, March 2009. Final Report. 81, 90
- S. P. Timoshenko and J. M. Gere. *Theory of Elastic Stability*. McGraw-Hill, 2nd edition, 1961. 64
- A. C. Urgural and S. K. Fenster. *Advanced Strength and Applied Elasticity*. Elsevier, 2nd SI edition, 1987. 210, 211
- Vishay TN515. Strain gage rosettes: Selection, application and data reduction. Technical Report TN-515-1, Vishay Micro-Measurements, January 2010. URL <http://www.vishaymg.com/>. 63, 211

## A Properties of CJ wave in H<sub>2</sub>-N<sub>2</sub>O

Table 23: Properties of CJ detonation in standard (0.3/0.7) H<sub>2</sub>-N<sub>2</sub>O mixture as computed with the Shock and Detonation Toolbox [Browne et al. \(2004\)](#). for nominal initial conditions of the present tests.

### Initial State

Pressure 101325 (Pa)  
Temperature 300.15 (K)  
Density 1.2755 (kg/m<sup>3</sup>)  
a1 (frozen) 321.7538 (m/s)  
gamma1 (frozen) 1.3032 (m/s)

Computing CJ state and isentrope for H2:0.3 N2O:0.7 using H2-N2O.cti  
CJ speed 2087.919 (m/s)

### CJ State

Pressure 2620896.2405 (Pa)  
Temperature 3383.9138 (K)  
Density 2.3323 (kg/m<sup>3</sup>)  
Entropy 10355.319 (J/kg-K)  
w2 (wave frame) 1141.7939 (m/s)  
u2 (lab frame) 946.1251 (m/s)  
a2 (frozen) 1187.2092 (m/s)  
a2 (equilibrium) 1140.0226 (m/s)  
Gamma2 (frozen) 1.2543 (m/s)  
Gamma2 (equilibrium) 1.1566 (m/s)

Detonation CJ Mach number) 6.4892 (m/s)  
2-gamma energy parameter q 6432142.8919 (J/kg)  
Reflected CJ shock (equilibrium) computation

Reflected wave speed 811.6828 (m/s)  
Pressure 6503420.5432 (Pa)  
Temperature 3785.0383 (K)  
Density 5.0537 (kg/m<sup>3</sup>)

### State 3

Pressure 954063.0488 (Pa)  
Temperature 3005.9407 (K)  
Volume 1.0268 (m<sup>3</sup>/kg)  
Sound speed (frozen) 1107.4628 (m/s)  
Sound speed (equilibrium) 1065.6272 (m/s)  
Gamma frozen) 1.252 (m/s)  
Gamma (equilibrium) 1.1592 (m/s)

## B Properties of Schedule 40 pipe

The material properties are nominal values that have been obtained from tables of properties for commercial materials.

Table 24: 2-in Schedule 40 Stainless Steel pipe, nominal properties.

Outer diameter	2.375	in	60.3	mm
Inner diameter	2.067	in	52.5	mm
Mean radius $R$	1.11	in	0.0282067	m
thickness $h$	0.154	in	0.0039116	m
Pipe metal cross-sectional area $A_p$	1.075	in <sup>2</sup>	$6.910 \times 10^{-4}$	m <sup>2</sup>
Flow cross-sectional area $A_i$	3.356	in <sup>2</sup>	$2.165 \times 10^{-3}$	m <sup>2</sup>
Young's modulus $E$	$2.79 \times 10^6$	psi	$1.93 \times 10^{11}$	Pa
mass density $\rho$	0.29	lb/in <sup>3</sup>	8040	kg/m <sup>3</sup>
Poisson ratio $\nu$	0.305			
Specific heat capacity $C_p$			500	J/kg-K
Thermal expansion coefficient (linear) $\alpha$			$16.9 \times 10^{-6}$	K <sup>-1</sup>
Thermal conductivity $k$			16.2	W/m-K

The elastic properties and wave speeds are based on standard definitions [Kolsky \(1963\)](#), [Meyers \(1994\)](#) and the critical wave speeds  $V_{ci}$  are those discussed by [Beltman and Shepherd \(2002\)](#).

Table 25: 2-in Schedule 40 Stainless Steel pipe elastic properties.

Shear correction factor $\kappa$	0.83	
Lame $\lambda$	$1.157 \times 10^{11}$	Pa
Lame $\mu$ (Shear modulus)	$7.395 \times 10^{10}$	Pa
Bulk modulus $K$	$1.65 \times 10^{11}$	Pa
Dilatational wave speed, $C_\ell$	5725.	m/s
Shear wave speed, $C_s$	3033.	m/s
Hoop frequency $f_{hoop}$	$2.904 \times 10^4$	Hz
Hoop period $T_{hoop}$	34.4	$\mu$ s
Bending length $\ell_b$	8.18	mm
$V_{c0}$ - Flexural wave, thin-shell approximation	1421.	m/s
$V_{c1}$ - shell (modified) shear wave speed	2763.	m/s
$V_{c2}$ - dilatation speed in bar	4899.	m/s
$V_{c3}$ - shell dilatational speed	5145.	m/s

For completeness, the definitions of the quantities in Table 25 are:

$$\mu = \frac{E}{2(1 + \nu)}$$

$$\lambda = \frac{E\nu}{(1 + \nu)(1 - 2\nu)}$$

$$K = \frac{E}{3(1 - 2\nu)}$$

$$C_s = \sqrt{\frac{\mu}{\rho}}$$

$$C_\ell = \sqrt{\frac{\lambda + 2\mu}{\rho}}$$

$$V_{c0} = \left[ \frac{E^2 h^2}{3\rho^2 R^2 (1 - \nu^2)} \right]^{1/4}$$

$$V_{c1} = \sqrt{\frac{\kappa\mu}{\rho}}$$

$$V_{c2} = \sqrt{\frac{E}{\rho}}$$

$$V_{c3} = \sqrt{\frac{E}{\rho(1 - \nu^2)}}$$

$$f_{hoop} = \frac{1}{2\pi R} \sqrt{\frac{E}{\rho(1 - \nu^2)}}$$

$$T_{hoop} = \frac{1}{f_{hoop}}$$

$$\ell_b = \left[ \frac{R^2 h^2}{3(1 - \nu^2)} \right]^{1/4}$$

# C Room 19 Plate Mounting Arrangement

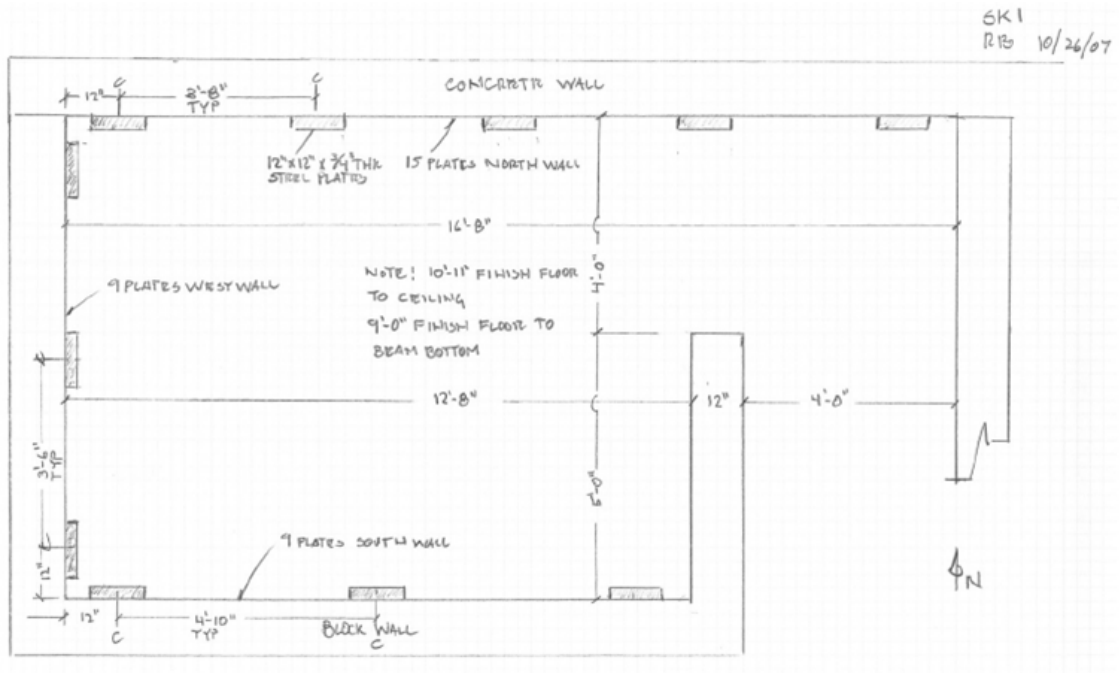


Figure 99: Nominal dimensions of Room 19 experiment area.

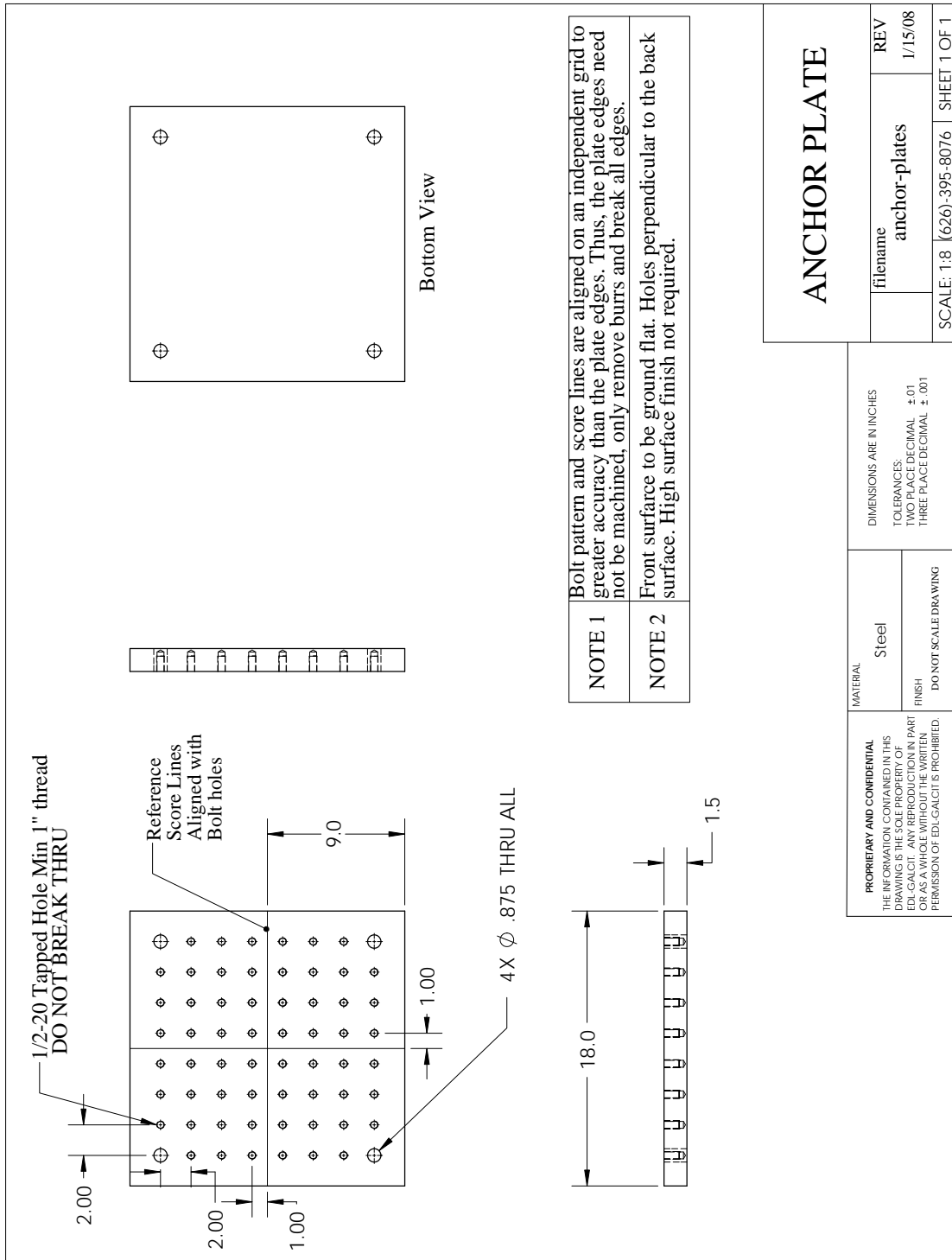


Figure 100: Engineering dimensions of anchor plate.

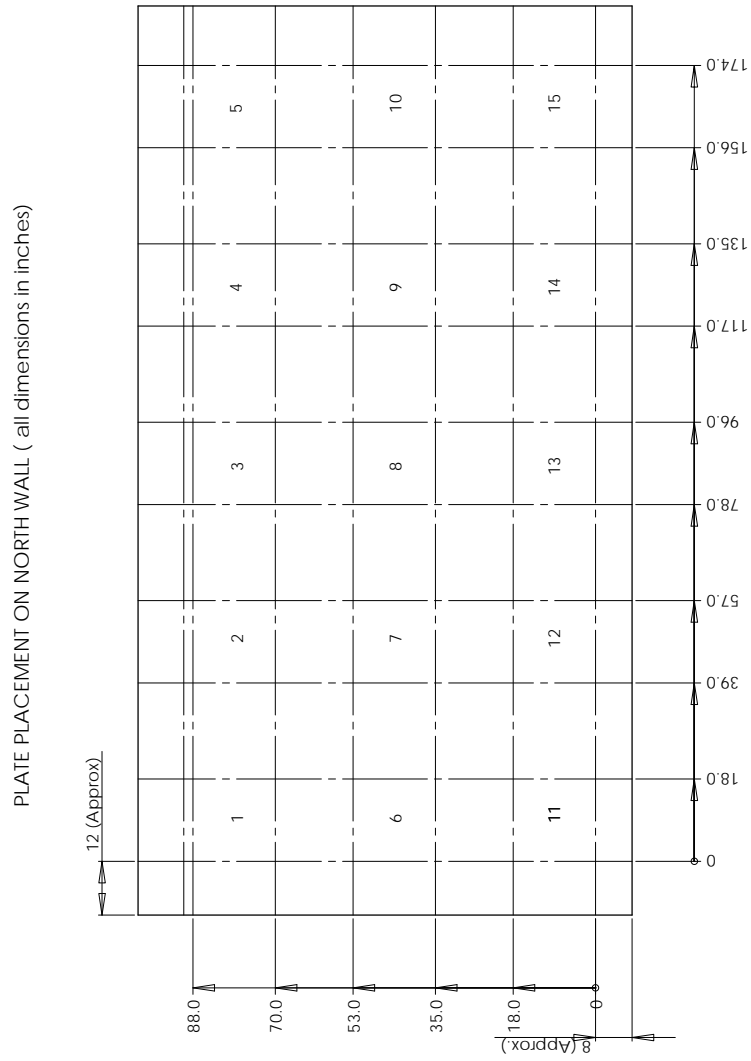


Figure 101: Plate layout on North wall.

PLATE PLACEMENT ON SOUTH WALL (all dimensions in inches)

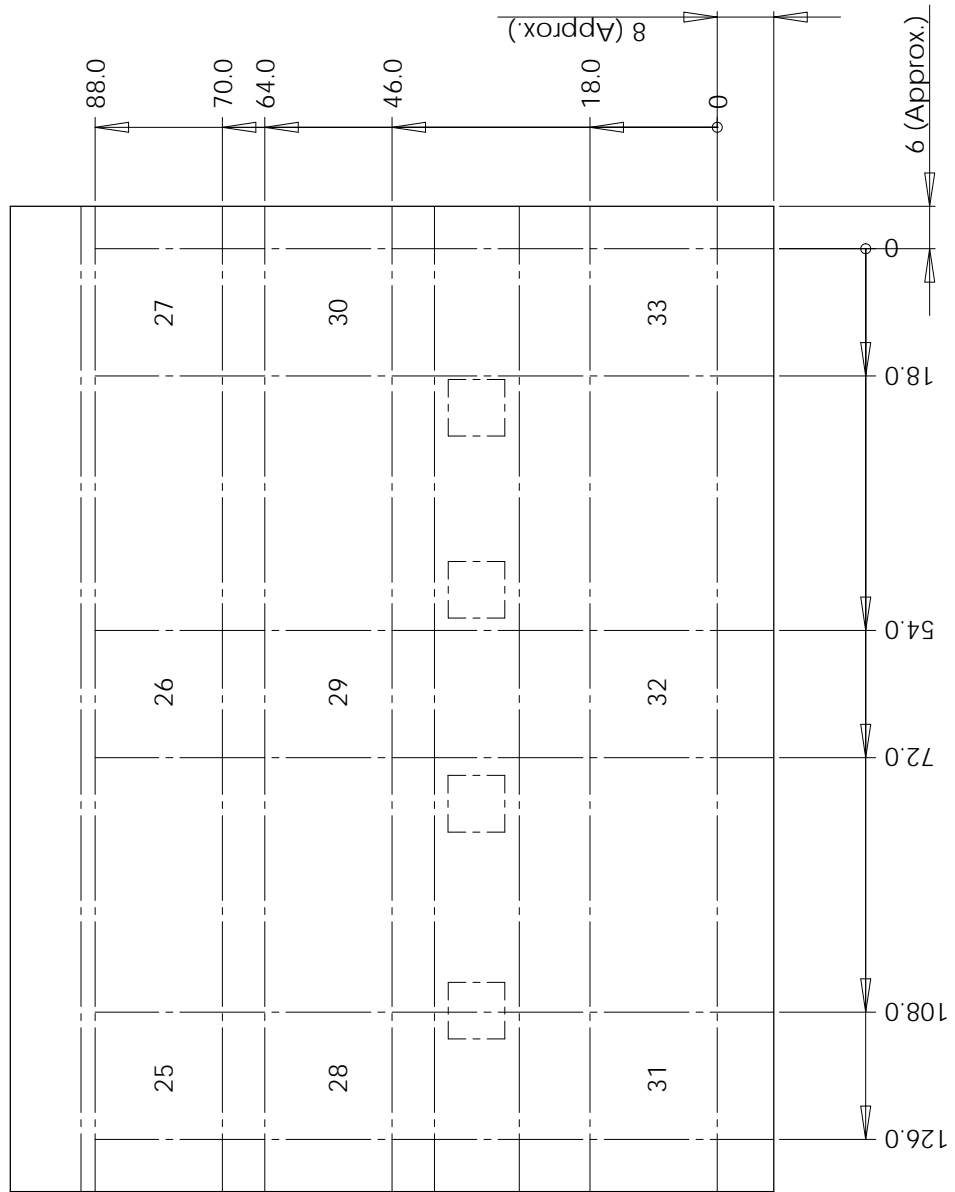


Figure 102: Plate layout on South wall.

PLATE PLACEMENT ON WEST WALL (all dimensions in inches)

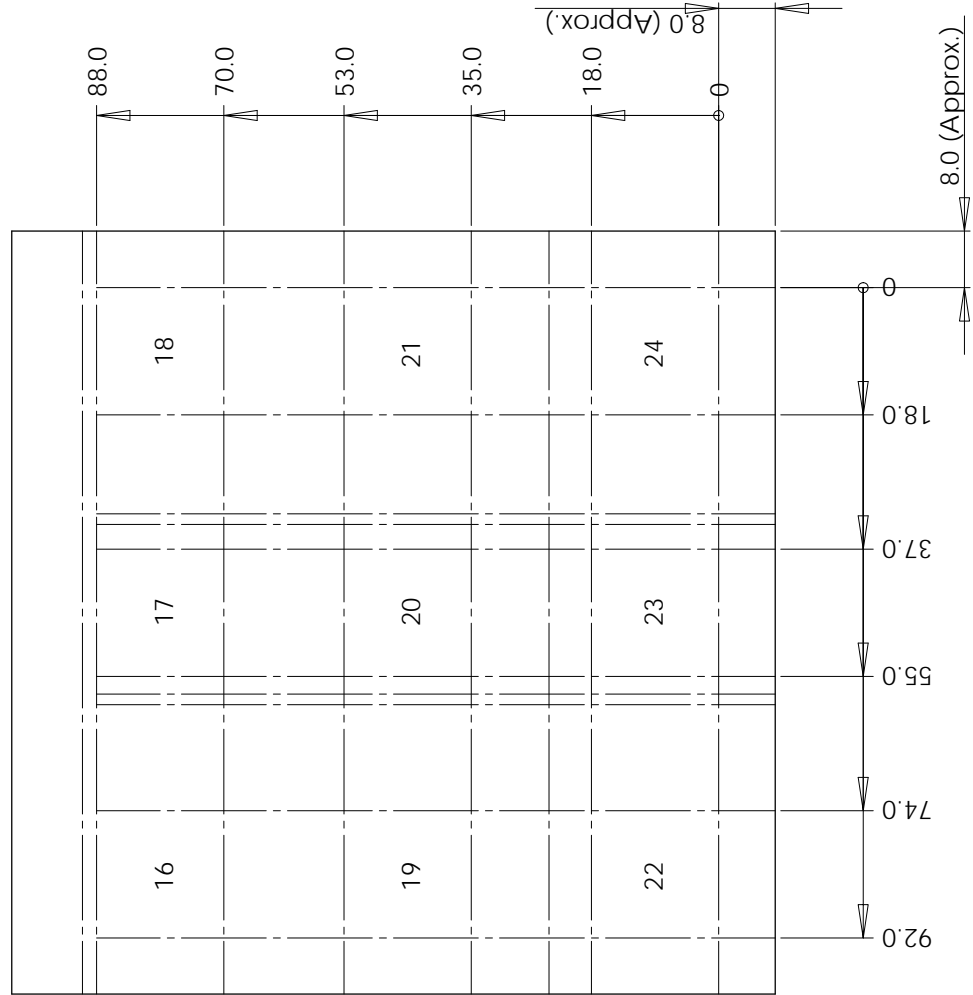


Figure 103: Plate layout on West wall.

# D Check List

JES.HPAV-1-PAC.HPAV

5/8/2009

## RM19 Combustion Test Checklist

:

**Test Number:** \_\_\_\_\_

**Test Specimen or Series:** \_\_\_\_\_

**Test Date:** \_\_\_\_\_

**Operator(s):** \_\_\_\_\_

**Instrumentation layout file:** \_\_\_\_\_

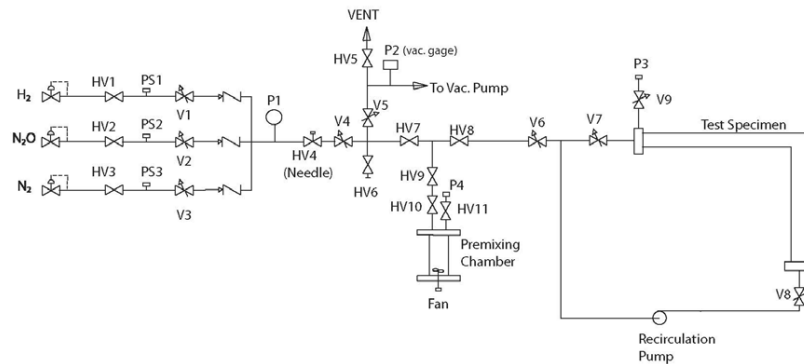
**Instrumentation setup file:** \_\_\_\_\_

### Before starting a series of tests *without* the mixing chamber:

1. \_\_\_\_ Turn on air supply to valves
2. \_\_\_\_ Turn on control panel in Rm 19, check circuit breaker in panel LXX
3. Verify remote valve operation and hand valve positions  
\_\_\_\_ Close all valves on panel (All green lights on?)  
\_\_\_\_ HV7, HV8 open.  
\_\_\_\_ HV9, HV10, HV11 closed.  
\_\_\_\_ HV6 closed and capped off.
4. \_\_\_\_ Turn on gas bottle. Check bottle pressures, replace if below 200 psi.  
\_\_\_\_ Set regulators at 15-20 psi  
\_\_\_\_ Open hand valves at regulator and gas lines (HV1, HV2, HV3).  
\_\_\_\_ Verify pressure in lines. Pressure switch indicator lights green?
5. \_\_\_\_ Close vacuum valve HV5 and V5. Turn on vacuum pump in closet, note hours since last oil change, and change if needed.
6. \_\_\_\_ Turn on TC vacuum gage P2. Pressure after pumping for 5 minutes \_\_\_\_\_
7. \_\_\_\_ Turn on video camera, vcr, and monitor, adjust video camera tripod, and focus.
8. \_\_\_\_ Verify operation of gas leak detectors.
9. \_\_\_\_ Verify power switch is on at spark box
10. \_\_\_\_ Verify circulation pump operation
11. \_\_\_\_ Verify operation of interlocks. Close vent, door, warning light on, reset gas detectors if needed, check for green light on fireset control panel
12. \_\_\_\_ Check fireset operation with dummy sparkplug. Remove key, safe fireset.

Prepared By: JES & Raza Akbar

1



For each explosion test:

Calculate composition target and estimate CJ parameters

Gas	Target Fraction	Target Partial P (mTorr)	Target Fill P (mTorr)	Actual Fill P (mTorr)
Starting pressure				
H2	0.30	228	228	
N2O	0.70	532	760	
Final preshot pressure (mTorr)				
Final preshot temperature (°C)				
CJ wave speed (m/s)				
CJ pressure (MPa)				

1. \_\_\_\_\_ Computer, DAQ and instrumentation amplifiers turned on and warmed up.
  - \_\_\_\_\_ Verify all signal cables and interconnect cables are in place.
  - \_\_\_\_\_ PCB signal conditioner gains set per setup sheet.
  - \_\_\_\_\_ Displacement gage power supply turned on. Verify gage operation.
  - \_\_\_\_\_ Strain gage fault check, set gain, excitations, and bandwidth
  - \_\_\_\_\_ Turn on MKS pressure gage P3 and omega thermocouple readout T1
2. Evacuate lines and test specimen.
  - \_\_\_\_\_ Open vent in 19A.
  - \_\_\_\_\_ Open V5, V6, V7, V8, and V9.
3. \_\_\_\_\_ Note ultimate pressure after pump down of \_\_\_\_\_ minutes
  - \_\_\_\_\_ Pressure P3
  - \_\_\_\_\_ Pressure P2
4. **Leak check.**
  - \_\_\_\_\_ Close V6, V5 and wait 5 minutes. Pressure P3 \_\_\_\_\_
5. **Flush lines from bottles.**
  - \_\_\_\_\_ Verify V6 is closed

- Activate key in gas panel  
 Set HV4 2-1/2 turns from closed and open V5.  
 Activate V4 and each of V1, V2, V3 for 2 s.
6. **Evacuate fill lines.**
- Close HV1, HV2, HV3.  
 Open V4 until P2 is stable.
7.  Open V6 and evacuate specimen.
8.  Close V5.
9.  Close door to 19A (check for green light)
10.  Warning light on
11.  Ear protection on.
12. **Fuel fill.**
- Open HV1.
13.  Open V1, and V4 to fill fuel to target pressure at P3.
14. Evacuate lines.
- Close V6 and HV1.  
 Open V4, HV4, V5. Evacuate until P2 is stable.
15. **Oxidizer fill.**
- Close V5 and open HV2.
16.  Open V2 and V4 to charge oxidizer line unit P1 is stable.
17.  Open V6. Fill by opening V4, adjust flow rate with HV4.
18.  Close V6, HV2
19.  Run circulation pump for 5 minutes. Turn pump off.
20.  Record final pressure and temperature
21.  Close V7, V8, V9.
22.  Open V6 and V5, pump until P2 is stable.
23.  Close V6 and V5
24. **Arming and Firing**
25.  Close vent in 19A
26.  Zero strain gages
27.  Verify interlock green (Check door switch if not)
28.  start video recording
29.  Arm the DAS
30.  Turn on power to fireset panel with key
31.  ARM FIRESET BY HOLDING ARM SWITCH ON FOR 3 s.
32.  KEEPING ARM SWITCH ON, PRESS FIRE BUTTON.
33.  Remove key from fireset, put back into gas panel.
34.  End video recording .  Video End time
35.  Save data from DAS- make archive copies on CD-ROM. Shot
- Time: \_\_\_\_\_

**36. Cool down and pump out**

- Monitor temperature gage T1, when this drops below 40C, open V9
- Record final pressure on P-3 \_\_\_\_\_
- Open vent in Rm 19A
- Open V5, V6, V7, V8.

Evacuate until P2 is stable. Run circulation pump if needed

**37. Shut down**

- 38.  Close V6, V7, V8, V9, and V5. Turn off circulation pump
- 39.  Turn off vacuum pump, open HV5
- 40.  Shut off gas bottles.
- 41.  Turn off displacement gage power, DAS, signal conditioners.
- 42.  Turn off P1, T1, P2
- 43.  Turn off Control Panel.

Comments:

**V1.5 23 July 2008**



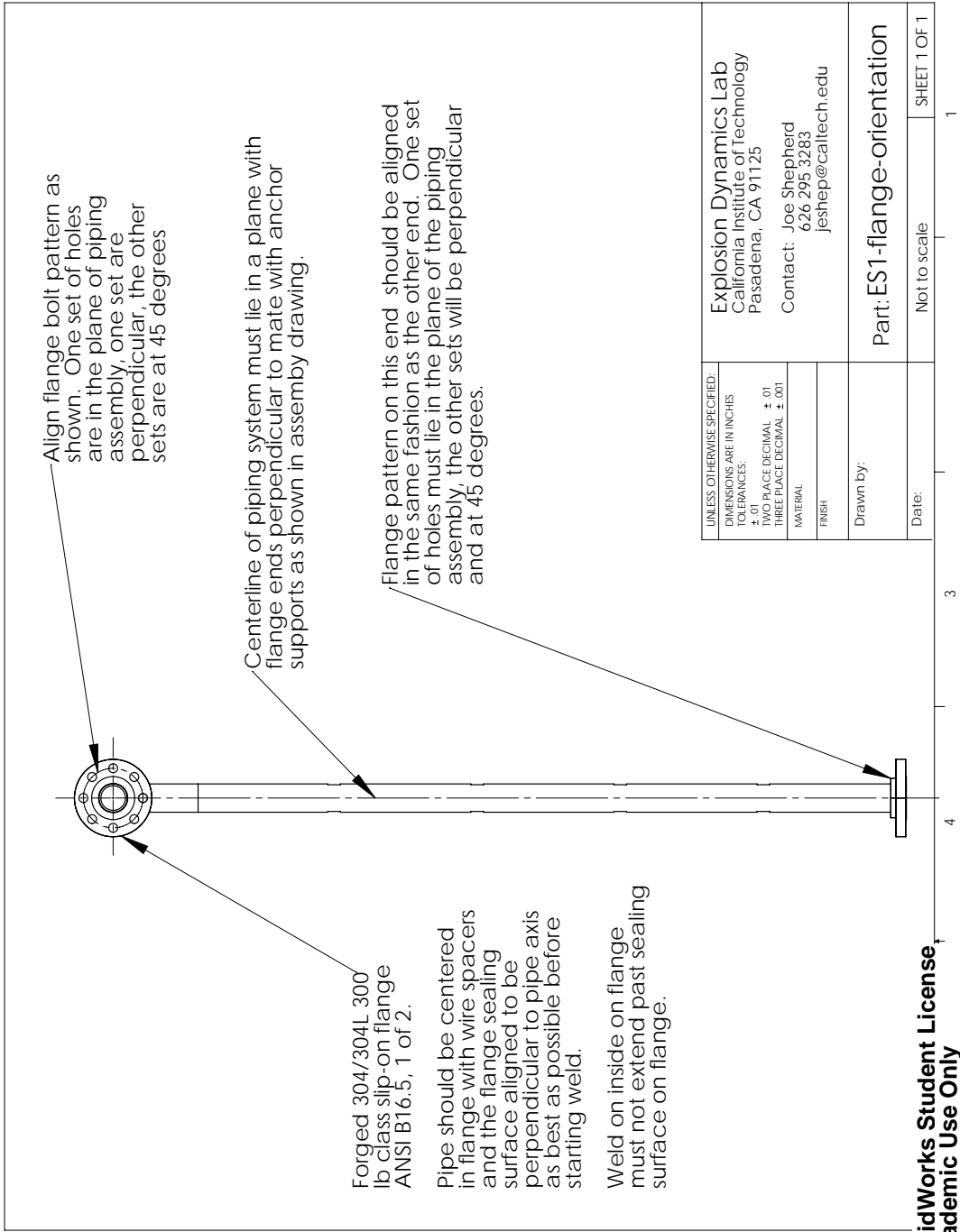


Figure 105: Engineering drawing of ES1 assembly. Side view.

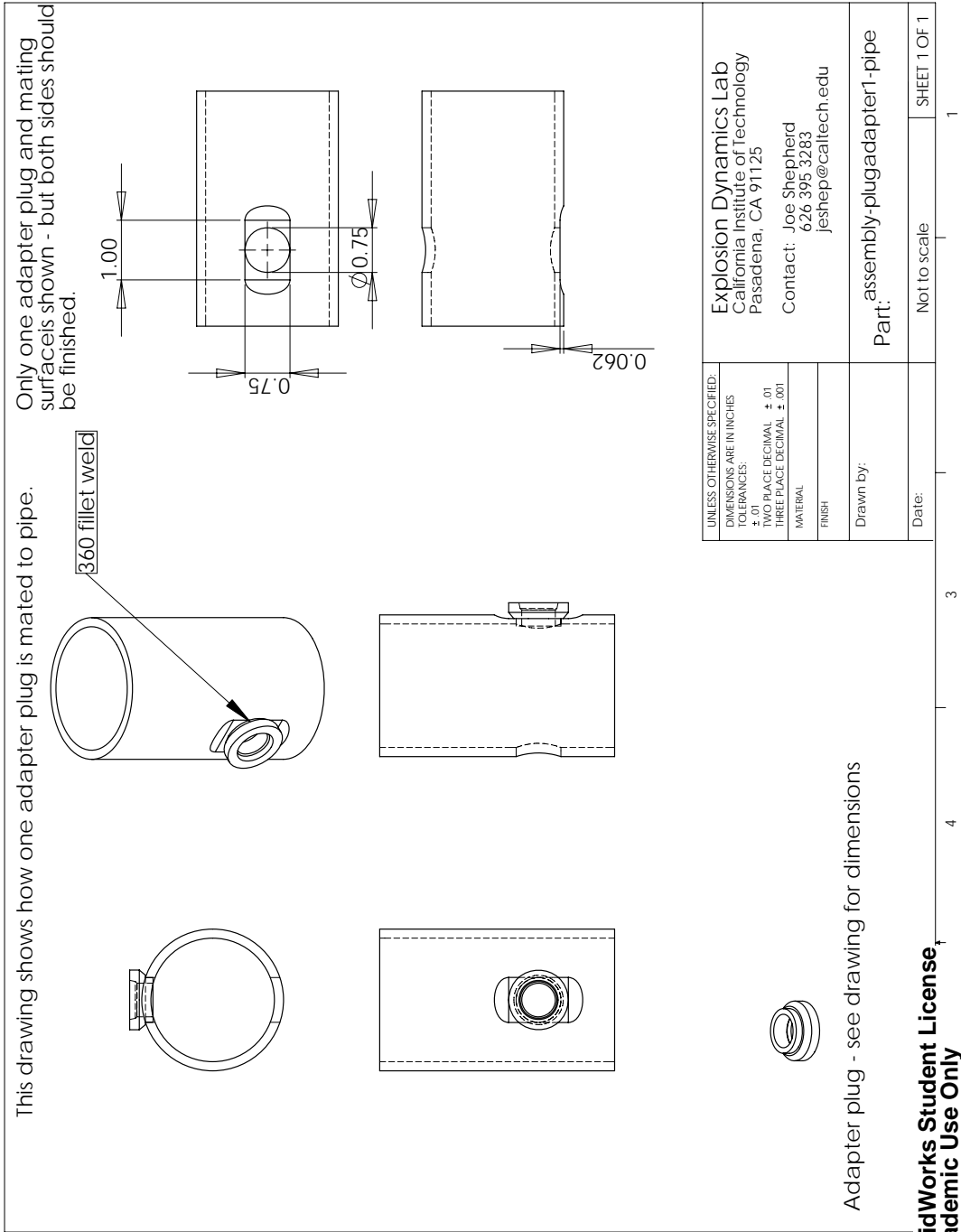
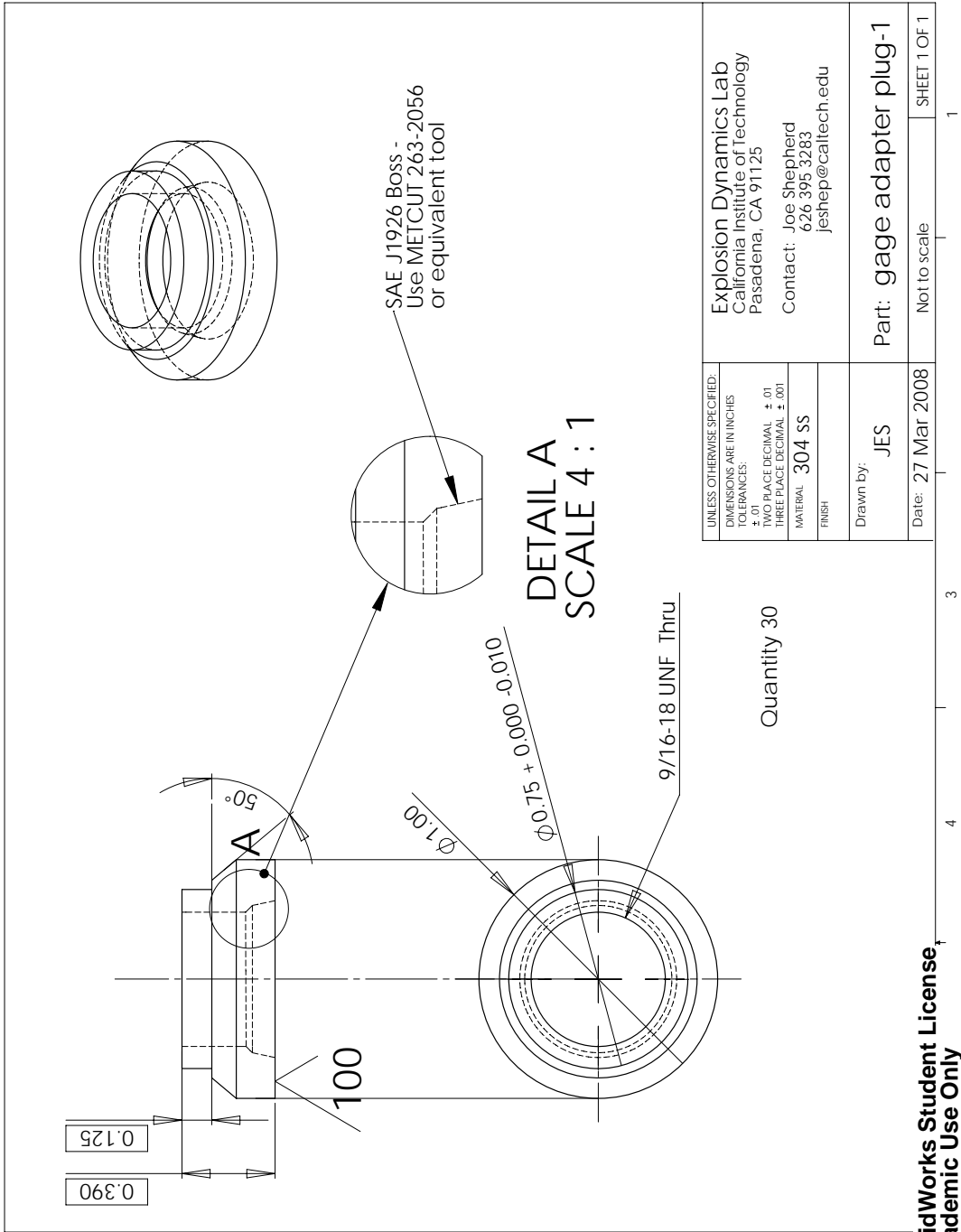
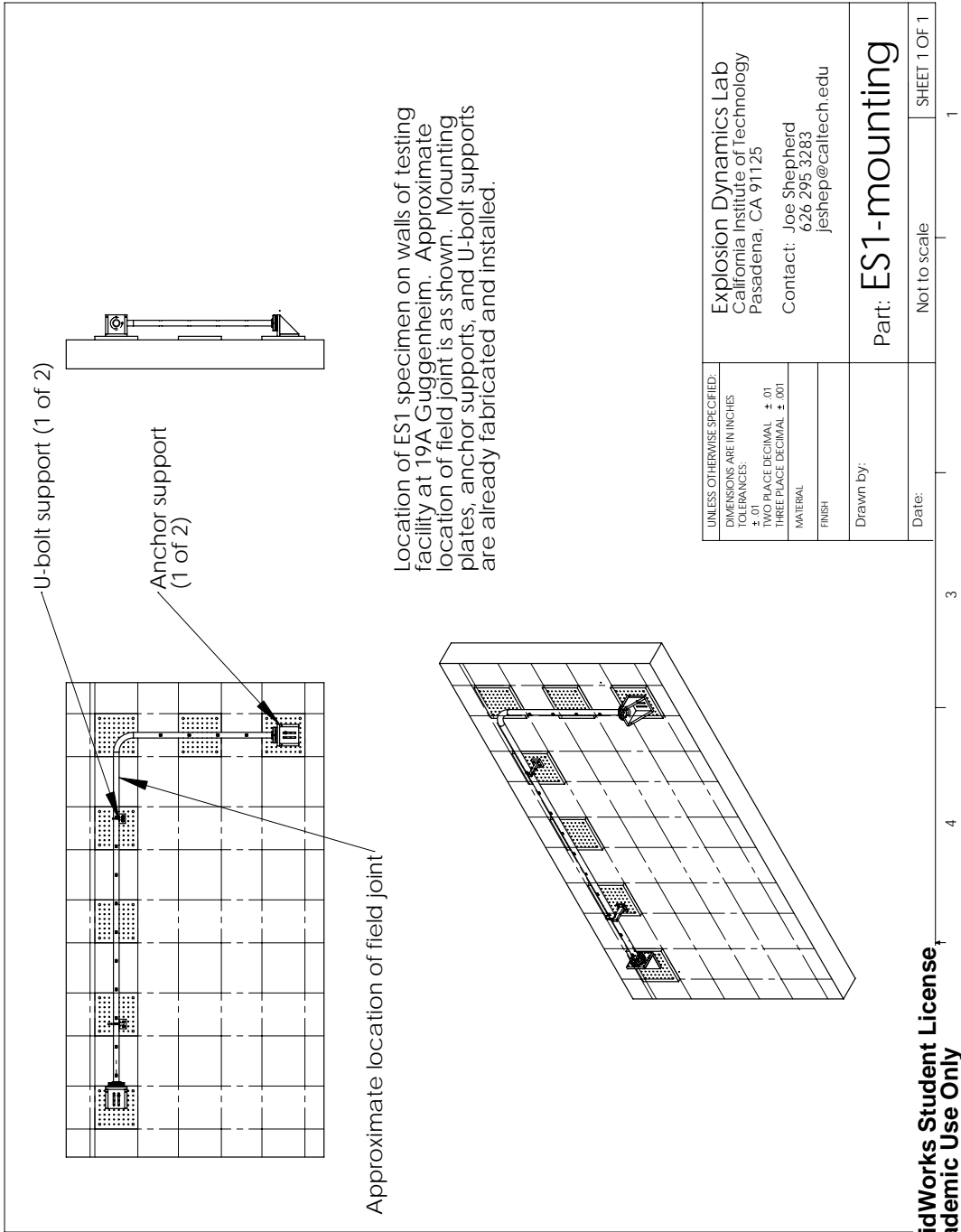


Figure 106: Engineering drawing showing assembly of the SAE boss onto the pipe.



SolidWorks Student License  
Academic Use Only

Figure 107: Engineering drawing of SAE boss.



SolidWorks Student License  
Academic Use Only

Figure 108: Perspective view of ES1 assembly mounted on the North wall.

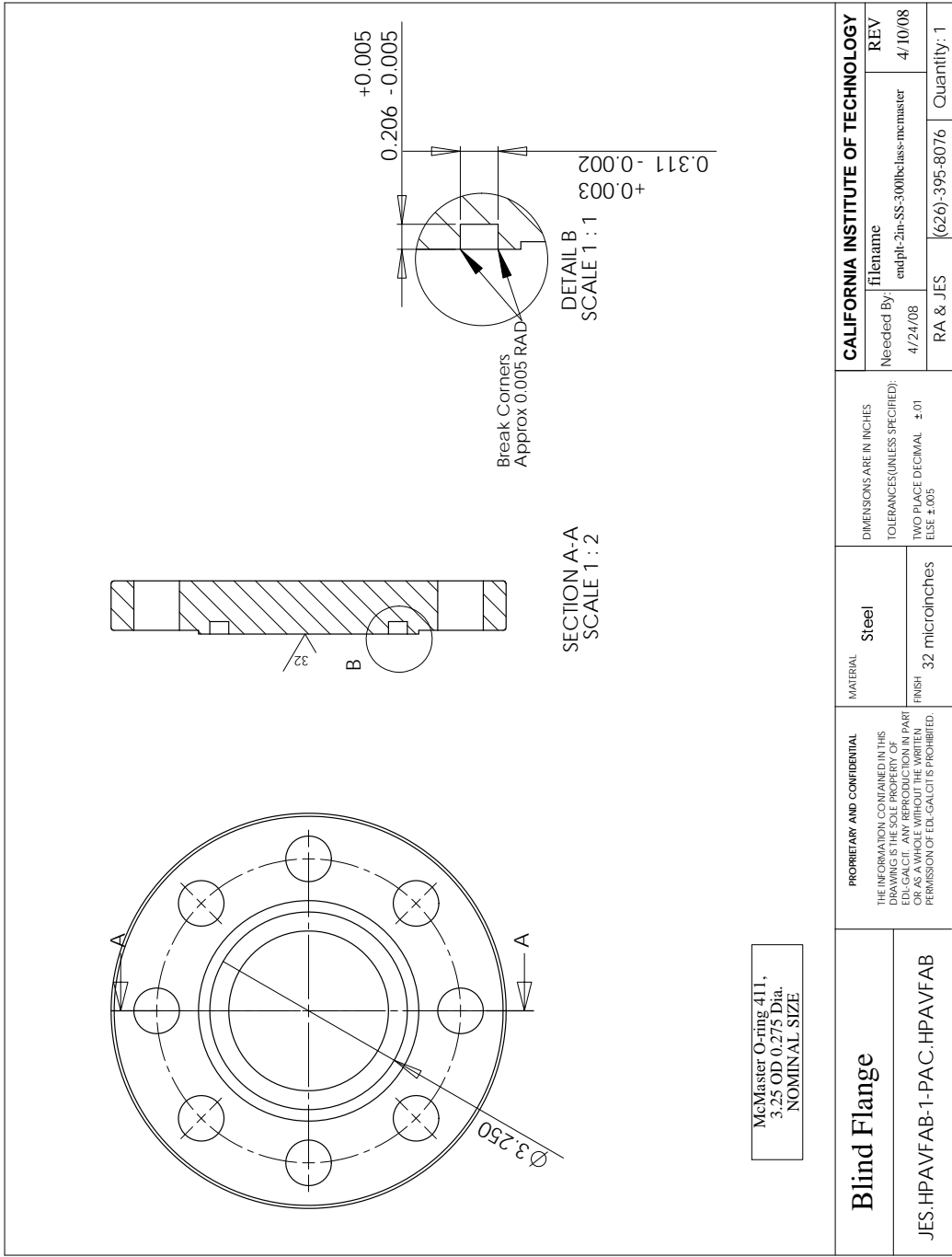


Figure 109: Engineering drawing of ES1 300 lb class blind flange.

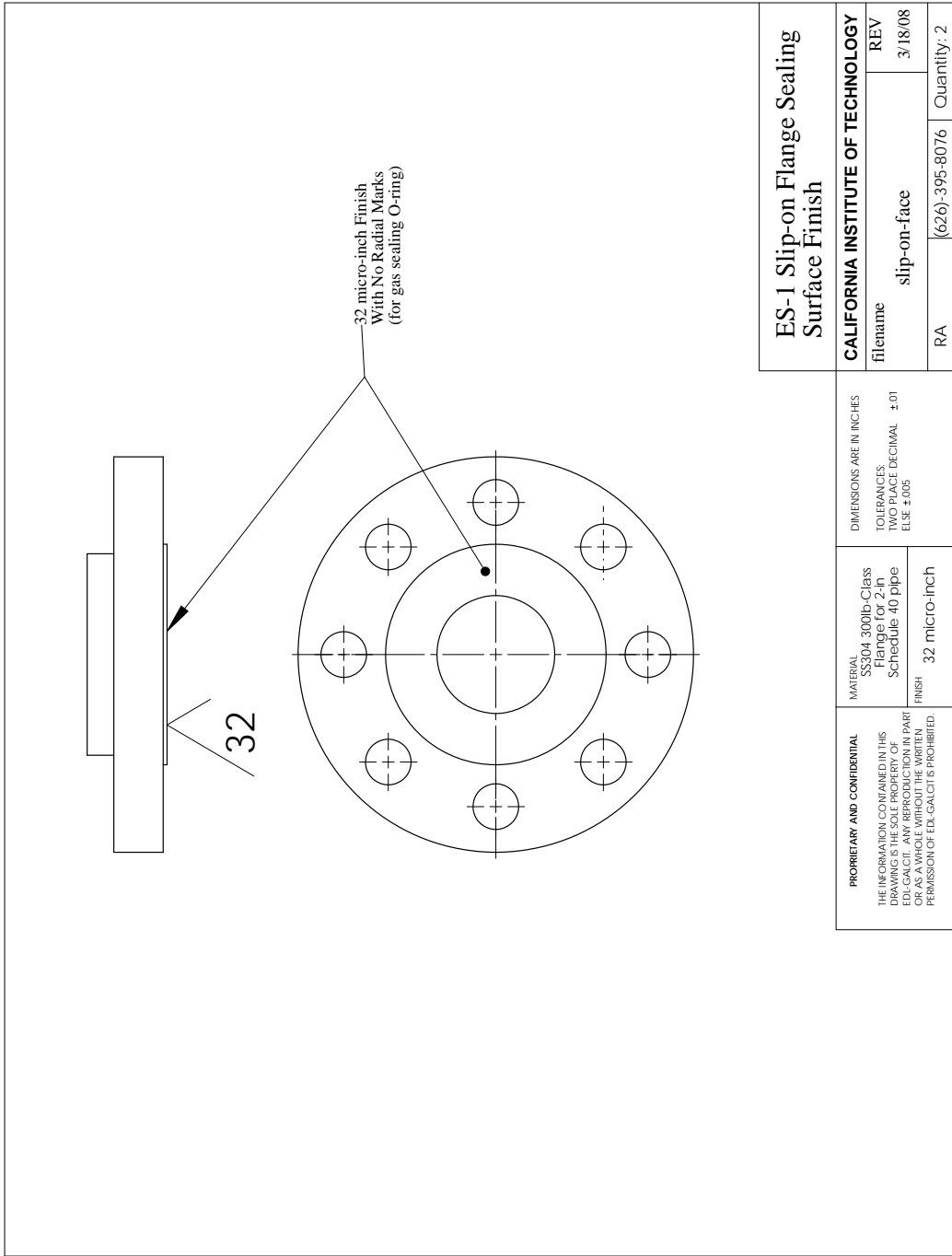


Figure 110: Engineering drawing of ES1 slip-on flange modification.

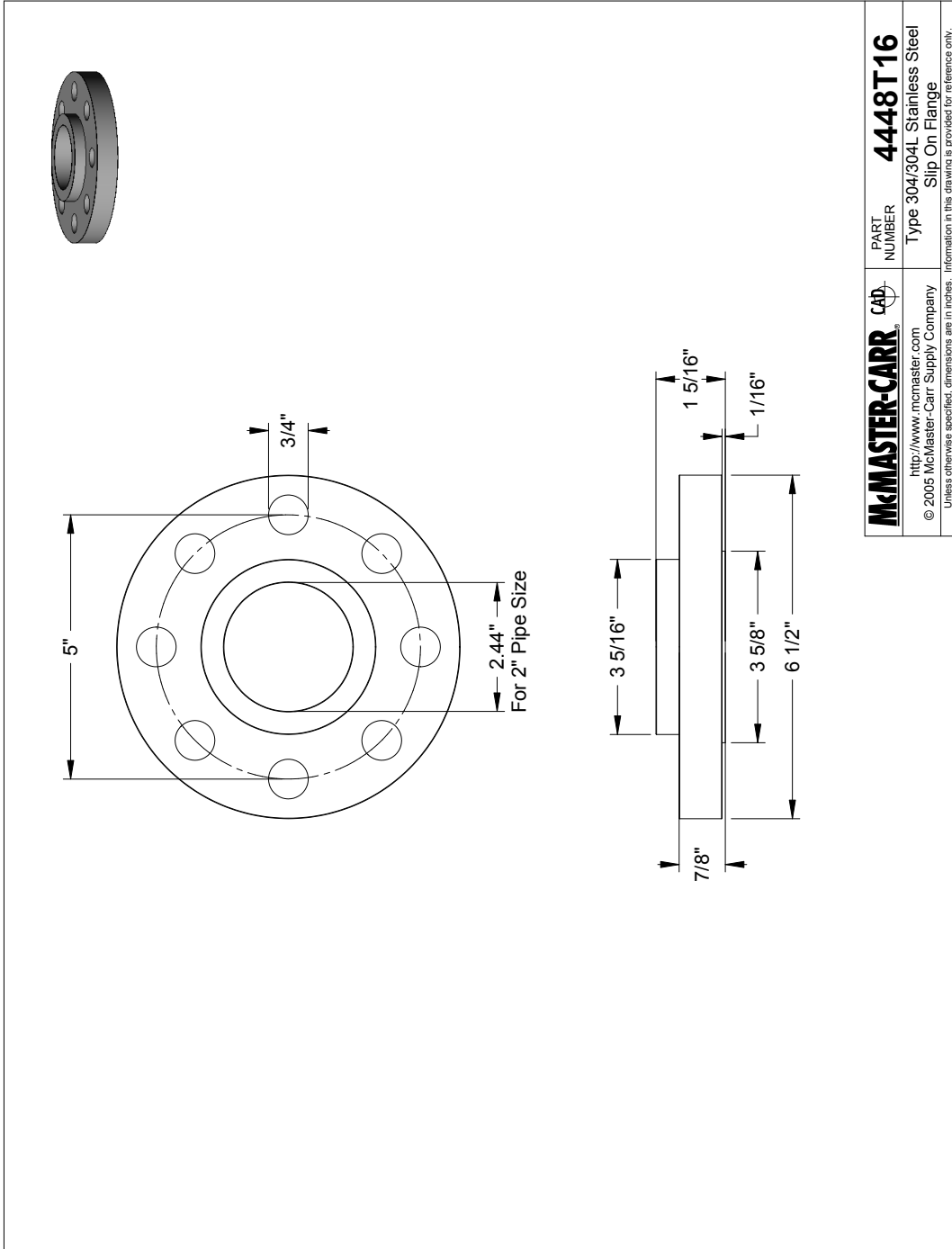
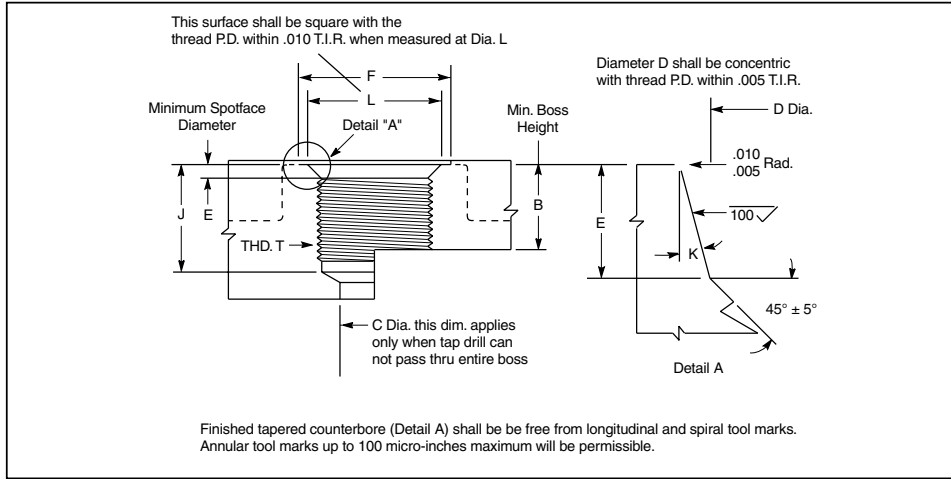


Figure 111: Engineering drawing of original ES1 slip-on flange.

**Design Table 4-7 — Tube Fitting Boss Seals**

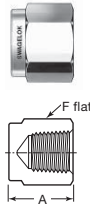


Design Table 4-7 — Boss Dimensions for Industrial Straight Thread Tube Fittings												
Parker O-ring Size No.	Actual O-Ring Dimensions		Tube OD	Thread T	B Min. Thread Depth	C Min.	D +.005 - .000	E +.015 - .000	F Min.	J Min.	K ±1°	L Min.
	W	ID										
3-902	.064 ± .003	.239 ± .005	1/8	5/16-24	.390	.062	.358	.074	.672	.468	12°	.438
3-903	.064 ± .003	.301 ± .005	3/16	3/8-24	.390	.125	.421	.074	.750	.468	12°	.500
3-904	.072 ± .003	.351 ± .005	1/4	7/16-20	.454	.172	.487	.093	.828	.547	12°	.563
3-905	.072 ± .003	.414 ± .005	5/16	1/2-20	.454	.234	.550	.093	.969	.547	12°	.625
3-906	.078 ± .003	.468 ± .005	3/8	9/16-18	.500	.297	.616	.097	.909	.609	12°	.688
3-908	.087 ± .003	.644 ± .009	1/2	3/4-16	.562	.391	.811	.100	1.188	.688	15°	.875
3-910	.097 ± .003	.755 ± .009	5/8	7/8-14	.656	.484	.942	.100	1.344	.781	15°	1.000
3-912	.116 ± .004	.924 ± .009	3/4	1 1/16-12	.750	.609	1.148	.130	1.625	.906	15°	1.250
3-913	.116 ± .004	.986 ± .010	13/16									
3-914	.116 ± .004	1.047 ± .010	7/8	1 3/16-12	.750	.719	1.273	.130	1.765	.906	15°	1.375
3-916	.116 ± .004	1.171 ± .010	1	1 5/16-12	.750	.844	1.398	.130	1.910	.906	15°	1.500
3-918	.116 ± .004	1.355 ± .012	1 1/8									
3-920	.118 ± .004	1.475 ± .014	1 1/4	1 5/8-12	.750	1.078	1.713	.132	2.270	.906	15°	1.875
3-941	.118 ± .004	1.720 ± .014	1 1/2	1 7/8-12	.750	1.312	1.962	.132	2.560	.906	15°	2.125
3-932	.118 ± .004	2.337 ± .018	2	2 1/2-12	.750	1.781	2.587	.132	3.480	.906	15°	2.750

**Design Table 4-7: Boss Dimensions for Industrial Straight Thread Tube Fitting O-ring Gaskets Per SAE J1926 and MS16142**

Figure 112: Engineering specifications of SAE1926 port.

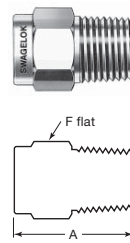
**Pipe Caps**



**Female NPT**

NPT Size in.	Basic Ordering Number	Dimensions in. (mm)	
		A	F
1/8	-2-CP	0.75 (19.1)	9/16
1/4	-4-CP	0.91 (23.1)	3/4
3/8	-6-CP	1.03 (26.2)	7/8
1/2	-8-CP	1.34 (34.0)	1 1/16
3/4	-12-CP	1.44 (36.6)	1 5/16
1	-16-CP	1.62 (41.1)	1 5/8
Heavy-Wall Female NPT			
1/4	SS-4-CP-10K	1.11 (28.2)	1
1/2	SS-8-CP-10K	1.58 (40.1)	1 1/2

**Pipe Plugs**

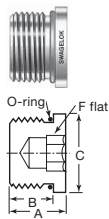


**Male NPT**

NPT Size in.	Basic Ordering Number	Dimensions in. (mm)	
		A	F
1/16	-1-P	0.75 (19.1)	5/16
1/8	-2-P	0.75 (19.1)	7/16
1/4	-4-P	0.96 (24.4)	9/16
3/8	-6-P	0.99 (25.1)	11/16
1/2	-8-P	1.21 (30.7)	7/8
3/4	-12-P	1.21 (30.7)	1 1/16
1	-16-P	1.50 (38.1)	1 3/8

For pipe plugs with male ISO/BSP parallel threads (RS), contact your authorized Swagelok representative.

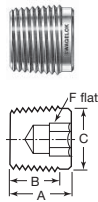
**Hollow Hex Plugs**



**Male SAE/MS Straight Thread (ST)**

SAE/MS Thread Size in.	Basic Ordering Number	Dimensions in. (mm)				Uniform O-ring <sup>①</sup> Size
		A	B	C	F	
7/16-20	-4-HPST	0.45 (11.4)	0.36 (9.1)	0.56 (14.2)	3/16	-904
9/16-18	-6-HPST	0.48 (12.2)	0.39 (9.9)	0.69 (17.5)	1/4	-906
3/4-16	-8-HPST	0.56 (14.2)	0.44 (11.2)	0.88 (22.4)	5/16	-908
1 1/16-12	-12-HPST	0.75 (19.1)	0.59 (15.0)	1.25 (31.8)	9/16	-912
1 5/16-12	-16-HPST	0.75 (19.1)	0.59 (15.0)	1.50 (38.1)	5/8	-916

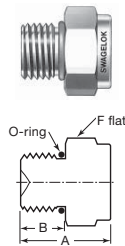
① O-ring material is 90 durometer fluorocarbon FKM.



**Male NPT**

NPT Size in.	Basic Ordering Number	Dimensions, in. (mm)			
		A	B	C	F
1/8	SS-2-HP	0.41 (10.4)	0.29 (7.4)	0.37 (9.4)	3/16
1/4	SS-4-HP	0.61 (15.5)	0.49 (12.4)	0.48 (12.1)	1/4
3/8	SS-6-HP	0.59 (15.0)	0.47 (11.9)	0.62 (15.7)	5/16
1/2	SS-8-HP	0.76 (19.3)	0.64 (16.2)	0.76 (19.3)	3/8

**Hex Head Plugs**



**Male SAE/MS Straight Thread (ST)**

SAE/MS Thread Size in.	Basic Ordering Number	Dimensions in. (mm)			Uniform O-ring <sup>①</sup> Size
		A	B	F	
7/16-20	-4-PST	0.76 (19.3)	0.36 (9.1)	9/16	-904
9/16-18	-6-PST	0.82 (20.8)	0.39 (9.9)	11/16	-906
3/4-16	-8-PST	0.89 (22.6)	0.44 (11.2)	7/8	-908
1 1/16-12	-12-PST	1.12 (28.4)	0.59 (15.0)	1 1/4	-912
1 5/16-12	-16-PST	1.18 (30.0)	0.59 (15.0)	1 1/2	-916

① O-ring material is 90 durometer fluorocarbon FKM.

Swagelok

Figure 113: Engineering specification of SAE hex head plugs.

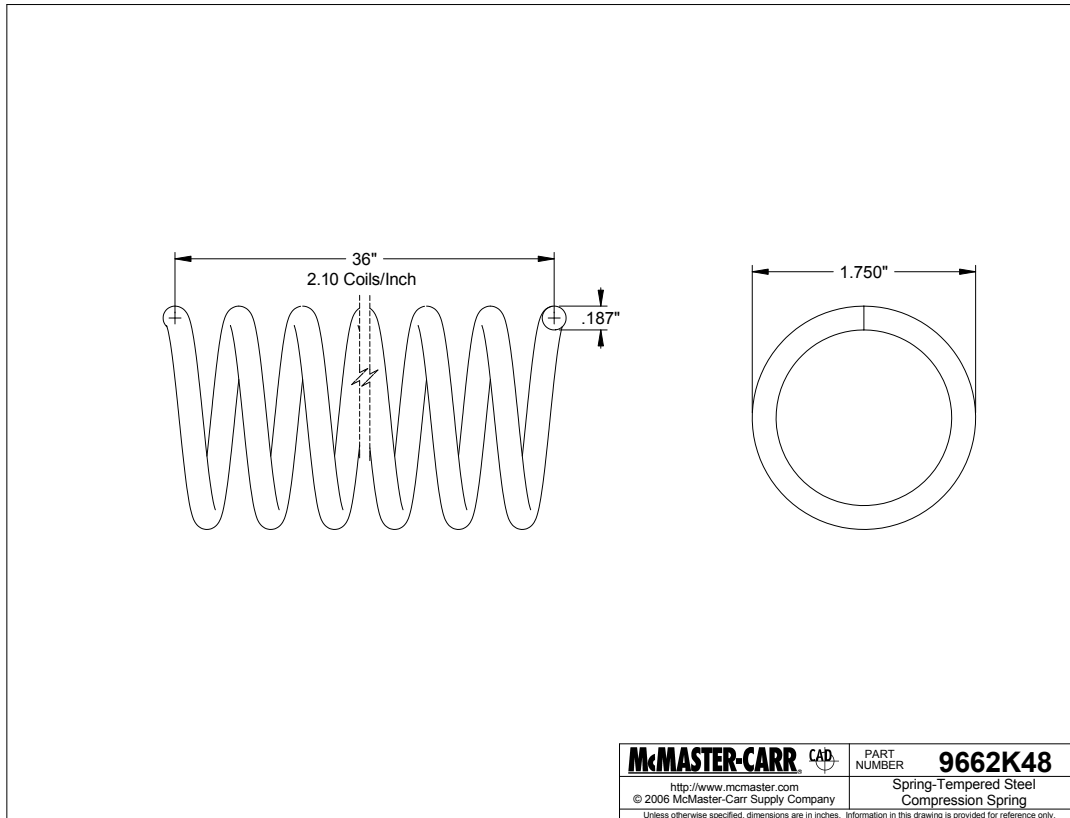


Figure 114: Engineering drawing of spring used for Shchelkin spiral.

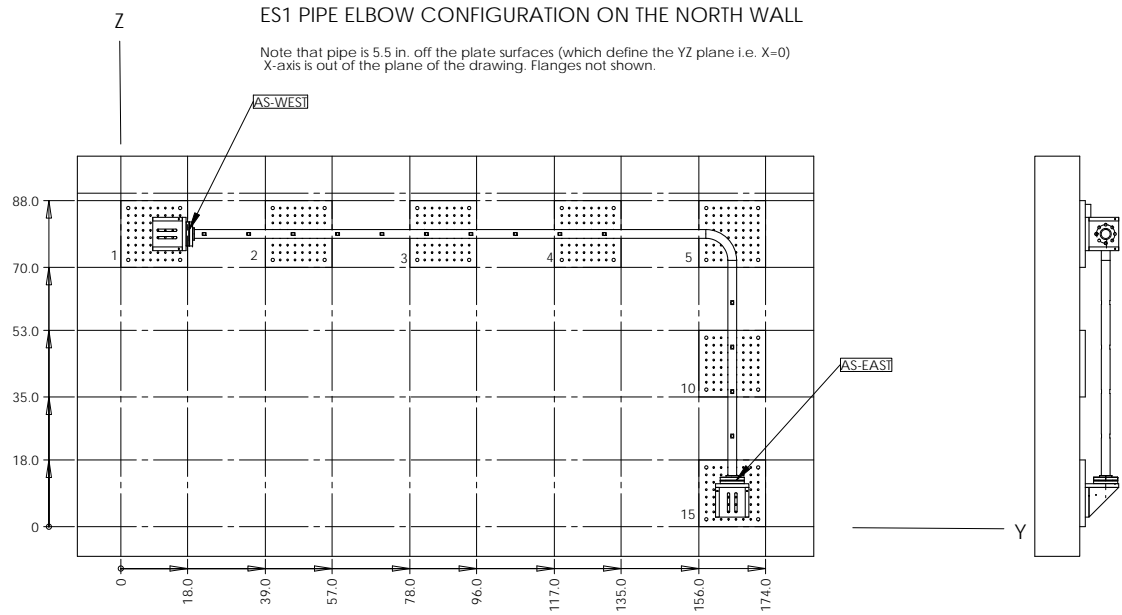


Figure 115: Orientation of ES1 as mounted on North wall.

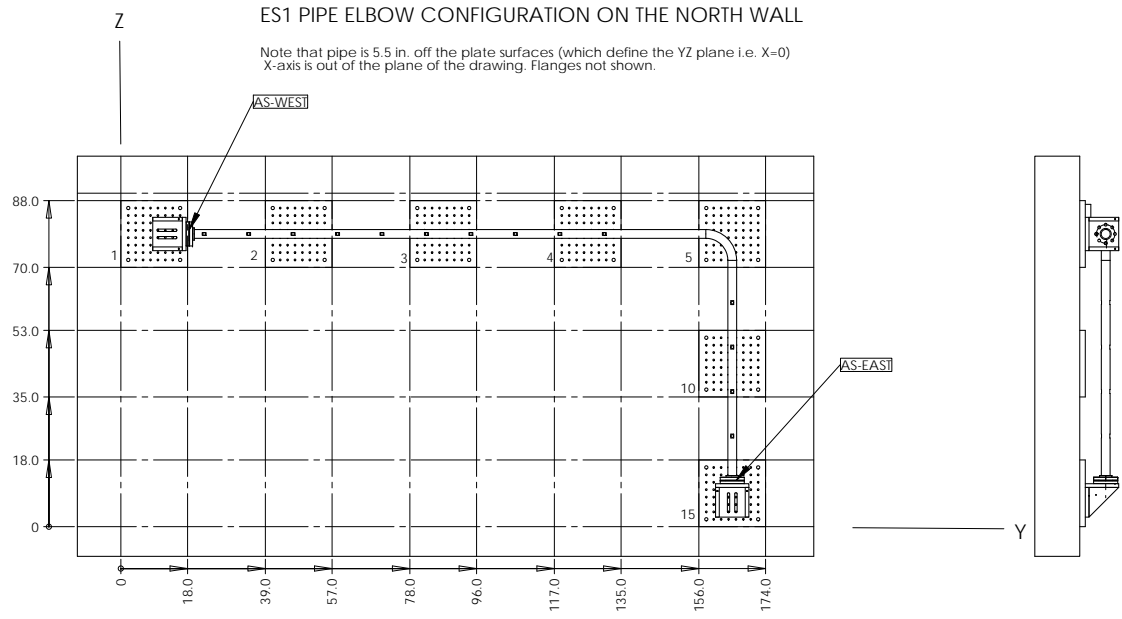


Figure 116: Orientation of ES1 as mounted on North wall.

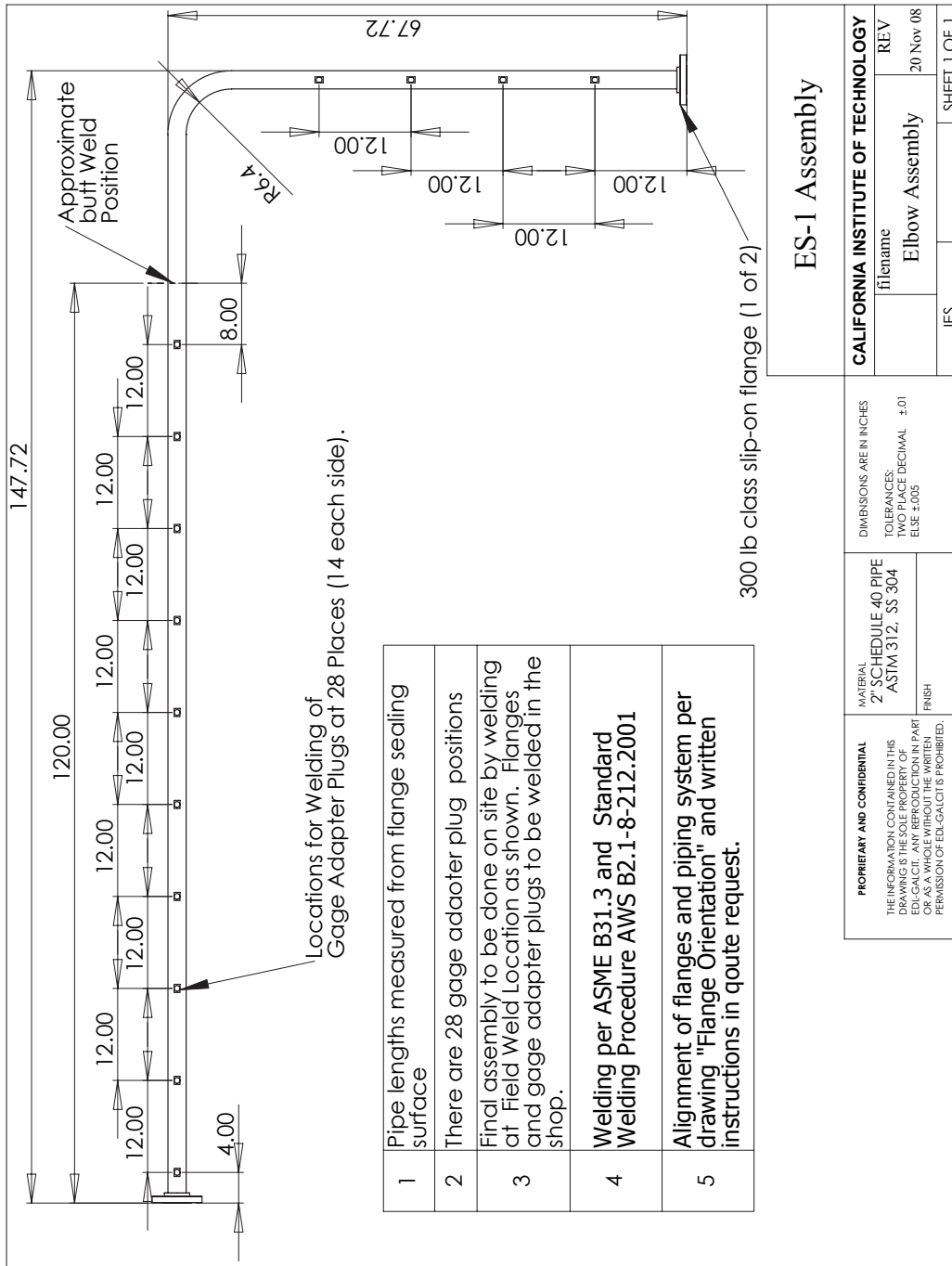


Figure 117: As built dimensions of ES1. Note bend radius is measured to pipe wall in this drawing.

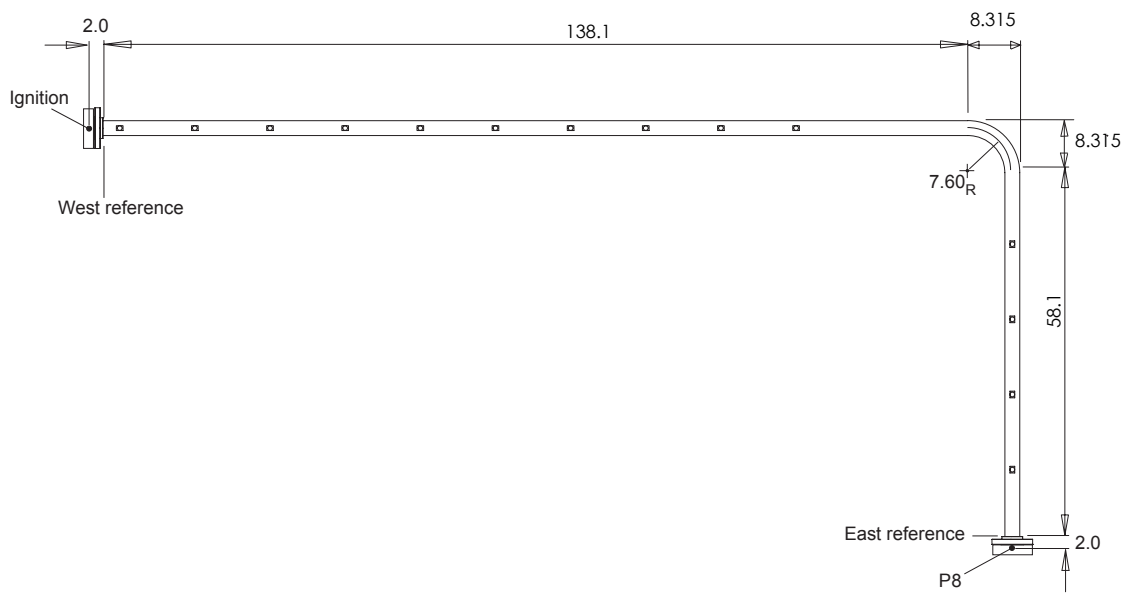


Figure 118: Overall dimensions of ES1. Note bend radius is measured to centerline in this drawing.

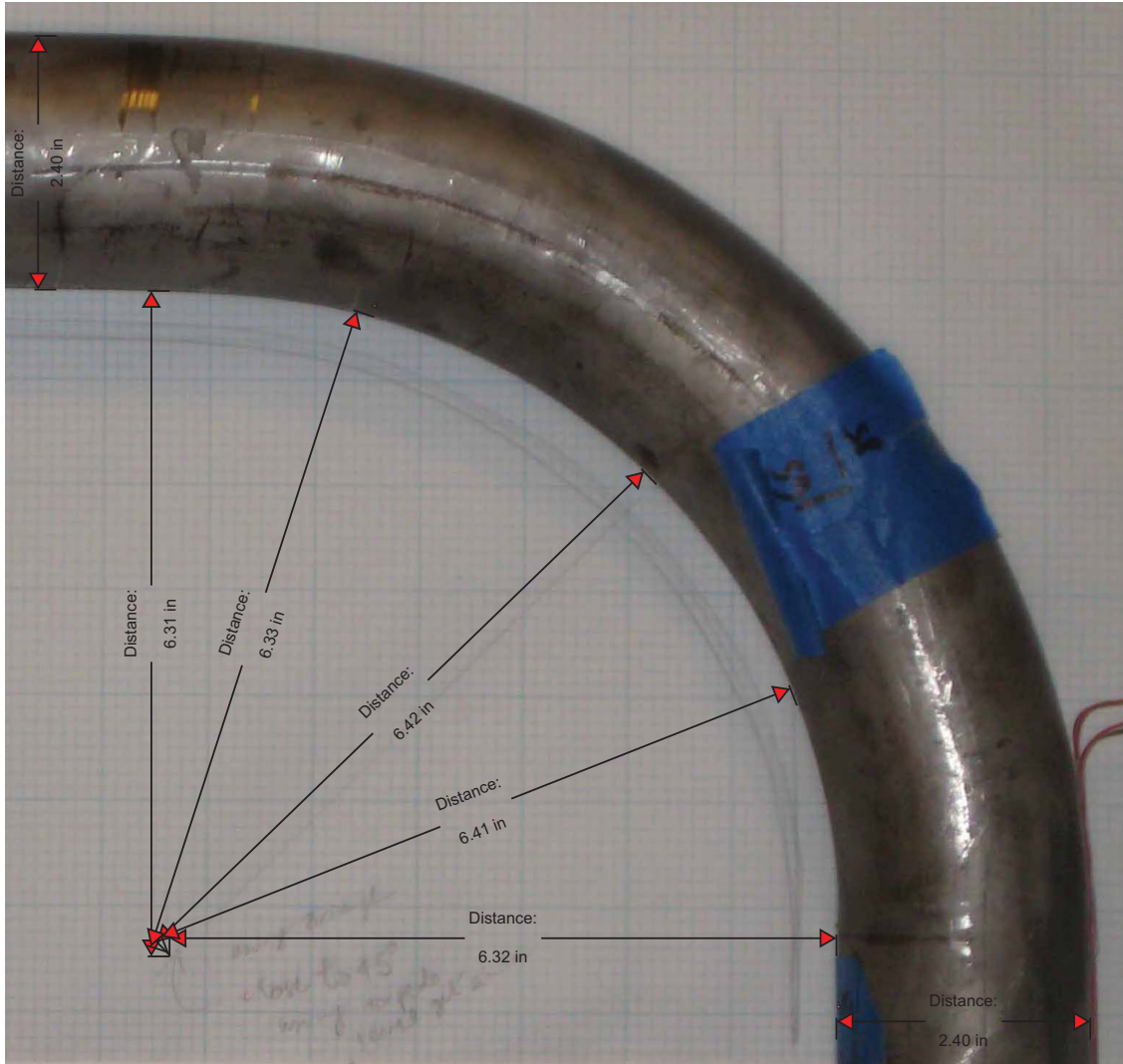


Figure 119: ES1 bend photograph annotated with measured dimensions used to create as-built specifications.

## F ES1 thickness measurements

The thickness of ES1 was measured using a Checkline TI-007 ultrasonic wall-thickness gauge calibrated with Olympus 2211E 304 stainless steel test block. The variation of thickness with axial distance is shown in Fig. 120. The thickness was measured at 90 degree increments with the 0 deg location on the top of the pipe on the horizontal section and on the east facing portion on the vertical section. The indexing was such that the 90 deg location is on the side away from the mounting wall and 270 deg is on the side facing the wall. ES1 was made up of two sections with a butt weld located at about 120 in from the west end. The section of pipe from 0 to 120 in was straight and used as delivered. The hydraulically formed bend was located between 140 and 150 in, the increase in thickness on the intrados (180 deg) and decrease on the extrados (0 deg) can be clearly observed. The average thickness of the piping was 0.149 in, about 3% smaller than the nominal value of 0.154 in quoted in the specifications. The outside diameter of the pipe was measured with a micrometer and away the region of the bend, the average value appeared to be within  $\pm 0.005$  of 2.375 in, the nominal value.

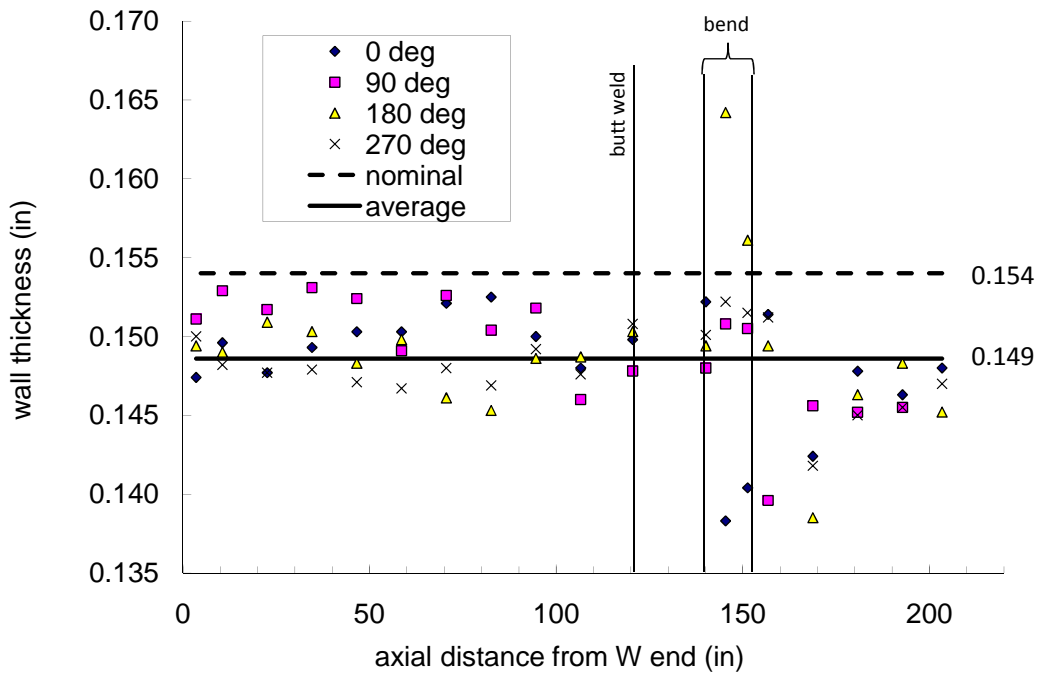


Figure 120: Thickness measurements on ES1 specimen.

## G Cantilever Beam Supports

The cantilever beams used as supports and for force measurement were constructed from mild steel, type A36. The beams were 1.25 in by 1 in in cross-section, 7 in long and attached to base 1 in thick and 4 × 4 in wide. Except for U2, the method of construction was to machine the beam and base together from a single block of material except for beam U2, which was constructed by welding the beam to the base. The dimensions are given in the drawings in the next section. The techniques for instrumenting the beam with strain gages and calibrating the strain-force response are described in Section G.2.

### G.1 Engineering Drawings

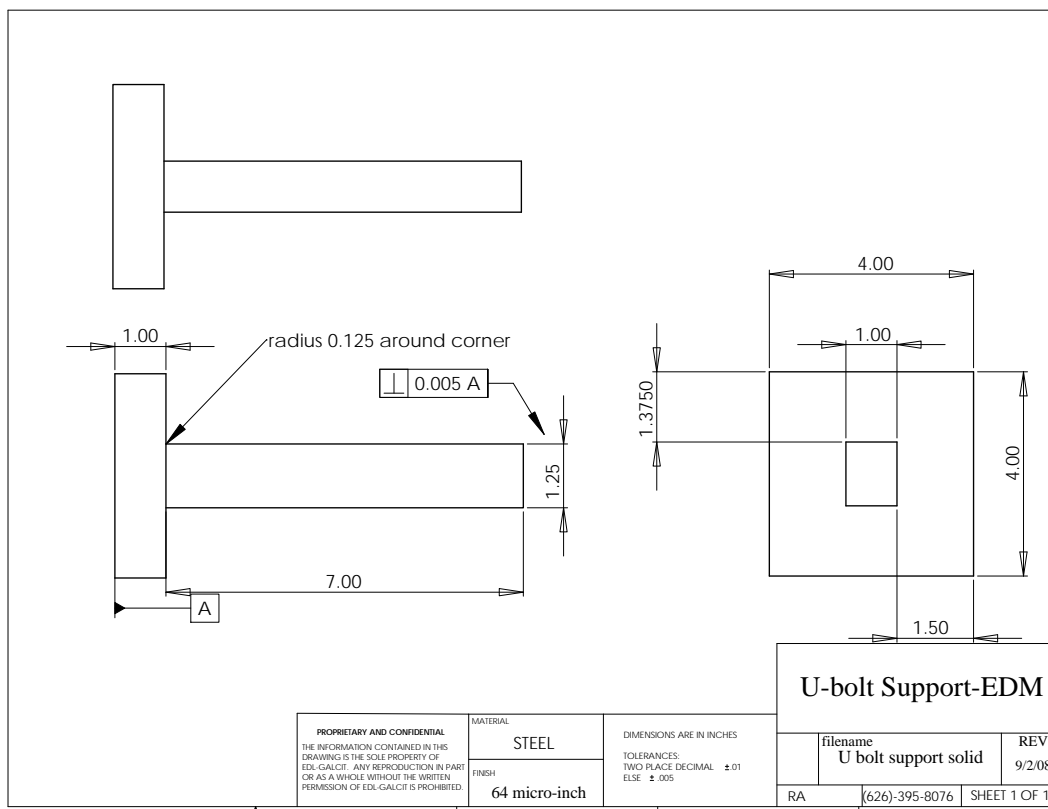


Figure 121: Engineering drawing of cantilever beam - basic outline.

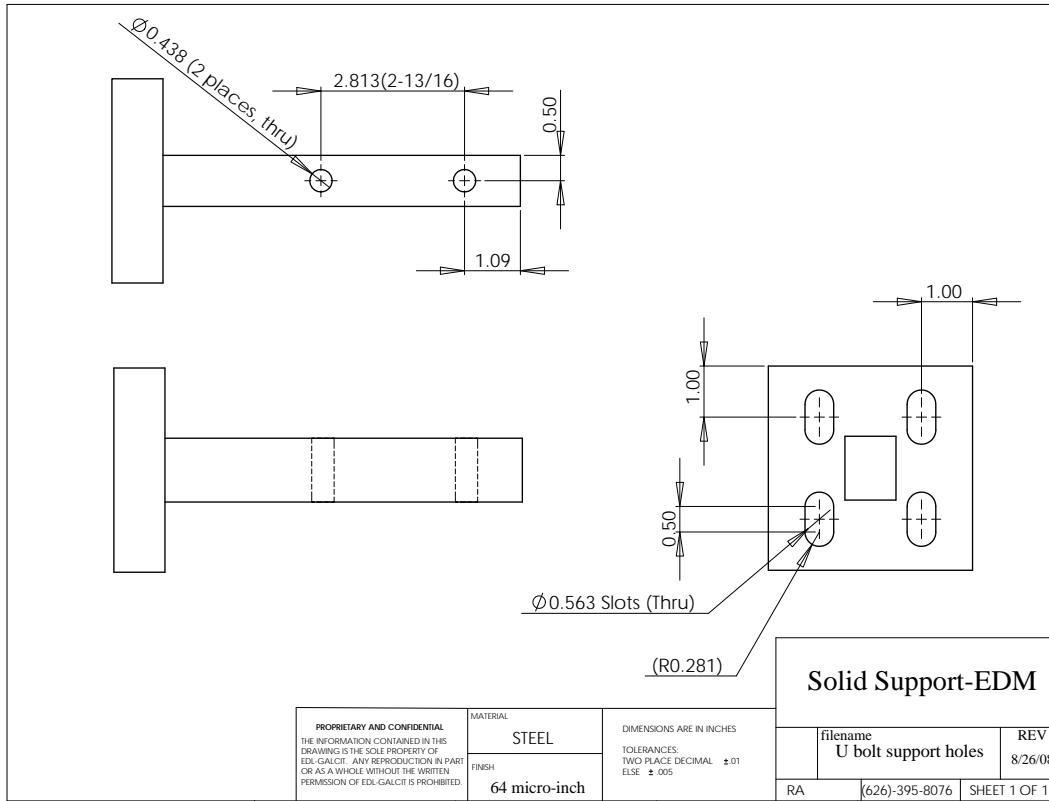


Figure 122: Engineering drawing of cantilever beam - hole locations.

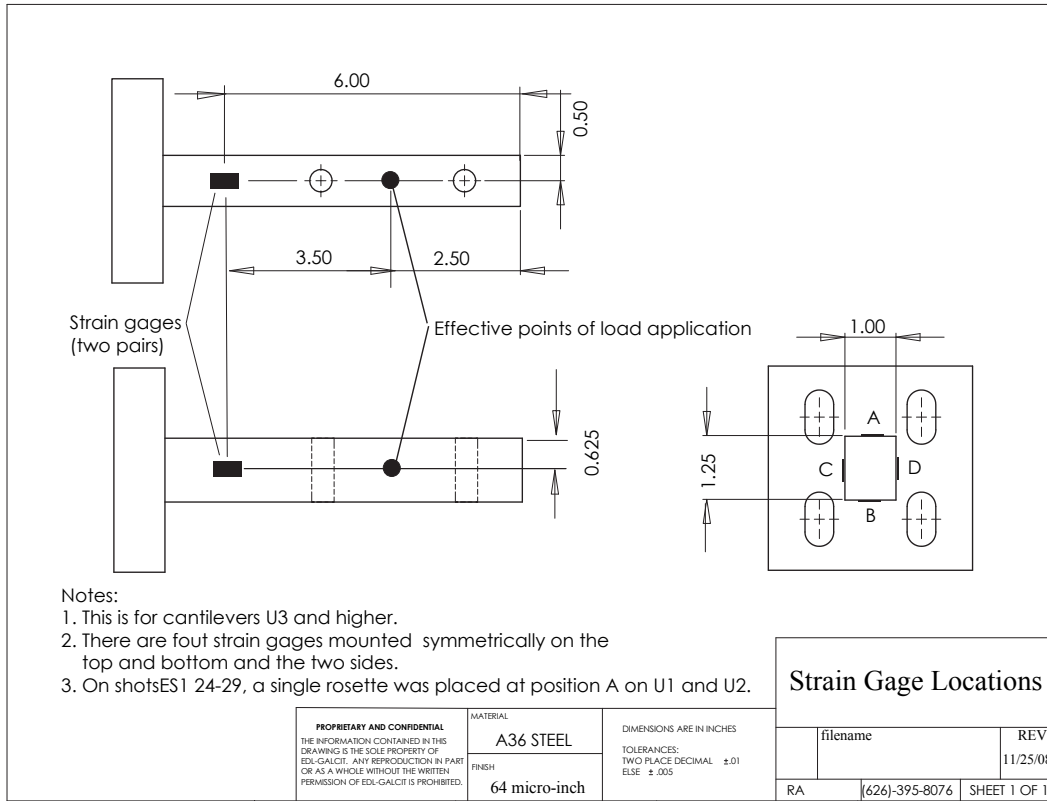


Figure 123: Strain gage locations on cantilever beams.

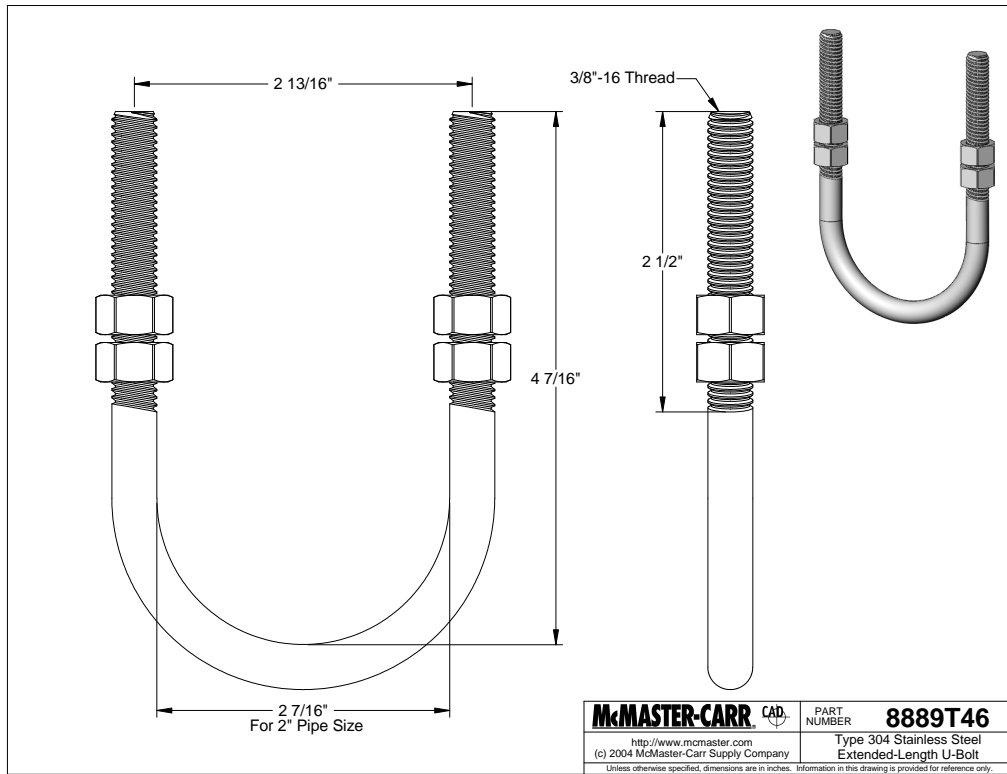


Figure 124: Dimensions of U-bolts used to fasten pipe to cantilever beams.

## G.2 Instrumentation and Calibration

Three types of configurations were used to measure strain on the beams. In all cases, strain gages were bonded to the beam about 1 in from the base. The gages respond to a combination of bending, axial, and thermal stresses as described by Bray et al. (1990), Perry (2008). As discussed in Section 3.5 and Table 3, gages were either used singly or in combinations. The three typical configurations are discussed below.

### G.2.1 Single Gage in a Quarter-Bridge Circuit

A single located on the beam surface and oriented to measure the bending strain is the simplest configuration. This is known as a “quarter-bridge” configuration and is shown in Fig. 125.

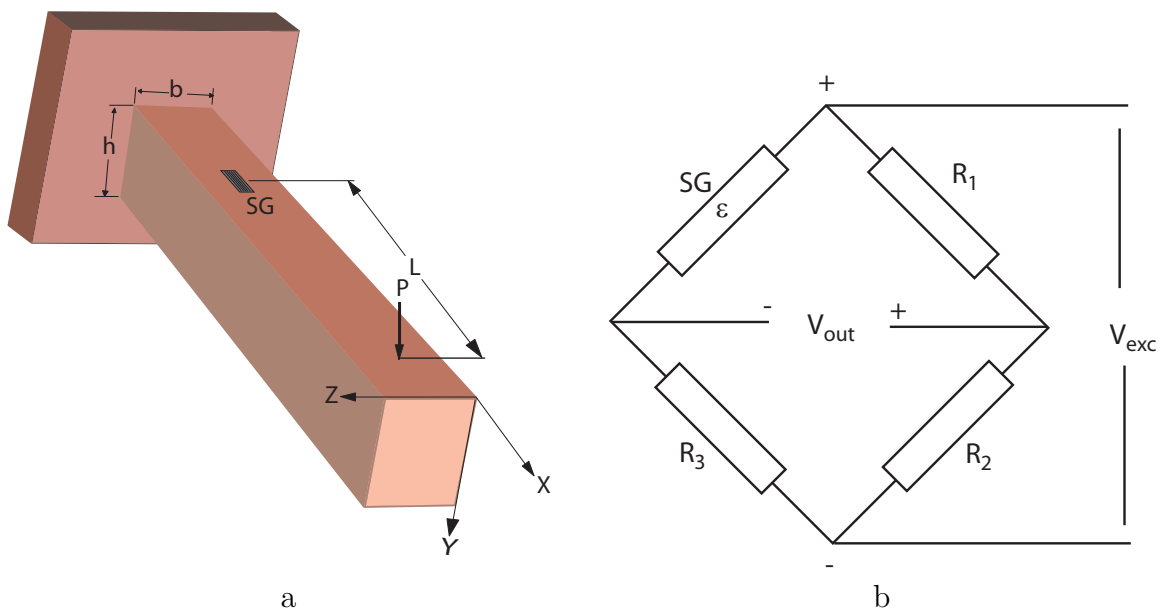


Figure 125: Quarter bridge configuration: a) Strain gage located on beam; b) bridge circuit.

The strain gage increases resistance under tension  $R_{SG} = R_{SG}^o(1 + K\epsilon_x)$ , where  $K$  is the *gage factor* which is approximately 2.1 for the gages used in this study. If the bridge starts out balanced  $R_{SG}^o = R_1 = R_2 = R_3$ , then application of elementary circuit theory yield the result

$$V_{out} = V_{exc} \frac{K\epsilon}{4 + 2K\epsilon} \approx V_{exc} \frac{K\epsilon}{4} . \quad (81)$$

The approximation of neglecting the variation of the denominator with strain (usually referred to as linearization) is valid as long as the strain  $\epsilon$  is not too large. This is reasonable because the strains in the present experiments are all less than  $2 \times 10^{-3} = 0.2\%$  or 2000  $\mu$ strain, which the nominal proportional limit where permanent deformation is considered to set in. Peak cantilever strains in the present tests do not exceed 200  $\mu$ strain.

The bending response of the beam to the applied load force  $P$  in the  $Y$  direction can be

calculated using Bernoulli-Euler beam theory [Urgural and Fenster \(1987\)](#),

$$\epsilon_x = \frac{6PL}{Ebh^2}, \quad (82)$$

where  $E$  is the modulus of elasticity (Young's modulus) which is about  $2.10 \times 10^{11}$  Pa for A36 steel. Note that only the distance  $L$  from the point of application of the load  $P$  to the strain gage SG location is important in this model. Combining (82) and (81), we obtain the relationship between load and strain

$$P = \frac{Ebh^2}{6L} \frac{4V_{out}}{KV_{exc}}. \quad (83)$$

If a load  $Q$  is applied in the  $+Y$  direction, this will also produce a strain. Considering the beam as a bar, the elementary strength of materials approach [Urgural and Fenster \(1987\)](#) yields

$$\epsilon_x = \frac{Q}{Ebh}. \quad (84)$$

This is one of the drawbacks of using a single gage to measure bending. Other drawbacks include the lack of temperature compensation (less important in dynamic applications like the present experiment) and the nonlinearity of a quarter bridge circuit response. The half-bridge circuit solves both of these problems, [Perry \(2008\)](#).

## G.2.2 Two Gages in a Half-Bridge Circuit

The two gage configuration simply adds a gage at a location directly opposite the first gage, [Fig. 126](#). The gages are both oriented to record the strain in the  $X$  direction. The key advantage is that the bending response is of equal and opposite signs for the upper and lower gage because when the top surface of the beam is in compression, the bottom surface is in tension and vice versa. However, both gages will register the same response for either temperature changes or strains resulting from axial (bar) loads in the  $X$  direction.

By connecting the two gages in adjacent arms of the Wheatstone bridge, the temperature and axial components of strain will cancel and only the bending response will be recorded.

$$\epsilon_1 = \epsilon_{bend} + \epsilon_{thermal} + \epsilon_{axial} \quad \epsilon_2 = -\epsilon_{bend} + \epsilon_{thermal} + \epsilon_{axial} \quad \epsilon_1 - \epsilon_2 = 2\epsilon_{bend} \quad (85)$$

The bridge output will also be precisely linear with strain and the double the approximate value for a single gage with the same strain, [Perry \(2008\)](#).

$$V_{out} = V_{exc} \frac{K\epsilon_{bend}}{2} \quad (86)$$

This is the configuration that was used for the cantilever is ES1 tests 28-35, and all TS1 tests. Two pairs of gages A-B and C-D were used on opposite faces as shown in [Fig. 123](#).

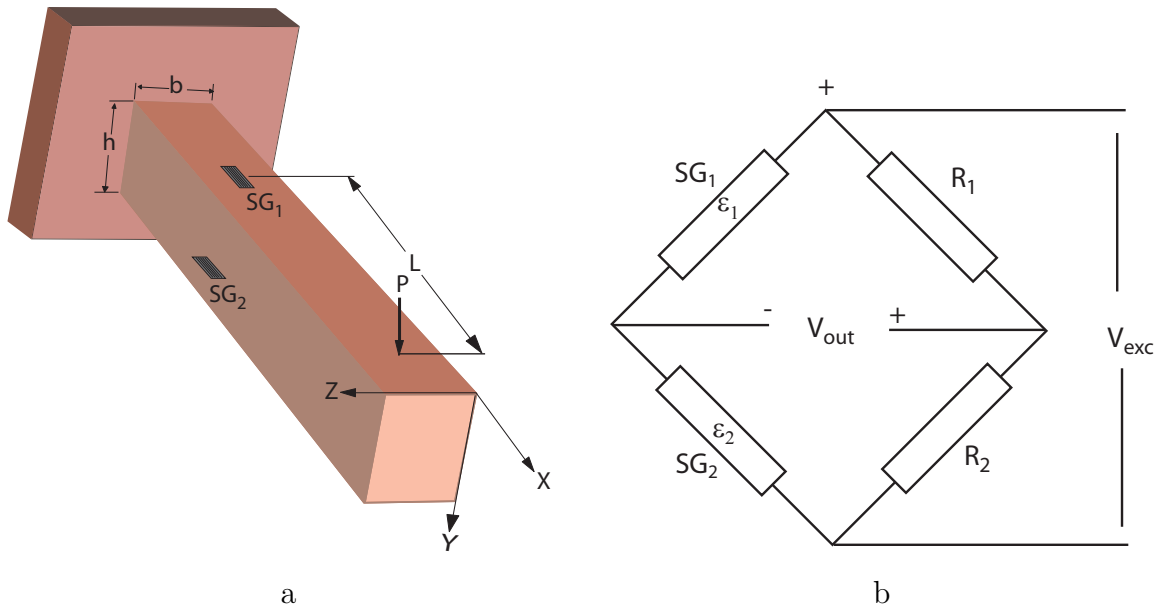


Figure 126: Half bridge configuration: a) Strain gages located on top and bottom of beam; b) bridge circuit.

### G.2.3 Two Gages Connected Independently

In order to measure the two components of the force (bending and axial) on the beam, each gage in a pair can be connected in a quarter-bridge configuration and either added (to obtain twice the axial+thermal component of strain) or else subtracted to obtain twice the bending component. The gages are zero immediately prior to testing and for such a short test, thermal effects are expected to be minimal so that this method enables us to separate the axial and bending components. This was done for two supports, using the A and B gages only, in the SS1 series of tests.

### G.2.4 Three-gage Rosettes

The advantage of the three-gage rosettes used on U1 and U2 and shown in Fig. 14, is that if all three gages are recorded, the principal strains and gage orientation can be recovered by processing the signals. From Bernoulli-Euler Beam theory, the principal strains in bending are in the  $X$  and  $Z$  direction with  $\epsilon_z = -\nu \epsilon_x$  where  $\nu$  is the Poisson ratio, about 0.29 for mild steel. The formulas for recovering the principal strains and gage orientation are based on the standard Mohr's circle construction (Urgural and Fenster, 1987) for strain transformation, as discussed by Vishay TN515 (2010). The principal strains  $\epsilon_p$  and  $\epsilon_q$  are

$$\epsilon_{p,q} = \frac{\epsilon_1 + \epsilon_3}{2} \pm \frac{1}{\sqrt{2}} \sqrt{(\epsilon_1 - \epsilon_2)^2 + (\epsilon_2 - \epsilon_3)^2} \quad (87)$$

and the angle  $\theta$  from the principal axis ( $\epsilon_p$ ) to the direction of gage 1 of the rosette is

$$\theta = \frac{1}{2} \tan^{-1} \left( \frac{\epsilon_1 - 2\epsilon_2 + \epsilon_3}{\epsilon_1 - \epsilon_3} \right) \quad (88)$$

Applying this procedure to the data from U1 and U2 shows that the maximum error due to gage not being precisely aligned with the beam axis is less than 1%. The average value of the ratio  $-\epsilon_q/\epsilon_p$  can be used to estimate  $\nu$  and a value of  $0.29 \pm 0.005$  is obtained.

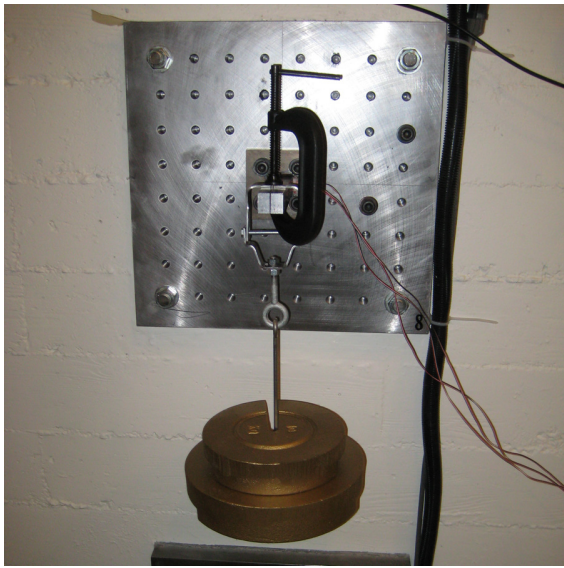
### G.2.5 Static Calibration

To calibrate the cantilevers, precision weights were used to load the beams with masses from 0 to 70 kg and the strains were recorded. The cantilevers were bolted to the wall plates and the masses were hung vertically (Fig. 127) from either the U-bolt or else a flattened pipe hanger clamped to the point of pipe contact. These simulate the pipe either pushing up on the U-bolt or down on the lever. The data was filtered to remove all the high frequency noise, 5000 samples were recorded over 25 s for each mass, and averaged to obtain the strain. The average strains were analyzed by fitting the measured strain against the applied force using linear regression to obtain the slope (N/ $\mu$ strain) of the fitted line. The gages were also calibrated using an impact hammer and the results are discussed in Appendix C of [Shepherd and Akbar \(2009\)](#).

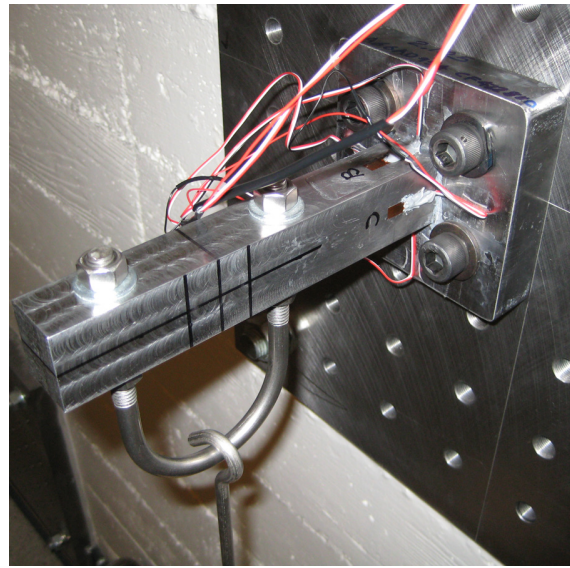
The results for the beams with rosettes are shown in Fig. 128. We can compare the calibration results with the ideal beam theory (82). For the nominal gage position, a sensitivity of 10.08 N/ $\mu$ strain is computed from (82) as compared to an average value of 10.20 for U1 and 9.86 for U2. The differences between the two beams are consistent with the observation variations in the axial location and orientation of the rosettes. The calibration data for the other beams are given in Figs. 129-130 and summarized in Table 26.

Table 26: Calibration constants for support beams

Beam	Direction	Calibration factor (N/ $\mu$ strain)
U1	AB	10.2
U2	AB	9.86
U3	AB	10.05
U3	CD	8.078
U4	AB	10.07
U4	CD	8.078



a



b

Figure 127: Calibration of support beams a) Fixture for creating bending simulation pipe pushing down on the lever b) fixture for simulating pipe pushing up on U-bolt.

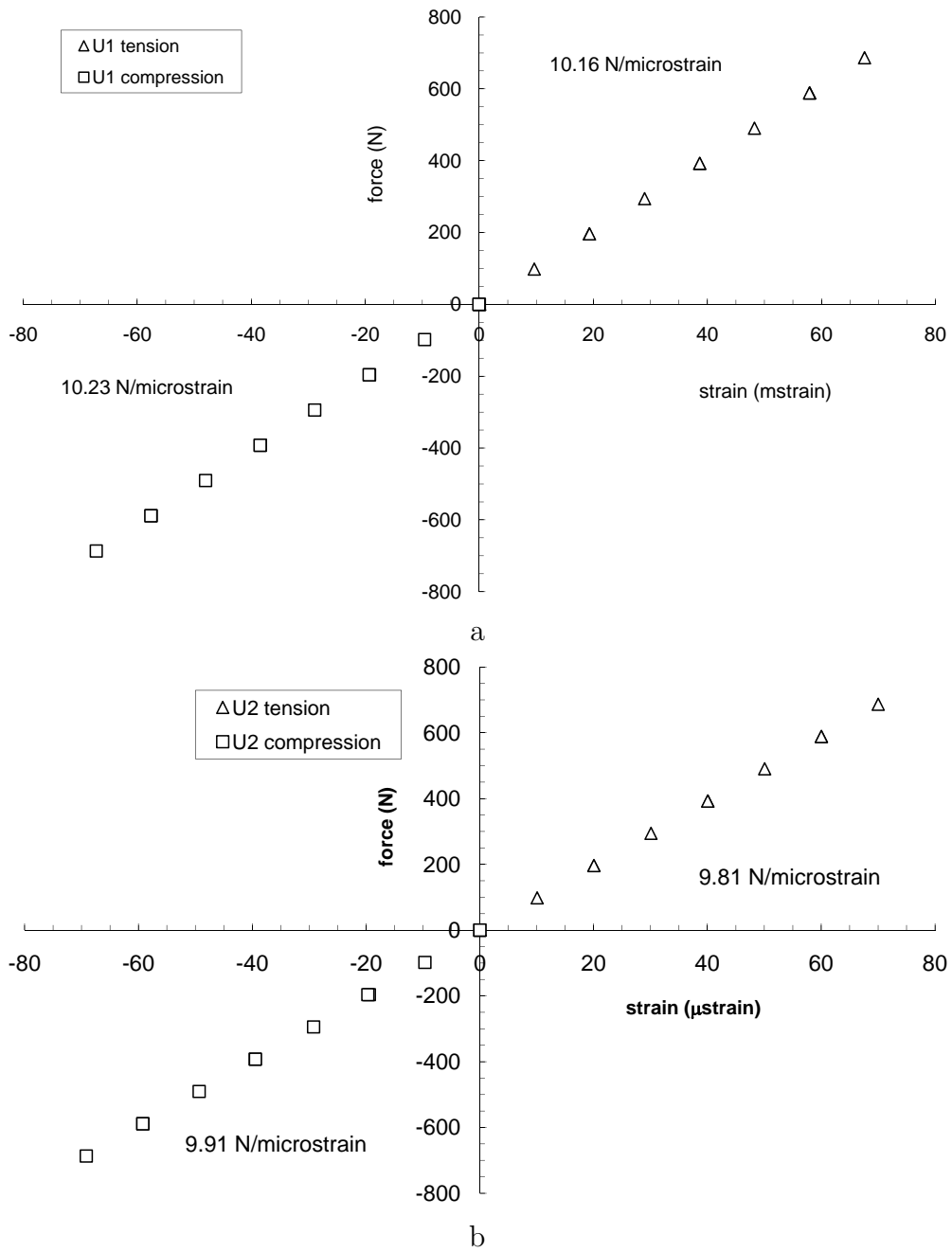
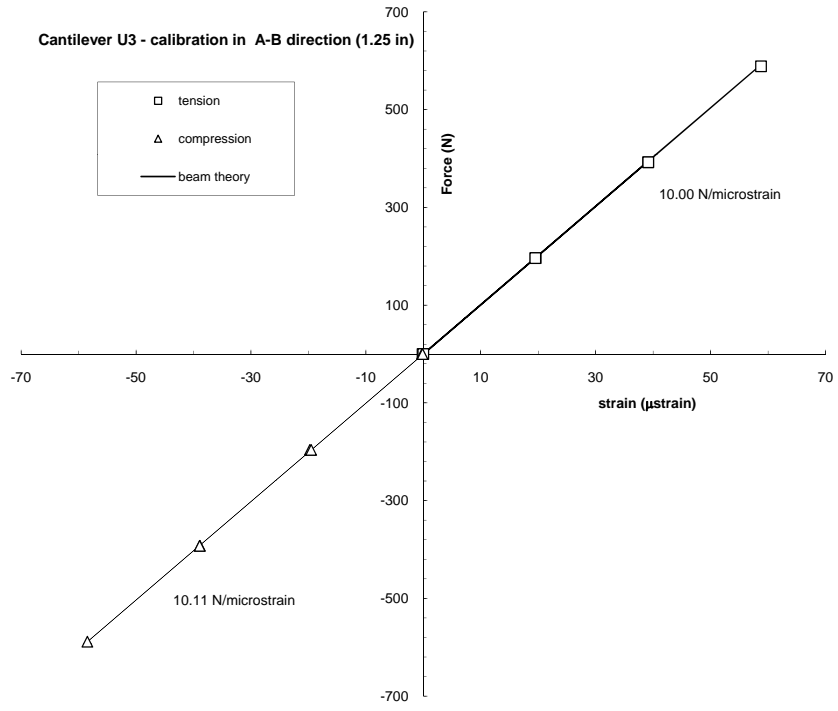
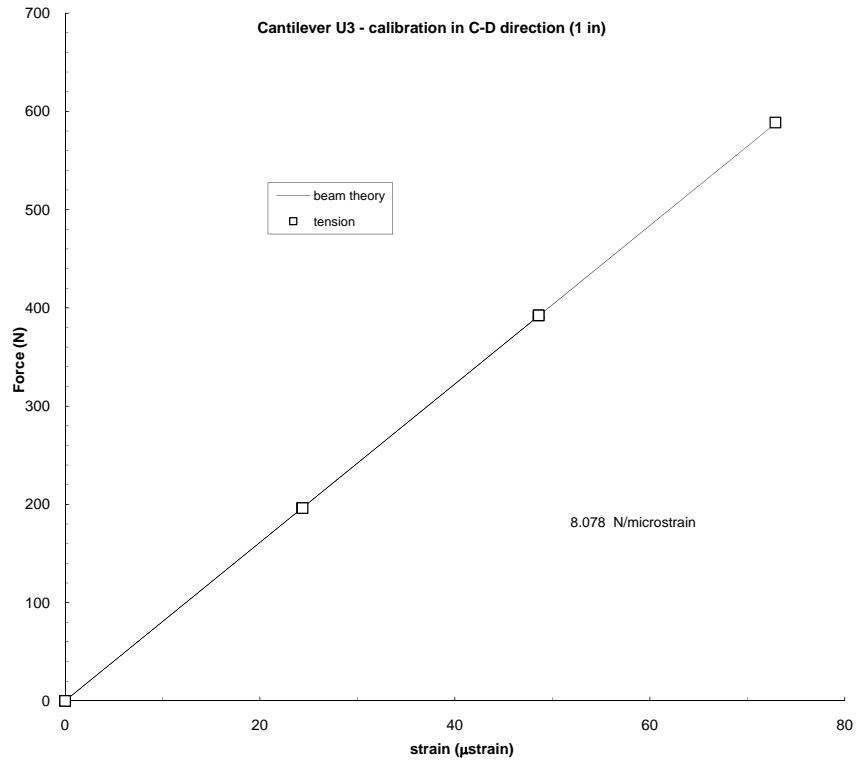


Figure 128: Calibration results using central gage (number 2) of rosette. a) U1 b) U2.



a



b

Figure 129: Calibration results for half-bridge configuration on U3. a) AB pair b) CD pair.

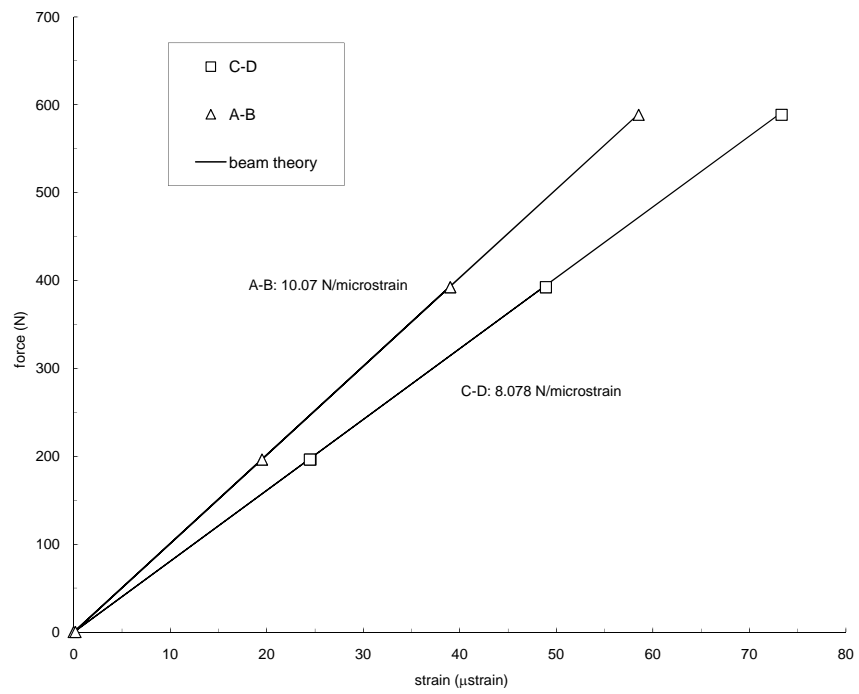


Figure 130: Calibration results for half-bridge configuration on U4.

# H Anchor Brackets

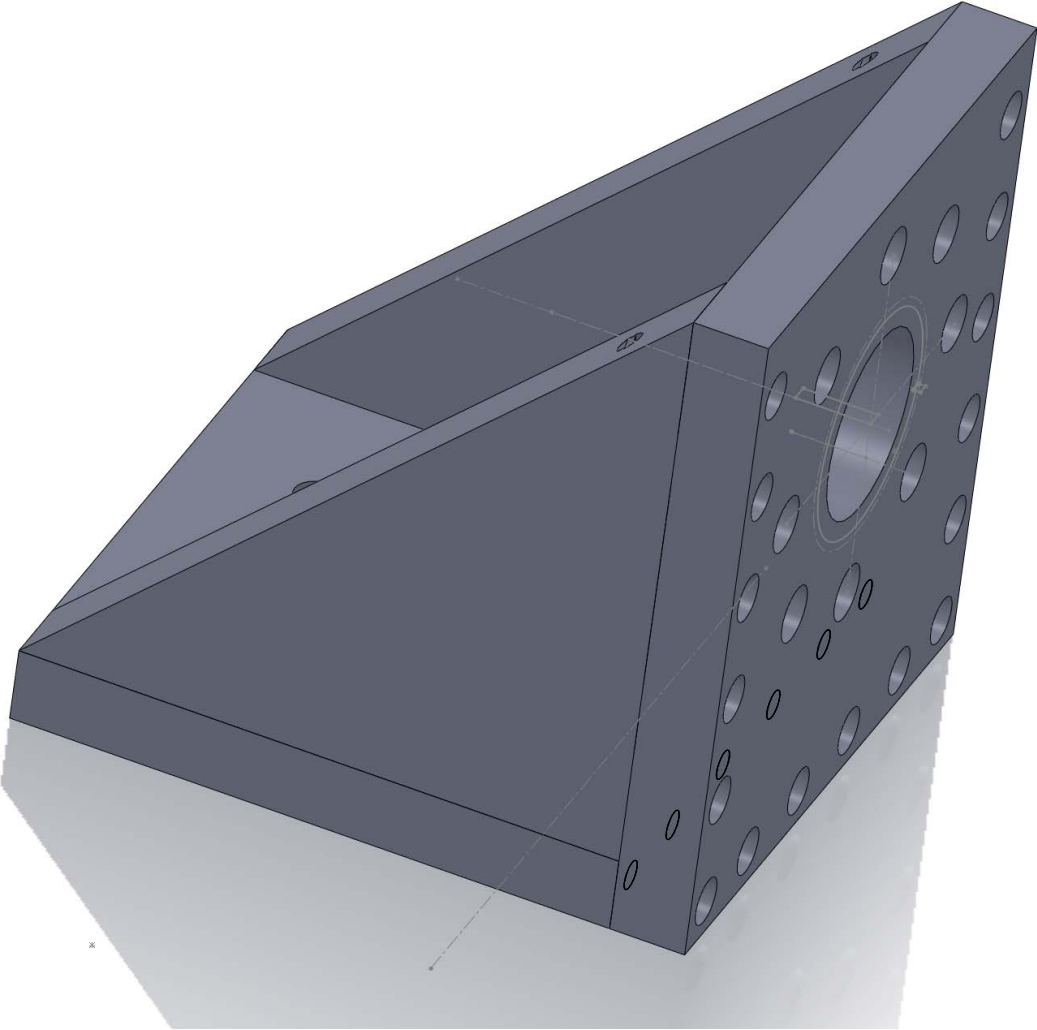


Figure 131: Perspective view of solid model for fixed end anchors.

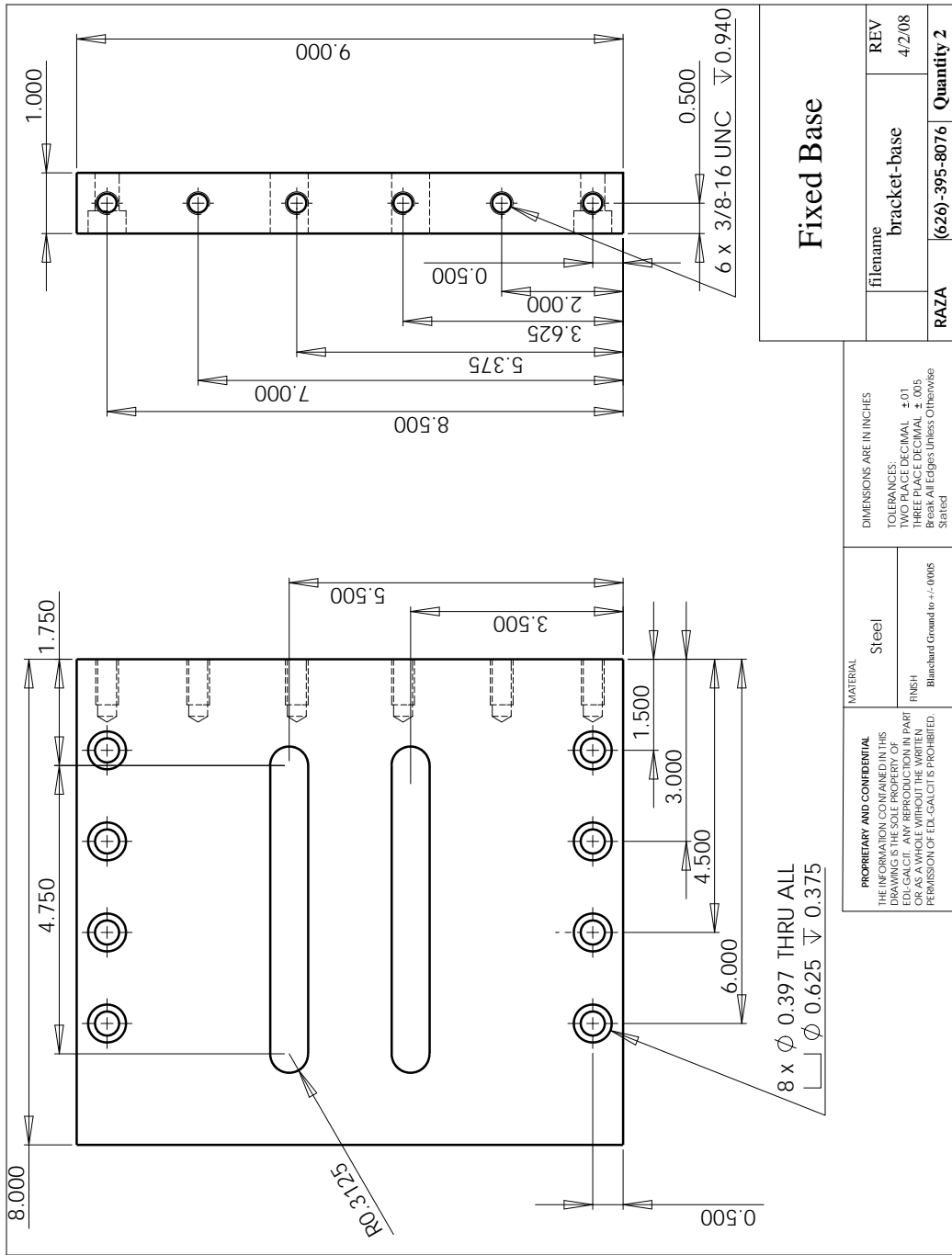


Figure 132: Engineering drawing of anchor base.

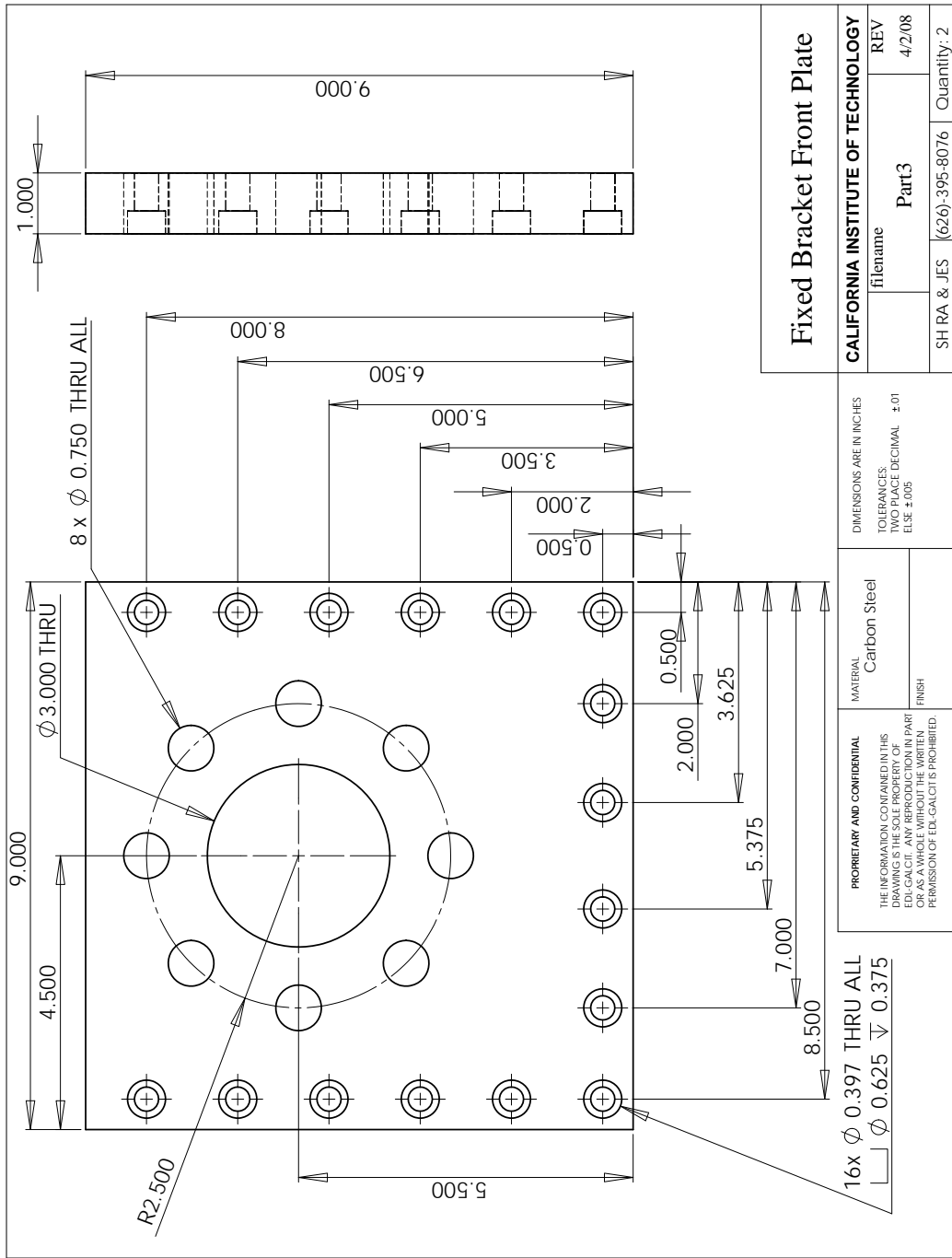


Figure 133: Engineering drawing of anchor front.

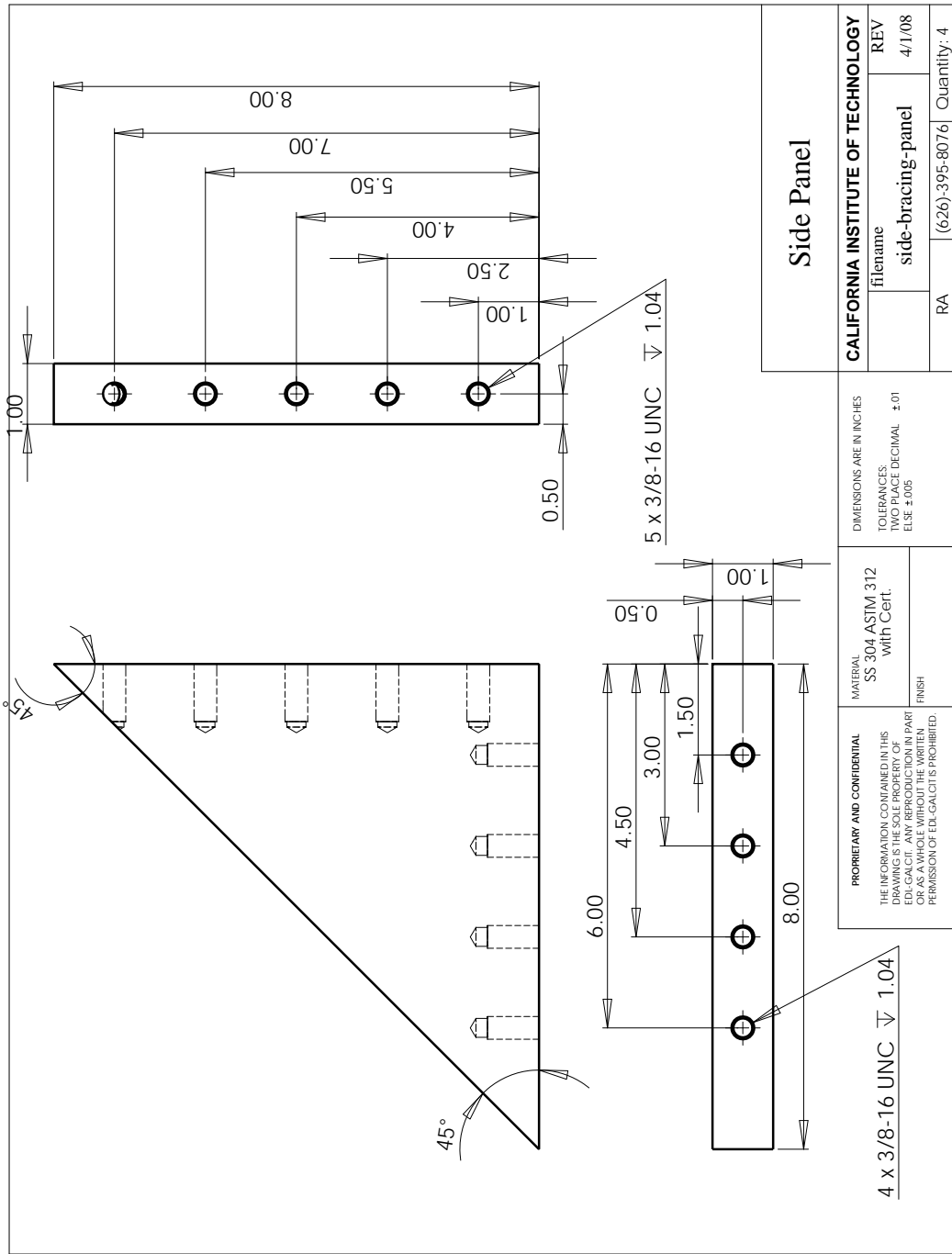


Figure 134: Engineering drawing of anchor side.

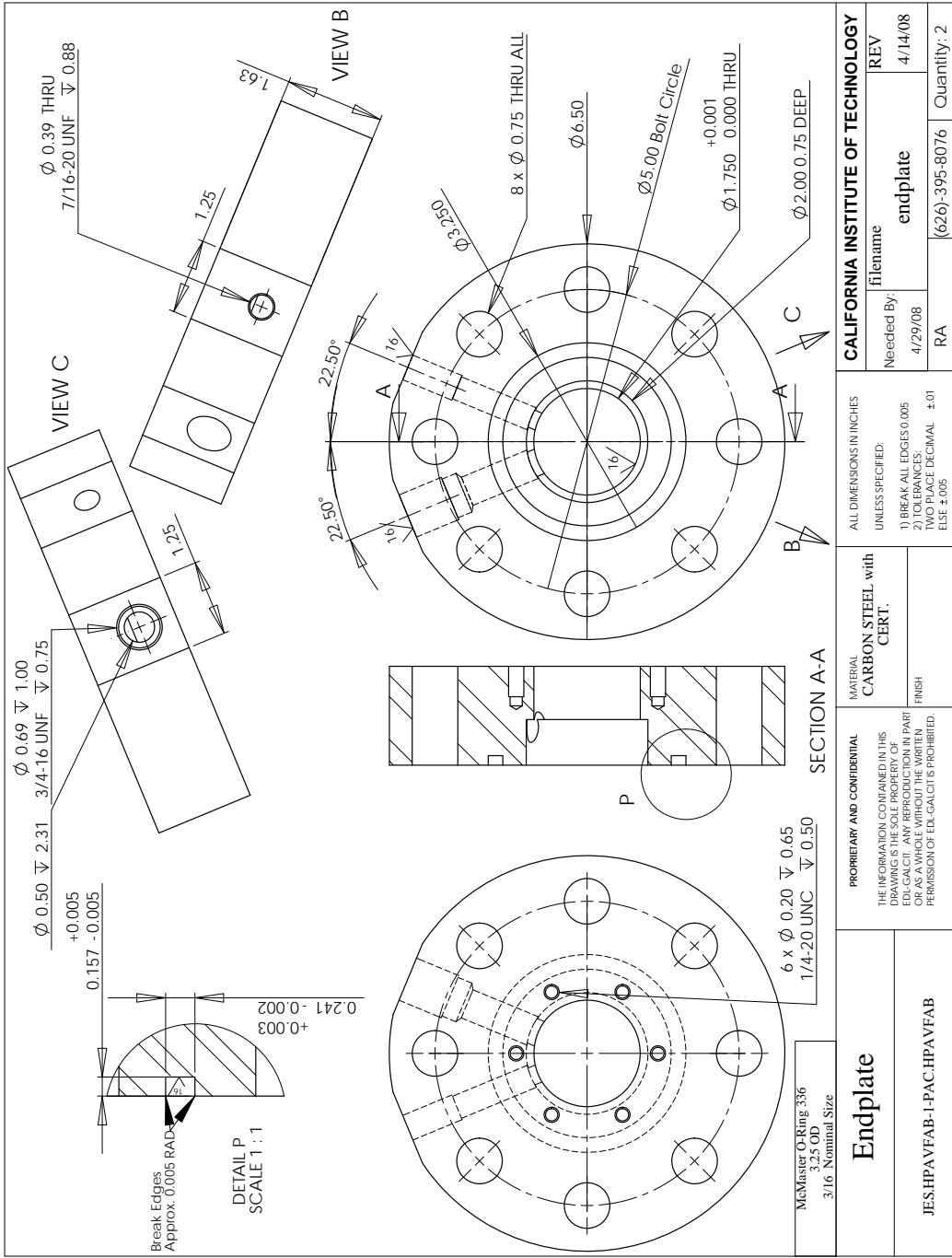


Figure 135: Engineering drawing of gas handling flange.

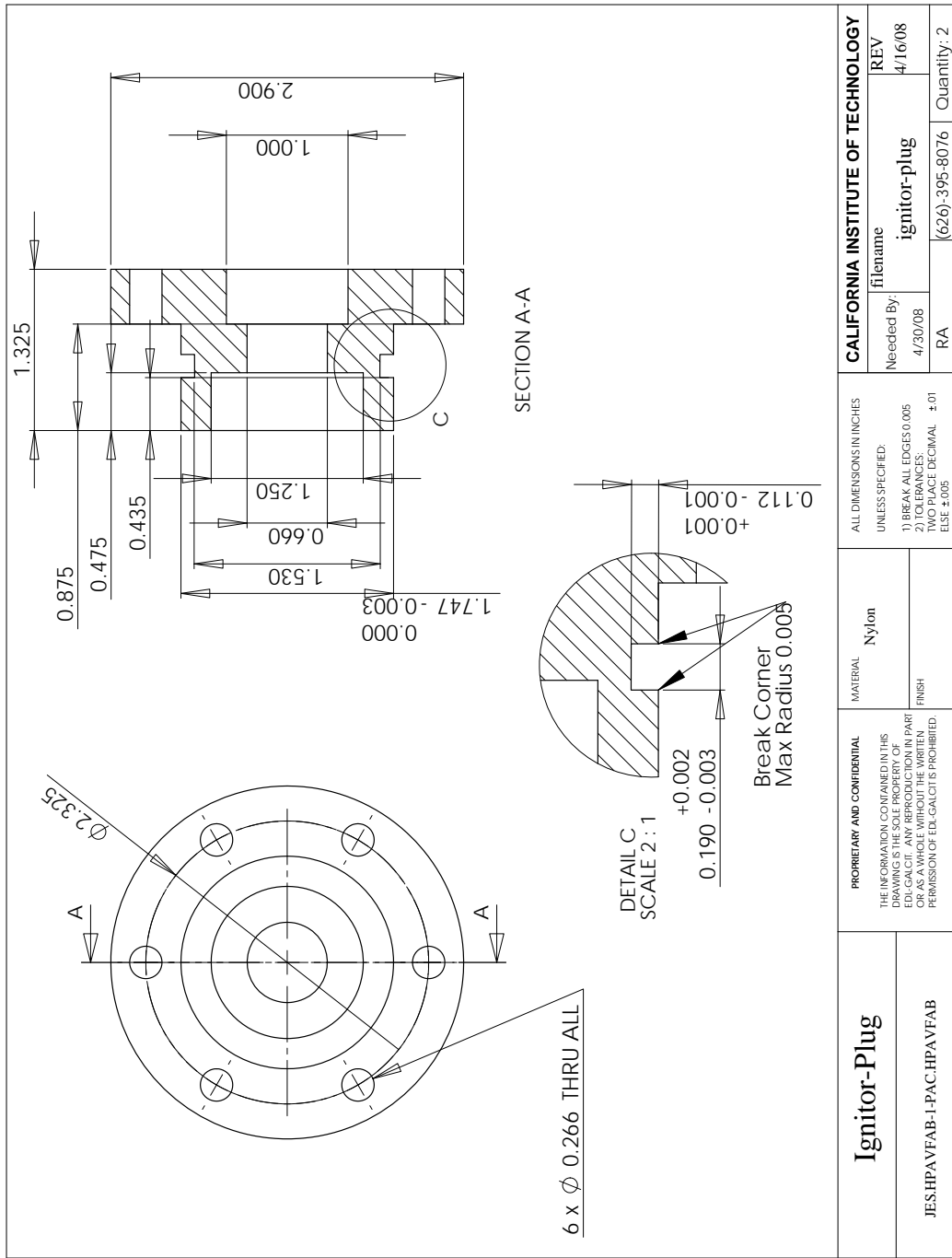


Figure 136: Engineering drawing of nylon spark plug insert.

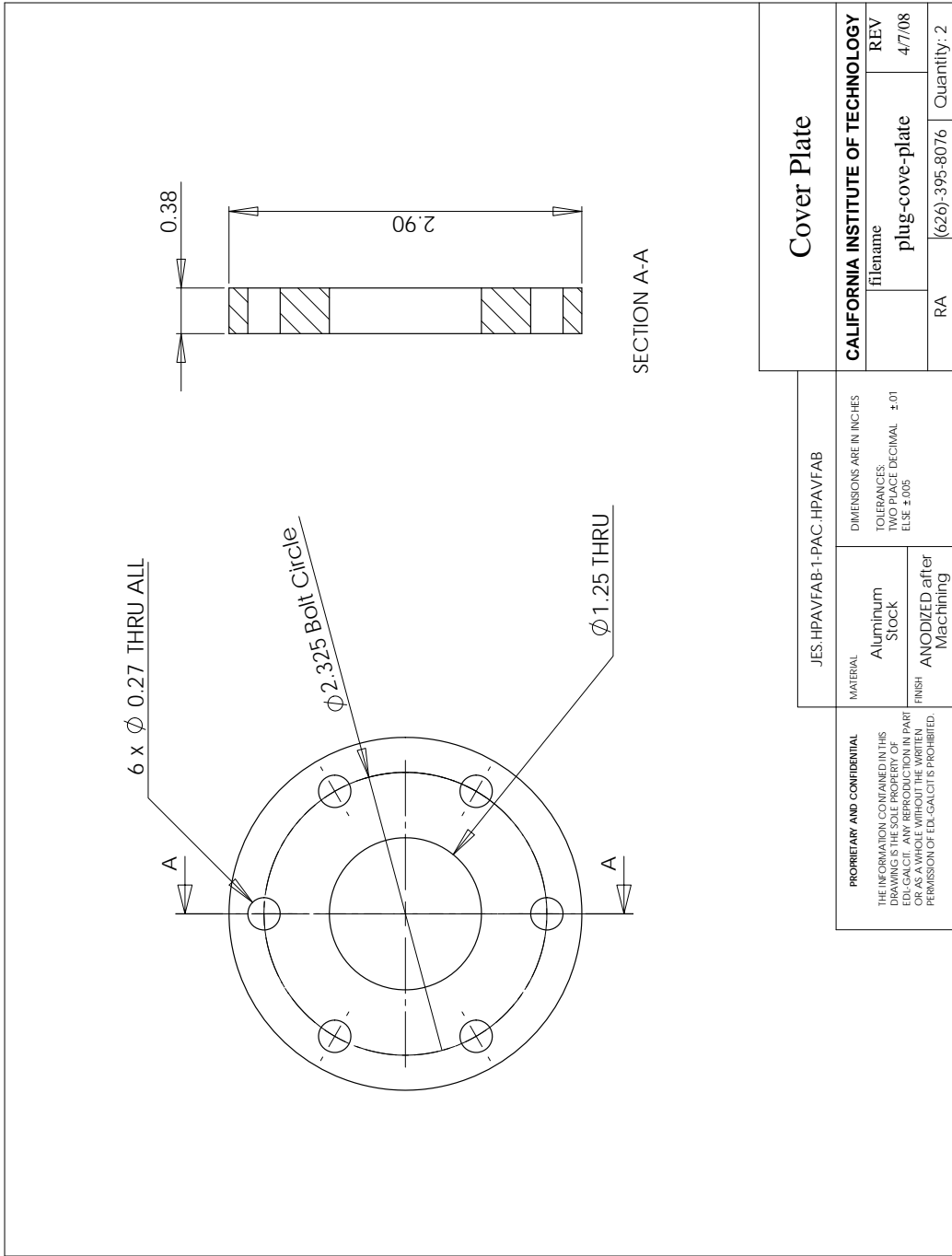


Figure 137: Engineering drawing of backing ring for nylon spark plug insert.

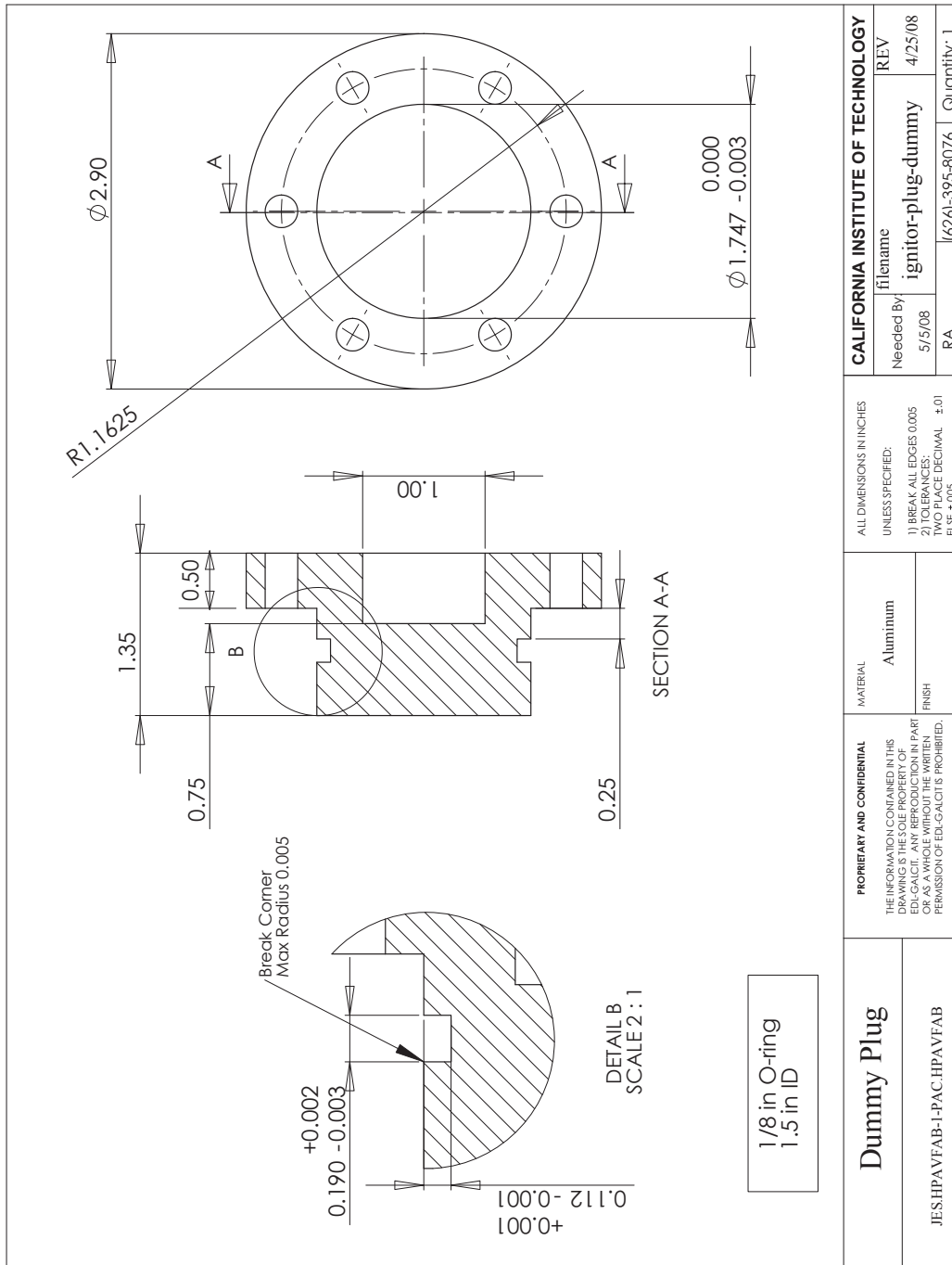


Figure 138: Engineering drawing of plug used to fill spark plug insert opening. A pressure transducer (PCB) was mounted in these plugs.

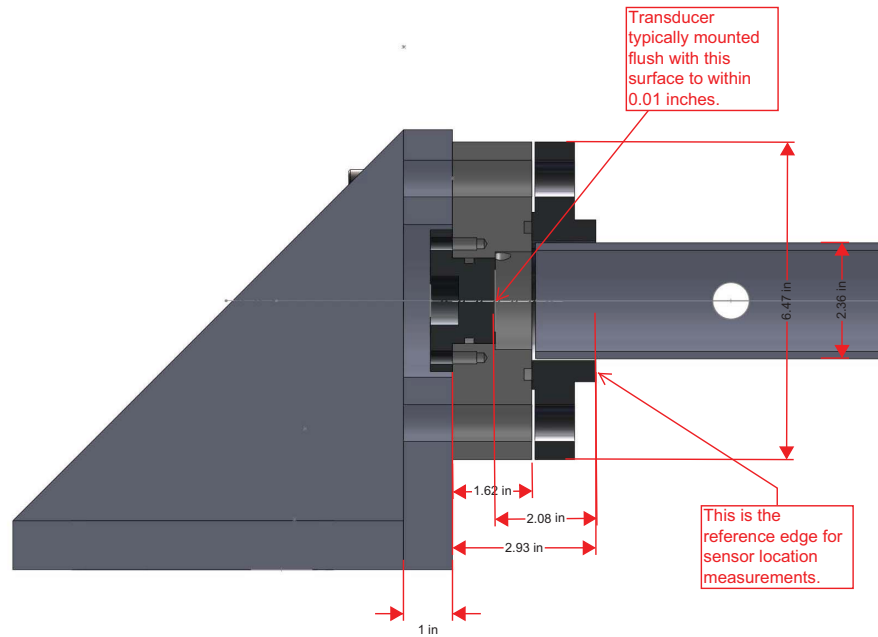


Figure 139: Dimensions of cut-away of assembled pipe, gas handling flange, end bracket, and insert plug.

# I ES1 Sensor Locations

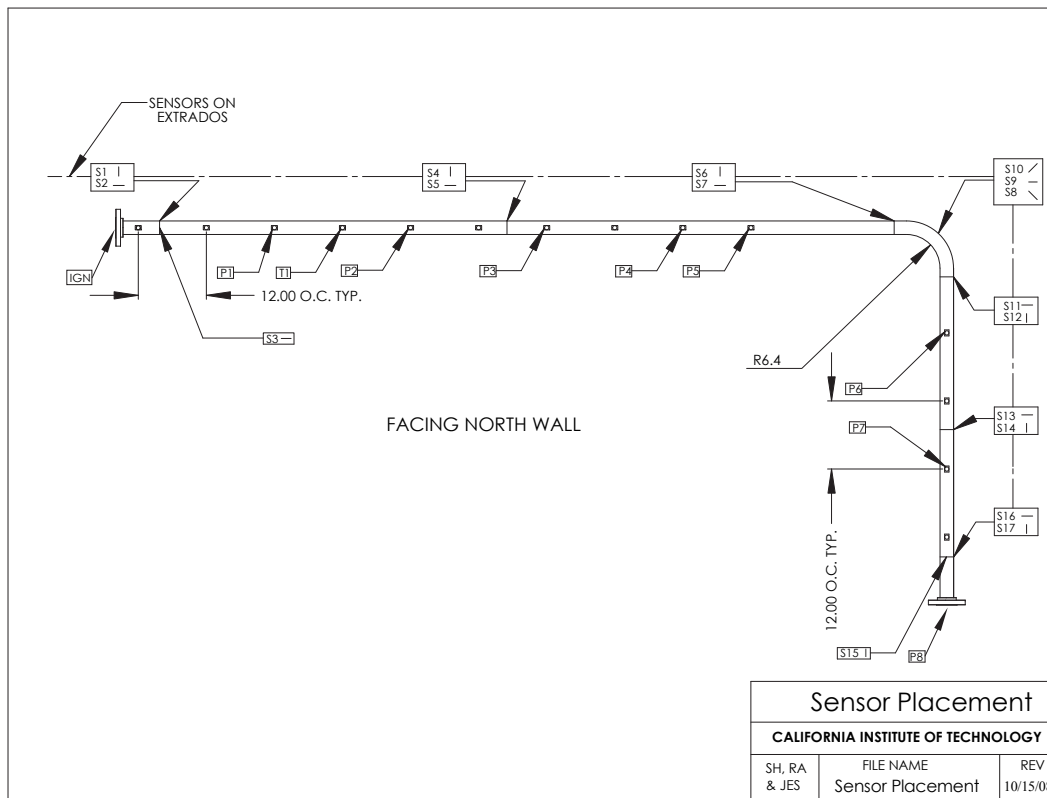


Figure 140: Location of sensors on ES1 for all tests except 22 and 23.

Notes for sensor placement in shots 1-14.

- 1 Reference plane for dimensions is outer-most slip-on flange surface. This is 1-5/16 in from the sealing surface of the slip on flange. See OutlineDimensions drawing for clarification. E = east reference W = west reference
- 2 The sealing surface of the slip on flange is 1-5/8 from the anchor plates.
- 3 H = hoop & L = Longitudinal
- 4 Angle is measured CW from plane of specimen starting from outer edge of the pipe - uppermost (top) on horizontal leg - eastmost (extrados of bend) on vertical leg
- 5 Axial locations of S8 & S9 & S10 (3-gage rosette) have been placed at midpoint of bend.
- 6 Accelerometers only used on shot 1 - overanged

Table 27: ES1 gage locations for tests 1-14.

Gage	Type	Orientation	Reference	Angle	Ref	Axial distance	
			(in)			(in)	(m)
S1	Strain	H	7.500	0	W	9.50	0.241
S2	Strain	L	7.500	0-	W	9.50	0.241
S3	Strain	L	7.375	90	W	9.38	0.238
S4	Strain	H	67.813	0	W	69.81	1.773
S5	Strain	L	67.813	0-	W	69.81	1.773
S6	Strain	H	135.875	0-	W	137.88	3.502
S7	Strain	L	135.875	0	W	137.88	3.502
S8	Strain	-45	145.000	0+	W	143.70	3.650
S9	Strain	L	64.000	0	E	143.70	3.650
S10	Strain	45	64.000	0-	E	143.70	3.650
S11	Strain	H	56.625	0	E	152.78	3.880
S12	Strain	L	56.625	0+	E	152.78	3.880
S13	Strain	H	29.625	0	E	179.78	4.566
S14	Strain	L	29.625	0+	E	179.78	4.566
S15	Strain	L	7.125	90	E	202.28	5.138
S16	Strain	H	7.125	0	E	202.28	5.138
S17	Strain	L	7.125	0+	E	202.28	5.138
P1	Pressure	-	26.563	90	W	28.56	0.725
P2	Pressure	-	50.625	90	W	52.63	1.337
P3	Pressure	-	74.750	90	W	76.75	1.949
P4	Pressure	-	98.563	90	W	100.56	2.554
P5	Pressure	-	110.563	90	W	112.56	2.859
P6	Pressure	-	46.625	90	E	162.78	4.134
P7	Pressure	-	22.625	90	E	186.78	4.744
P8	Pressure	-	-2.050	90	E	211.45	5.371
D1	Displacement		68.000	180	W	70.00	1.778
D2	Displacement		31.625	180	E	177.78	4.515
D3	Displacement		31.688	90	E	177.71	4.514
ACC1	Acceleration (6)	E-W	49.000	0	E	160.40	4.074
ACC2	Acceleration (6)	N-S	49.000	90	E	160.40	4.074
T1	Temperature		38.563	90	W	40.56	1.030
WELD	Girth		118.500	-	W	120.50	3.061
IGN	Spark plug		-2.000		W	0.00	0.000

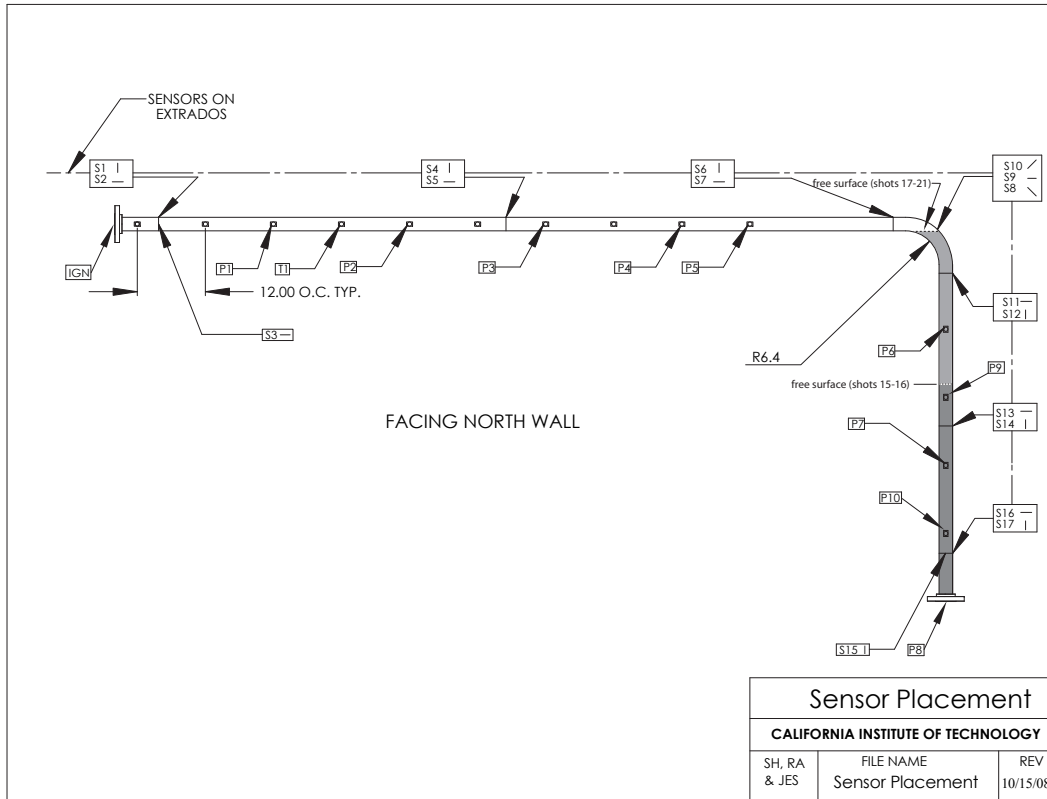


Figure 141: Location of sensors on ES1 for tests 15-21 with water in vertical leg.

Notes for sensor placement in shots 15-21.

The sensors were the same as in 1-14 except for the addition of gages P9 and P10 in the water-filled section and the removal of gage D3.

Table 28: ES1 gage locations for tests 15-21.

Gage	Type	Orientation	Reference (in)	Angle	Ref	Axial distance (in) (m)	
S1	Strain	H	7.500	0	W	9.50	0.241
S2	Strain	L	7.500	0-	W	9.50	0.241
S3	Strain	L	7.375	90	W	9.38	0.238
S4	Strain	H	67.813	0	W	69.81	1.773
S5	Strain	L	67.813	0-	W	69.81	1.773
S6	Strain	H	135.875	0-	W	137.88	3.502
S7	Strain	L	135.875	0	W	137.88	3.502
S8	Strain	-45	145.000	0+	W	143.70	3.650
S9	Strain	L	64.000	0	E	143.70	3.650
S10	Strain	45	64.000	0-	E	143.70	3.650
S11	Strain	H	56.625	0	E	152.78	3.880
S12	Strain	L	56.625	0+	E	152.78	3.880
S13	Strain	H	29.625	0	E	179.78	4.566
S14	Strain	L	29.625	0+	E	179.78	4.566
S15	Strain	L	7.125	90	E	202.28	5.138
S16	Strain	H	7.125	0	E	202.28	5.138
S17	Strain	L	7.125	0+	E	202.28	5.138
P1	Pressure	-	26.563	90	W	28.56	0.725
P2	Pressure	-	50.625	90	W	52.63	1.337
P3	Pressure	-	74.750	90	W	76.75	1.949
P4	Pressure	-	98.563	90	W	100.56	2.554
P5	Pressure	-	110.563	90	W	112.56	2.859
P6	Pressure	-	46.625	90	E	162.78	4.134
P7	Pressure	-	22.625	90	E	186.78	4.744
P8	Pressure	-	-2.050	90	E	211.45	5.371
P9	Pressure	-	34.625	90	E	174.78	4.439
P10	Pressure	-	10.625	90	E	198.78	5.049
D1	Displacement		68.000	180	W	70.00	1.778
D2	Displacement		31.625	180	E	177.78	4.515
D3	Displacement	Not used					
ACC1	Acceleration	Not used					
ACC2	Acceleration	Not used					
T1	Temperature		38.563	90	W	40.56	1.030
WELD	Girth		118.500	-	W	120.50	3.061
IGN	Spark plug		-2.000		W	0.00	0.000

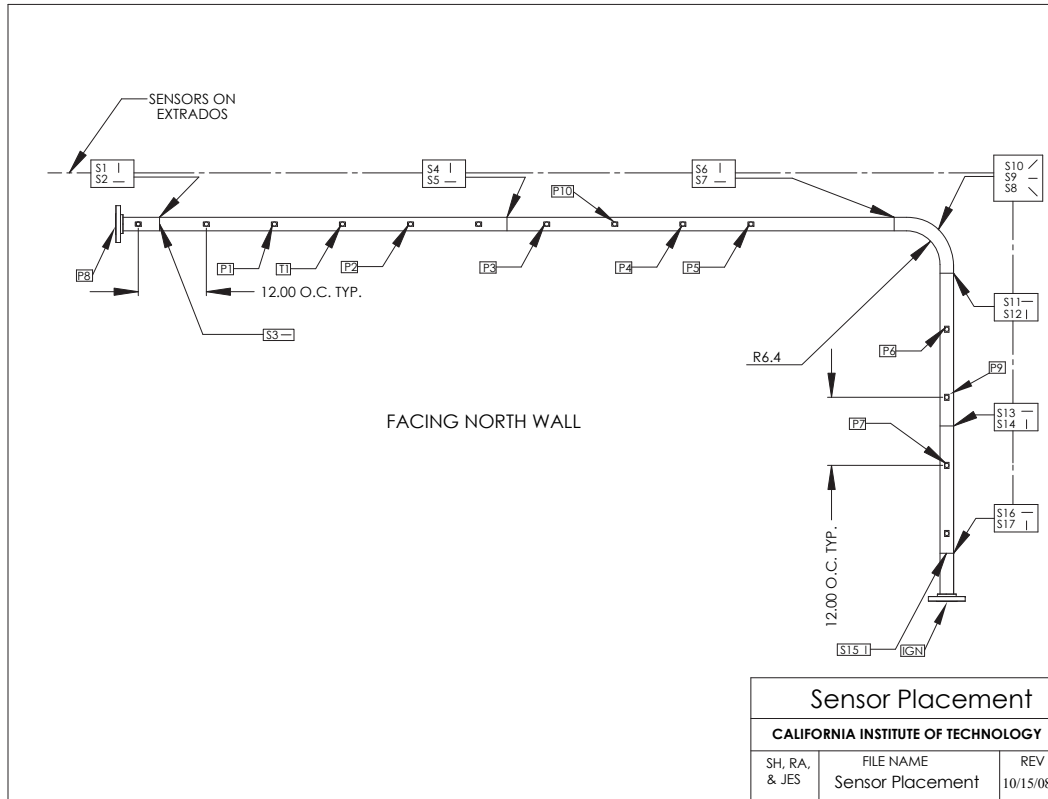


Figure 142: Location of sensors on ES1 for tests 22-24.

Notes on tests 22-24.

For these tests, pressure transducer P8 was swapped with the spark plug so that P8 was on the west end and the ignition was on the east end.

For test 24, P10 was moved to the location between P3 and P4, the cantilever support strain rosettes (R) were hooked up (S18-S23). The cantilevers were not bolted to the pipe yet and the accelerometers were moved to the tips of the cantilever supports. ACC1 was on the tip of U1, and ACC2 was on the tip of U2.

Table 29: ES1 gage locations for tests 22-23.

Gage	Type	Orientation	Reference (in)	Angle	Ref	Axial distance	
						(in)	(m)
S1	Strain	H	7.500	0	W	9.50	0.241
S2	Strain	L	7.500	0-	W	9.50	0.241
S3	Strain	L	7.375	90	W	9.38	0.238
S4	Strain	H	67.813	0	W	69.81	1.773
S5	Strain	L	67.813	0-	W	69.81	1.773
S6	Strain	H	135.875	0-	W	137.88	3.502
S7	Strain	L	135.875	0	W	137.88	3.502
S8	Strain	-45	145.000	0+	W	143.70	3.650
S9	Strain	L	64.000	0	E	143.70	3.650
S10	Strain	45	64.000	0-	E	143.70	3.650
S11	Strain	H	56.625	0	E	152.78	3.880
S12	Strain	L	56.625	0+	E	152.78	3.880
S13	Strain	H	29.625	0	E	179.78	4.566
S14	Strain	L	29.625	0+	E	179.78	4.566
S15	Strain	L	7.125	90	E	202.28	5.138
S16	Strain	H	7.125	0	E	202.28	5.138
S17	Strain	L	7.125	0+	E	202.28	5.138
P1	Pressure	-	26.563	90	W	28.56	0.725
P2	Pressure	-	50.625	90	W	52.63	1.337
P3	Pressure	-	74.750	90	W	76.75	1.949
P4	Pressure	-	98.563	90	W	100.56	2.554
P5	Pressure	-	110.563	90	W	112.56	2.859
P6	Pressure	-	46.625	90	E	162.78	4.134
P7	Pressure	-	22.625	90	E	186.78	4.744
P8	Pressure	-	-2.000	-	W	0.00	0.000
P9	Pressure	-	34.625	90	E	174.78	4.439
P10	Pressure	-	10.625	90	E	198.78	5.049
D1	Displacement		68.000	180	W	70.00	1.778
D2	Displacement		31.625	180	E	177.78	4.515
D3	Displacement	Not used					
ACC1	Acceleration					Located on west anchor	
ACC2	Acceleration					Located on west anchor	
T1	Temperature		38.563	90	W	40.56	1.030
WELD	Girth		118.500	-	W	120.50	3.061
IGN	Spark plug		-2.000		E	211.40	5.370

Table 30: ES1 gage locations for test 24.

Gage	Type	Orientation	Reference	Angle	Ref	Axial distance	
			(in)			(in)	(m)
S1	Strain	H	7.500	0	W	9.50	0.241
S2	Strain	L	7.500	0-	W	9.50	0.241
S3	Strain	L	7.375	90	W	9.38	0.238
S4	Strain	H	67.813	0	W	69.81	1.773
S5	Strain	L	67.813	0-	W	69.81	1.773
S6	Strain	H	135.875	0-	W	137.88	3.502
S7	Strain	L	135.875	0	W	137.88	3.502
S8	Strain	-45	145.000	0+	W	143.70	3.650
S9	Strain	L	64.000	0	E	143.70	3.650
S10	Strain	45	64.000	0-	E	143.70	3.650
S11	Strain	H	56.625	0	E	152.78	3.880
S12	Strain	L	56.625	0+	E	152.78	3.880
S13	Strain	H	29.625	0	E	179.78	4.566
S14	Strain	L	29.625	0+	E	179.78	4.566
S15	Strain	L	7.125	90	E	202.28	5.138
S16	Strain	H	7.125	0	E	202.28	5.138
S17	Strain	L	7.125	0+	E	202.28	5.138
S18	Strain	R1	104.7	-	W	106.07	2.694
S19	Strain	R2	104.7	-	W	106.07	2.694
S20	Strain	R3	104.7	-	W	106.07	2.694
S21	Strain	R1	28.20	-	E	183.20	4.653
S22	Strain	R2	28.20	-	E	183.20	4.653
S23	Strain	R3	28.20	-	E	183.20	4.653
P1	Pressure	-	26.563	90	W	28.56	0.725
P2	Pressure	-	50.625	90	W	52.63	1.337
P3	Pressure	-	74.750	90	W	76.75	1.949
P4	Pressure	-	98.563	90	W	100.56	2.554
P5	Pressure	-	110.563	90	W	112.56	2.859
P6	Pressure	-	46.625	90	E	162.78	4.134
P7	Pressure	-	22.625	90	E	186.78	4.744
P8	Pressure	-	-2.000	-	W	0.00	0.000
P9	Pressure	-	34.625	90	E	174.78	4.439
P10	Pressure	-	86.625	90	W	88.63	2.251
D1	Displacement	-	68.000	180	W	70.00	1.778
D2	Displacement	-	31.625	180	E	177.78	4.515
D3	Displacement	Not used					
ACC1	Acceleration	V	104.07	0	W	106.07	2.694
ACC2	Acceleration	H	26.20	90	E	183.20	4.653
T1	Temperature	-	38.563	90	W	40.56	1.030
WELD	Girth	-	118.500	-	W	120.50	3.061
IGN	Spark plug	-	-2.000	-	E	211.4	5.370

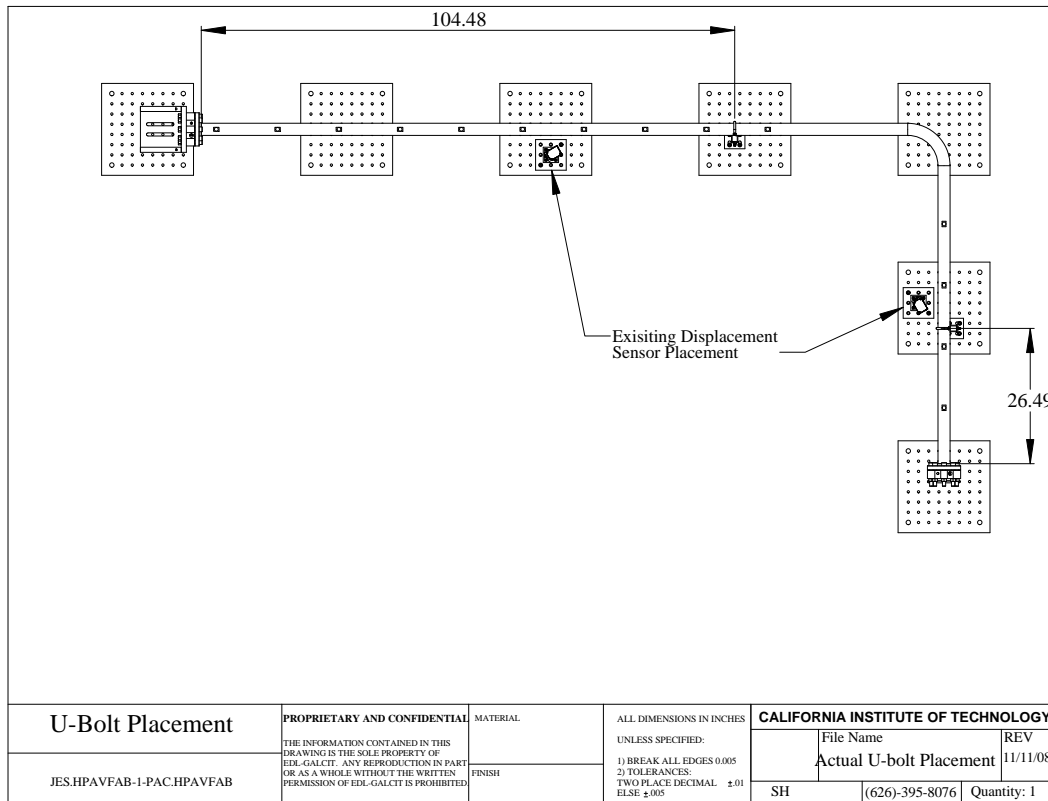


Figure 143: Location of U-bolts in tests 25-27 and 34-35.

In test 25, the cantilever supports were in place with the U-bolts located around the pipe but not torqued down. The pipe was still fastened to the east anchor - the purpose was to look at the cross talk that might be created during ignition and reflection of the detonation in the pipe. The ignition location was moved back to the W anchor and pressure gage P8 was moved to the east end.

For tests 26-27, the cantilever supports U1 and U2 were fastened to the pipe firmly with the U-bolts, located as shown in Fig. 143. The east end of pipe was freed from the anchor and the accelerometers were moved to the east flange. Otherwise, the instrument locations and channels are the same as for shot 25.

U1 is mounted on the belly of the specimen (lower or intrados side) and the signal S19 is positive when the cantilever moves downward. Signals S18 and S20 are the +/- 45 deg legs of the rosette - these signals are sensitive to torsion and transverse bending and were not analyzed. U2 is mounted along the spine of the specimen (east or extrados side) and signal S22 is positive when the cantilever moves toward the east. Signals S21 and S23 are the +/- 45 deg legs of the rosette - these signals are sensitive to torsion and transverse bending and were not analyzed.

For tests 28-33, the east end of the pipe was connected to the force link, which was fastened to a cantilever. In test 28, the cantilever U2 was used in the force link and the

cantilever U1 was located as in tests 26-27.

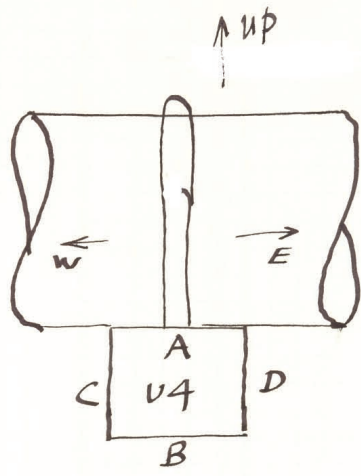
In tests 29-33, the cantilever U1 was removed and the pipe was supported only by the west anchor and the force link, which used cantilever U3 with two half-bridges. Signal S24 corresponds to the AB gage pair (vertical deflection) and signal S25 to the CD gage pair (horizontal deflection). Only data for shots 32-33 was distributed since shots 29-31

For tests 34-35, the east end of the pipe was free and the cantilevers U3 and U4 were located in the same positions as U2 and U1 in tests 25-27. The orientation of the cantilevers and strain gages are shown in Fig. [144](#).

1-5-2009

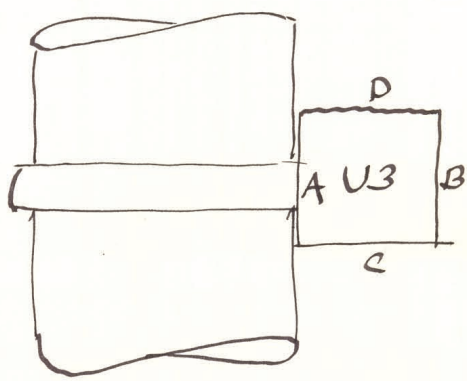
### Cantilever Beam Arrangements for shots 34 & 35 ESI.

Plate 4



Half-bridge  
works:  
A-B S24  
C-D S25

Plate 10



UP  
E  
A-B S26  
C-D S27

Output is + from half-bridge pair when  
A - tension & C - tension if  
push cantilever U4 with a downward force or  
force directed to East.

No. 937 811E  
 Engineer's Computation Pad  
 STAEDTLER®

Figure 144: Arrangement of strain gages for cantilevers in shots 34-35.

Table 31: ES1 gages for shots 25-28. Except for the accelerometers, locations are also valid for shots 26 and 27. In shot 28, U2 was moved to the force link location.

Gage	Type	Orientation	Reference (in)	Angle	Ref	Axial distance (in)	(m)
S1	Strain	H	7.500	0	W	9.50	0.241
S2	Strain	L	7.500	0-	W	9.50	0.241
S3	Strain	L	7.375	90	W	9.38	0.238
S4	Strain	H	67.813	0	W	69.81	1.773
S5	Strain	L	67.813	0-	W	69.81	1.773
S6	Strain	H	135.875	0-	W	137.88	3.502
S7	Strain	L	135.875	0	W	137.88	3.502
S8	Strain	-45	145.000	0+	W	143.70	3.650
S9	Strain	L	64.000	0	E	143.70	3.650
S10	Strain	45	64.000	0-	E	143.70	3.650
S11	Strain	H	56.625	0	E	152.78	3.880
S12	Strain	L	56.625	0+	E	152.78	3.880
S13	Strain	H	29.625	0	E	179.78	4.566
S14	Strain	L	29.625	0+	E	179.78	4.566
S15	Strain	L	7.125	90	E	202.28	5.138
S16	Strain	H	7.125	0	E	202.28	5.138
S17	Strain	L	7.125	0+	E	202.28	5.138
S18	Strain - U1	R1	104.7	-	W	106.07	2.694
S19	Strain - U1	R2	104.7	-	W	106.07	2.694
S20	Strain - U1	R3	104.7	-	W	106.07	2.694
S21	Strain - U2	R1	28.20	-	E	183.20	4.653
S22	Strain - U2	R2	28.20	-	E	183.20	4.653
S23	Strain - U2	R3	28.20	-	E	183.20	4.653
P1	Pressure	-	26.563	90	W	28.56	0.725
P2	Pressure	-	50.625	90	W	52.63	1.337
P3	Pressure	-	74.750	90	W	76.75	1.949
P4	Pressure	-	98.563	90	W	100.56	2.554
P5	Pressure	-	110.563	90	W	112.56	2.859
P6	Pressure	-	46.625	90	E	162.78	4.134
P7	Pressure	-	22.625	90	E	186.78	4.744
P8	Pressure	-	-2.000	-	W	211.45	5.371
P9	Pressure	-	34.625	90	E	174.78	4.439
P10	Pressure	-	86.625	90	W	88.63	2.251
D1	Displacement	-	68.000	180	W	70.00	1.778
D2	Displacement	-	31.625	180	E	177.78	4.515
D3	Displacement	Not used					
ACC1	Acceleration	V	104.07	0	W	106.07	2.694
ACC2	Acceleration	H	26.20	90	E	183.20	4.653
T1	Temperature	-	38.563	90	W	40.56	1.030
WELD	Girth	-	118.500	-	W	120.50	3.061
IGN	Spark plug	-	-2.000	-	W	0.0	0.0

Table 32: ES1 gage locations for shots 32-33. Cantilever U3 was mounted in the force link at the bottom of the east flange. Gage D4 was Keyence measurement of out-of-plane motion of the bend.

Gage	Type	Orientation	Reference (in)	Angle	Ref	Axial distance (in)	(m)
S1	Strain	H	7.500	0	W	9.50	0.241
S2	Strain	L	7.500	0-	W	9.50	0.241
S3	Strain	L	7.375	90	W	9.38	0.238
S4	Strain	H	67.813	0	W	69.81	1.773
S5	Strain	L	67.813	0-	W	69.81	1.773
S6	Strain	H	135.875	0-	W	137.88	3.502
S7	Strain	L	135.875	0	W	137.88	3.502
S8	Strain	-45	145.000	0+	W	143.70	3.650
S9	Strain	L	64.000	0	E	143.70	3.650
S10	Strain	45	64.000	0-	E	143.70	3.650
S11	Strain	H	56.625	0	E	152.78	3.880
S12	Strain	L	56.625	0+	E	152.78	3.880
S13	Strain	H	29.625	0	E	179.78	4.566
S14	Strain	L	29.625	0+	E	179.78	4.566
S15	Strain	L	7.125	90	E	202.28	5.138
S16	Strain	H	7.125	0	E	202.28	5.138
S17	Strain	L	7.125	0+	E	202.28	5.138
S24	Strain - U3	AB	-	-	-	-	force link
S25	Strain - U3	CD	-	-	-	-	force link
P1	Pressure	-	26.563	90	W	28.56	0.725
P2	Pressure	-	50.625	90	W	52.63	1.337
P3	Pressure	-	74.750	90	W	76.75	1.949
P4	Pressure	-	98.563	90	W	100.56	2.554
P5	Pressure	-	110.563	90	W	112.56	2.859
P6	Pressure	-	46.625	90	E	162.78	4.134
P7	Pressure	-	22.625	90	E	186.78	4.744
P8	Pressure	-	-2.000	-	W	211.45	5.371
P9	Pressure	-	34.625	90	E	174.78	4.439
P10	Pressure	-	86.625	90	W	88.63	2.251
D4	Displacement	Out of plane bend motion					
ACC1	Acceleration	V	104.07	0	W	106.07	2.694
ACC2	Acceleration	H	26.20	90	E	183.20	4.653
T1	Temperature	-	38.563	90	W	40.56	1.030
WELD	Girth	-	118.500	-	W	120.50	3.061
IGN	Spark plug	-	-2.000	-	W	0.0	0.0

Table 33: ES1 gage locations for shots 34-35. Cantilevers U3 and U4 mounted in same locations as U2 and U1 in tests 26 and 27.

Gage	Type	Orientation	Reference (in)	Angle	Ref	Axial distance (in) (m)	
S1	Strain	H	7.500	0	W	9.50	0.241
S2	Strain	L	7.500	0-	W	9.50	0.241
S3	Strain	L	7.375	90	W	9.38	0.238
S4	Strain	H	67.813	0	W	69.81	1.773
S5	Strain	L	67.813	0-	W	69.81	1.773
S6	Strain	H	135.875	0-	W	137.88	3.502
S7	Strain	L	135.875	0	W	137.88	3.502
S8	Strain	-45	145.000	0+	W	143.70	3.650
S9	Strain	L	64.000	0	E	143.70	3.650
S10	Strain	45	64.000	0-	E	143.70	3.650
S11	Strain	H	56.625	0	E	152.78	3.880
S12	Strain	L	56.625	0+	E	152.78	3.880
S13	Strain	H	29.625	0	E	179.78	4.566
S14	Strain	L	29.625	0+	E	179.78	4.566
S15	Strain	L	7.125	90	E	202.28	5.138
S16	Strain	H	7.125	0	E	202.28	5.138
S17	Strain	L	7.125	0+	E	202.28	5.138
S24	Strain - U3	AB	28.20	-	E	183.20	4.653
S25	Strain - U3	CD	28.20	-	E	183.20	4.653
S26	Strain - U4	AB	104.7	-	W	106.07	2.694
S27	Strain - U4	CD	104.7	-	W	106.07	2.694
P1	Pressure	-	26.563	90	W	28.56	0.725
P2	Pressure	-	50.625	90	W	52.63	1.337
P3	Pressure	-	74.750	90	W	76.75	1.949
P4	Pressure	-	98.563	90	W	100.56	2.554
P5	Pressure	-	110.563	90	W	112.56	2.859
P6	Pressure	-	46.625	90	E	162.78	4.134
P7	Pressure	-	22.625	90	E	186.78	4.744
P8	Pressure	-	-2.000	-	W	211.45	5.371
P9	Pressure	-	34.625	90	E	174.78	4.439
P10	Pressure	-	86.625	90	W	88.63	2.251
D4	Displacement	Out of plane bend motion					
ACC1	Acceleration	V	104.07	0	W	106.07	2.694
ACC2	Acceleration	H	26.20	90	E	183.20	4.653
T1	Temperature	-	38.563	90	W	40.56	1.030
WELD	Girth	-	118.500	-	W	120.50	3.061
IGN	Spark plug	-	-2.000	-	W	0.0	0.0

## J ES1 Data Plots

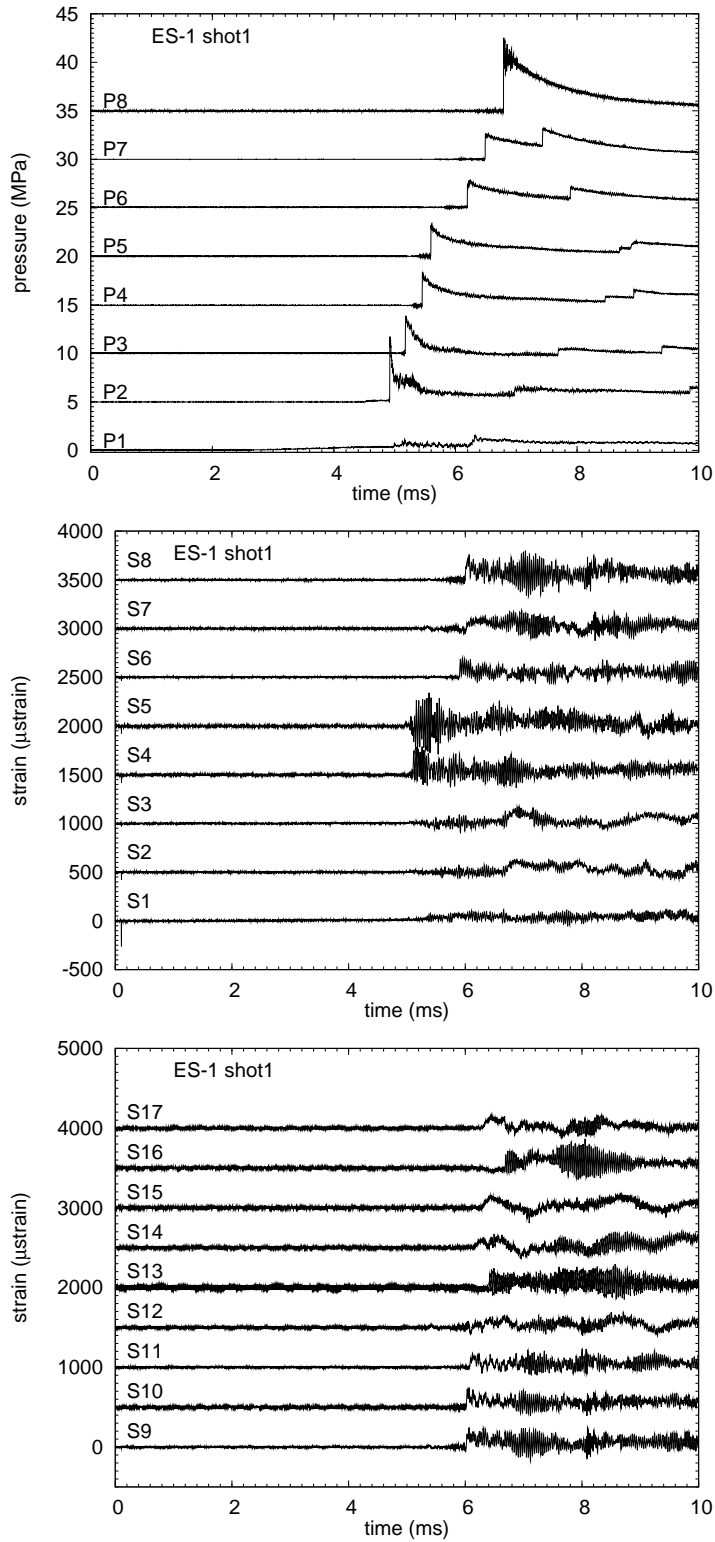


Figure 145: ES1 Shot 1. Pressure and strain gage signals.

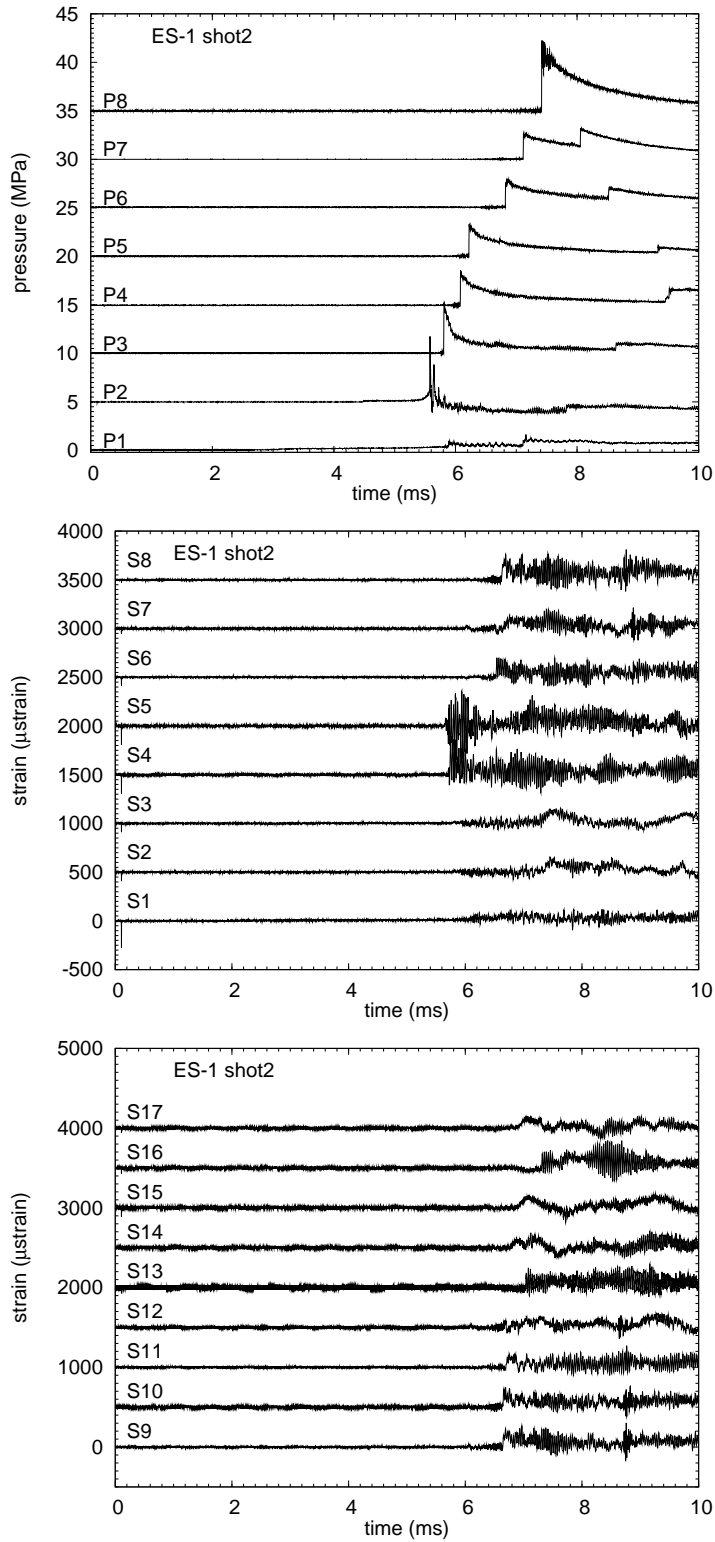


Figure 146: ES1 Shot 2. Pressure and strain gage signals.

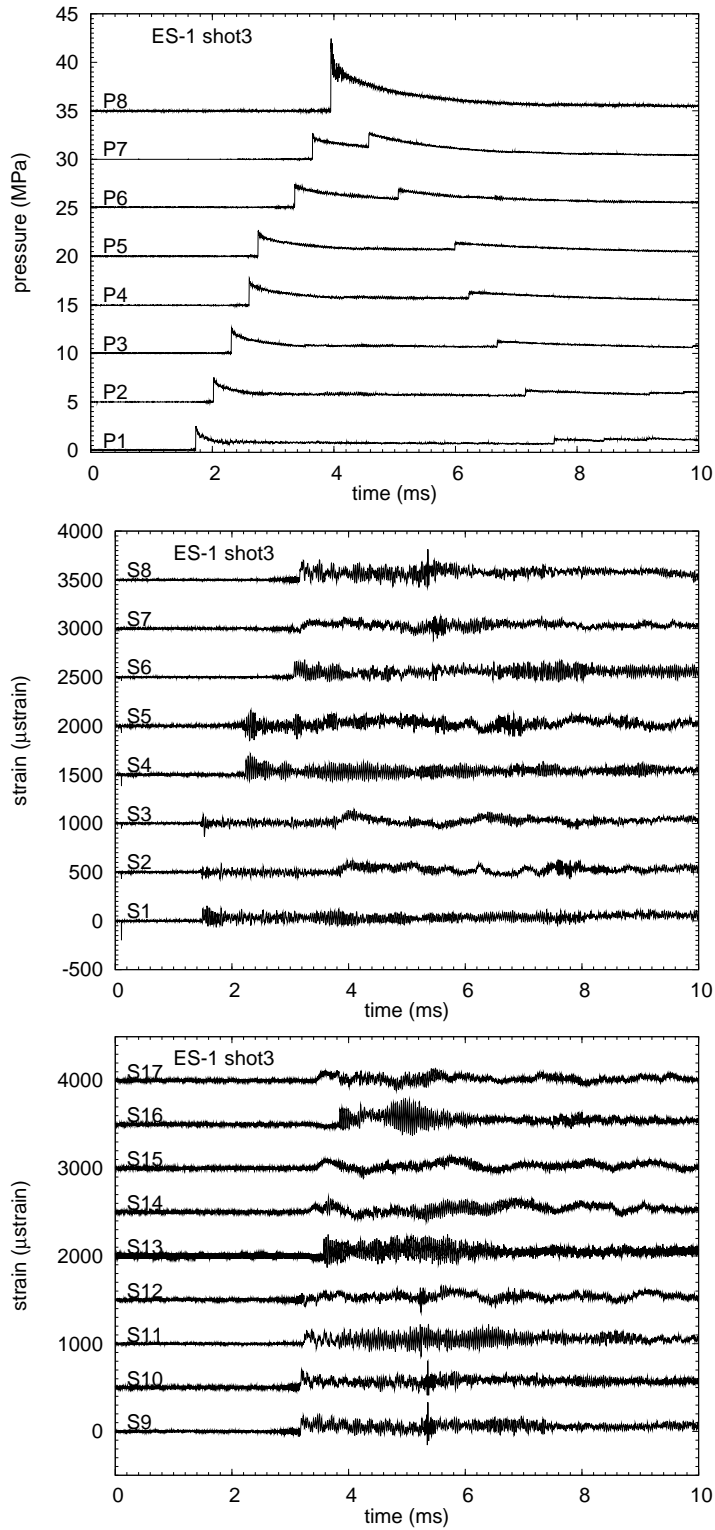


Figure 147: ES1 Shot 3. Pressure and strain gage signals.

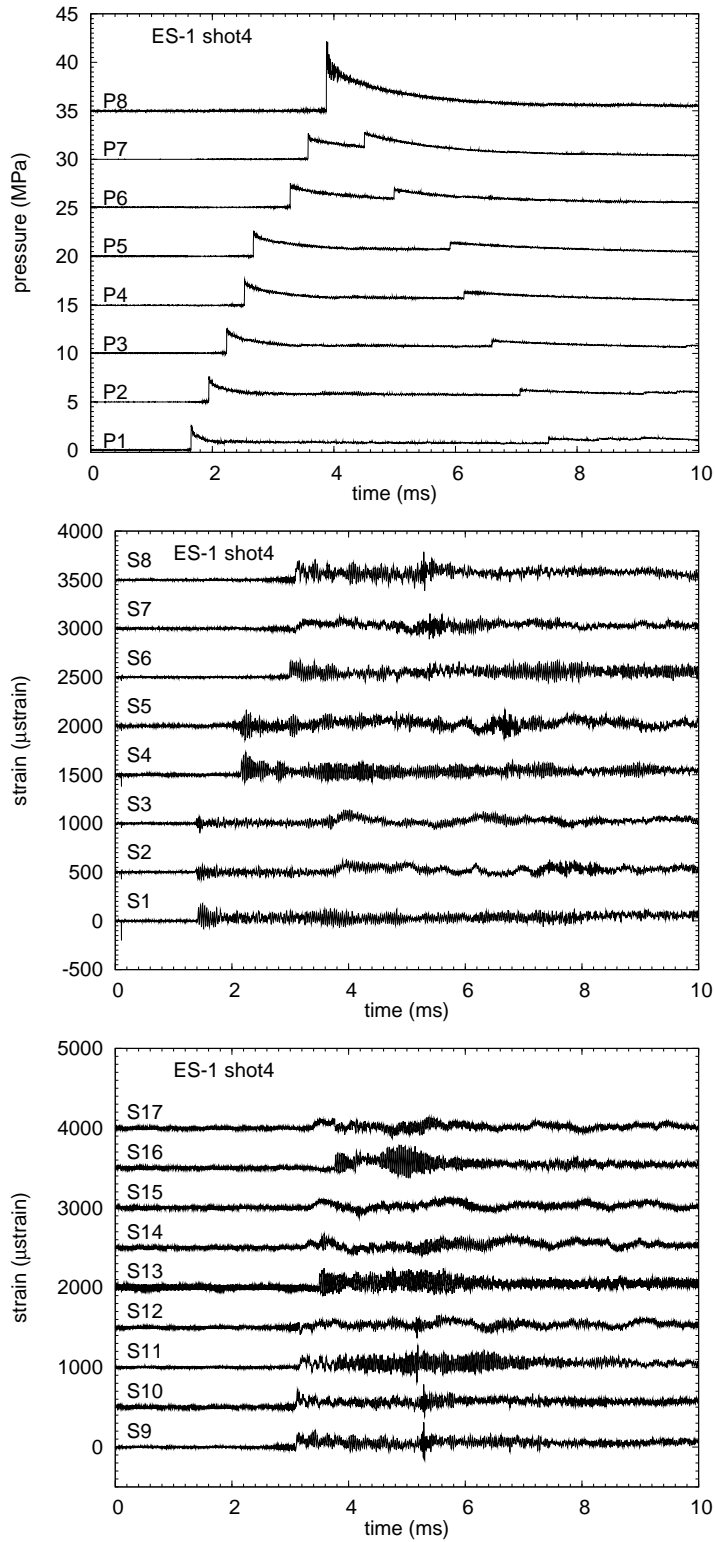


Figure 148: ES1 Shot 4. Pressure and strain gage signals.

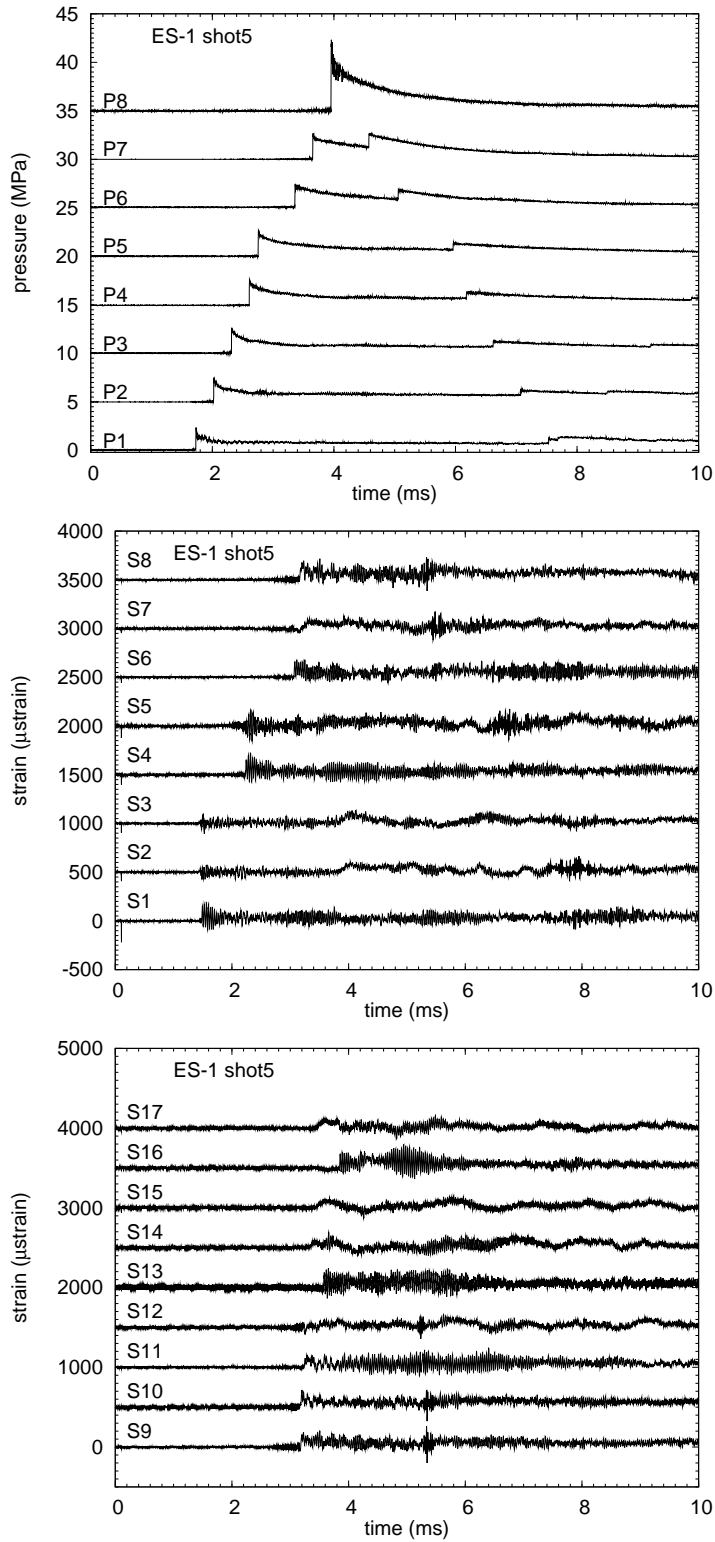


Figure 149: ES1 Shot 5. Pressure and strain gage signals.

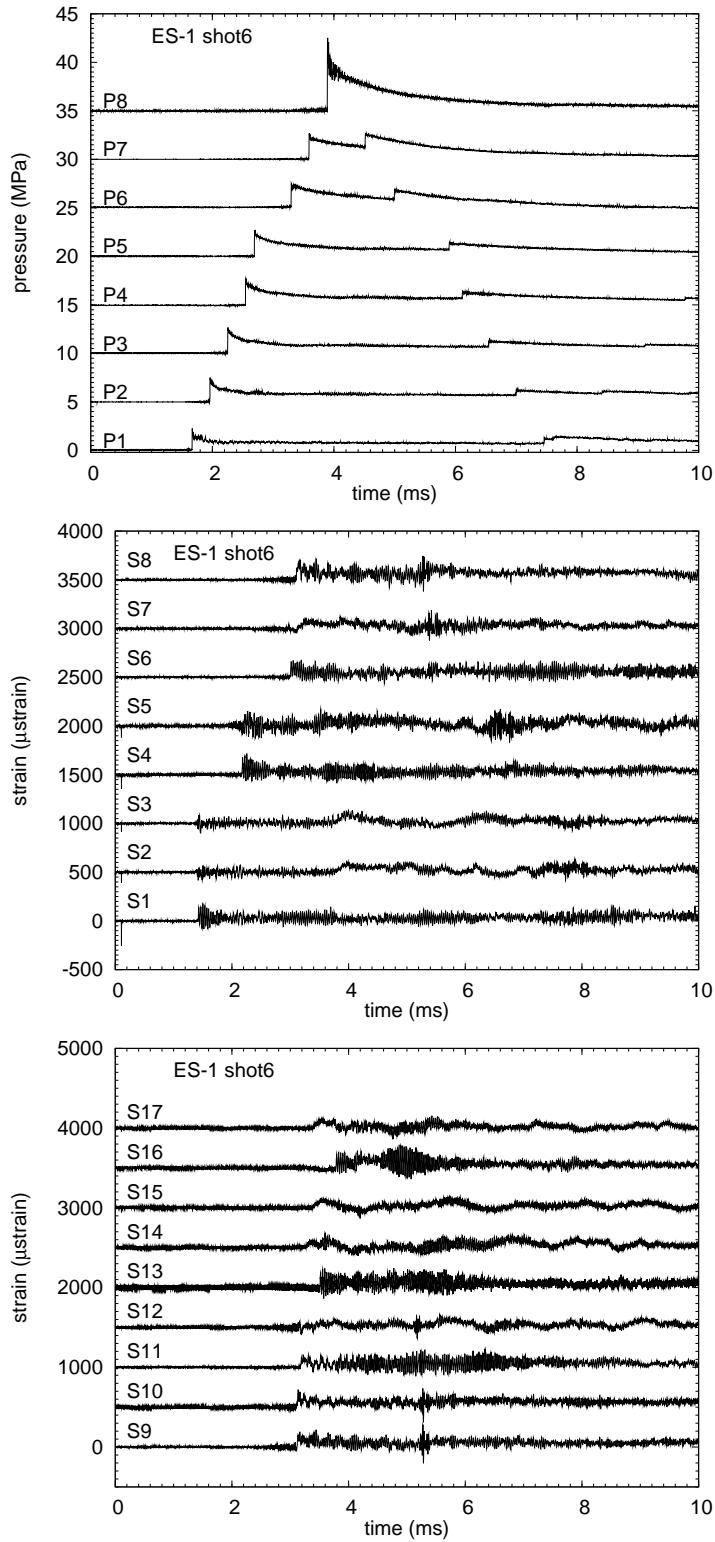


Figure 150: ES1 Shot 6. Pressure and strain gage signals.

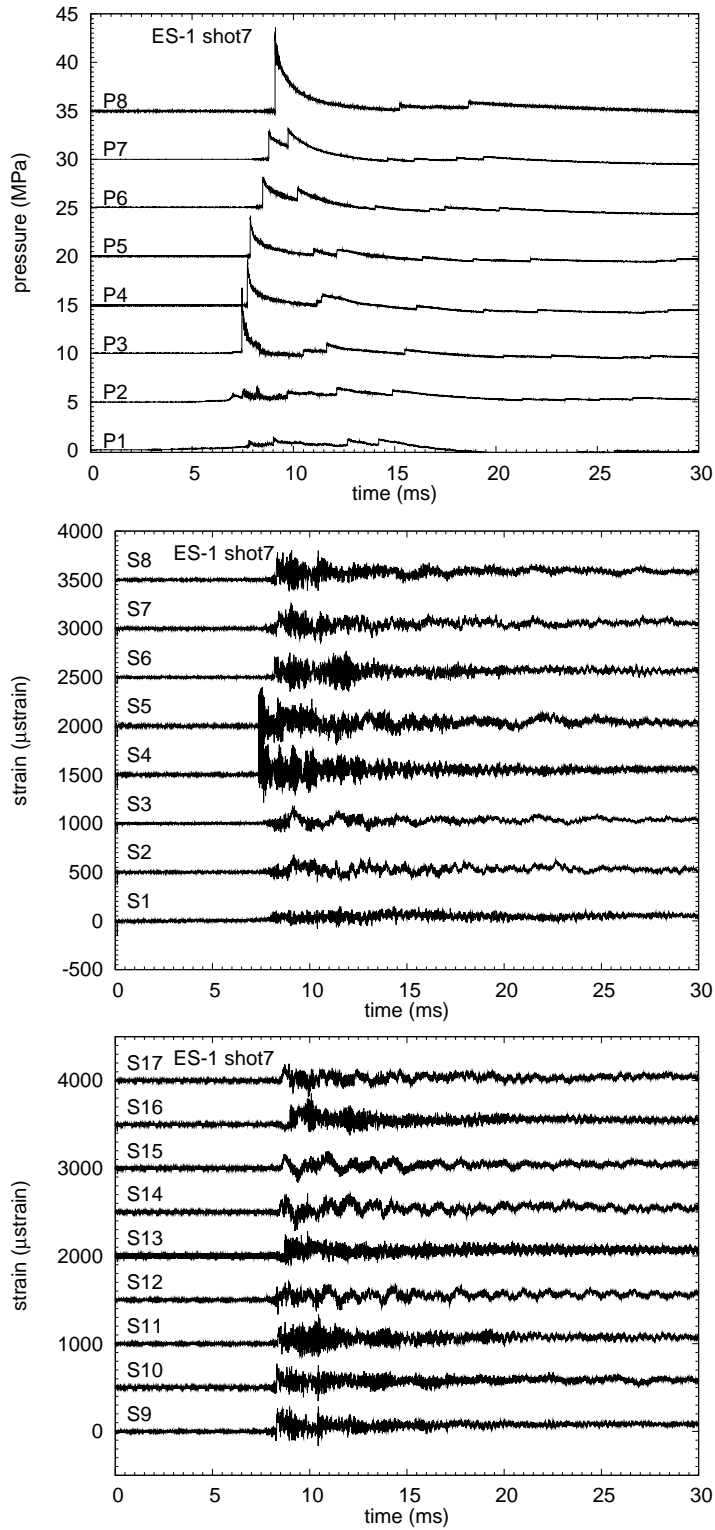


Figure 151: ES1 Shot 7. Pressure and strain gage signals.

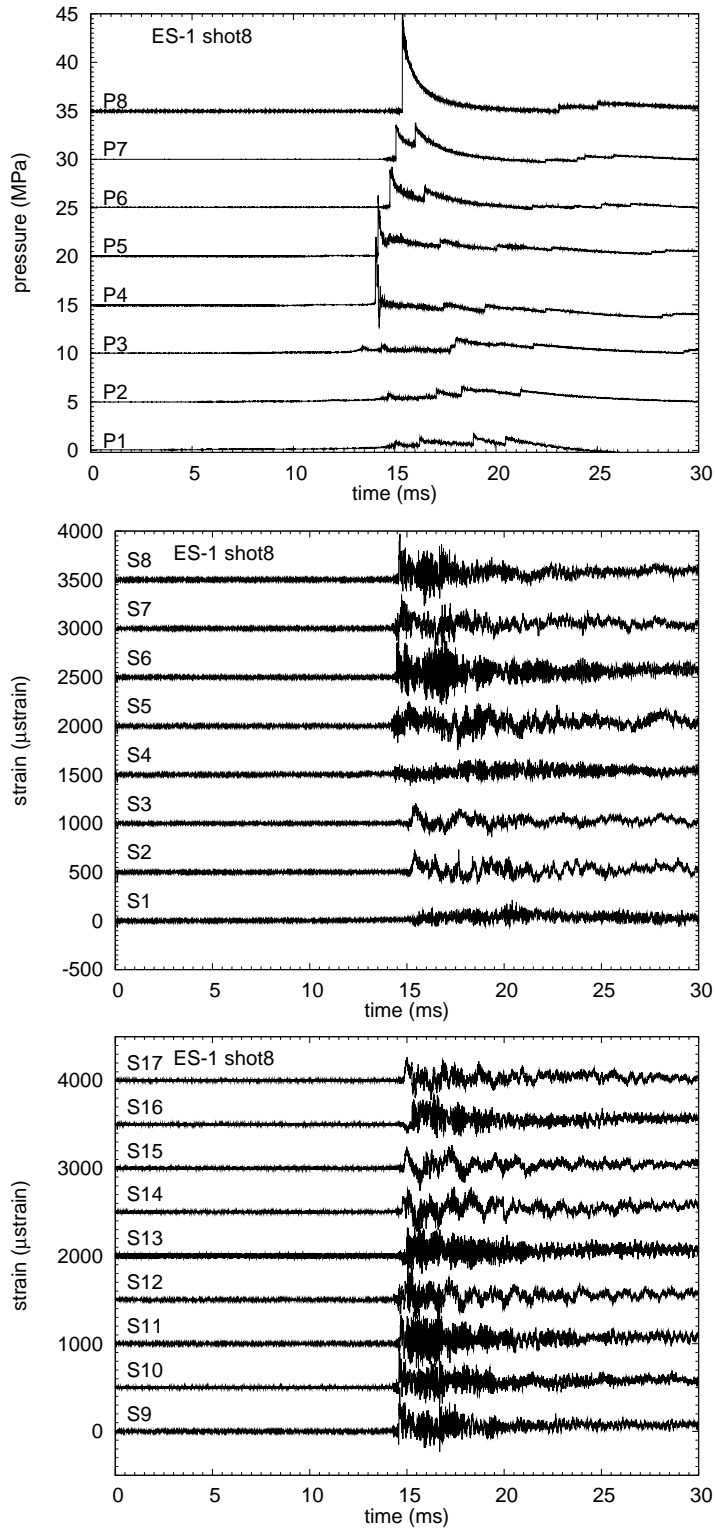


Figure 152: ES1 Shot 8. Pressure and strain gage signals.

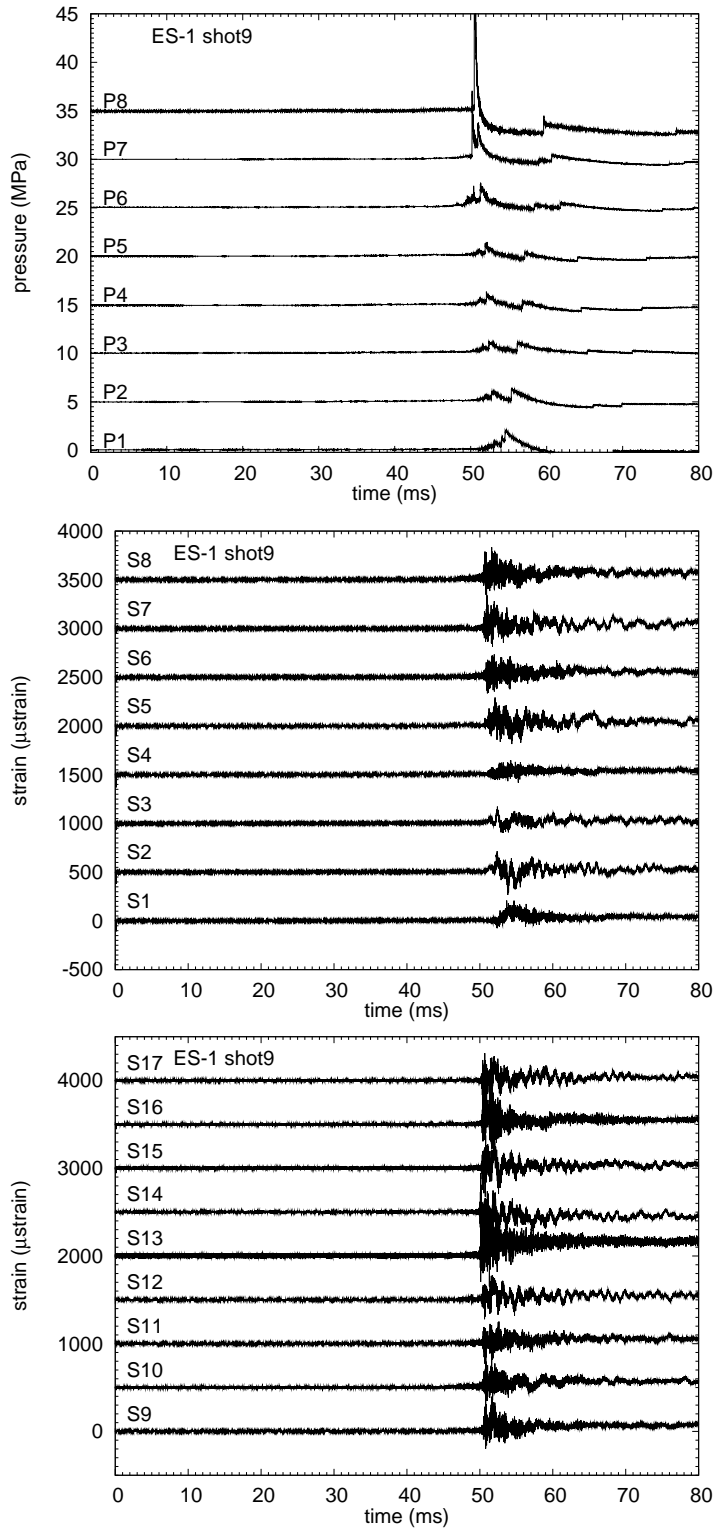


Figure 153: ES1 Shot 9. Pressure and strain gage signals.

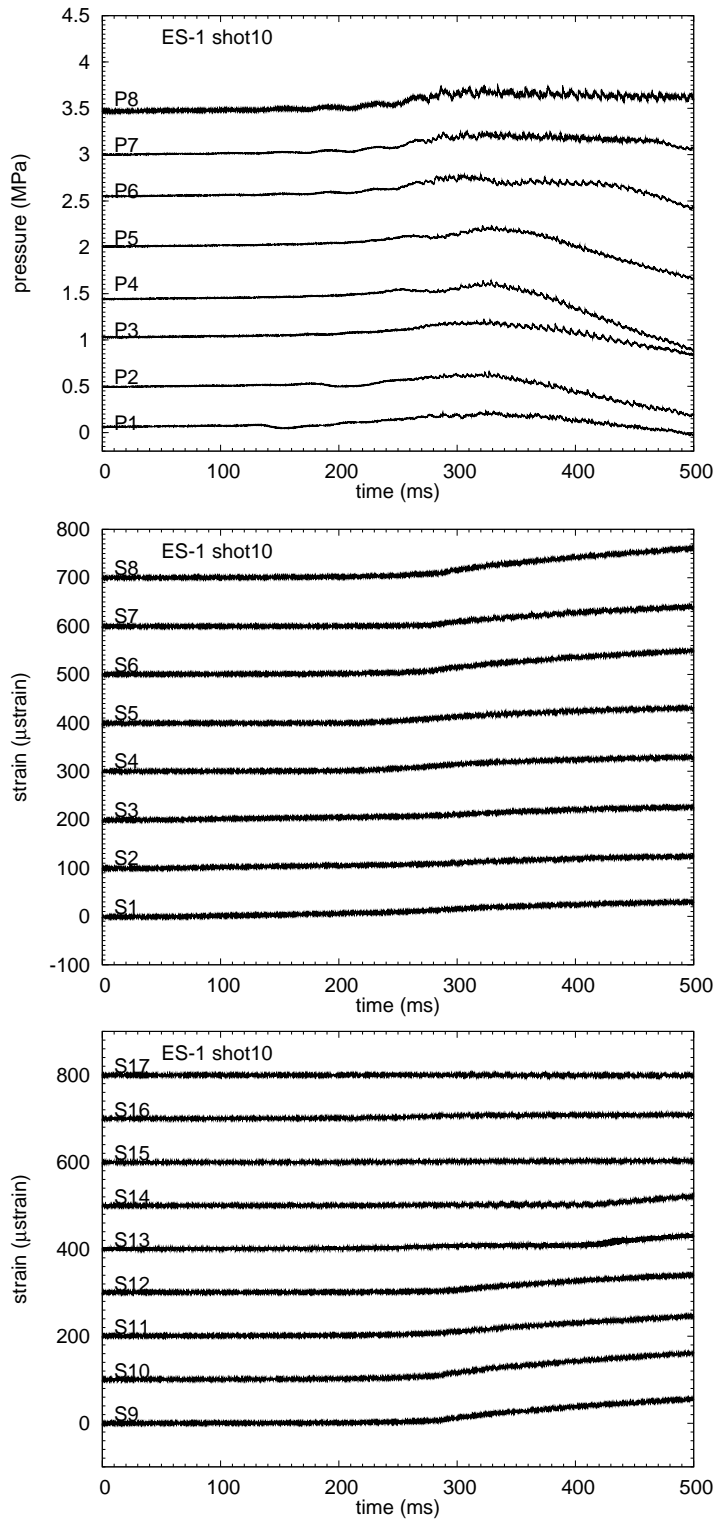


Figure 154: ES1 Shot 10. Pressure and strain gage signals.

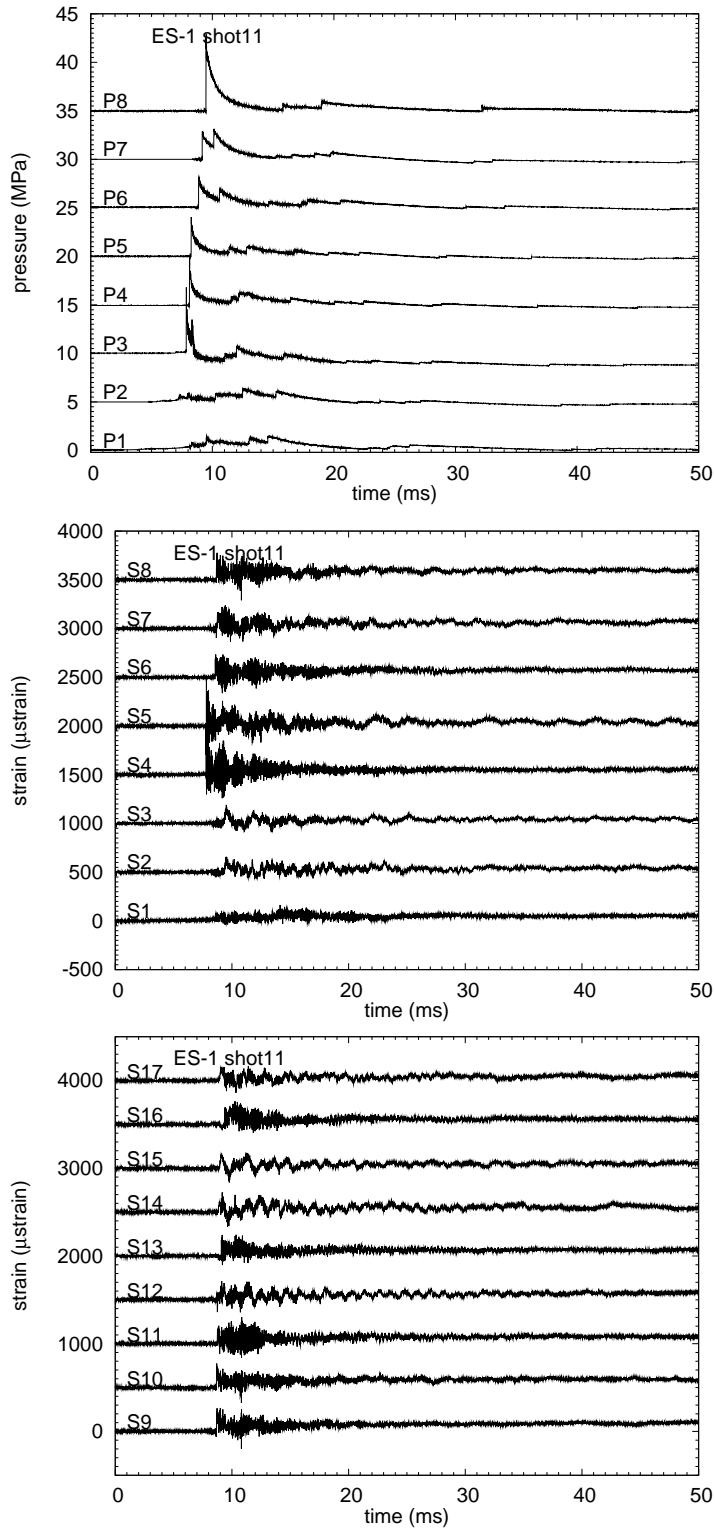


Figure 155: ES1 Shot 11. Pressure and strain gage signals.

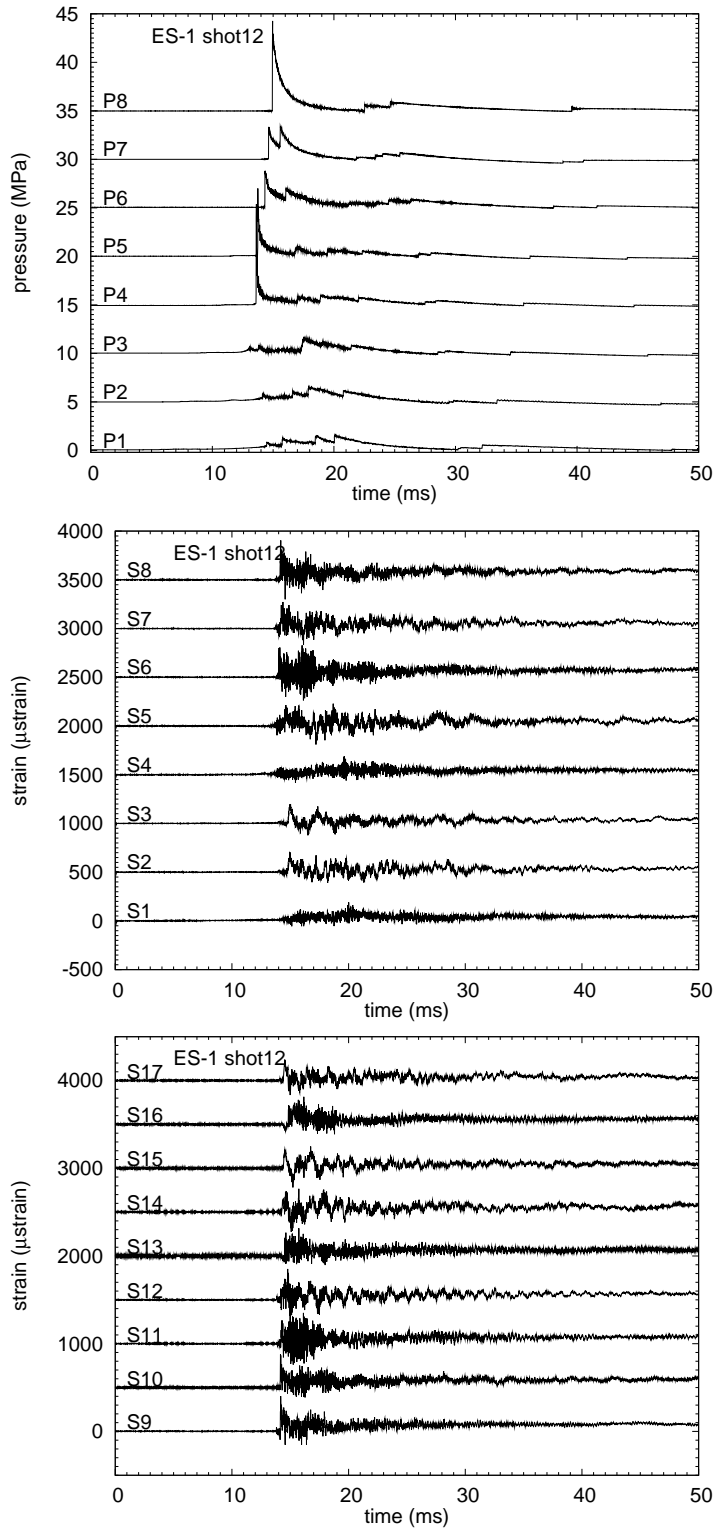


Figure 156: ES1 Shot 12. Pressure and strain gage signals.

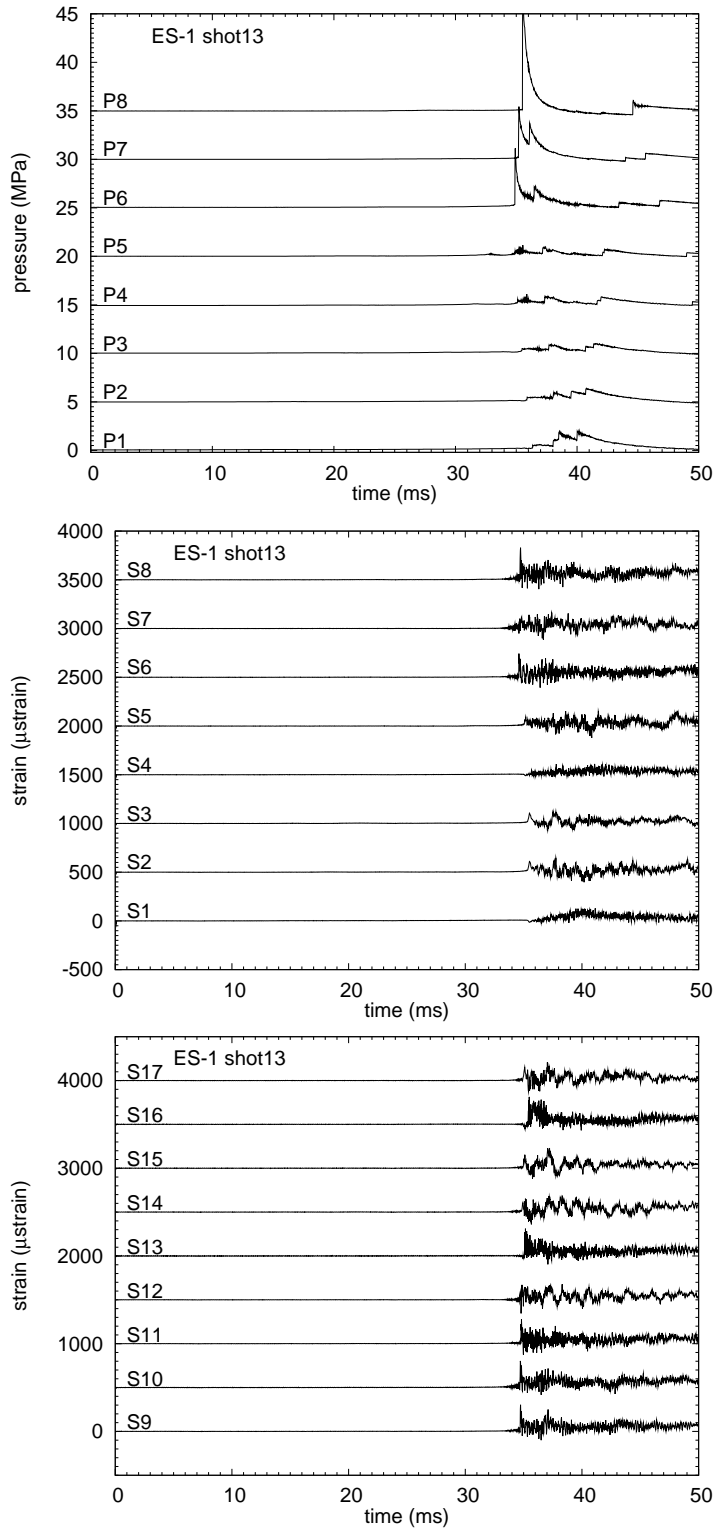


Figure 157: ES1 Shot 13. Pressure and strain gage signals.

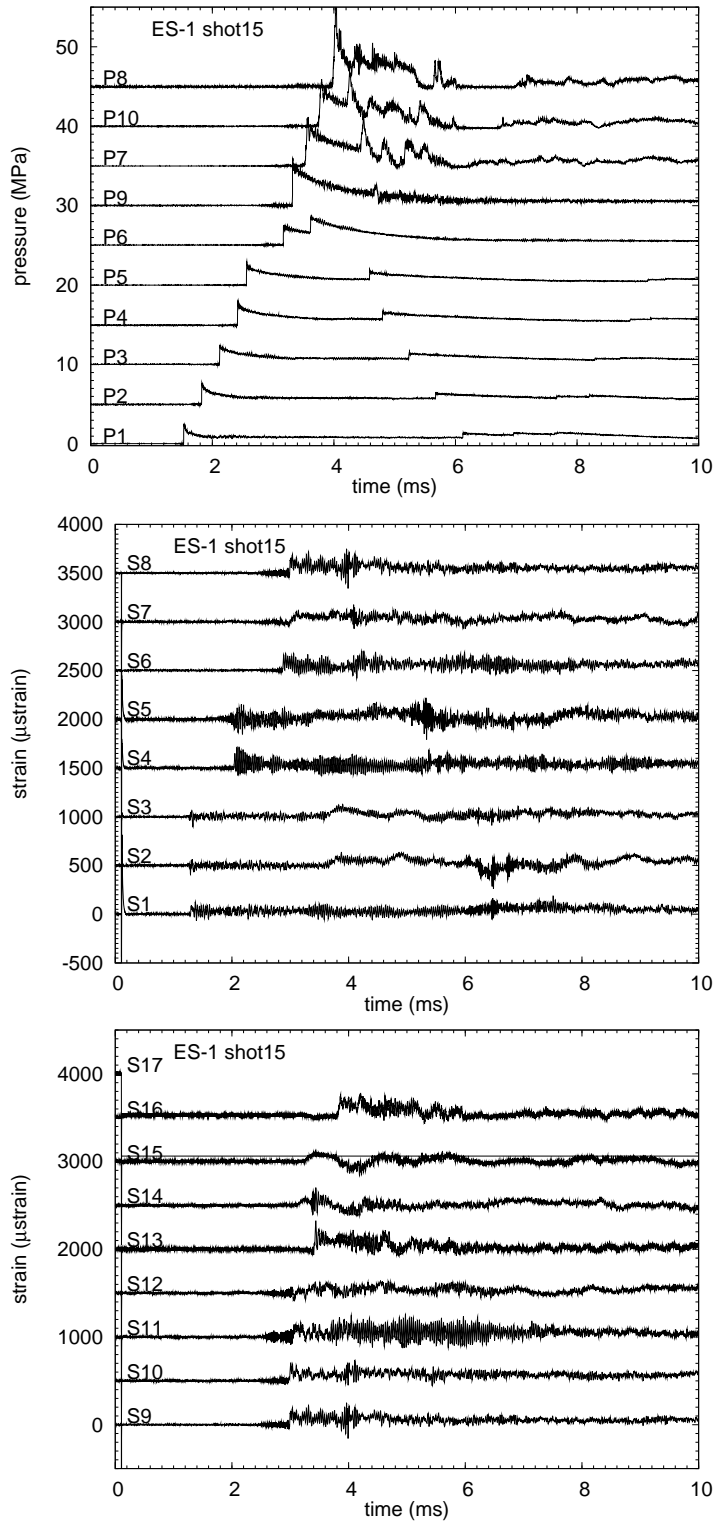


Figure 158: ES1 Shot 15. Pressure and strain gage signals.

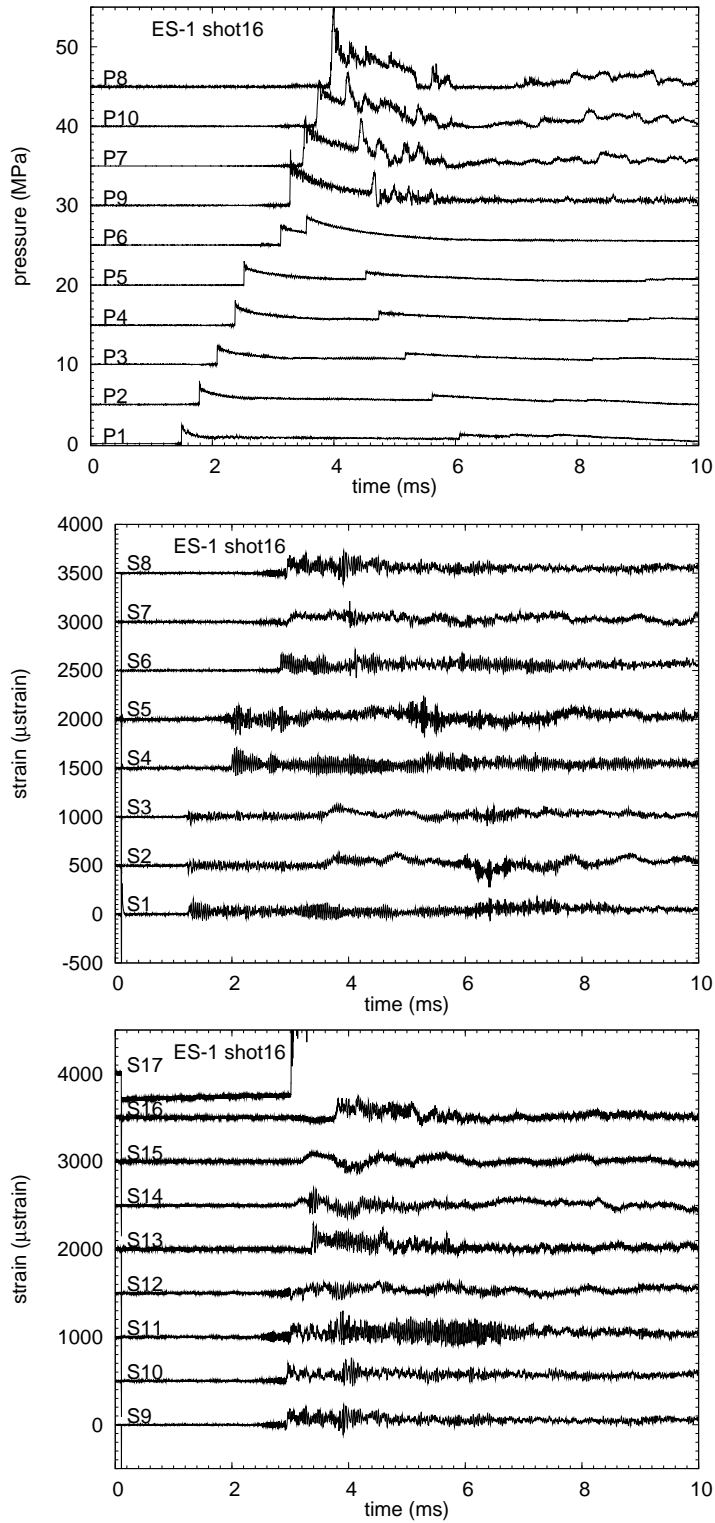


Figure 159: ES1 Shot 16. Pressure and strain gage signals.

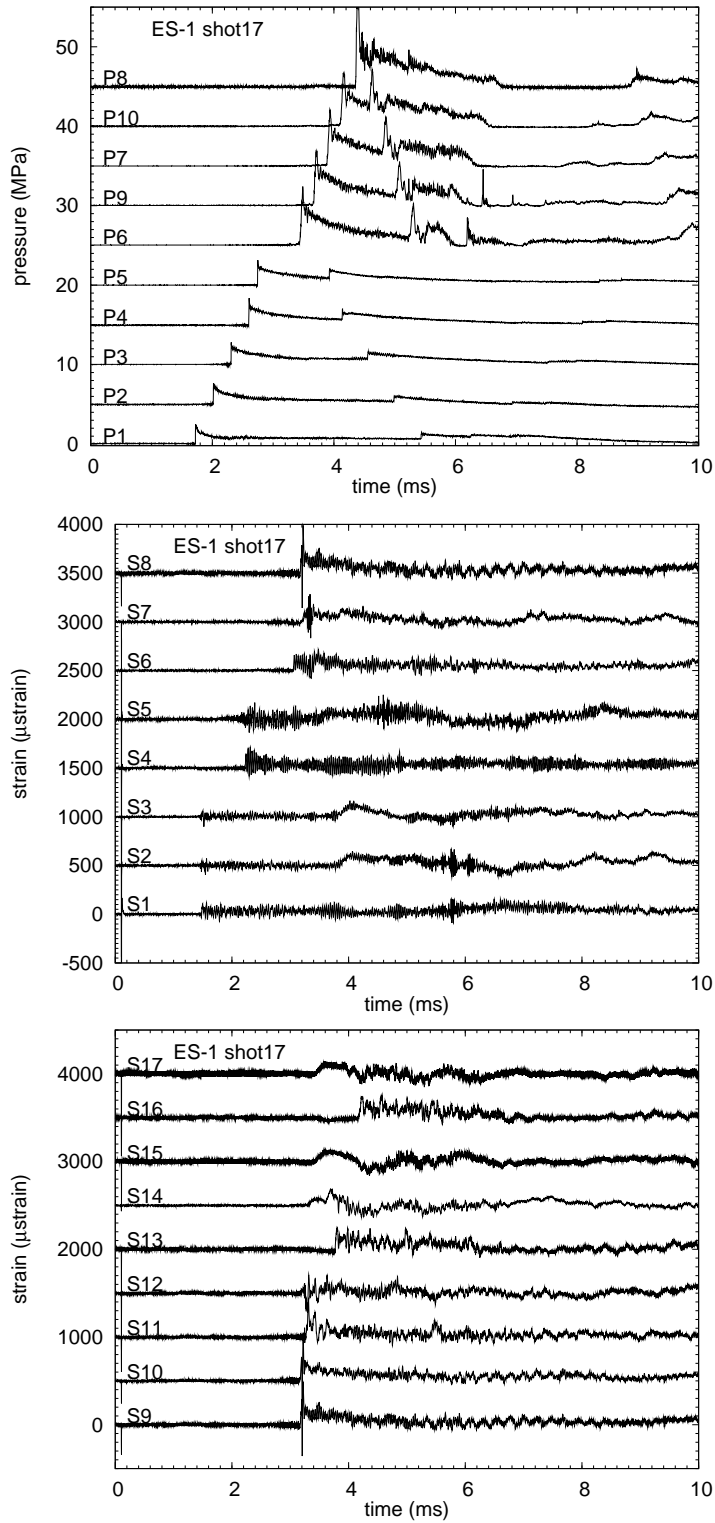


Figure 160: ES1 Shot 17. Pressure and strain gage signals.

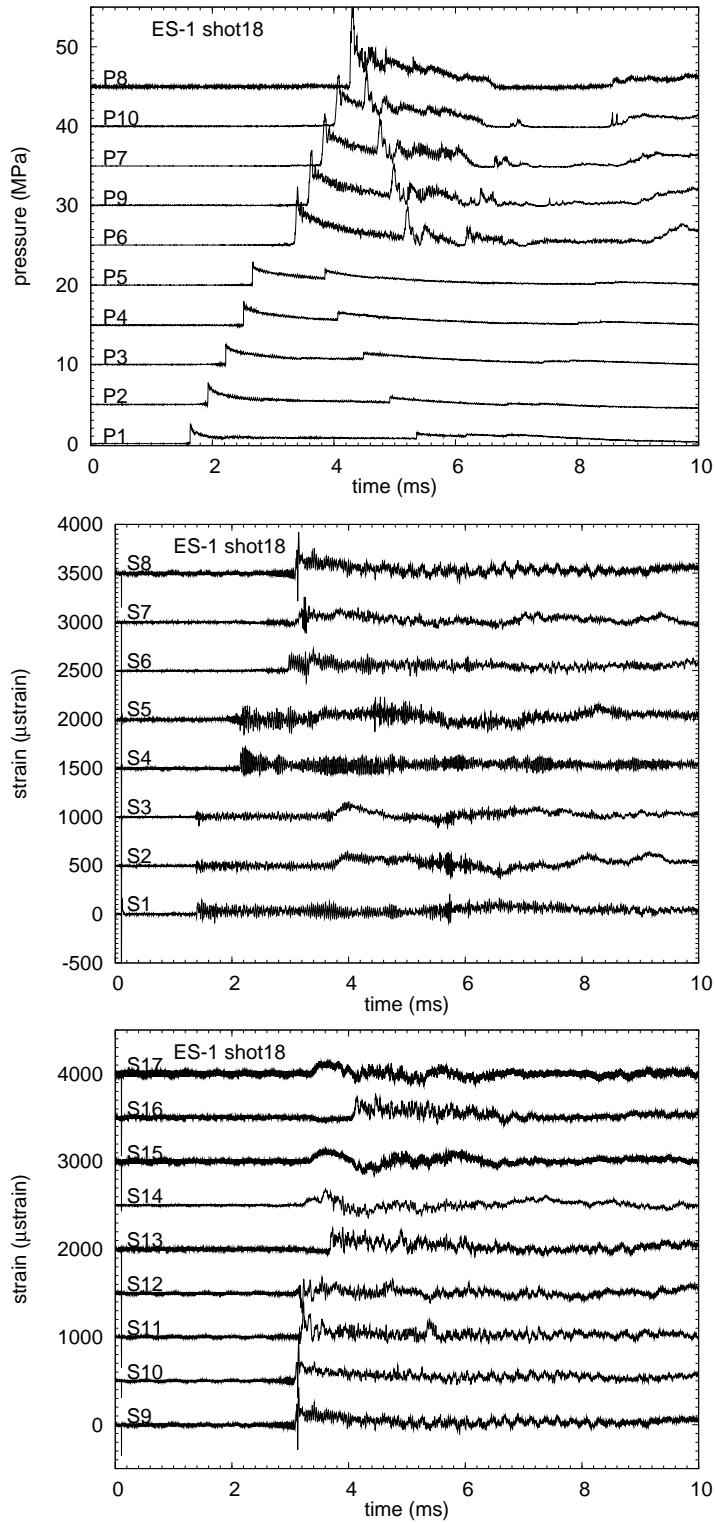


Figure 161: ES1 Shot 18. Pressure and strain gage signals.

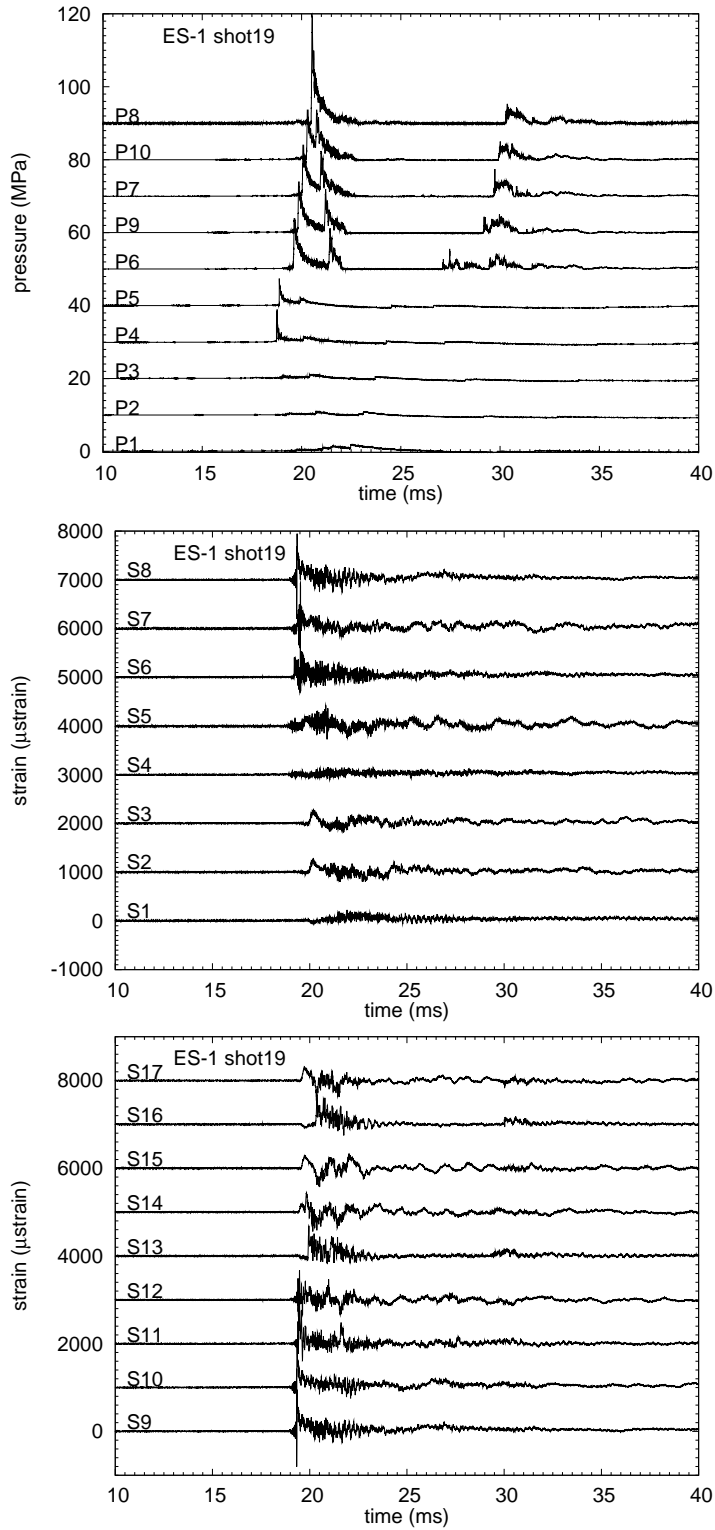


Figure 162: ES1 Shot 19. Pressure and strain gage signals.

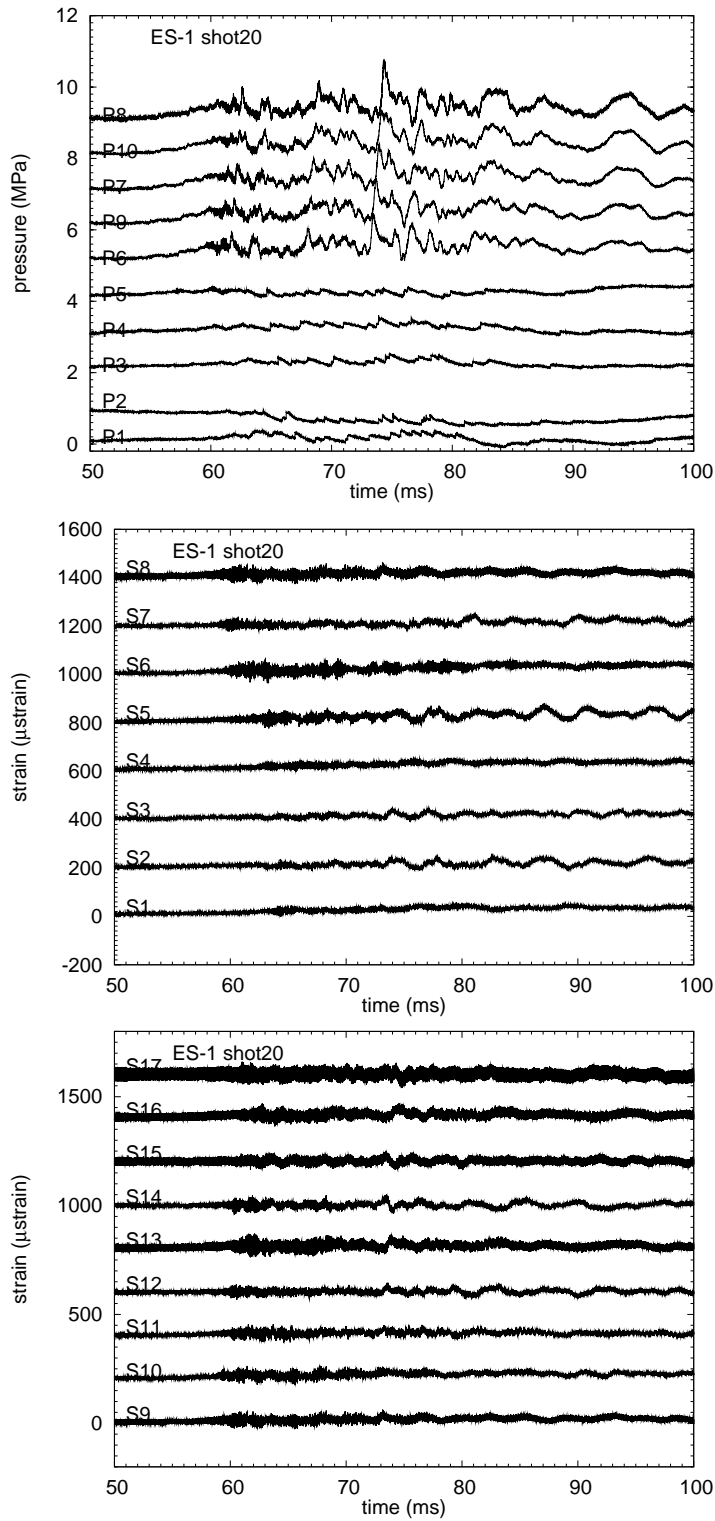


Figure 163: ES1 Shot 20. Pressure and strain gage signals.

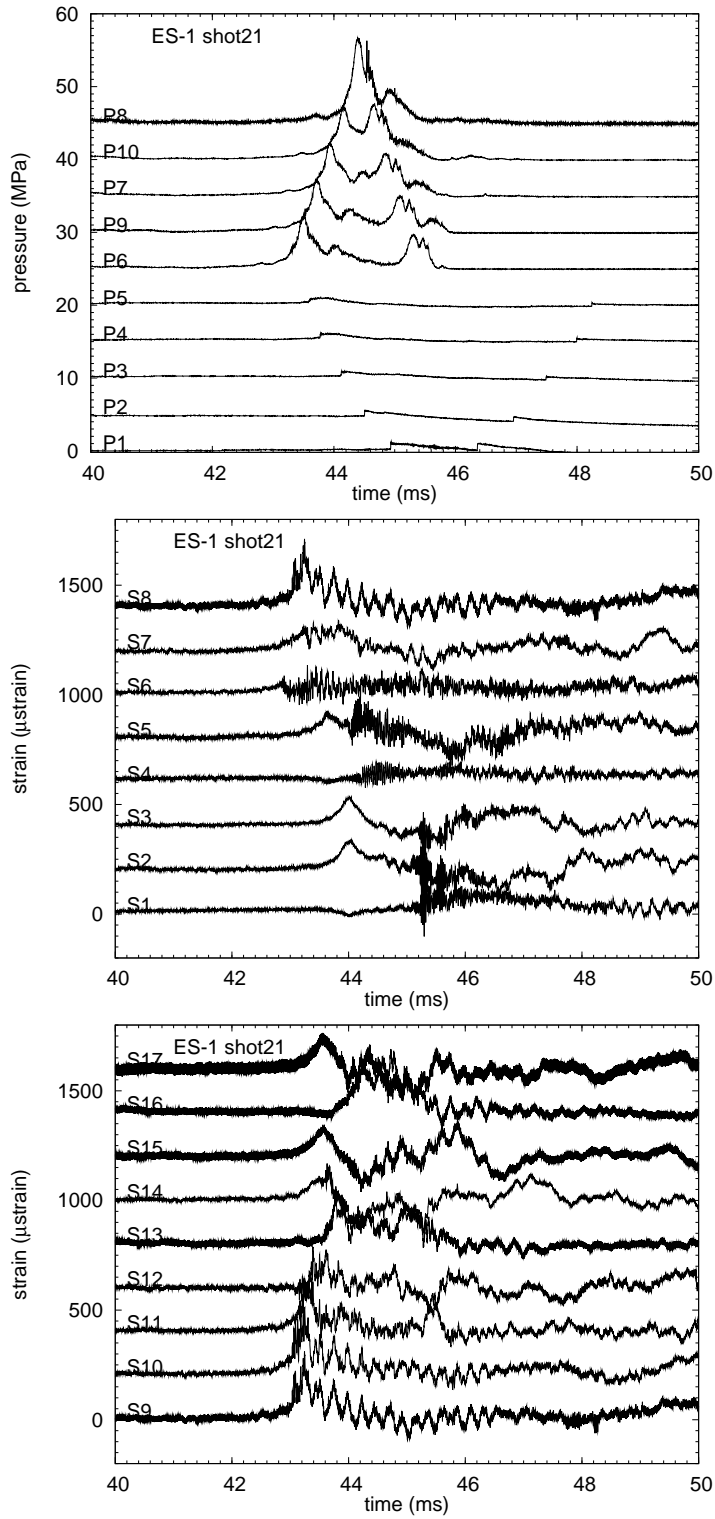


Figure 164: ES1 Shot 21. Pressure and strain gage signals.

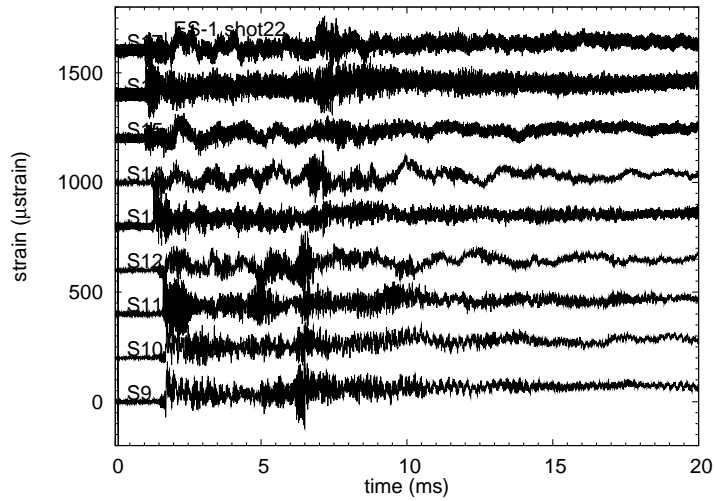
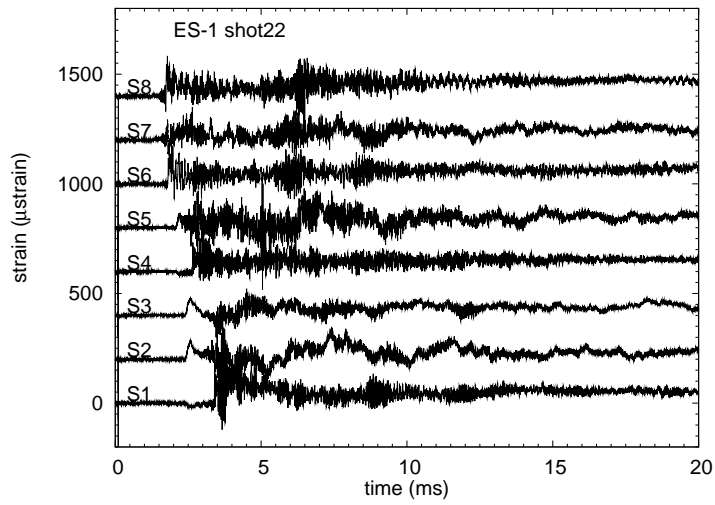
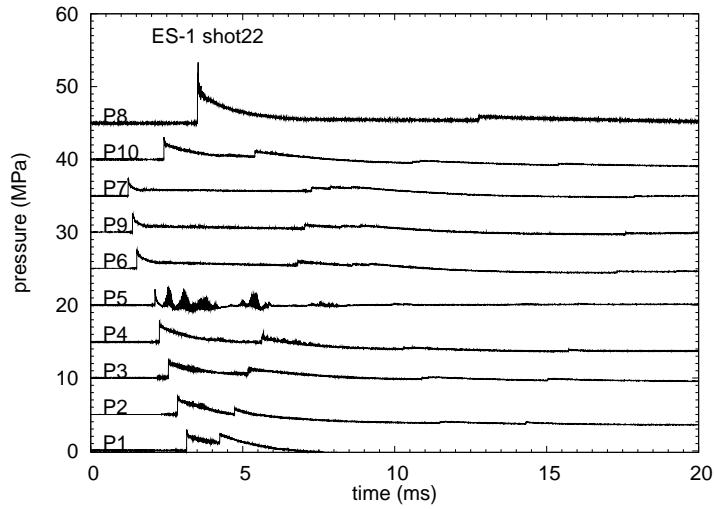


Figure 165: ES1 Shot 22. Pressure and strain gage signals.

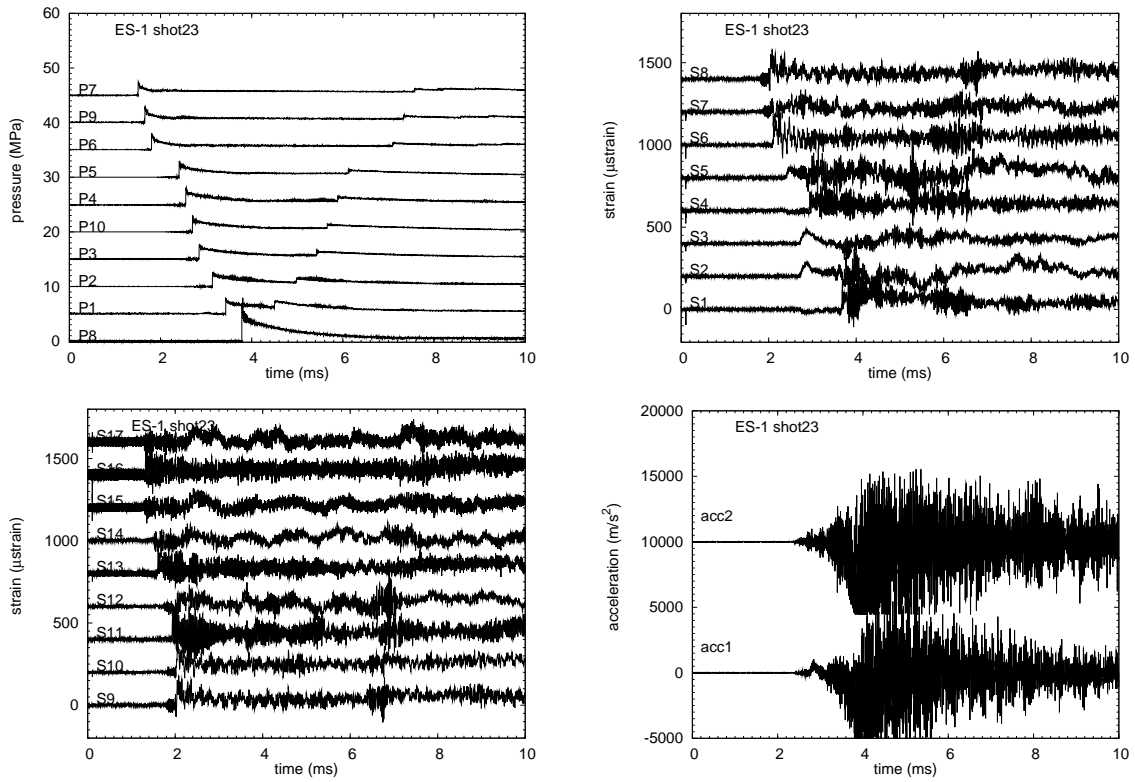


Figure 166: ES1 Shot 23. Pressure and strain gage signals. 10 ms, unfiltered.

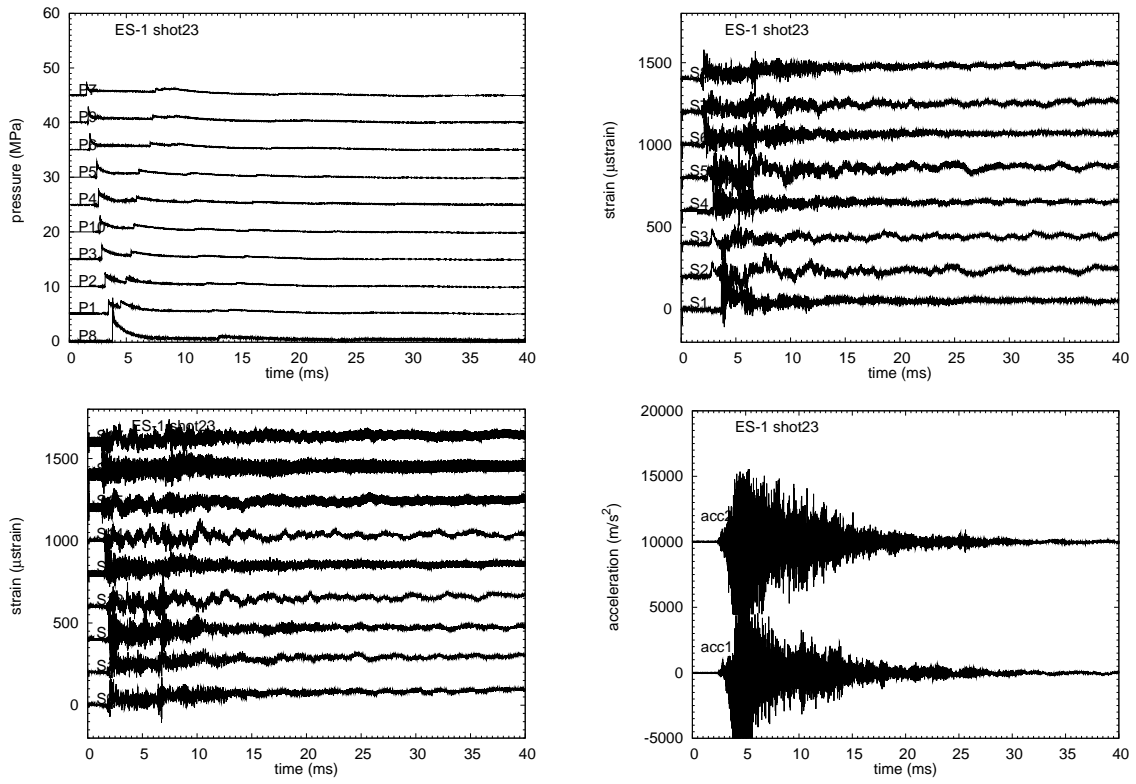


Figure 167: ES1 Shot 23. Pressure and strain gage signals. 40 ms, unfiltered.

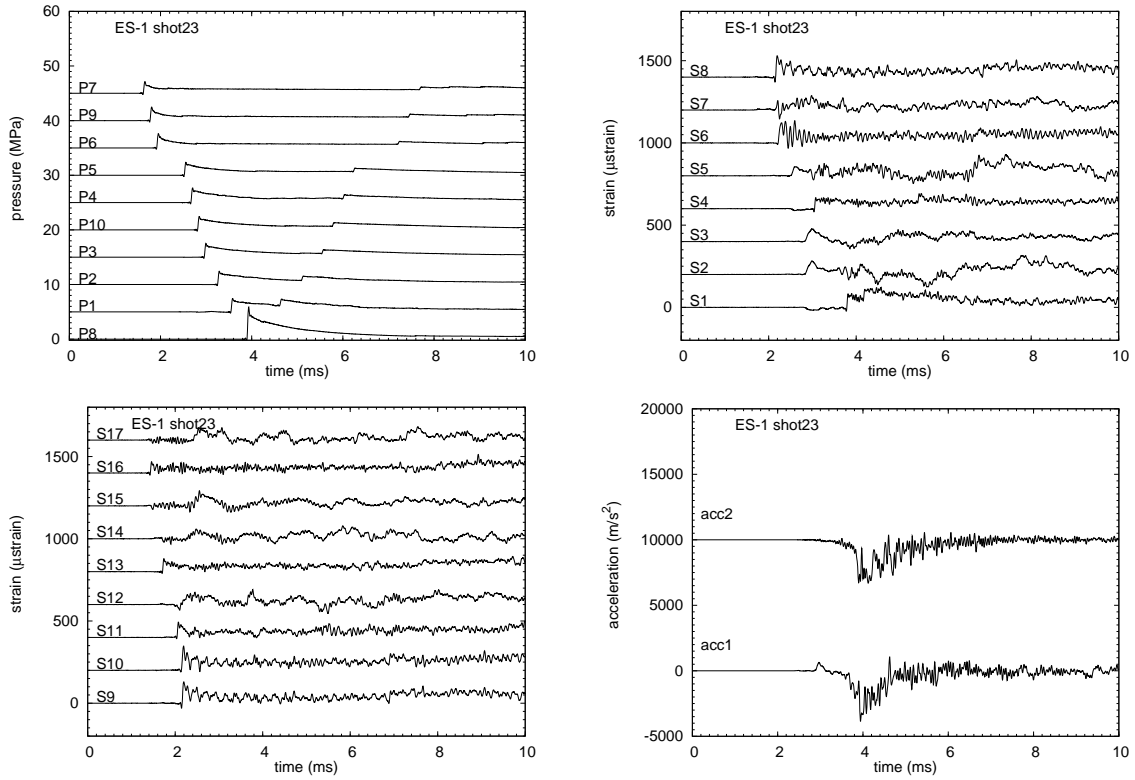


Figure 168: ES1 Shot 23. Pressure and strain gage signals. 10 ms, 20 kHz low-pass filter.

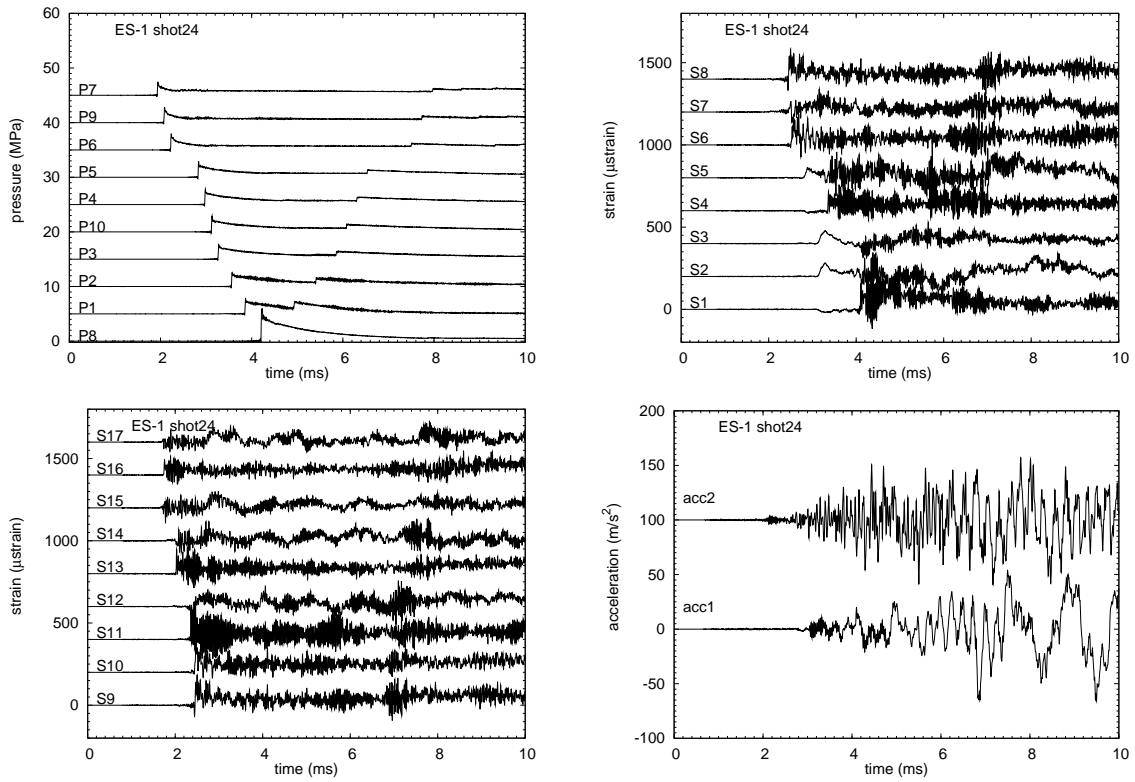


Figure 169: ES1 Shot 24. Pressure, strain gage, and accelerometer signals. 10 ms, 50 kHz low-pass filter.

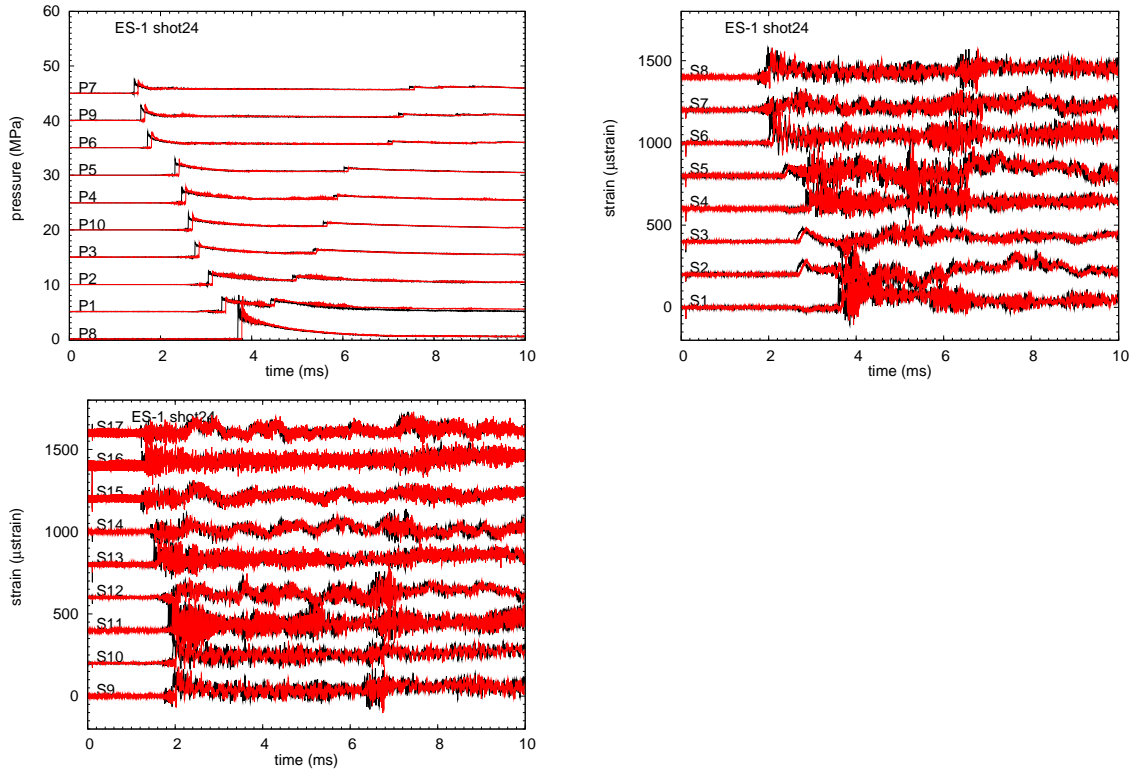


Figure 170: ES1 Shot 24 vs 23. Pressure and strain gage signal comparisons, 10 ms.

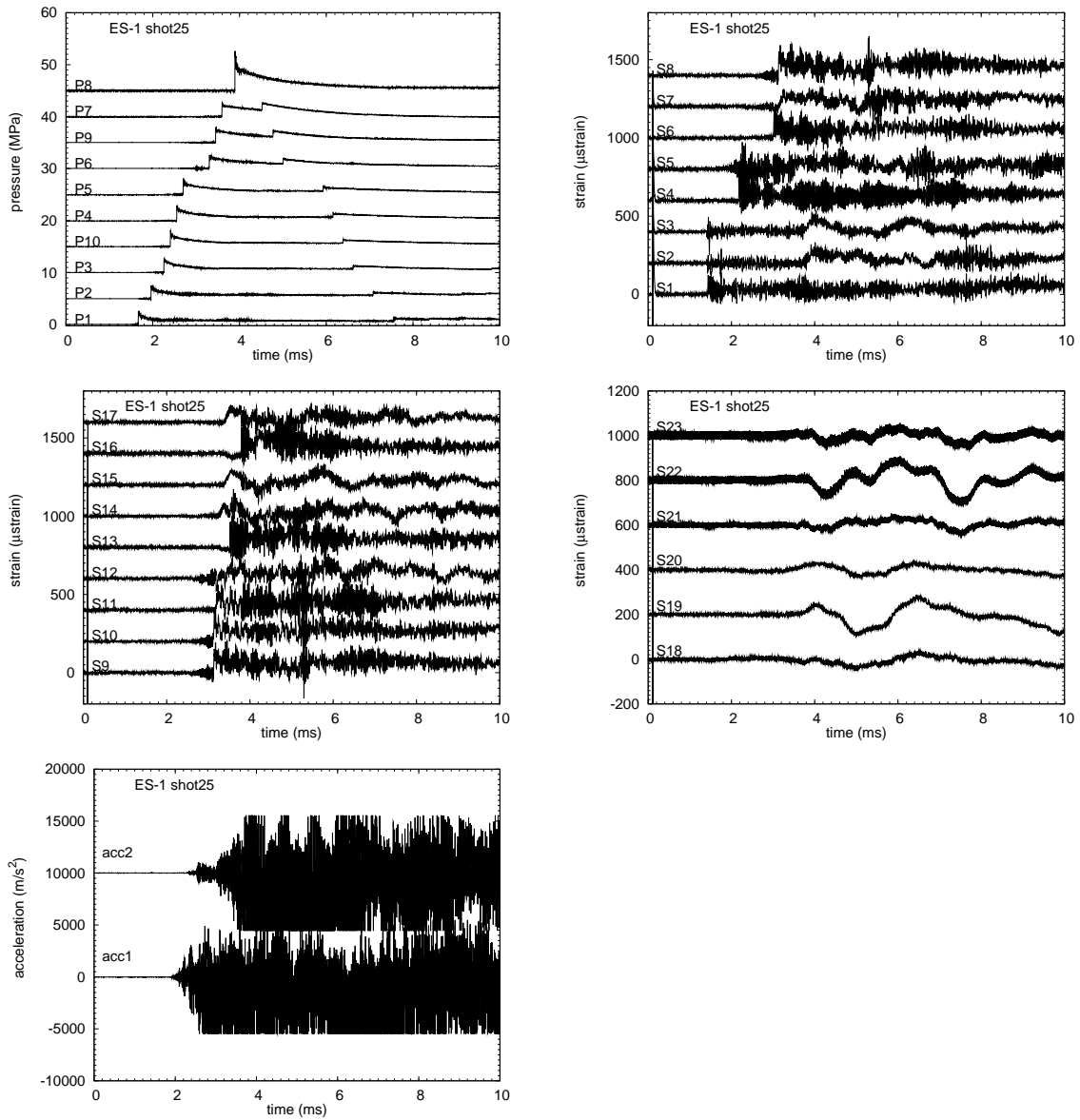


Figure 171: ES1 Shot 25. Pressure, strain gage, and accelerometer signals. 10 ms raw data.

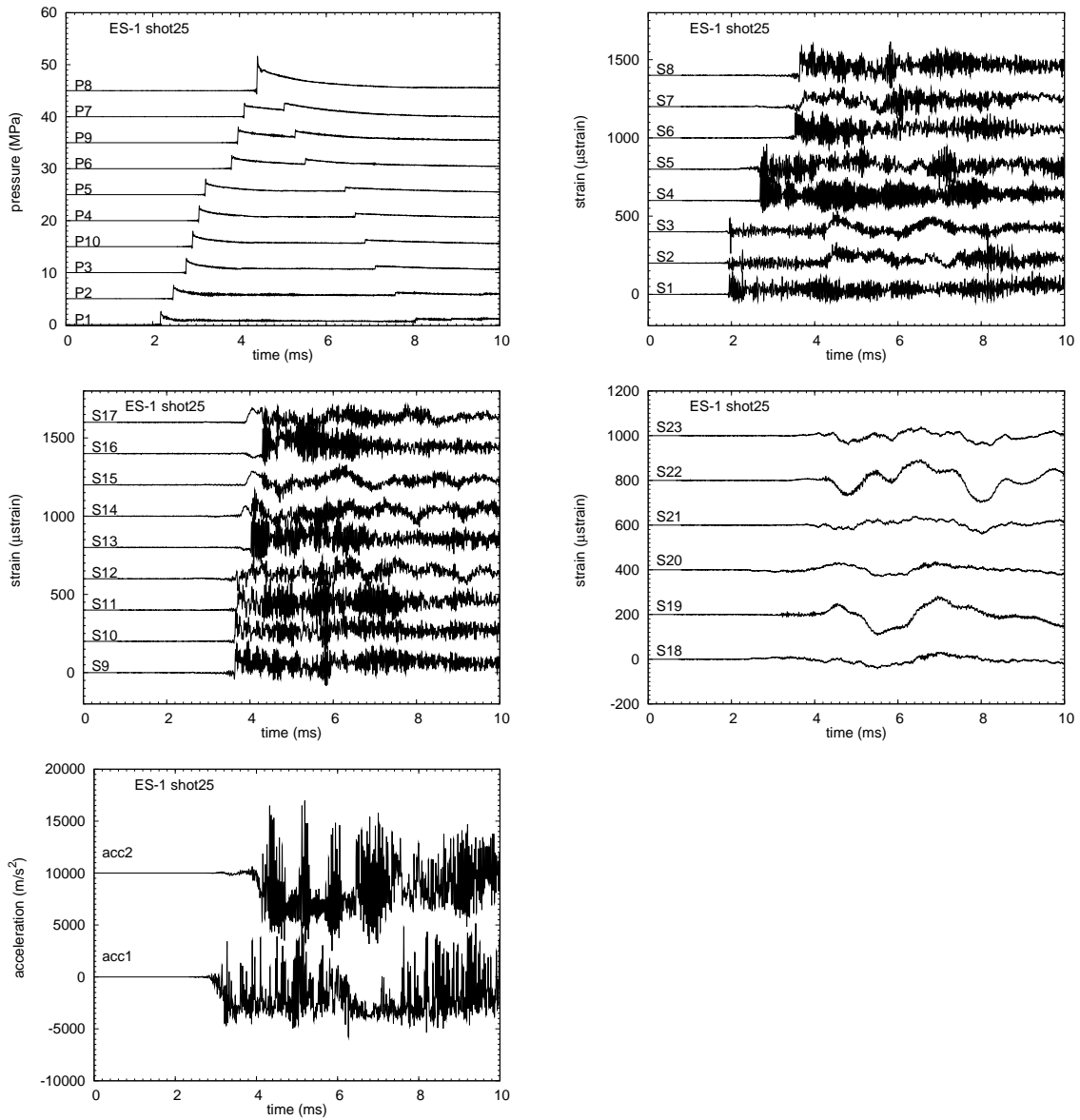


Figure 172: ES1 Shot 25. Pressure, strain gage, and accelerometer signals. 10 ms, 50 kHz low-pass filter.

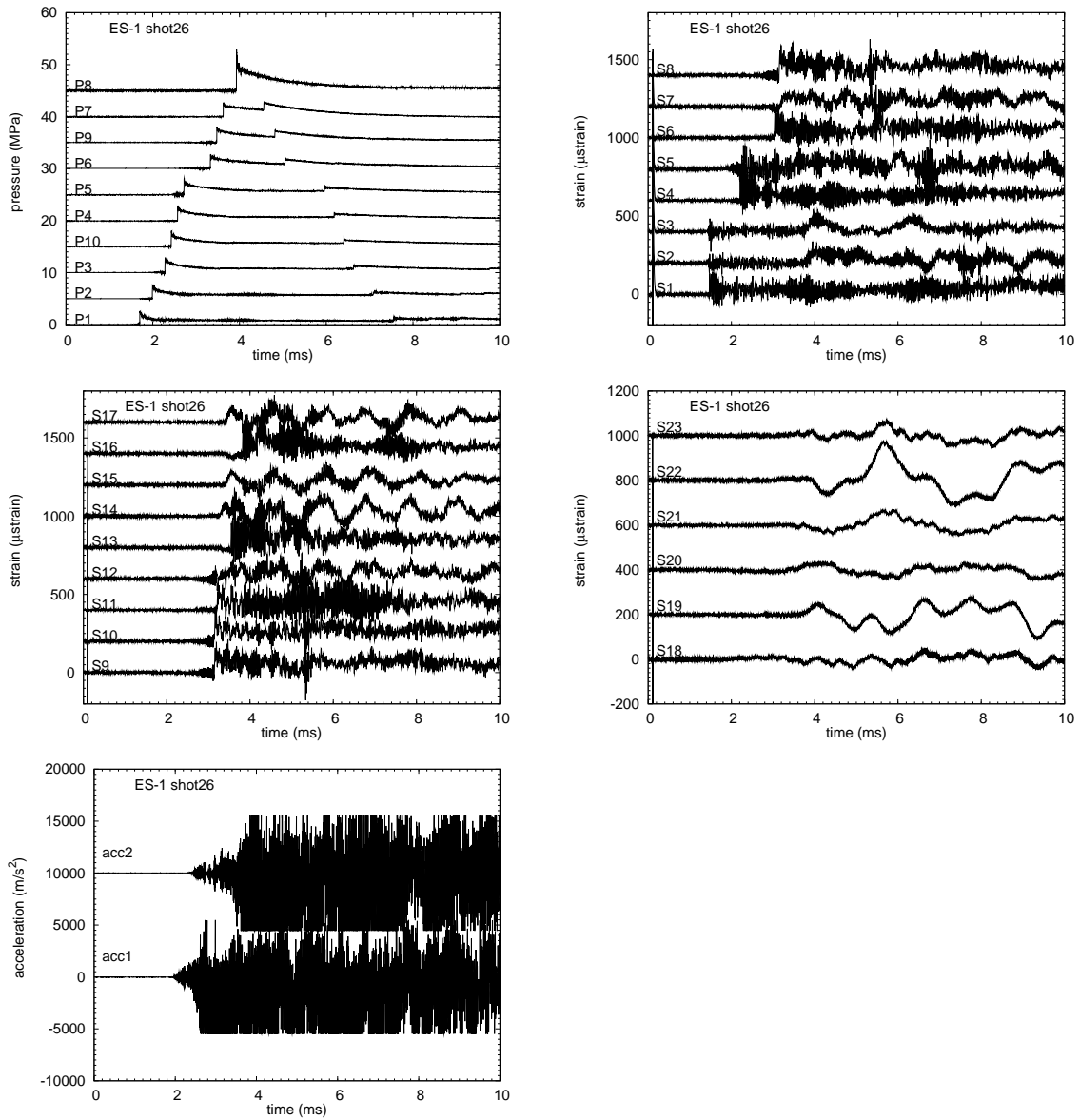


Figure 173: ES1 Shot 26. Pressure, strain gage, and accelerometer signals. 10 ms raw data.

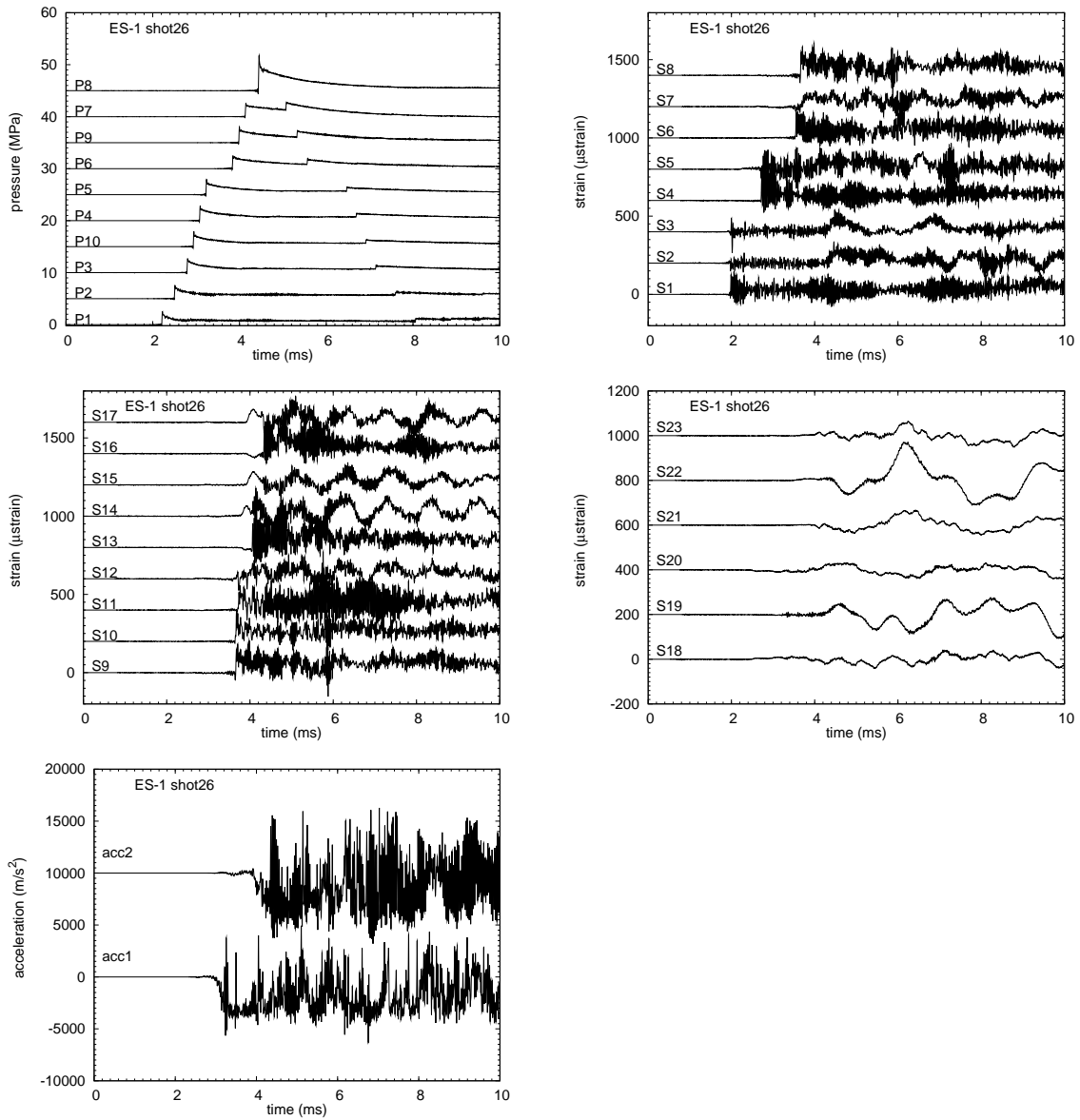


Figure 174: ES1 Shot 26. Pressure, strain gage, and accelerometer signals. 10 ms, 50 kHz low-pass filter.

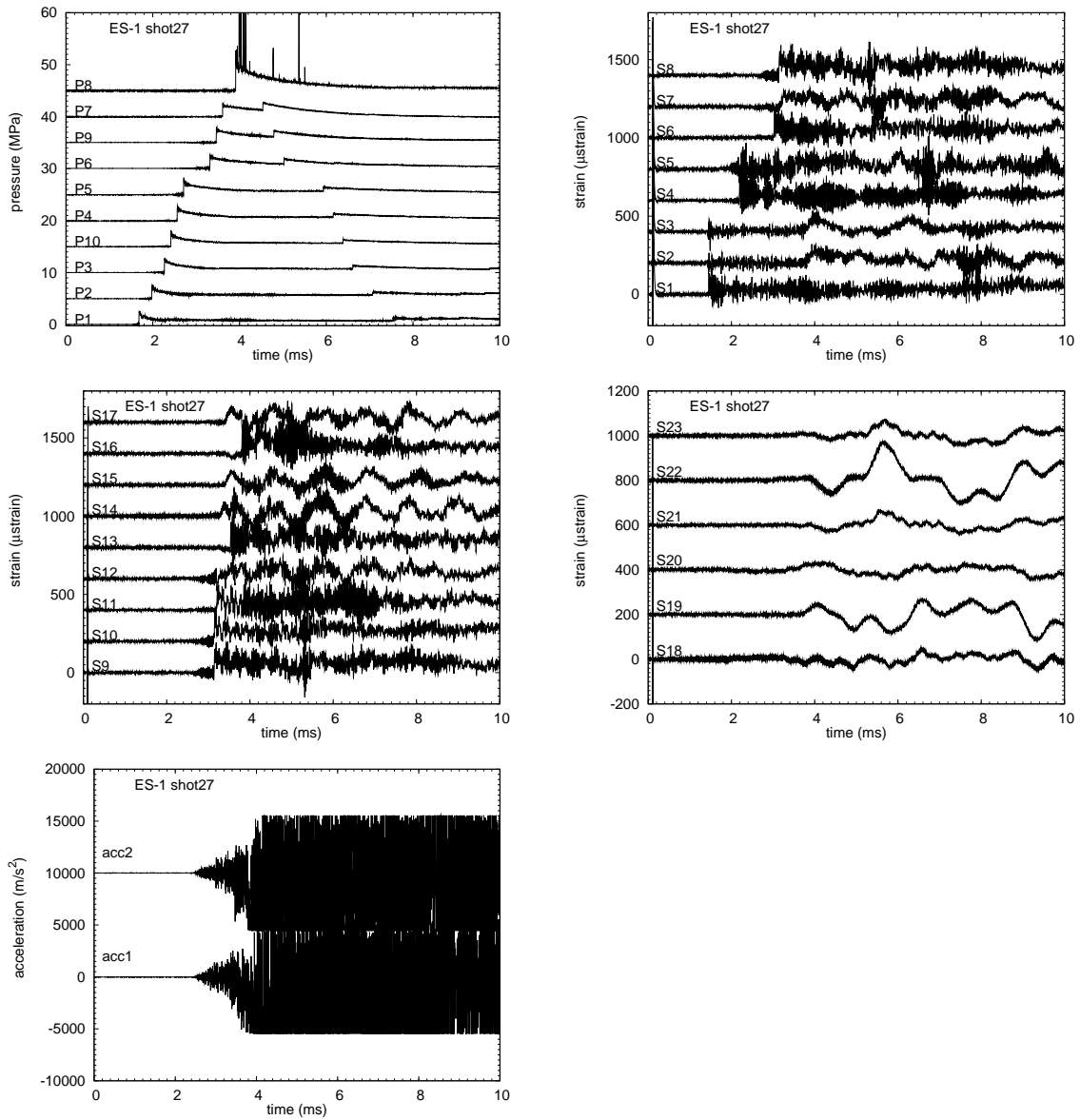


Figure 175: ES1 Shot 27. Pressure, strain gage, and accelerometer signals. 10 ms raw data.

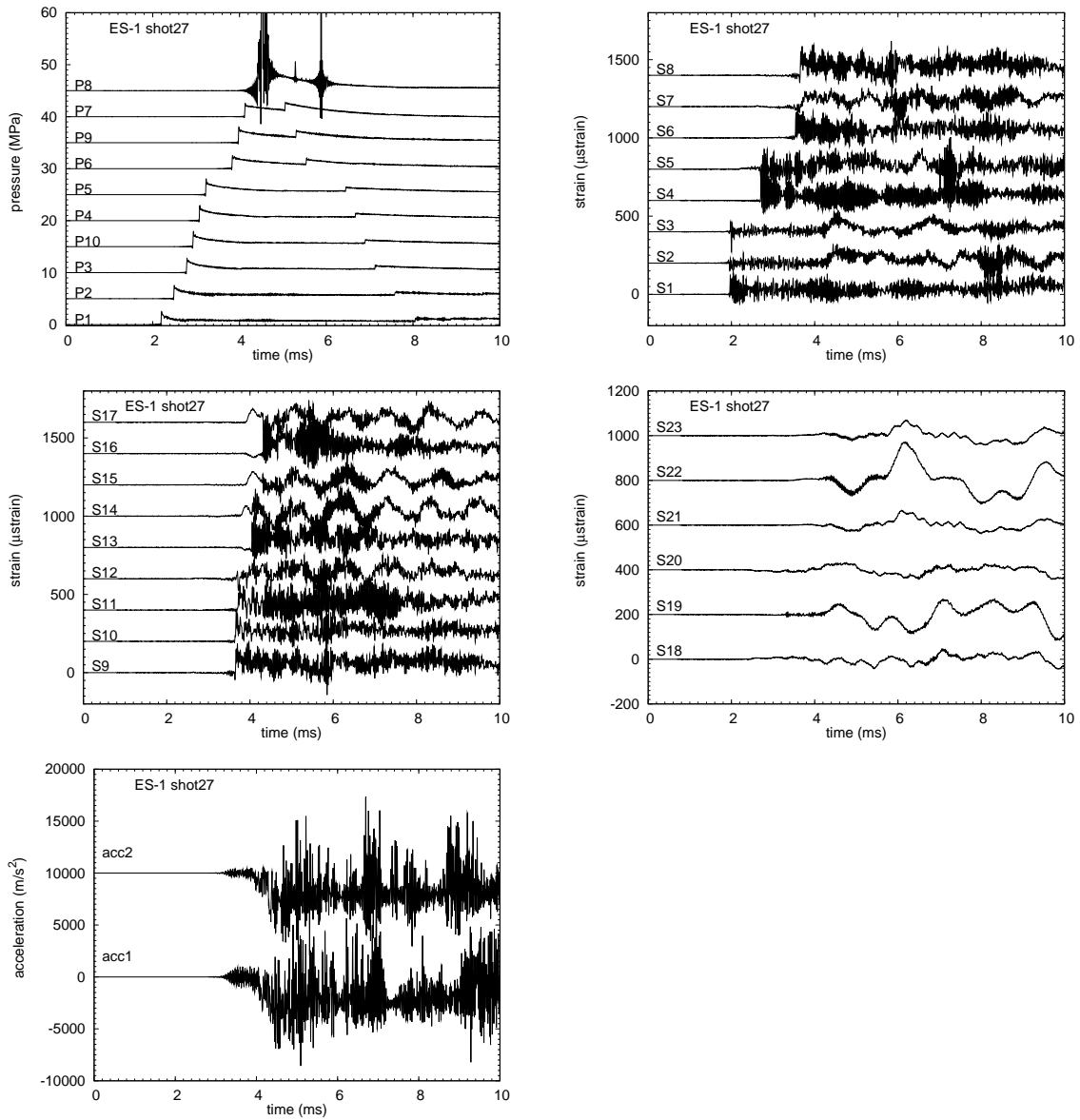


Figure 176: ES1 Shot 27. Pressure, strain gage, and accelerometer signals. 10 ms, 50 kHz low-pass filter.

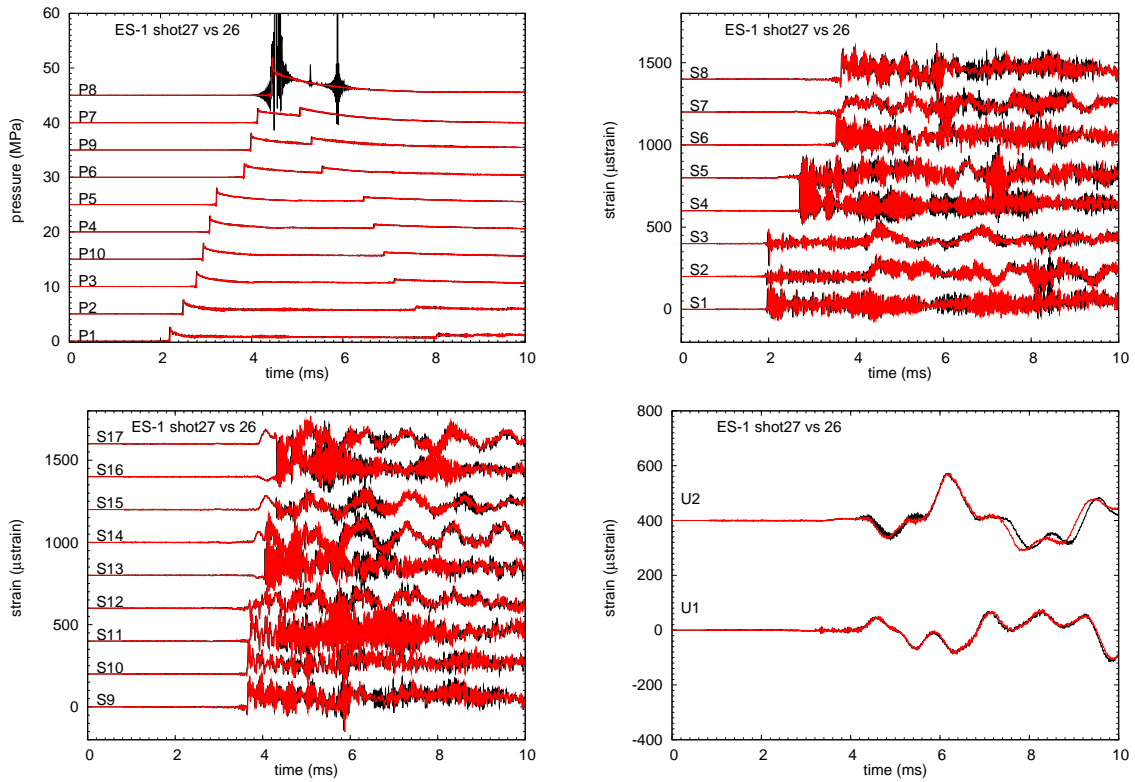


Figure 177: ES1 Shot 27 vs 26. Pressure, strain gage, and accelerometer signals. 10 ms, 50 kHz low-pass filter.

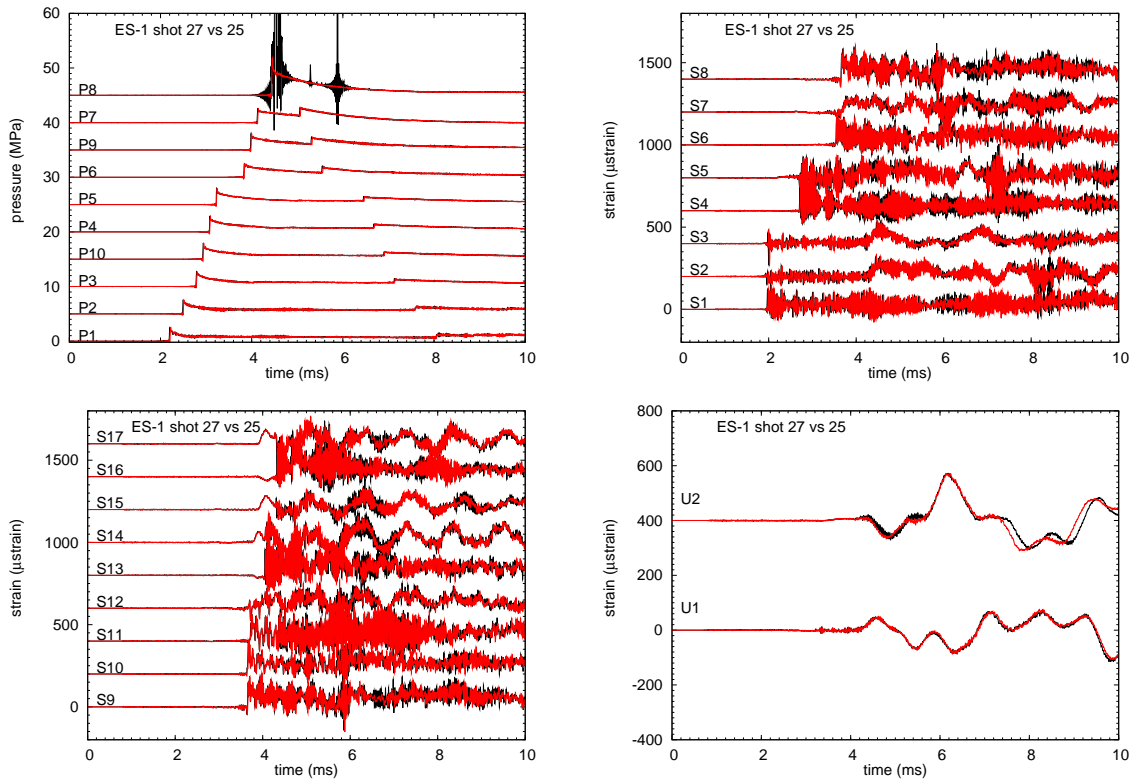


Figure 178: ES1 Shot 27 vs 25. Pressure, strain gage, and accelerometer signals. 10 ms, 50 kHz low-pass filter.

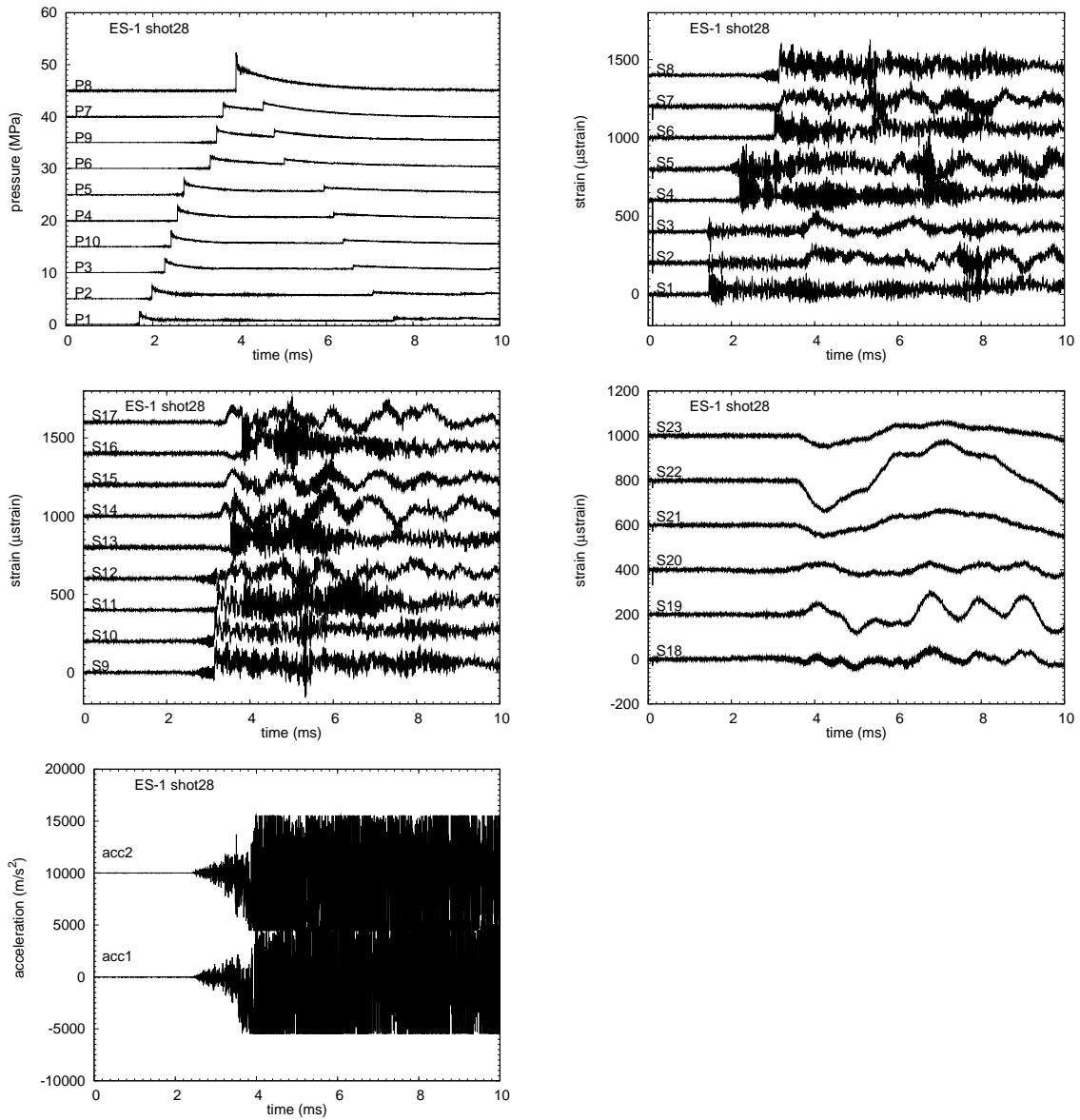


Figure 179: ES1 Shot 28. Pressure, strain gage, and accelerometer signals. 10 ms raw data.

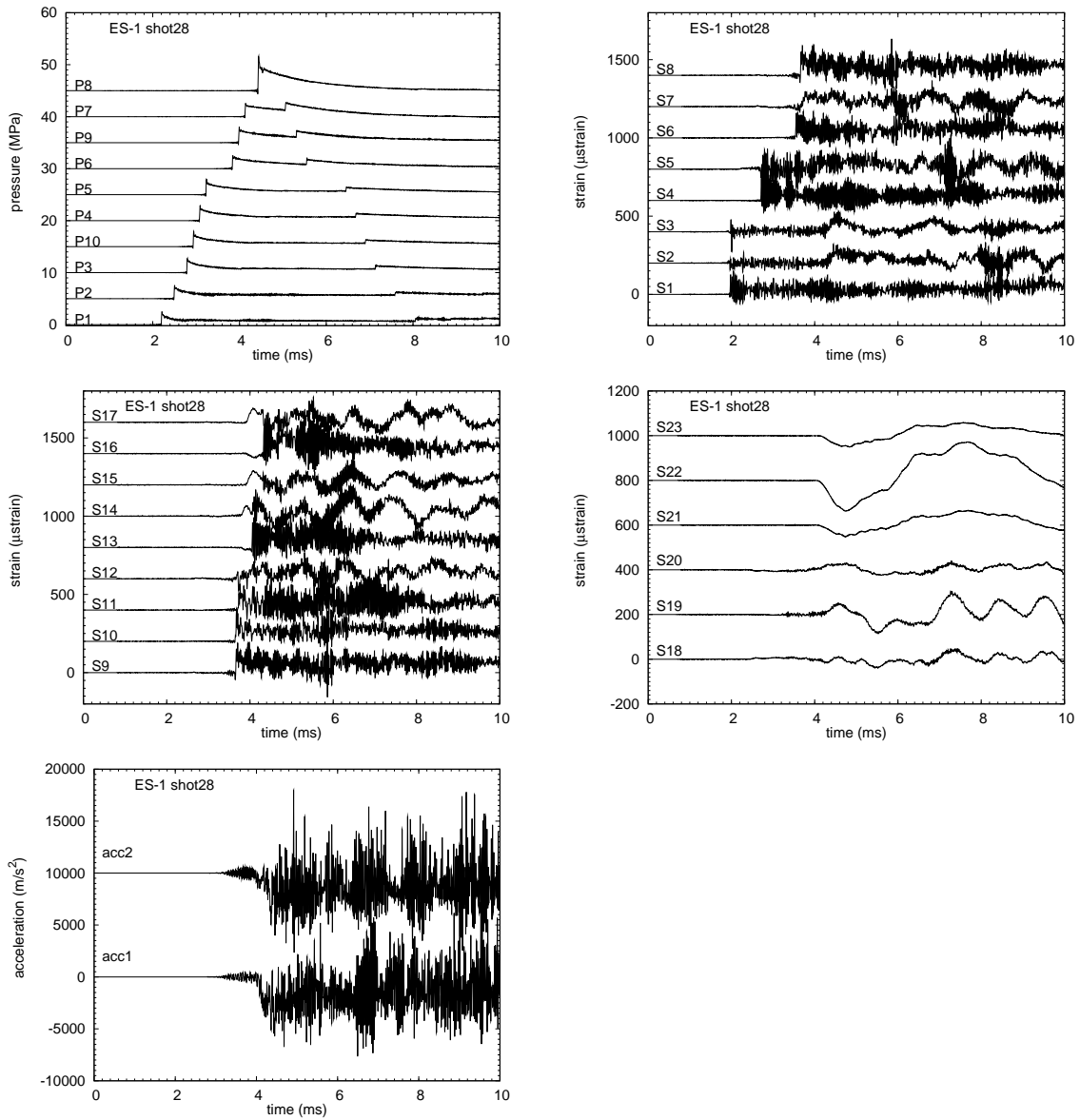


Figure 180: ES1 Shot 28. Pressure, strain gage, and accelerometer signals. 10 ms, 50 kHz low-pass filter.

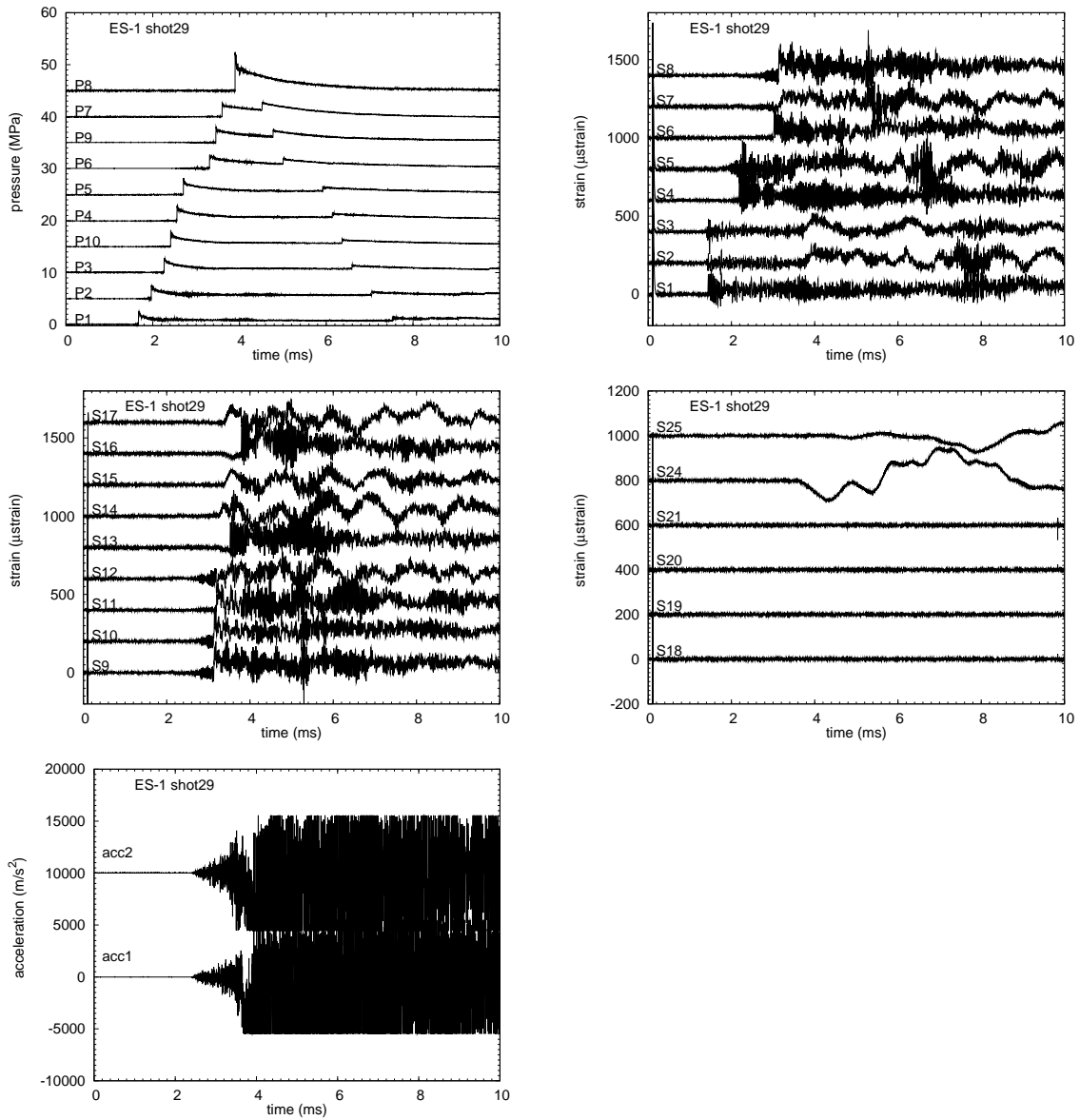


Figure 181: ES1 Shot 29. Pressure, strain gage, and accelerometer signals. 10 ms raw data.

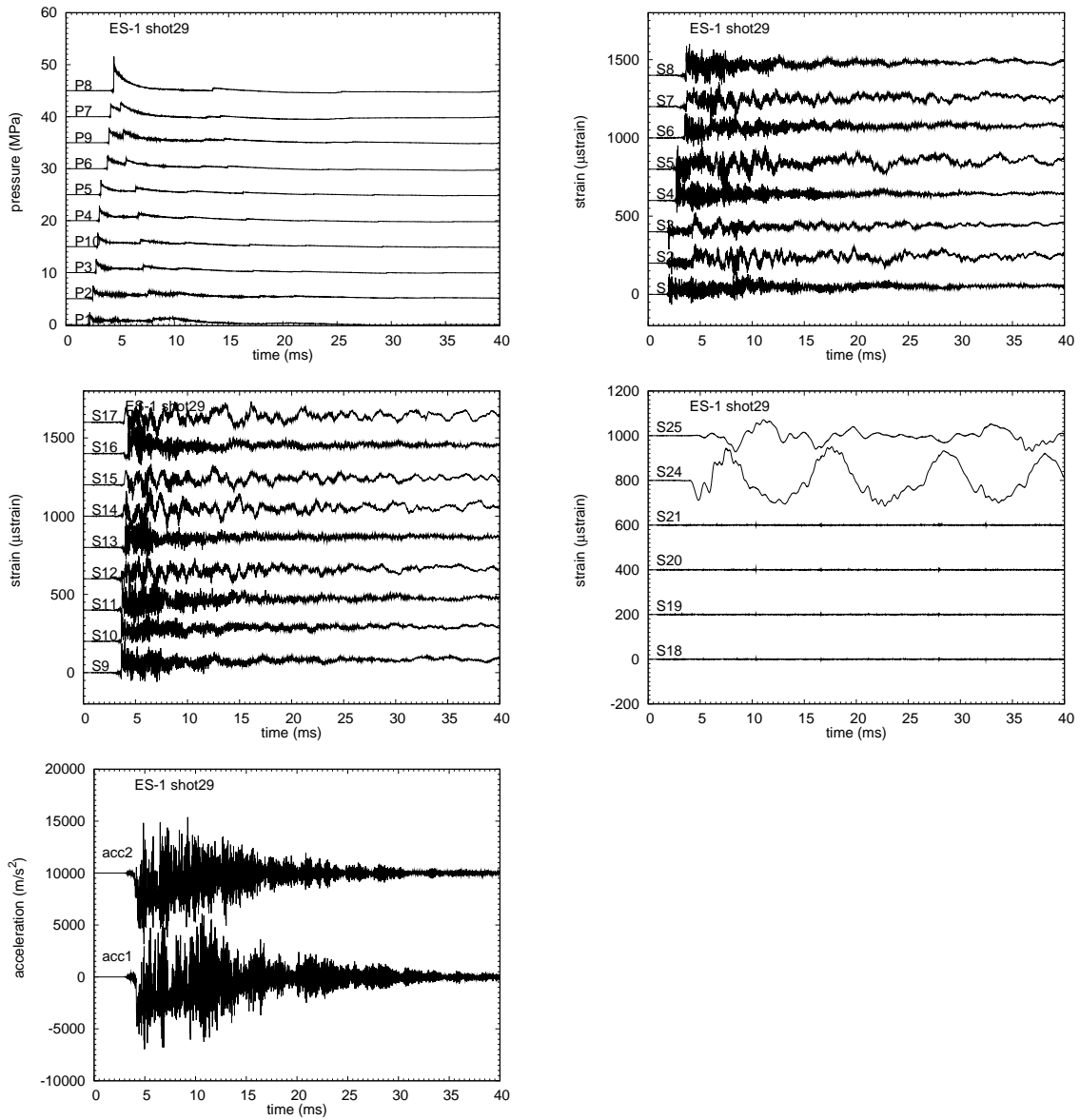


Figure 182: ES1 Shot 29. Pressure, strain gage, and accelerometer signals. 40 ms, 50 kHz low-pass filter.

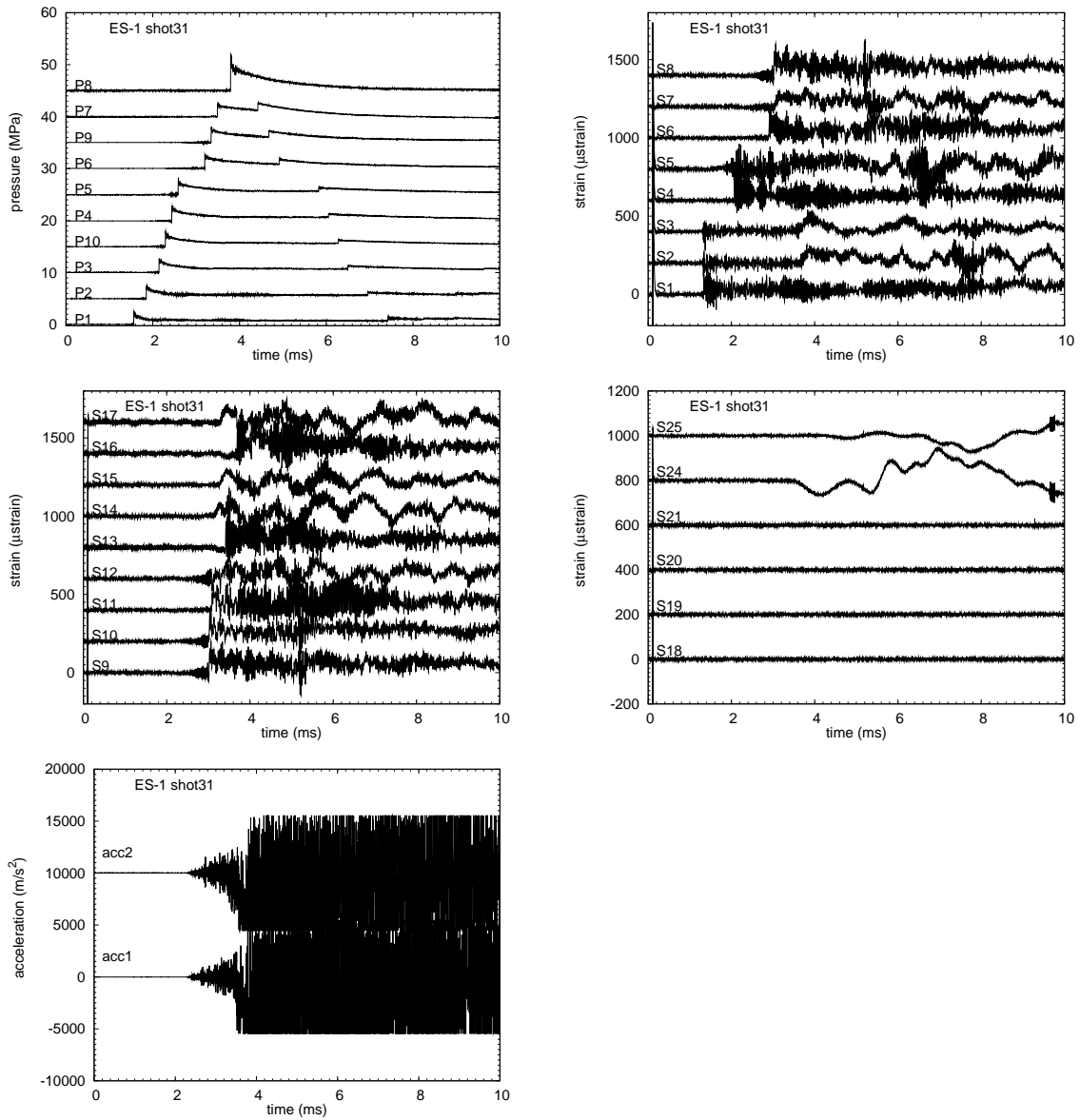


Figure 183: ES1 Shot 31. Pressure, strain gage, and accelerometer signals. 10 ms raw data.

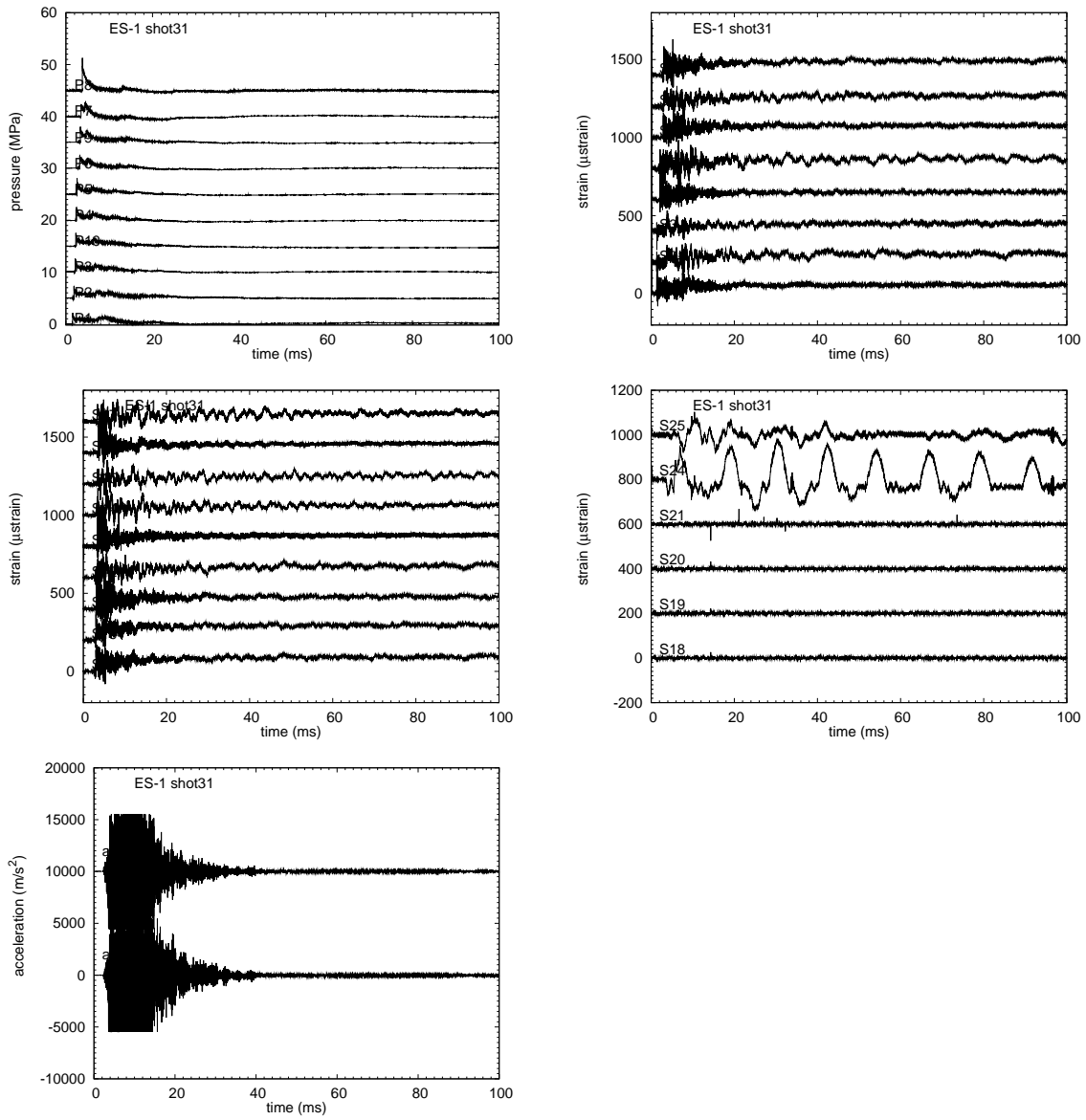


Figure 184: ES1 Shot 31. Pressure, strain gage, and accelerometer signals. 100 ms raw data.

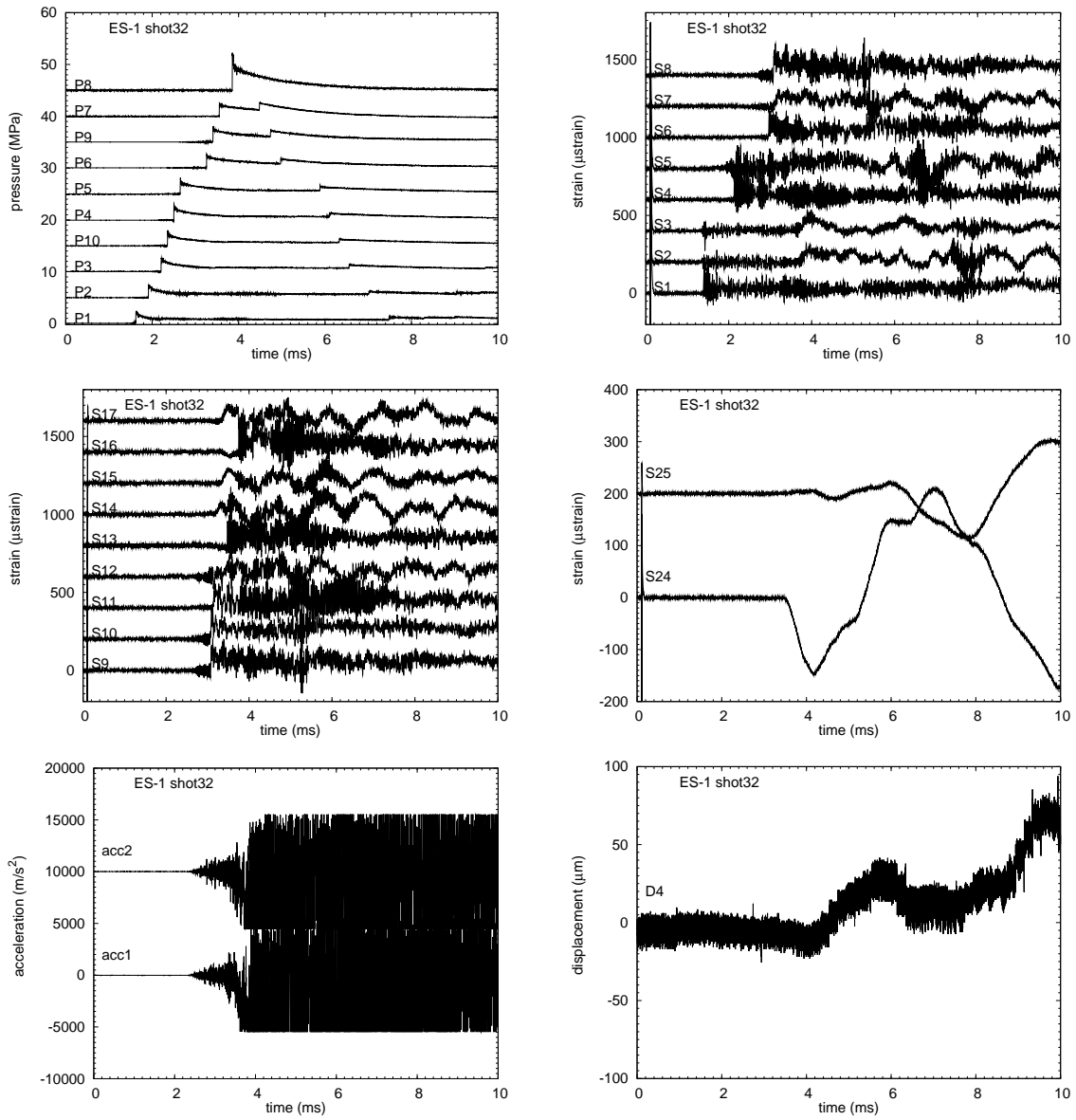


Figure 185: ES1 Shot 32. Pressure, strain gage, accelerometer signals. 10 ms raw data.

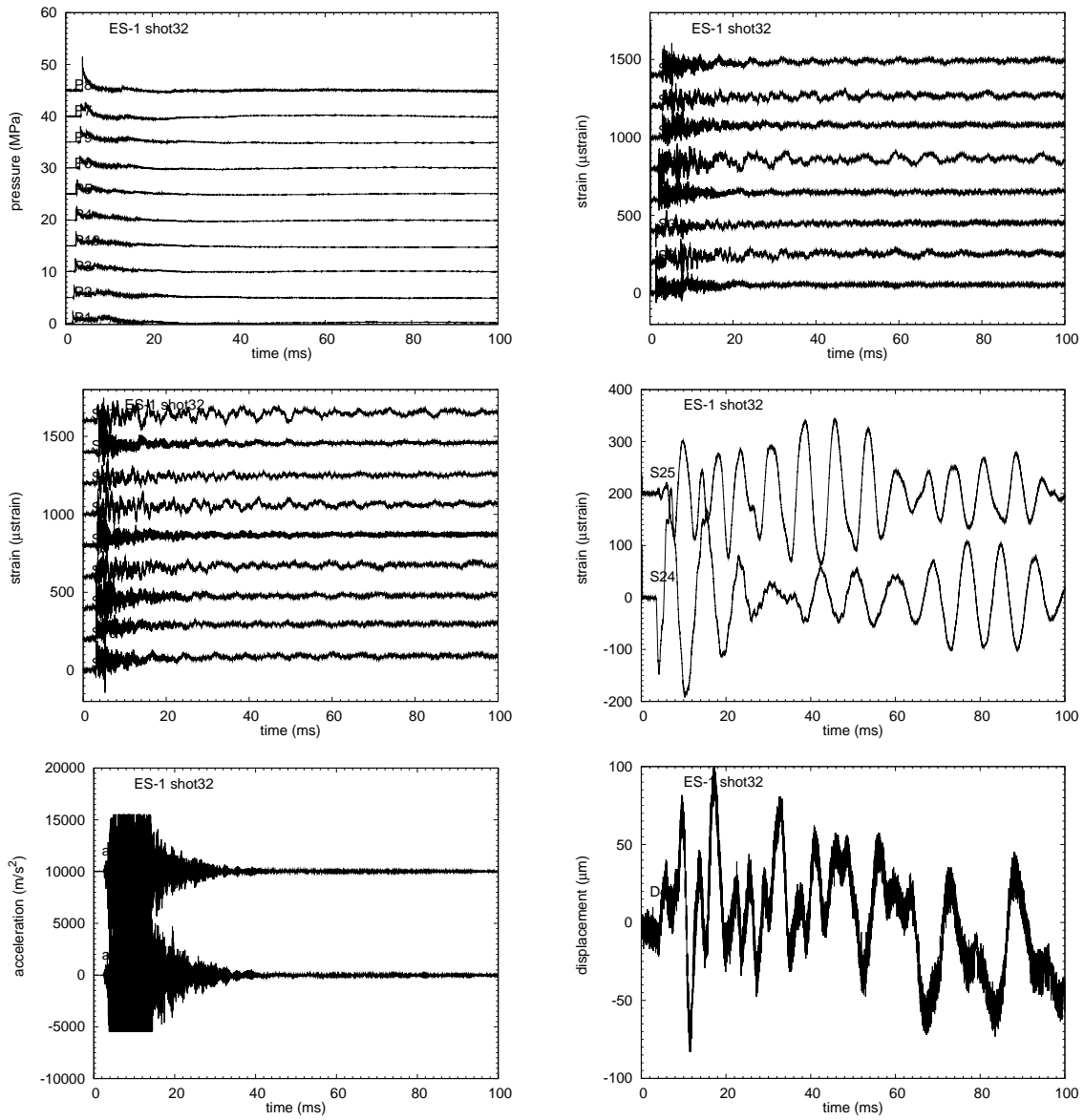


Figure 186: ES1 Shot 32. Pressure, strain gage, accelerometer, and displacement signals. 100 ms raw data.

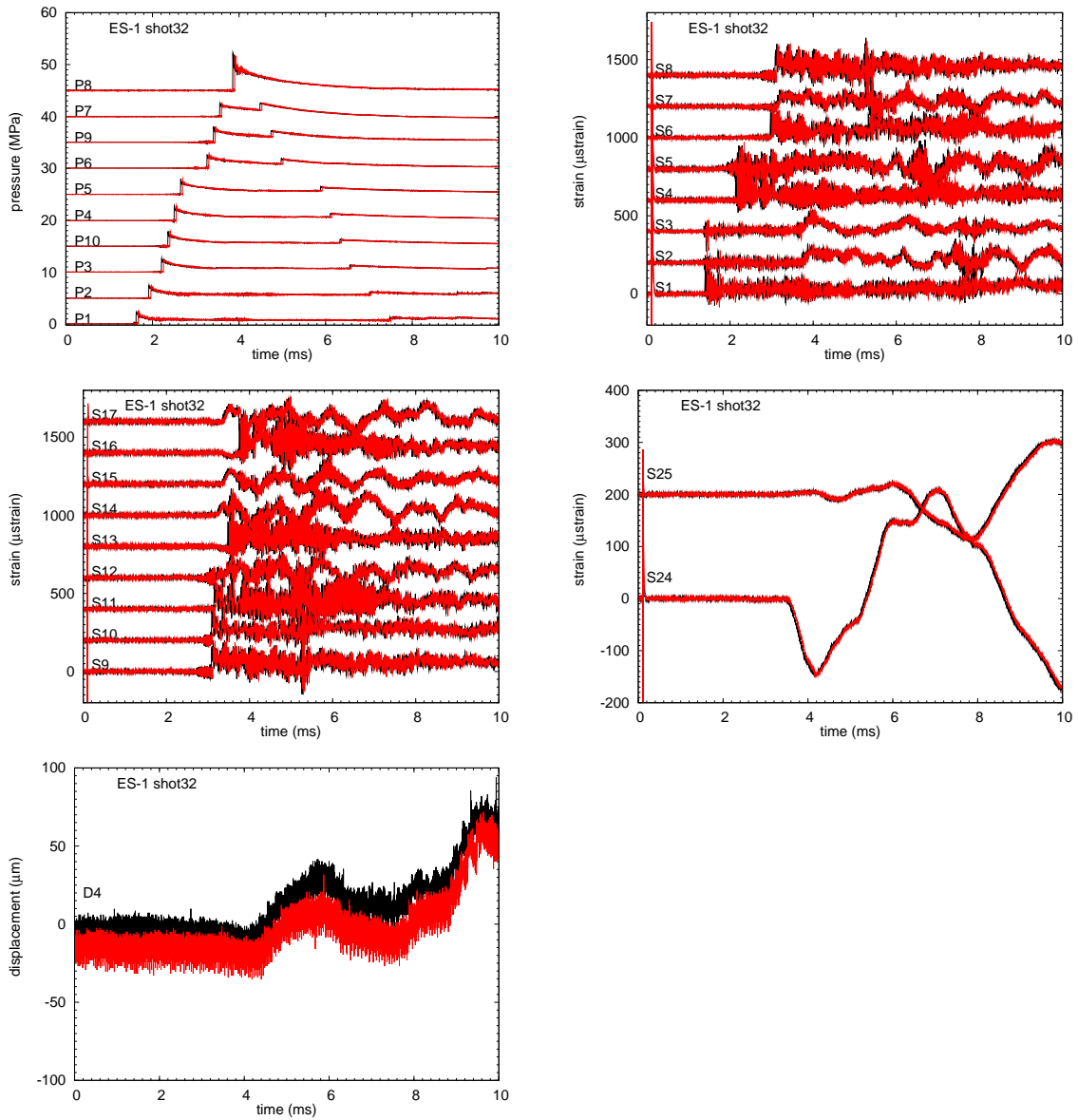


Figure 187: ES1 Shot 32 vs 33. Pressure, strain gage, and displacement signals. 10 ms raw data.

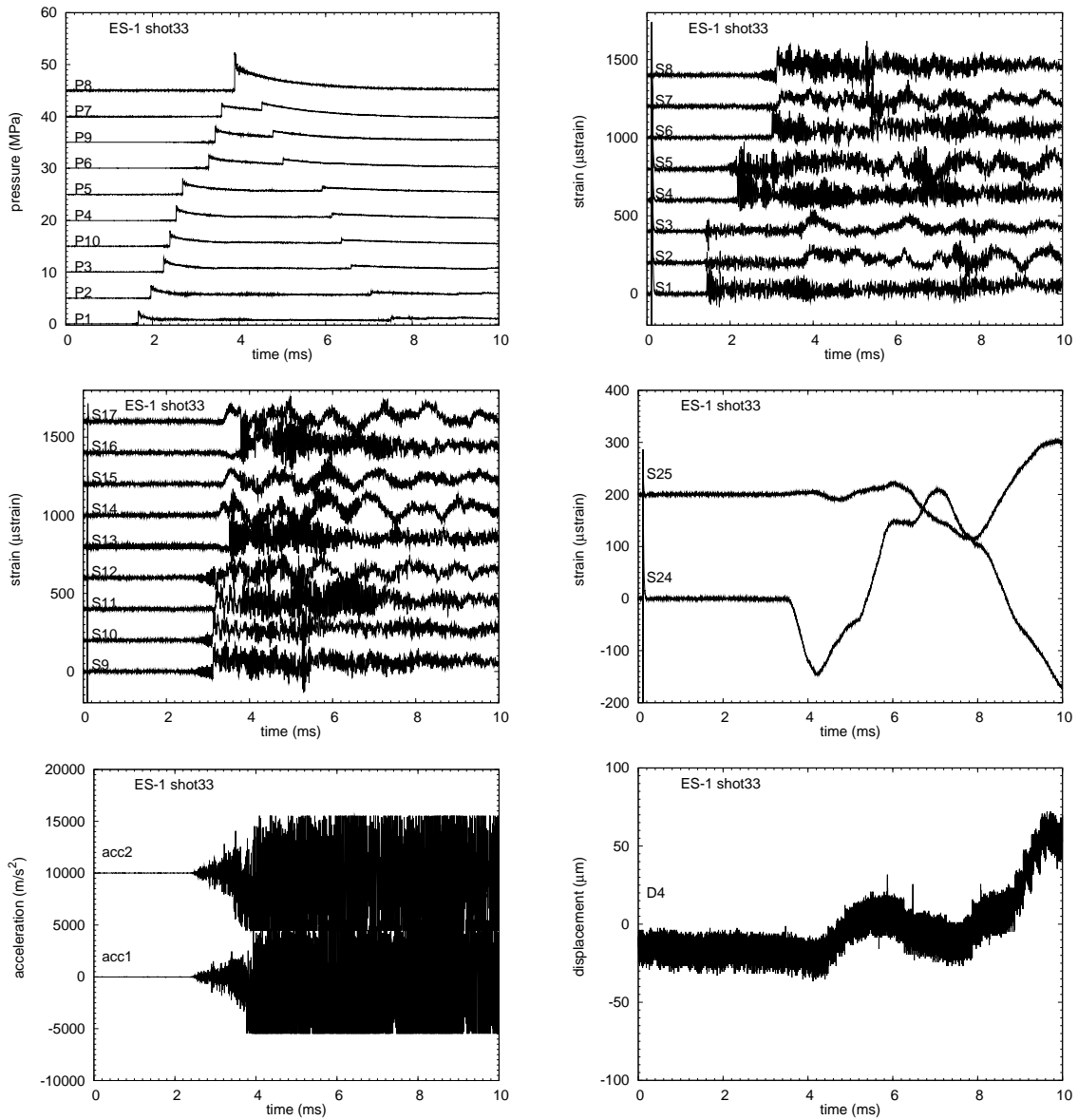


Figure 188: ES1 Shot 33. Pressure, strain gage, accelerometer signals. 10 ms raw data.

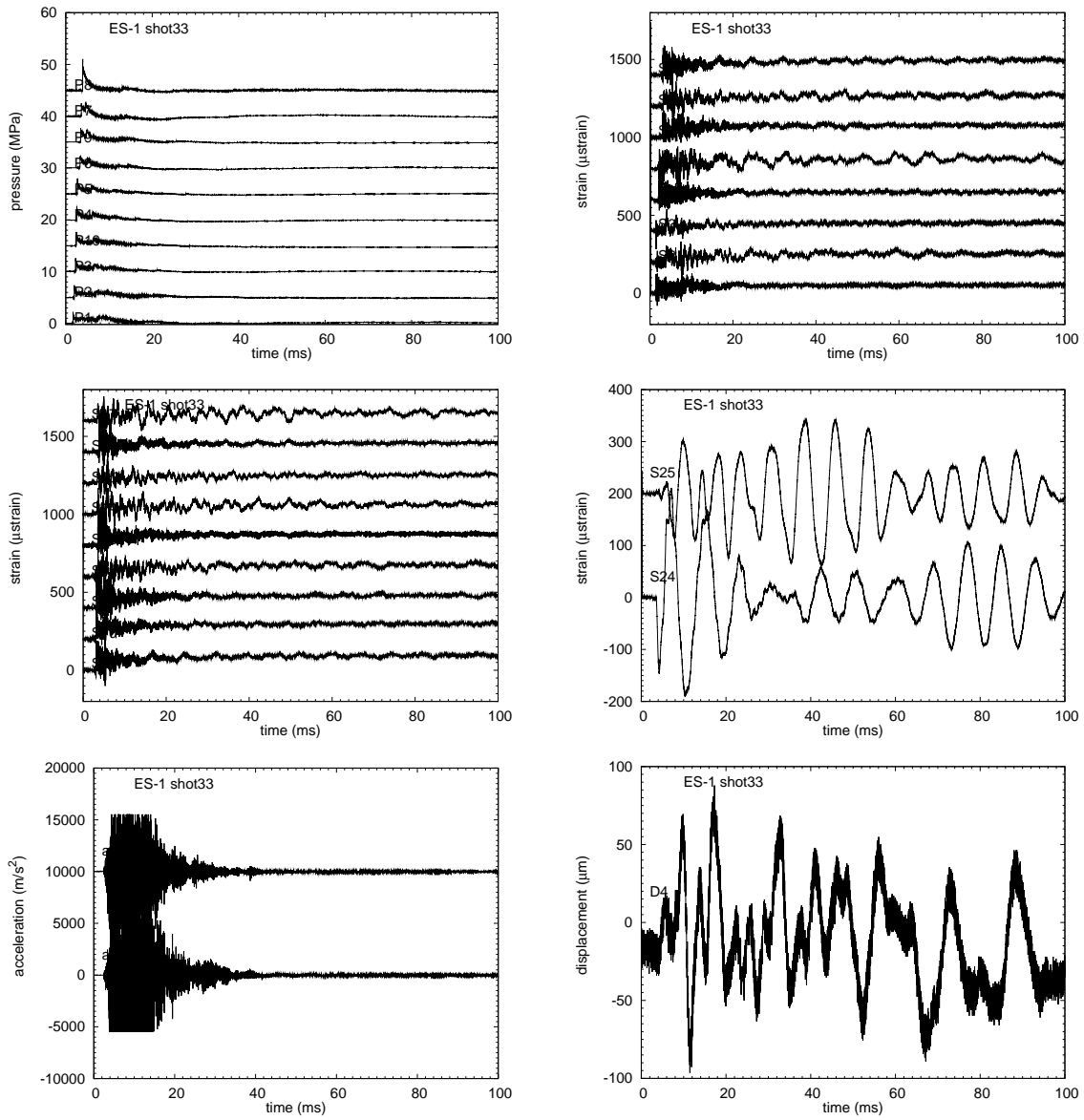


Figure 189: ES1 Shot 33. Pressure, strain gage, accelerometer, and displacement signals. 100 ms raw data.

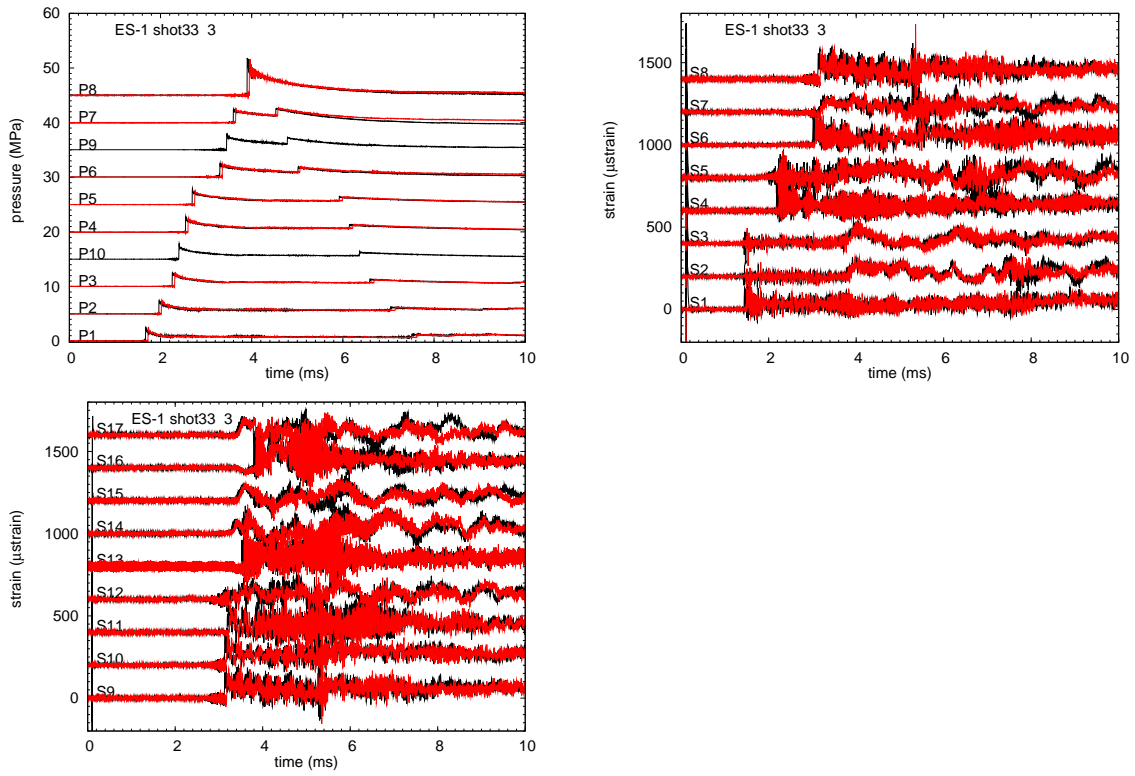


Figure 190: ES1 Shot 33 vs 3. Pressure, strain gage, and displacement signals. 10 ms raw data.

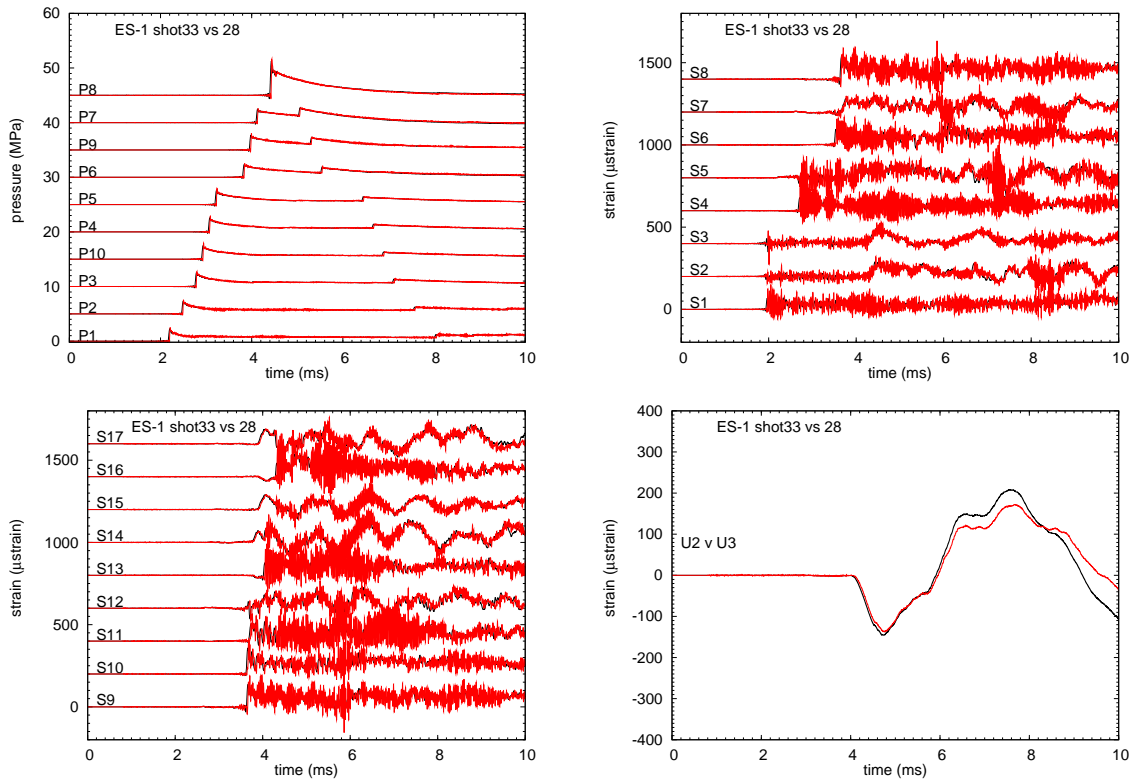


Figure 191: ES1 Shot 33 vs 28. Pressure, strain gage, and displacement signals. 10 ms, 50 kHz low-pass filtered data.

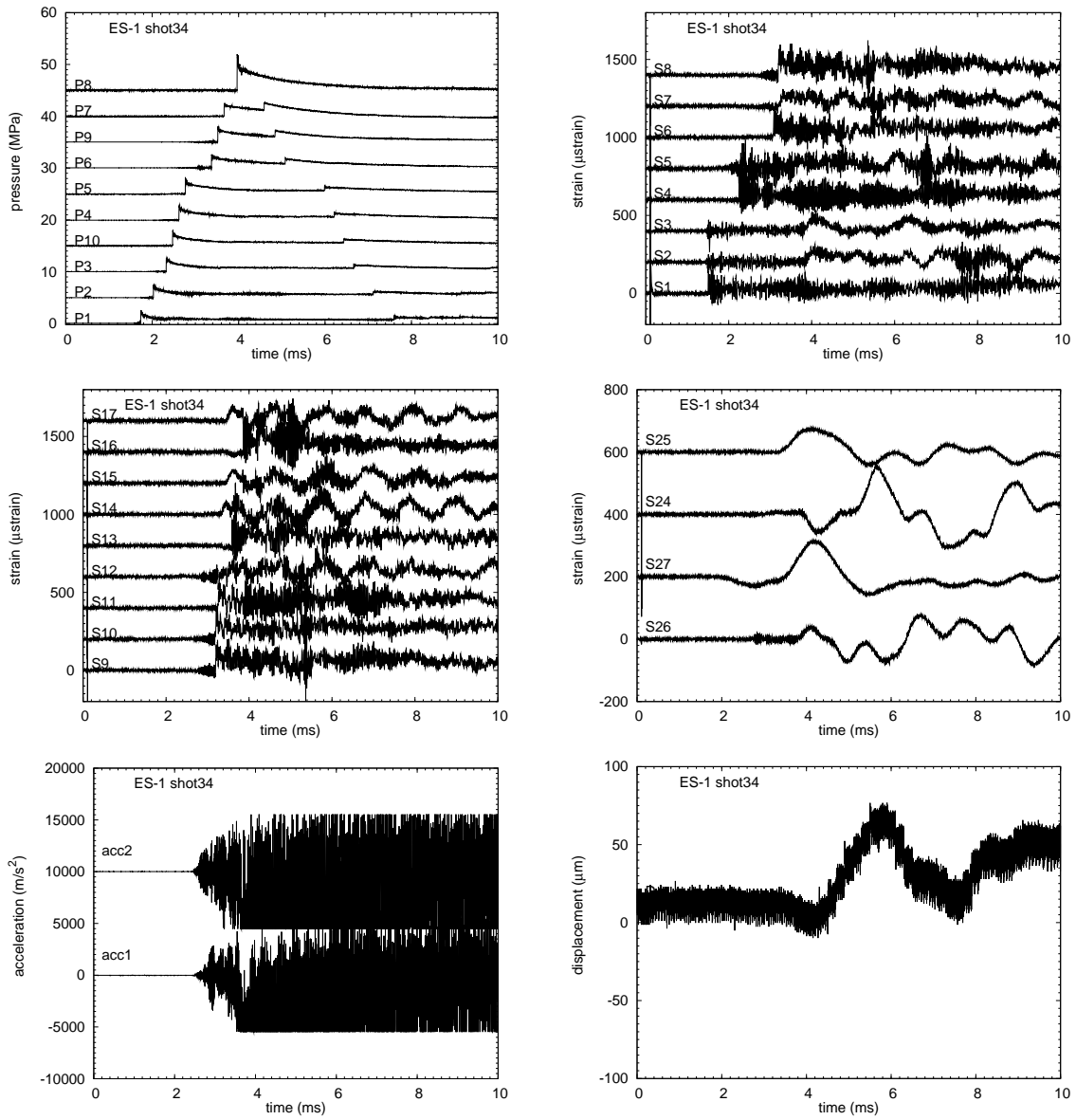


Figure 192: ES1 Shot 34. Pressure, strain gage, accelerometer signals. 10 ms raw data.

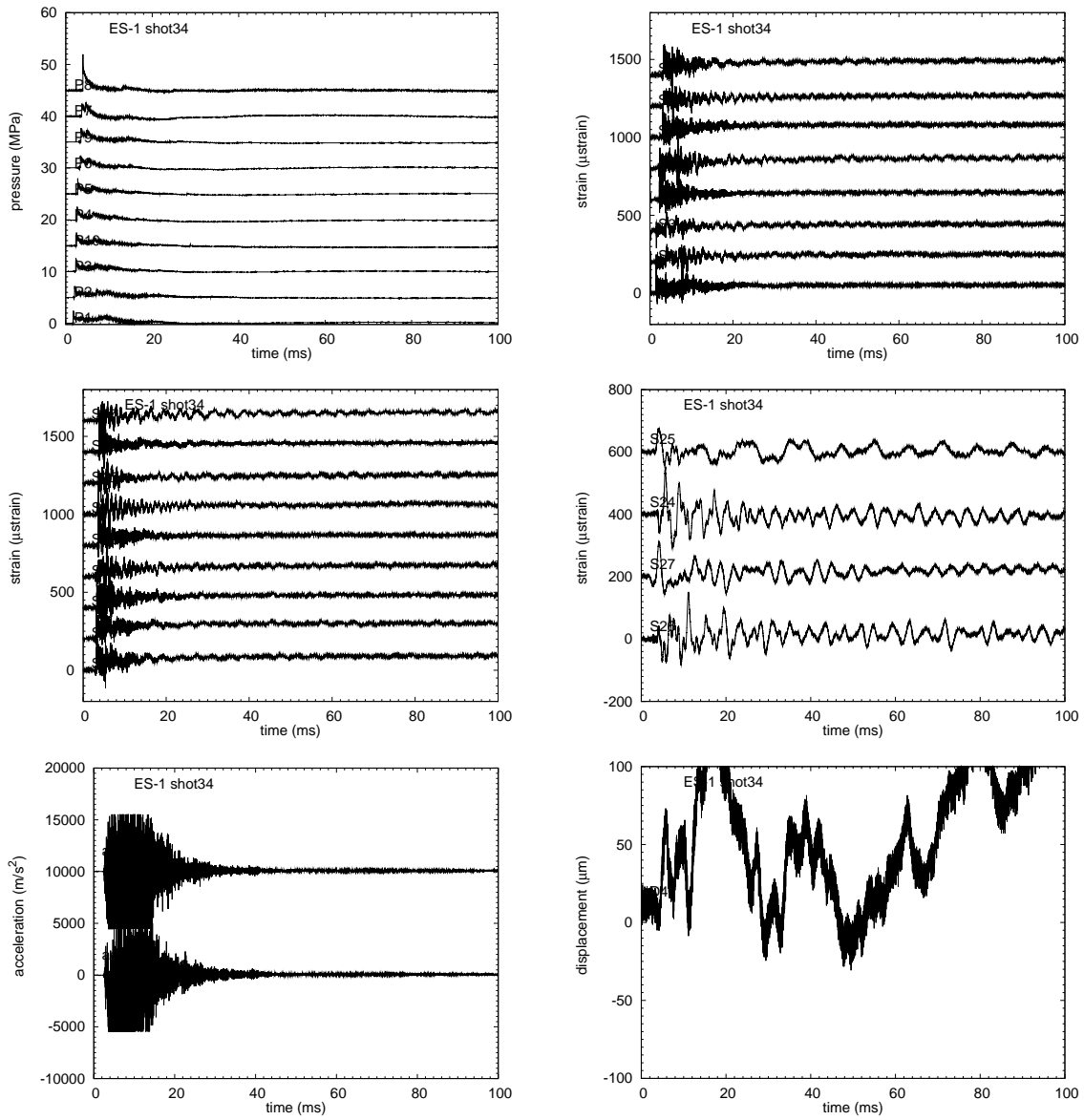


Figure 193: ES1 Shot 34. Pressure, strain gage, accelerometer, and displacement signals. 100 ms raw data.

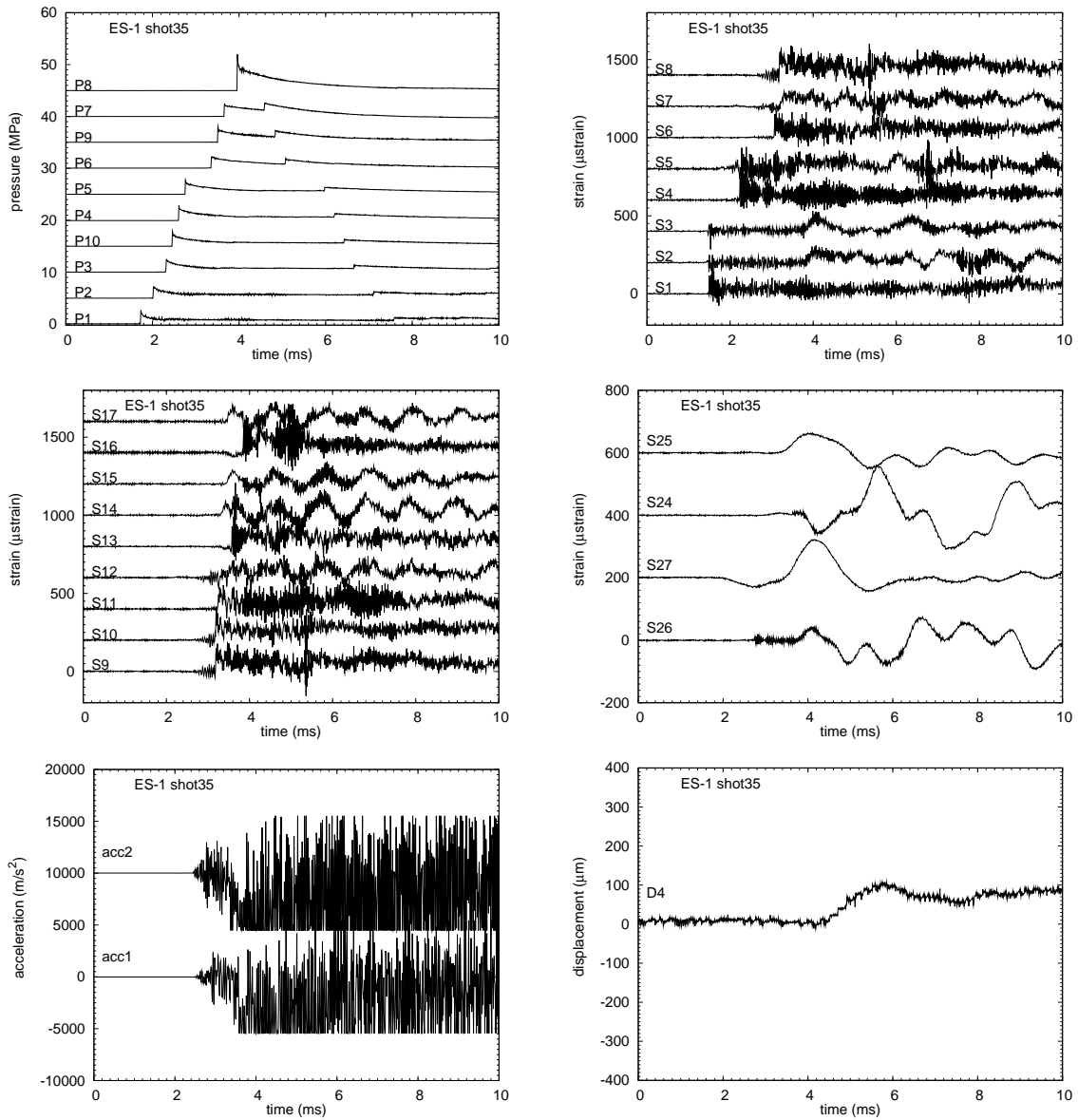


Figure 194: ES1 Shot 35. Pressure, strain gage, accelerometer signals. 10 ms raw data.

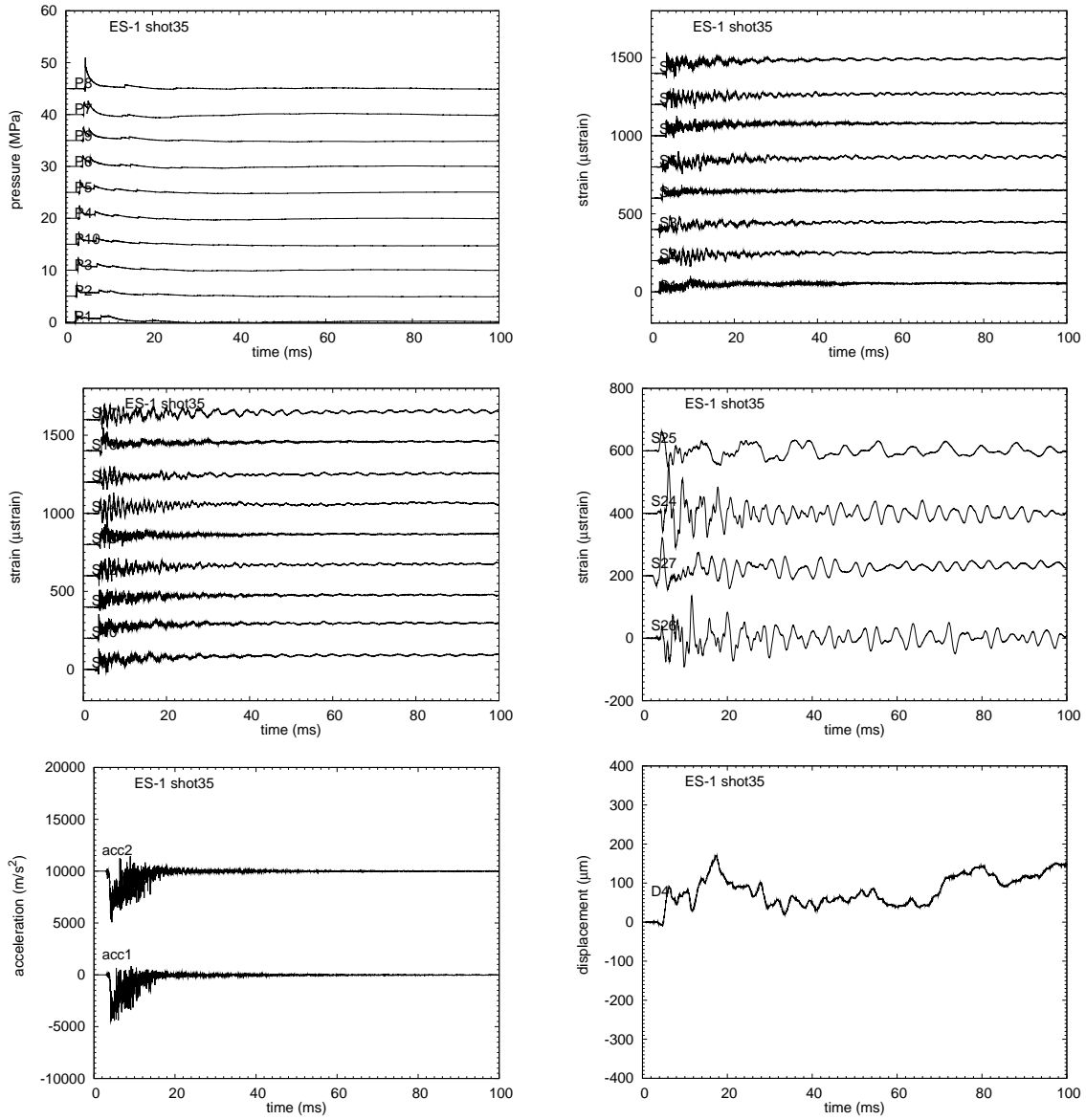


Figure 195: ES1 Shot 35. Pressure, strain gage, accelerometer signals. 100 ms of 50 kHz low-pass filtered data.

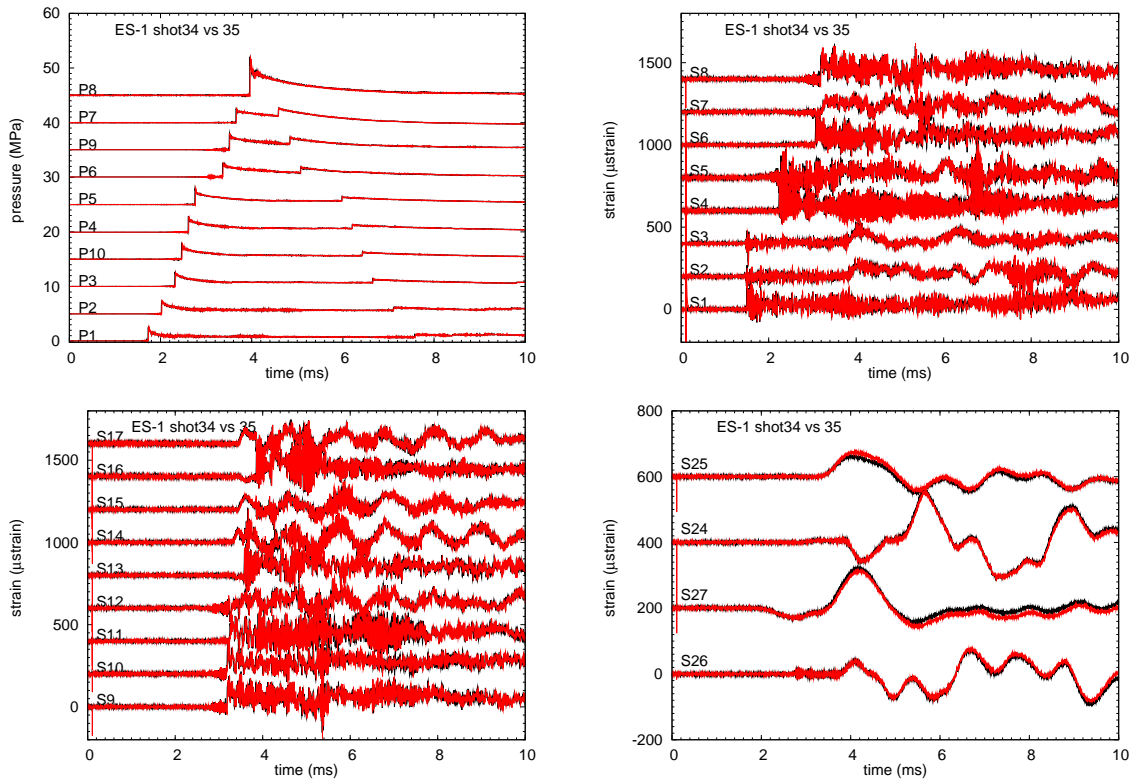


Figure 196: ES1 Shot 34 vs 35. Pressure, strain gage, accelerometer signals. 10 ms raw data.

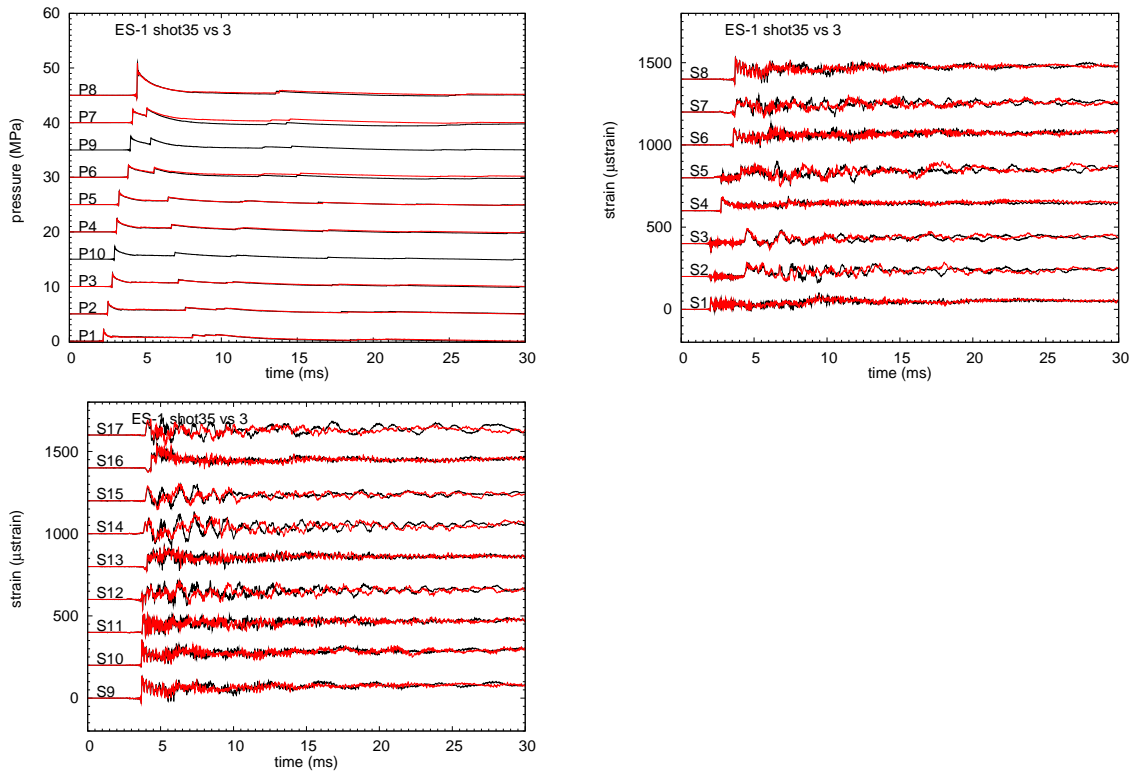


Figure 197: ES1 Shot 35 vs 3. Pressure, strain gage, accelerometer signals. 30 ms of 50 kHz low-pass filtered data.

# K TS1 Engineering Drawings

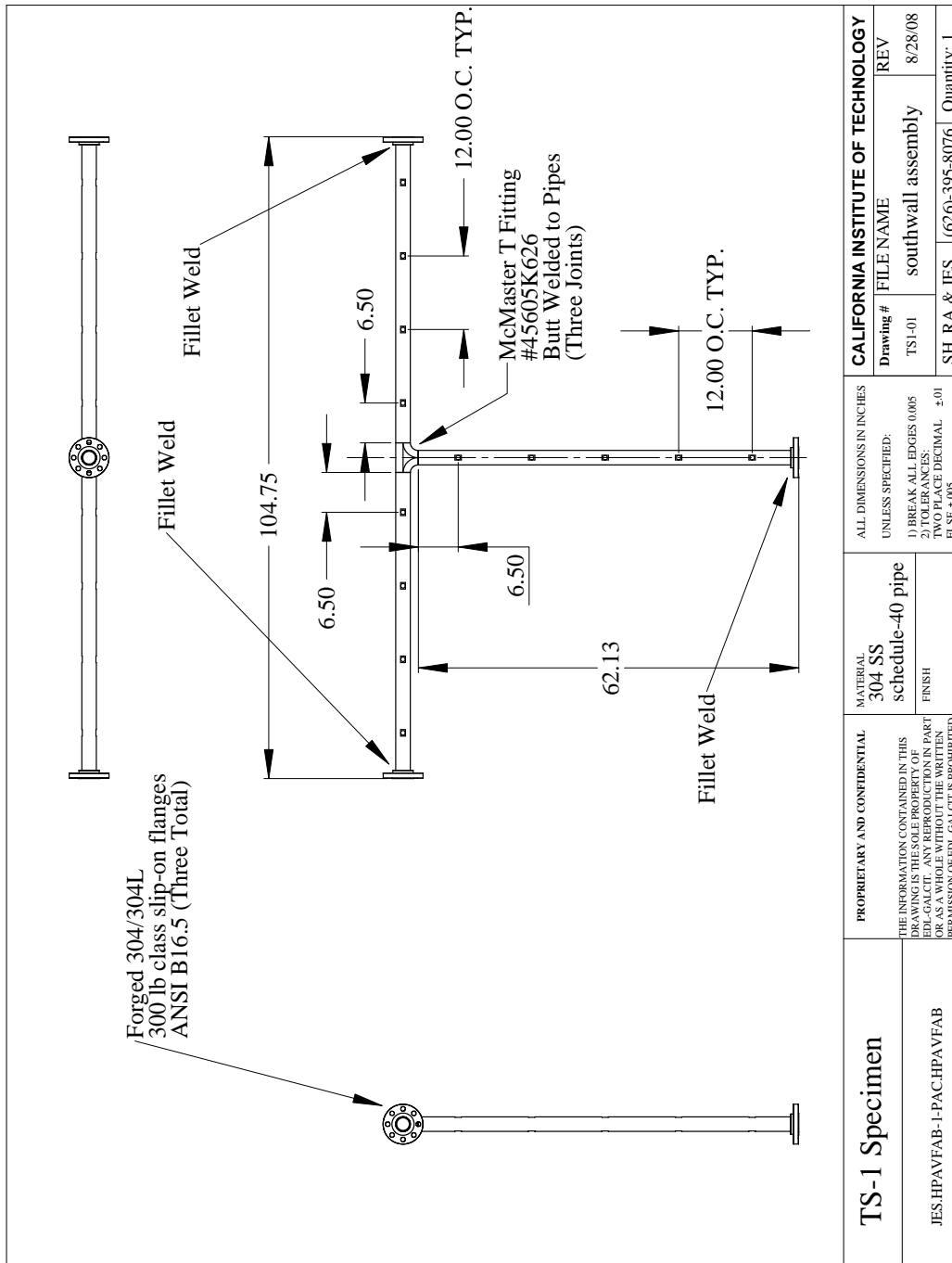


Figure 198: Engineering drawing of TS1 assembly. Front, top, and side views.

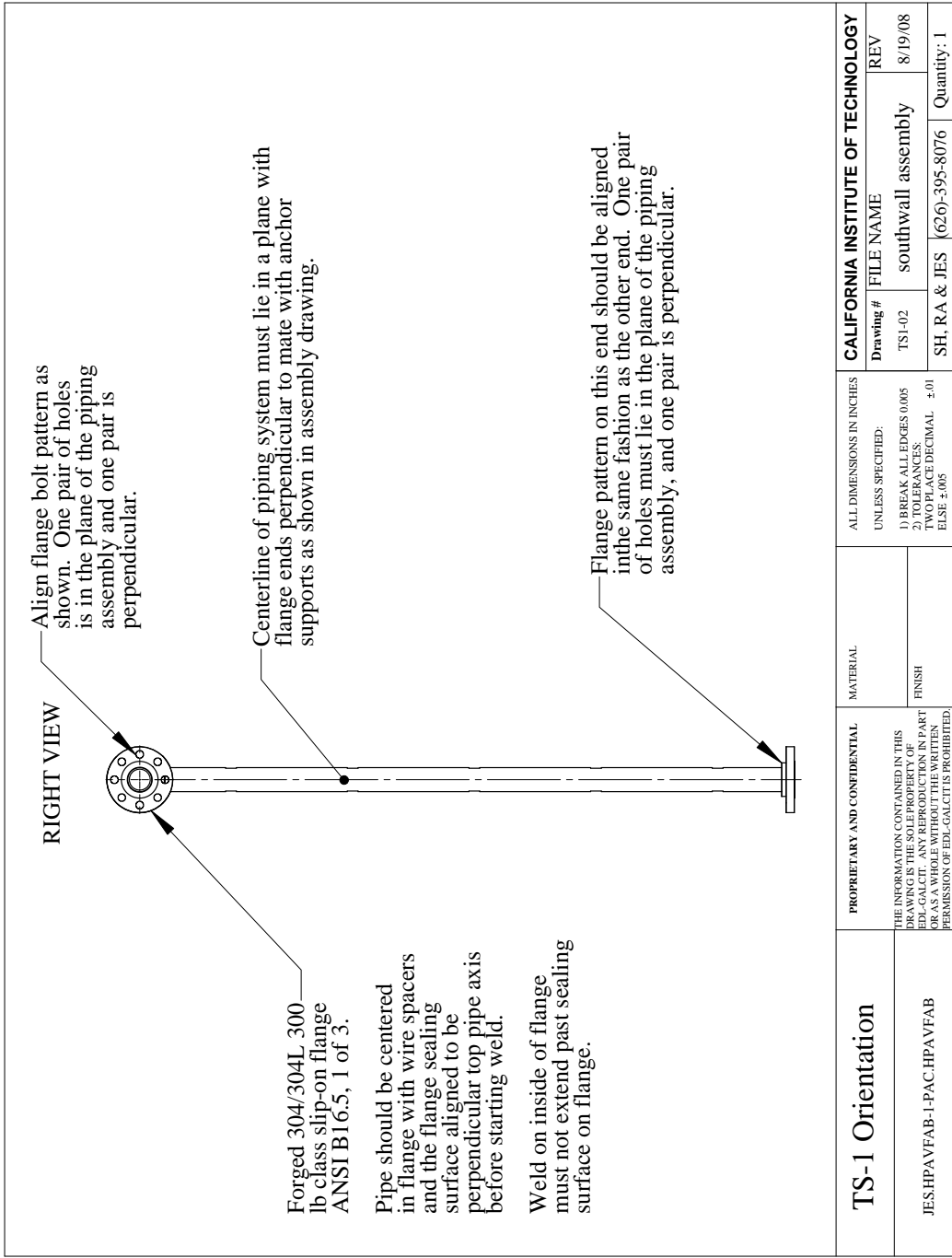


Figure 199: Engineering drawing of TS1 assembly. Side view.

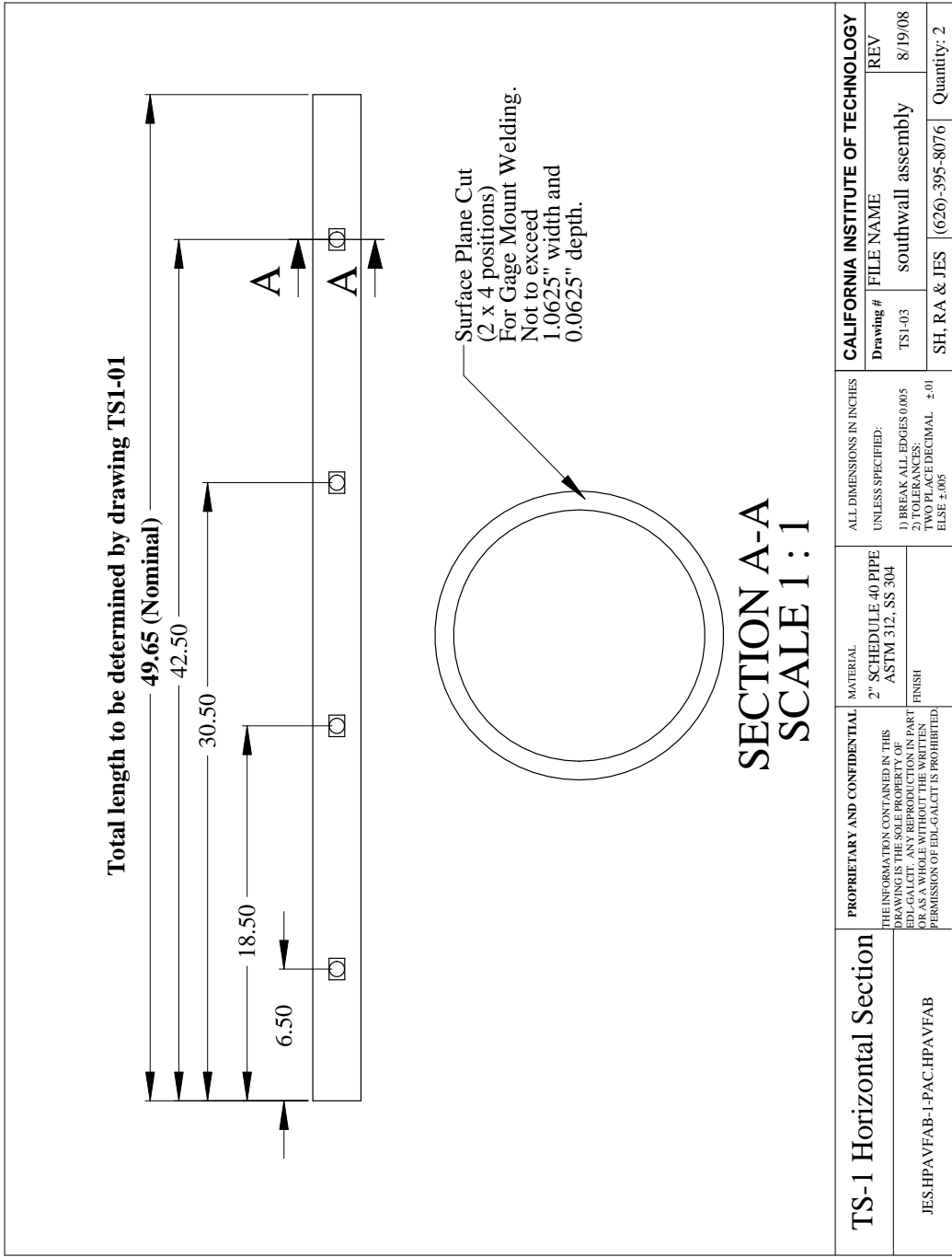


Figure 200: Engineering drawing of TS1 assembly. Instrument port locations on tee run pipe segment.

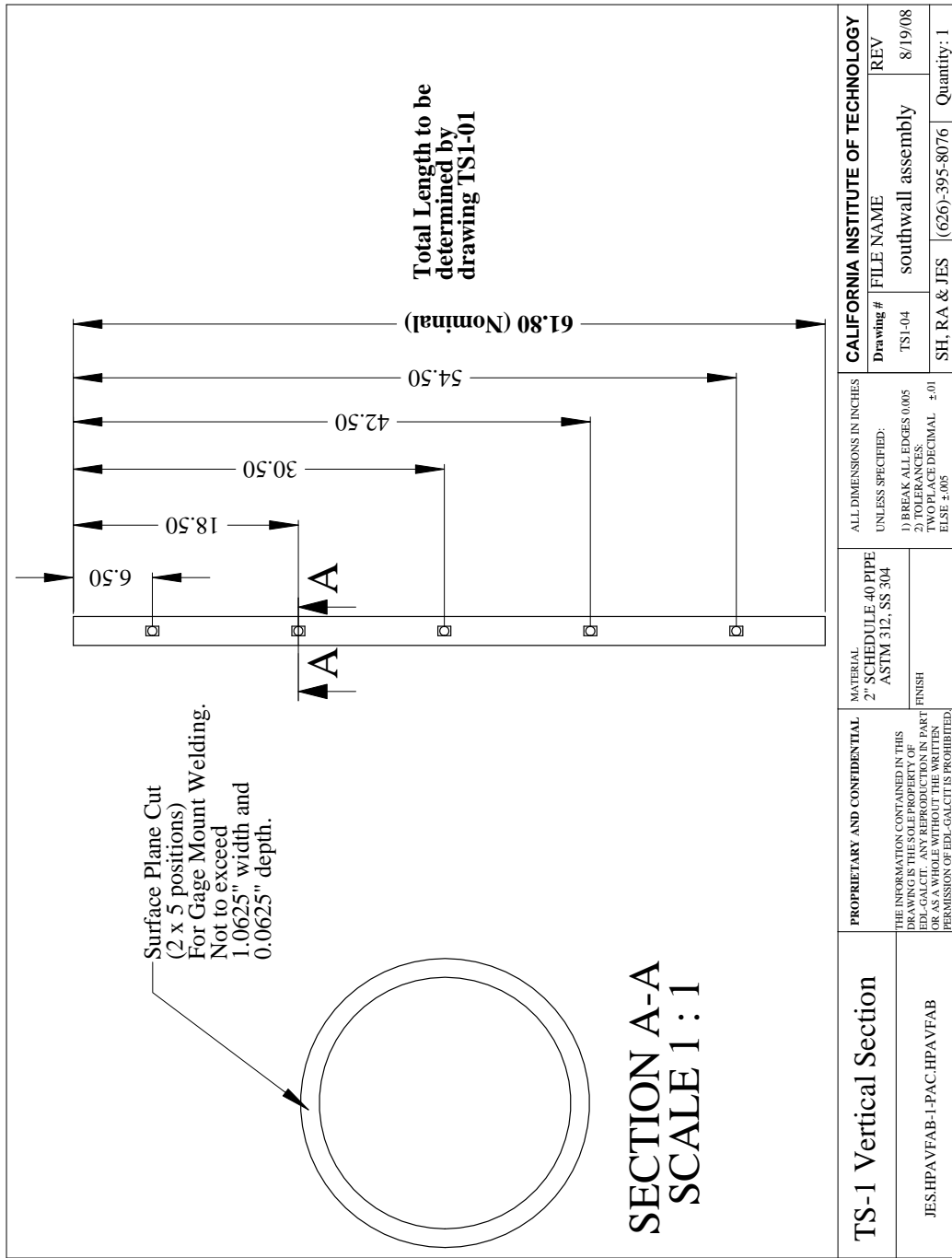


Figure 201: Engineering drawing of TS1 assembly. Instrument port locations on tee branch pipe segment.

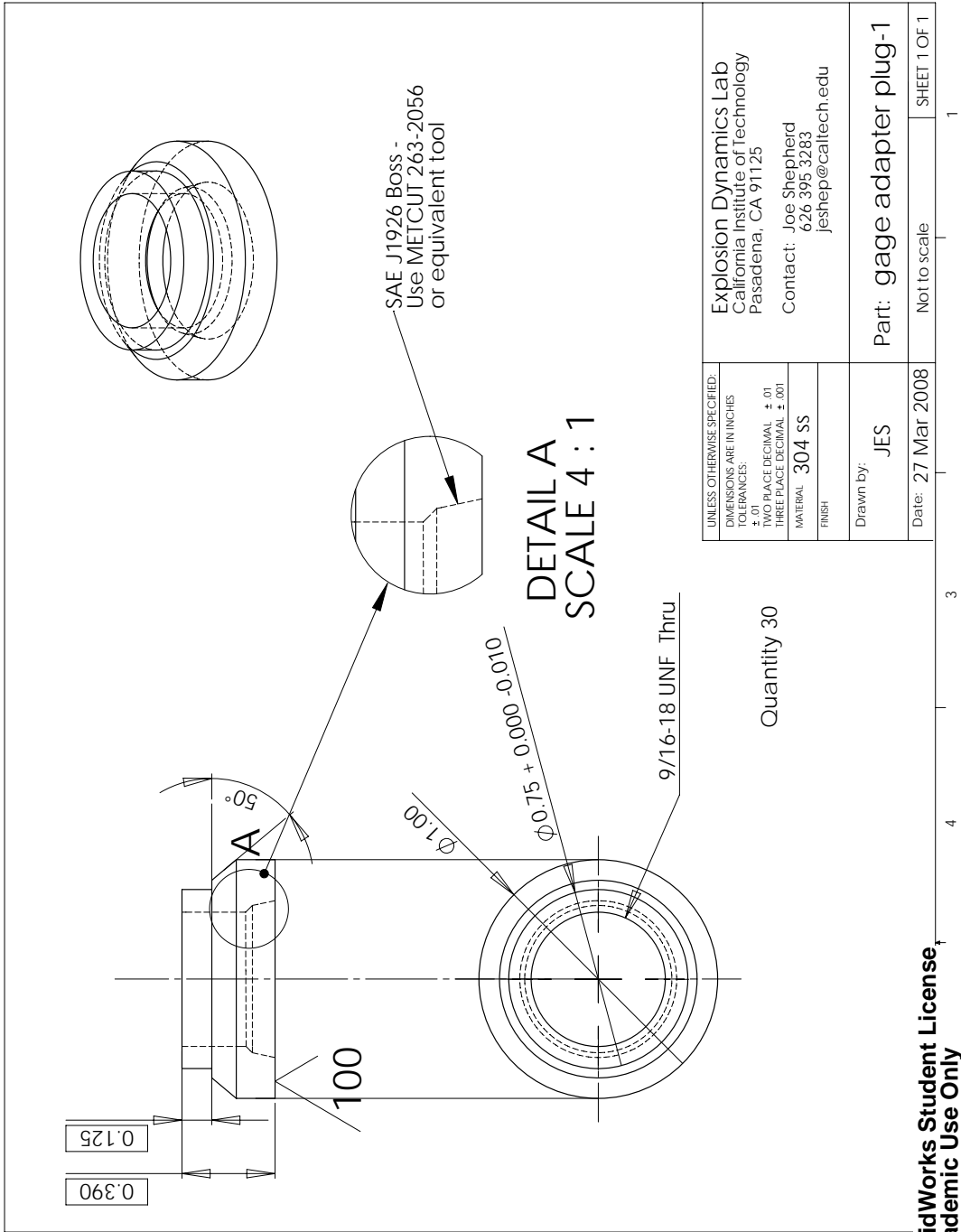


Figure 202: Engineering drawing of TS1 SAE port adapter boss.

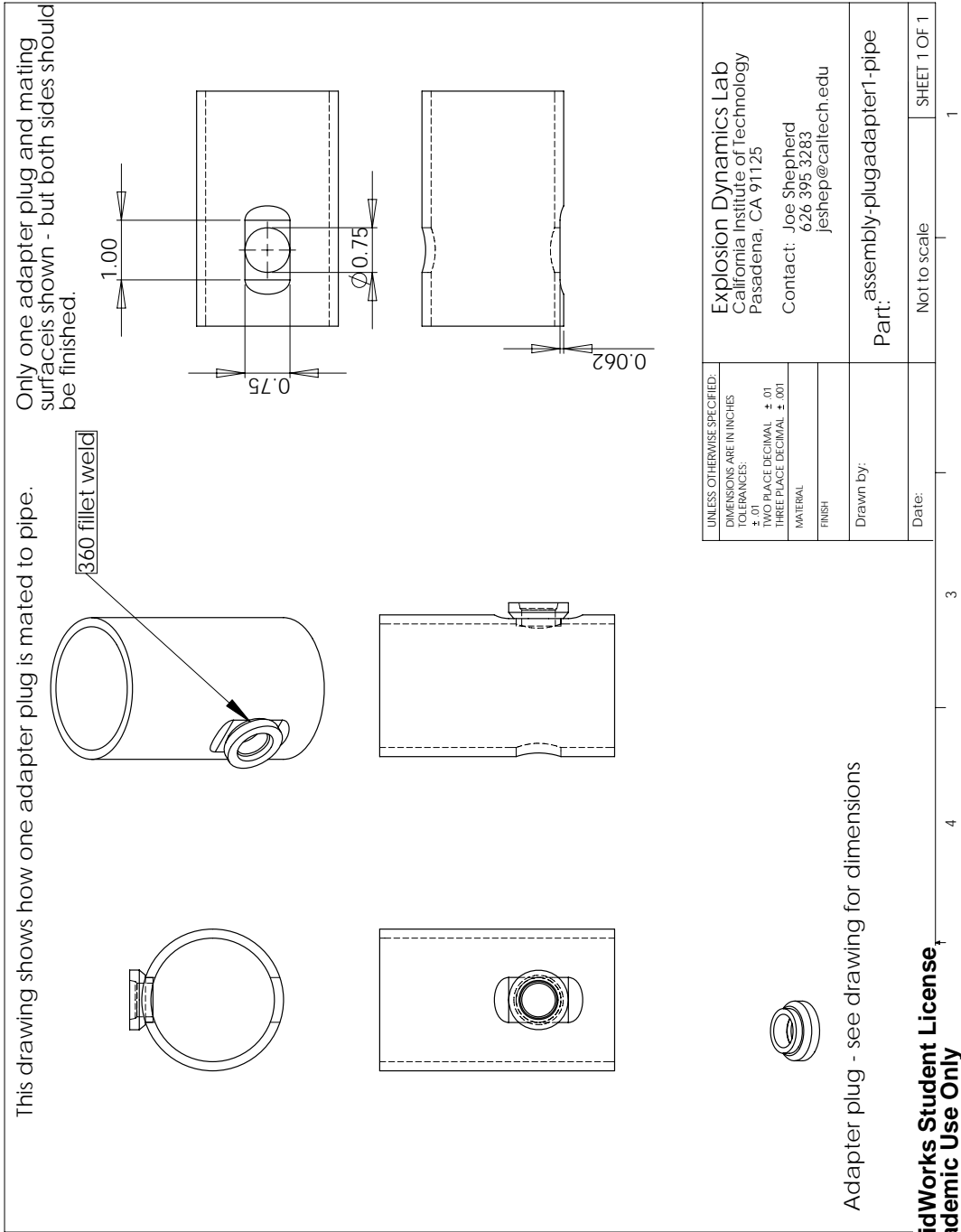


Figure 203: Engineering drawing of SAE port assembly to piping.

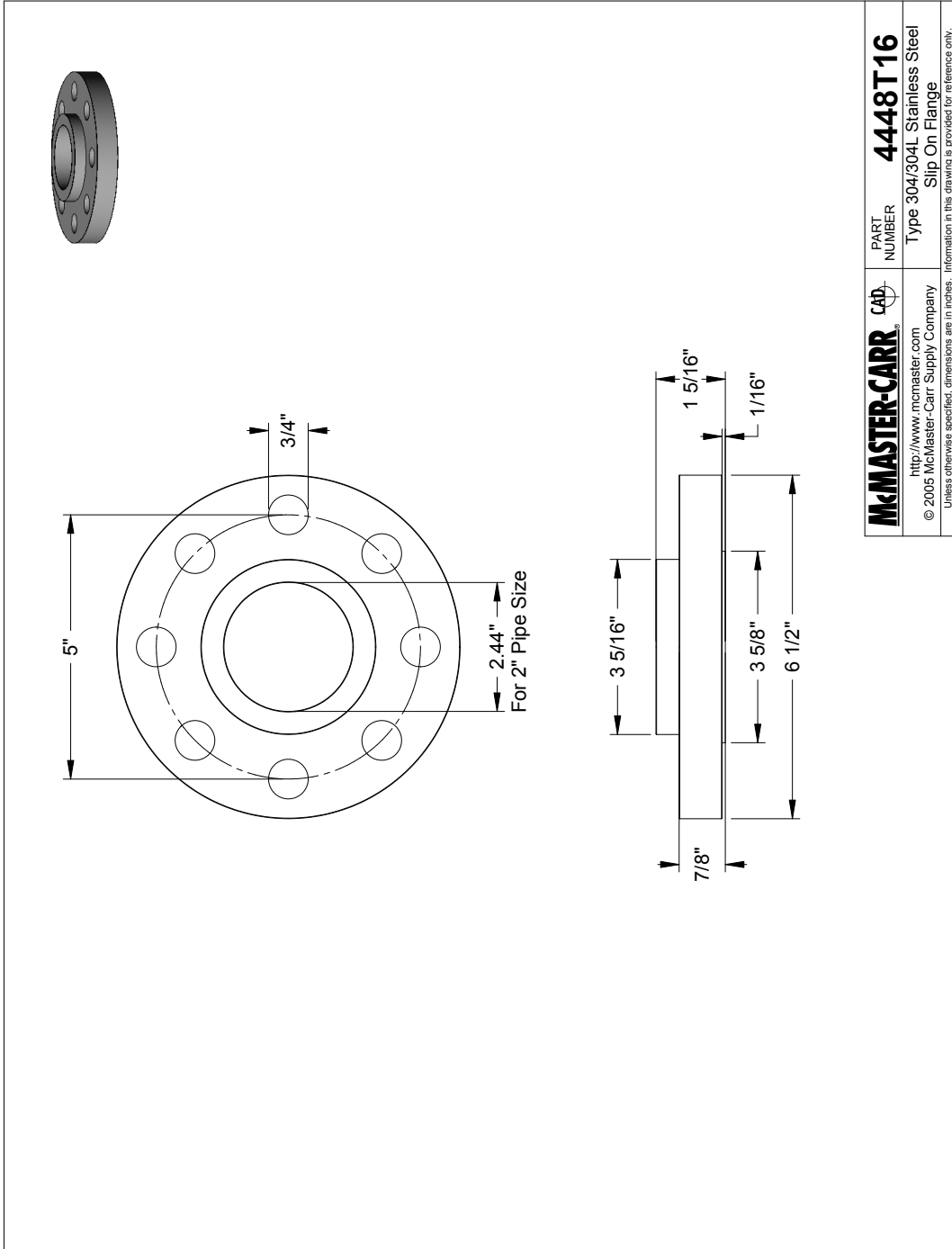


Figure 204: Engineering drawing of tee component used in TS1.

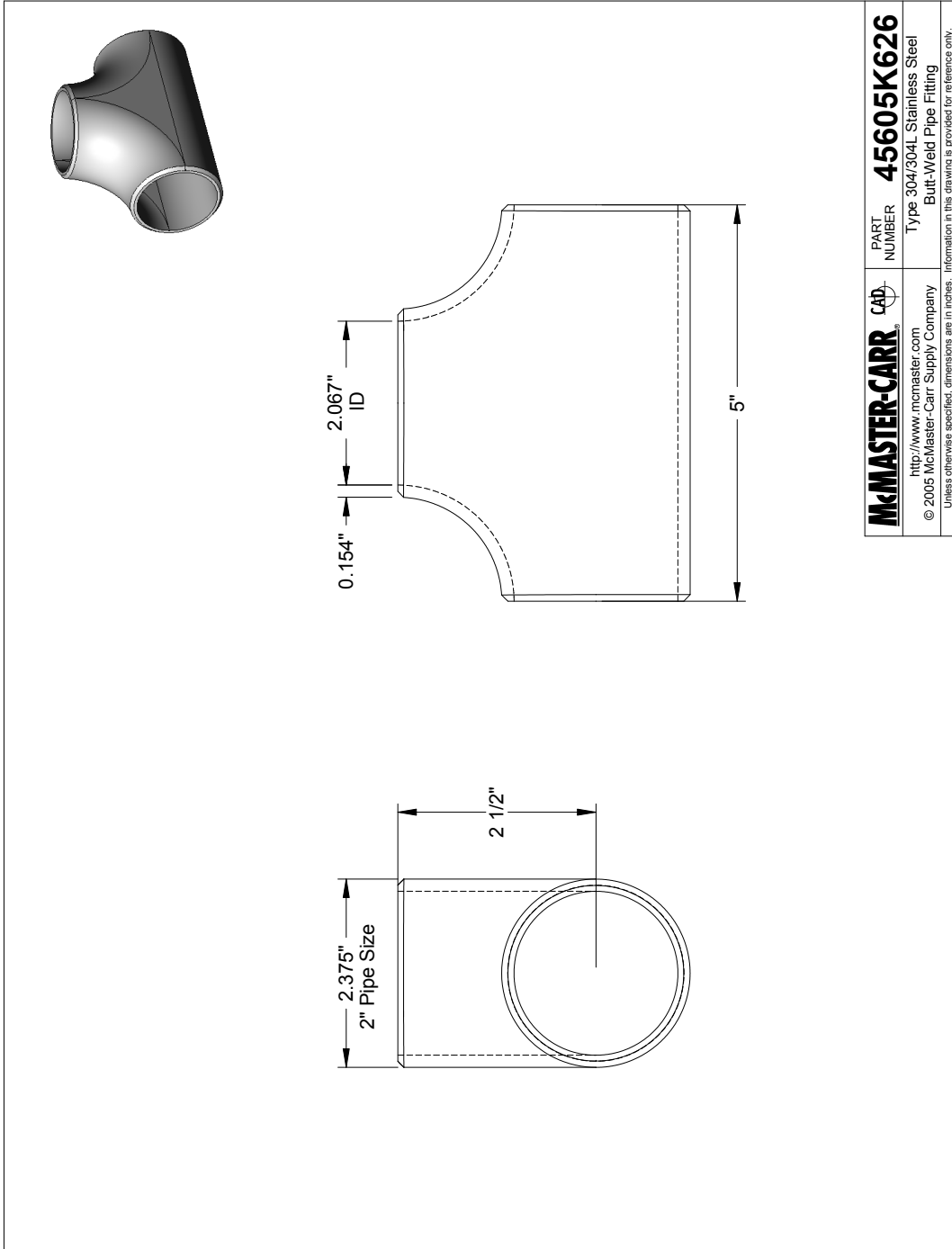


Figure 205: Engineering drawing of slip-on flange used in TS1.

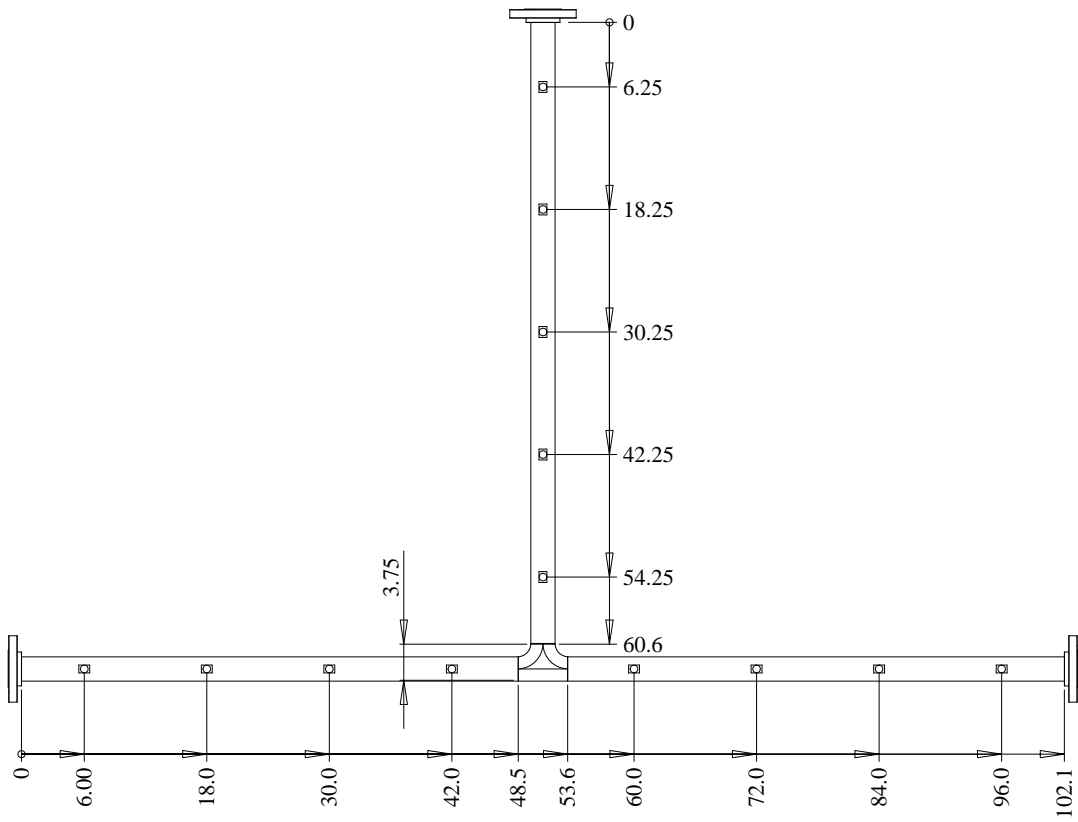


Figure 206: Dimensions of key features of TS1.

## L TS1 Sensor Locations

Table 34: TS1 sensor location.

Sensor	Type	Orientation	Location	Reference	Distance to igniter				
					Top (in)	East (in)	Top (m)	East (m)	
P1	pressure	N	30.25	top	32.25	85.80	0.819	2.179	
P2	pressure	N	42.25	top	44.25	73.80	1.124	1.875	
P3	pressure	N	54.25	top	56.25	61.80	1.429	1.570	
P4	pressure	N	60.00	east	71.95	62.00	1.828	1.575	
P5	pressure	N	84.00	east	95.95	86.00	2.437	2.184	
P6	pressure	N	104.10	east	116.05	106.10	2.948	2.695	
P7	pressure	N	42.00	east	72.05	44.00	1.830	1.118	
P8	pressure	N	18.00	east	96.05	20.00	2.440	0.508	
P9	pressure	N	-2.00	east	116.05	0.00	2.948	0.000	
P9	pressure	N	-2.00	top	0.00	118.05	0.000	2.998	
Fire	t-zero	-	-	-	-	-	-	-	
D4	displacement	vertical	-	64.35	top	66.35	51.05	1.685	1.297
ACC3	acceleration	vertical	-	0.00	top	2.00	116.05	0.051	2.948
S1	strain	H	E	18.25	top	20.25	97.80	0.514	2.484
S2	strain	A	E	18.25	top	20.25	97.80	0.514	2.484
S3	strain	A	W	18.25	top	20.25	97.80	0.514	2.484
S4	strain	A	W	36.06	top	38.06	79.99	0.967	2.032
S5	strain	H	U	44.00	east	70.05	46.00	1.779	1.168
S6	strain	A	U	44.00	east	70.05	46.00	1.779	1.168
S7	strain	A	L	44.00	east	70.05	46.00	1.779	1.168
S8	strain	H	U	58.00	east	69.95	60.00	1.777	1.524
S9	strain	A	U	58.00	east	69.95	60.00	1.777	1.524
S10	strain	A	L	58.00	east	69.95	60.00	1.777	1.524
S11	strain	H	U	89.88	east	101.83	91.88	2.586	2.334
S12	strain	A	L	89.88	east	101.83	91.88	2.586	2.334
S13	strain	A	L	89.88	east	101.83	91.88	2.586	2.334
T1	temperature		18.25	top	20.25	97.80			
	Centerline of horizontal leg		63.00	top					
	flange-to-flange horizontal leg		102.10	east					
	centerline of vertical leg		51.05	east					

Notes:

H = hoop strain

A = axial (longitudinal) strain

E = east side of vertical segment

W = west side of vertical segment  
 U = upper side of horizontal segment  
 L = lower side of horizontal segment  
 N = north side of either vertical or horizontal segment

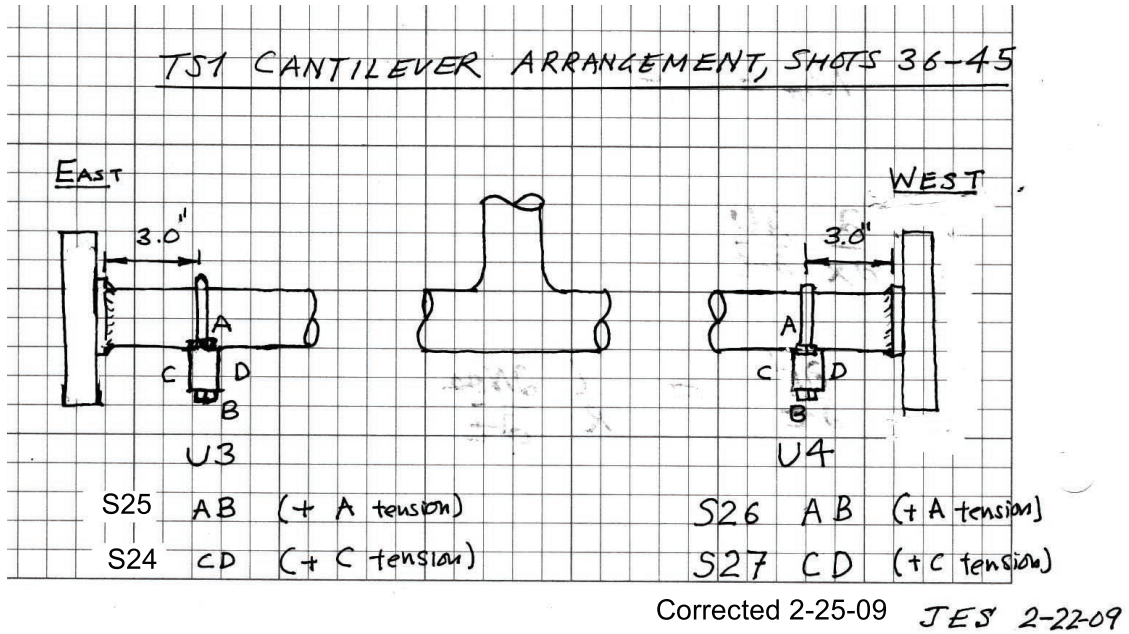


Figure 207: Arrangement of strain gages for cantilevers in shots 36-45.

# M TS1 Data Plots

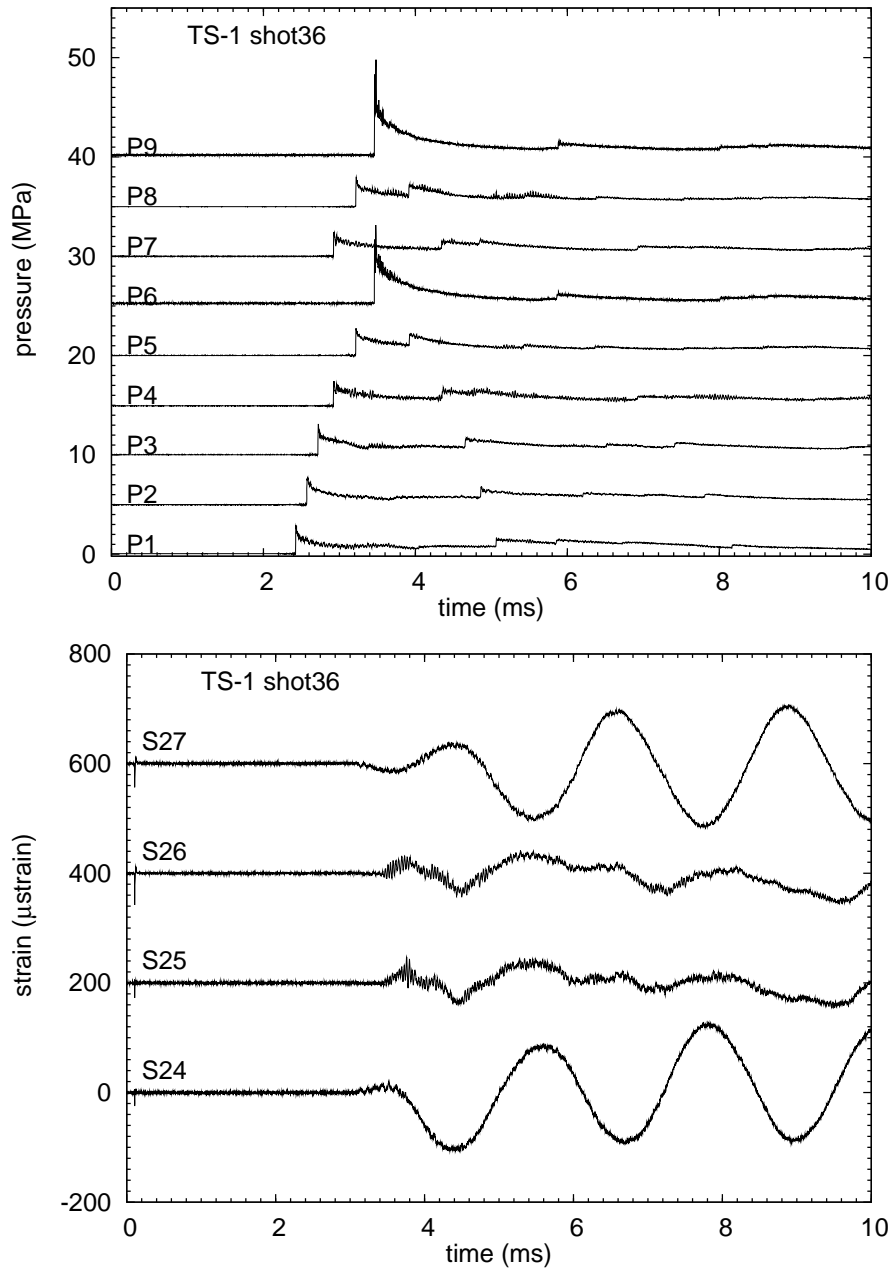


Figure 208: TS1 Shot 36. Pressure and cantilever strain gage signals. 10 ms raw data.

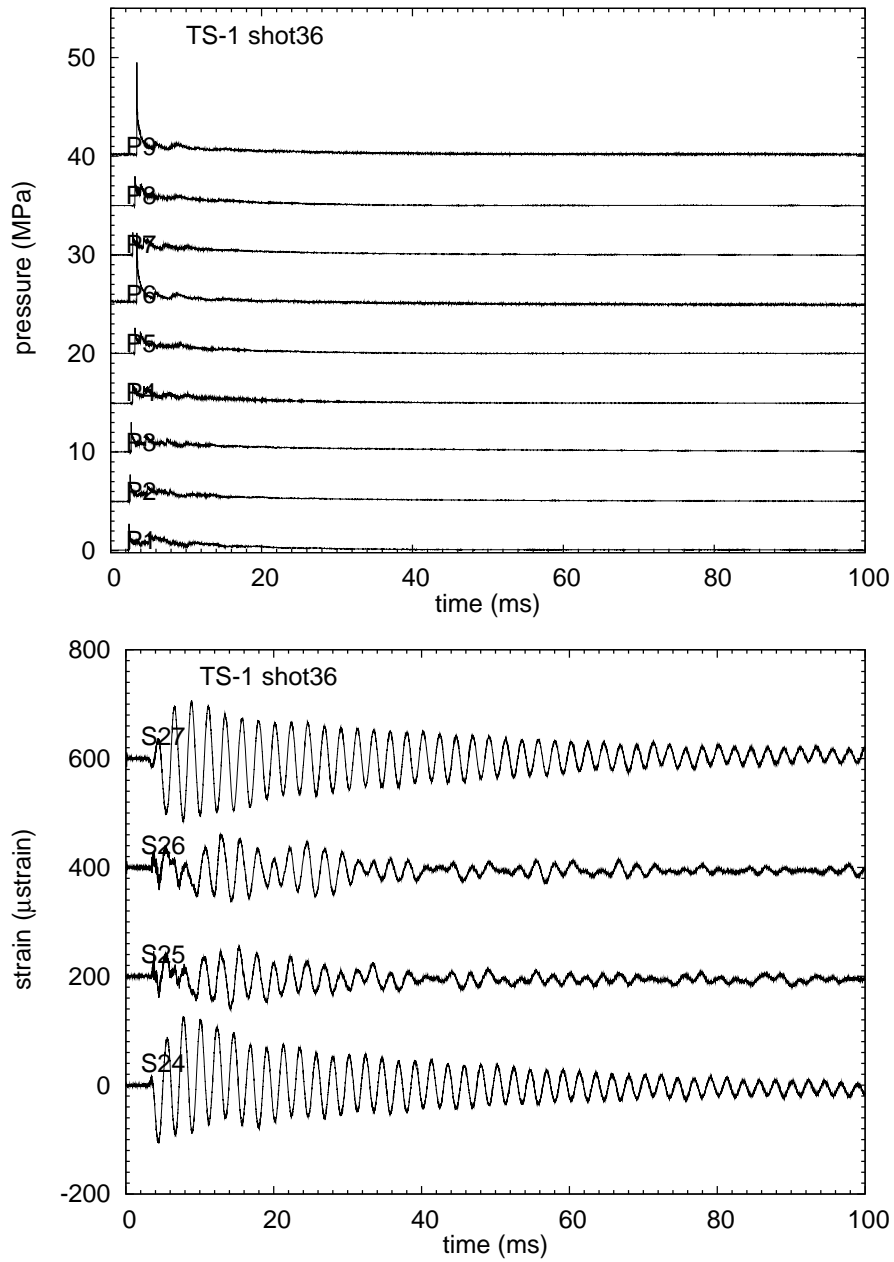


Figure 209: TS1 Shot 36. Pressure and cantilever strain gage signals. 10 ms raw data.

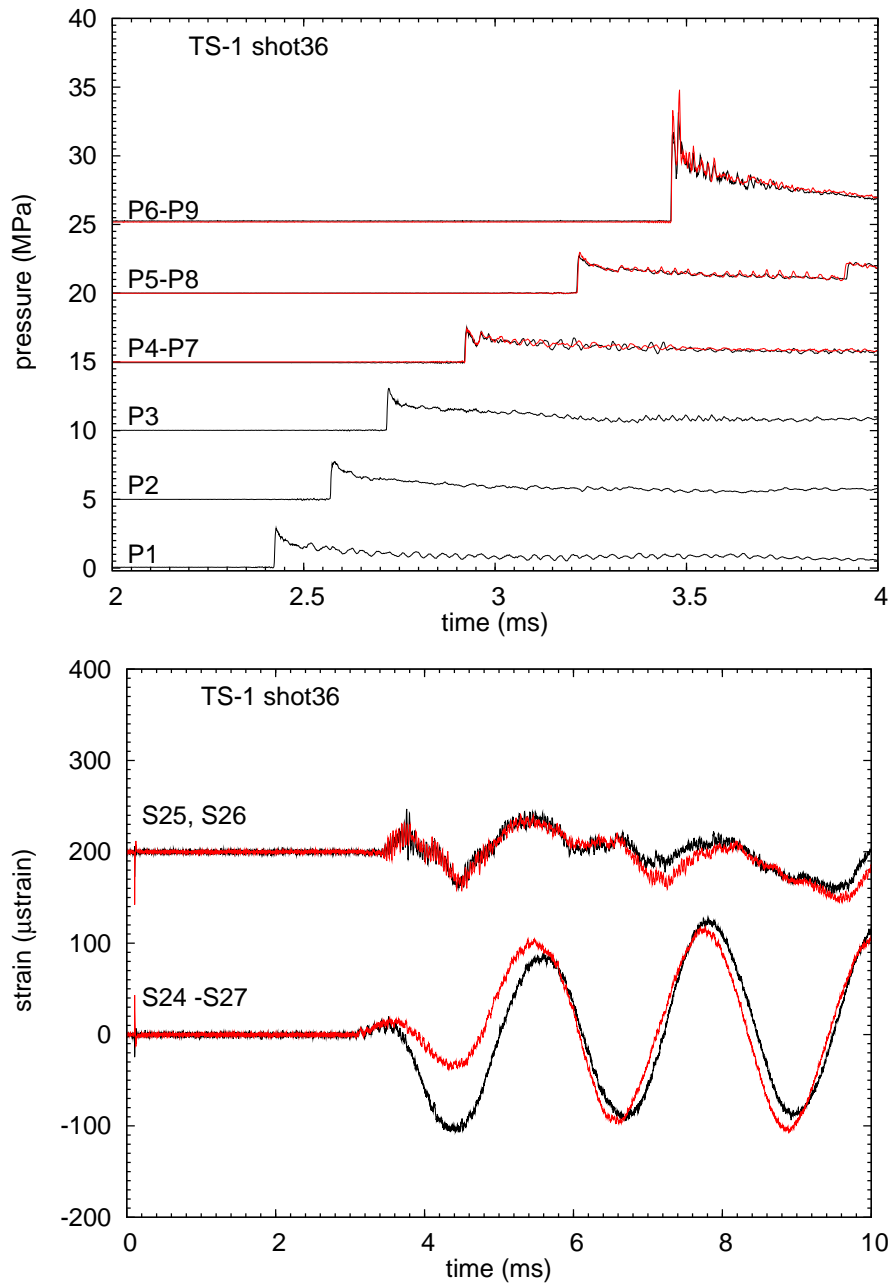


Figure 210: TS1 Shot 36. Check of pressure and cantilever beam symmetry. 10 ms raw data.

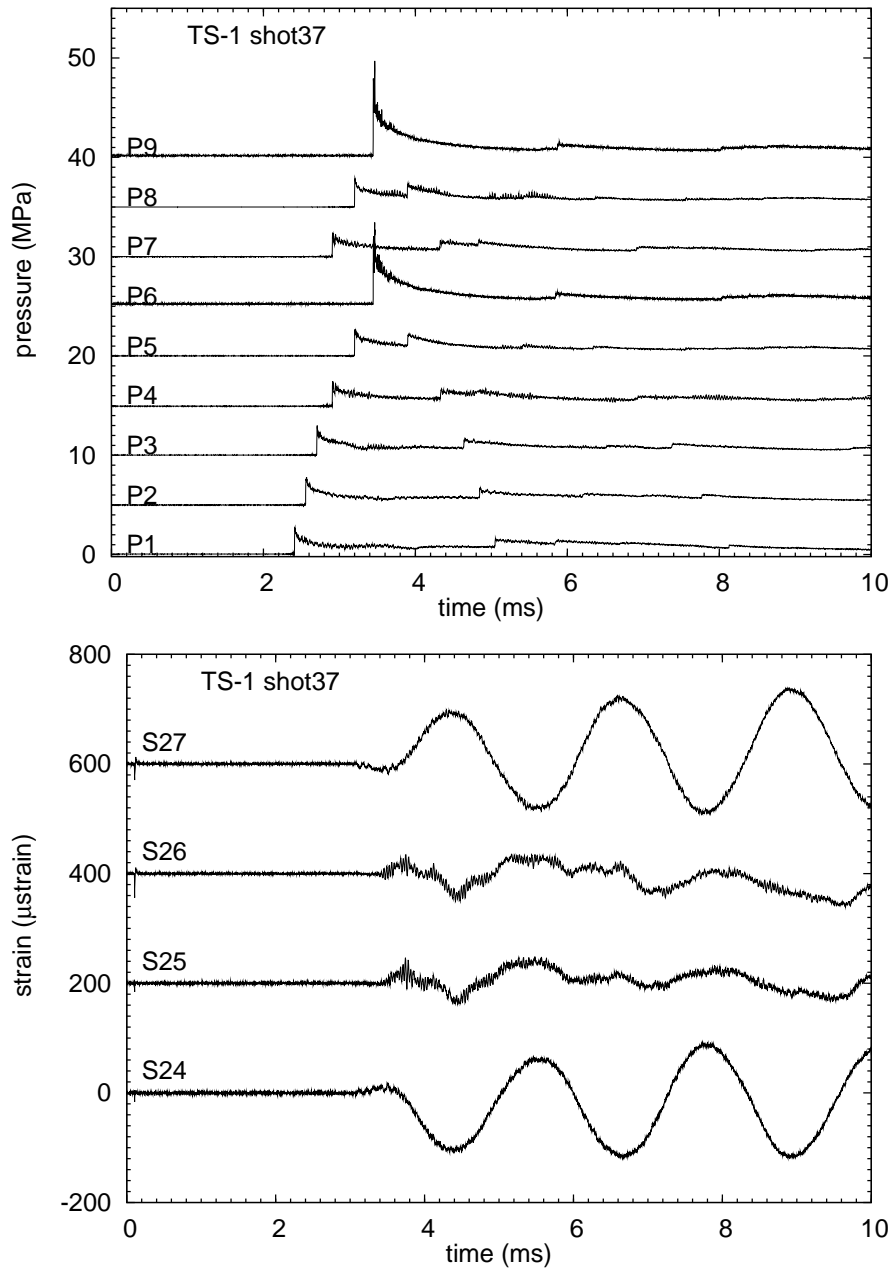


Figure 211: TS1 Shot 37. Pressure and cantilever strain gage signals. 10 ms raw data.

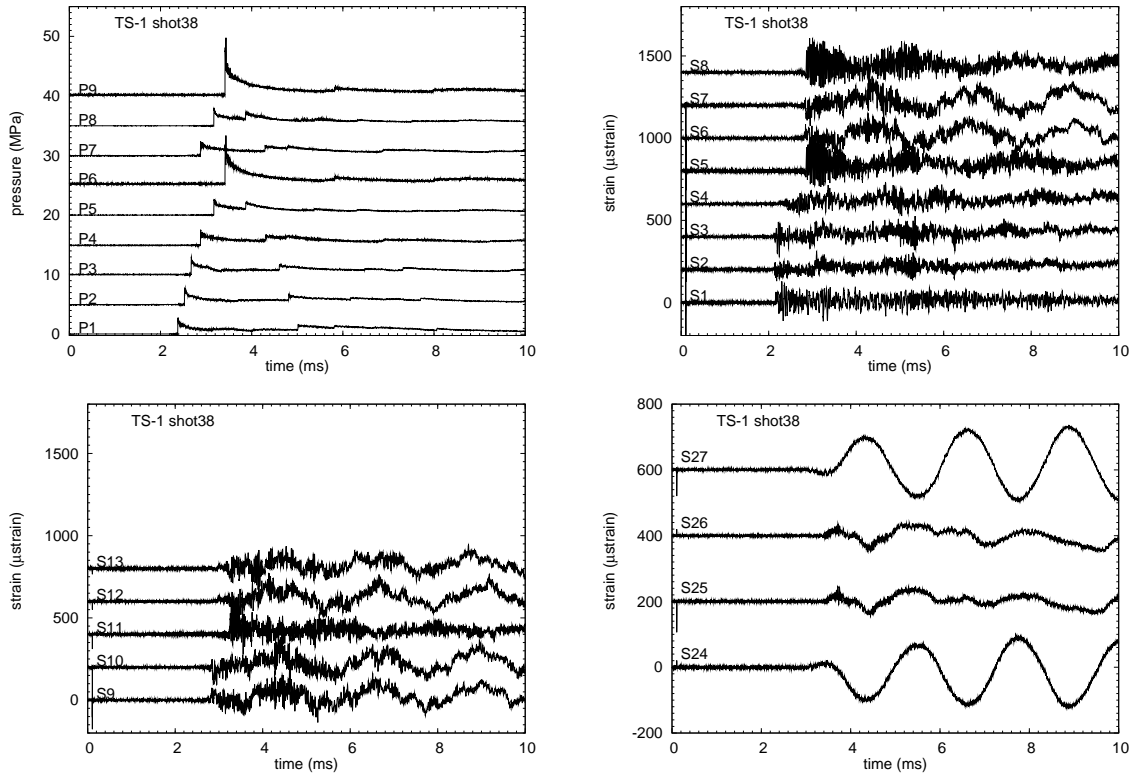


Figure 212: TS1 Shot 38. Pressure, strain gage, and cantilever strain gage signals. 10 ms raw data.

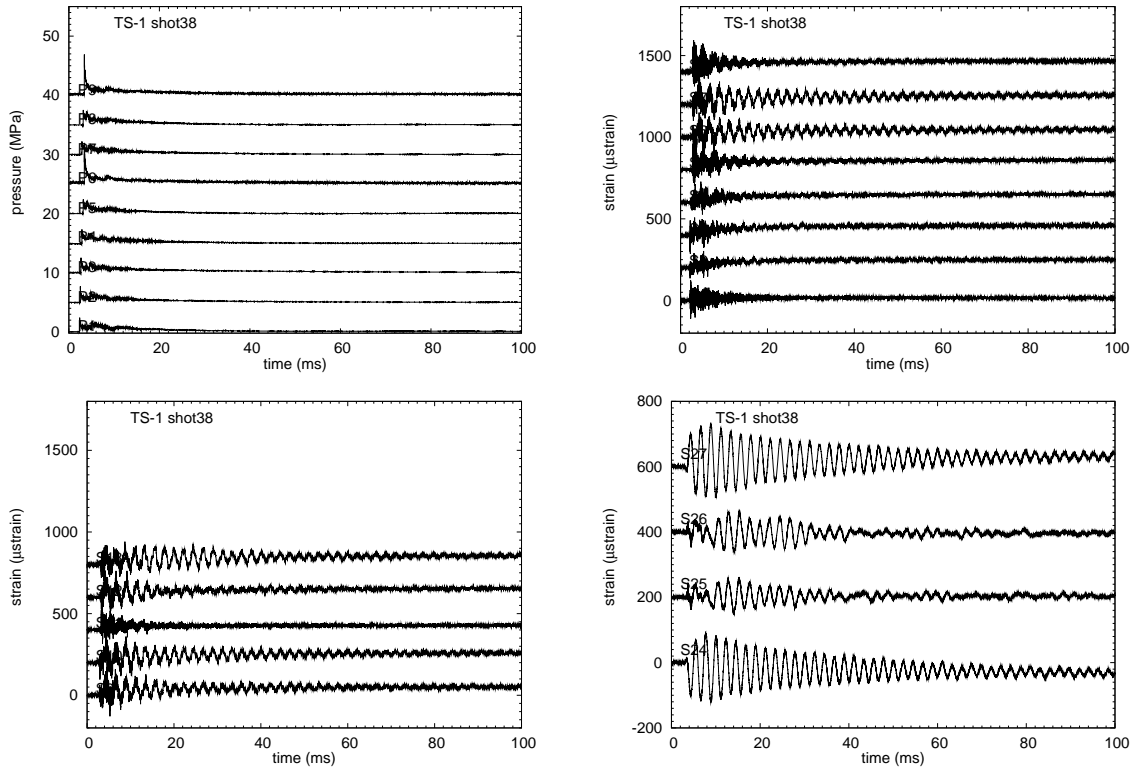


Figure 213: TS1 Shot 38. Pressure, strain gage, and cantilever strain gage signals. 100 ms raw data.

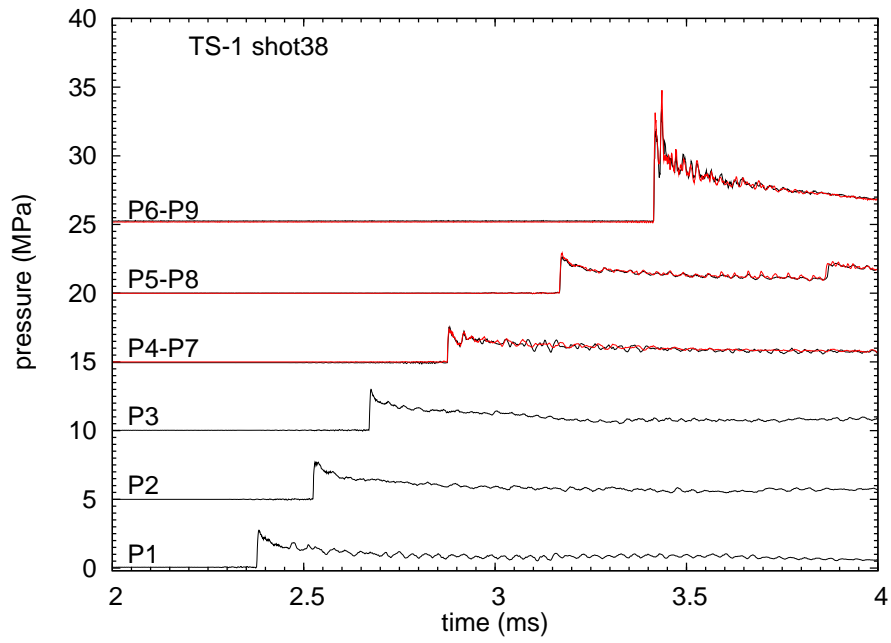


Figure 214: TS1 Shot 38. Check of pressure symmetry. 10 ms raw data.

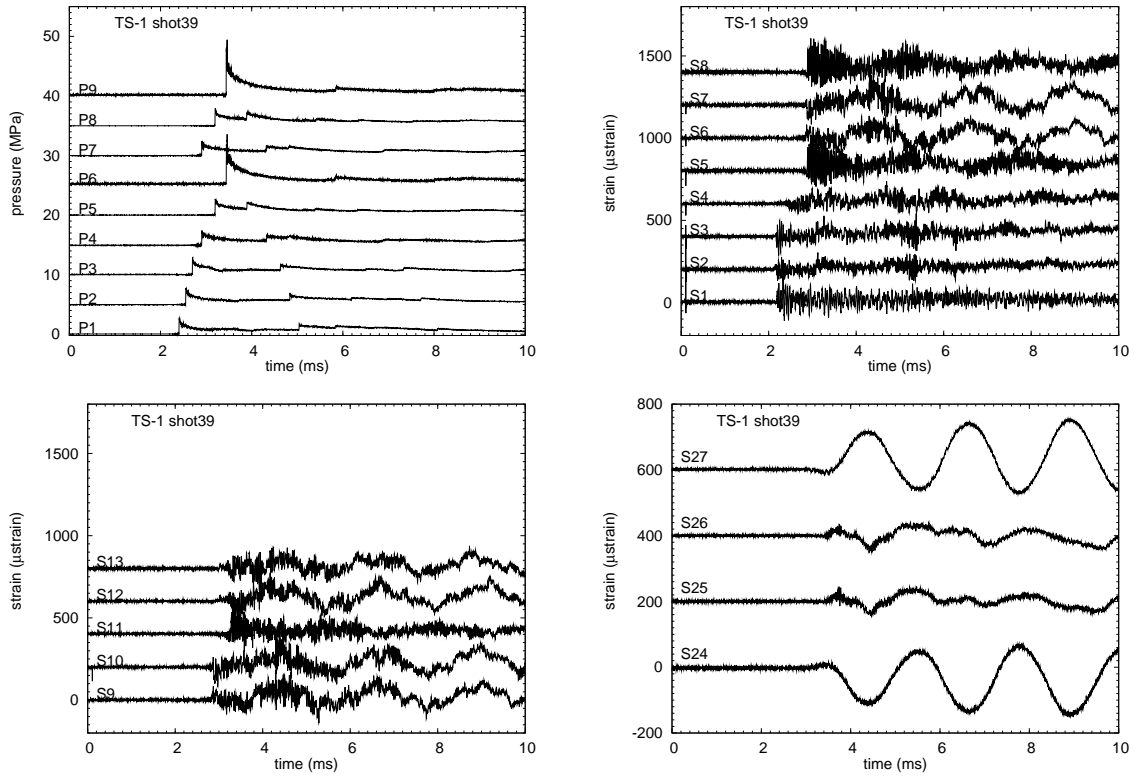


Figure 215: TS1 Shot 39. Pressure, strain gage, and cantilever strain gage signals. 10 ms raw data.

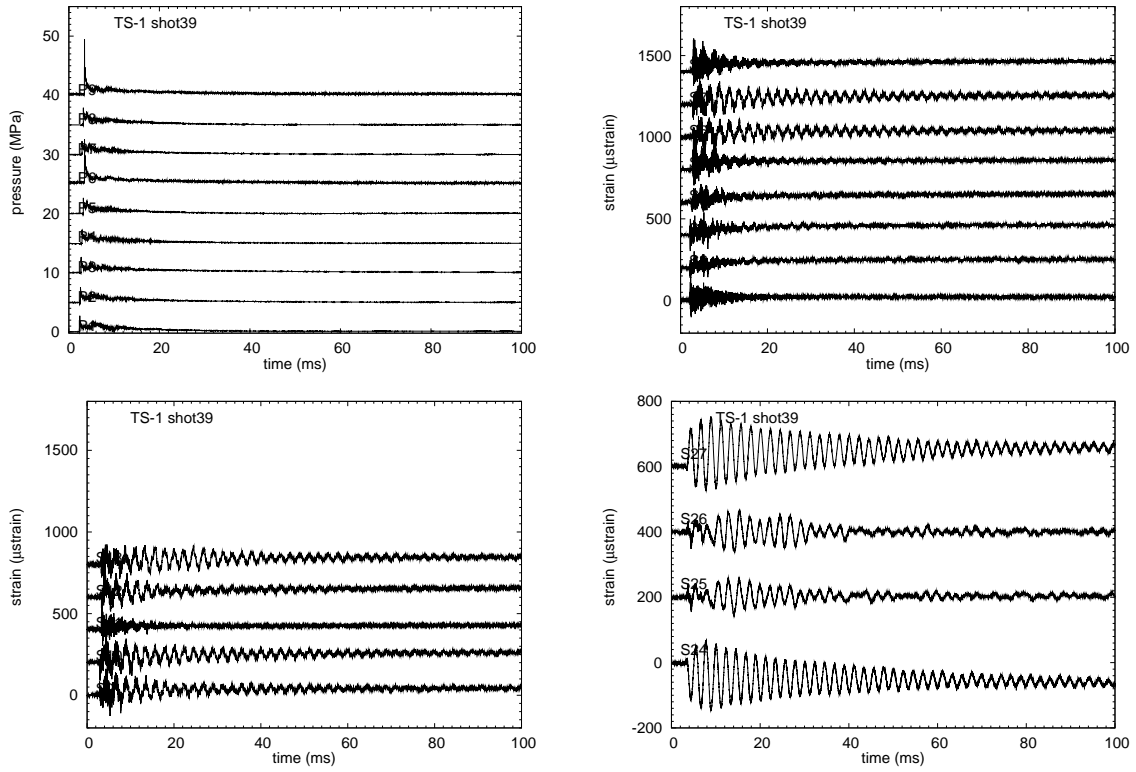


Figure 216: TS1 Shot 39. Pressure, strain gage, and cantilever strain gage signals. 100 ms raw data.

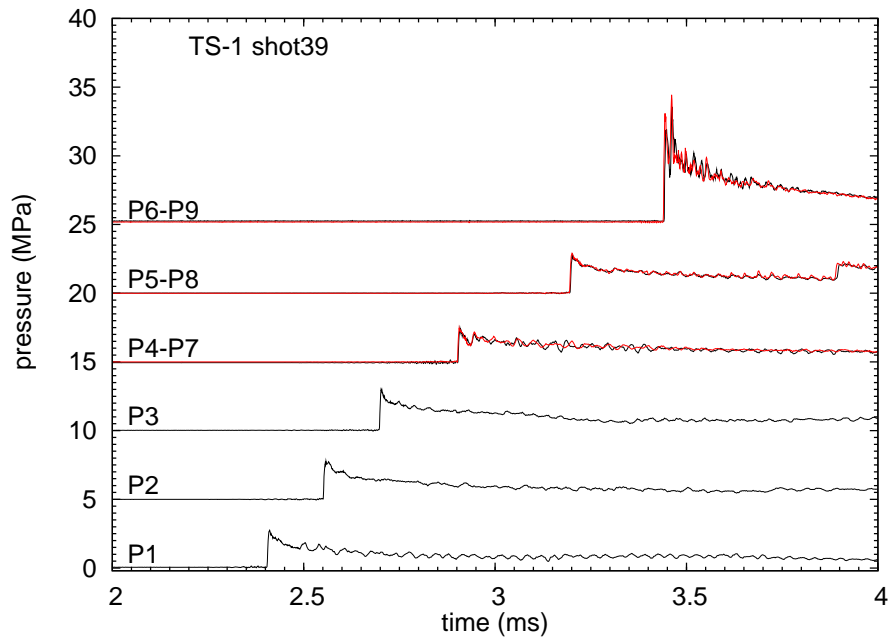


Figure 217: TS1 Shot 39. Check of pressure symmetry. 10 ms raw data.

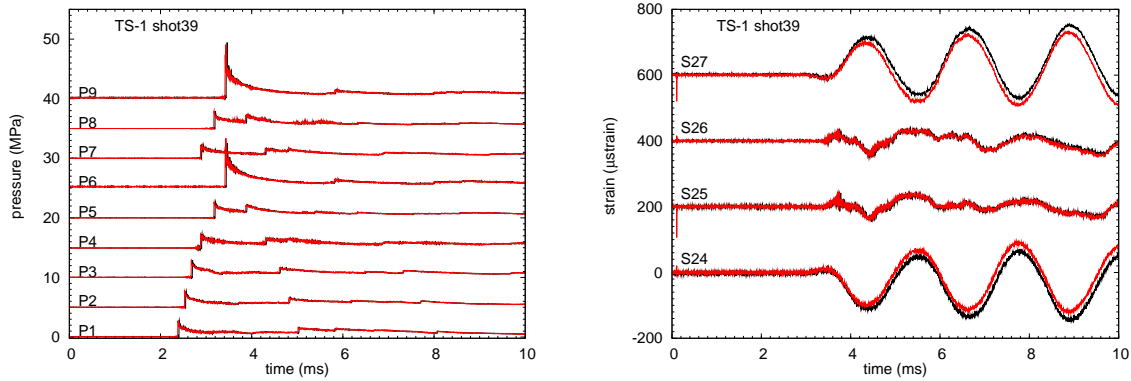


Figure 218: TS1 Shot 39 vs 38 comparisons. Pressure, and cantilever strain gage signals. 10 ms raw data.

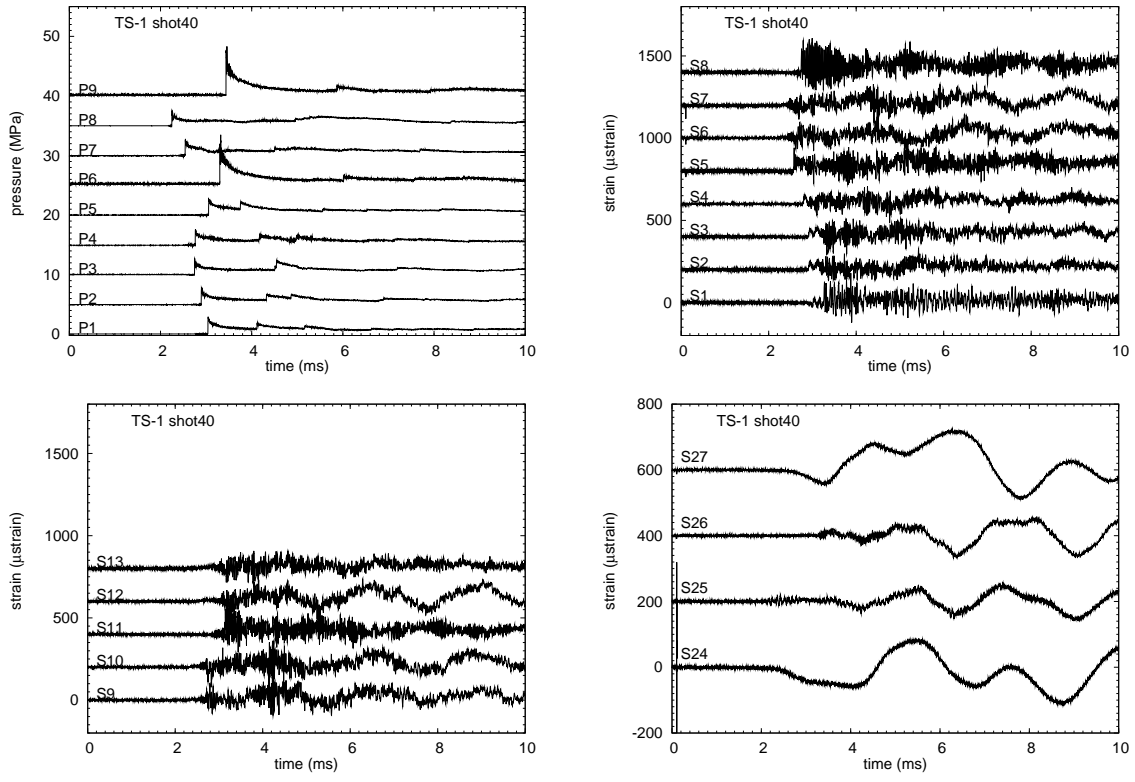


Figure 219: TS1 Shot 40. Pressure, strain gage, and cantilever strain gage signals. 10 ms raw data.

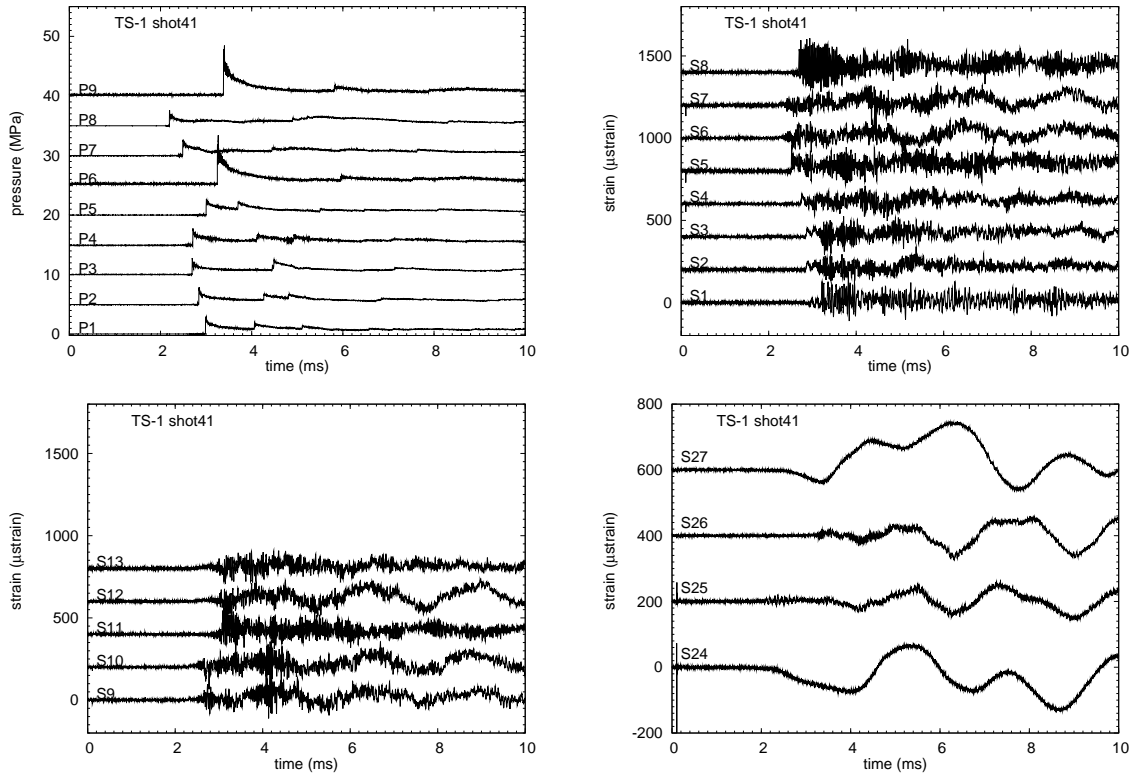


Figure 220: TS1 Shot 41. Pressure, strain gage, and cantilever strain gage signals. 10 ms raw data.

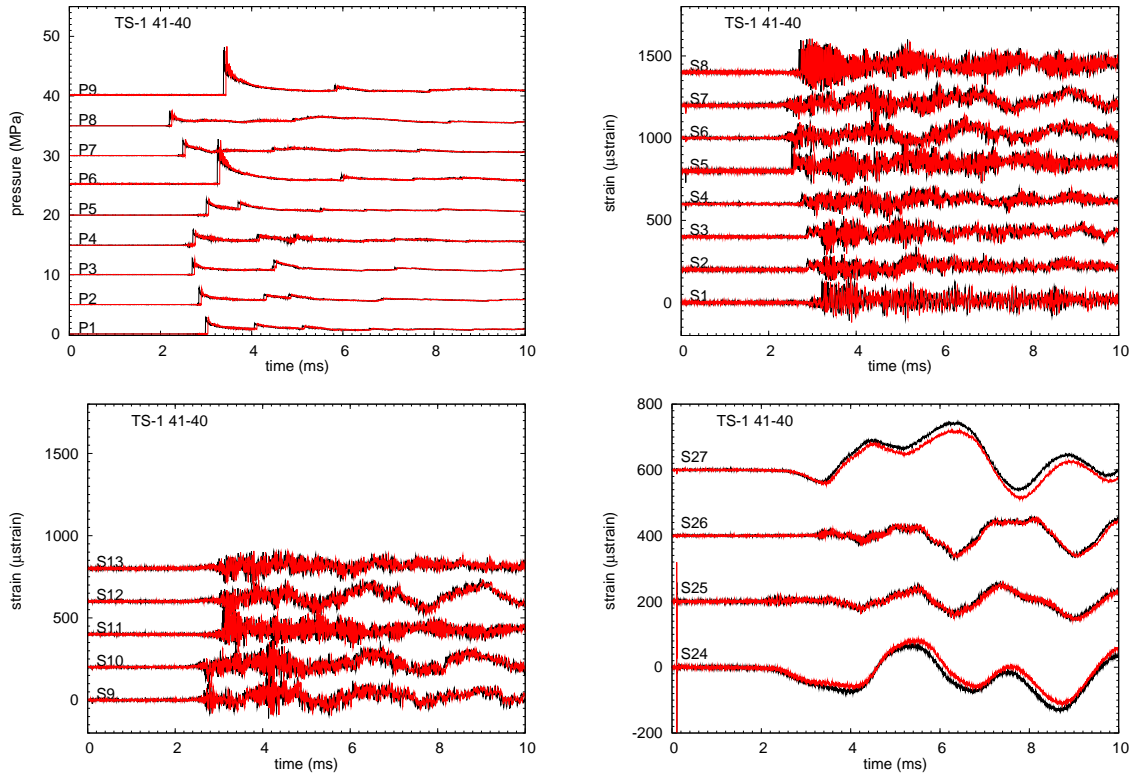


Figure 221: TS1 Shot 41 vs 40. Pressure, strain gage, and cantilever strain gage signals. 10 ms raw data.

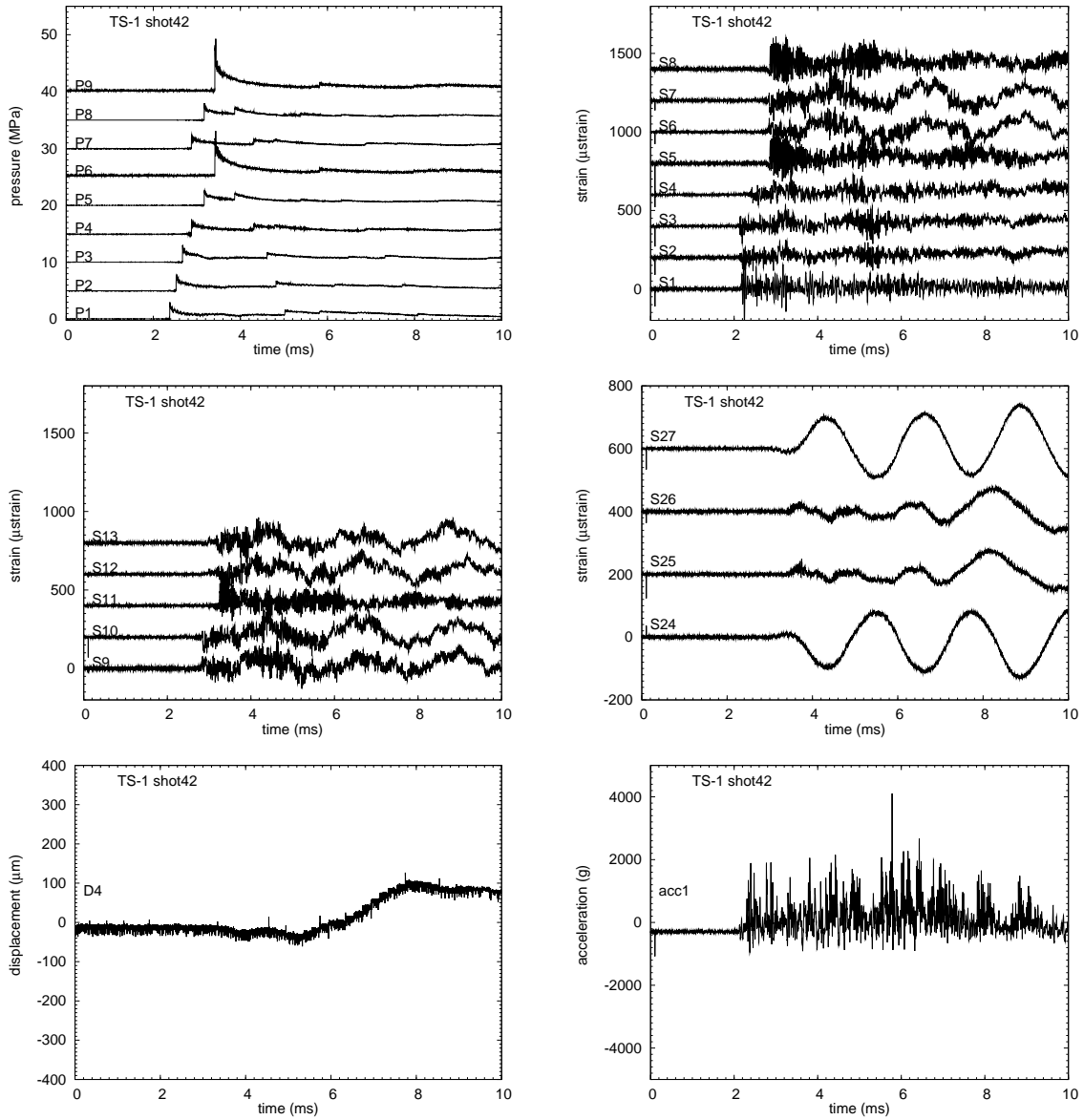


Figure 222: TS1 Shot 42. Pressure, strain gage, cantilever strain gage, displacement, and accelerometer signals. 10 ms raw data.

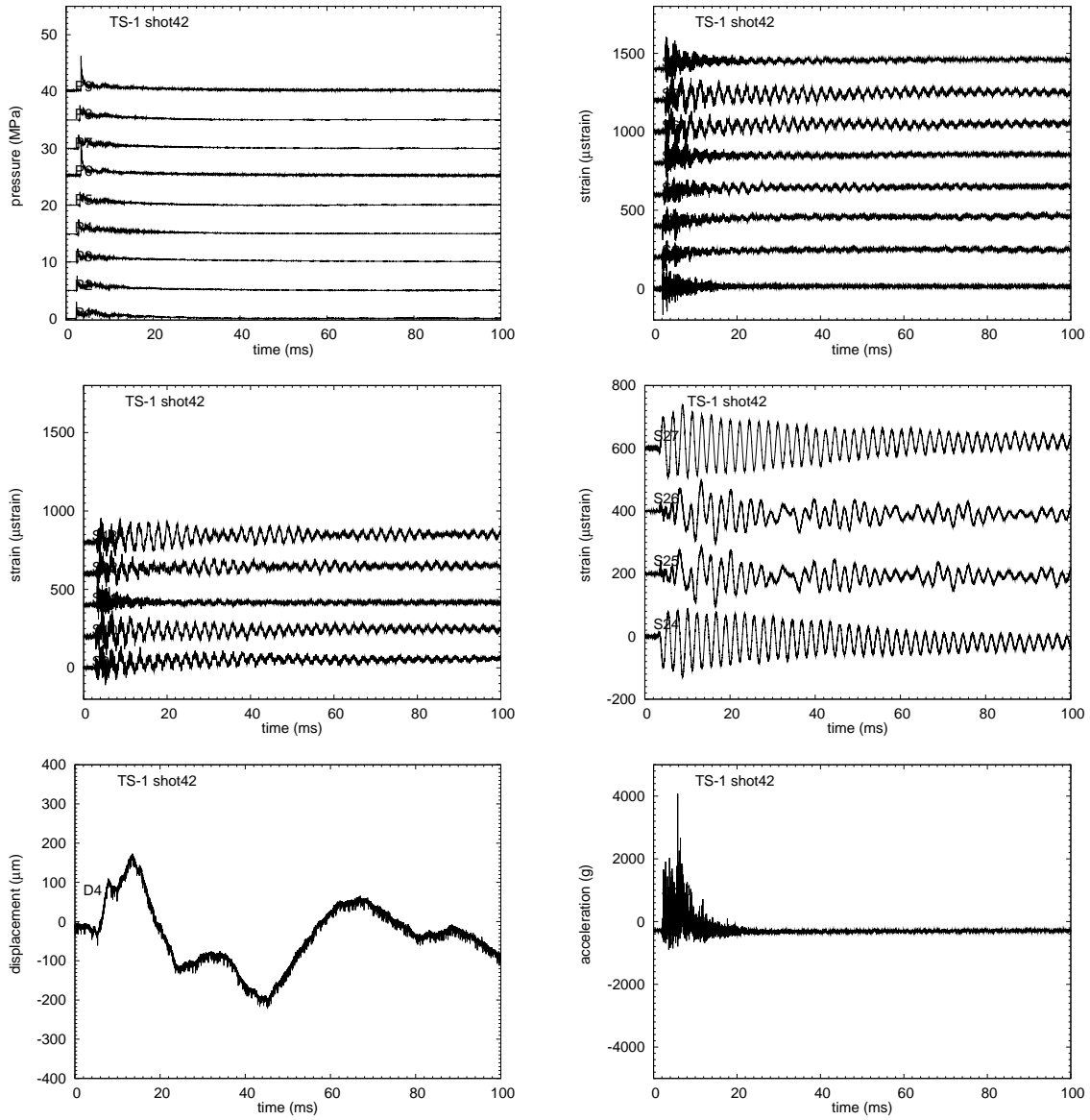


Figure 223: TS1 Shot 42. Pressure, strain gage, cantilever strain gage, displacement, and accelerometer signals. 100 ms raw data.

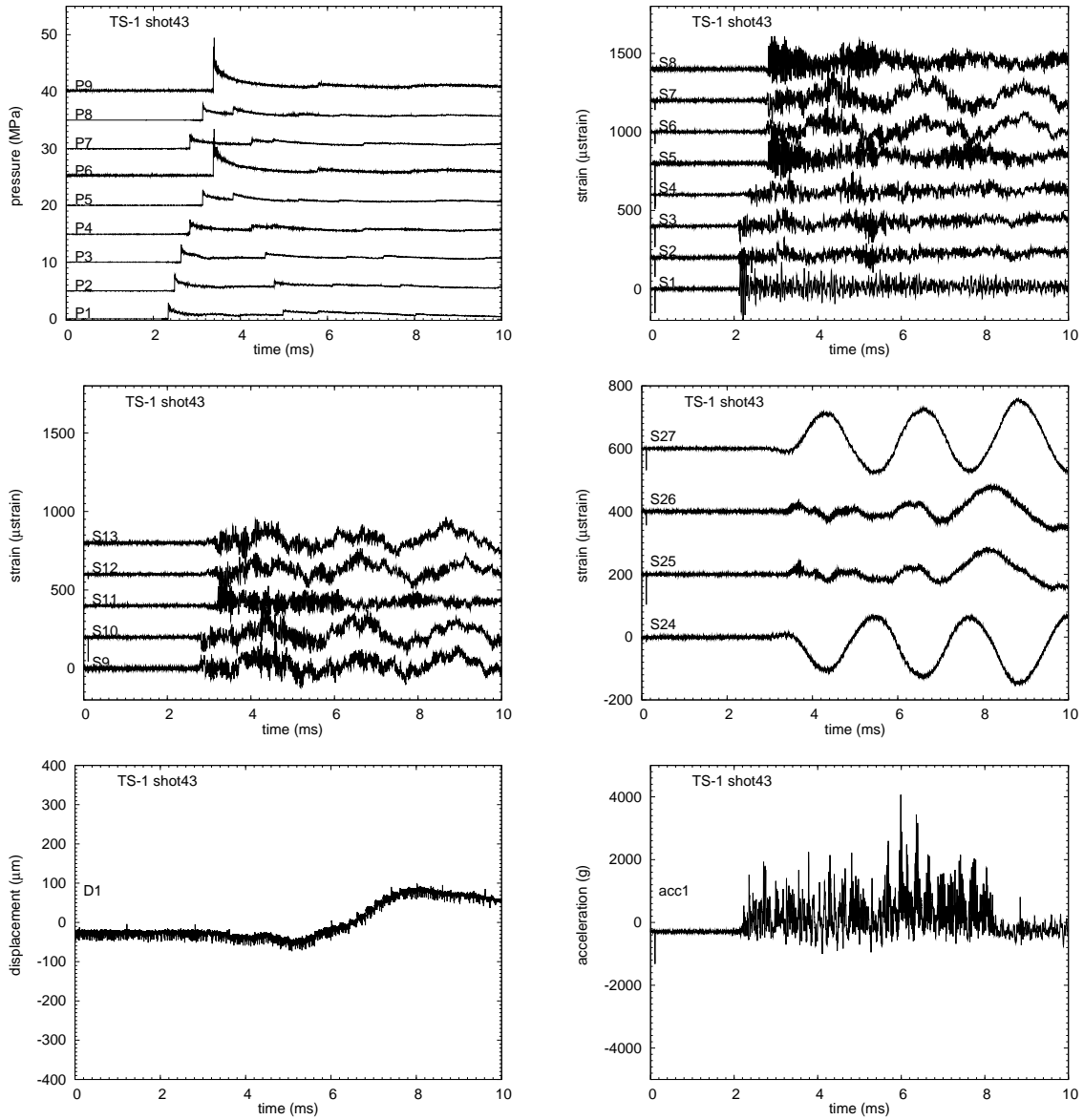


Figure 224: TS1 Shot 43. Pressure, strain gage, cantilever strain gage, displacement, and accelerometer signals. 10 ms raw data.

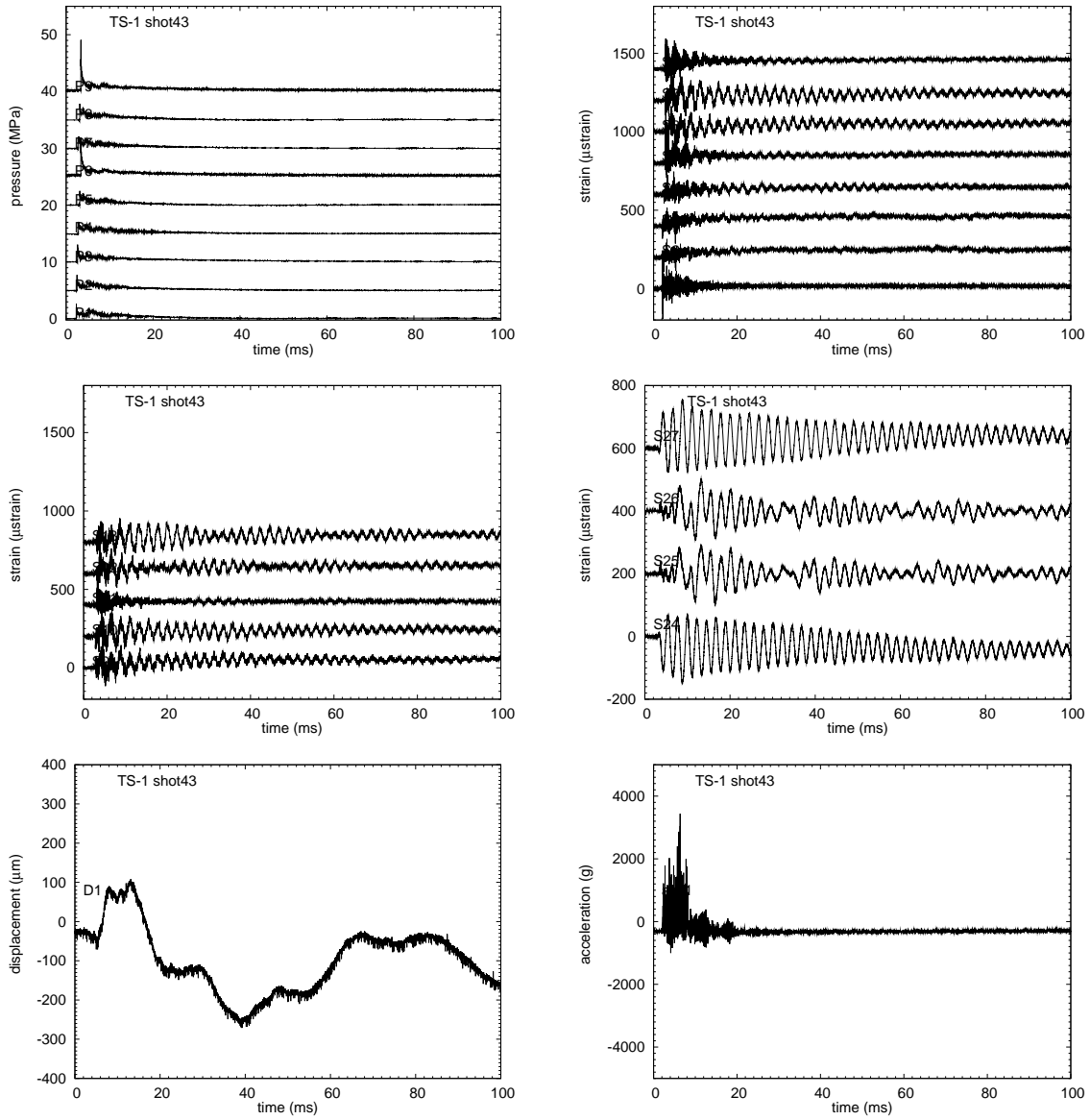


Figure 225: TS1 Shot 43. Pressure, strain gage, cantilever strain gage, displacement, and accelerometer signals. 100 ms raw data.

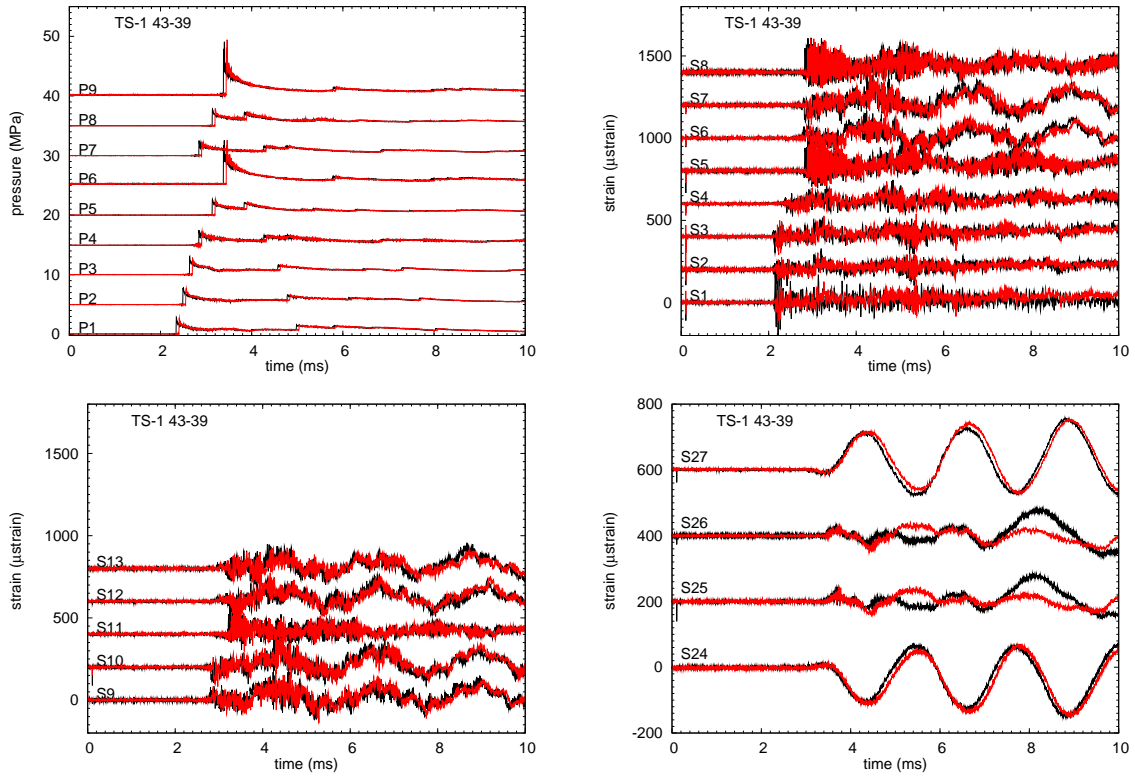


Figure 226: TS1 Shot 43 vs 39 . Pressure, strain gage, cantilever strain gage signals. 10 ms raw data.

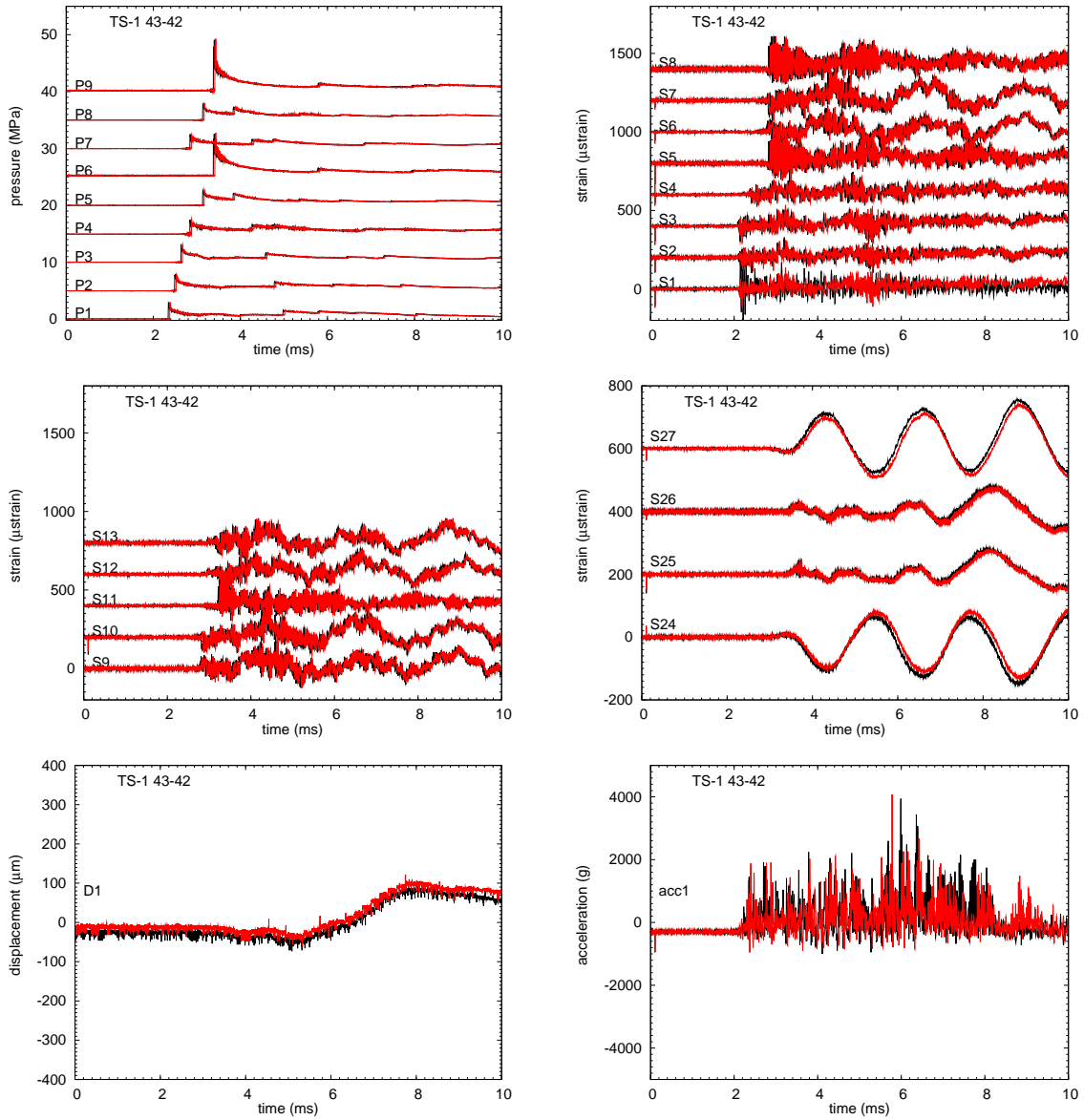


Figure 227: TS1 Shot 43 vs 42. Pressure, strain gage, cantilever strain gage, displacement, and accelerometer signals. 10 ms raw data.

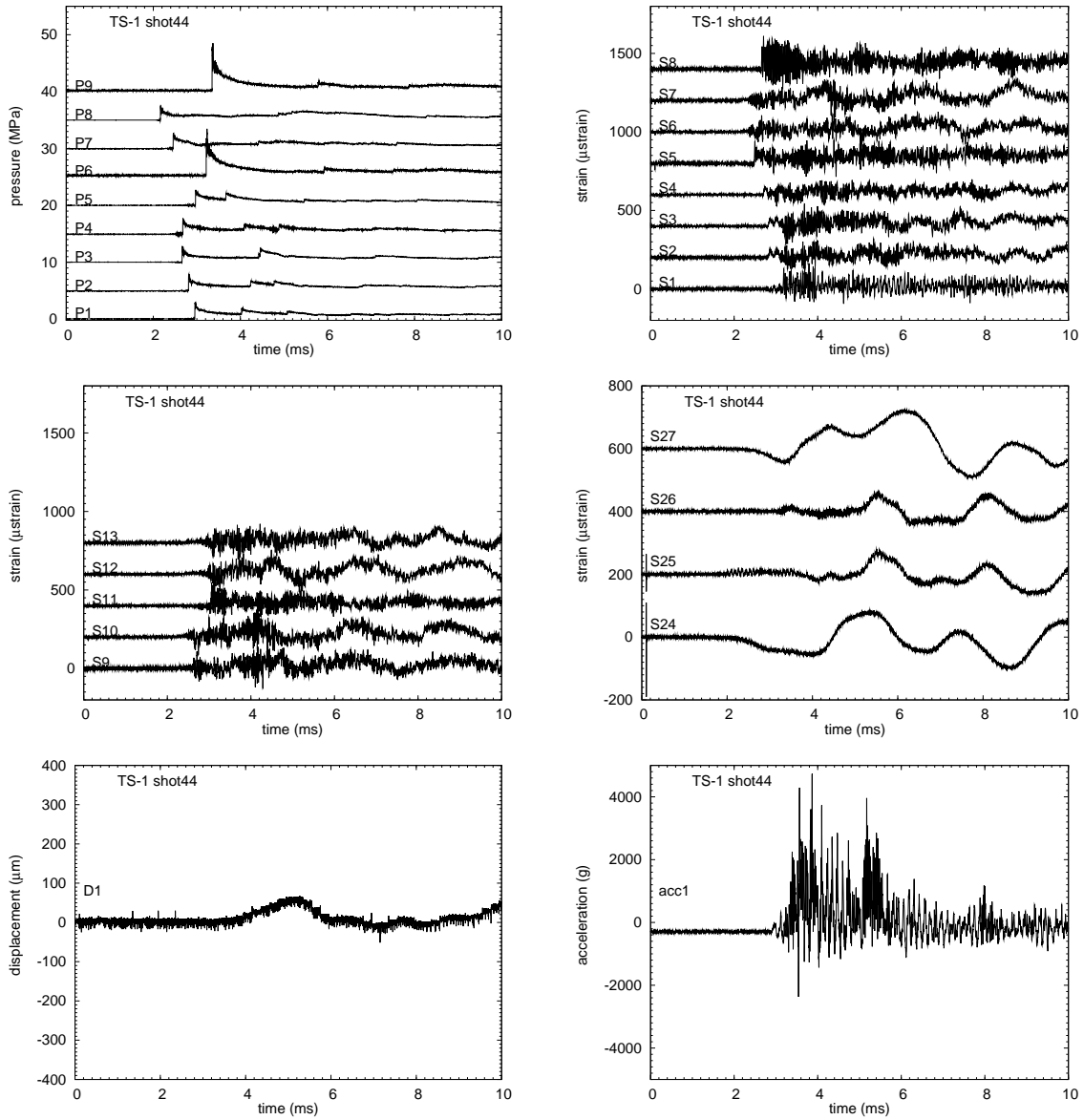


Figure 228: TS1 Shot 44. Pressure, strain gage, cantilever strain gage, displacement, and accelerometer signals. 10 ms raw data.

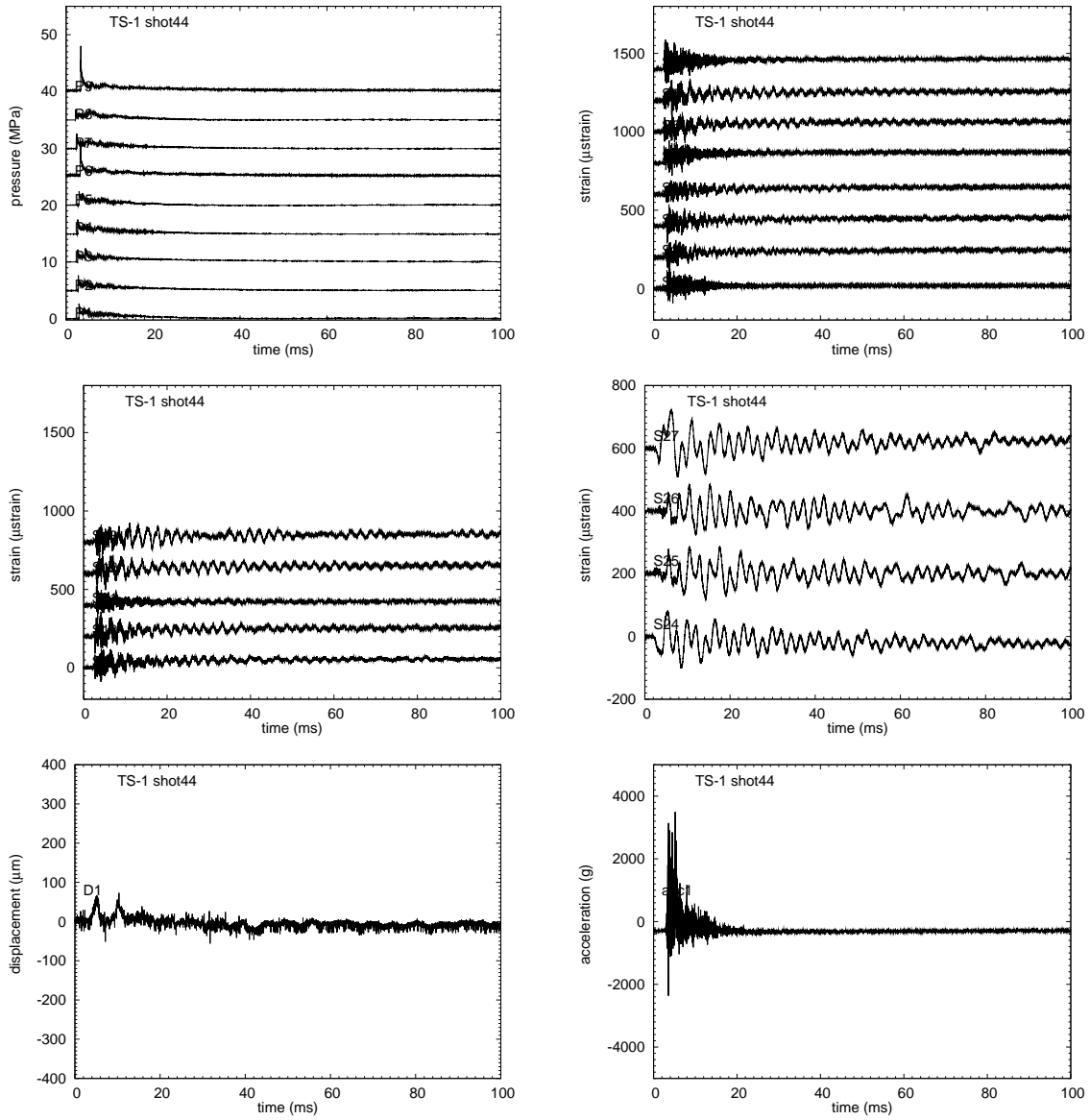


Figure 229: TS1 Shot 44. Pressure, strain gage, cantilever strain gage, displacement, and accelerometer signals. 100 ms raw data.

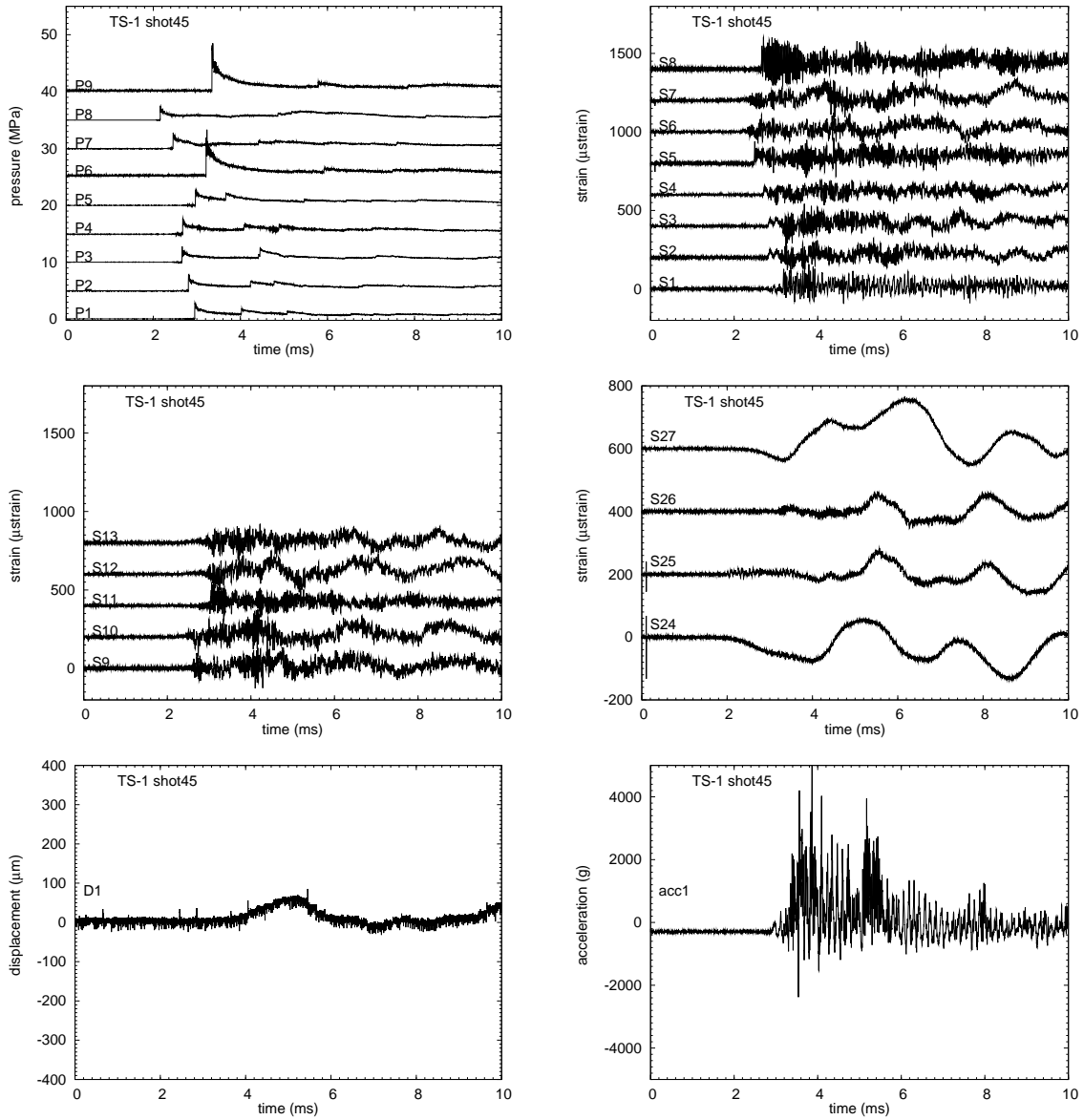


Figure 230: TS1 Shot 45. Pressure, strain gage, cantilever strain gage, displacement, and accelerometer signals. 10 ms raw data.

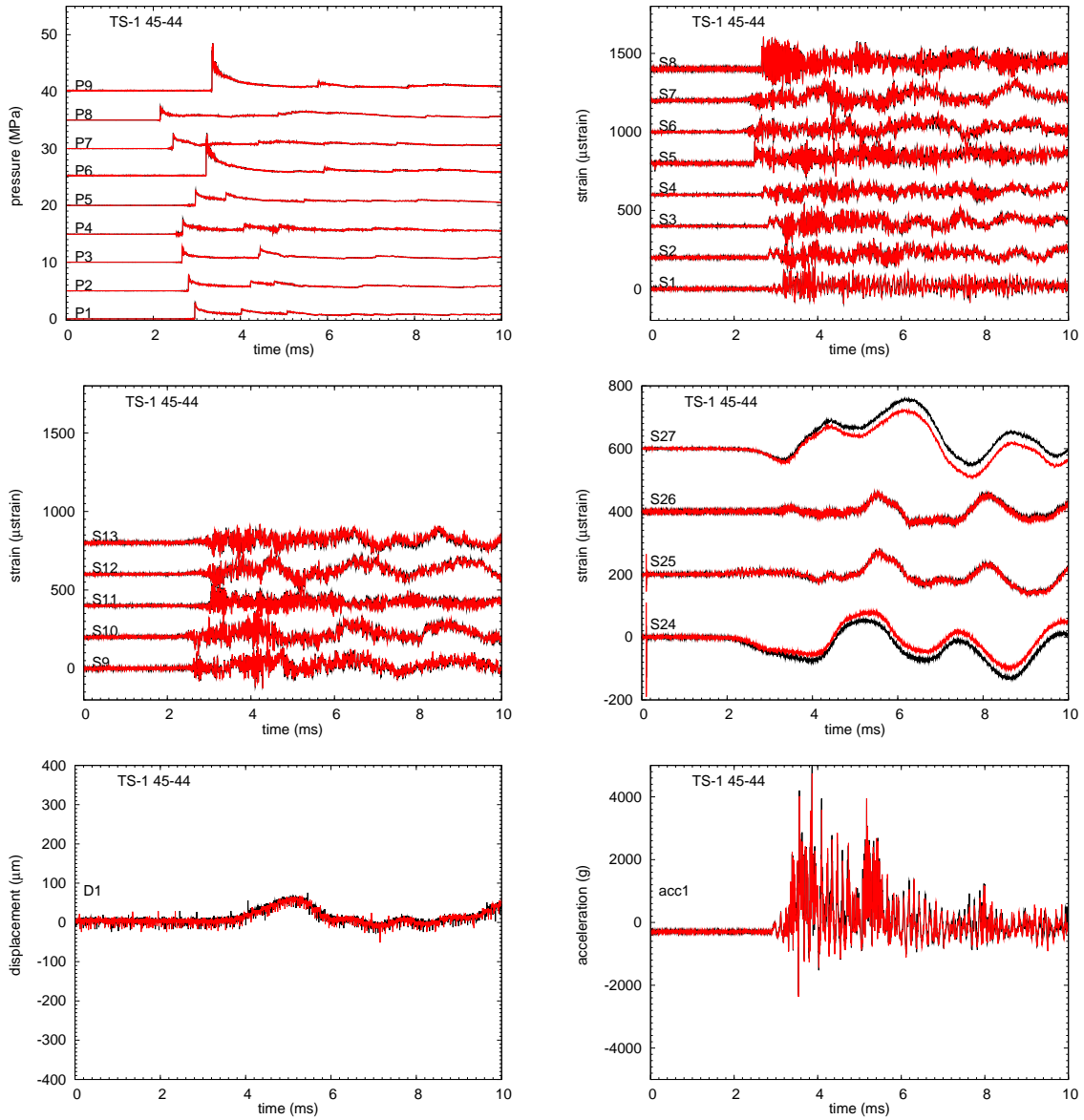


Figure 231: TS1 Shot 45 vs 44. Pressure, strain gage, cantilever strain gage, displacement, and accelerometer signals. 10 ms raw data.

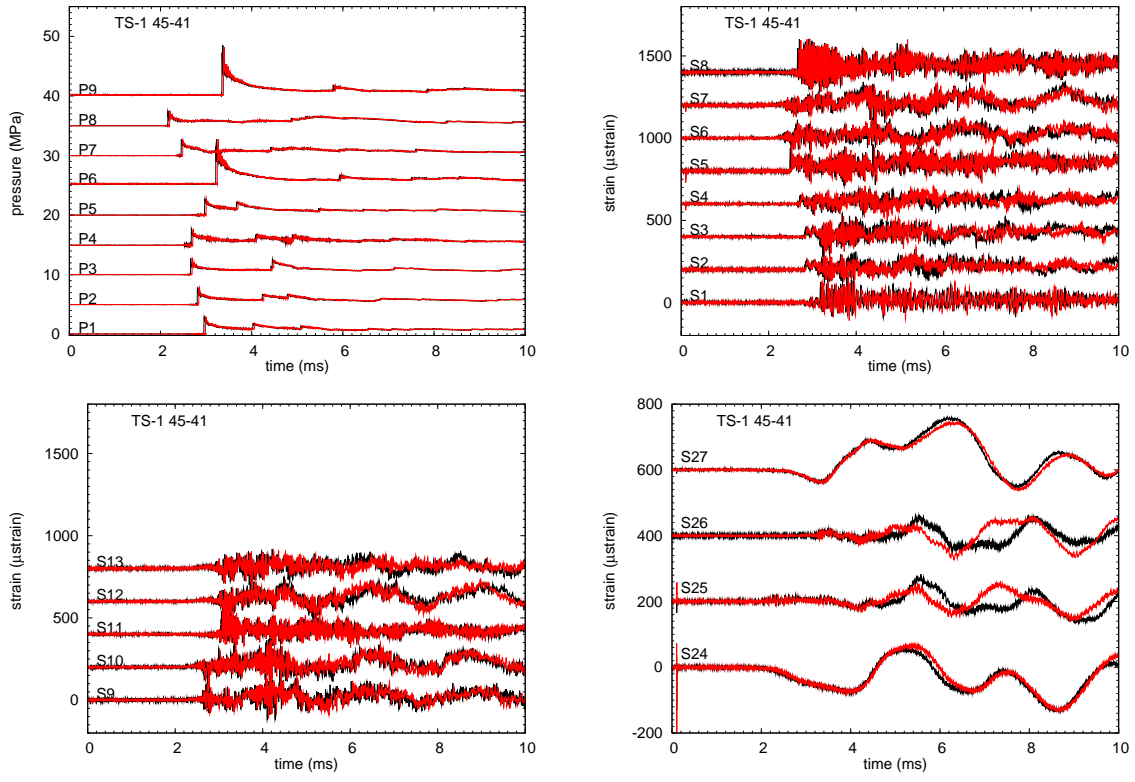


Figure 232: TS1 Shot 45 vs 41. Pressure, strain gage, and cantilever strain gage signals. 10 ms raw data.

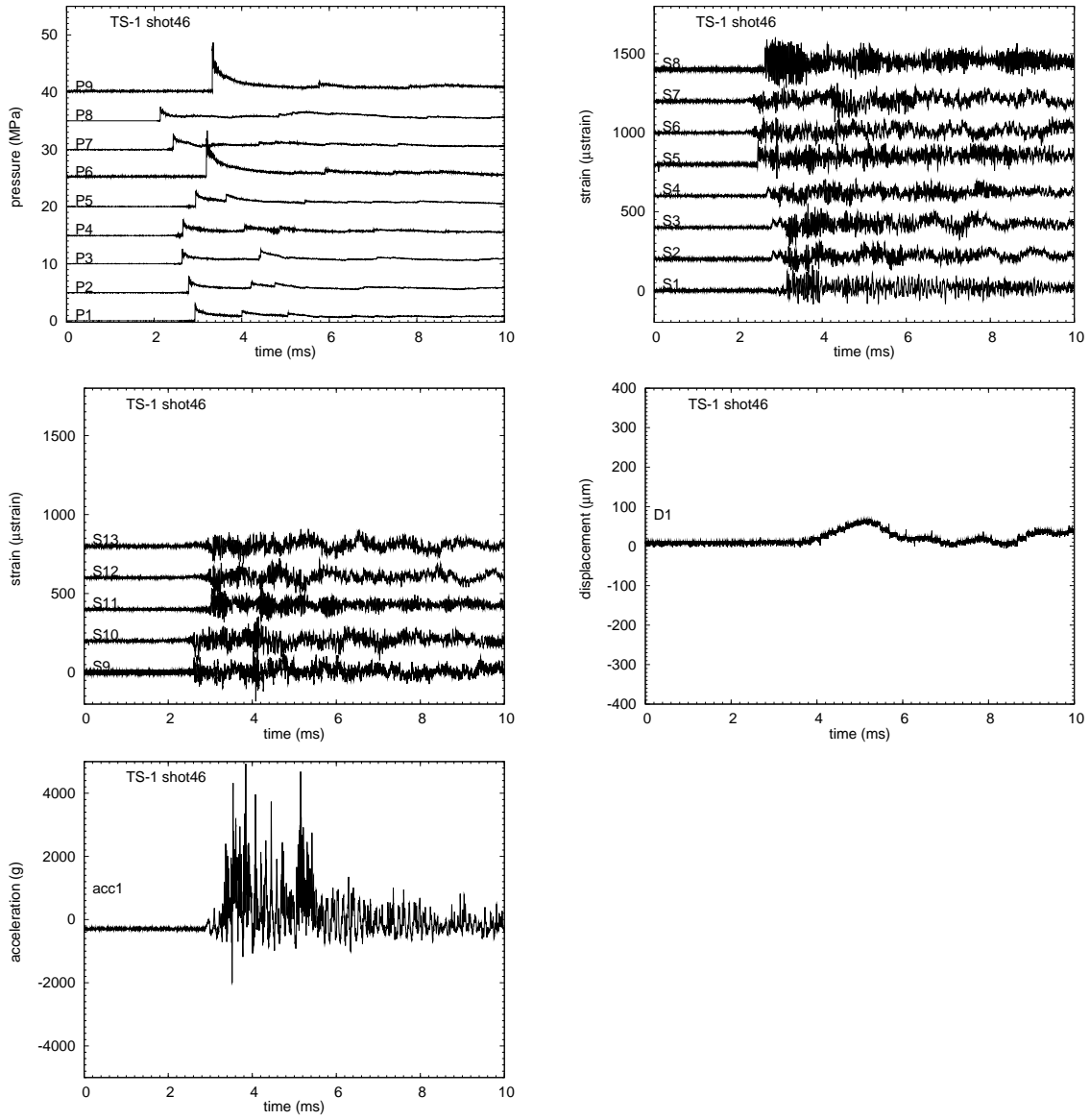


Figure 233: TS1 Shot 46. Pressure, strain gage, displacement, and accelerometer signals. 10 ms raw data.

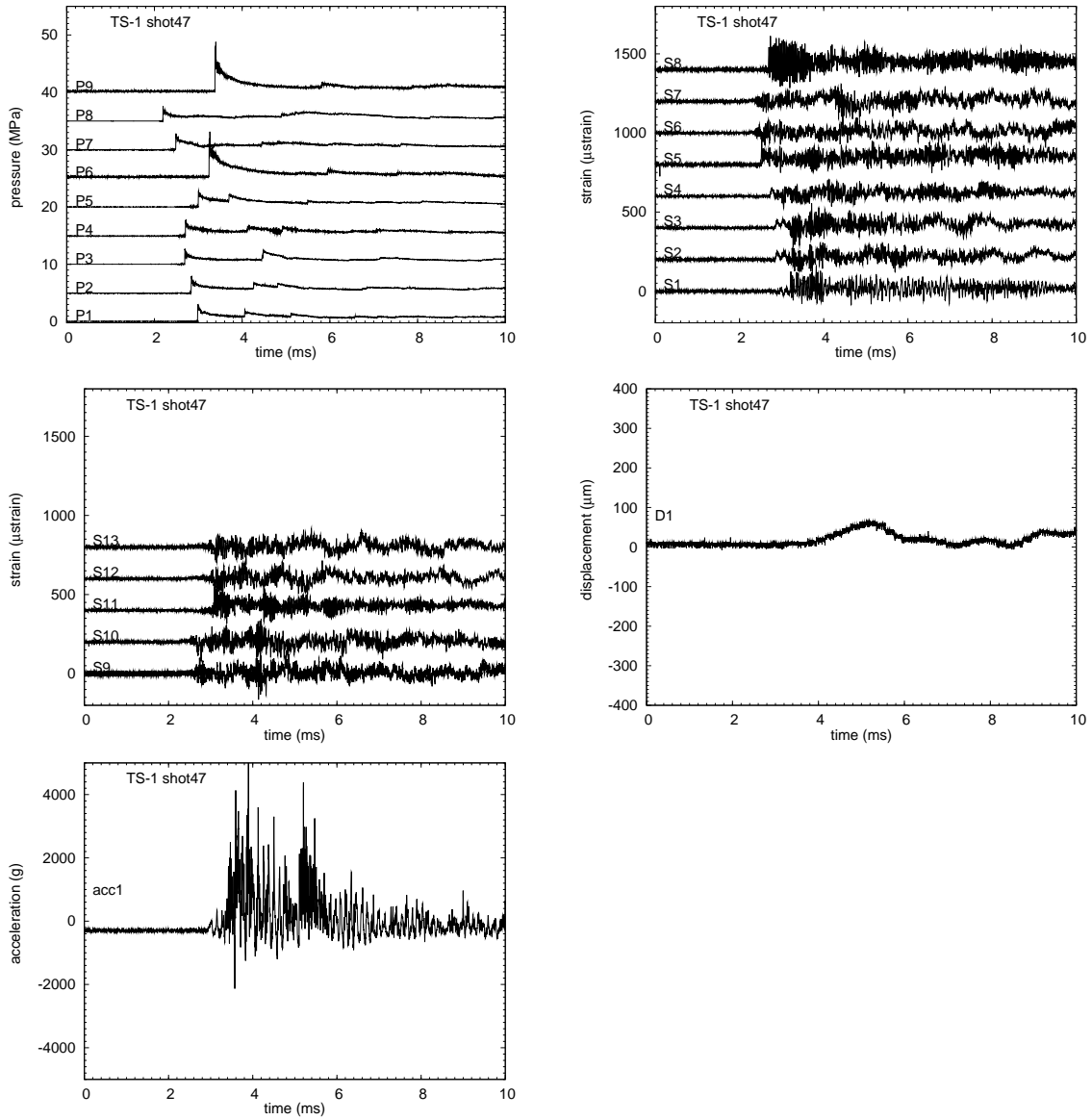


Figure 234: TS1 Shot 47. Pressure, strain gage, displacement, and accelerometer signals. 10 ms raw data.

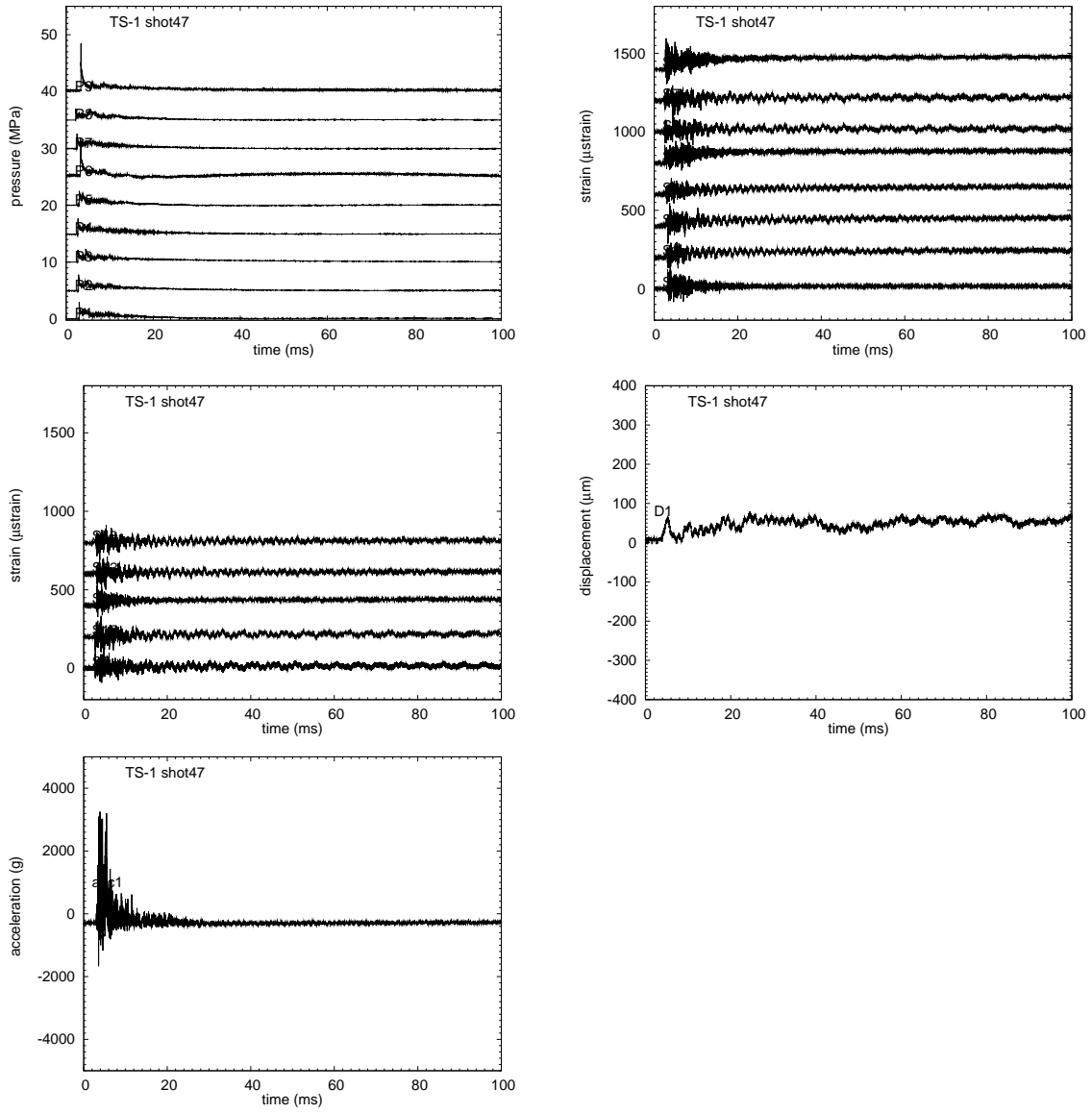


Figure 235: TS1 Shot 47. Pressure, strain gage, displacement, and accelerometer signals. 100 ms raw data.

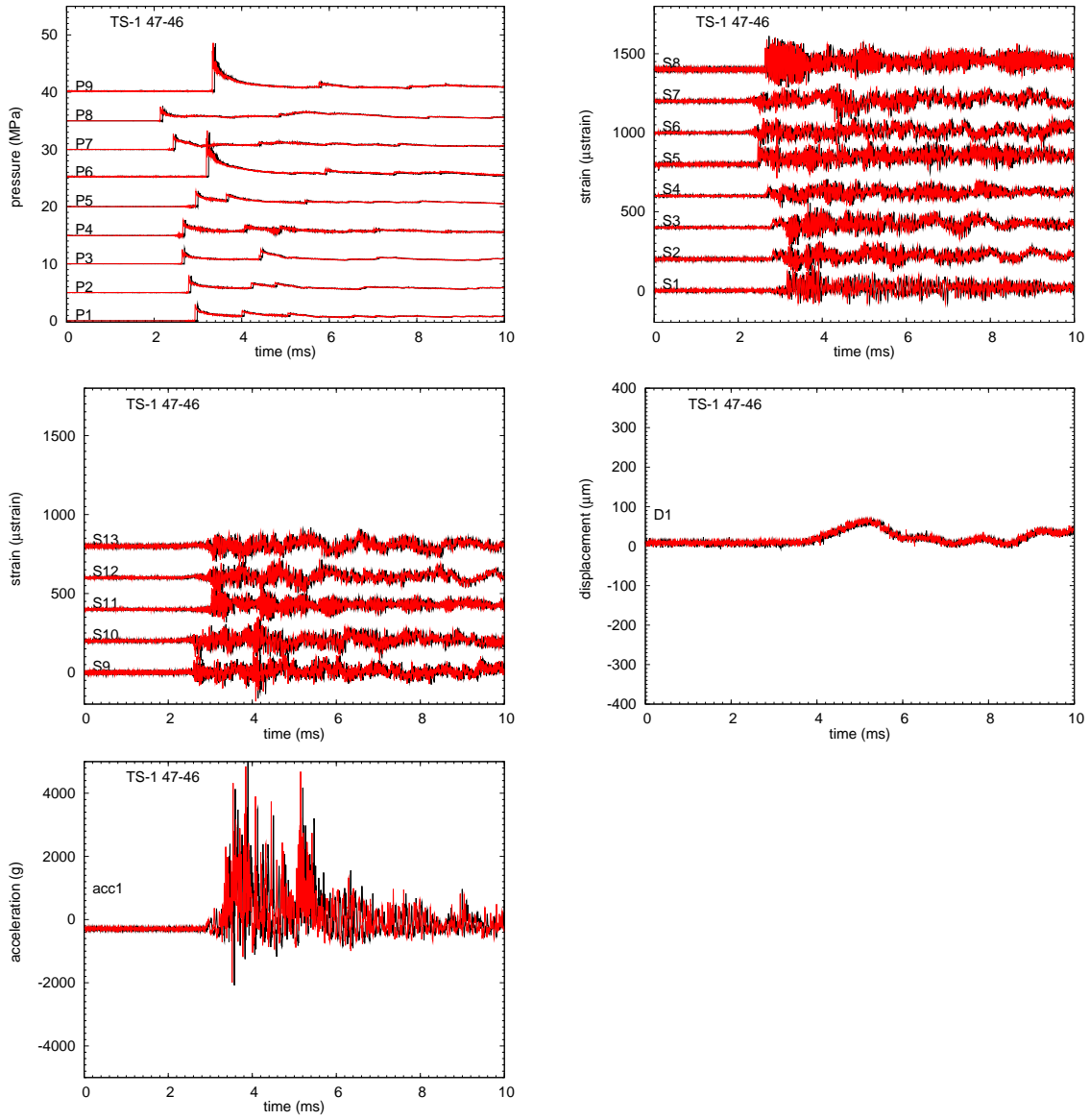


Figure 236: TS1 Shot 47 vs 46. Pressure, strain gage, displacement, and accelerometer signals. 10 ms raw data.

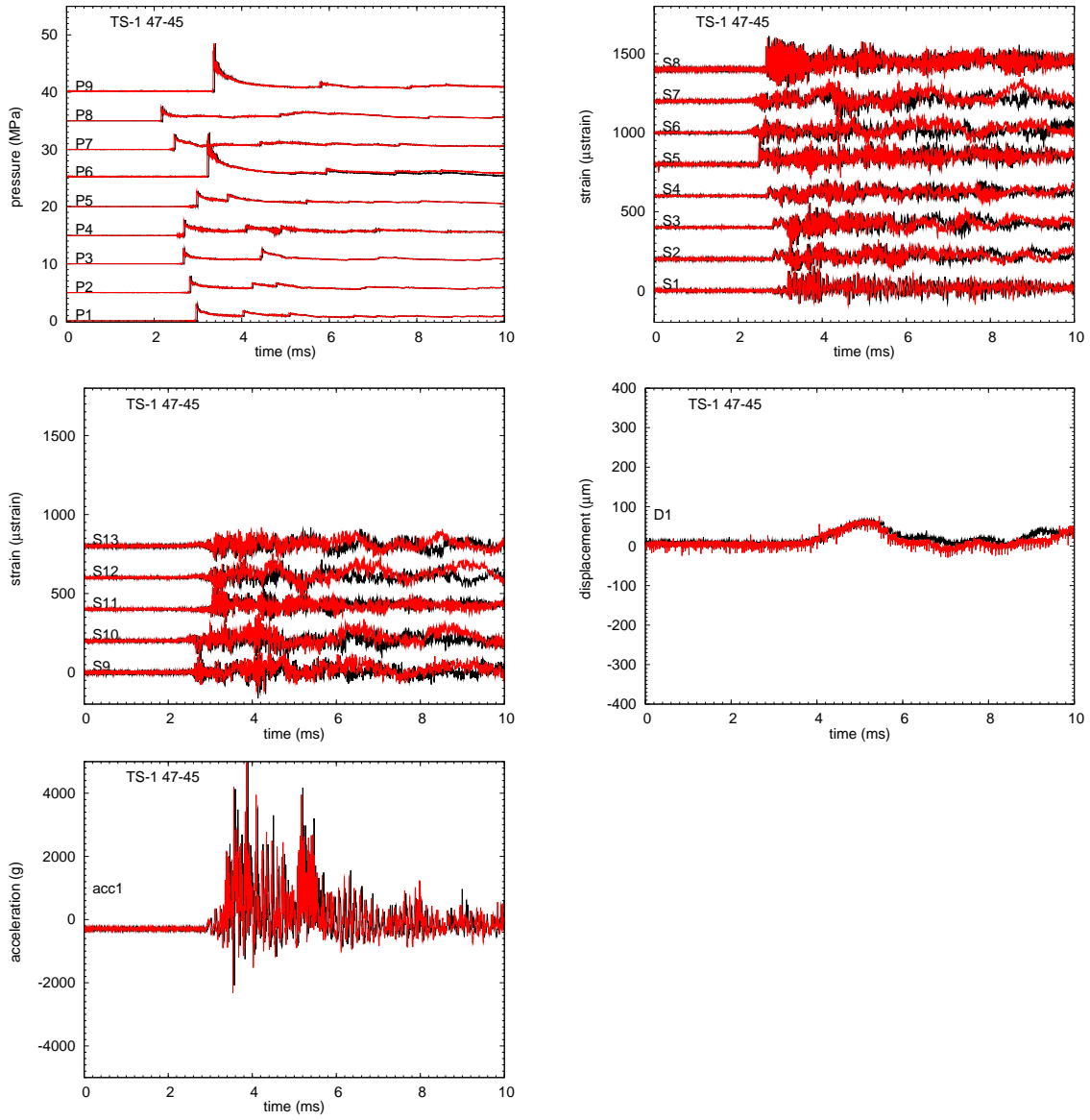


Figure 237: TS1 Shot 47 vs 45. Pressure, strain gage, displacement, and accelerometer signals. 10 ms raw data.

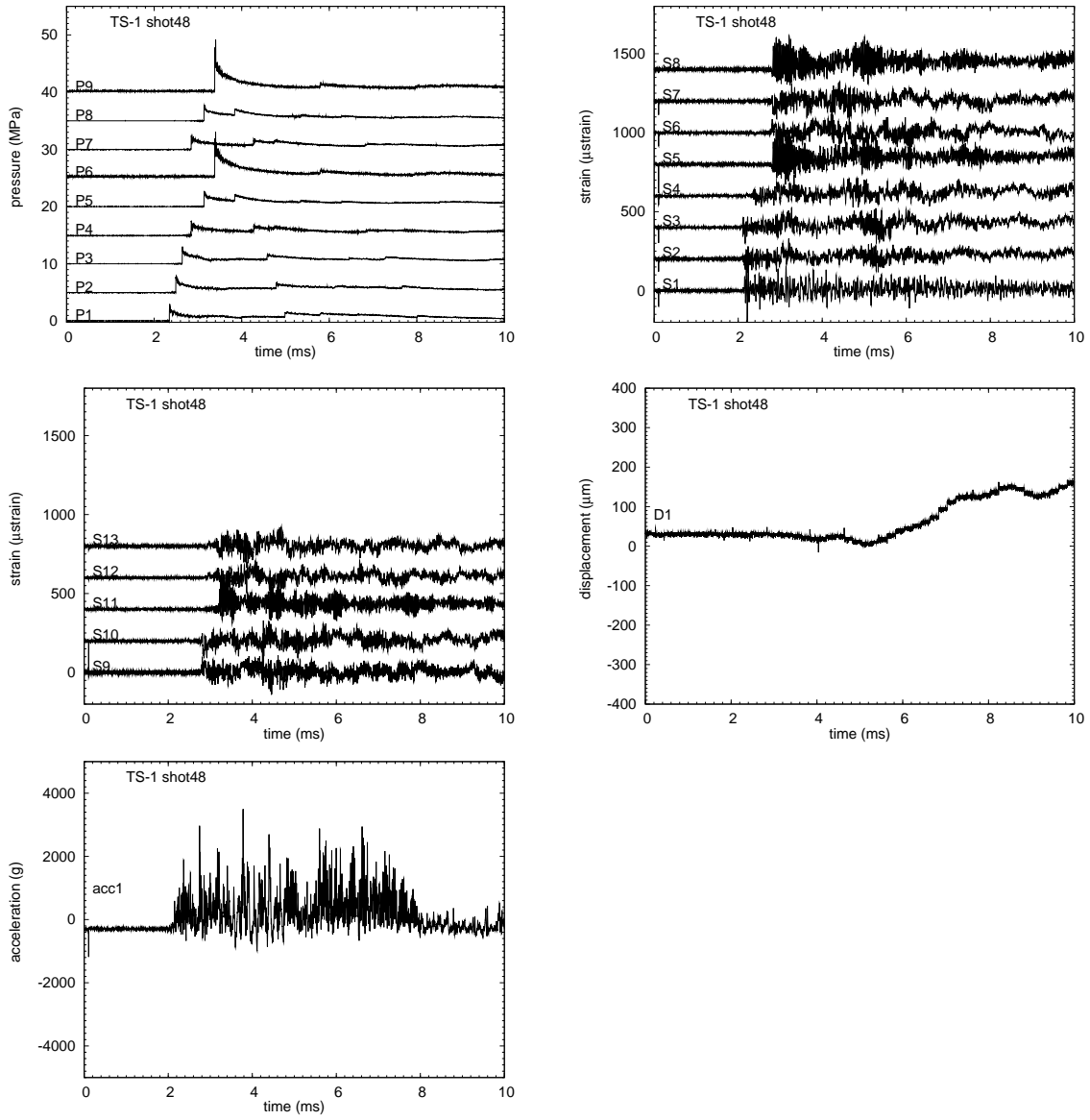


Figure 238: TS1 Shot 48. Pressure, strain gage, displacement, and accelerometer signals. 10 ms raw data.

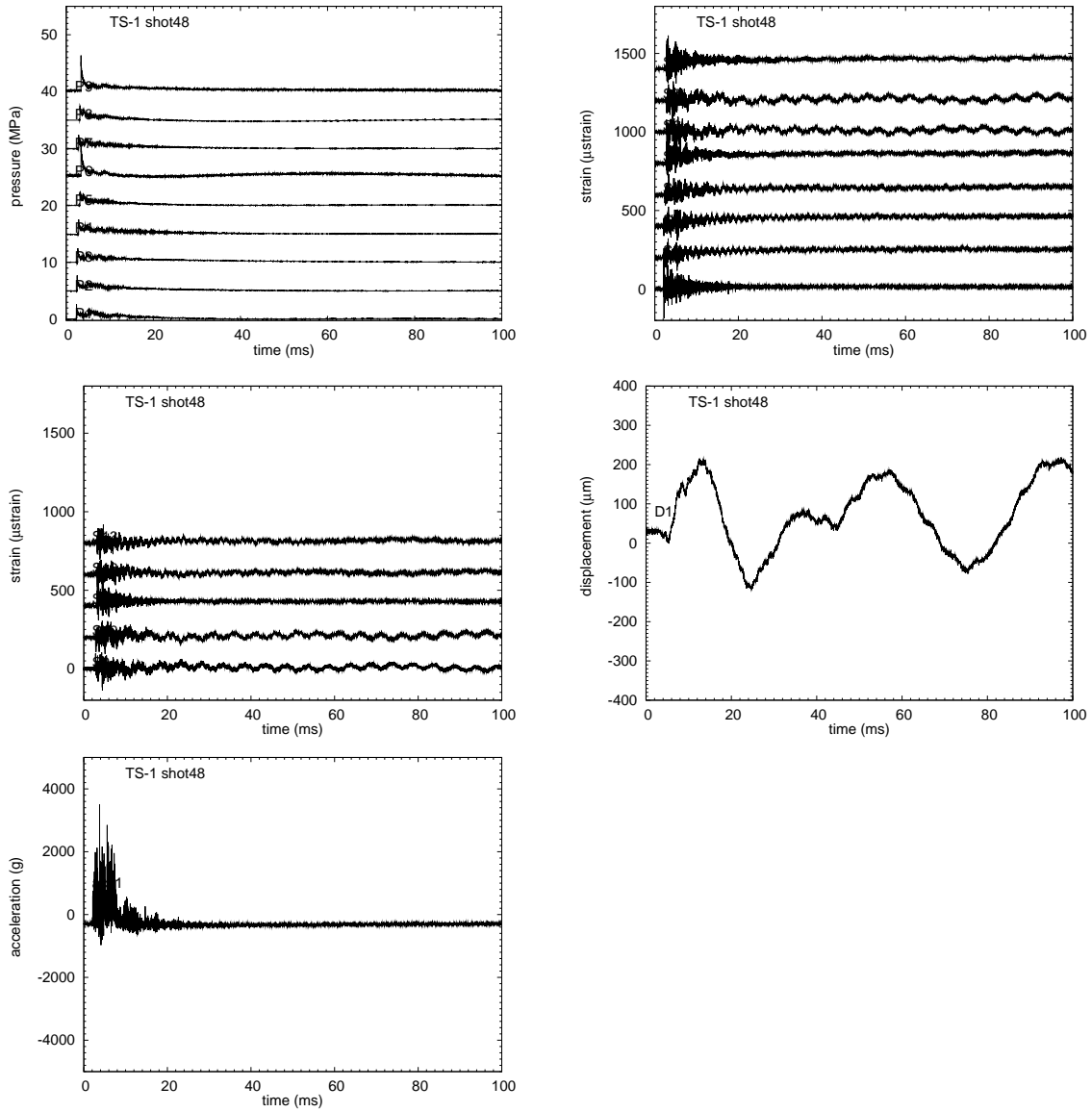


Figure 239: TS1 Shot 48. Pressure, strain gage, displacement, and accelerometer signals. 100 ms raw data.

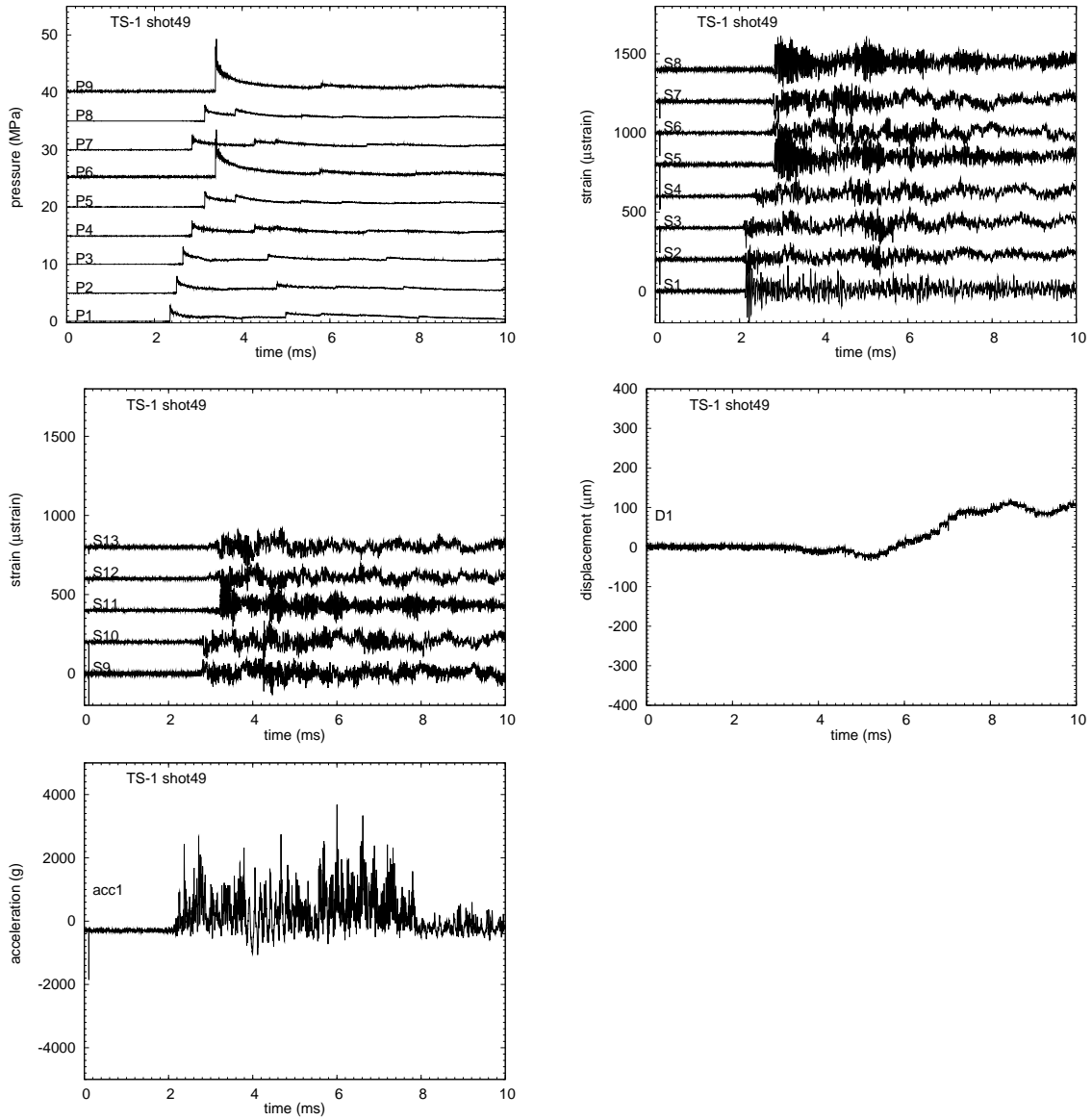


Figure 240: TS1 Shot 49. Pressure, strain gage, displacement, and accelerometer signals. 10 ms raw data.

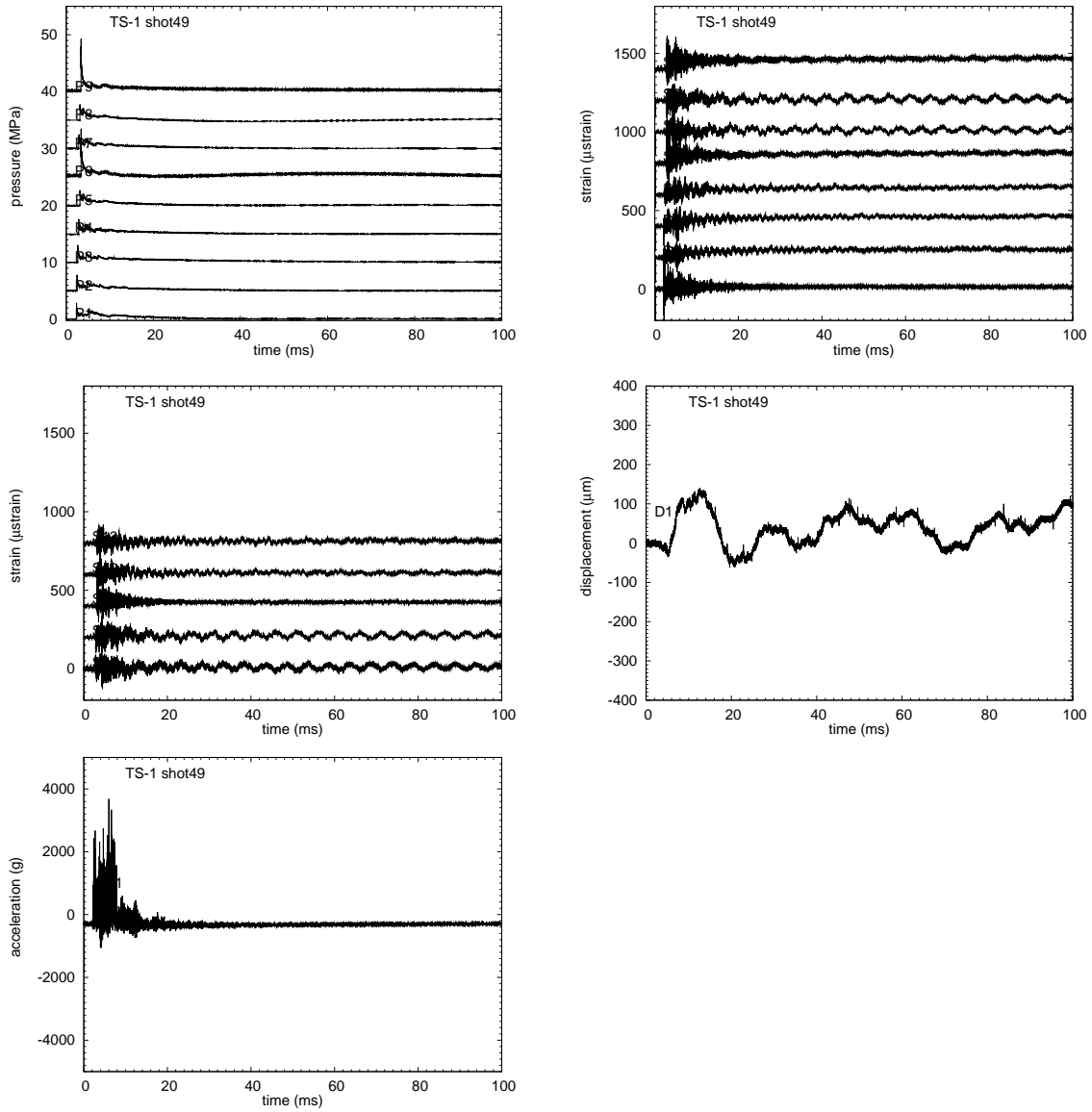


Figure 241: TS1 Shot 49. Pressure, strain gage, displacement, and accelerometer signals. 100 ms raw data.

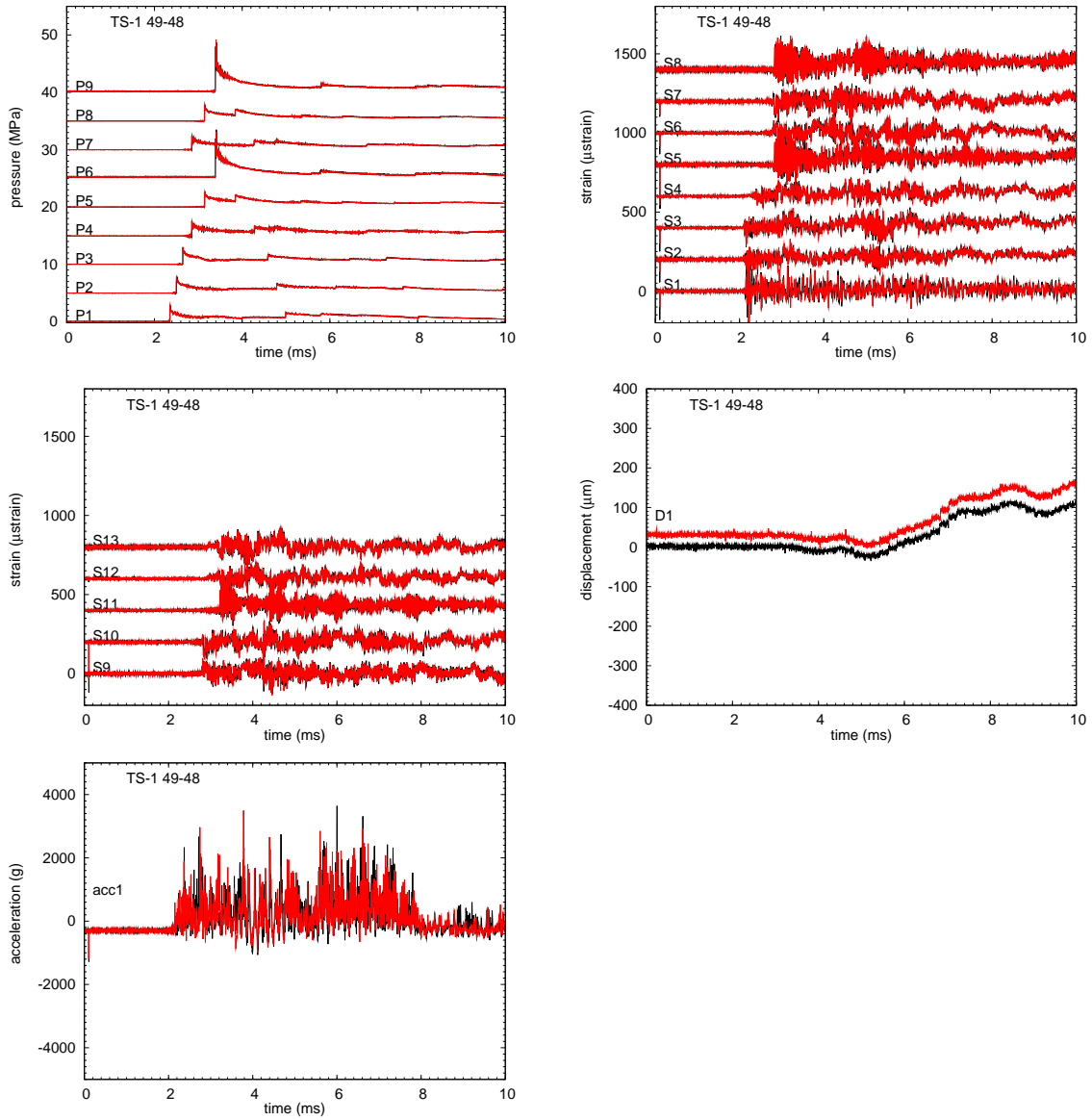


Figure 242: TS1 Shot 49 vs 48. Pressure, strain gage, displacement, and accelerometer signals. 10 ms raw data.

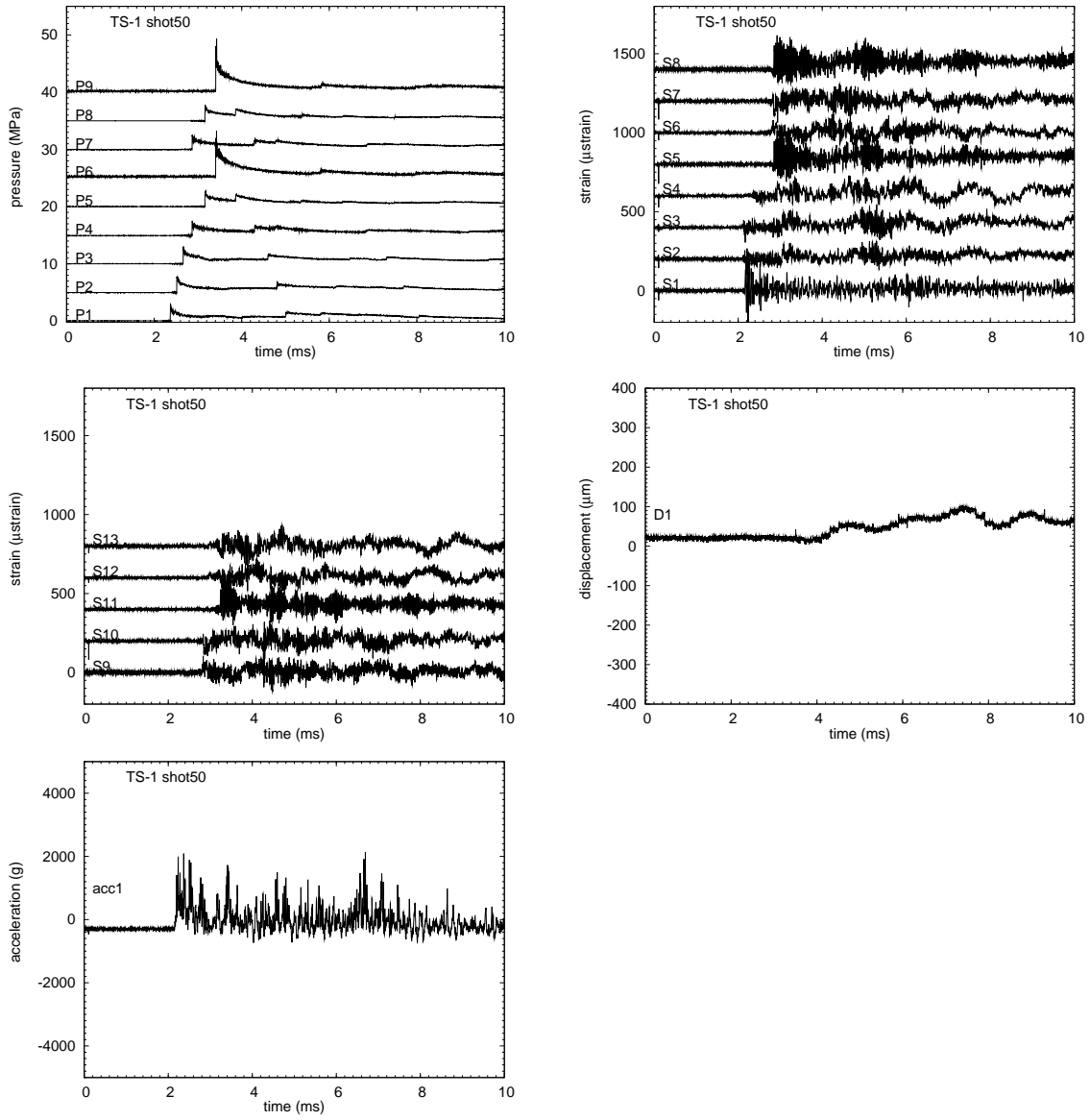


Figure 243: TS1 Shot 50. Pressure, strain gage, displacement, and accelerometer signals. 10 ms raw data.

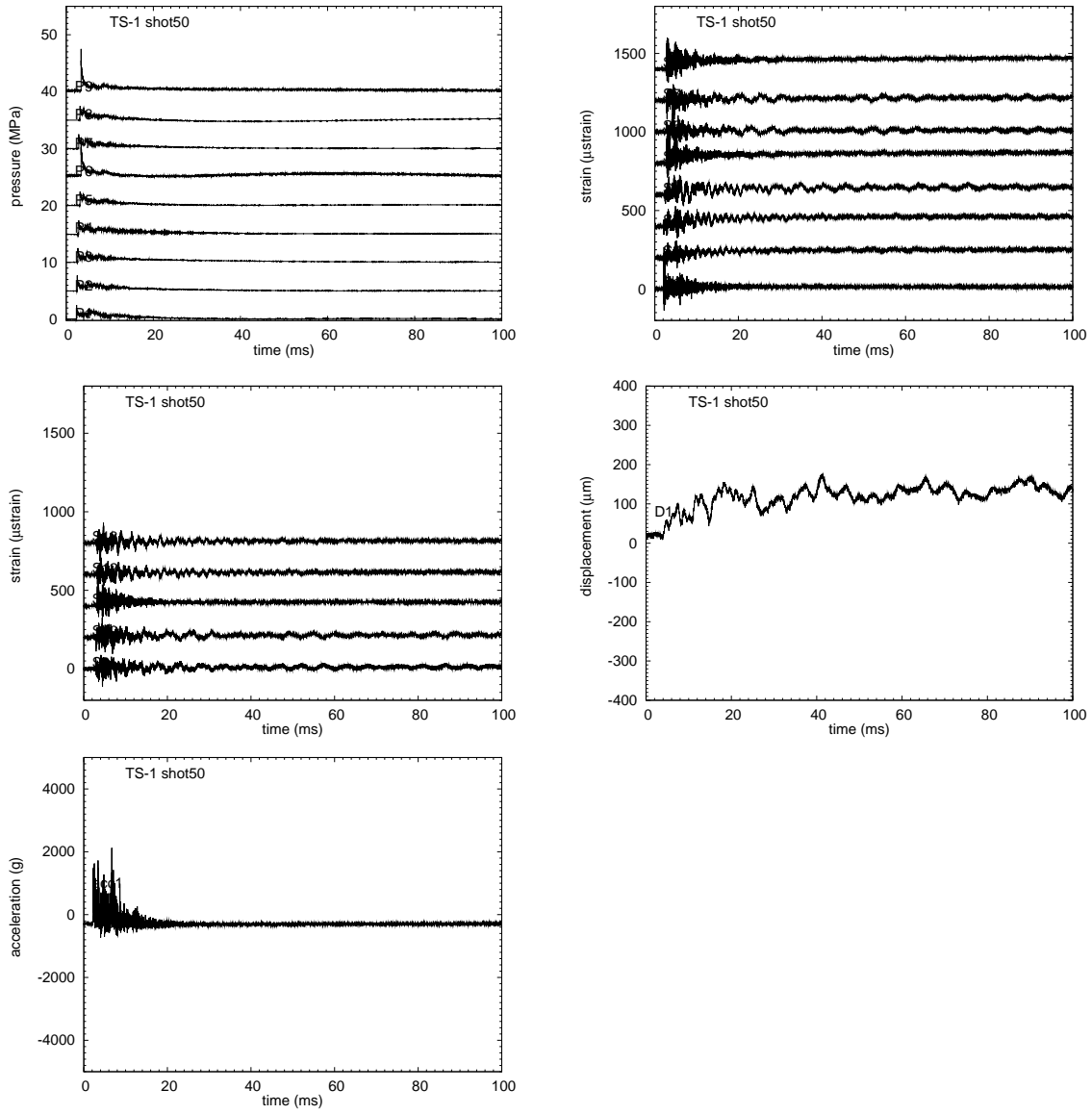


Figure 244: TS1 Shot 50. Pressure, strain gage, displacement, and accelerometer signals. 100 ms raw data.

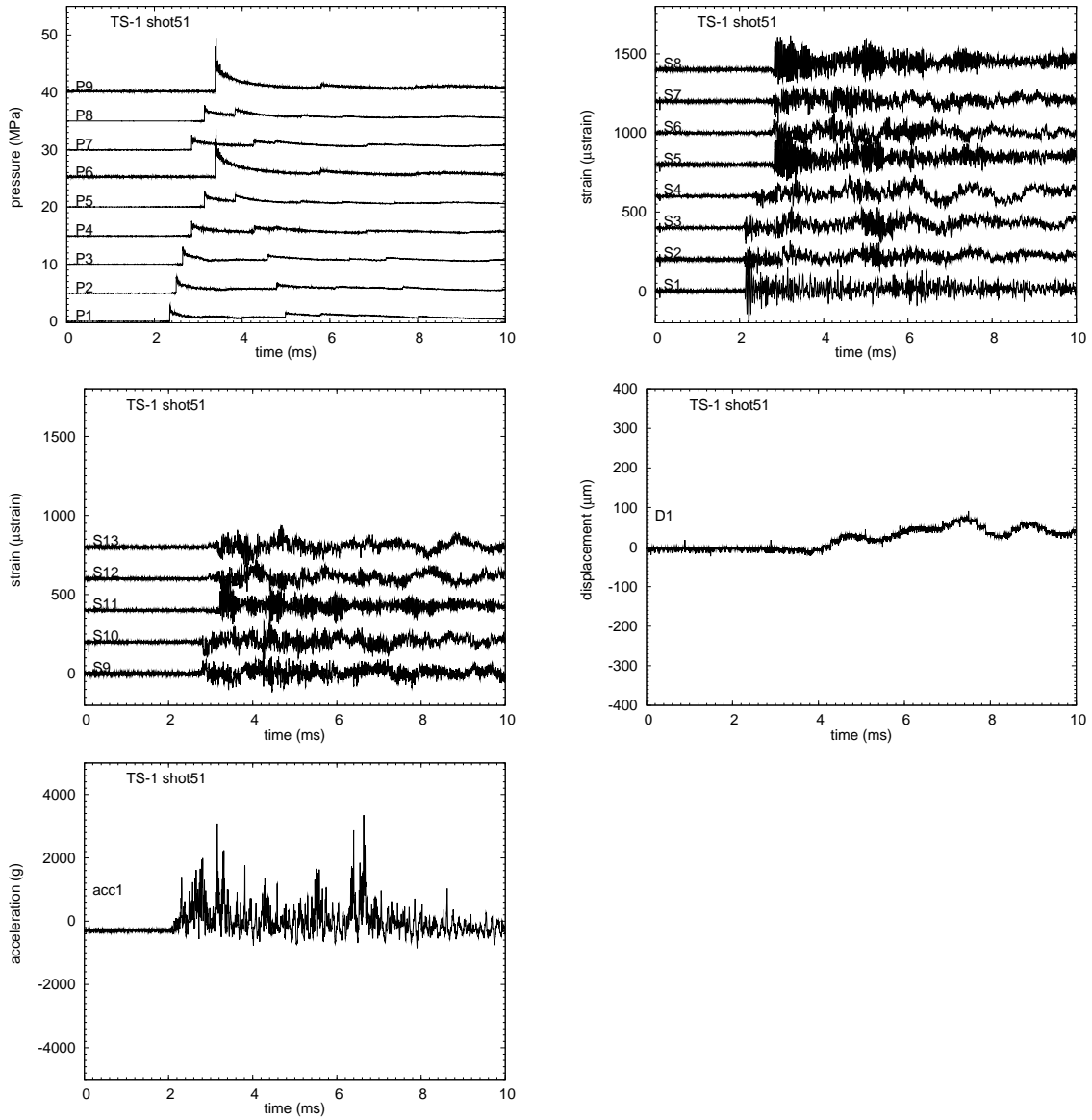


Figure 245: TS1 Shot 51. Pressure, strain gage, displacement, and accelerometer signals. 10 ms raw data.

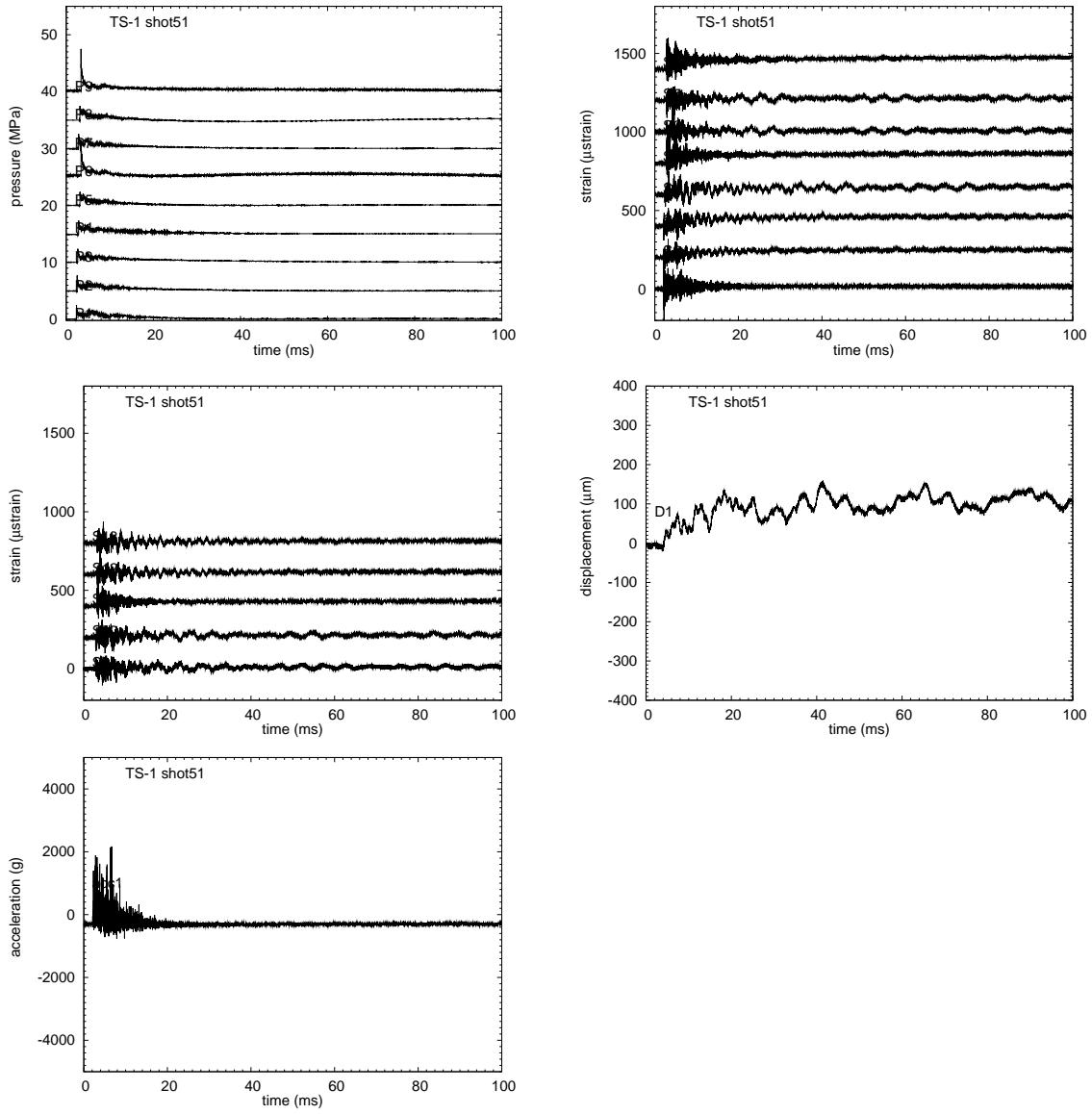


Figure 246: TS1 Shot 51. Pressure, strain gage, displacement, and accelerometer signals. 100 ms raw data.

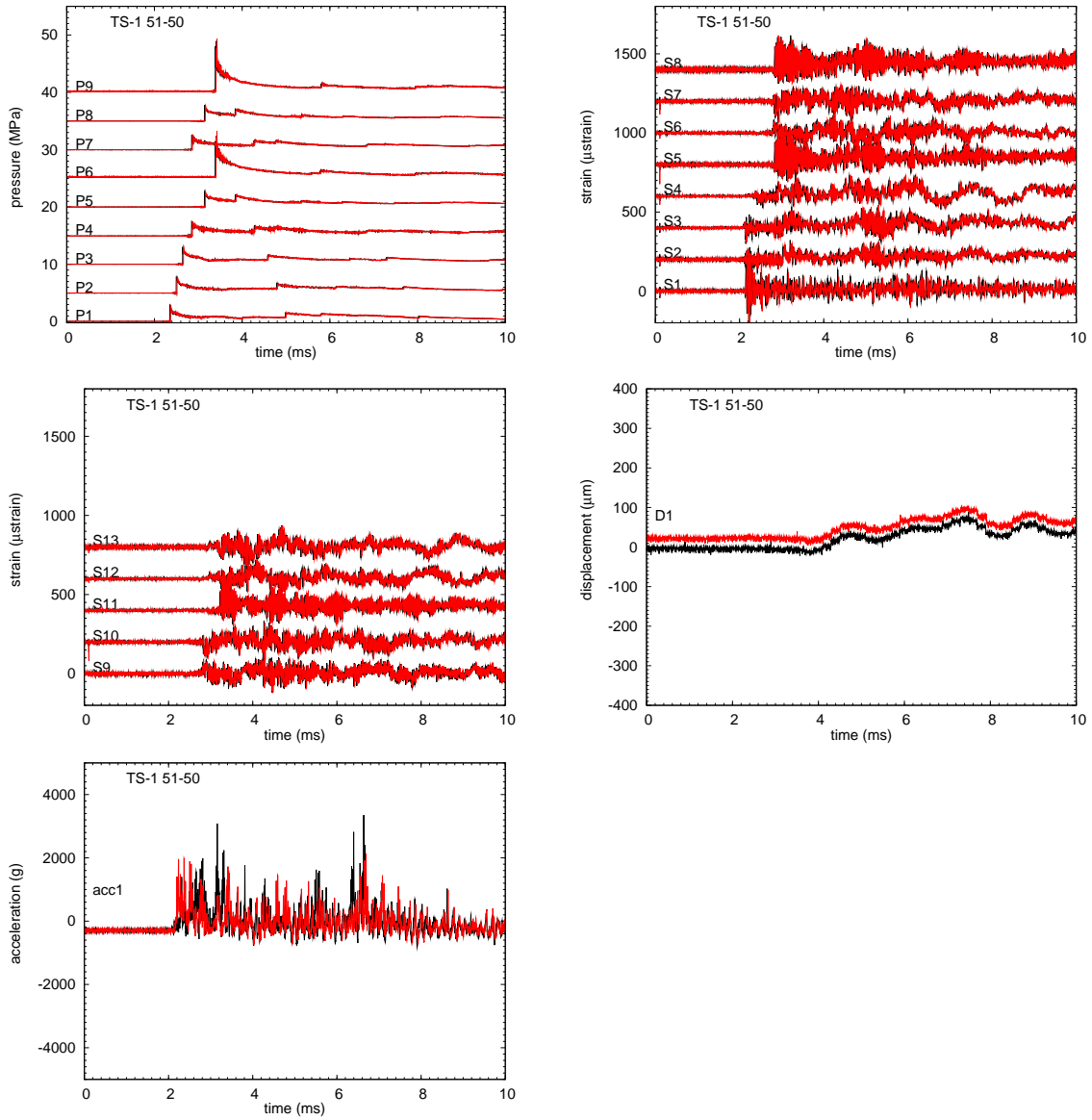


Figure 247: TS1 Shot 51 vs 50. Pressure, strain gage, displacement, and accelerometer signals. 10 ms raw data.

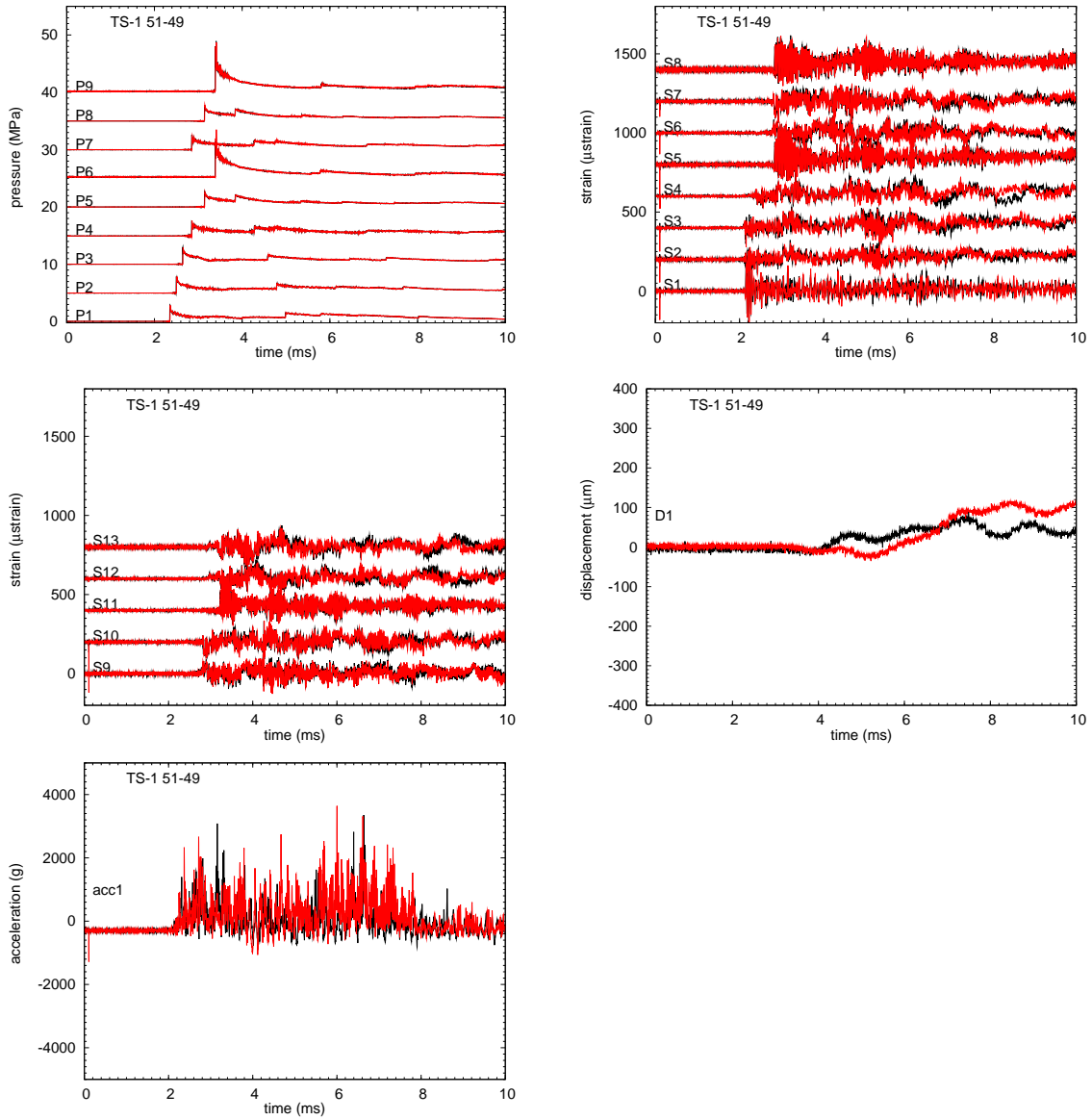


Figure 248: TS1 Shot 51 vs 49. Pressure, strain gage, displacement, and accelerometer signals. 10 ms raw data.

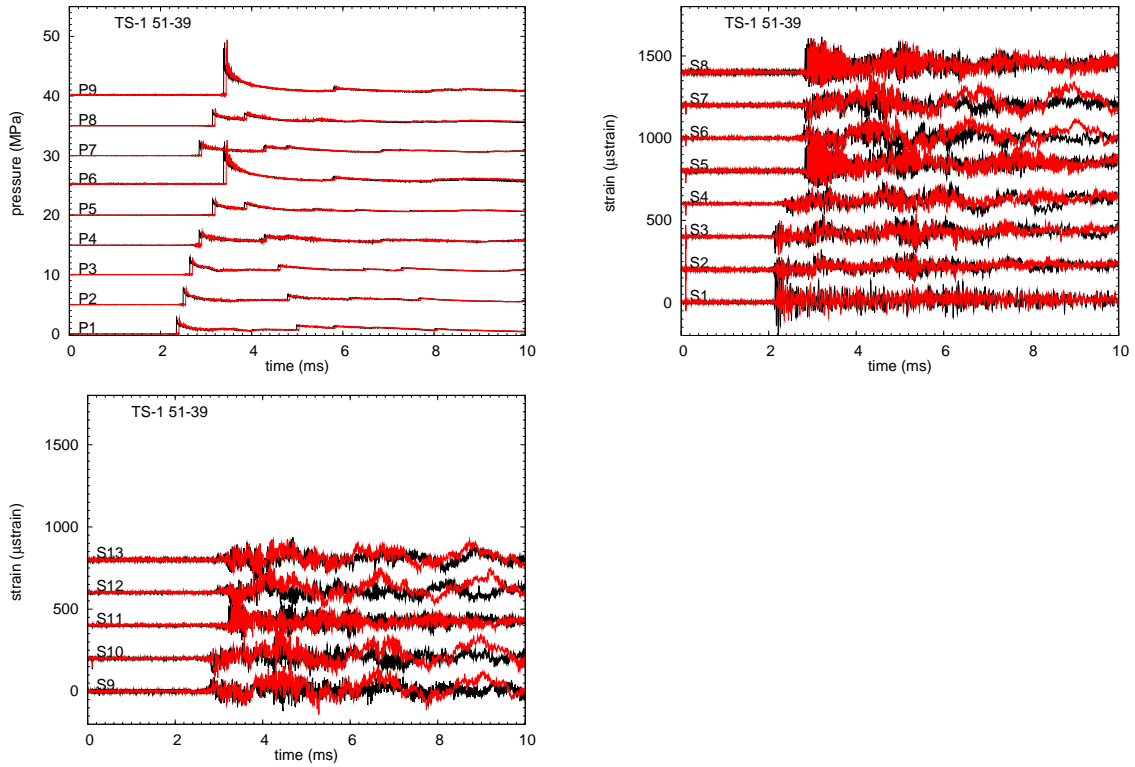


Figure 249: TS1 Shot 51 vs 39. Pressure, strain gage, displacement, and accelerometer signals. 10 ms raw data.

# N SS1 Engineering Drawings

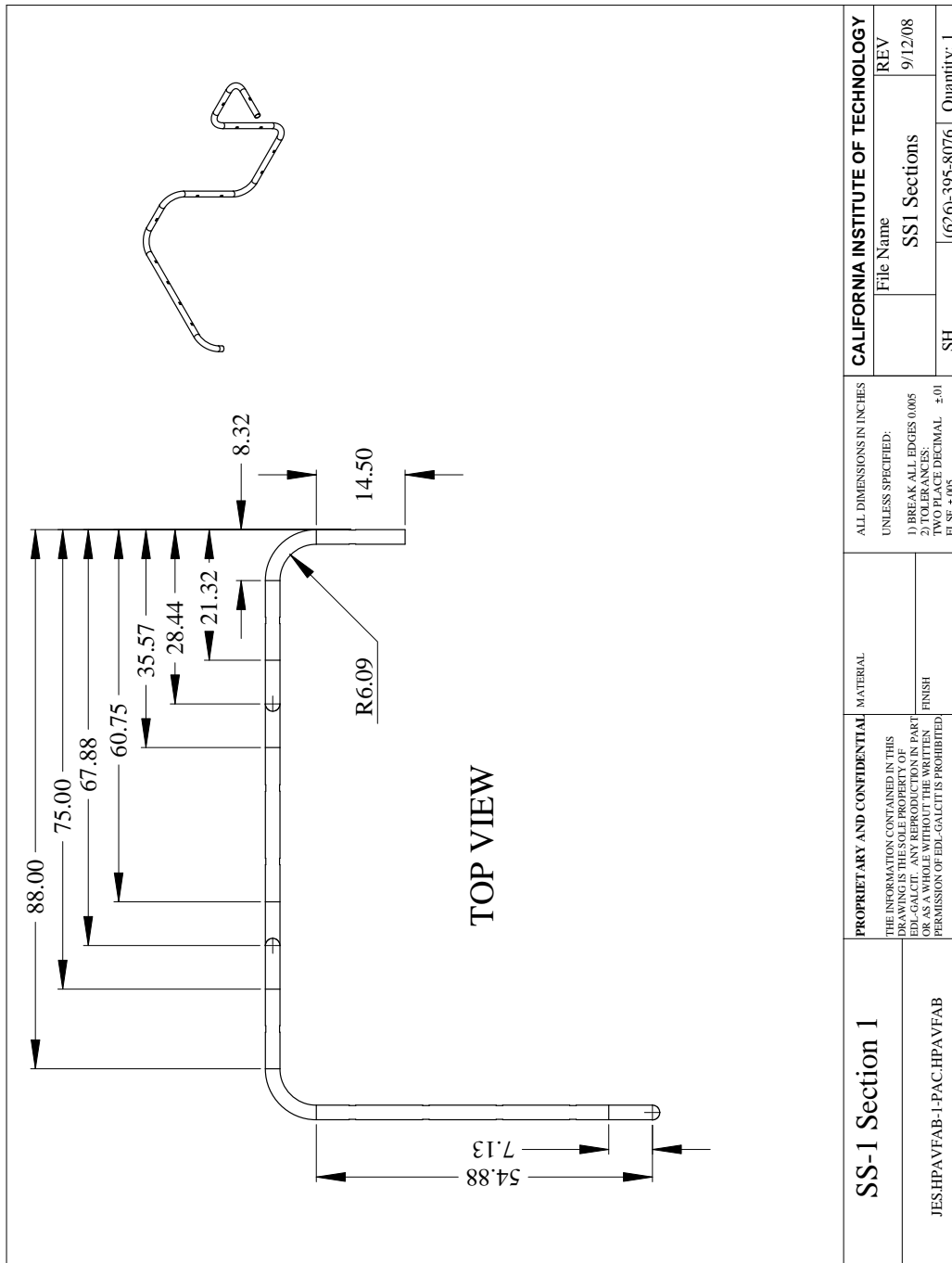


Figure 250: Engineering drawing of SS1 assembly.

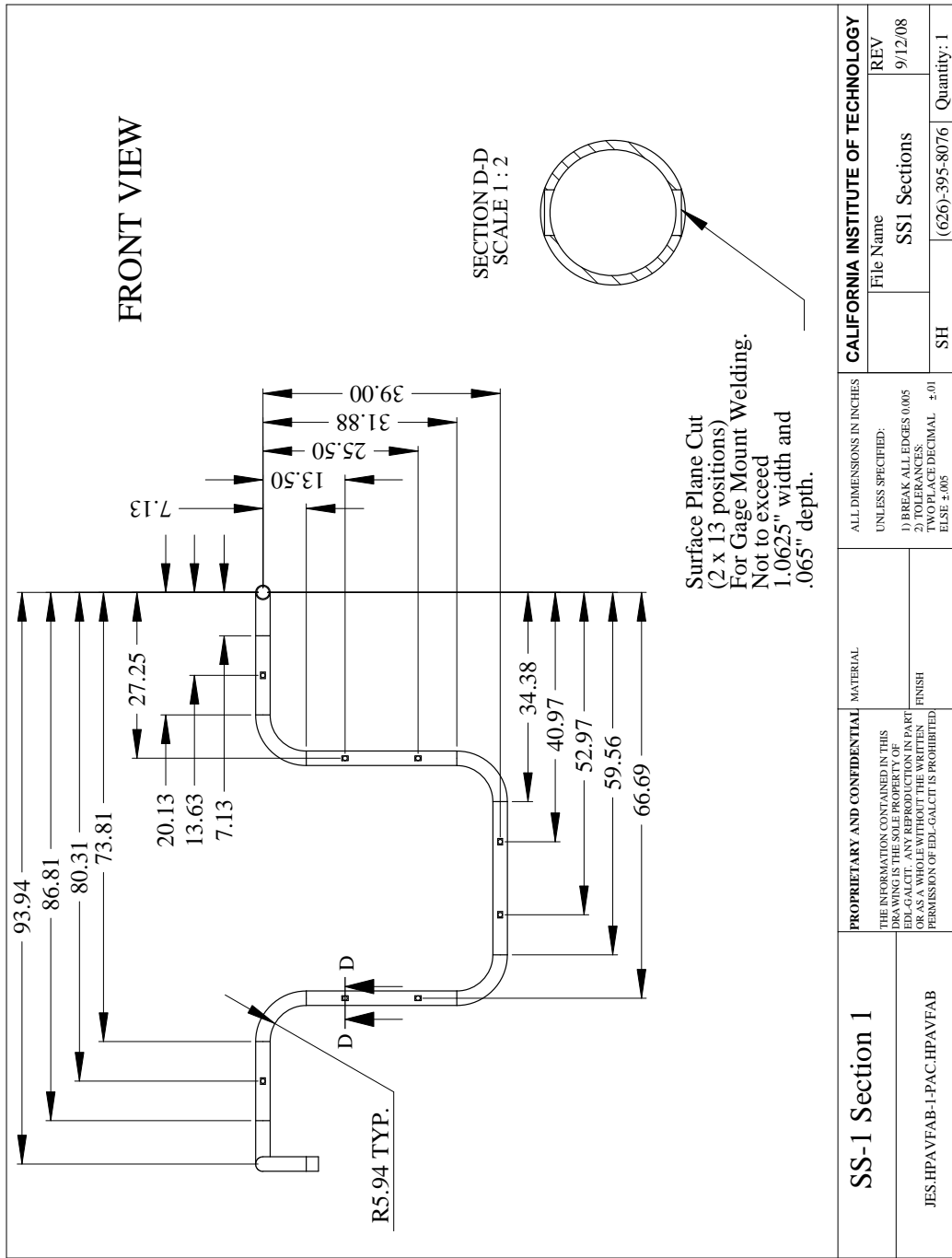


Figure 251: Engineering drawing of SS1 assembly.

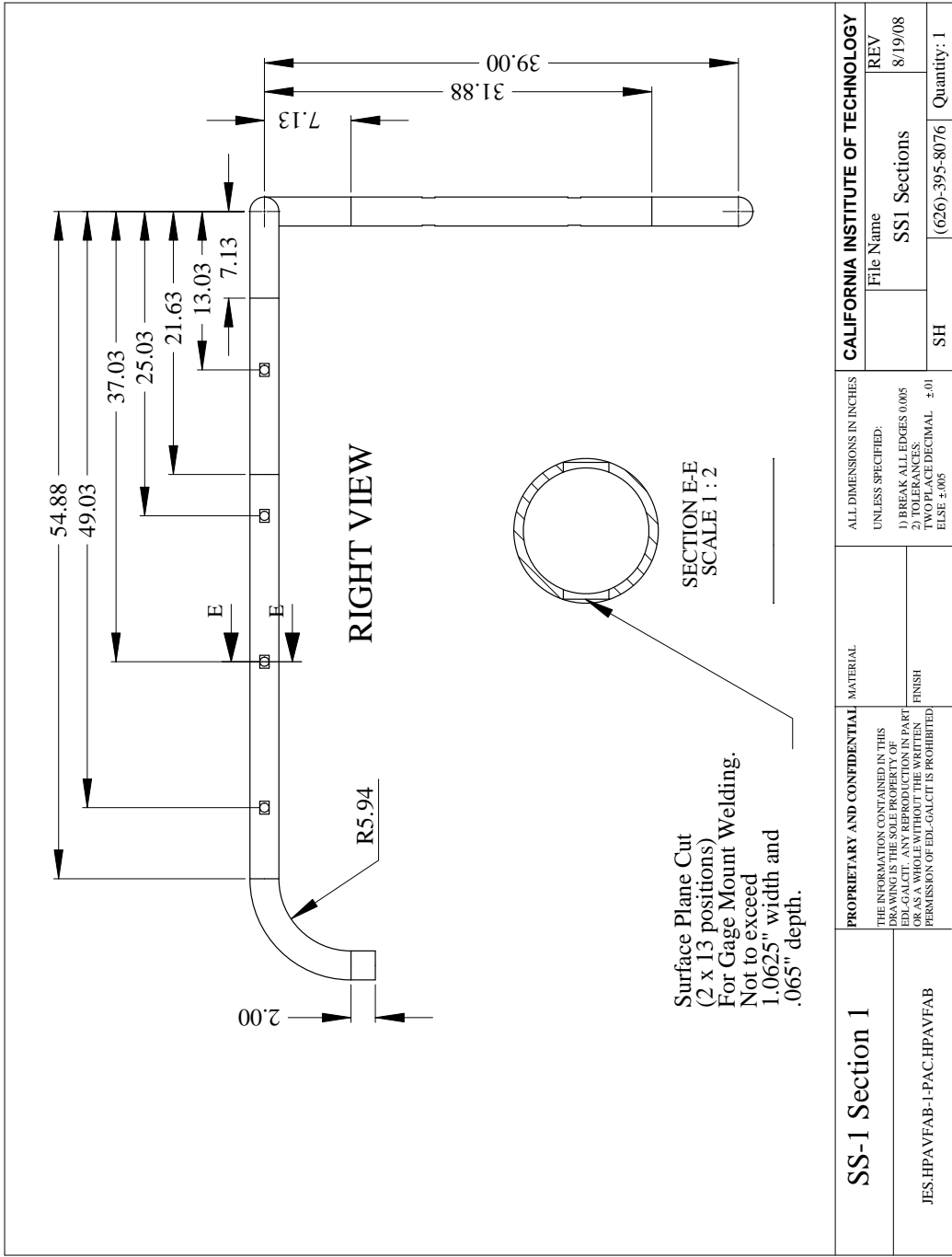


Figure 252: Engineering drawing of SS1 assembly.

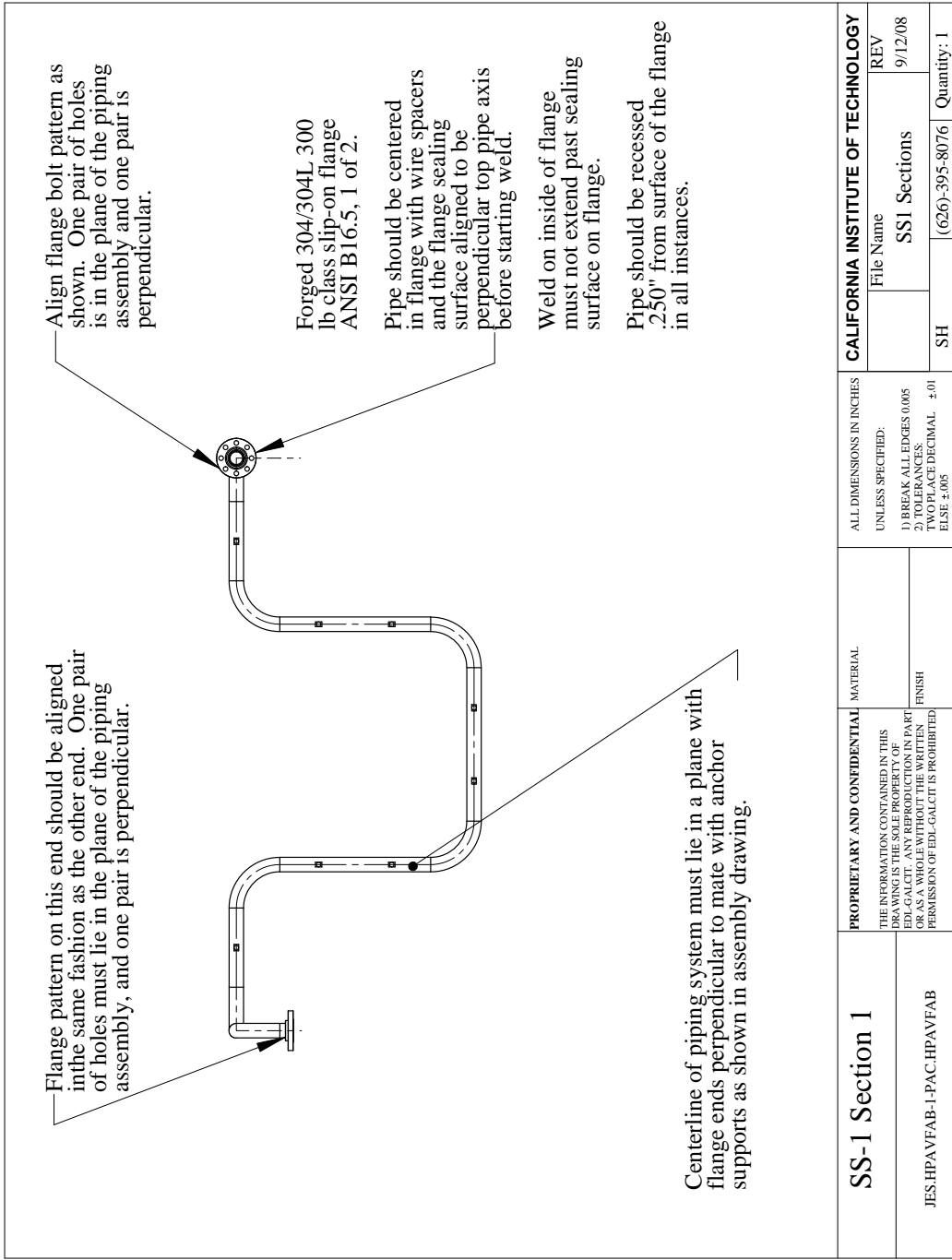


Figure 253: Engineering drawing of SS1 assembly.

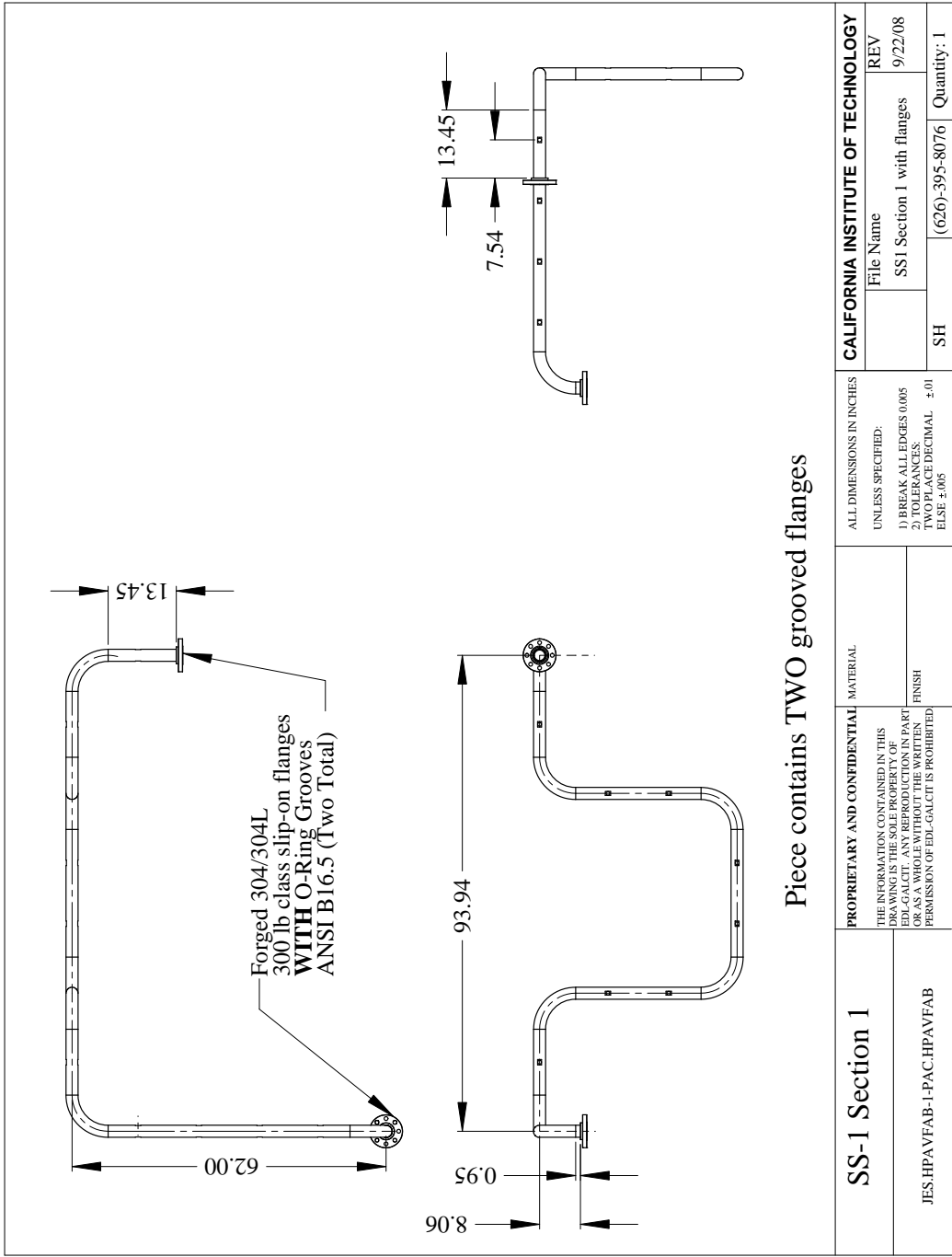


Figure 254: Engineering drawing of SS1 assembly.

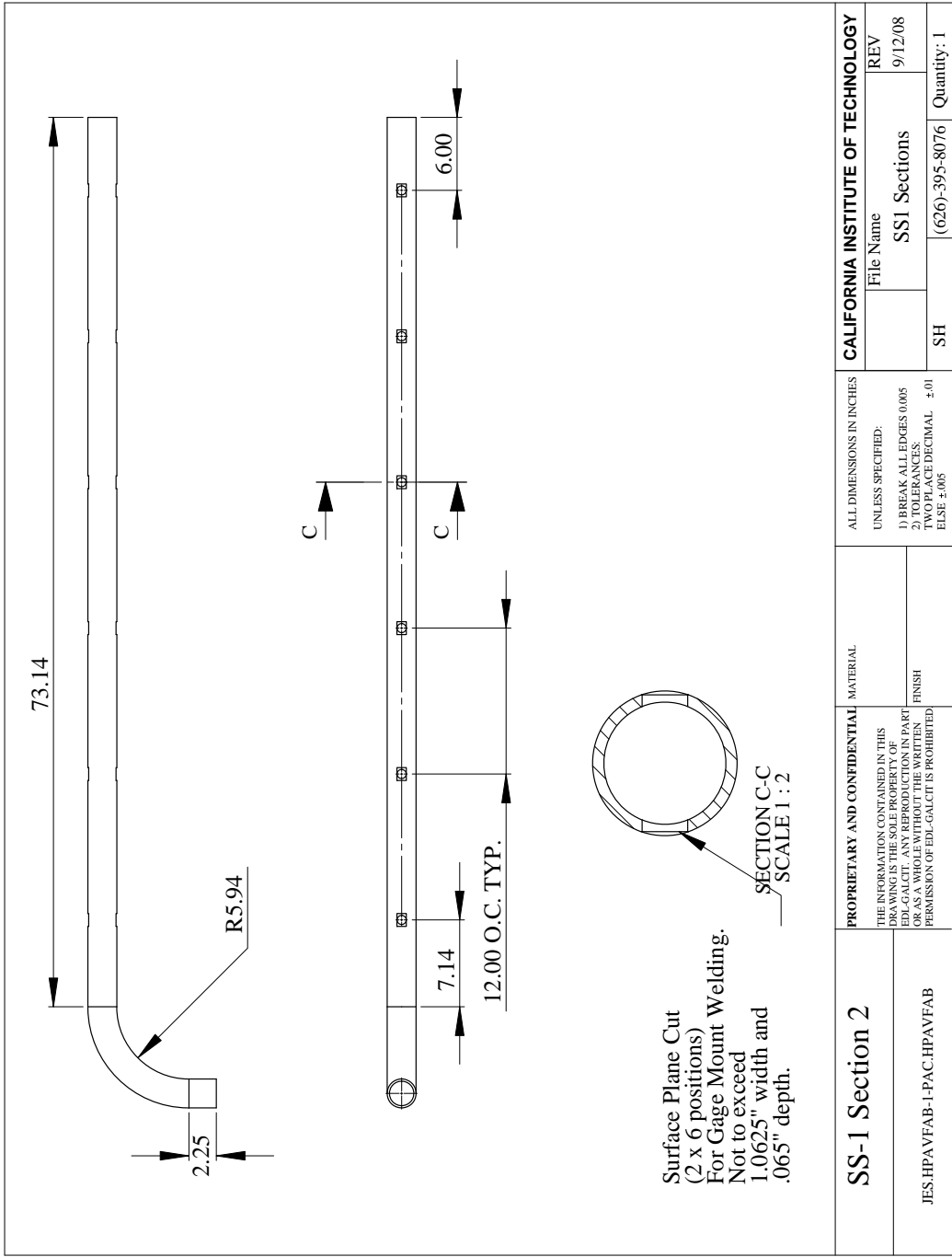


Figure 255: Engineering drawing of SS1 assembly.

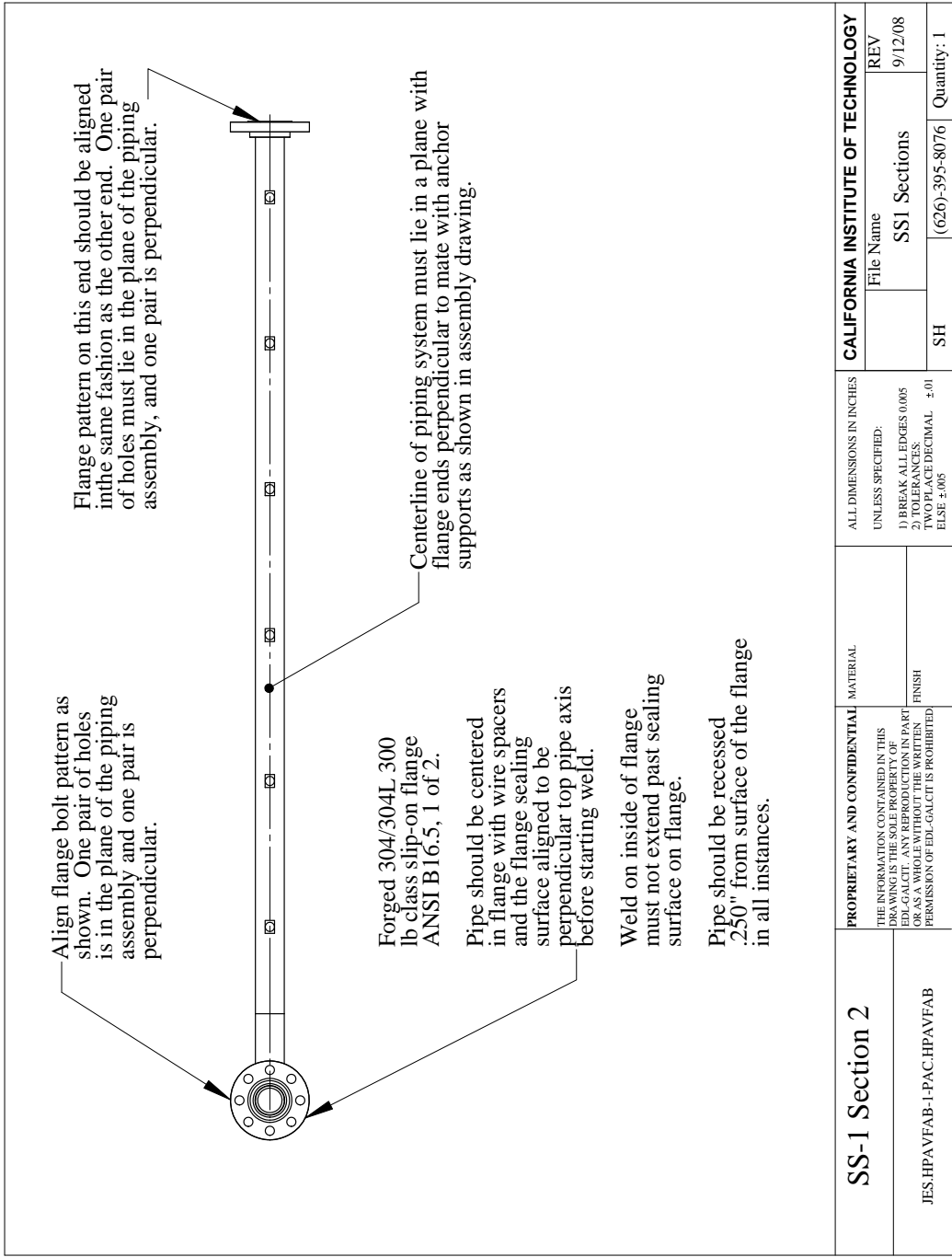


Figure 256: Engineering drawing of SS1 assembly.

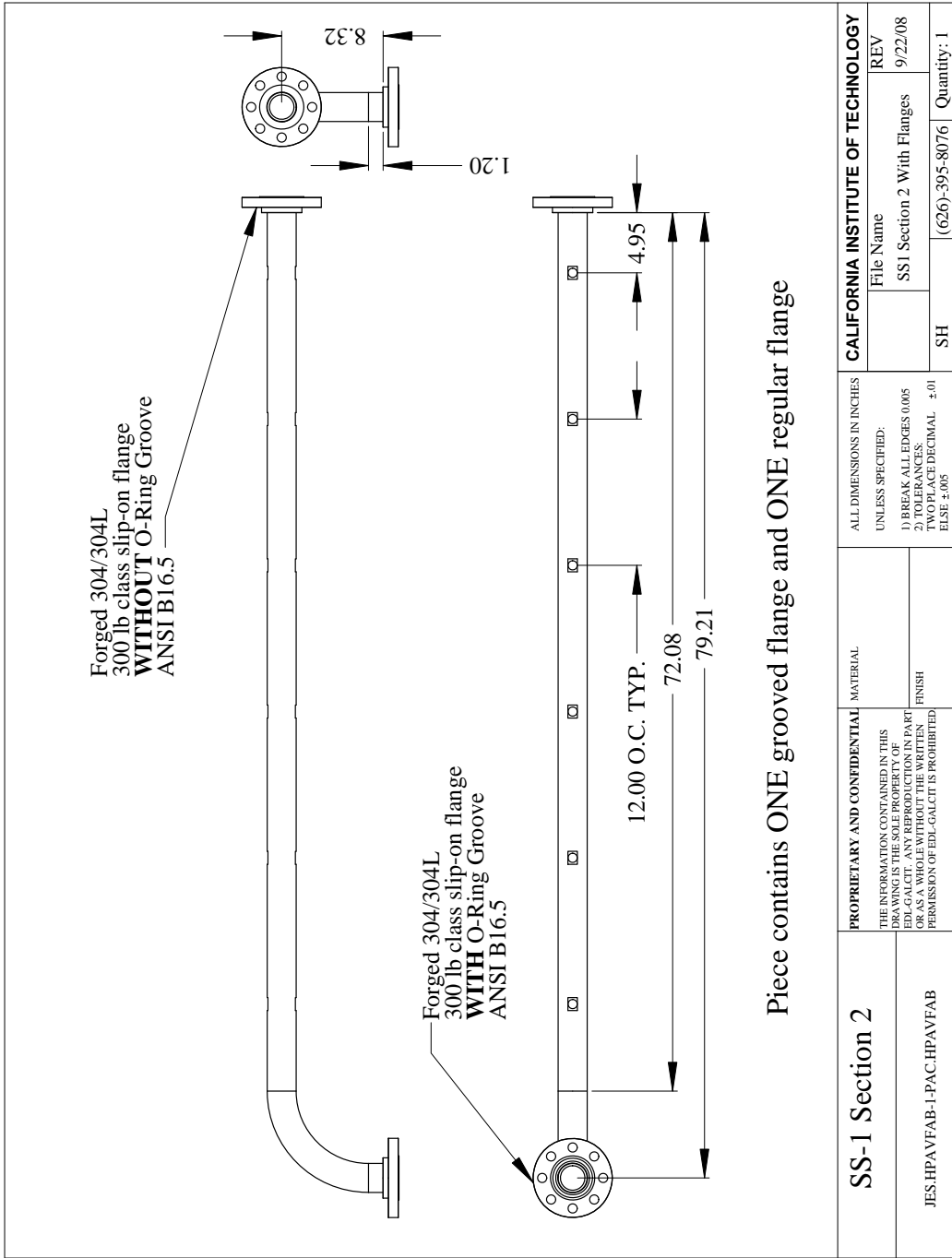


Figure 257: Engineering drawing of SS1 assembly.

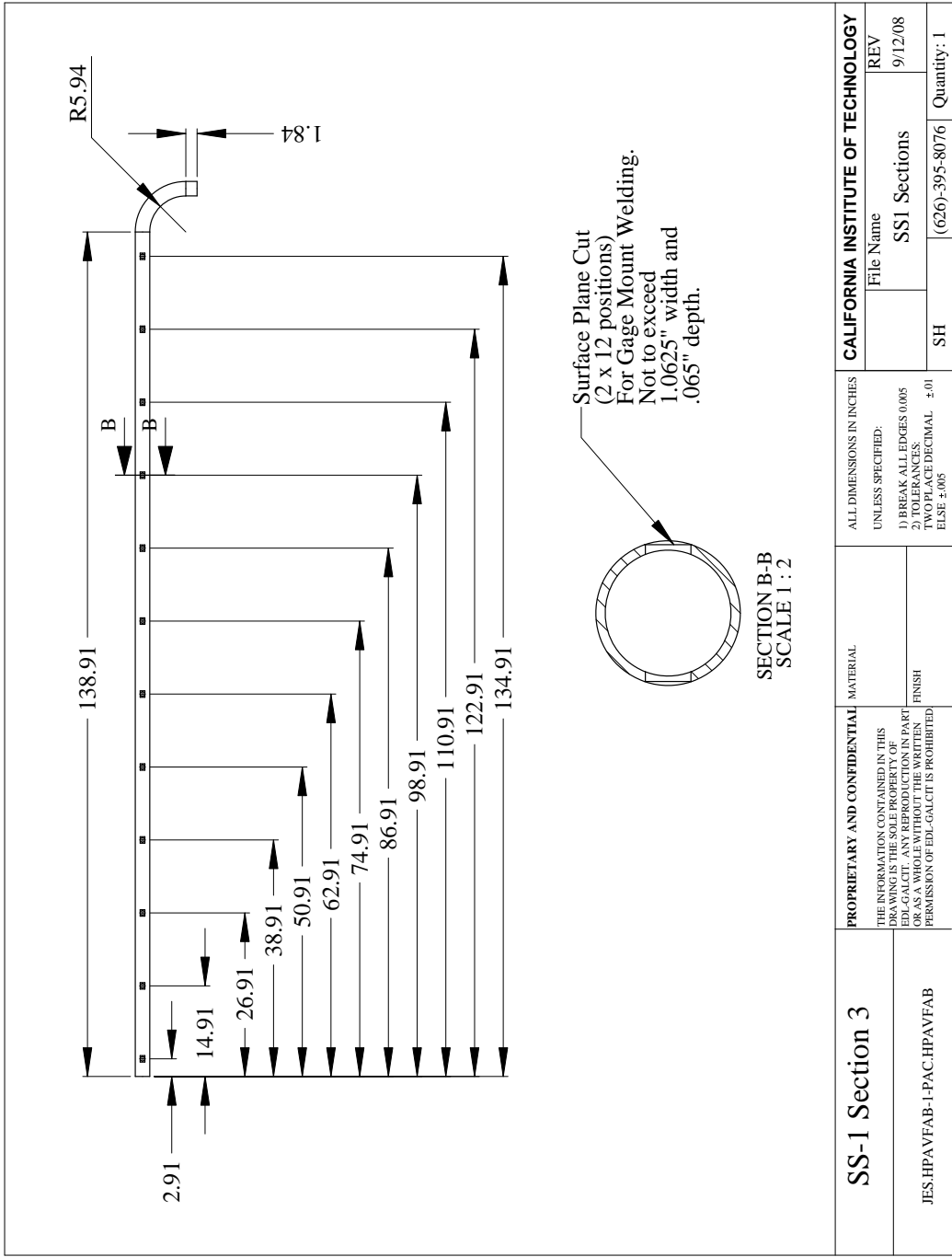


Figure 258: Engineering drawing of SS1 assembly.

<b>SS-1 Section 3</b>	PROPRIETARY AND CONFIDENTIAL THE INFORMATION CONTAINED IN THIS DRAWING IS THE SOLE PROPERTY OF EDL-GALCIT. ANY REPRODUCTION IN PART OR AS A WHOLE WITHOUT THE WRITTEN PERMISSION OF EDL-GALCIT IS PROHIBITED.	MATERIAL	ALL DIMENSIONS IN INCHES UNLESS SPECIFIED: 1) BREAK ALL EDGES 0.005 2) TOLERANCES: TWO PLACE DECIMAL ±.01 ELSE ±.005	CALIFORNIA INSTITUTE OF TECHNOLOGY	
				File Name	REV
JES.HPAVFAB-1-PAC.HPAVFAB		FINISH		SS1 Sections	9/12/08
				SH (626)-395-8076	Quantity: 1

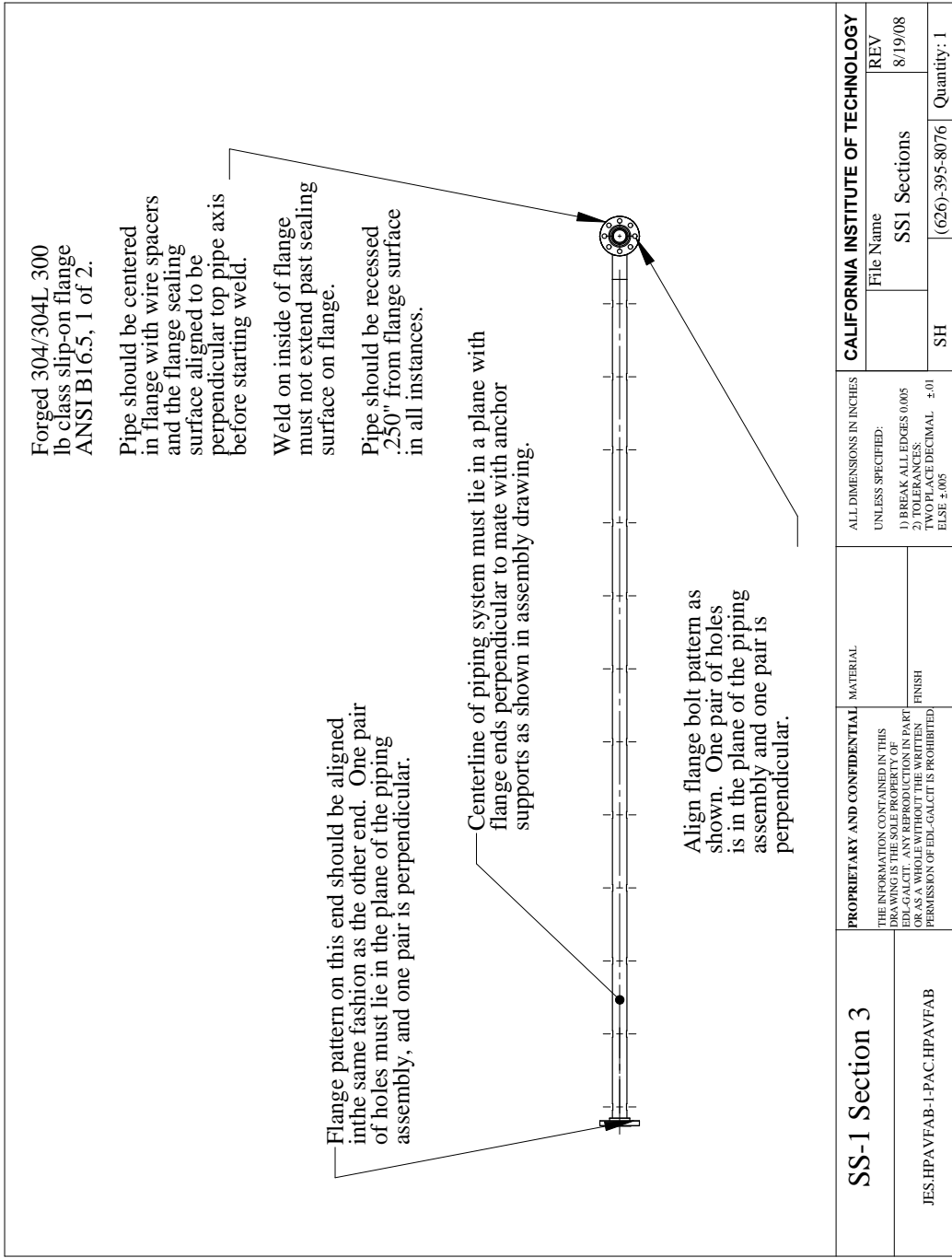


Figure 259: Engineering drawing of SS1 assembly.

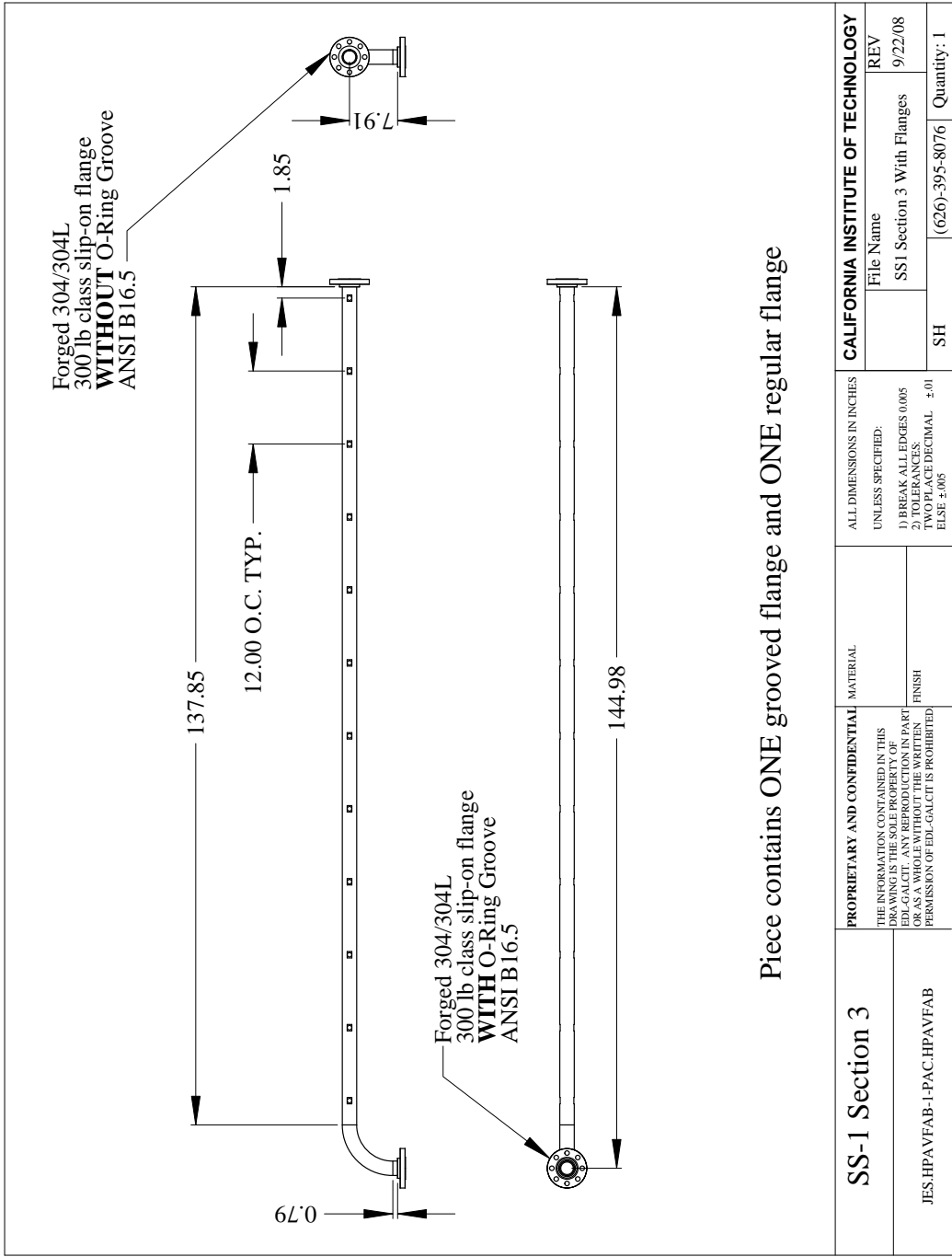


Figure 260: Engineering drawing of SS1 assembly.

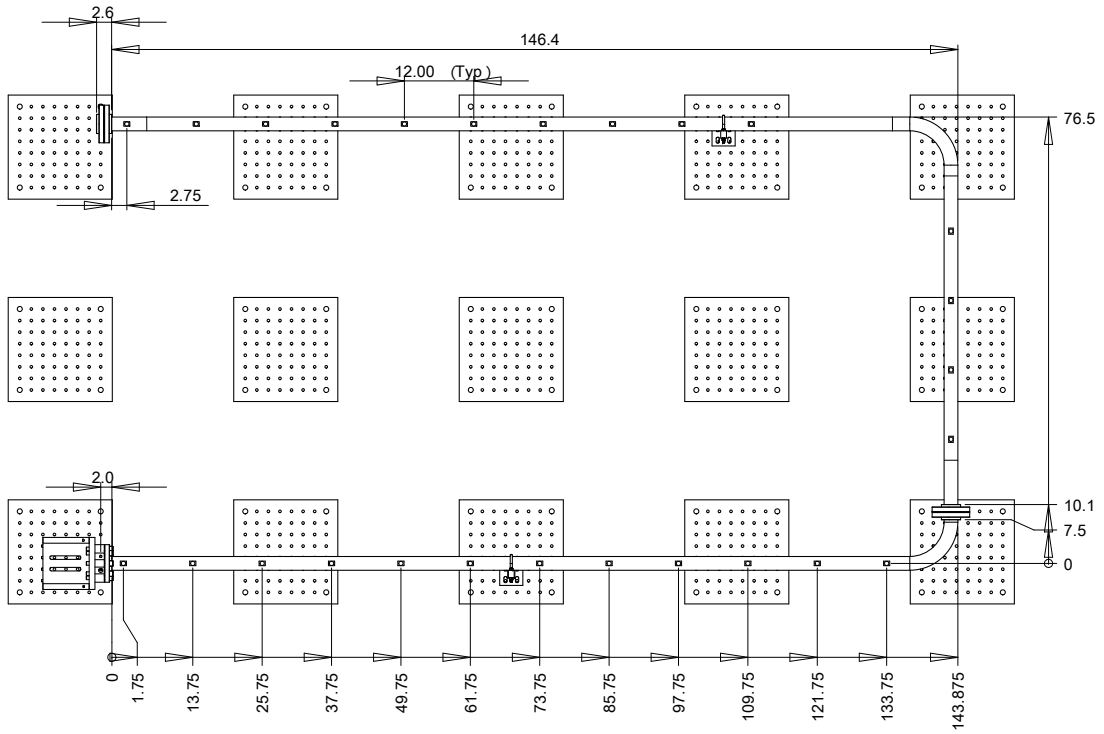


Figure 261: SS1 North wall port locations.

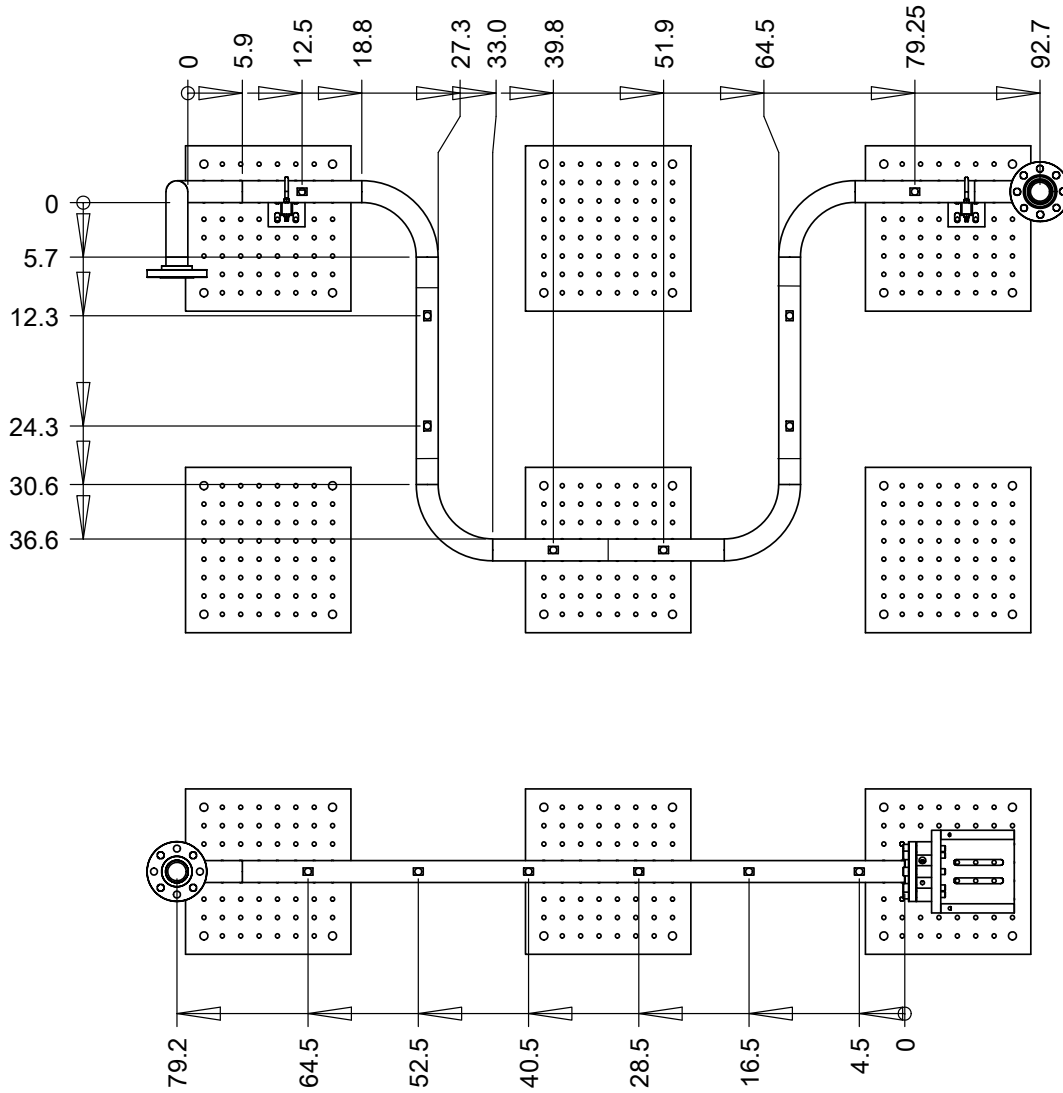


Figure 262: SS1 West wall port locations.

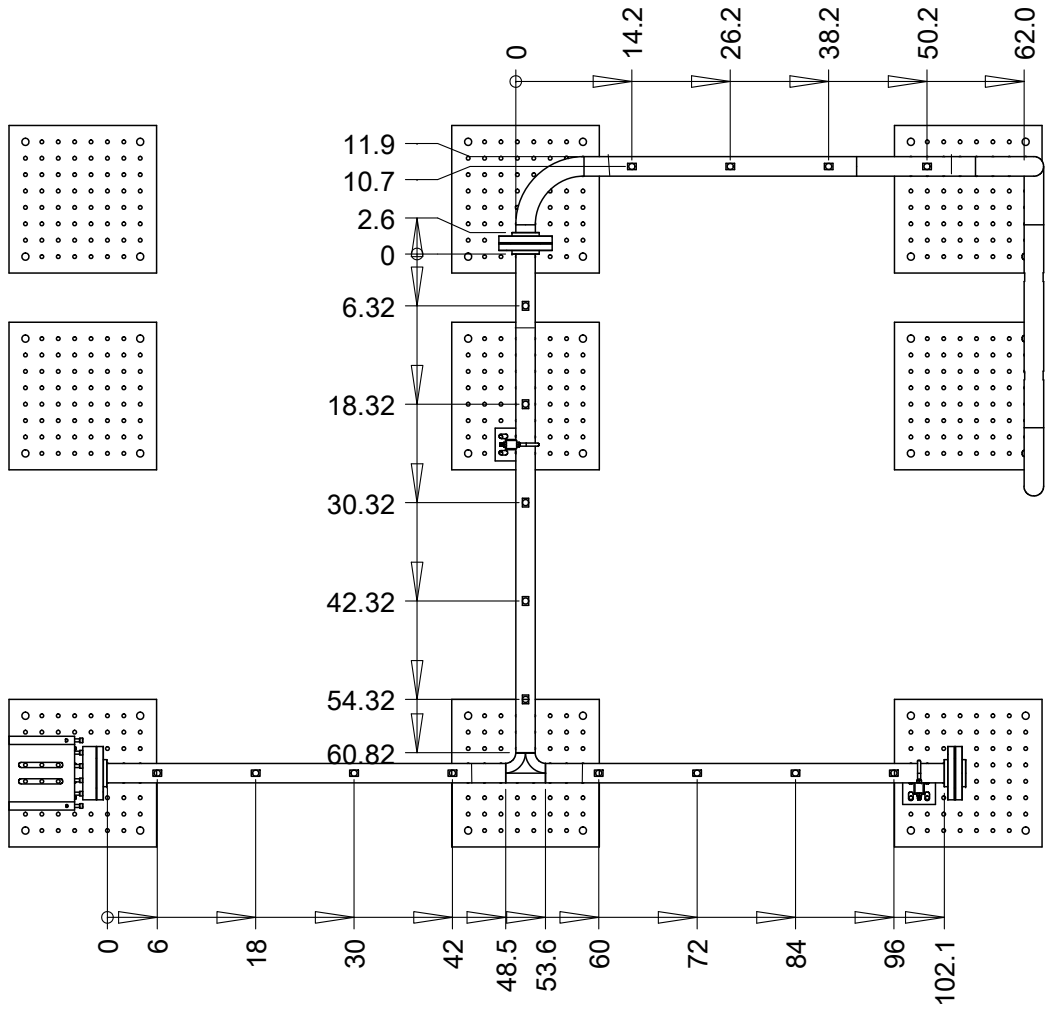


Figure 263: SS1 South wall port locations.

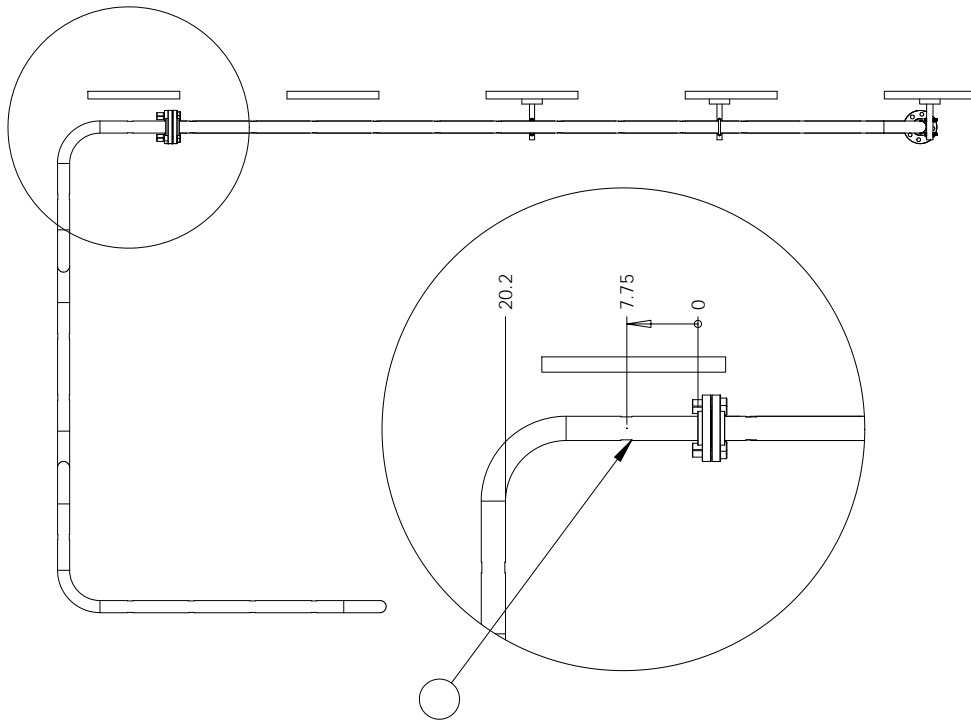


Figure 264: SS1NW corner port locations, overhead view.

## O SS1 Data Plots

The location of the sensors and components of the piping system required tedious measurements along the axis and corrections for the bends and flanges. Despite repeated measurements there remains some residual uncertainty in the locations and some inconsistencies. As a consequence, the locations used for the arrival time analysis in the main text are slightly different than the locations given below. In most cases, the differences are less than 50 mm.

### O.1 Sensor Locations

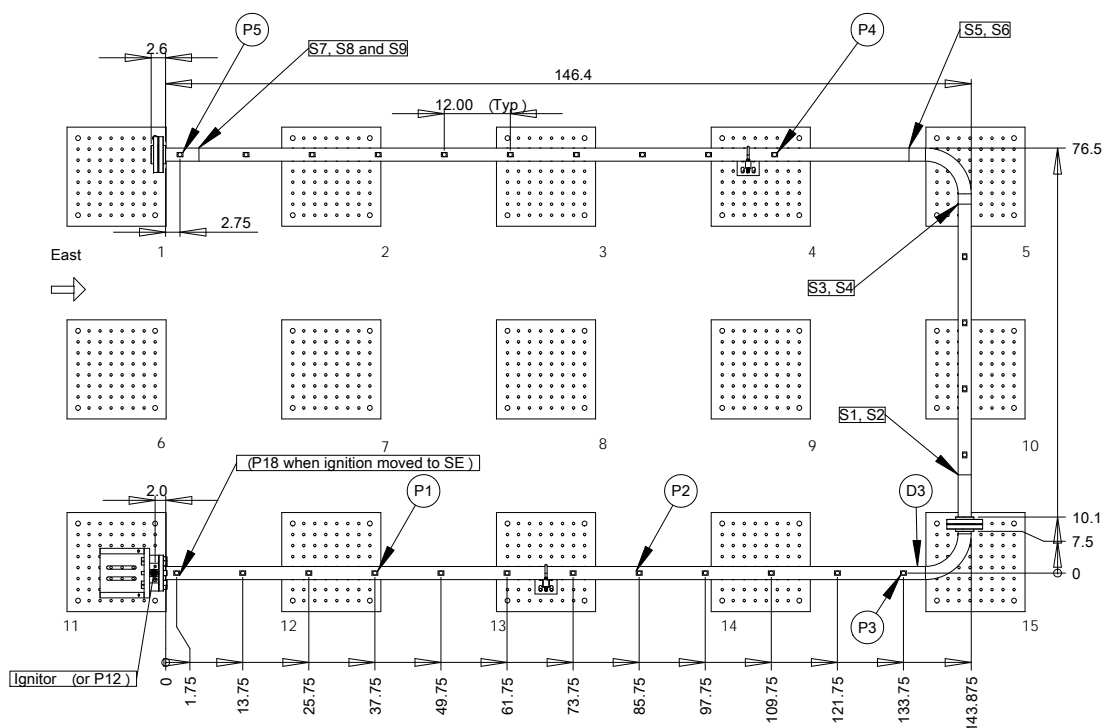


Figure 265: SS1 North wall sensor locations. Pressure transducer locations correct only for shots 53, 54, 58, and 59; some changes were made for other shots.

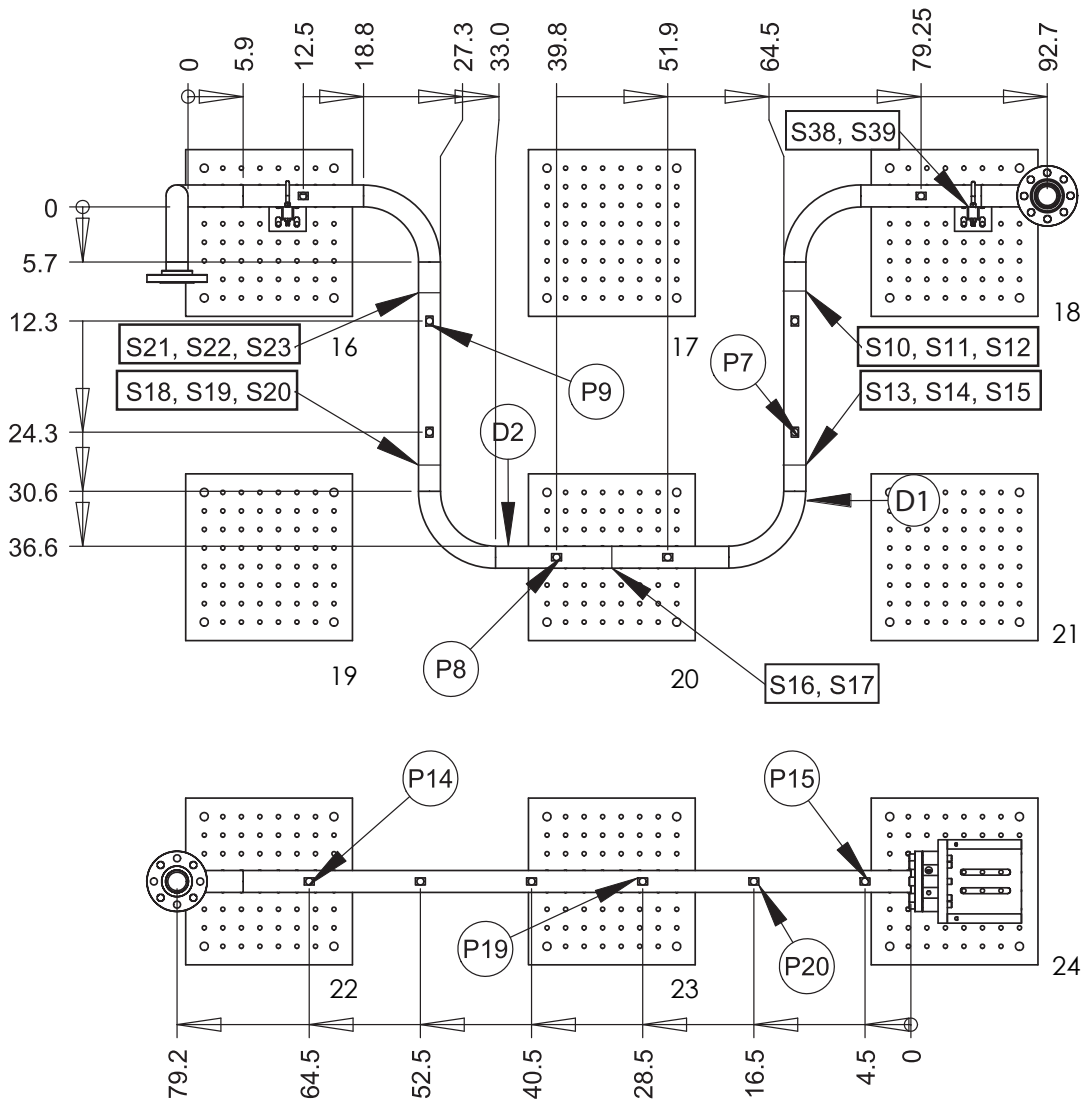


Figure 266: SS1 West wall sensor locations. Pressure transducer locations correct only for shots 53, 54, 58, and 59; some changes were made for other shots.

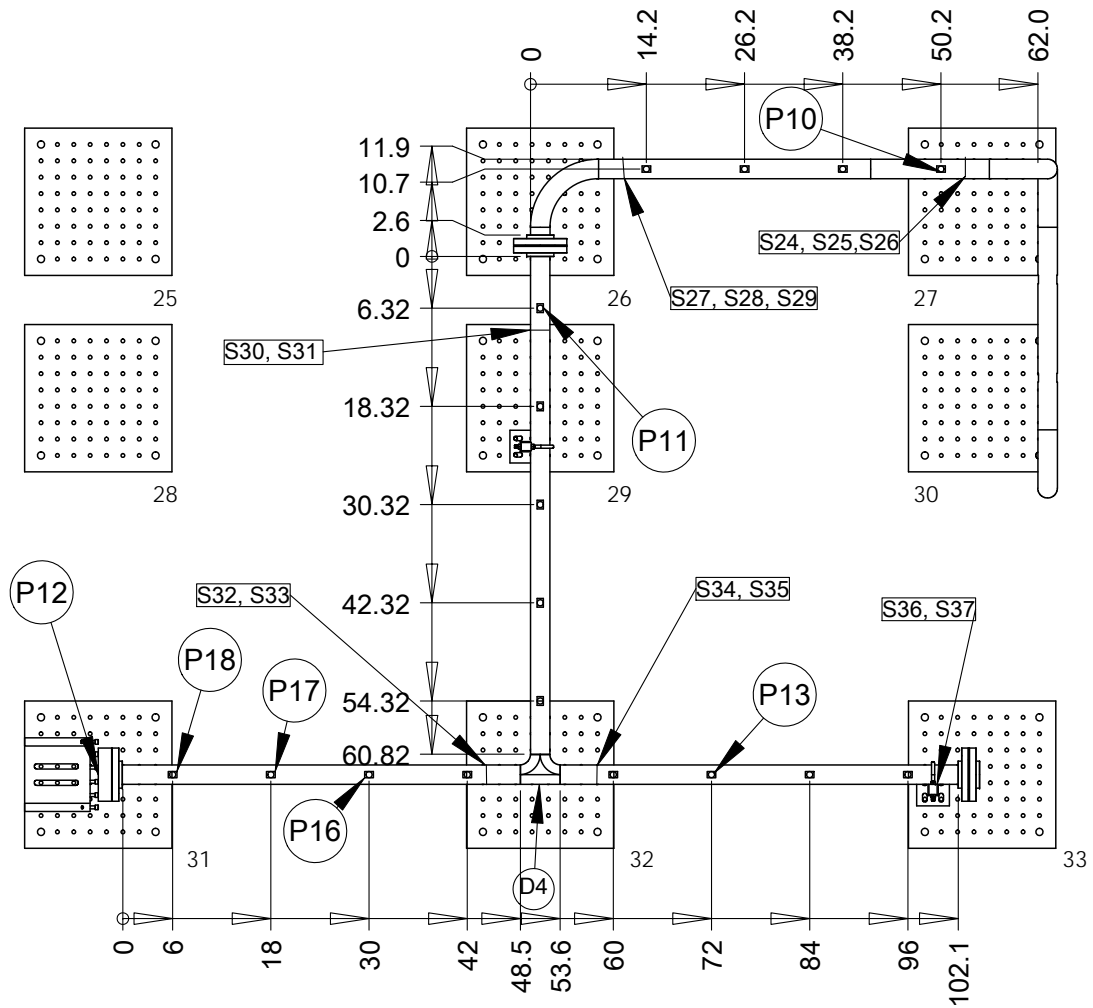


Figure 267: SS1 South wall sensor locations. Pressure transducer locations correct only for shots 53, 54, 58, and 59; some changes were made for other shots.

Table 35: SS1 tests 53-56, location of gages and key features as a distance from the ignition source at E3.

Gage or Feature	Specimen	Distance (m)
E3 - Ignitor	SS1-3	0.000
P1	SS1-3	1.010
U-Bolt Support- SU7	SS1-3	1.796
P2	SS1-3	2.229
P3	SS1-3	3.448
D3	SS1-3	3.543
S1,S2	ES1	4.105
S3,S4	ES1	5.362
S5,S6	ES1	5.740
P4	ES1	6.383
U-Bolt Support- SU6	ES1	6.462
S7,S8,S9	ES1	9.001
P5	ES1	9.122
BOLTED CONNECTION		9.258
U-Bolt Support-SU5	SS1-1	9.337
P6	SS1-1	9.455
S38, S39 U-Bolt Support SU4	SS1-1	9.882
S10, S11, S12	SS1-1	10.585
P7	SS1-1	10.974
S13,S14,S15	SS1-1	11.033
D1	SS1-1	11.174
S16,S17	SS1-1	11.741
P8	SS1-1	11.894
D2	SS1-1	12.050
S18,S19,S20	SS1-1	12.453
P9	SS1-1	12.815
S21,S22,S23	SS1-1	12.894
U-Bolt Support SU3	SS1-1	13.473
S24,S25,S26	SS1-1	13.994
P10	SS1-1	14.038
S27,S28,S29	SS1-1	15.005
P11	TS1	15.642
S30,S31	TS1	15.805
U-Bolt Support SU2	TS1	16.072
T-Fitting	TS1	17.090
D4	TS1	17.090
S32,S33	TS1	17.269
P16	TS1	17.624
P17	TS1	17.929
P18	TS1	18.234
E1 - P12	TS1	18.437
S34,S35	TS1	17.266
P13	TS1	17.622
S36, S37 U-Bolt Support SU1	TS1	18.312
P14	SS1-2	18.958
P19	SS1-2	19.872
P20	SS1-2	20.177
P15	SS1-2	20.482
E2 - flange	SS1-2	20.596

Table 36: SS1 tests 57-61, location of gages and key features as a distance from the ignition source at E1.

Gage or Feature	Specimen	Distance (m)
P12 - E3	SS1-3	18.437
P18	SS1-3	18.342
P1	SS1-3	17.427
U-Bolt Support- SU7	SS1-3	16.641
P3	SS1-3	14.989
D3	SS1-3	14.894
S1,S2	ES1	14.332
S3,S4	ES1	13.075
S5,S6	ES1	12.697
P4	ES1	12.054
U-Bolt Support- SU6	ES1	11.975
S7,S8,S9	ES1	9.436
P5	ES1	9.315
U-Bolt Support-SU5	SS1-1	9.100
P6	SS1-1	8.982
S38, S39 U-Bolt Support SU4	SS1-1	8.555
S10, S11, S12	SS1-1	7.852
P7	SS1-1	7.463
S13,S14,S15	SS1-1	7.404
D1	SS1-1	7.263
S16, S17	SS1-1	6.696
P8	SS1-1	6.543
D2	SS1-1	6.387
S18, S19, S20	SS1-1	5.984
P9	SS1-1	5.622
S21,S22, S23	SS1-1	5.543
U-Bolt Support SU3	SS1-1	4.964
S24, S25, S26	SS1-1	4.443
P10	SS1-1	4.399
S27, S28, S29	SS1-1	3.432
P11	TS1	2.795
S30,S31	TS1	2.632
U-Bolt Support SU2	TS1	2.365
T-Fitting	TS1	1.347
D4	TS1	1.347
S32,S33	TS1	1.168
P16	TS1	0.813
P17	TS1	0.508
E3 Ignition	TS1	0.000
S34,S35	TS1	1.524
P13	TS1	1.829
S36, S37 U-Bolt Support S1	TS1	2.519
P14	SS1-2	3.165
P19	SS1-2	4.079
P20	SS1-2	4.384
P15	SS1-2	4.689
Flange E2	SS1-2	4.803

## O.2 Shot 53

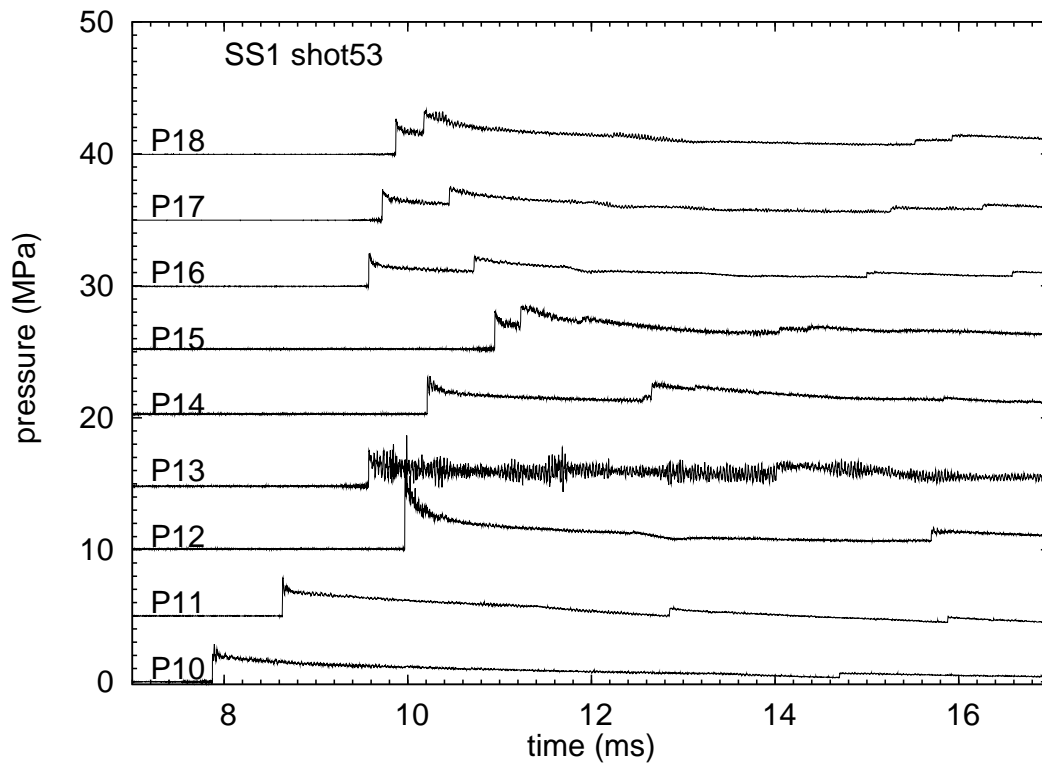
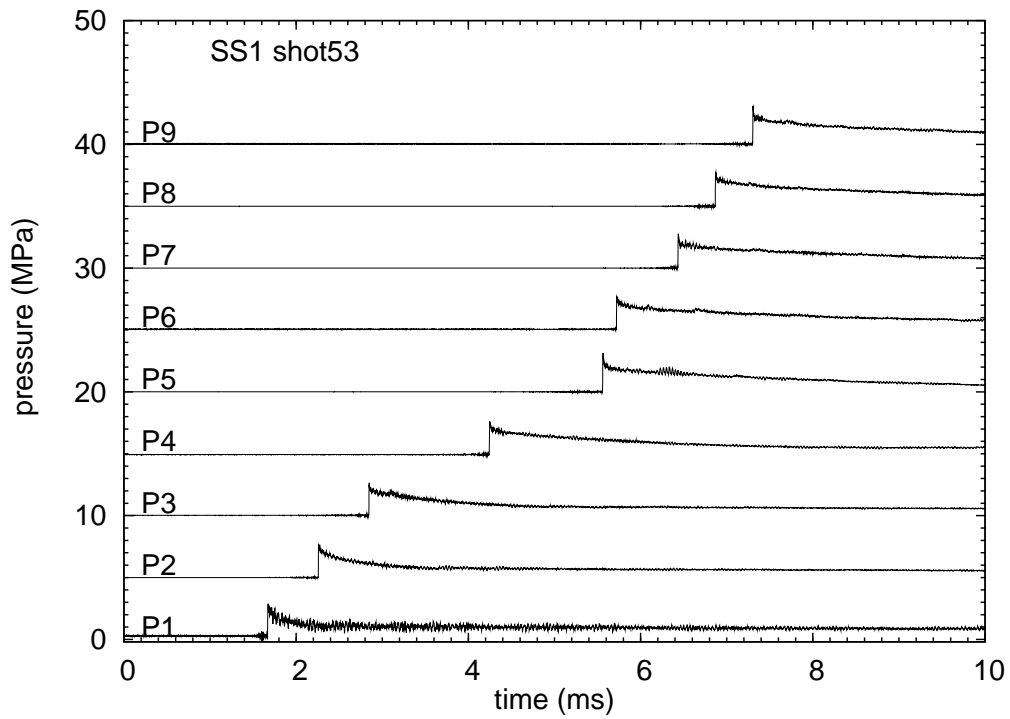


Figure 268: SS1 Shot 53. Pressure gage signals. 10 ms raw data.

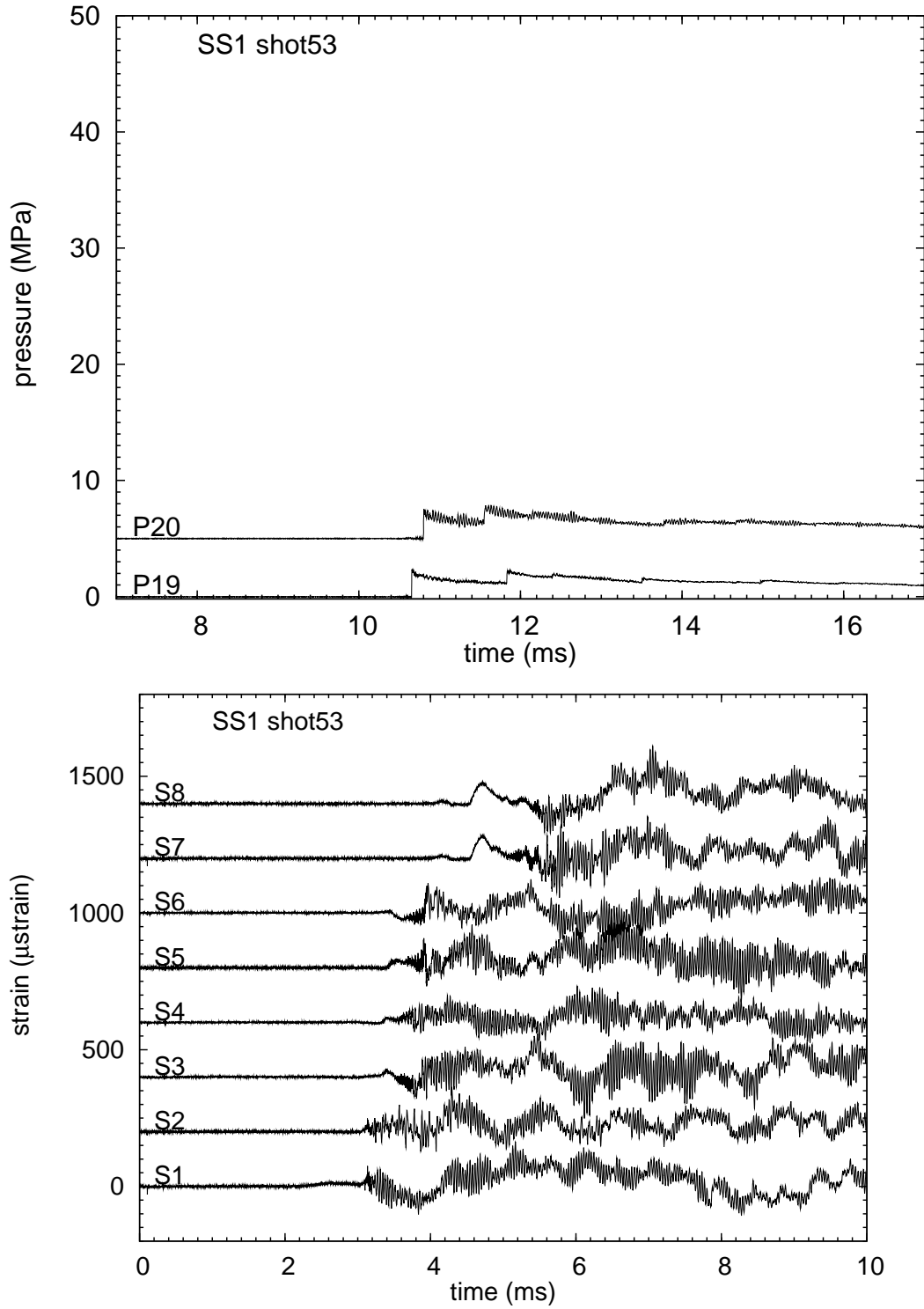


Figure 269: SS1 Shot 53. Pressure and strain gage signals. 10 ms raw data.

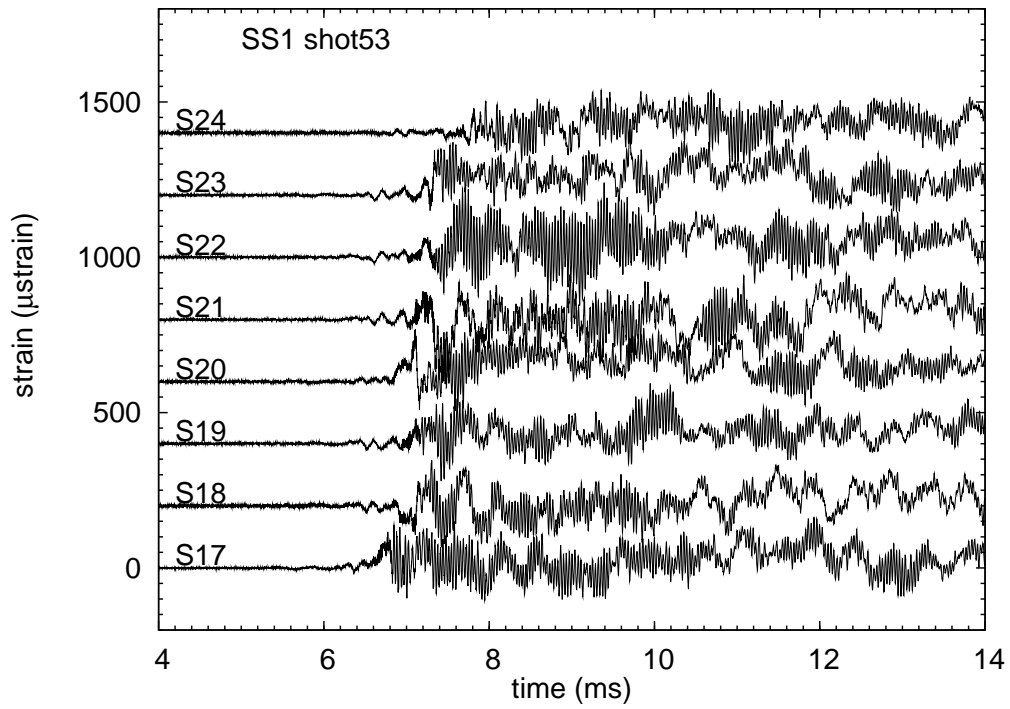
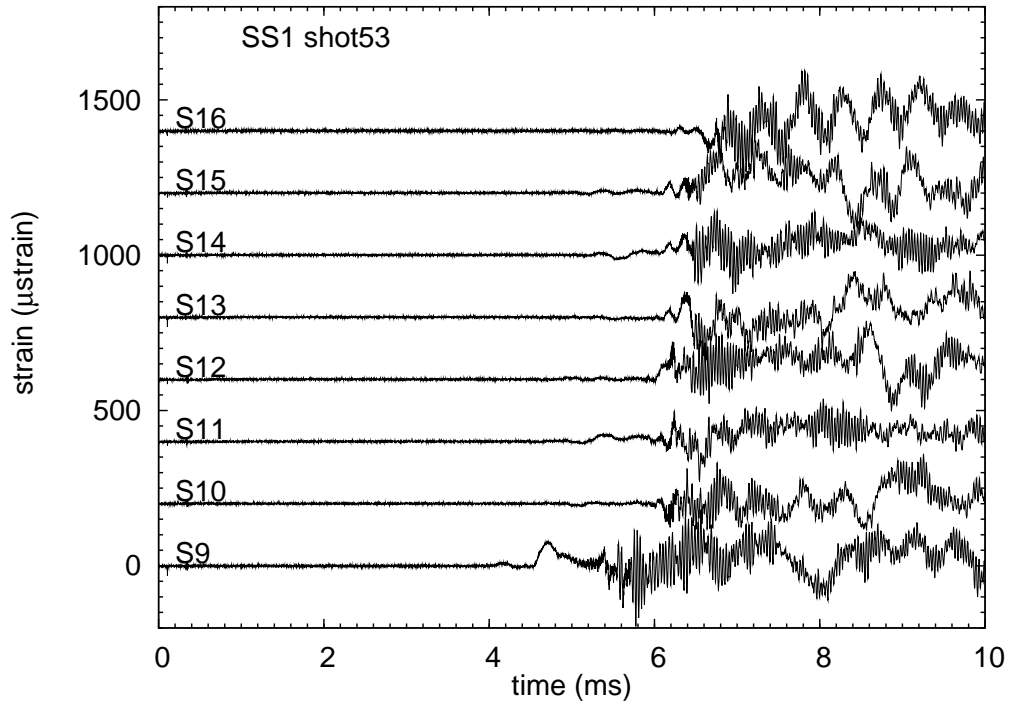


Figure 270: SS1 Shot 53. Strain gage signals. 10 ms raw data.

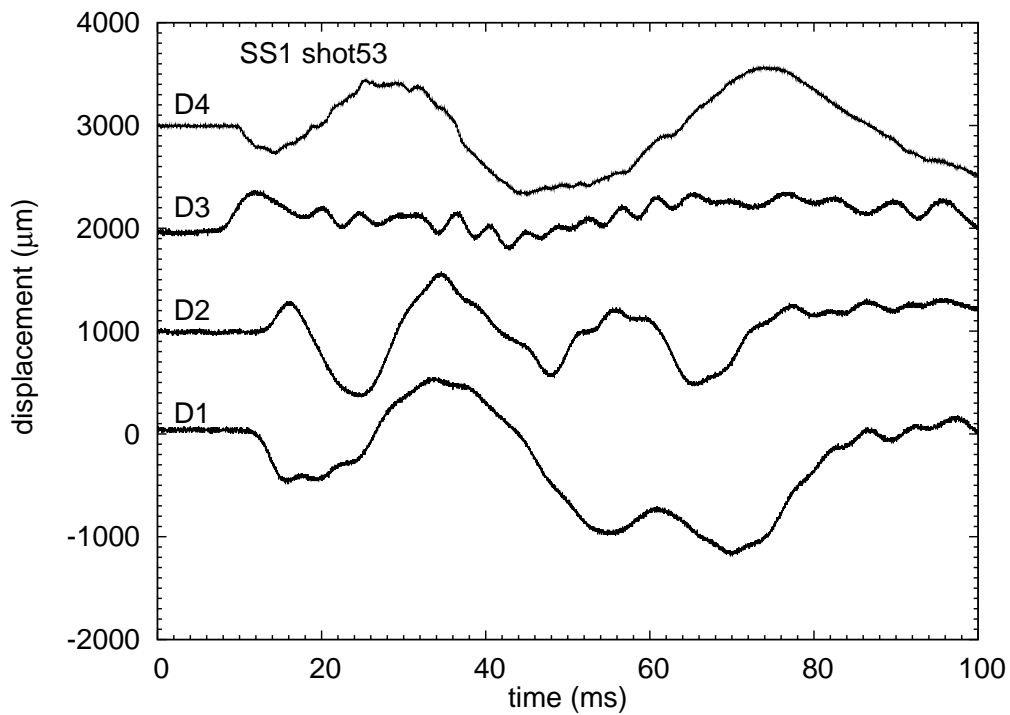
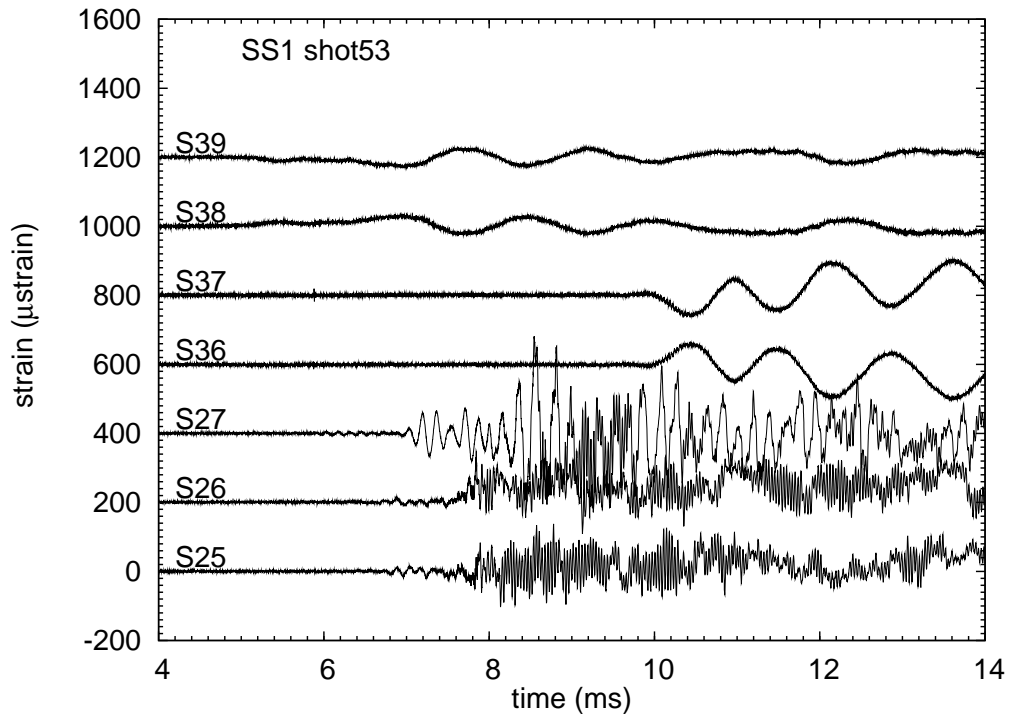


Figure 271: SS1 Shot 53. Strain gage, cantilever strain gage, and displacement signals. 10 ms raw data.

### O.3 Shot 54

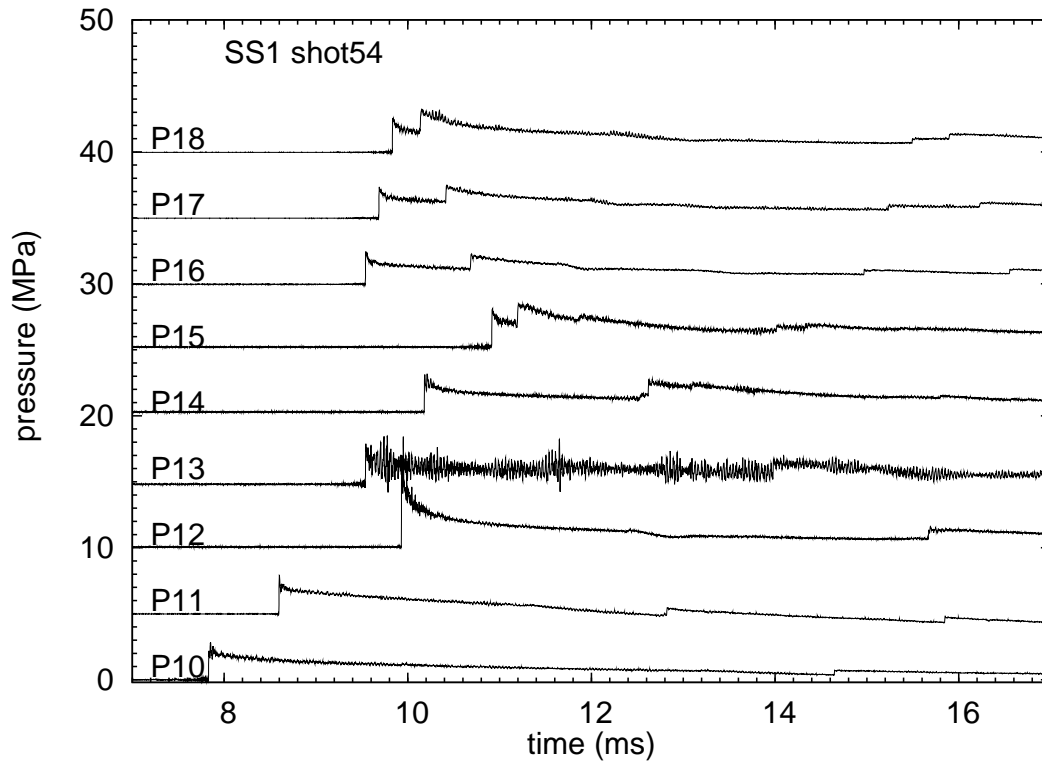
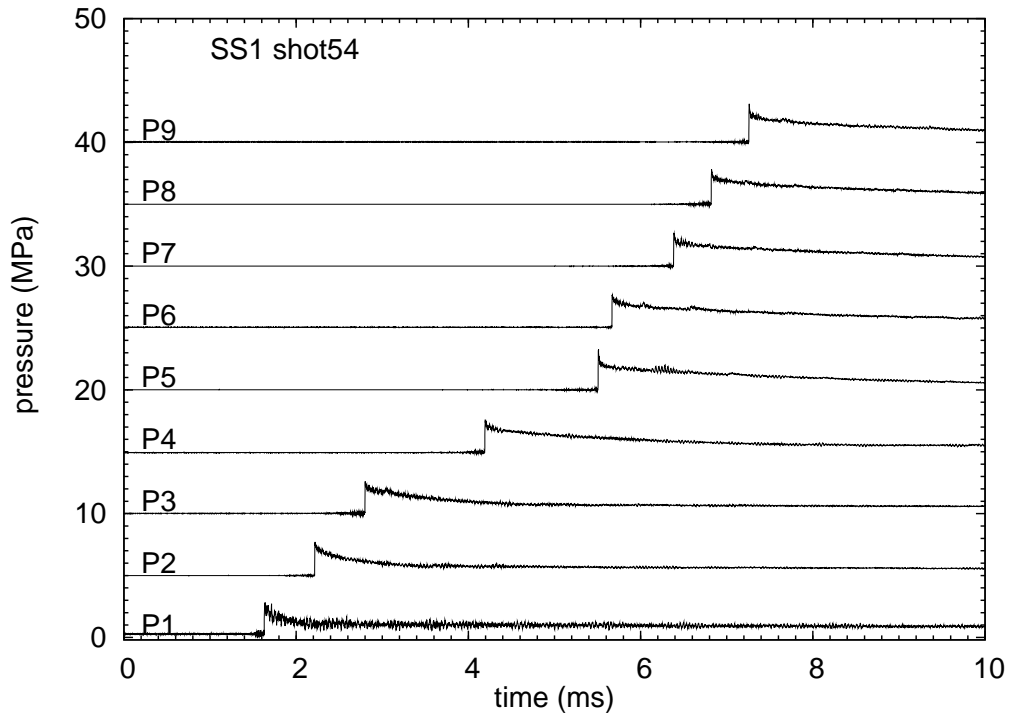


Figure 272: SS1 Shot 54. Pressure gage signals. 10 ms raw data.

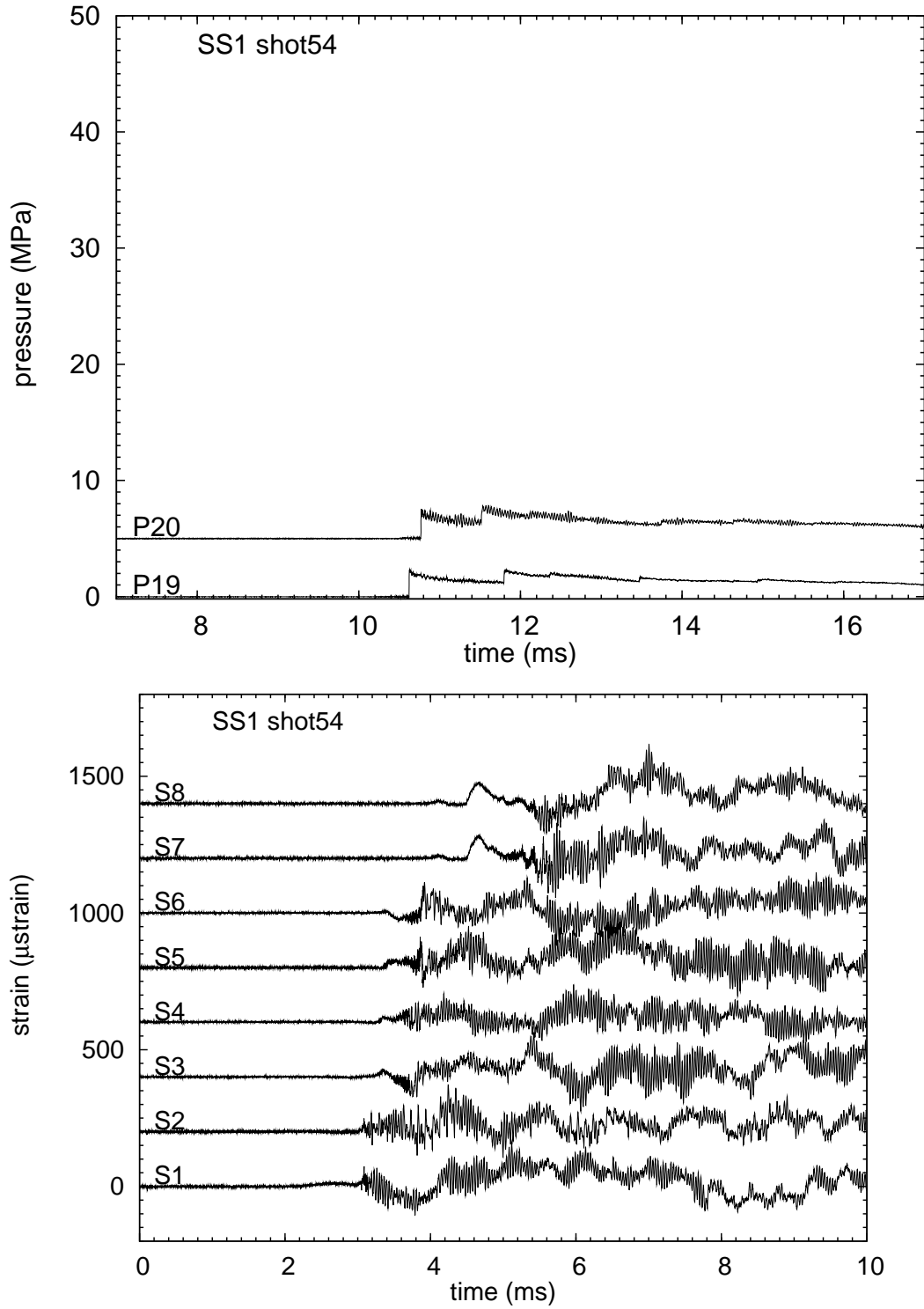


Figure 273: SS1 Shot 54. Pressure and strain gage signals. 10 ms raw data.

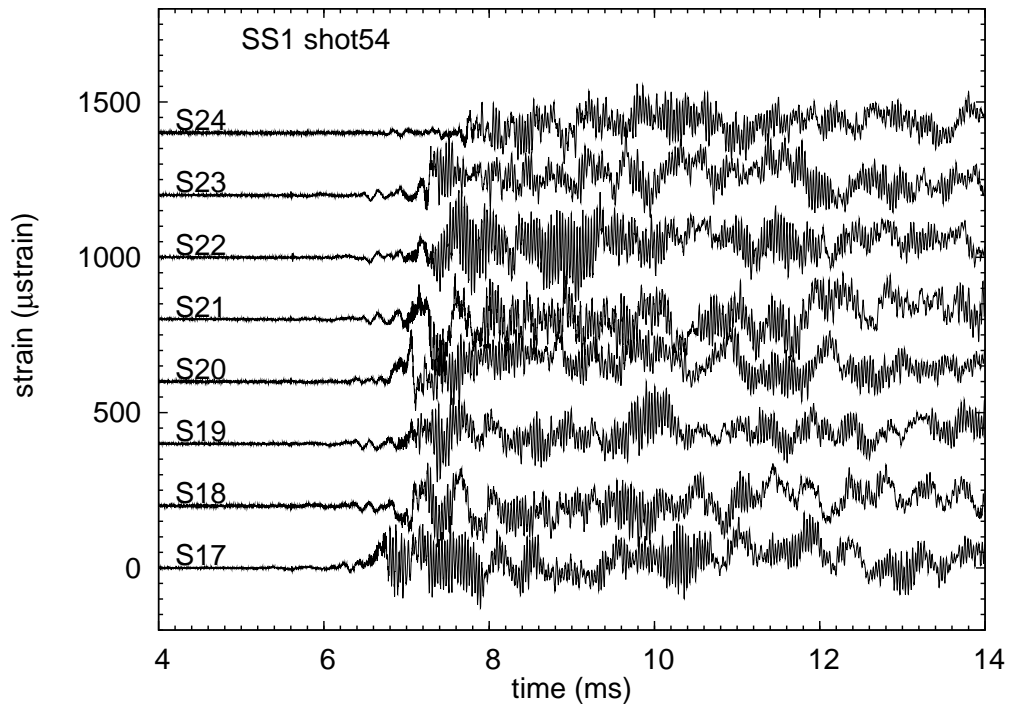
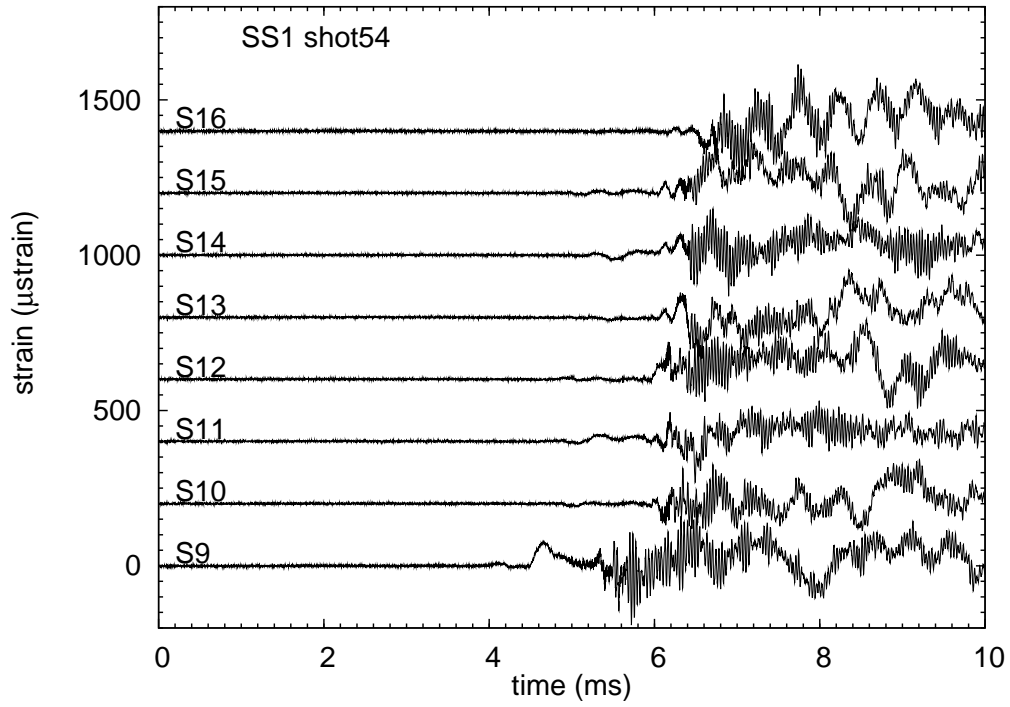


Figure 274: SS1 Shot 54. Strain gage signals. 10 ms raw data.

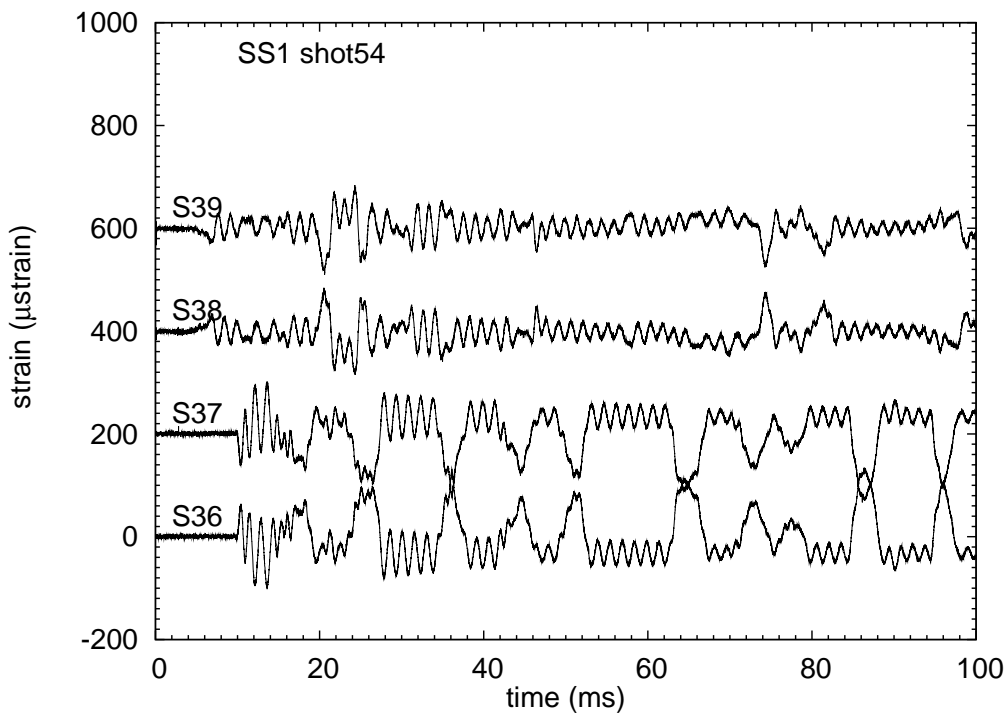
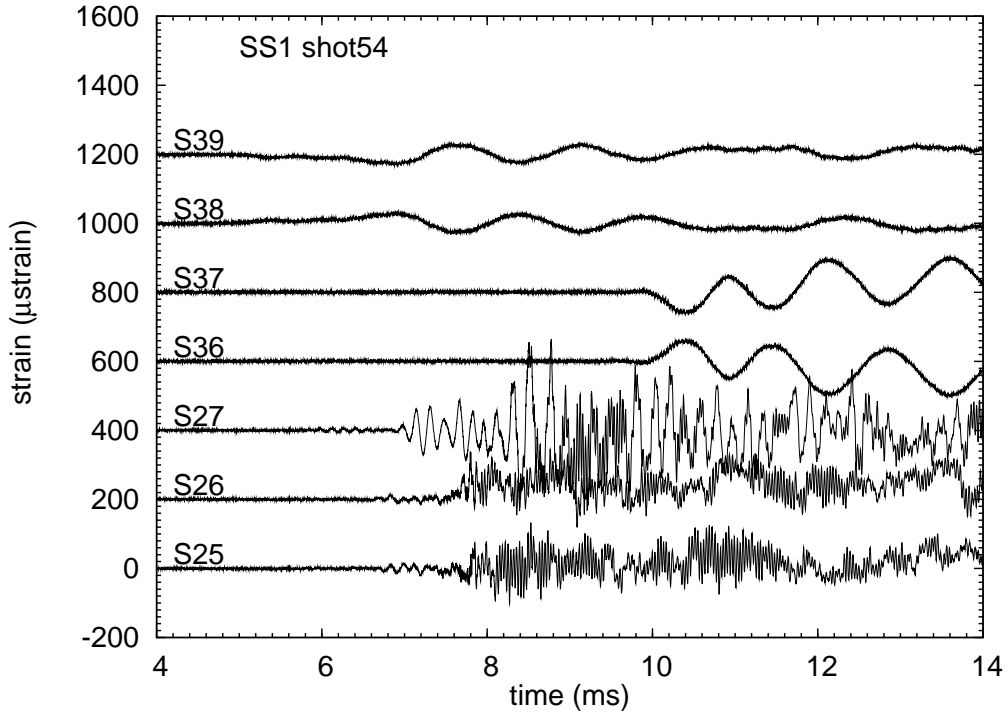


Figure 275: SS1 Shot 54. Pipe strain and cantilever strain gage signals. 10 ms and 100 ms raw data.

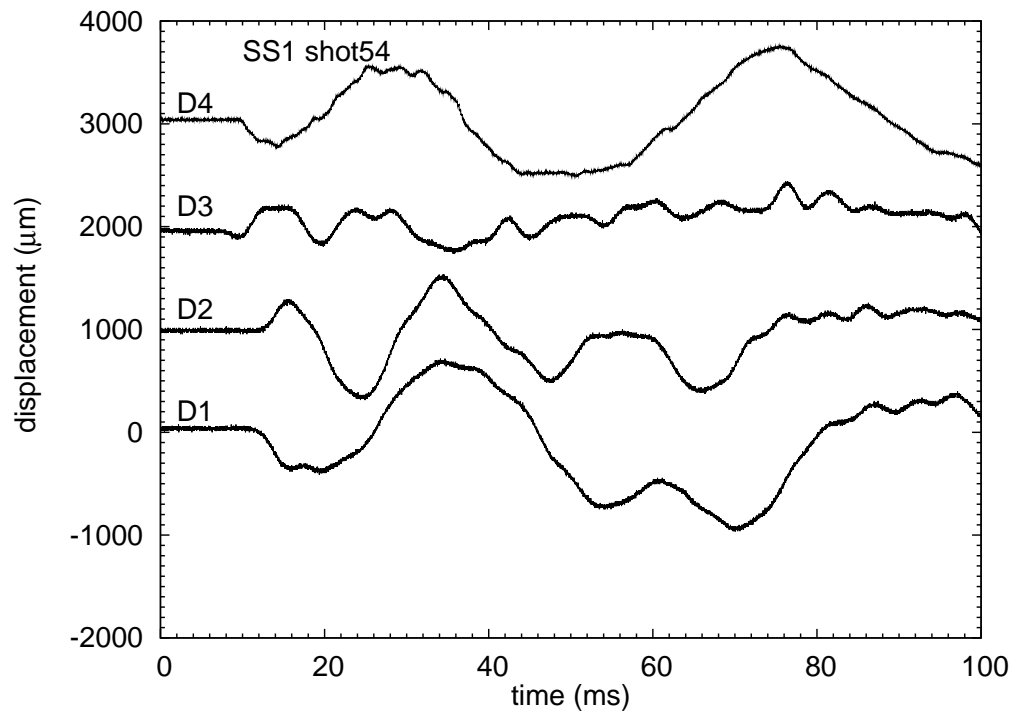


Figure 276: SS1 Shot 54. Displacement gage signals. 100 ms raw data.

## O.4 Shot 55

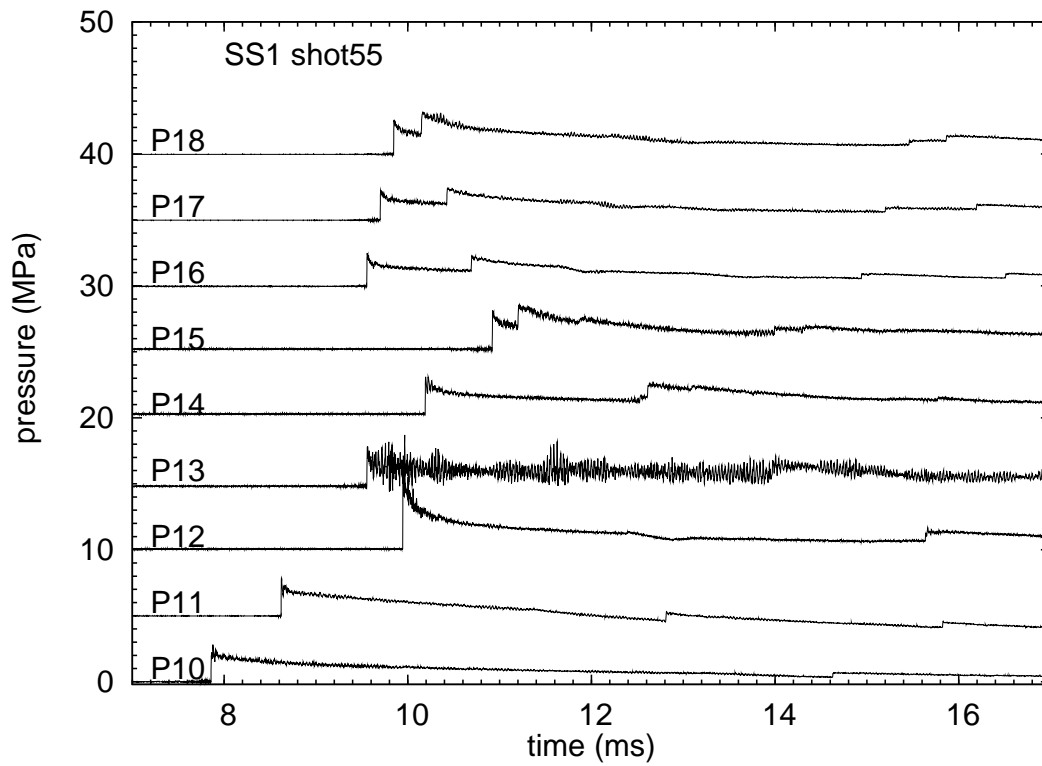
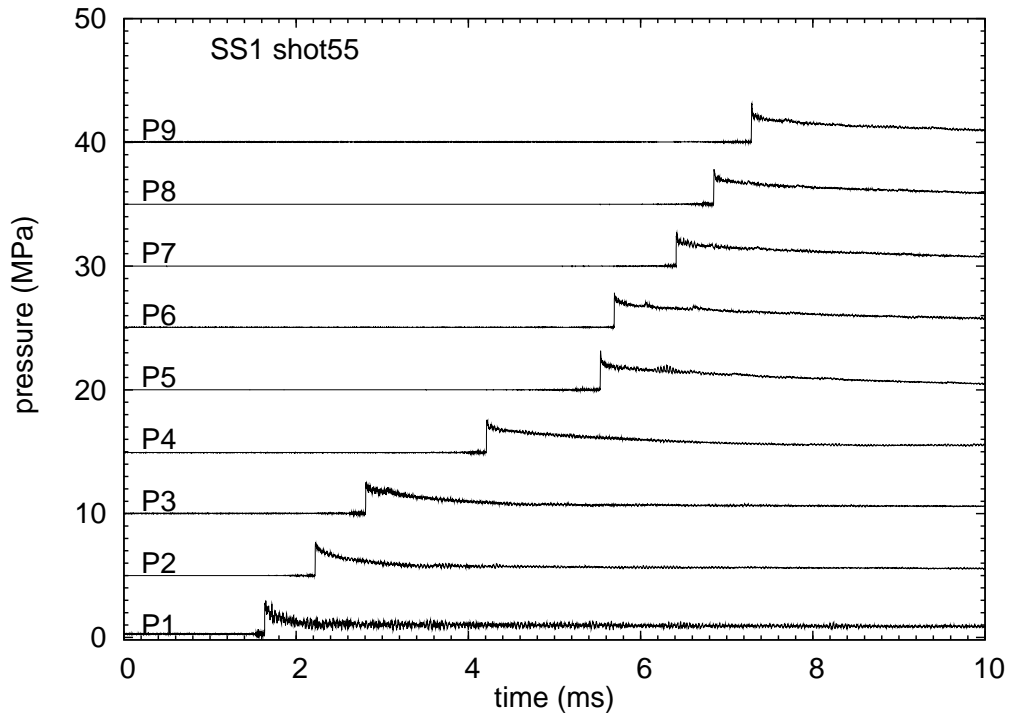


Figure 277: SS1 Shot 55. Pressure gage signals. 10 ms raw data.

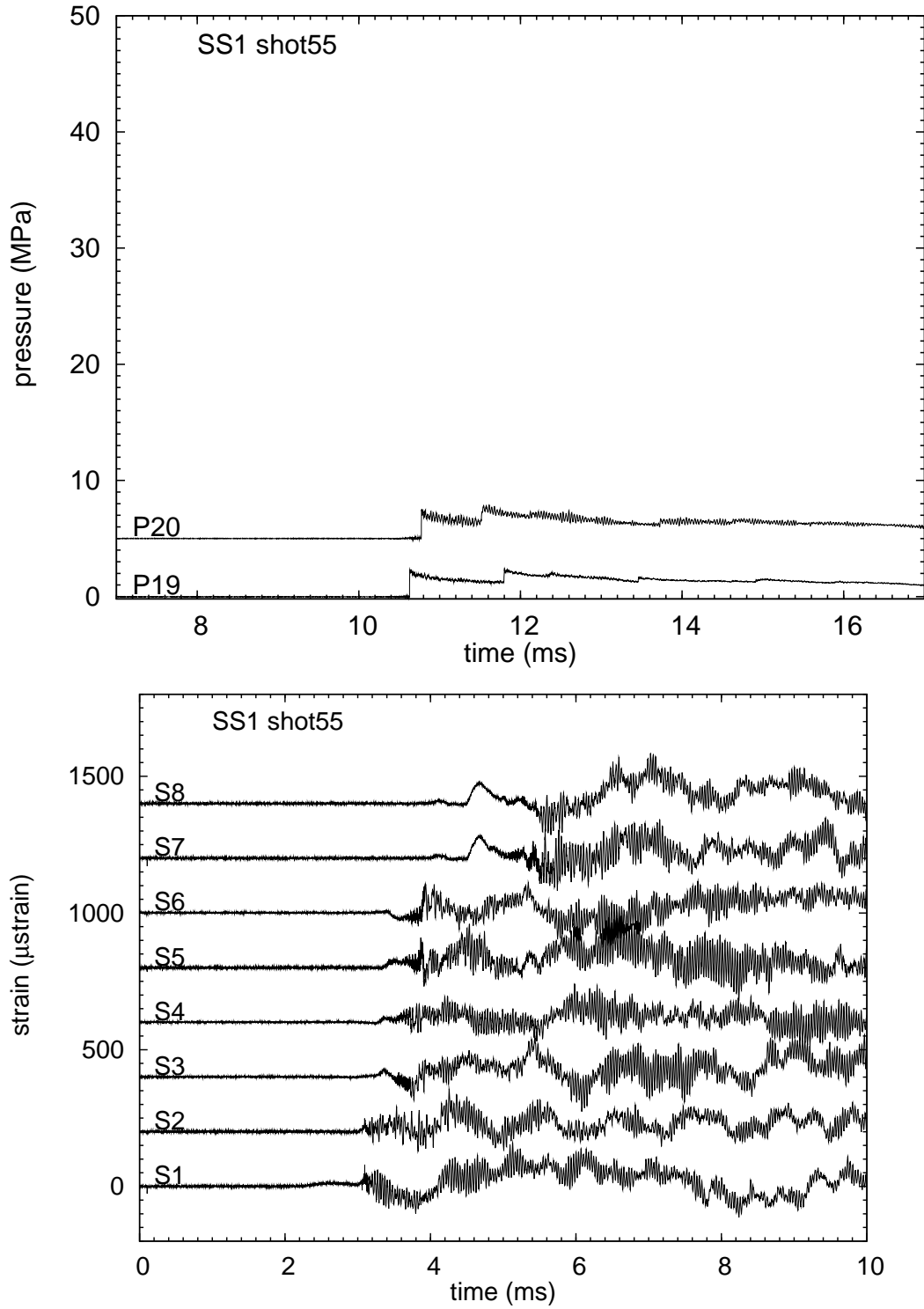


Figure 278: SS1 Shot 55. Pressure and strain gage signals. 10 ms raw data.

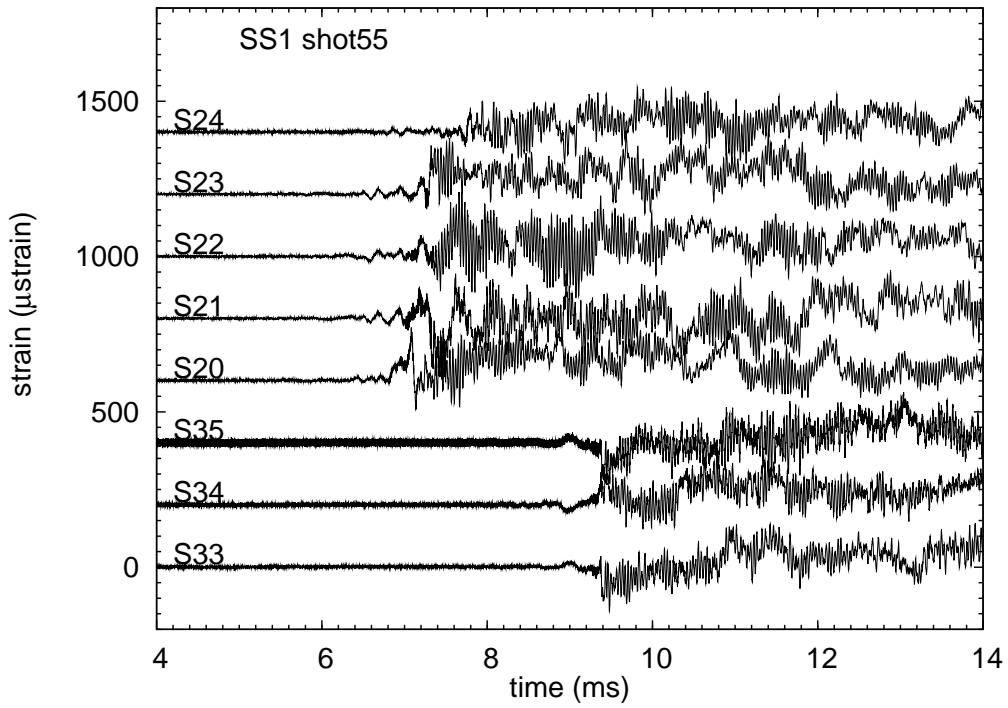
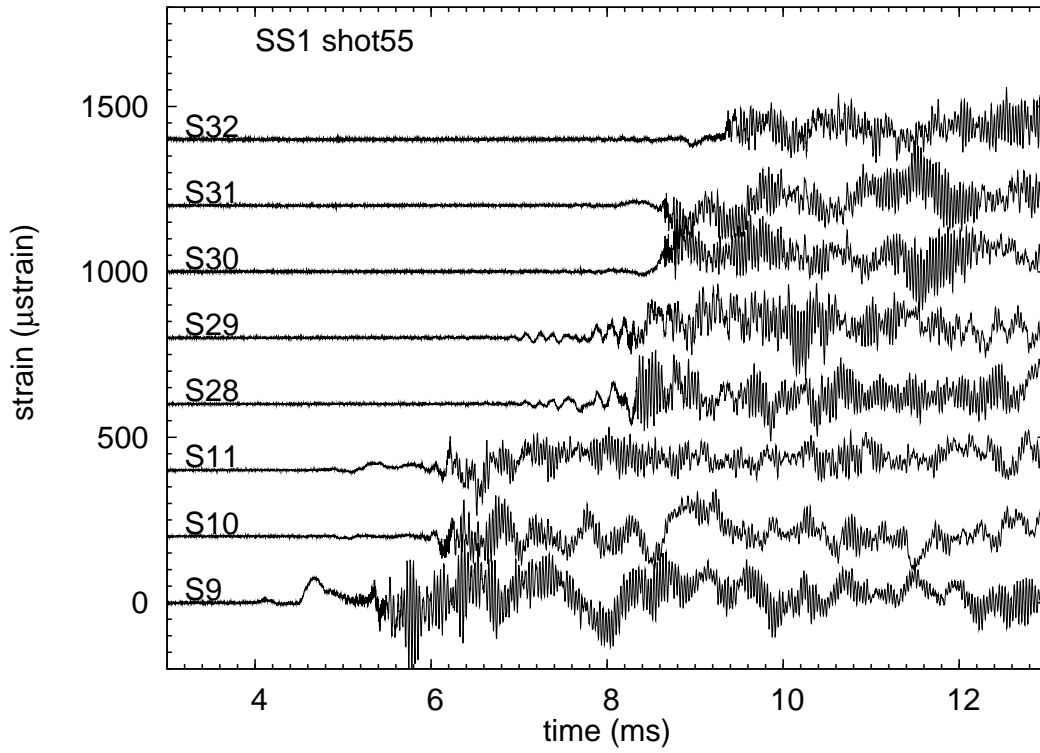


Figure 279: SS1 Shot 55. Strain gage signals. 10 ms raw data.

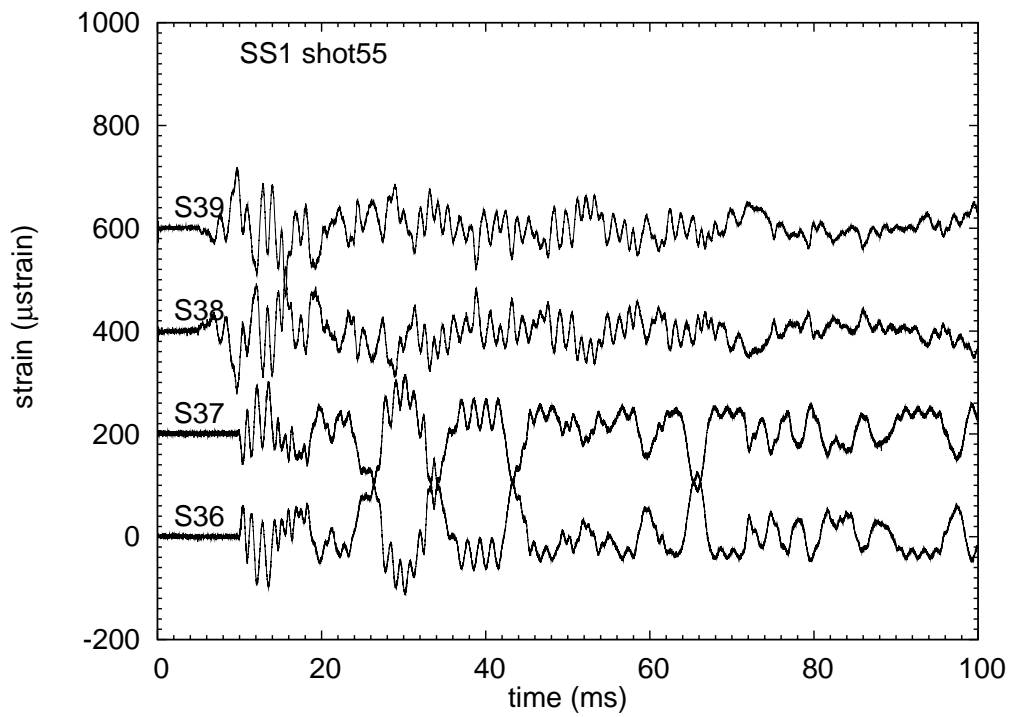
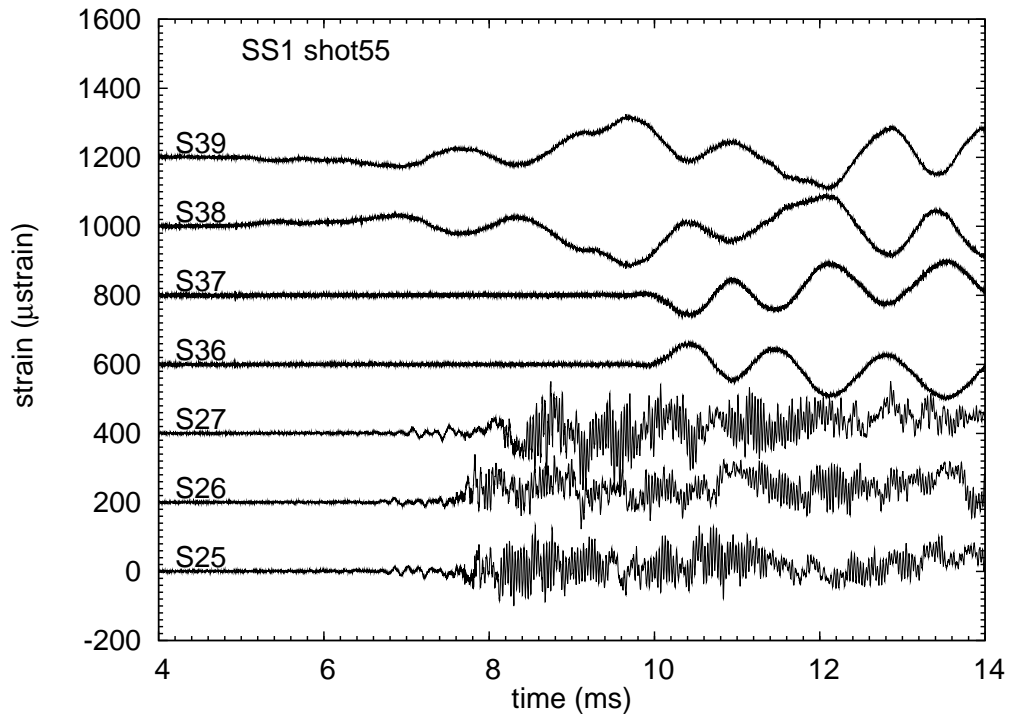


Figure 280: SS1 Shot 55. Pipe strain and cantilever strain gage signals. 10 ms and 100 ms raw data.

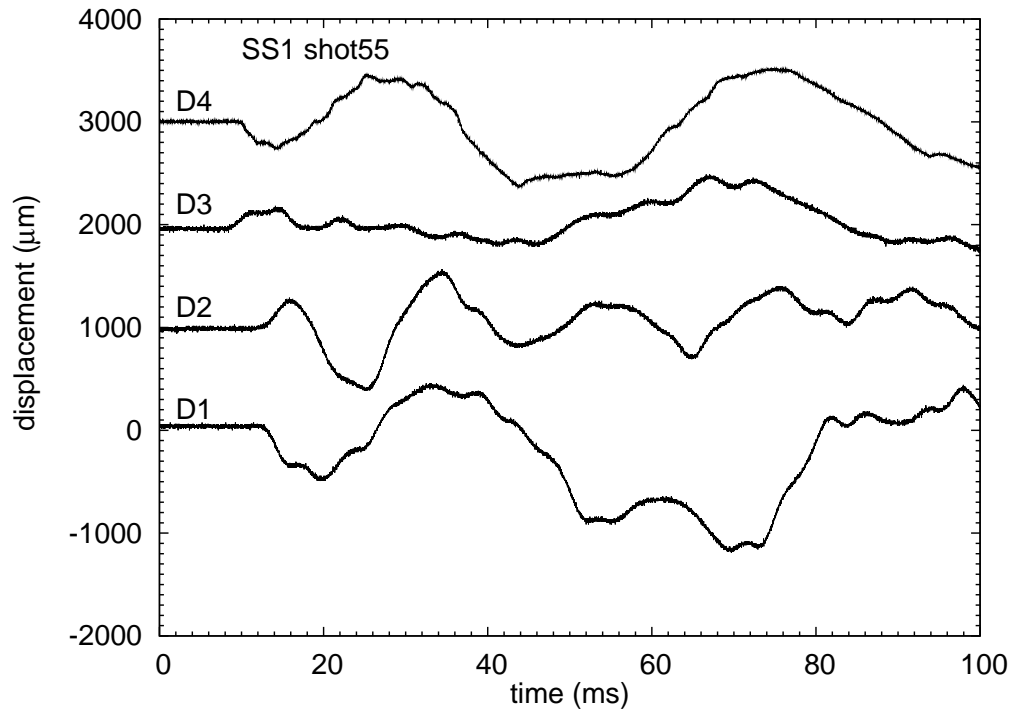


Figure 281: SS1 Shot 55. Displacement gage signals. 100 ms raw data.

## O.5 Shot 56

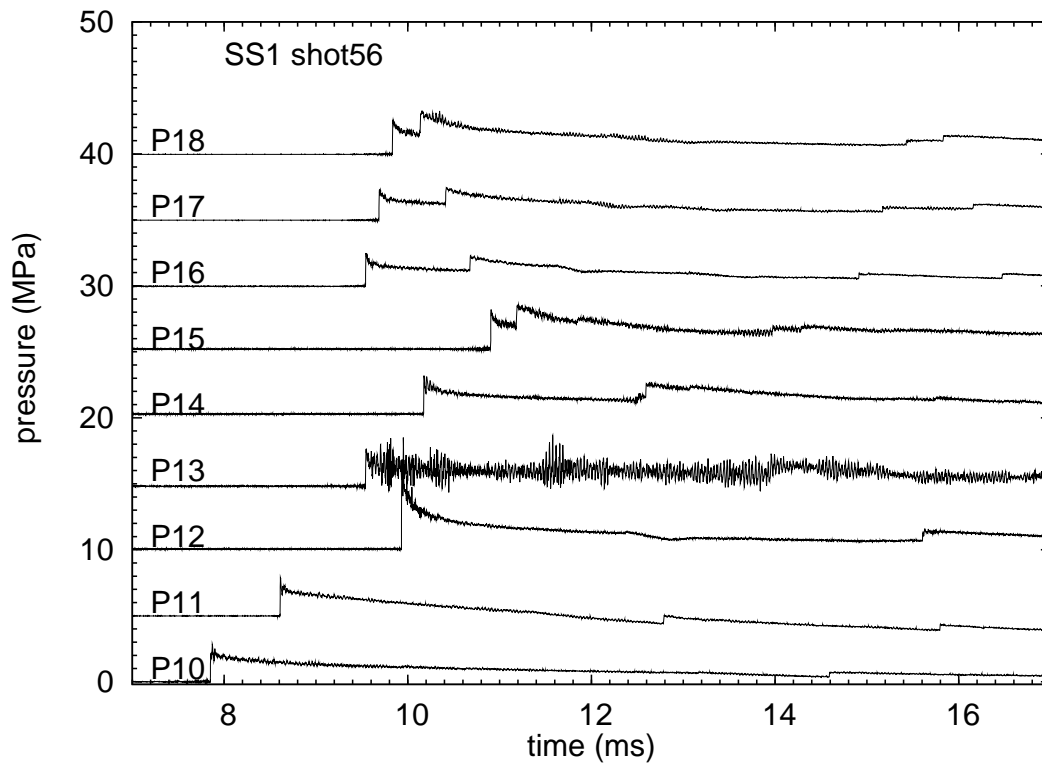
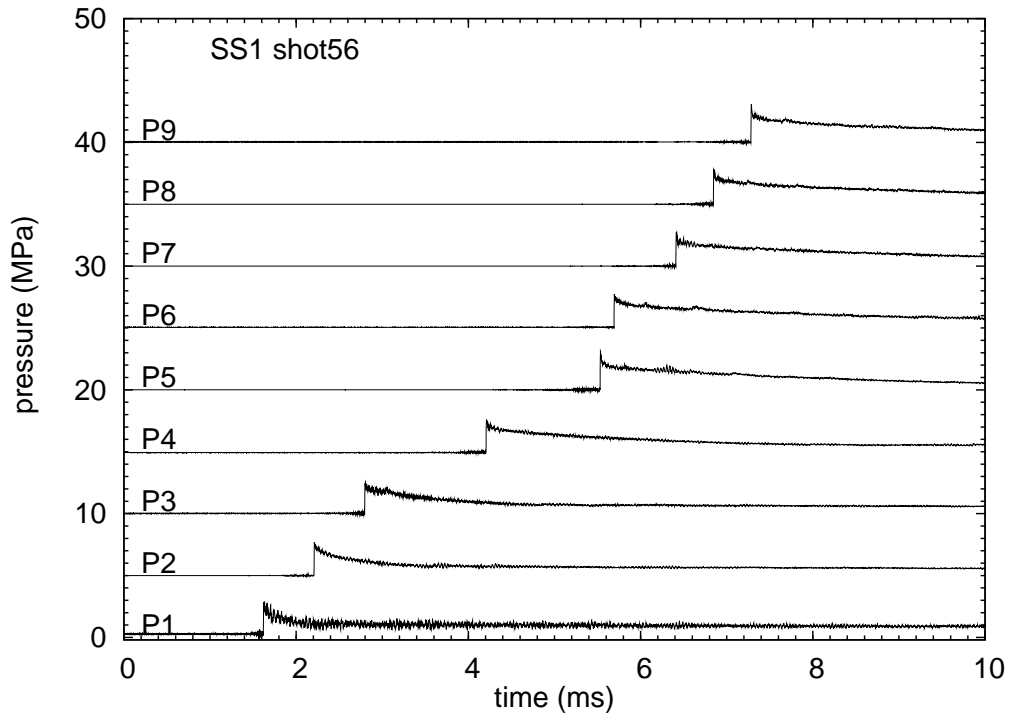


Figure 282: SS1 Shot 56. Pressure gage signals. 10 ms raw data.

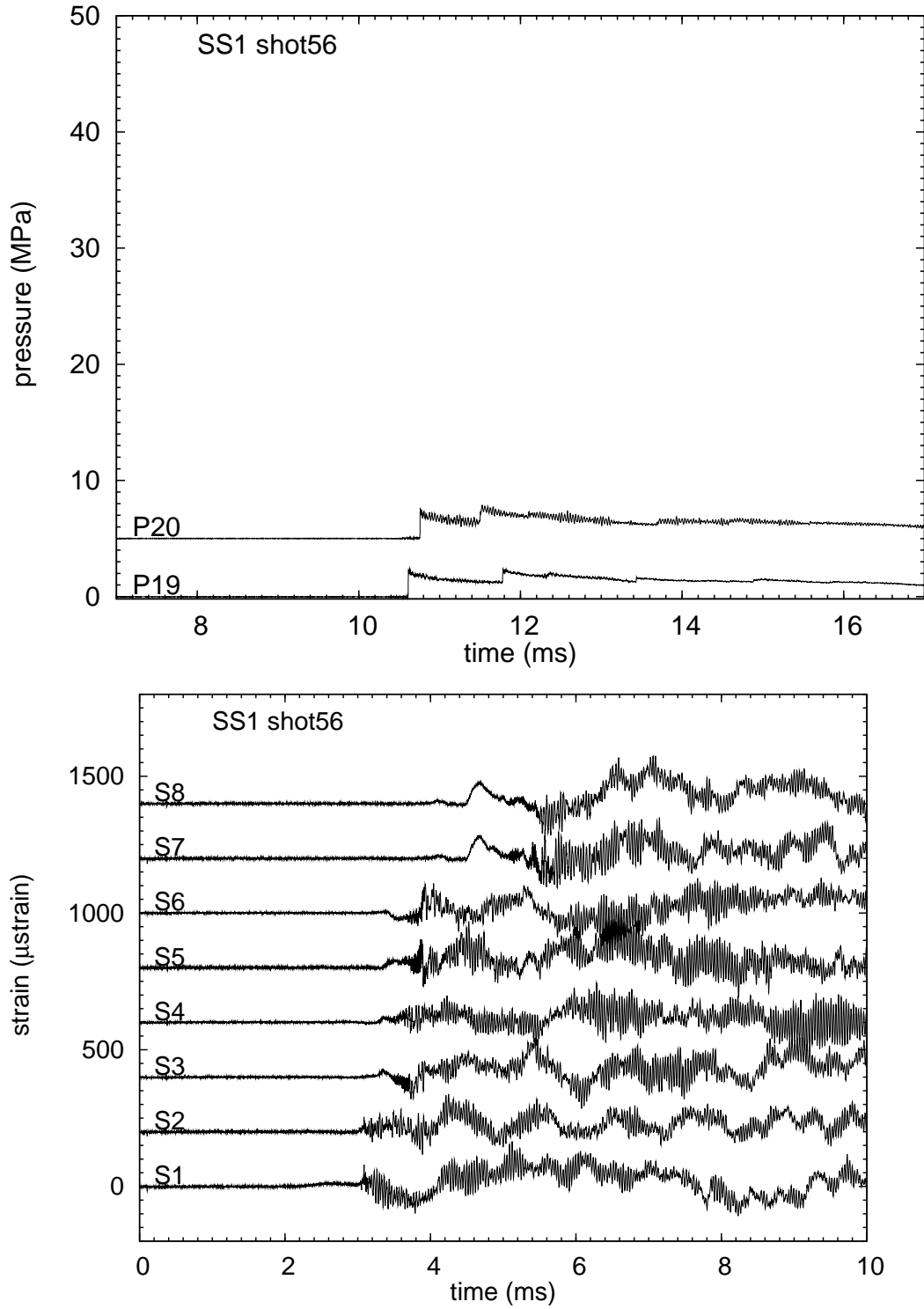


Figure 283: SS1 Shot 56. Pressure and strain gage signals. 10 ms raw data.

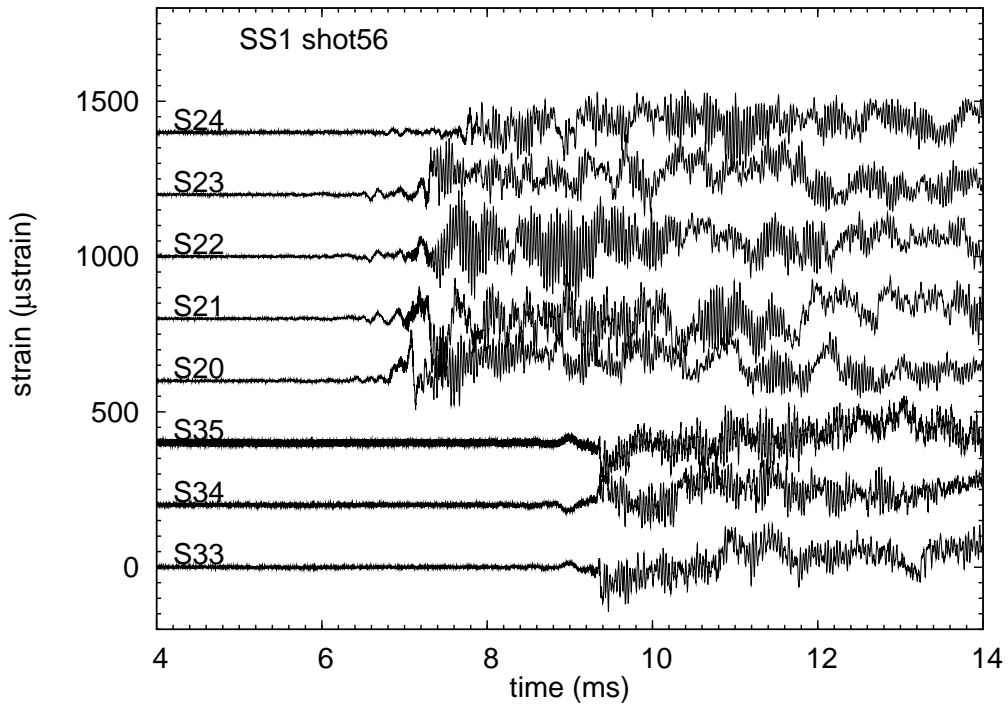
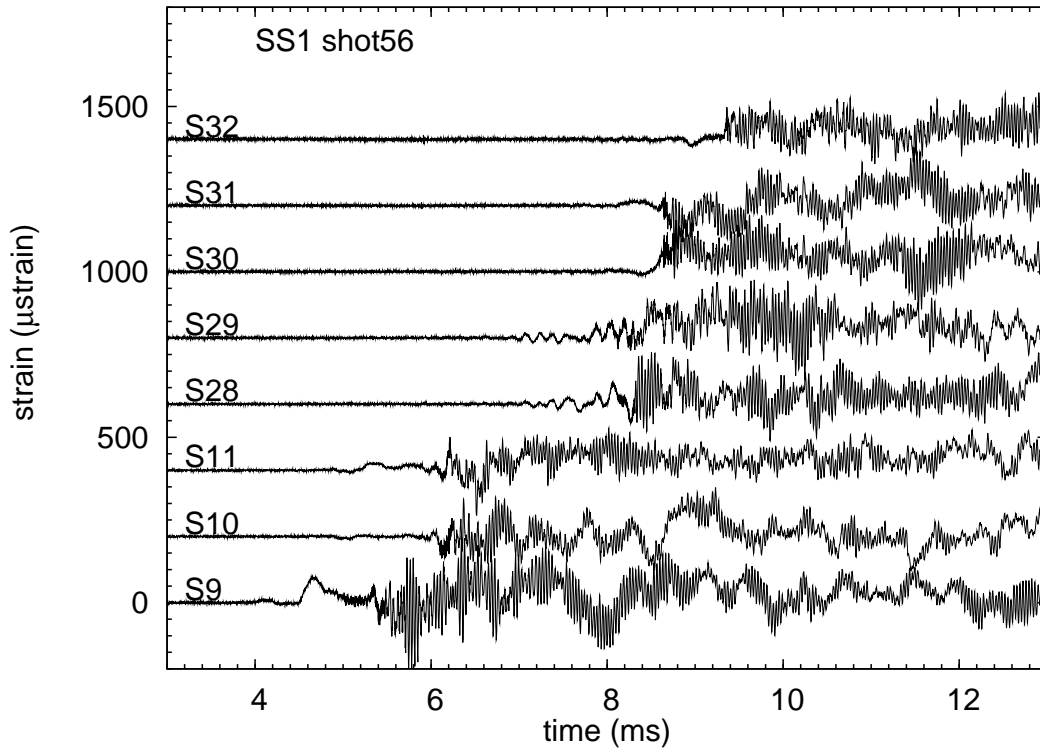


Figure 284: SS1 Shot 56. Strain gage signals. 10 ms raw data.

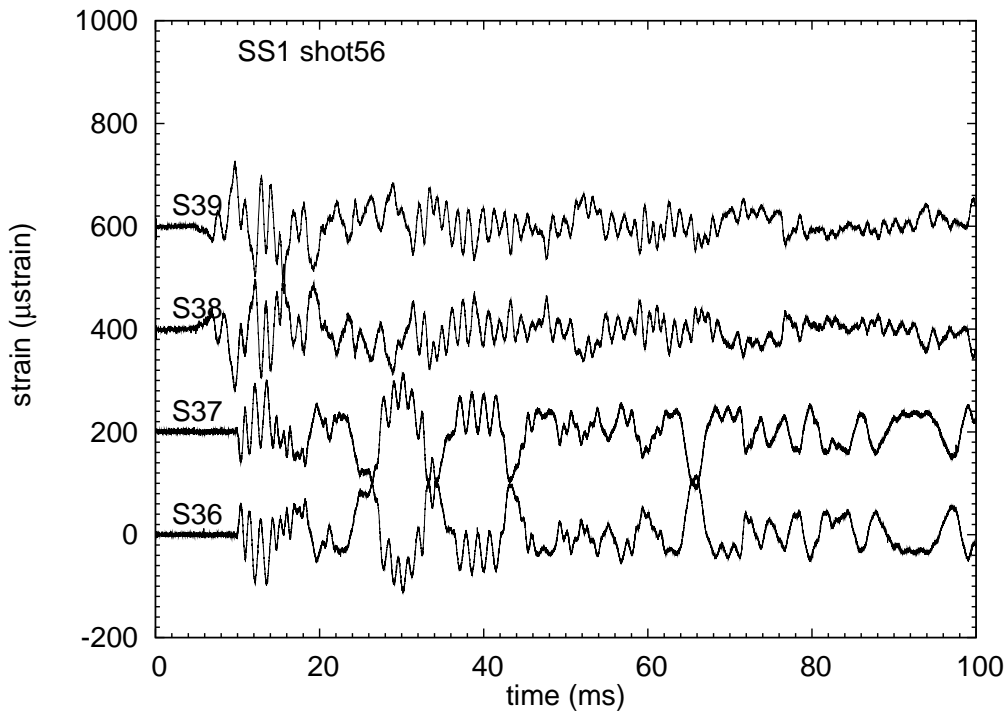
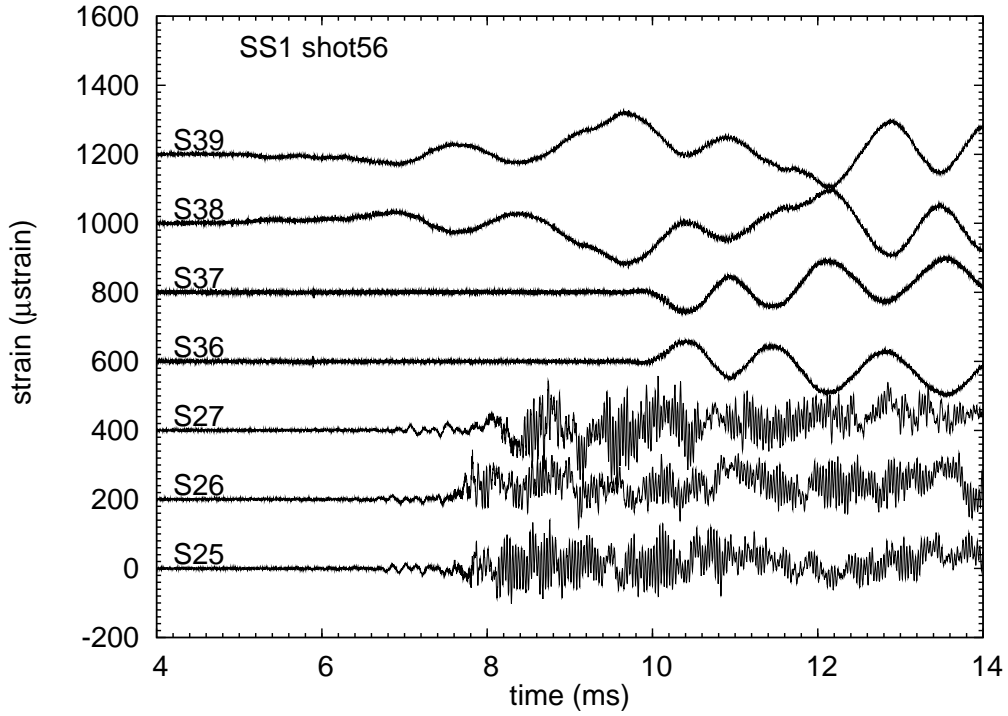


Figure 285: SS1 Shot 56. Pipe strain and cantilever strain gage signals. 10 ms and 100 ms raw data.

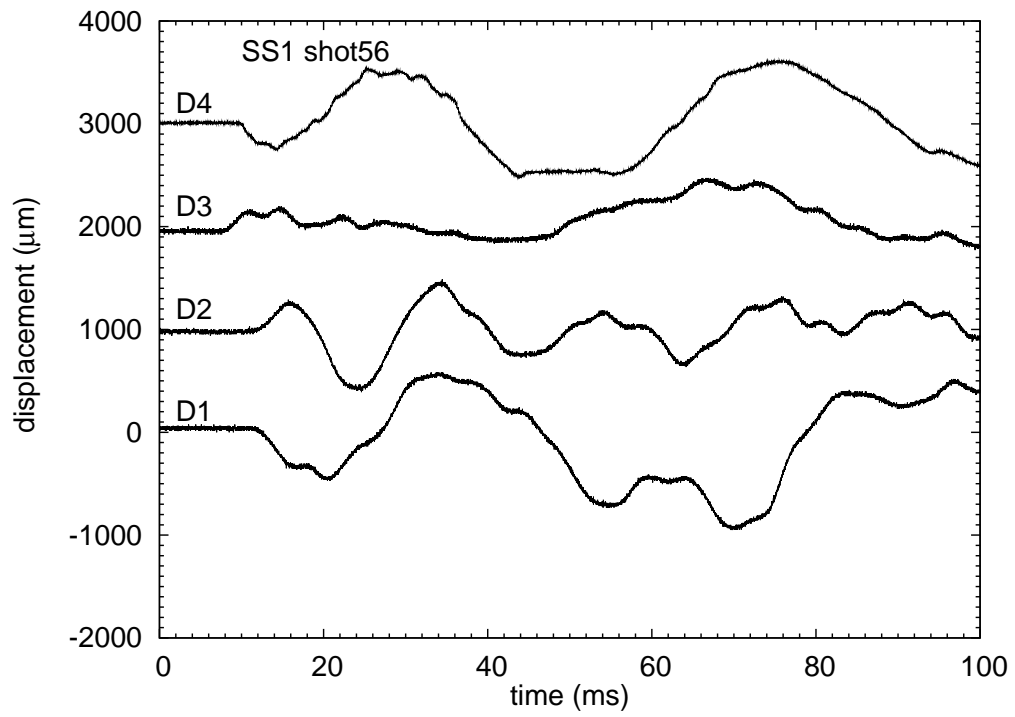


Figure 286: SS1 Shot 56. Displacement gage signals. 100 ms raw data.

## O.6 Shot 58

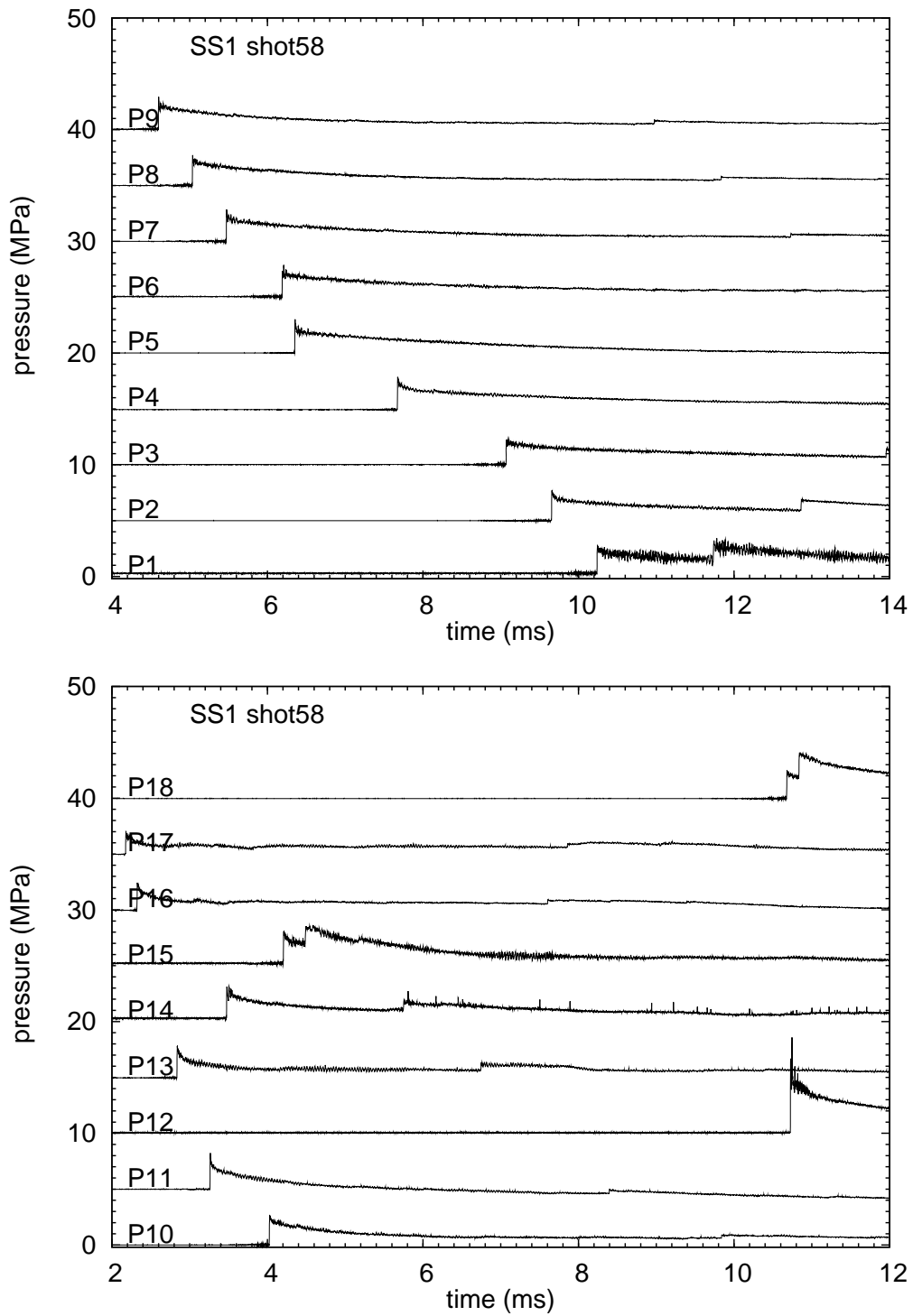


Figure 287: SS1 Shot 58. Pressure gage signals. 10 ms raw data.

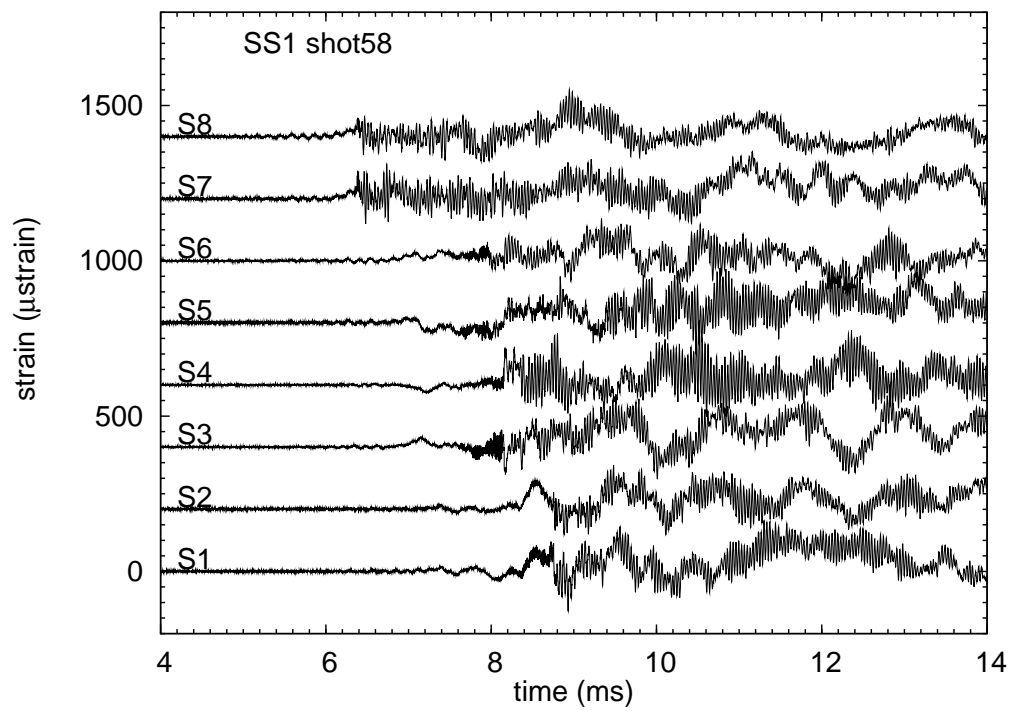
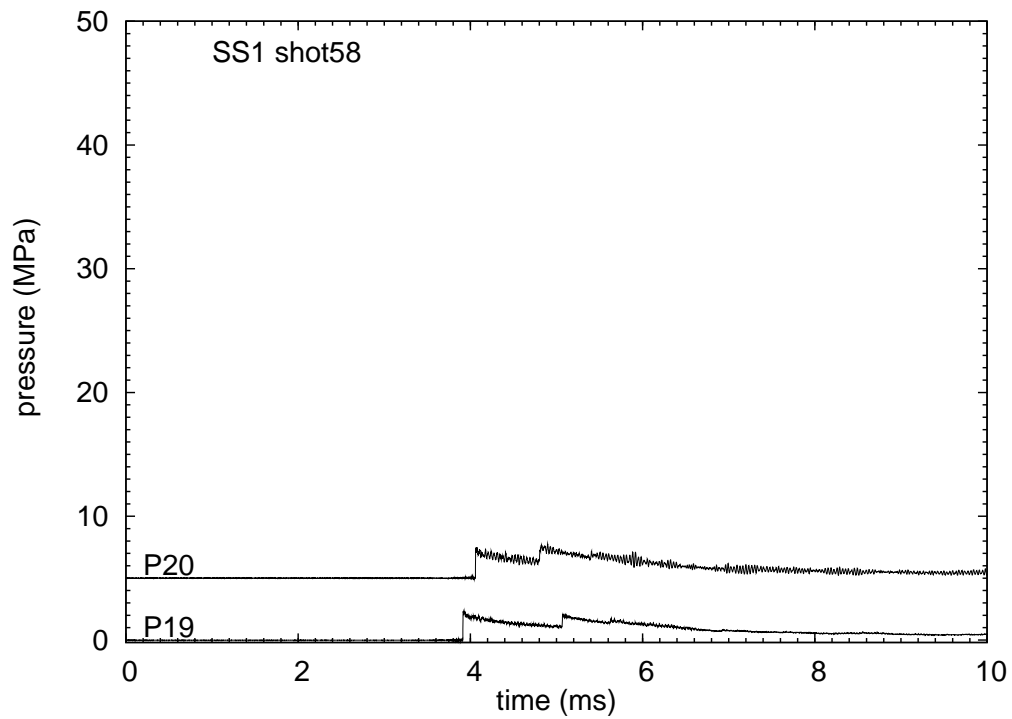


Figure 288: SS1 Shot 58. Pressure and strain gage signals. 10 ms raw data.

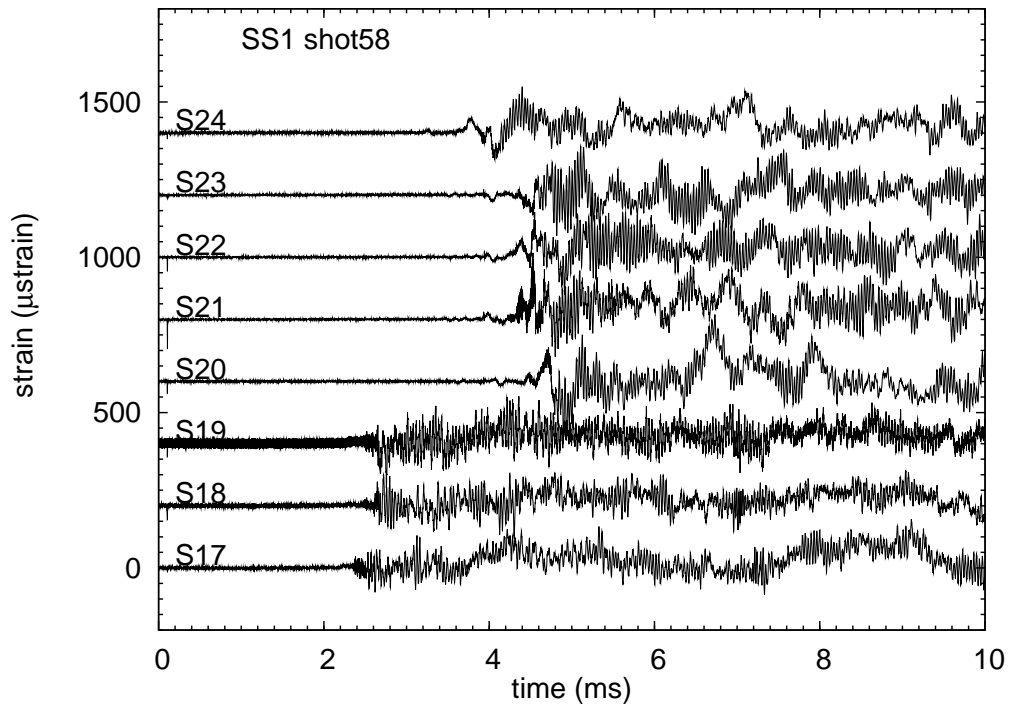
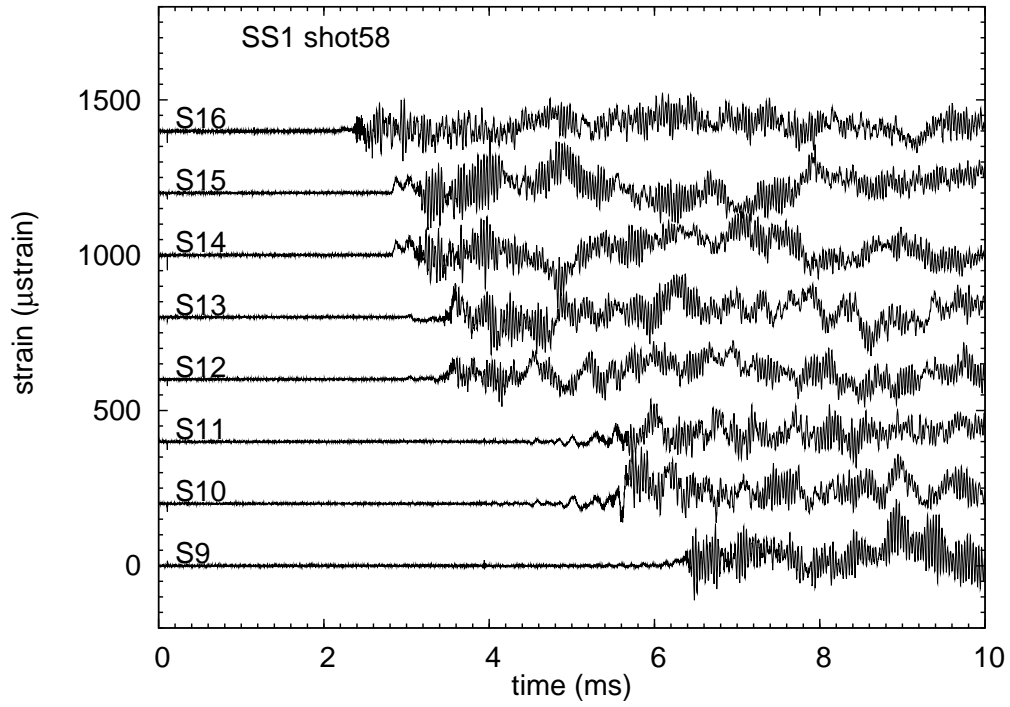


Figure 289: SS1 Shot 58. Strain gage signals. 10 ms raw data.

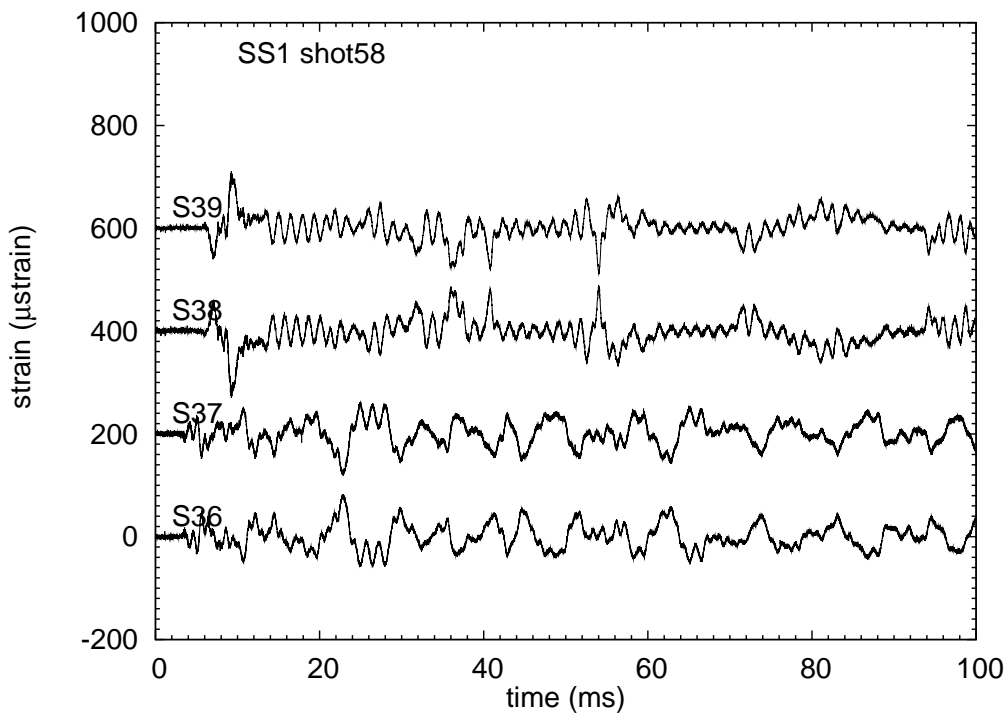
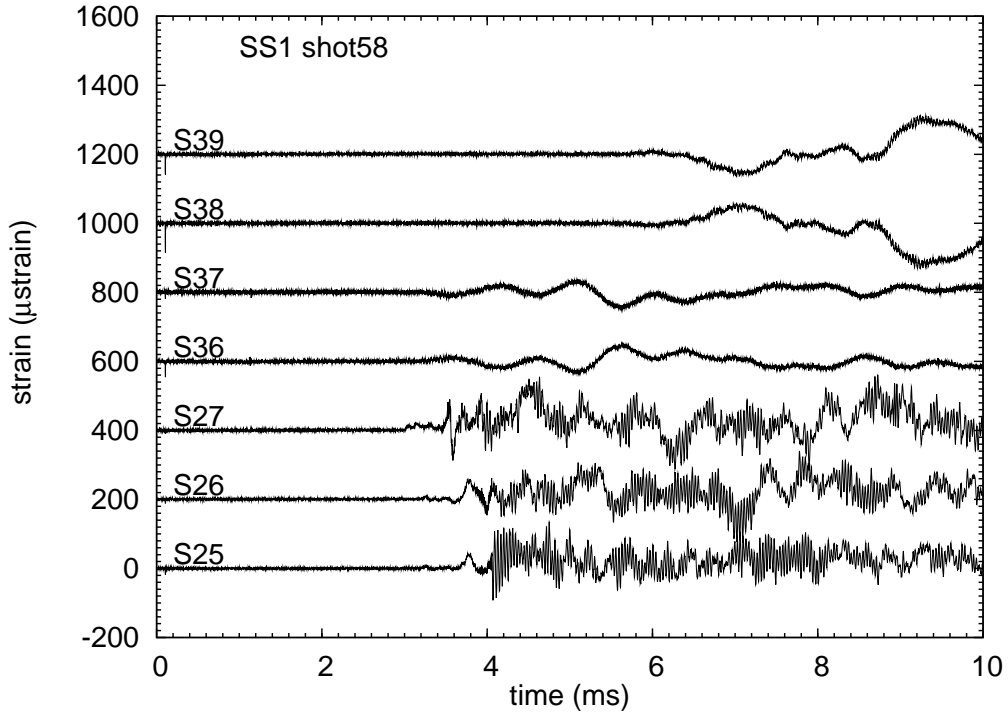


Figure 290: SS1 Shot 58. Pipe strain and cantilever strain gage signals. 10 ms and 100 ms raw data.

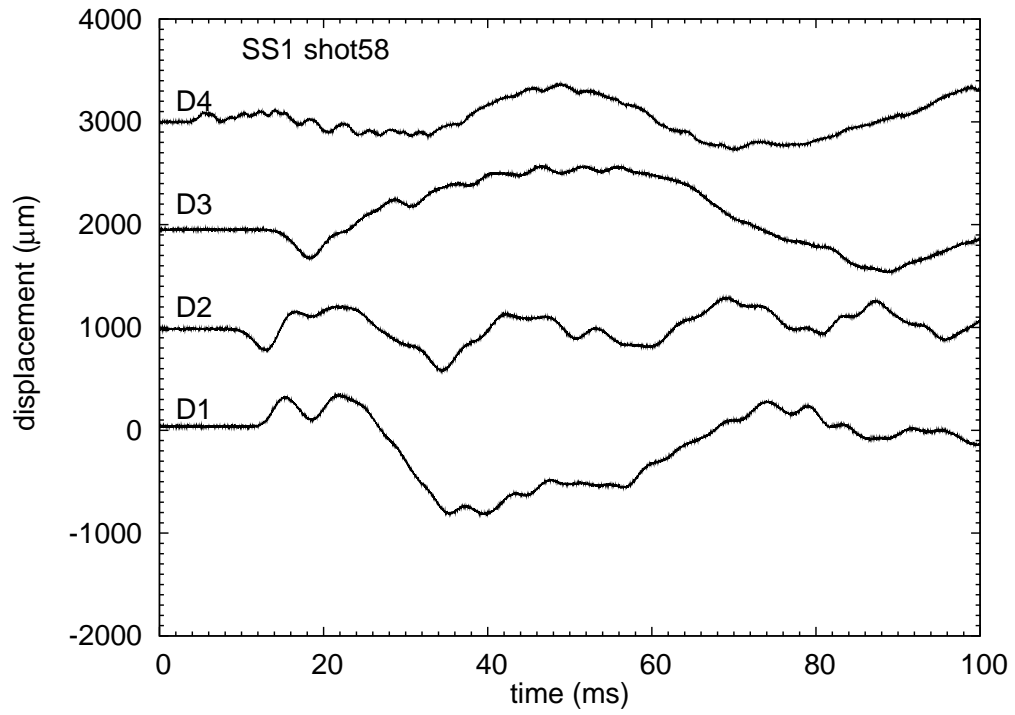


Figure 291: SS1 Shot 58. Displacement gage signals. 100 ms raw data.

## O.7 Shot 59

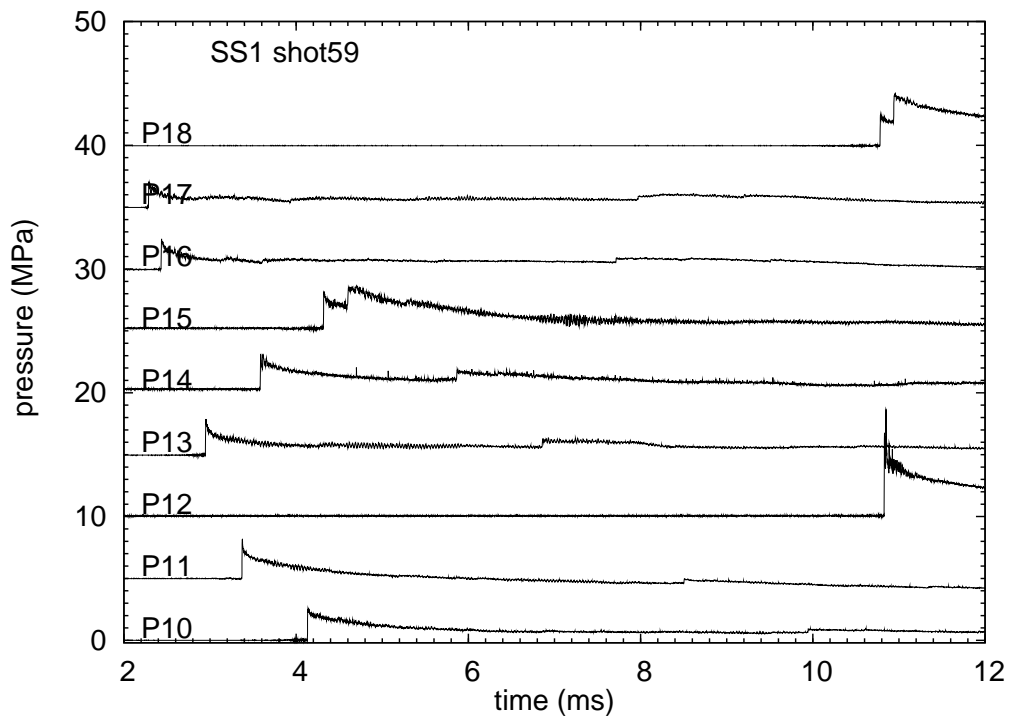
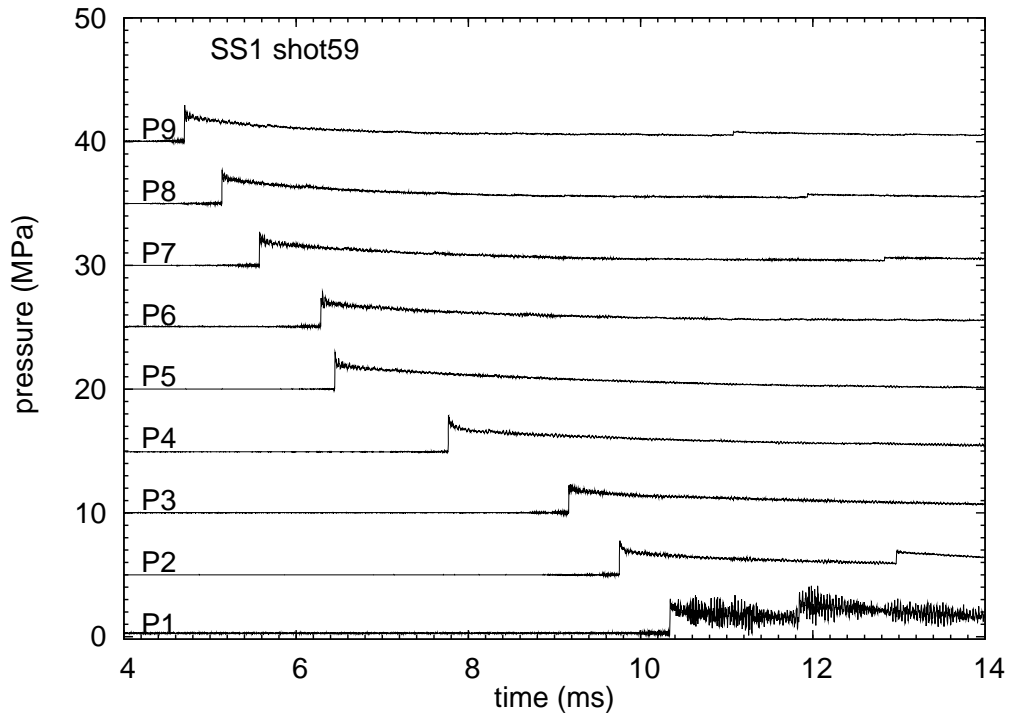


Figure 292: SS1 Shot 59. Pressure gage signals. 10 ms raw data.

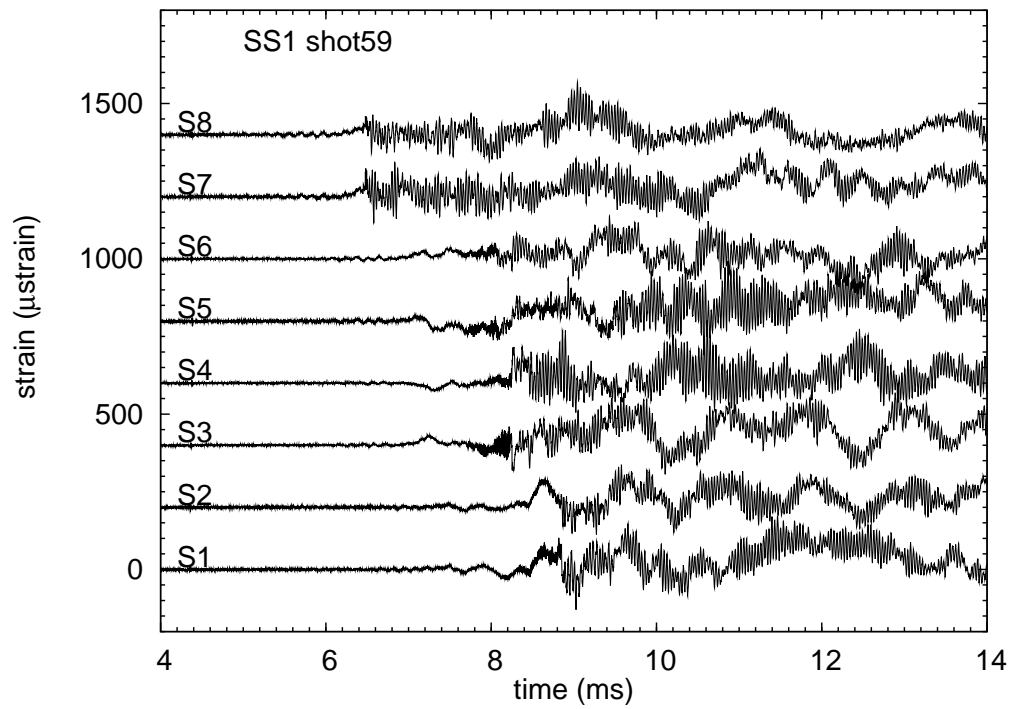
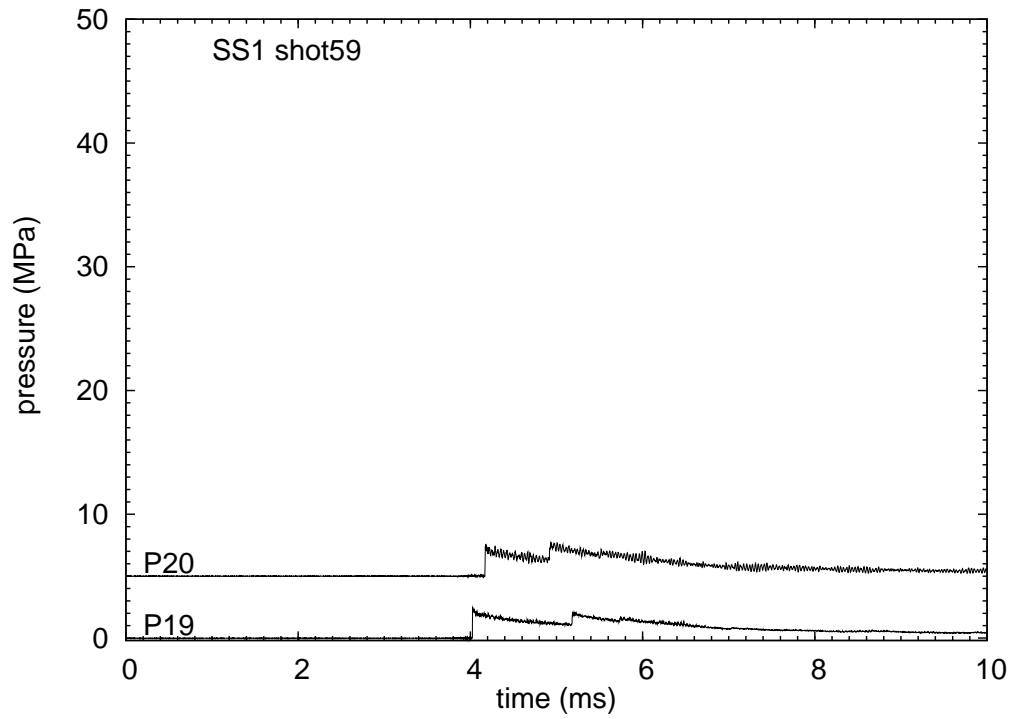


Figure 293: SS1 Shot 59. Pressure and strain gage signals. 10 ms raw data.

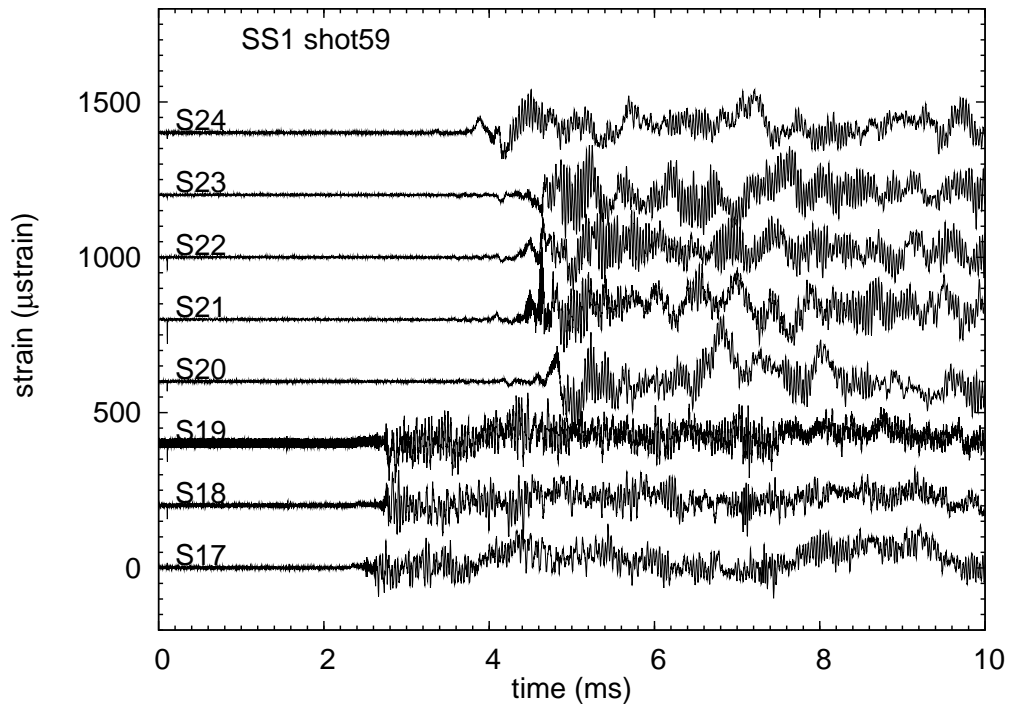
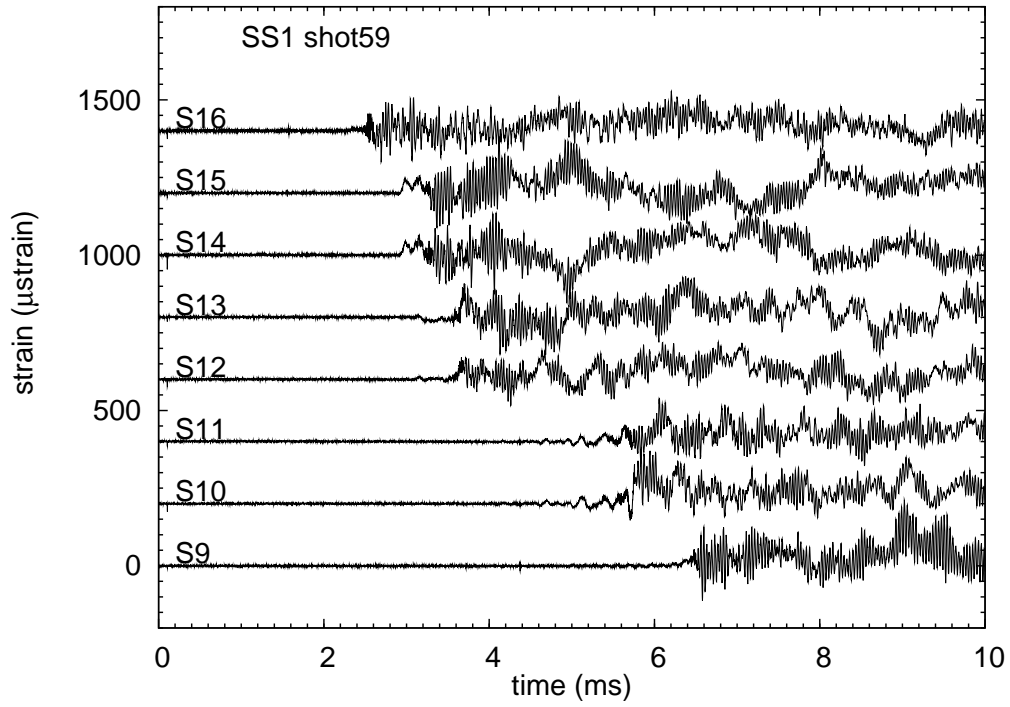


Figure 294: SS1 Shot 59. Strain gage signals. 10 ms raw data.

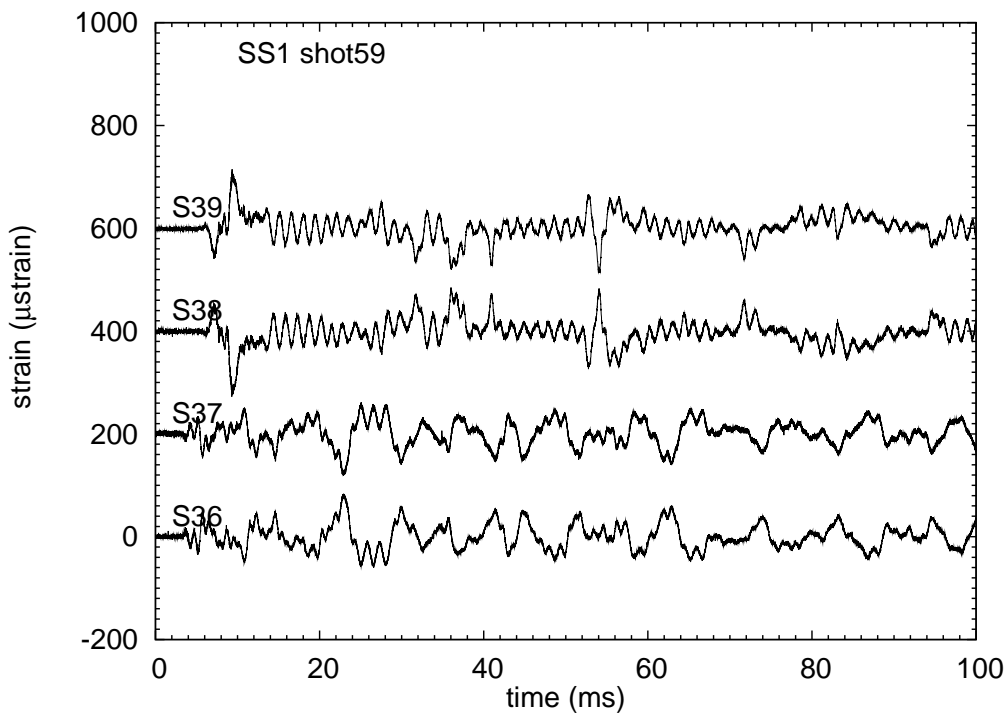
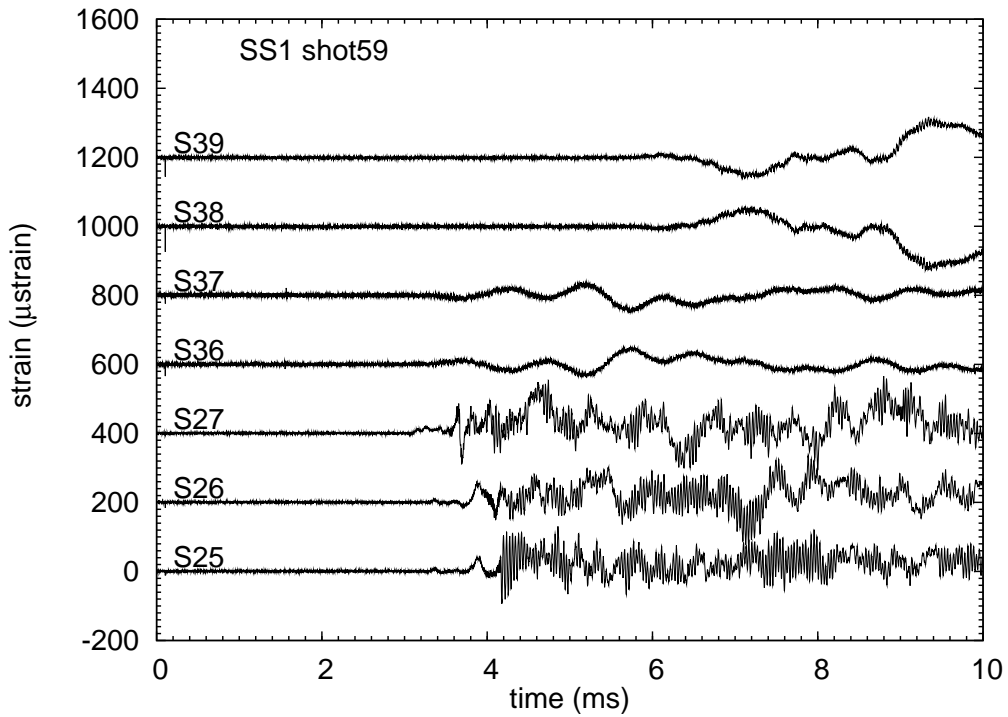


Figure 295: SS1 Shot 59. Pipe strain and cantilever strain gage signals. 10 ms and 100 ms raw data.

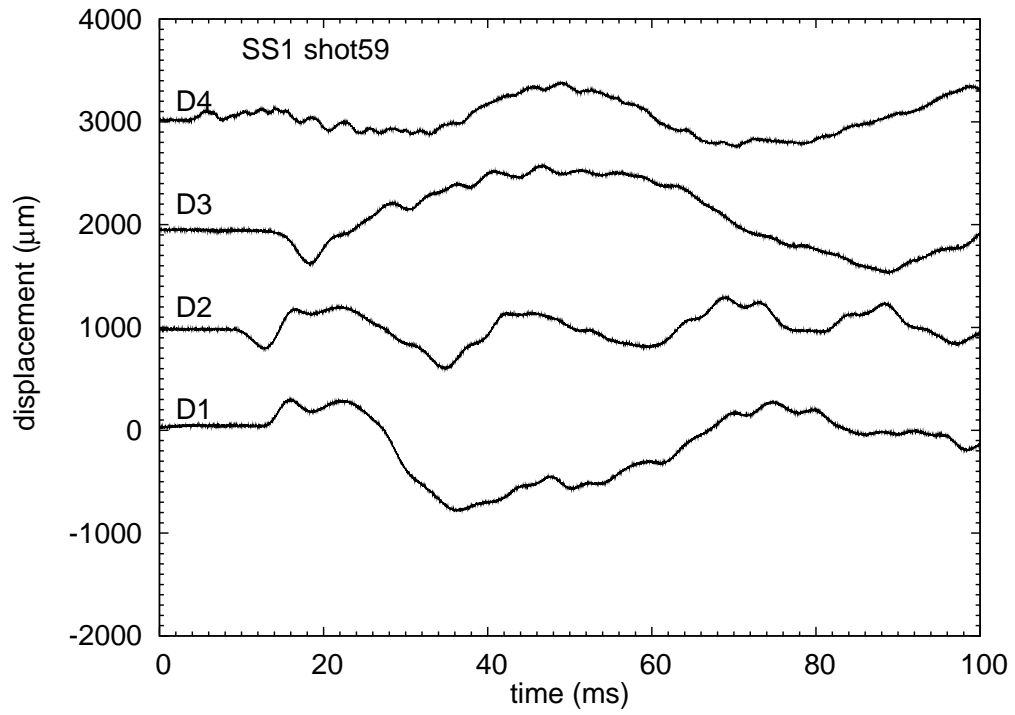


Figure 296: SS1 Shot 59. Displacement gage signals. 100 ms raw data.

## O.8 Shot 60

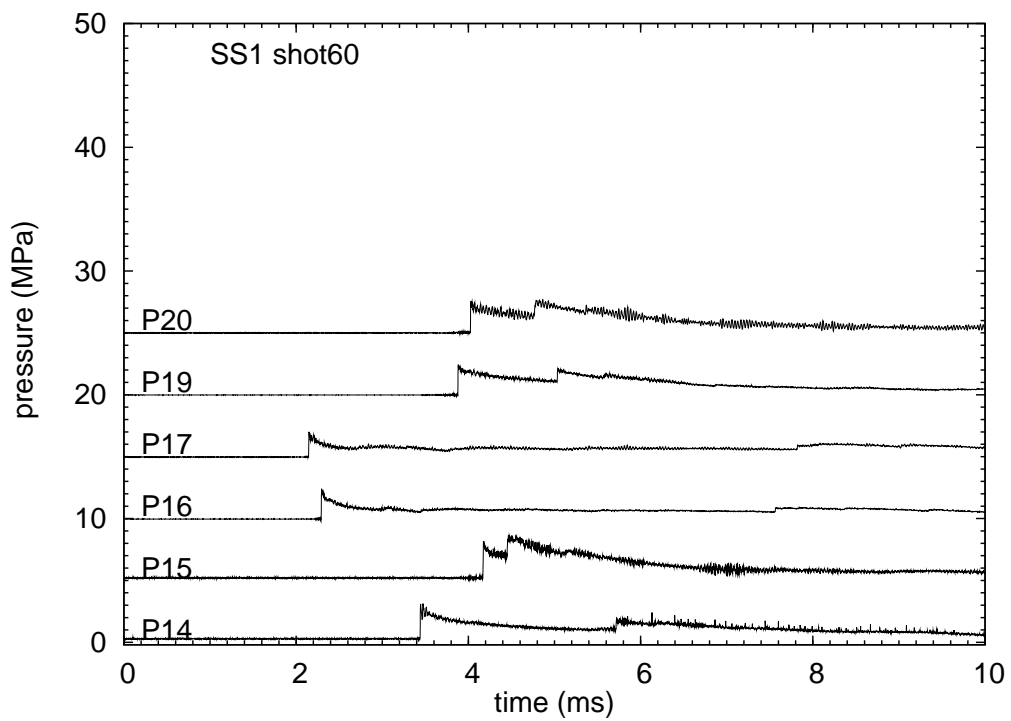
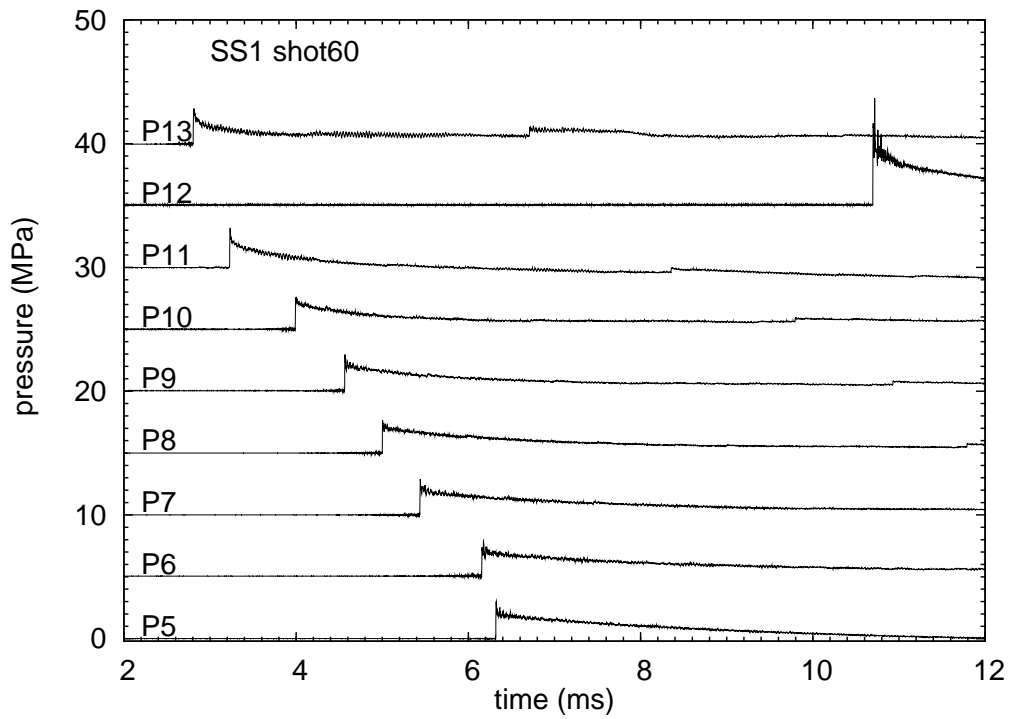


Figure 297: SS1 Shot 60. Pressure gage signals. 10 ms raw data.

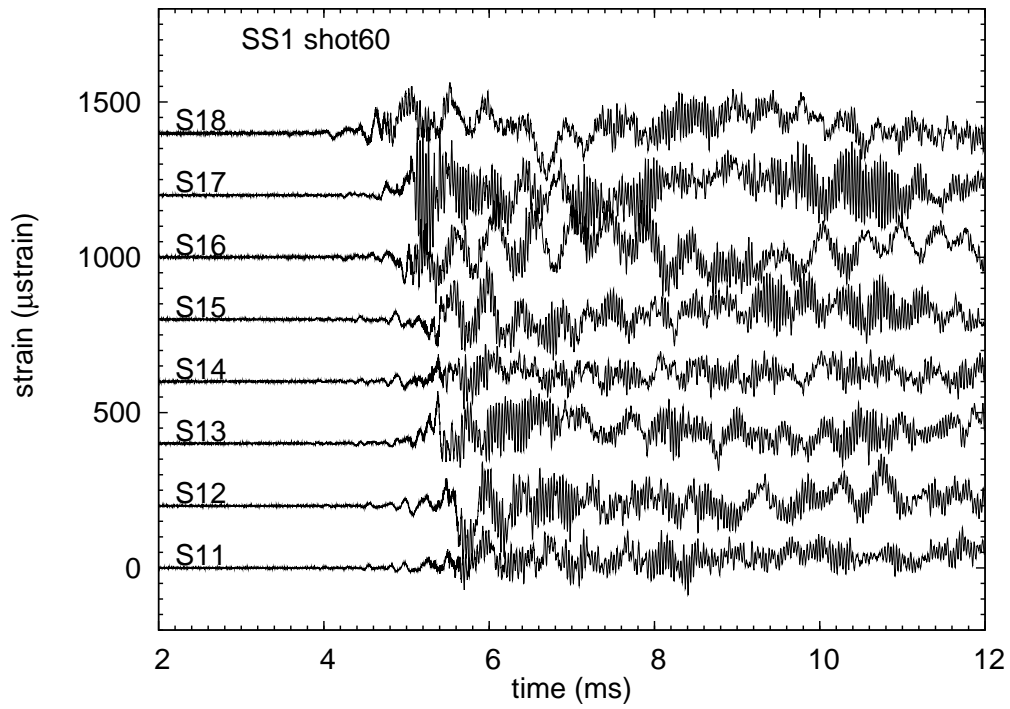
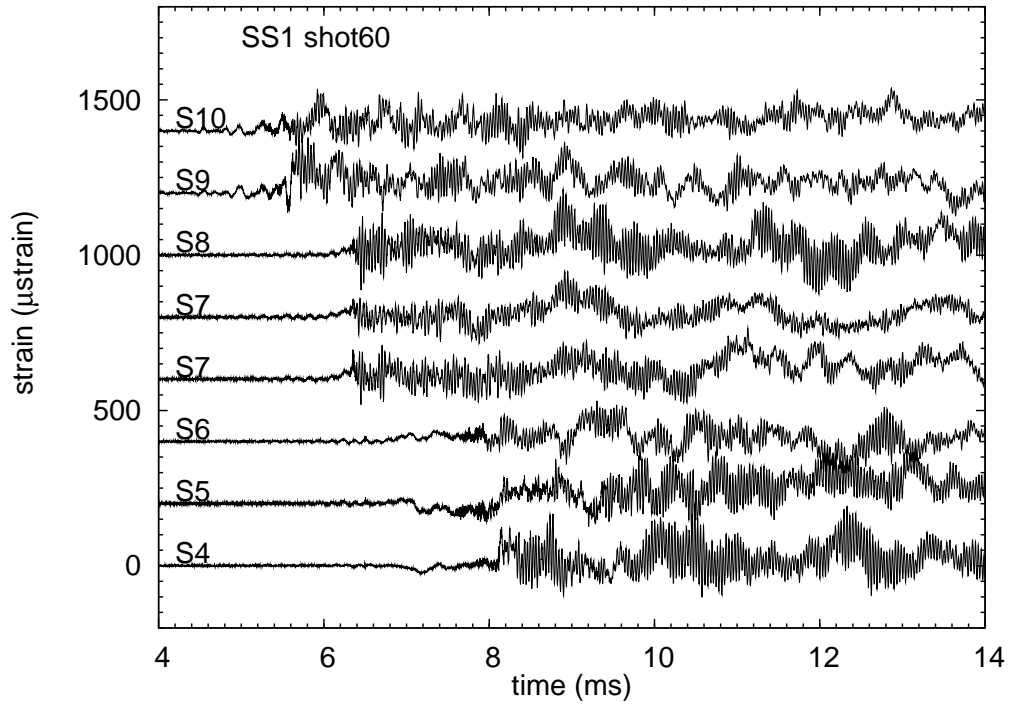


Figure 298: SS1 Shot 60. Pressure and strain gage signals. 10 ms raw data.

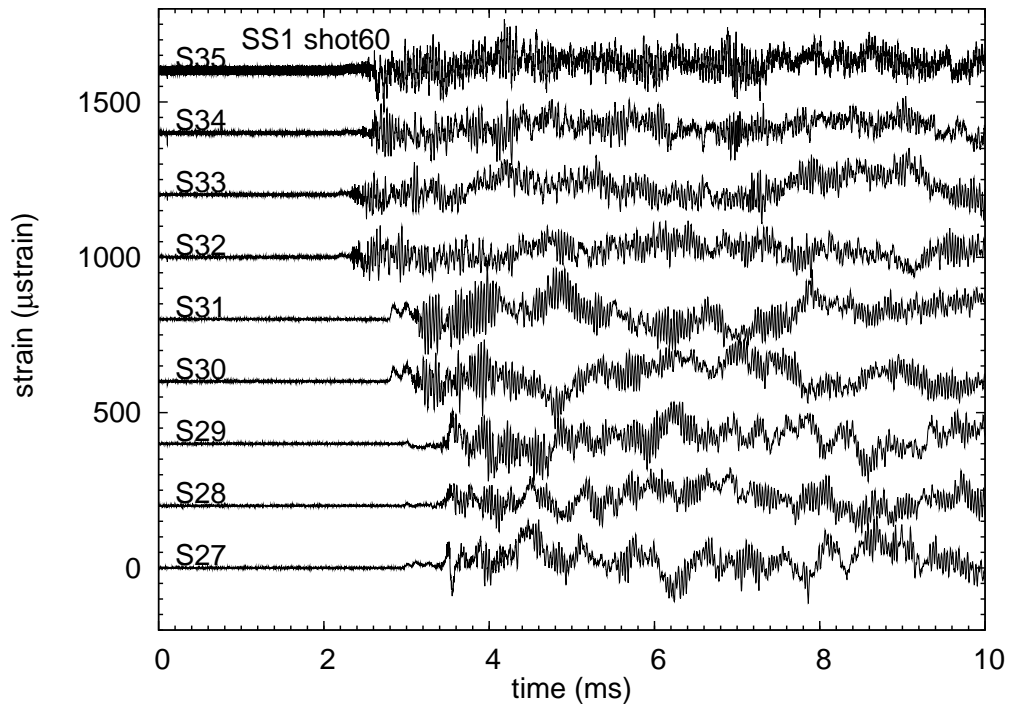
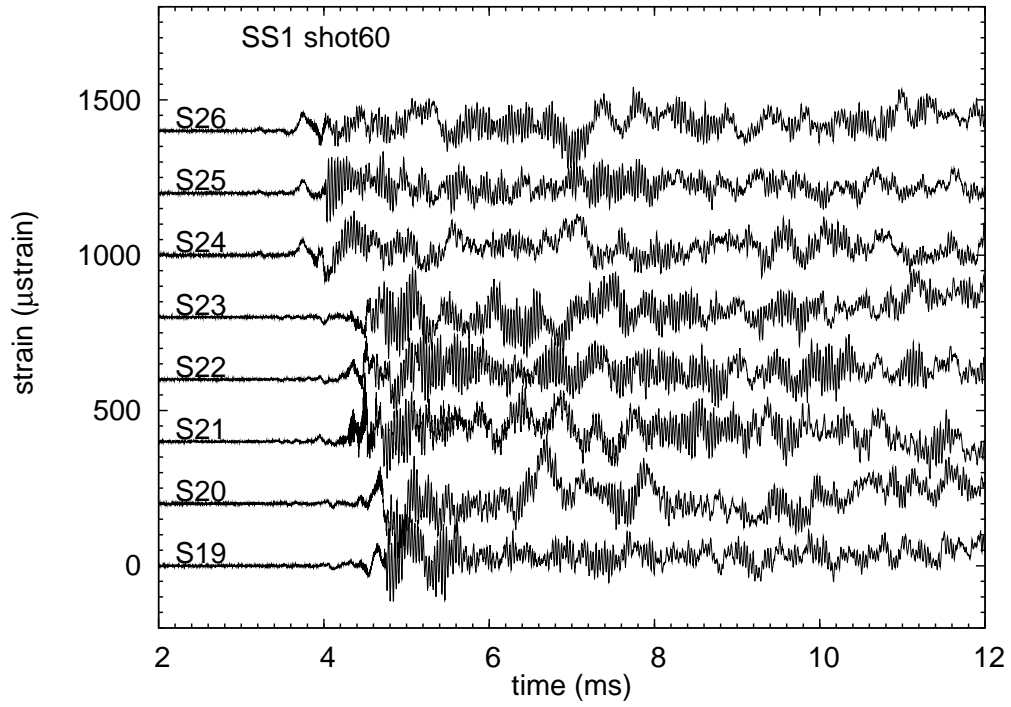


Figure 299: SS1 Shot 60. Strain gage signals. 10 ms raw data.

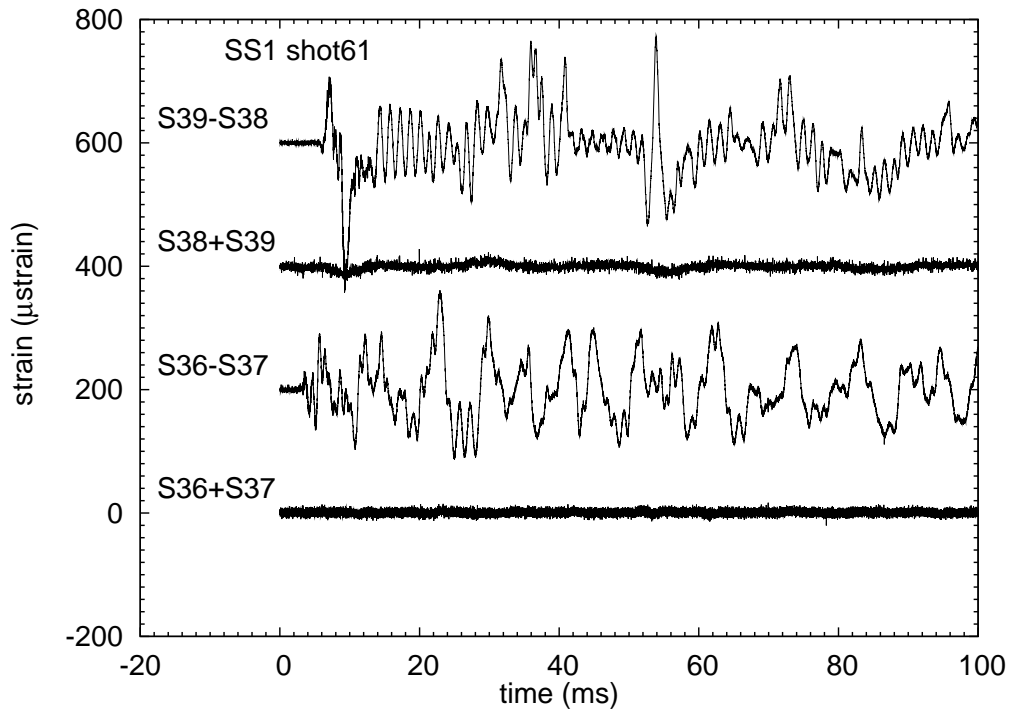
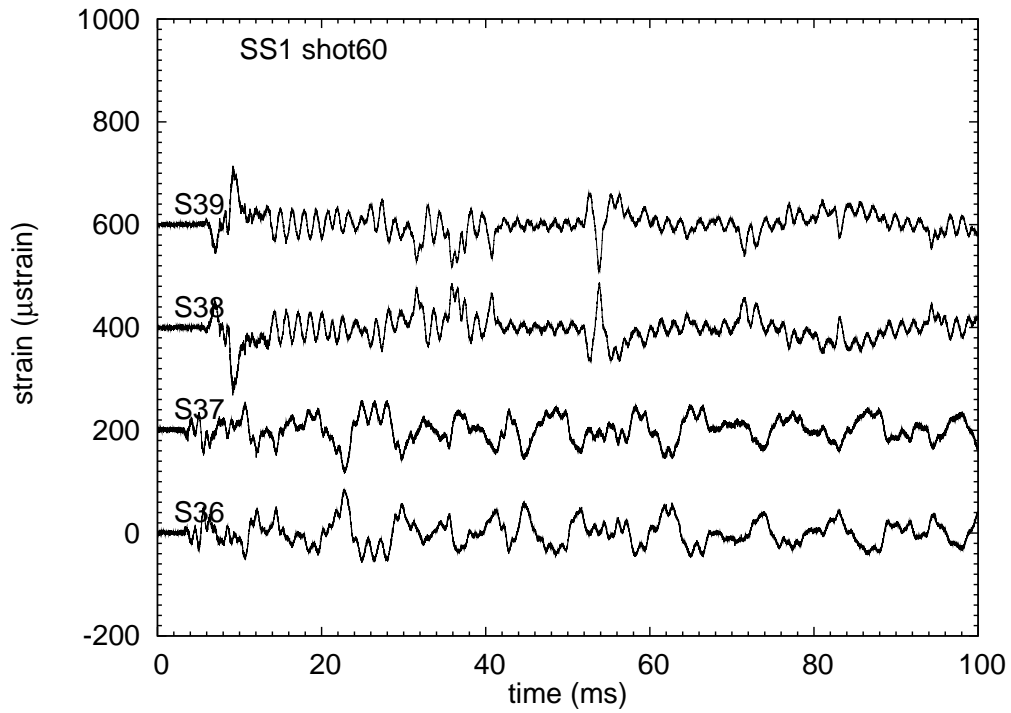


Figure 300: SS1 Shot 60. Cantilever strain gage signals. 100 ms raw and processed data.

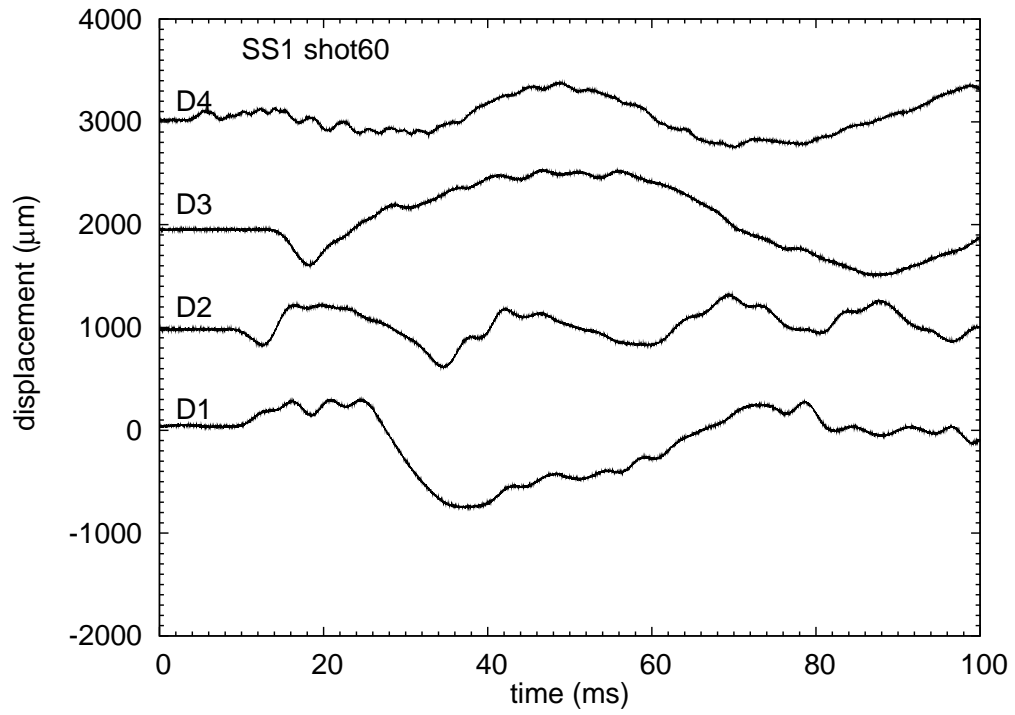


Figure 301: SS1 Shot 60. Displacement gage signals. 100 ms raw data.

## O.9 Shot 61

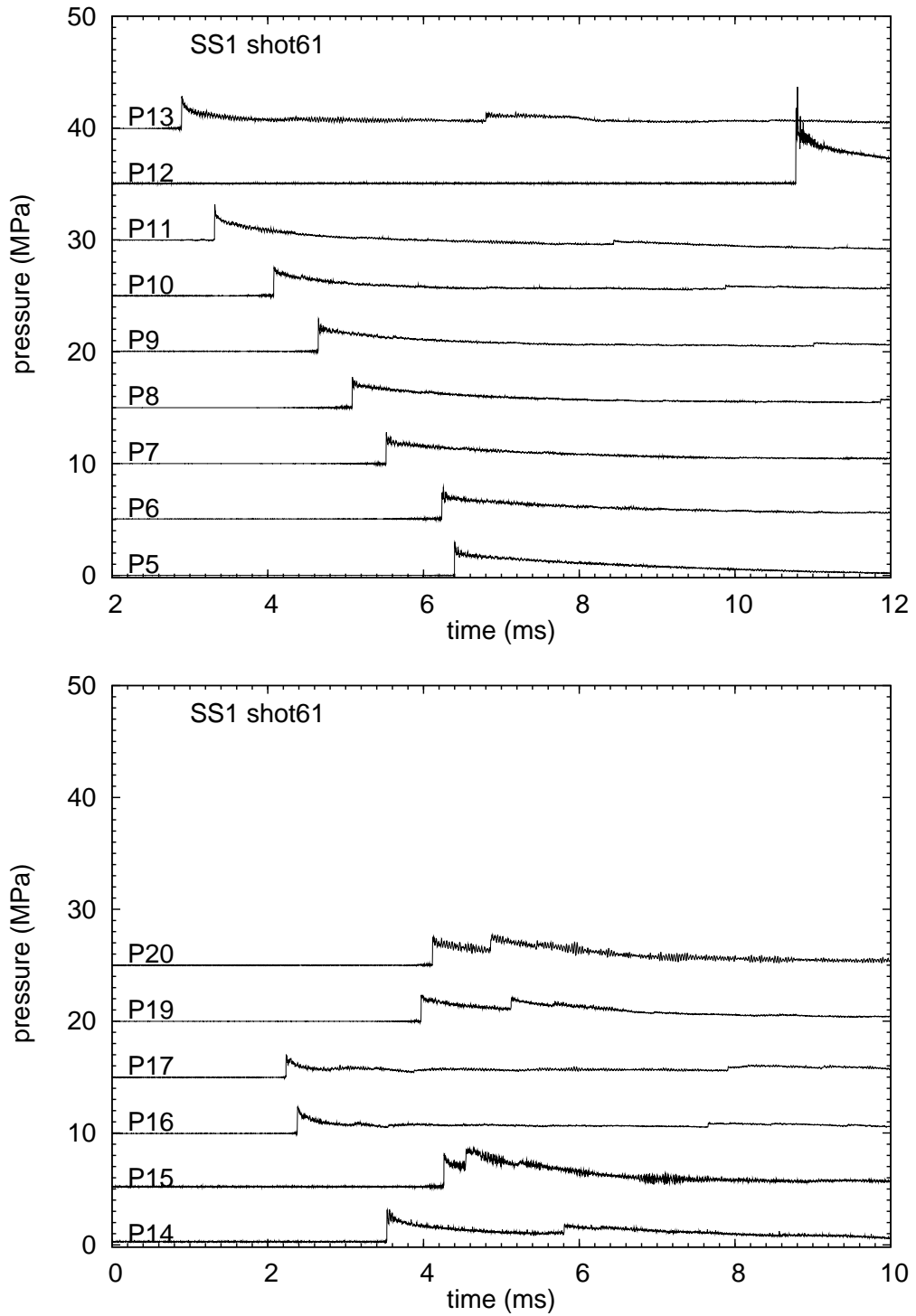


Figure 302: SS1 Shot 61. Pressure gage signals. 10 ms raw data.

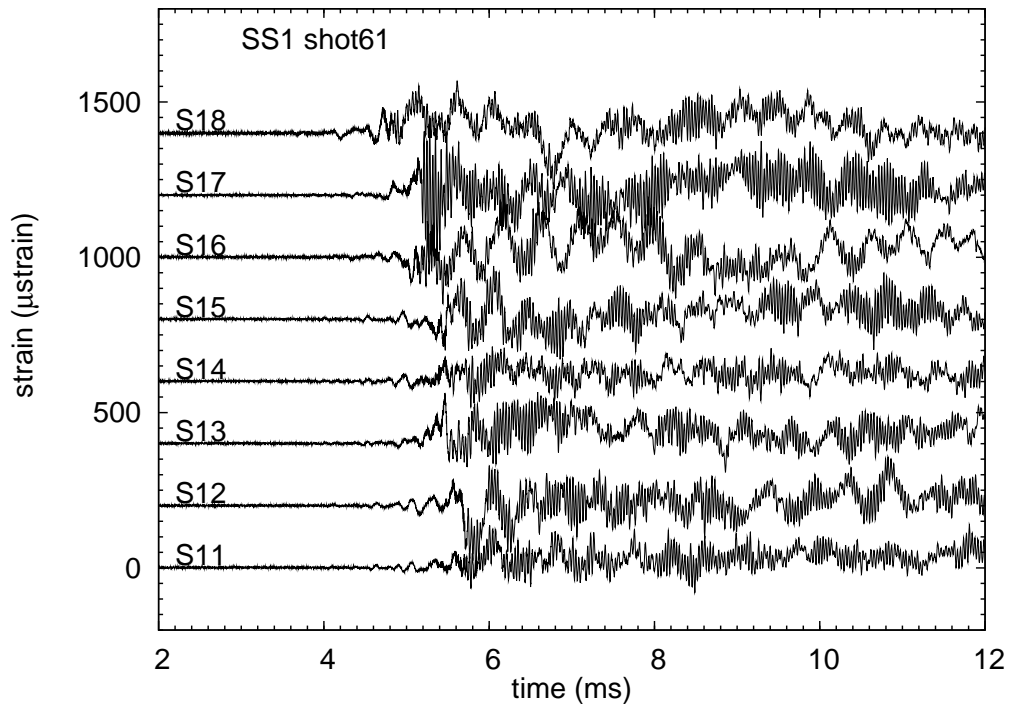
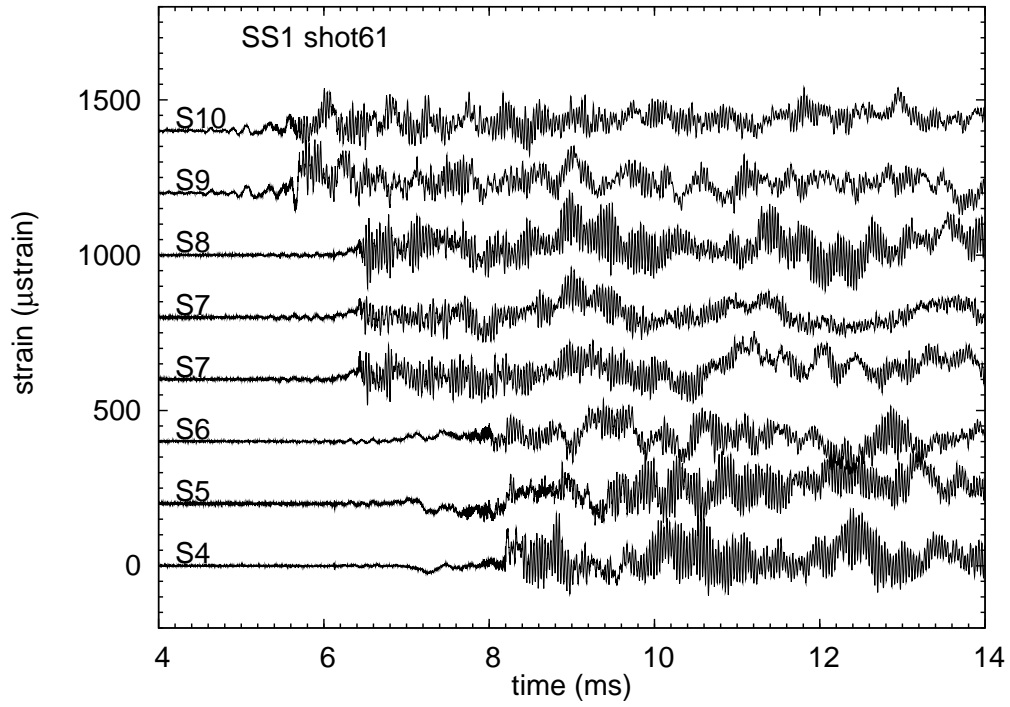


Figure 303: SS1 Shot 61. Pressure and strain gage signals. 10 ms raw data.

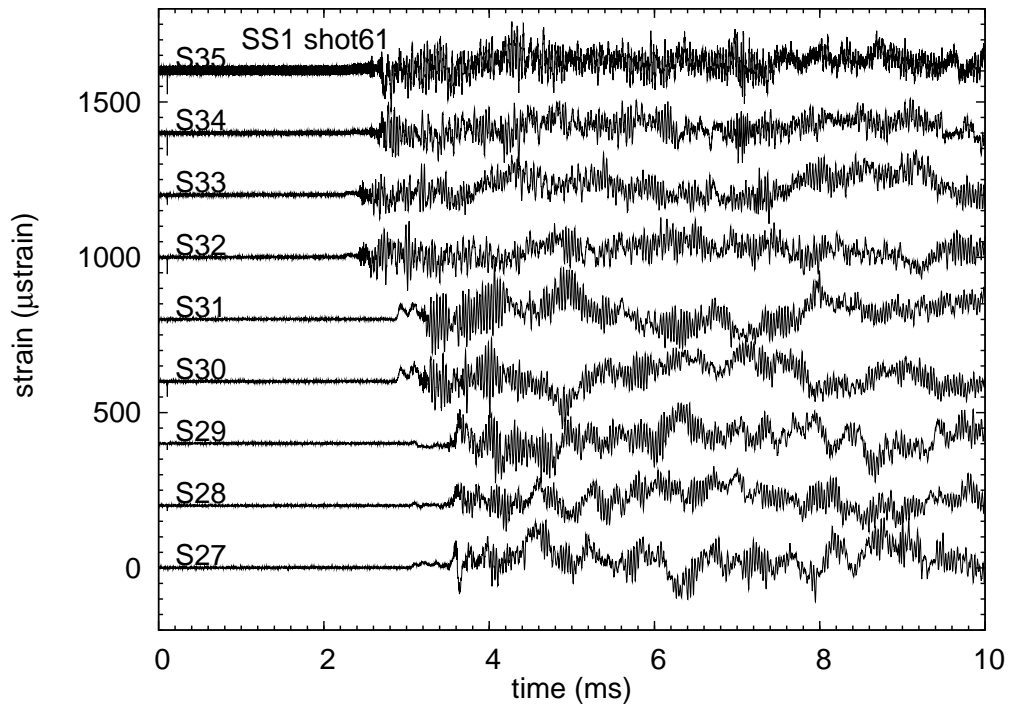
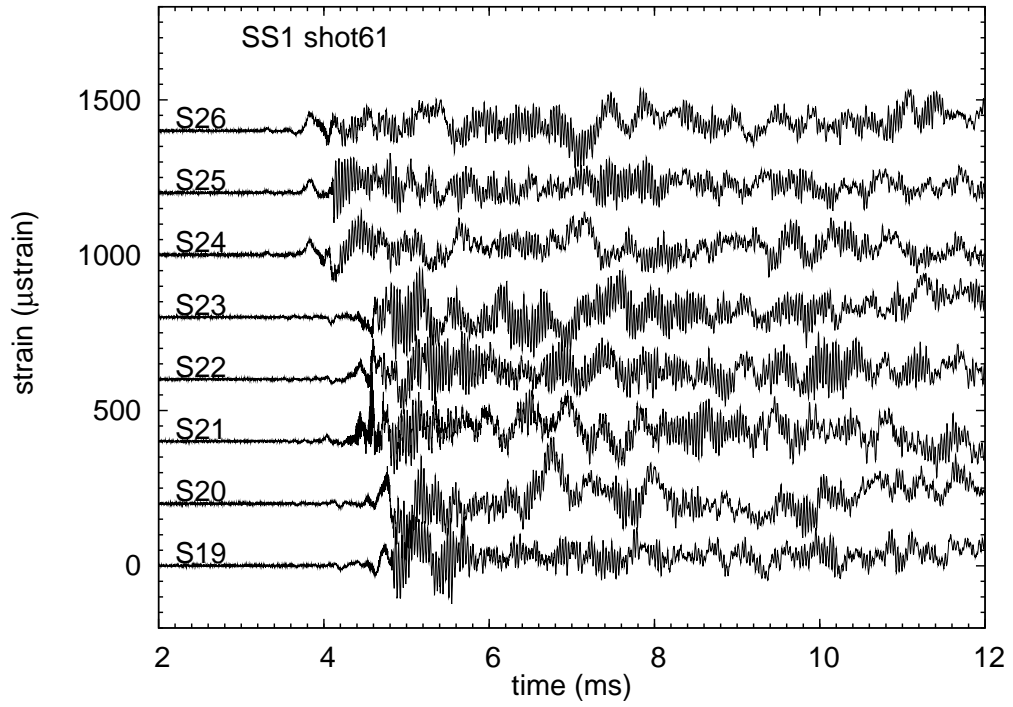


Figure 304: SS1 Shot 61. Strain gage signals. 10 ms raw data.

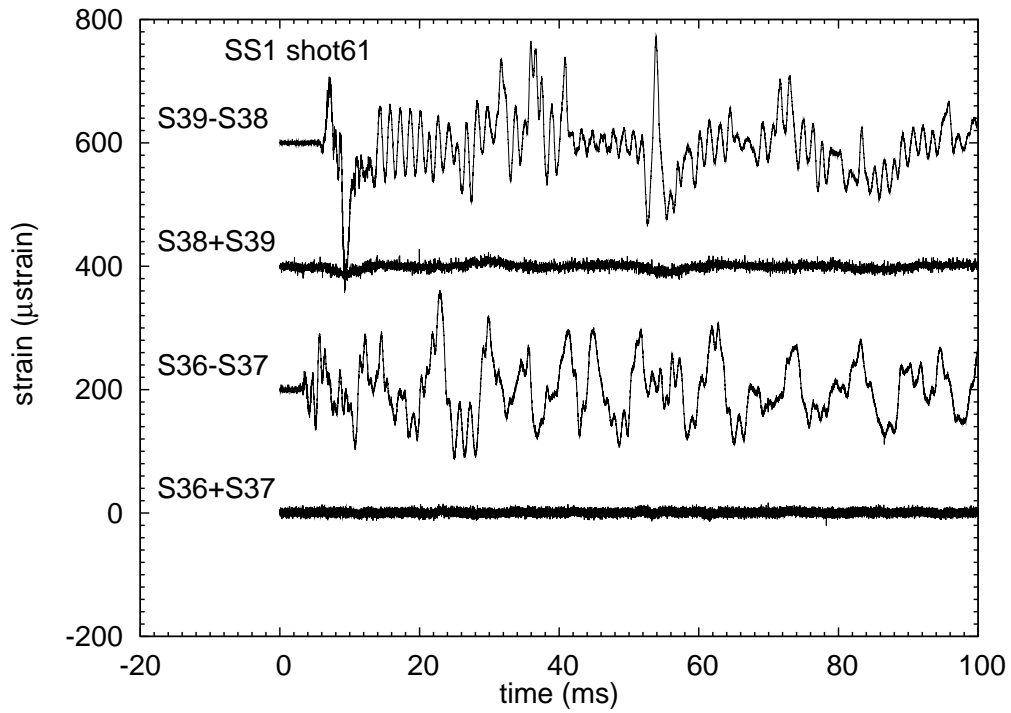
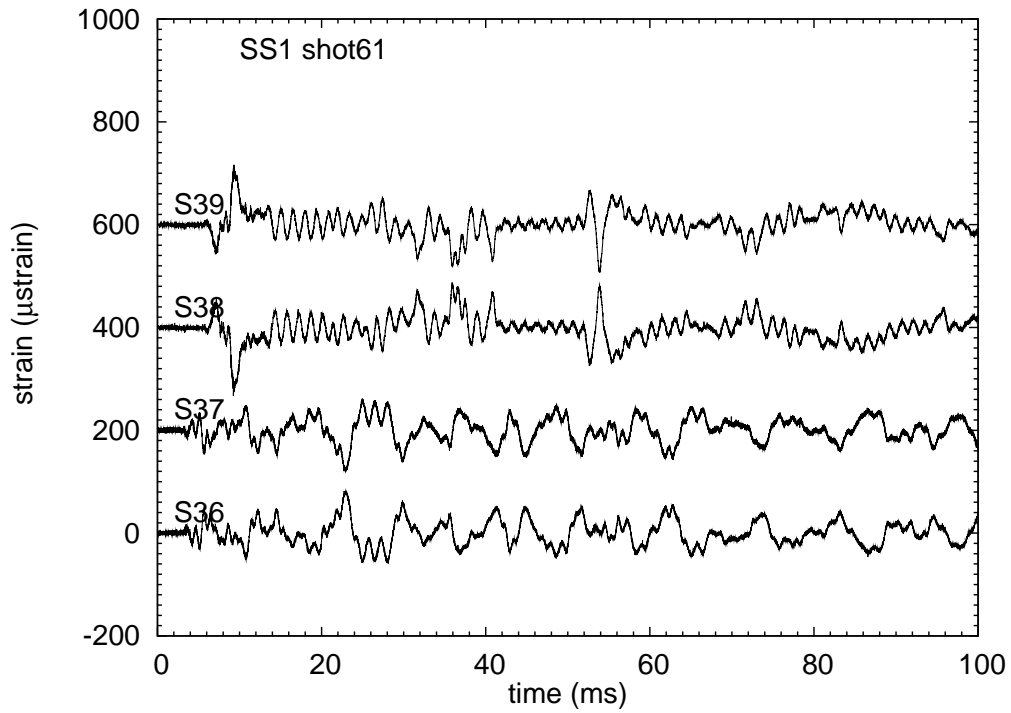


Figure 305: SS1 Shot 61. Cantilever strain gage signals. 100 ms raw and processed data.

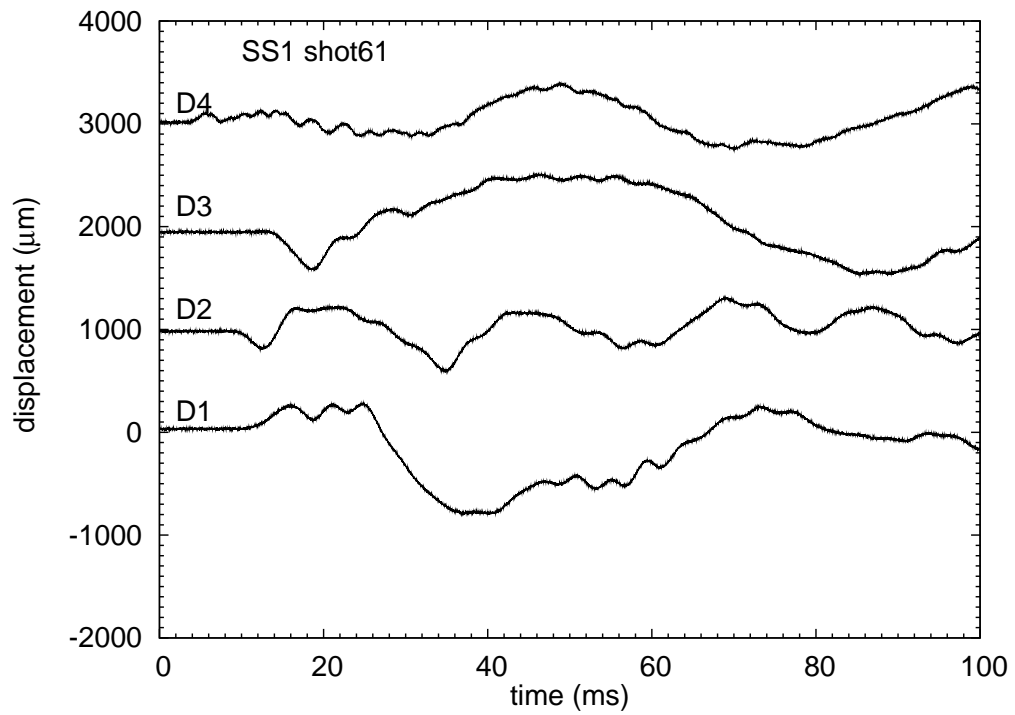


Figure 306: SS1 Shot 61. Displacement gage signals. 100 ms raw data.

# P Quality Assurance Plan

Page 1

6/5/2008

## Research Quality Plan Explosion Dynamics Laboratory

Joseph E. Shepherd  
Explosion Dynamics Laboratory  
California Institute of Technology  
Pasadena, CA 91125

March 12, 2008

### 1 Scope

This quality plan is based on ANSI/ASQ Z1.13-1999 "Guidelines for Research" and will apply to all work being carried out at Caltech under the sponsored research program, "Response of Piping and Support Systems to Detonations and Deflagrations".

### 2 Responsibilities

#### 2.1 Principal Investigator

Research in the Explosion Dynamics Laboratory (EDL) at the California Institute of Technology (Caltech) is carried out under the supervision of Joseph Shepherd, C. J. "Kelly" Johnson Professor of Aeronautics and Professor of Mechanical Engineering. A brief CV is attached in Appendix A.

The day-to-day responsibility for executing this project is delegated to Raza Akbar, a Research Engineer employed by Caltech. A brief CV is attached in Appendix A.

#### 2.2 Funding Agency and Primary Sponsor

**Sponsor Award:** ORP-CAL.001  
**Sponsor:** Project Assistance Corporation PAC  
**Prime Sponsor:** US Department of Energy, Office of River Protection  
**Award title:** Response of Piping and Support Systems to Detonations and Deflagrations

The primary sponsor of this work is the US Department of Energy, Office of River Protection. The work was initiated under Lew Miller as the technical contact and as of February 15, 2008, the technical oversight was shifted to Greg Jones.

Page 1

6/5/2008

### **3 Research Planning**

The research plan is described in depth in the Research Proposal, which is attached as Appendix B.

#### **3.1 Technical Approach**

The technical approach is described in detail in the Research Proposal, Section 1, Introduction; Section 4, Scaling and Modeling; Section 5, Instrumentation, and Section 6, Test Plan.

#### **3.2 Schedule and Deliverables**

The schedule and deliverables are described in detail in the Research Proposal, Section 8, Schedule, and Section 9, Deliverables.

#### **3.3 Facilities**

The facilities and capabilities are described in the Research Proposal, Section 3. Test Facility and Section 5, Instrumentation.

### **4 Performing and Documenting the Research**

The outline of the test plan is given in the Research Proposal, Section 6, Test Plan. Details of the performance and documentation of specific areas related to quality assurance are given in the subsequent sections.

#### **4.1 Role of Principal Investigator**

The Principal Investigator (PI) and/or his delegate are responsible for:

1. Interactions with the program sponsors' technical personnel.
2. Planning research and managing resources to implement the plan.
3. Oversight of professional staff and graduate students carrying out the research.
4. Assuring technical correctness of research plan implementation.
5. Calibrating and maintaining records on instruments used in the conduct of research.
6. Record keeping and documentation of the research project.
7. Verifying and validating computer programs used in the conduct of research.
8. Assuring the integrity of data.
9. Documenting and maintaining data archives of research results.
10. Carrying out measurement uncertainty analyses and documenting the results.

## 4.2 Instrument Calibration

The Measurement and Test Equipment (MTE) is of two types. *Critical M&TE* is used for data acquisition of key parameters or instruments and is directly in the chain of measurement. Critical M&TE will have either factory calibration (if new), recalibration by the factory or calibration by a certified testing laboratory (if used). Examples of critical M&TE are the primary static pressure gauge used for partial fill measurements, strain gauges, strain gauge amplifiers, dynamic pressure, force, and acceleration transducers, associated amplifiers, and transient digitizers. *Noncritical M&TE* is used for diagnostics that verify equipment function (but do not have a calibration function), for example, utility voltmeters or oscilloscopes. Other non-critical M&TE include portions of the signal chain or facility measurements that are secondary. Examples include non-regulated power supplies, backup systems, pressure regulator gauges.

The procedures for calibration of M&TE include:

1. Calibration of critical existing instruments prior to test
  - a. Certified labs
  - b. NIST primary standard traceable
2. Archival storage of certification supplied with new instruments
3. Checkout procedures (pre/post test)
  - a. End-to-end testing using known loads for static measurements
  - b. Voltage/current calibration of data acquisition system for dynamic measurements
  - c. Use of secondary-standard calibrated devices for cross-checking functionality of primary instruments
4. All uncalibrated M&TE equipment used in the laboratory will be clearly marked and stored with the label "Uncalibrated".

## 4.3 Process Control

The "process" that will be important to document in our work is the experimental test set-up and act of testing. The test setup will be documented in the lab notebook and associated electronic files and the testing process is documented on the test log sheet and associated electronic file. The information that will be documented includes:

1. Test matrix - electronic record of test conditions, test numbers, parameters and associated data files for each test.
2. Parameter acceptance range for pre-test conditions - there will be pre-determined parameter ranges for maximum vacuum and pressure leak rates, number of operational channels, and maximum noise levels and dropouts in signals.
3. Test procedure. Test procedure will be noted in the lab notebook and test log sheets.
4. Checklist control of experiments will serve as a safety process and also help insure correctness of the experimental procedure.
5. Post-test documentation for all aspects of testing including fixtures, procedures, specimens, data assessment, and analysis.

#### **4.4 Data Quality and Integrity**

The data quality and integrity are assured by using critical M&TE that is specified and calibrated for the specific needs of our research program. Key steps in the data quality and integrity process include:

1. Specification of critical M&TE capabilities required to execute the test program.
2. Calibration of critical instruments and archival storage of calibration information.
3. Post-test validity assessment on all signals. Signal quality will be determined by examining
  - a. Signal appearance (open/shorted), noise level.
  - b. Signal amplitude, comparison with other tests, engineering judgment based on order-of-magnitude estimates.
  - c. Artifacts. These include noise due to loose cables or EMI, negative pressures due to thermal effects, off-scale signals due to amplifier or transducer failure.Exceptions will be noted in the test log and reports.
4. Engineering analysis. Data will be checked using post-processing and comparison to engineering computations. For example, detonation velocities and peak will be compared with CJ values. Single-degree-of-freedom computations and measured or estimated peak pressures will be used to check the data. There are two types of checks.
  - a. Internal consistency - Data of different types can be compared.
  - b. Engineering hand calculations - Data can be compared with simple computation, which may include computer analyses if they are sufficiently reliable.
5. Criteria for data acceptance. Data will be judged as acceptable based on the following factors:
  - a. Test parameters are within the acceptable range and testing was free of anomalies.
  - b. Signals appear to be valid.
  - c. Signals pass engineering analysis consistency test.
6. Corrective action if test data are unacceptable or designs are incorrect. Following a test or a series of tests, the data quality will be reviewed.
  - a. Based on the results of Items 3-5 above, correction actions will be taken. These may include changing the test procedure, replacing instruments, or recalibration of instruments.
7. Archival storage. This will be accomplished by a combination of print on paper storage in indexed and labeled binders in the laboratory, bound lab notes, electronic

files and scanned-in records stored on multiple computer storage systems with redundant backup. The archival documents will be kept for a minimum of 10 years.

- a. Calibration sheets will be stored in an indexed loose leaf notebook that is kept in the laboratory area and digital copies will be kept in the project directory on the GALCIT filer.
- b. Notes on testing will be kept in a bound and labeled lab notebook with numbered pages.
- c. A record of test setup and performance will be kept in the test log which is stored electronically and in an indexed binder in the laboratory.
- d. Paper notes on design and procurement will be kept in an indexed binder in the laboratory. Electronic copies will be kept on the computer system.
- e. Critical test data will be stored on redundant disk arrays and backed up onto CD-ROMs or DVDs that will be labeled and stored in a separate location. There is a fire safe in the Karman building that can be used for this purpose.

#### **4.5 Assessing the Performance of Research**

The research performance will be assessed in the following ways:

1. Internally. As discussed in 4.4, data and test procedures will be reviewed at Caltech following the completion of individual tests and test series.
2. Externally. Reports (written and oral) of the research project will be prepared and given to the DOE and the contractor complex. Caltech expects to receive written and oral feedback on the research performance.

The internal and external assessments will be used to take corrective actions in improving research quality. Caltech will propose specific changes to test configuration, M&TE specifications, and test procedures in response to the assessments.

#### **4.6 Transferring the Results of the Research**

Progress reports will be submitted to the sponsor as indicated in the award. A summary of the research results will be transferred to the sponsor by written and oral reports at the conclusion of each major phase of the program. Preliminary data and interim reports will be transferred to the sponsor electronically. Final reports and electronic data sets will be transmitted to the sponsor electronically. In addition, journal and conference papers resulting from this study will be prepared and submitted.

### **5 Institutional Quality Management**

The California Institute of Technology is an independent, privately supported, non-profit university. Caltech conducts instruction at both the undergraduate and graduate levels and, including its off-campus facilities, is one of the world's major research institutions. In FY

2007, Caltech received grant, contract, and subcontract awards valued at \$250 million. The official mission statement is:

*The mission of the California Institute of Technology is to expand human knowledge and benefit society through research integrated with education. We investigate the most challenging, fundamental problems in science and technology in a singularly collegial, interdisciplinary atmosphere, while educating outstanding students to become creative members of society.*

The California Institute of Technology is committed to quality and integrity in the research process and there are a number of organizations at Caltech that support researchers directly and indirectly in developing and maintaining quality research programs.

### **5.1 Provost's Office**

As the chief academic officer for Caltech, the provost is responsible for overseeing all of the Institute's research and educational programs. The Office of the Provost at the California Institute of Technology is responsible for policies for ethical conduct of research and integrity of research process. Primary responsibility for integrity in the research process is assigned to Principal Investigators and faculty supervising research.

<http://provost.caltech.edu/>

### **5.2 Division of Engineering and Applied Science**

Caltech is divided into six academic divisions and a number of business and support organizations. The Graduate Aeronautical Laboratories is a member of the Division of Engineering and Applied Science.

<http://www.eas.caltech.edu/>

### **5.3 Graduate Aeronautical Laboratories (GALCIT)**

The Explosion Dynamics Laboratory is located in the Guggenheim Building and is part of the Graduate Aeronautical Laboratories.

<http://www.galcit.caltech.edu/>

### **5.4 Environmental, Health and Safety**

The mission of the Environment, Health and Safety (EHS) Office is to facilitate innovative research at Caltech through a comprehensive safety program, which promotes the health and safety of students, faculty, staff, and visitors. Through education, training and information, safety awareness and practices are integrated into all activities at Caltech.

The EHS Office assists the Institute community by providing consultations, evaluations, and inspections, which reduce or eliminate conditions which may lead to injury or loss of institute resources.

The EHS Office is responsible for implementing the Caltech Injury and Illness Prevention Program and compliance with Cal-OSHA workplace safety regulations. Primary responsibility for day-to-day safety in lab operations is assigned to the principal investigators, faculty supervisors and their delegates.

<http://www.safety.caltech.edu/>

### **5.5 Research Administration**

Research Administration includes the Office of Sponsored Research, Project Accounting, Financial Compliance and Training, and Export Compliance. The Office of Sponsored Research handles pre-award and non-financial post-award project administration.

<http://osr.caltech.edu/>

### **5.6 Office of Technology Transfer**

The Office of Technology Transfer (OTT) is responsible for the licensing and the transfer of technologies from Caltech and JPL to the commercial sector. OTT protects and manages the intellectual property developed by faculty members, students, other researchers, and JPL technologists.

<http://www.ott.caltech.edu/>

### **5.7 Human Resources**

Employee services and personnel matters are handled by the Caltech Human Resources office.

<http://hr.caltech.edu/>

### **5.8 Office of Financial Services and Controller**

All post-award financial reporting is handled by the Project Accounting and Cost Studies group. The Procurement Services group is responsible for procurement services that effectively and efficiently respond to Caltech's operating needs. These services are supported by established policies and procedures, which promote fair, ethical and legal acquisition and payment.

<http://www.businessandfinance.caltech.edu/>

### **5.9 Security Department**

Caltech's Security Department is responsible for physical security and personal safety on campus and campus buildings. <http://security.caltech.edu/>

### **5.10 Information Management Systems and Services**

Caltech's IMSS is responsible for computer network infrastructure and security. IMSS manages portions of the computing system used in GALCIT. <http://www.imss.caltech.edu/>



**U.S. Department of Energy**  
**Office of River Protection**  
P.O. Box 450, MSIN H6-60  
Richland, Washington 99352

10-NSD-038

MAY 06 2010

Mr. R. W. Bradford, Project Manager  
Bechtel National, Inc.  
2435 Stevens Center Place  
Richland, Washington 99354

Dear Mr. Bradford:

CONTRACT NO. DE-AC27-01RV14136 – BECHTEL NATIONAL, INC. (BNI) USAGE OF CALIFORNIA INSTITUTE OF TECHNOLOGY (CIT) DATA GENERATED IN SUPPORT OF HYDROGEN IN PIPING AND ANCILLARY VESSELS (HPAV)

- References:
1. Office of River Protection Operational Awareness Data Base, "Surveillance of CalTech QA Program," Report 3766, July 3, 2008.
  2. ORP letter G. L. Jones to file, "In Process Surveillance of California Institute of Technology (CIT) Testing Program in support of Hydrogen in Piping and Ancillary Vessels," 09-NSD-023, March 25, 2009.
  3. Office of River Protection Operational Awareness Data Base, "Surveillance of California Institute of Technology (CIT) Hydrogen in Piping and Ancillary Vessels," Report 10417, dated May 6, 2010.

This letter authorizes BNI to utilize published data by CIT provided under the U.S. Department of Energy, Office of River Protection (ORP) contracts for use in supporting development of methods and criteria by which HPAV is evaluated. The data is controlled by CIT and is located on the CIT/Explosion Dynamics Laboratory (EDL) website.

ORP and BNI contracted testing in support of HPAV criteria and methods for evaluating hydrogen hazards in 2008 and 2009 to CIT and Southwest Research Institute. This letter is specific to the CIT contracts data collected in 2008 and 2009 and summarized by the following scopes of work:

2008 contract DE-AB27-03RV14546:

1. Validation of structural response modeling of piping systems. EDL at CIT will provide test data that can be used to validate models for forces and structural response predictions by Finite Element Models and BNI structural response code ME101.
2. EDL will provide fundamental test data on peak forces and strains for high-speed deflagrations and transition from deflagration-to-detonation.

Mr. R. W. Bradford  
10-NSD-038

-2-

3. EDL will provide fundamental data on the propagation of shock waves in tubes partially filled with liquid and liquid-solid suspensions.

2009 Contract DE-AC27-09-RV15086:

1. Conduct a quantification of minimum detonable geometries of gas pockets using 2 inch pipes.
2. Conduct visualization tests in a rectangular channel to determine the actual dispersion of the liquids simulating the Waste Treatment and Immobilization Plant waste with high speed video imaging.
3. Provide significant new data on flame and detonation propagation in pockets bounded by horizontal liquid layers.
4. Work with BNI and subcontractors to provide information and editorial comments for a review of the propagation above liquid levels.

Both of these contracts have the following statement regarding the data quality under Environmental, Health, Safety, and Quality Requirements necessary:

*"The Contractor will comply with DOE Order 414.1C, "Quality Assurance," requirements as implemented through the NQA-1-2000, Subpart 4.2, "Guidance on Graded Application of Quality Assurance for Nuclear-related Research and Development," or demonstrated compliance with this Subpart 4.2 based on implementation of the ANSI/ASQ Z1.13 consensus standard."*

The testing at CIT was managed as "Applied Research" defined in NQA-1, Subpart 4.2, Section 103.2. Both contracts have Quality Assurance Plans (QAP). The QAP was initially approved in March 2008 with supporting surveillances by ORP Quality Assurance (QA) and follow-up surveillances performed by Nuclear Safety Division. An initial surveillance by ORP QA (Reference 1) concluded that:

*"By separate assessment, ORP has determined that ANSI/ASQ Z1.13-1999 meets the expectations of NQA-1, Subpart 4.2...as implemented by CalTECHs Project Proposal and Quality Assurance Program documents."*

Separate follow-up surveillance (Reference 2 and 3) determined that CIT continued to adequately implement the requirements of the contract.

Therefore, the data generated by CIT and published on the CIT website can be used by BNI in support of the methods and criteria for evaluating HPAV hazards.

MAY 06 2010

Mr. R. W. Bradford  
10-NSD-038

-3-

This letter is not considered to constitute a change to the Contract. In the event the Contractor disagrees with this interpretation, it must immediately notify the Contracting Officer orally, and otherwise comply with the requirements of the Contract clause entitled 52.243-7, "Notification of Changes."

If you have any questions, please contact me, or your staff may contact Victor L. Callahan, Director, Nuclear Safety Division, (509) 373-9880.

Sincerely,



Guy A. Girard, Acting Assistant Manager  
Waste Treatment and Immobilization Plant

NSD:GLJ

cc: Gregory R. Ashley, BNI  
David J. Jantosik, BNI  
Mike G. Wentink, BNI  
BNI Correspondence

Proceedings of 2009 ASME Pressure Vessels and Piping Division Conference  
PVP2009  
July 26-30, 2009, Prague, Czech Republic

**PVP2009-77734**

## GASEOUS DETONATION IN PIPING SYSTEMS PARTIALLY FILLED WITH LIQUID

**Joseph E. Shepherd and R. Akbar**  
Graduate Aeronautical Laboratories  
California Institute of Technology  
Pasadena, California, 91125

**E. A. Rodriguez**  
Global Nuclear Network Analysis, LLC  
Box 4850  
Los Alamos, NM 87544

### ABSTRACT

*In this paper, we report the results of our investigation into the transmission of a detonation from a gas-filled section of pipe into a water-filled portion. Experimental studies were performed using a detonation in a  $H_2-N_2O$  mixture within a 2-inch, Schedule 40 pipe. The detonation wave impinges on a vertical column of water just downstream of a 90-degree bend. A shock wave is transmitted into the water-filled section and propagates slower than the sound speed in the water due to the coupling of flexural waves in the pipe with pressure waves in the liquid. Incident, transmitted, and reflected pressures in the gas are monitored, along with hoop and longitudinal strain throughout the pipe length. Results are presented for a both prompt initiation of an ideal (Chapman-Jouguet) detonation and deflagration-to-detonation transition (DDT) occurring just upstream of the gas-liquid interface. The results of the experiments are analyzed using computational modeling and simulation with an Eulerian hydrodynamic code as well as classical wave interaction methods. For a Chapman-Jouguet (CJ) detonation, the reflected and transmitted pressures agree with the classical one-dimensional theory of wave interaction. The values of the peak reflected pressure are close to those that would be obtained considering the water as a perfectly reflecting boundary. The transmitted wave propagates at a speed consistent with the Korteweg speed of classical water hammer theory and little to no attenuation in amplitude over*

*1.5 m of travel. In one DDT event, peak pressures up to 11 times the CJ pressure were observed at the end of the water-filled section.*

### INTRODUCTION

Gaseous detonations in piping systems are a potential and real hazard in both the petrochemical and nuclear industries. Notable examples of piping failures resulting from internal explosions were reported at Hamaoka-1 NPP [1, 2] and Brunsbuettel KBB [3], resulting from generation of a  $H_2-O_2$  mixture by radiolysis, which further accumulated in stagnant pipe legs since these piping configurations lacked high-point vents or off-gas systems. In those cases, the piping failure was attributed to extreme pressures developed by deflagration-to-detonation transition occurring near an elbow close to the surface of the water-filled portion of the pipe. Factors contributed to the failures are believed to include pressurization during the flame propagation stage followed by detonation wave reflection from the water surface and bend.

Laboratory testing and analysis during the last decade, reviewed by Shepherd [4], has advanced our understanding of structural loading for relatively ideal situations of straight pipe runs filled with explosive gases. However, industrial power and processing plants contain many other features such as bends and liquid or slurry-filled pipe portions that may play a significant

---

Address all correspondence to this author.

role in determining the structural loading. This study extends the previous work to examine these non-ideal features and is part of a larger effort to provide guidance for the design of piping systems with potential internal explosion hazards. Our goals in the part of the study presented in this paper are to characterize the detonation interaction at the gas-water interface and to determine the magnitude of the peak pressures in the gas and strains in the piping system. In the course of our work, we have examined the application of simple models for detonation reflection and shock wave propagation for the estimation of hoop and axial strains in the piping system. In addition, we have used a multi-material shock wave physics simulation tool to probe the details of the fluid-structure interaction.

### EXPERIMENTAL APPARATUS AND TEST PROCEDURE

Our tests are carried out in an instrumented piping system partly filled with water. The piping system (Fig. 1) was fabricated from 304 stainless steel, schedule 40, 2-in ASTM 312 type commercial pipe and 300 lb class slip-on flanges, see Table 1. The flanges and one joint just upstream of the bend were joined by welding certified to ASME B31.3 standards. The pipe had a nominal outer diameter of 60.3 mm and a wall thickness of 3.81 mm.

Table 1. 2-in Schedule 40 Type 304 Stainless Steel pipe, nominal properties.

Outer diameter	60.3	mm
Inner diameter	52.5	mm
thickness $h$	3.912	mm
Mean radius $R$	28.2	mm
Young's modulus $E$	$1.93 \cdot 10^{11}$	Pa
mass density $\rho$	8040	$\text{kg/m}^3$
Poisson ratio $\nu$	0.305	
Specific heat capacity $C_p$	500	J/kg-K
Thermal expansion coefficient (linear) $\alpha$	$16.9 \cdot 10^{-6}$	$\text{K}^{-1}$
Thermal conductivity $k$	16.2	W/m-K
hoop frequency $f_{hoop}$	29.0	kHz

The piping system was made up of two segments butt welded just upstream of a 90-degree bend as shown in Fig. 1. The horizontal run is approximately 3.5 m, followed by the bend and a vertical section of approximately 1.5 m. The bend was made using a hydraulic bending machine and a mandrel to create a 19.3 cm radius (centerline of pipe) bend connecting the vertical and horizontal segments. The pipe was instrumented with bonded strain gages at selected locations and oriented as shown in Fig. 1. Piezo-electric pressure transducers were flush-mounted along the side and at the end of the pipe. The strain gages were operated in quarter-bridge mode using a Vishay 2310B signal conditioner operated in the wide-band (140 kHz, -3 dB point) mode. The pressure gages are fast-response (rise times on the order of  $1 \mu\text{s}$ ) units (PCB 113A type) designed for shock wave measurements. Pressure and strain signals were recorded with a 14-bit transient digitizer at a sample interval of  $1 \mu\text{s}$  per point.

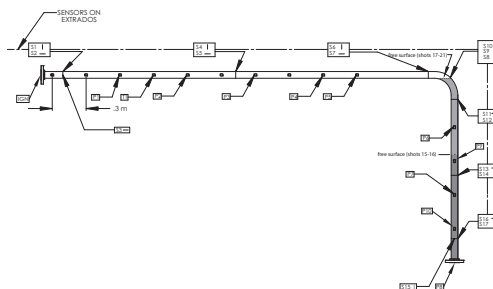


Figure 1. Experimental test fixture showing pipe and sensor locations.

The procedure was to first evacuate the piping system to less than 40 mTorr), fill the pipe with the test mixture ( $\text{H}_2$  and  $\text{N}_2\text{O}$ ) using the method of partial pressures, and mix the gas by circulating it through the pipe using a bellows pump connecting the two ends. The total pressure of the gas at the end of the filling process was set to a value less than atmospheric so that after the water was added, the pressure within the pipe would be 1 atm. After mixing the gas, the pipe was closed off at each end with ball valves and a secondary valve used to introduce water at the lowest point of the vertical leg of the piping system. The water was supplied by a carboy mounted next to the pipe system with sufficient head to insure that we could reach the desired level of the free surface within the pipe.

Two sets of water levels were used in a series of tests that examined the effect of water level, gas composition, and ignition method. The combustion event was started with an ordinary spark plug. In order to investigate ideal detonations, a short (305 mm) insert of coiled spring or Shchelkin spiral was used to accelerate the flame quickly to a detonation for a 30% H<sub>2</sub> and 70% N<sub>2</sub>O mixture (see Table 4 for detonation parameters). The spiral was removed in order to test deflagration-to-detonation transition (DDT) events with lower concentrations of H<sub>2</sub>.

### Results

We carried out a set of 7 tests with water in the vertical leg. Four of the tests (15-18) were with the Shchelkin spiral to promptly create CJ detonations and three tests (19-21) used spark ignition without the spiral to examine DDT events. Two water levels were used as shown in Fig. 1 and the specific test conditions are described in Table 2. In addition to these tests, a number (a total of 36) of other tests were carried out to obtain data on pipes without water in order to validate models of forces induced by the detonation propagation around the bend and reflection from the pipe end. Test 3 provides reference data for comparison of strains and pressures without water in the vertical leg.

Table 2. Test conditions. For all tests, the initial pressure  $P_o = 101.3$  kPa and temperature  $T_o = 27$  C.

test	H <sub>2</sub>	N <sub>2</sub> O	$U_{CJ}$ (m/s)	$P_{CJ}$ (MPa)	Spiral	Water (cc)
3	0.30	0.70	2087.5	2.62	Y	0
15	0.30	0.70	2087.5	2.62	Y	2250
16	0.30	0.70	2087.5	2.62	Y	2250
17	0.30	0.70	2087.5	2.62	Y	3750
18	0.30	0.70	2087.5	2.62	Y	3750
19	0.17	0.83	1917.5	2.57	N	3750
20	0.15	0.85	1891.9	2.56	N	3750
21	0.17	0.83	1917.5	2.57	N	3750

### CJ Detonation

**No water** Test 3 was carried out with only gas within the pipe and gives base line data that we can compare to the cases with water in the vertical leg. Referring to Figs. 2 - 4, we observe that the detonation was initiated at the left side of the pipe system and propagates with a constant velocity (within 1% of the CJ velocity given in Table 4) and is nearly unaffected by the bend. We estimate the detonation cell width is about 3 mm in this mixture [6], sufficiently small that the detonation will behave in a relatively ideal fashion. At the lower right-hand side of the pipe system, the detonation reflects from the closed end of the pipe and a shock wave proceeds back toward the ignition end. The peak strains in the pipe are in the hoop direction and about 200-300  $\mu$ strain in magnitude, which corresponds to a dynamic load factor of 2 to 2.5 applied to the CJ pressure and modeling the hoop response as a single degree of freedom harmonic oscillator.

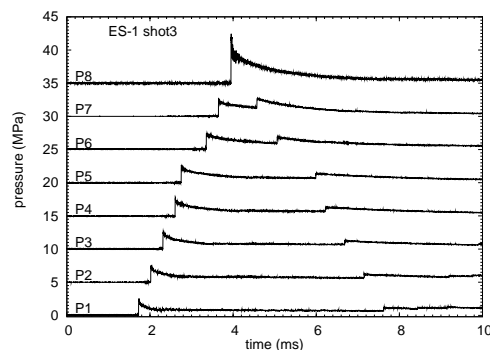


Figure 2. Test 3 pressure measurements.

**2250 cc water** We filled the the lower portion of the vertical leg of the pipe system with about 2250 cc of water in tests 15 and 16, reaching the lower level shown in Fig. 1. The total pressure before adding the water was about 617 Torr and after filling, 760 Torr. The nominal water level was just above pressure gage P9 and the total length of the water column was about 0.97 m as measured from the gage P8 at the bottom of the vertical section. Pressure and strain data are shown for test 15 in Figs. 5-7 for the same sensor locations as in test 3.

The pressure data (Fig. 5) show a transmitted shock wave

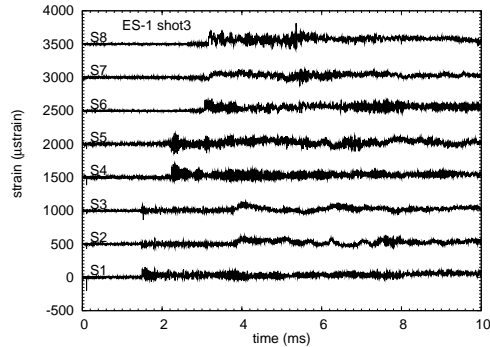


Figure 3. Test 3 strain gage set 1 measurements.

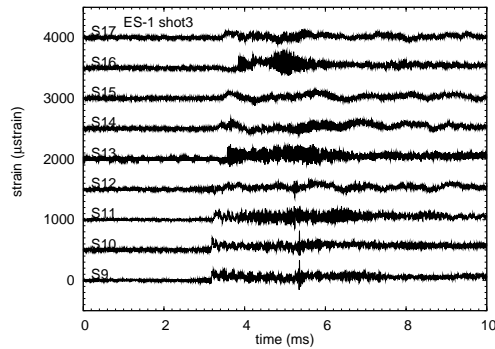


Figure 4. Test 3 strain gage set 2 measurements.

in the water and a reflected shock wave in the gas. The peak pressures of the incident waves in the gas (2.7 MPa vs. a CJ pressure of 2.5) and water (6 MPa) are consistent with standard detonation wave-free surface interaction analysis using pressure-velocity diagrams, described in [7]. The analysis (Fig. 8) predicts a peak pressure in the water (6.35 MPa) that is almost identical to the peak pressure (6.4 MPa) obtained in reflecting the detonation from a hard surface. The propagation speed of the deto-

nation is within 0.5% of the CJ velocity (see the x-t diagrams in Fig. 9) and the propagation of the lead shock wave in the water is about 1310 m/s, substantially slower than the shock speed in water alone<sup>1</sup> due to the coupling of the pressure wave in the water with the stress waves in the pipe, see [8] and discussion of the numerical results below. The peak strains (Fig. 7) in the water-filled segment are similar to those observed at the same location in the gas-filled test (Fig. 4). Although the pressures are higher, the wave speeds in the water-filled case are lower than for the gas-filled case. The lower wave speeds and the effect of fluid-structure coupling results in lower strains in water-filled section than would be expected on the basis of peak pressure alone.

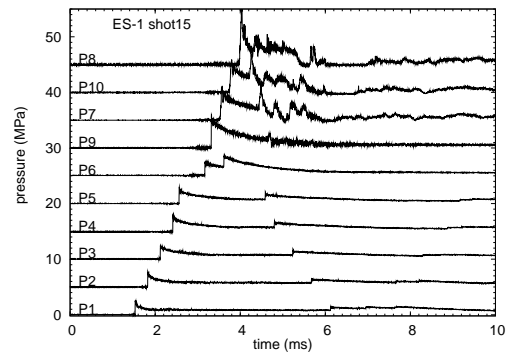


Figure 5. Test 15 pressure measurements.

The amplitude of the shock wave in the water does not appreciably attenuate in the 1 m of travel between the free surface and the bottom of the pipe (Fig. 5) although there is an expansion wave following the shock. The shock wave in the water reflects from the bottom and the peak amplitude (10.7 MPa) is slightly lower than double the incident wave (see signal P8 of Fig. 5). This is consistent with transmission of a wave into the steel supporting structure at the bottom of the pipe. Although this structure is very stiff, it is not completely rigid and in addition to the standard wave interaction processes at the water-steel interface, there will be some flexing of the support structure. The reflected

<sup>1</sup>The shock speed obtained in a ideal one-dimensional test will be only slightly (10-40 m/s) higher than the sound speed of 1480 m/s for the pressure amplitudes encountered in the present cases.

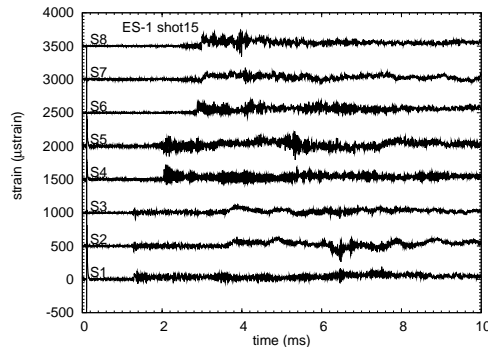


Figure 6. Test 15 strain gage set 1 measurements.

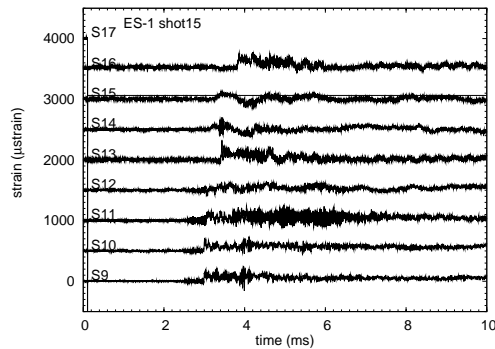


Figure 7. Test 15 strain gage set 2 measurements.

wave rapidly attenuates as it moves through the pressure drop in the expansion wave.

After the reflected shock reaches the free surface of the water, it reflects with a change in sign and creates a tension wave that propagates back to the bottom on the pipe. The amplitude of the tension wave increases on reflection from the bottom and causes cavitation of the water. The presence of cavitation is signaled by the portions of the pressure signal that are flat and close

to or below zero in gages P8, P10, and P7 between 5.8 and 7 ms in Fig. 5. Since the pressure measured by the gages is relative to the initial pressure in the pipe (101 kPa), a level less than -0.1 MPa corresponds to tension in the water. The greatest tension was observed on gage 10 of Fig. 5, for which the average gage pressure between 6.2 and 6.6 ms is approximately -0.23 MPa for an absolute tension of -120 kPa. The lowest pressures observed on the other gages ranged from +20 to +70 kPa. By comparison, the vapor pressure of water is 3 kPa at 297 C.

The location of the free surface of the water was not directly measured but we can use an  $x-t$  diagram (Fig. 9) to extrapolate the wave trajectories to estimate the location of the free surface from the intersection of the trajectories. The trajectories were estimated using a linear least squares fit of the arrival time-distance data. As shown in the enlarged  $x-t$  diagram in Fig. 9, the free surface was approximately 30 mm above gage P9. There is some uncertainty in this value but from the appearance of the pressure signals, it is clear that gage P9 was submerged in the water.

The strain gage records (S13-S16) in the water-filled section (Fig. 7) are similar in overall appearance to the corresponding gages in the gas-only test (Fig. 4). The strains are slightly lower in peak amplitude and the high frequency oscillations are significantly damped in comparison to the tests without water. The longitudinal strain wave precursor on S15 and S14 (gage S17 failed on test 15) is almost identical to the precursor in the gas only tests, confirming that this signal is associated with the detonation wave propagating through the elbow. The strain signals in the water-filled section are consistent with those observed in separate tests carried out at Caltech using impact to generate stress waves in water-filled tubes [8].

**3750 cc water** In tests 17-21, more water was added than in 15-16 so that the nominal water level was just below the bottom of the horizontal piping segment and within the bend itself as shown in Fig. 1. The total length of the water column was about 1.77 m as determined by the interpolating time of arrival data on an  $x-t$  diagram. In tests 17 and 18, the detonation was initiated using the Shchelkin spiral so that a detonation rapidly formed in the horizontal segment and reflected from the water surface in a fashion that was similar to tests 15-16. The test data shown in Fig. 10 is qualitatively very similar to that shown in Fig. 5 with expected difference in arrival time due to the length of the water column. Test 18 was a replica of test 17 that demonstrated the reproducibility of the data. A better estimate of the water shock wave speed can be obtained in these tests due to the larger number of transducers in the water. A water shock wave speed of 1370 m/s, close to the predicted Korteweg speed is observed in

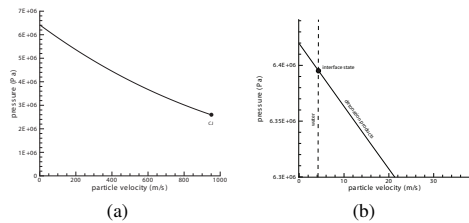


Figure 8. Pressure-velocity diagrams for shock wave propagation in detonation products behind a detonation in  $H_2/N_2O$  (30/70 mixture at 1 atm initial pressure, 295 K). a) Complete range of flow speed behind the detonation. b) Enlarged view of region near axis with water shock adiabat (nearly vertical dashed line) showing solution for detonation reflection on water free surface. See Browne et al. [5] for details.

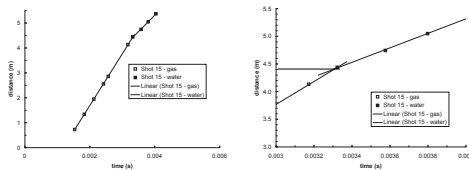


Figure 9. Distance-arrival time ( $x-t$ ) plots for test 15 showing detonation wave in gas (2075 m/s) and shock wave in water (1310 m/s). Right hand figure is an enlargement showing extrapolated location of free surface of water.

tests 17 and 18. The peak strains (not shown) are very similar for all gages except 8, 9, and 10 which are located on the extrados of the bend half-way between the vertical and horizontal piping segments. The higher strains in tests 17 and 18 occur at this location since the reflected wave is strongest just above the location of the water free surface.

### Deflagration and DDT

Tests 19, 20, and 21 were carried out without the Shchelkin spiral and with lower concentrations of  $H_2$  in order to create conditions for deflagration-to-detonation transition near the water surface. In test 19, see Figs. 11–13, a very clear DDT event is observed, with peak pressures (Fig. 16) of 14 MPa in the transmitted shock in the water and up to 30 MPa upon reflection from the end of the vertical section. Peak strains (Fig. 17) of up to

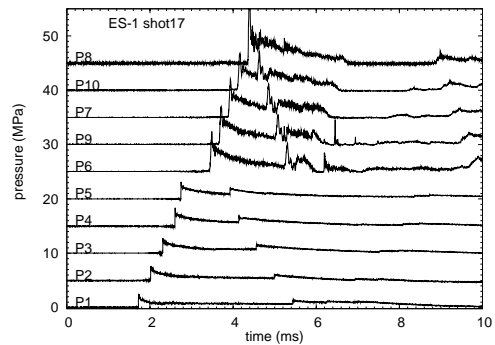


Figure 10. Test 17 pressure measurements.

1000  $\mu$ strain are observed in both gas-filled section and up to 700  $\mu$ strain in the liquid-filled section. Only a deflagration occurred in test 20 (Fig. 14) and resulting peak pressures (Fig. 16) are only about 1/2 the CJ value and the peak strains are between 50-100  $\mu$ strain. Test 21 was intended to be a replica of test 19 but due to the variability of the DDT process, the event in test 21 was much weaker and the resulting pressures (Fig. 15) and strains are more similar to CJ values than the extremes observed in test 19. The strains and peak pressures observed in test 19 are similar to those in test 9 (not shown) which was carried out without water and at a concentration of 15%  $H_2$ . The event in test 19 is of the type that has been proposed as occurring in the Hamaoka NPP and led to the catastrophic failure of the NPP piping near a bend.

### Numerical Simulation

A numerical simulation of a  $H_2-N_2O$  detonation wave impacting a liquid surface was developed with the aid of shock-wave propagation code, CTH. CTH is a multi-material, large deformation, strong shock-wave, solid mechanics code developed at Sandia National Laboratories [9, 10]. CTH has models for multiphase, elastic-viscoplastic, porous, and explosive materials. Three-dimensional rectangular meshes, two-dimensional rectangular and cylindrical meshes, and one-dimensional rectangular, cylindrical, and spherical meshes are available. It uses second-order accurate numerical methods to reduce dispersion and dissipation and to produce accurate, efficient results. Hydrodynamic codes, as the name implies, are based on the funda-

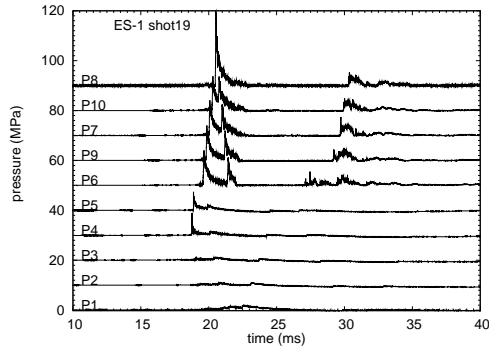


Figure 11. Test 19 pressure measurements.

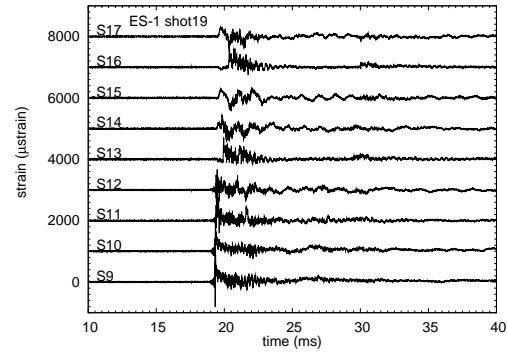


Figure 13. Test 19 strain gage set 2 measurements.

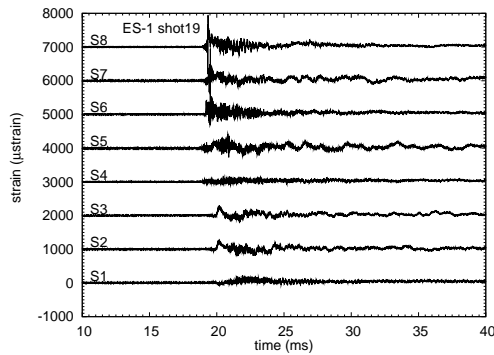


Figure 12. Test 19 strain gage set 1 measurements.

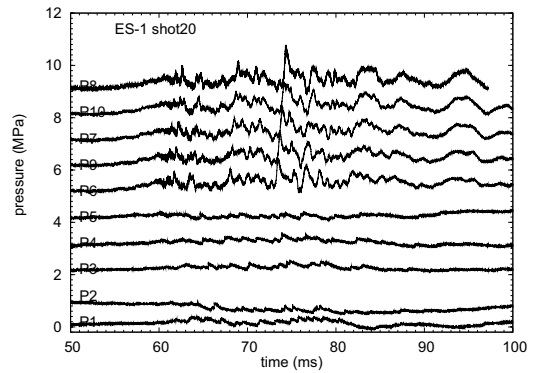


Figure 14. Test 20 pressure measurements.

mental equations of fluid dynamics; conservation of mass, momentum, and energy. The goal is to determine certain features associated with the detonation wave, specifically the incident, reflected, and transmitted pressures from the liquid surface, and the incident and reflected pressures at the closed-end of the piping run. Further, we endeavor to gain additional insight relative to precursor stresses developed in the pipe wall, which are generated from a traveling detonation front.

### Materials and Equations-of-State

The properties listed in Table 3 are utilized in the hydrocode model for the separate materials and detonation condition. It should be emphasized that the 304L stainless steel pipe encompasses both the hydrostatic and deviatoric response. The hydrostatic (or spherical) portion is defined by the equation-of-state (EOS) for steel, and the deviatoric portion is defined by the constitutive behavior, i.e., stress-strain representation. The Steinberg-Guinan constitutive model was utilized due to its ro-

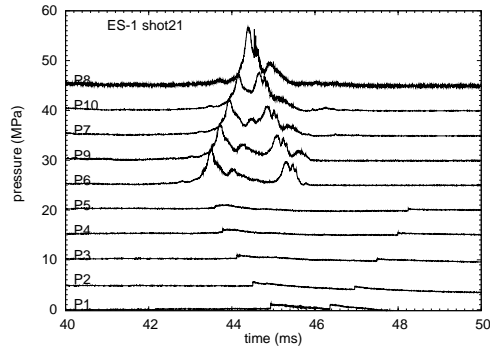


Figure 15. Test 21 pressure measurements.

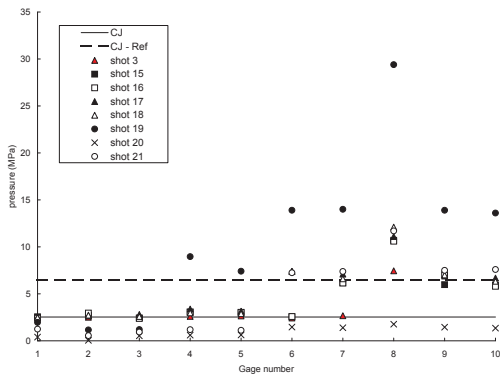


Figure 16. Peak pressures on all gages. CJ - computed ideal CJ detonation pressure, CJ - Ref - computed ideal reflected CJ detonation pressure.

bust capability in the viscoplastic region. Although the model is robust and quite accurate for 304L stainless steel, the penalty associated with such a model is the longer run-times. The detonation products are modeled with the JWL EOS, which at the pressures of interest is simplified to be just the ideal gas model. The SESAME EOS for water was used with a cavitation threshold of -2 MPa, substantially lower than what was observed in

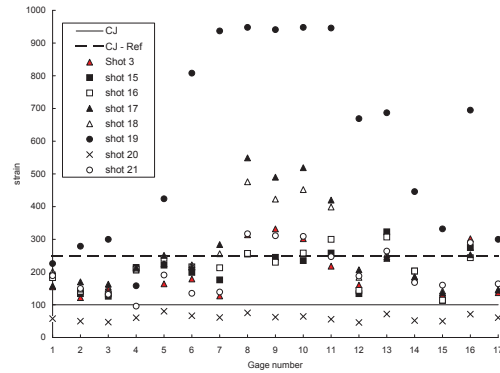


Figure 17. Peak strains on all gages; reference strains are computed using membrane stress and a dynamic load factor of 1.

the experiment. Cavitation phenomena will therefore not be correctly reproduced but this is not the focus of the present study.

### Geometric Configuration

Figure 18 shows a representation of the piping system utilized in the numerical model. The simulation geometry did not include the bend shown in Fig. 1 but did model the entire length of piping equivalent to the experimental apparatus. That is, the total volume of fuel and oxidizer in the experimental apparatus was duplicated in the numerical model, including the point of ignition. This treatment was adopted to maintain a 2D approximation and thus ensure a tractable solution. The vertical segment of piping up to approximately 127 cm, contained a column of water. The Eulerian mesh is subdivided into 0.5-mm cell sizes from the closed-end (Datum) to 160-cm height of piping. This approach was taken to obtain a high-fidelity resolution of pressures and densities within the gas region, detonation front at gas-liquid interface, water column, and pipe wall. The remainder of the pipe length from 160-cm to the ignition end at 542-cm, received slightly coarser mesh sizing of 2.5-mm cells to alleviate excessive run-times.

Tracer particles are located within the Eulerian mesh to access state variables during the transient event. Tracer particles within the gas or liquid are offset from a symmetry or structural boundary to minimize the cell-averaging. For example, a boundary may have both liquid cells and steel structure; however, it

Table 3. Equation of state and constitutive model parameters used in CTH simulations.

Equation of State Parameters				
Material	Density (kg/(m <sup>3</sup> ))	Sound Speed (m/s)	EOS model	
304L Steel	7.896	10 <sup>3</sup>	4569	Mie Gruneisen
Water	1.000	10 <sup>3</sup>	1480	Sesame
H <sub>2</sub> -N <sub>2</sub> O	1.2754	-	-	JWL
Steinberg-Guinan Strength Model				
Material	Modulus (GPa)	Shear Modulus (GPa)	Yield (MPa)	
304L Steel	200.	77.0	340	
JWL detonation Parameters for 0.3H <sub>2</sub> -0.7N <sub>2</sub> O				
$\gamma$	$P_{CJ}$ (MPa)	$D_{CJ}$ (m/s)	$T_{CJ}$ (K)	
1.1566	2.7	2088	3385	

would be erroneous to average the "pressure" or "density" from adjacent cells because these are different materials and different equations-of-state. As such, when determining actual pressure, velocity, and density, in either the gas or liquid, tracer particles are placed at 1.5 cell-widths from the boundary.

### CTH Results

Comparing Figs. 19 and 5, we observe that the simulation results reproduce qualitatively and quantitatively the general features observed in the experiment. The incident detonation, reflected pressure wave in the gas as well as the transmitted and reflected shock waves in the water are clearly shown. The wave speeds and amplitudes are consistent with those observed in the experiment and the theoretical analysis of wave interactions with the water-gas interface. In particular, by tracking the peak pressure of the reflected shock wave in the gas, we can extrapolate to determine that the peak pressure created by detonation reflection at the water surface is 6.4 MPa essentially identical to the value given by the analysis leading to Fig. 8. The pressure signals in the water-filled section show very substantial fluctuations and there are pressure spikes near the gas-water interface that

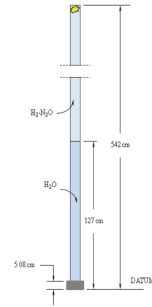


Figure 18. Geometry for numerical simulations.

appear to be artifacts that are much larger in magnitude than any fluctuations that are observed in the experimental data.

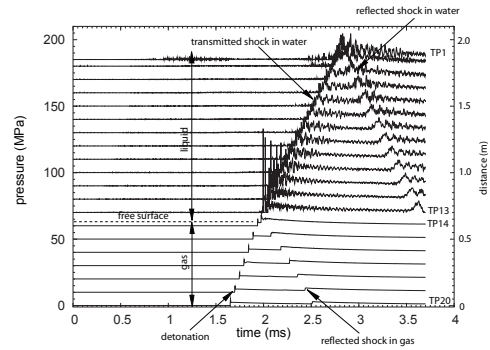


Figure 19. Pressure histories for 20 locations - numerical simulations.

The details of the interaction of the detonation wave with the pipe wall are shown in Fig. 20. The pressure of the detonation wave in the gas creates radial and longitudinal stress waves in the pipe wall. The main stress in the pipe is due to radial deflection and the hoop strain front propagates with the detonation speed in gas-filled pipes as discussed by Beltmann and Shepherd [11]. In addition, a series of oscillatory precursor waves can be observed

ahead of the main disturbance. The theoretical origin of the precursor waves is due to the propagation of longitudinal waves at the bar speed of about 5000 m/s, approximately 2.5 times faster than the detonation wave. The stresses predicted in the numerical simulations are consistent with the strains observed in the experiment, as shown in Fig. 3-4 and Figs. 6-7.

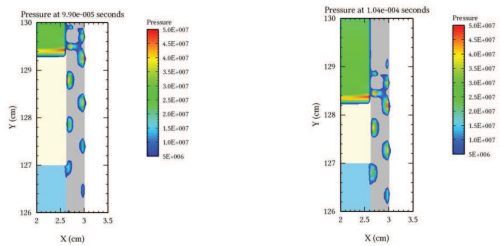


Figure 20. Interaction of detonation pipe wall to create stress precursor waves - numerical simulations.

Snapshots of the interaction of the detonation wave with the water-gas interface are shown in Fig. 21. The interface remains nearly planar as do the initial transmitted and reflected shock waves. An oscillatory structure can be observed close to the interface which subsequently develops into an extended oscillatory precursor wave that is shown in Fig. 22.

The theory of wave propagation in water-filled pipes has been developed in the context of water hammer by Skalak [12]. The shock wave propagating in the water is coupled with the radial deformation wave in the pipe wall to an extent that depend of the effective stiffness in the pipe as compared to the compressibility of the water [8]. As a consequence, the coupled wave system propagates with the Korteweg speed, 1370 m/s in the present case, which is slower than either the sound speed in the water or the bar speed in the pipe. Skalak's theory also predicts a precursor wave propagating at close the bar speed and consisting of primarily longitudinal strain. The results shown in Fig. 22 reveal that the precursor wave is actually a complex structure with radial and longitudinal spatial oscillations extending a substantial distance ahead of the main disturbance. These oscillations are induced in the water by the oscillation of the pipe wall associated with the precursor waves shown in Fig. 18. However, the magnitude is quite small and only a small amplitude oscillation can be observed ahead of the main pressure jump on gages P9, P10,

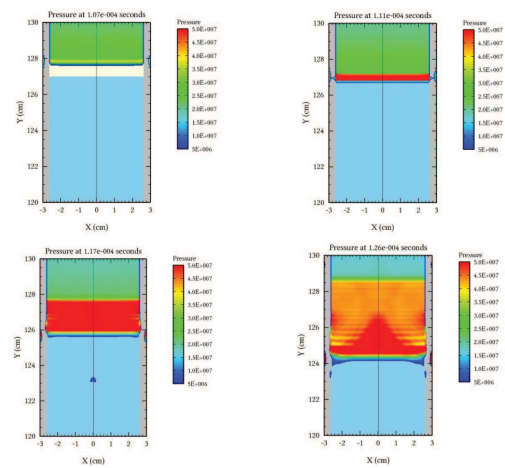


Figure 21. Interaction of detonation with water free surface - numerical simulations.

and P8 in Figs. 5 and 10. The oscillations are stronger behind the main pressure front and this gives rise to the noisy appearance of the signals on pressure gages in the water-filled section as compared to the pressure gages in the gas-filled section.

## Conclusion

Detonations reflecting from the free surface of a water-filled section produce peak reflected shock pressures (Fig. 16) that are comparable to reflection from a rigid surface. The transmitted shock waves in the water maintain their shape and peak amplitude with minimal attenuation a substantial distance from the water surface. The transmitted shock in the water propagates close to the Korteweg speed predicted by the theory of water hammer. The peak strains (Fig. 17) are comparable for the gas and water-filled cases. Peak strains and pressures observed in a DDT event are comparable in piping with and without water-filled segments, with peak pressures up to 30 MPa and peak strains up to 1000  $\mu$ strain. The force on the pipe due to the detonation propagation around the bend is manifested as an axial strain wave propagating away from the bend at approximately the bar speed. On the downstream side of the bend, the axial strain wave can be

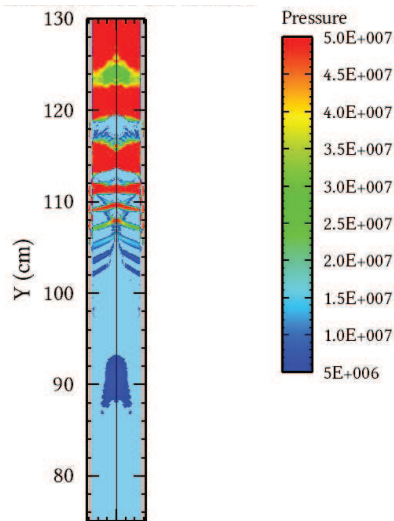


Figure 22. Pressure contours in water at 2.05 ms - numerical simulations.

observed propagating ahead of the detonation wave.

#### ACKNOWLEDGMENT

This research was sponsored by the US Department of Energy, Office of River Protection, Richland, WA.

#### REFERENCES

- [1] Naitoh, M., Kasahara, F., Kubota, R., and Ohshima, I., 2003. "Analysis of pipe rupture of steam condensation line at Hamoaka-1, (I) Accumulation of noncondensable gas in a pipe". *Journal of Nuclear Science and Technology*, **40**(12), p. 1032.
- [2] Naitoh, M., Kasahara, F., Kubota, R., and Ohshima, I., 2003. "Analysis of pipe rupture of steam condensation line at Hamoaka-1, (II) Hydrogen combustion and generation". *Journal of Nuclear Science and Technology*, **40**(12), pp. 1041–1051.
- [3] Kuznetsov, M., Breitung, W., Grüne, J., and Singh, R. K.,

2005. "Structural response of DN15-tubes under radiolysis gas detonation loads for BWR safety applications". In 18th International Conference on Structural Mechanics in Reactor Technology, no. SMiRT 18-J09-1.

- [4] Shepherd, J. E., 2006. "Structural response of piping to internal gas detonation". In ASME Pressure Vessels and Piping Conference., ASME. PVP2006-ICPVT11-93670, presented July 23-27 2006, Vancouver BC Canada.
- [5] Browne, S., Ziegler, J., and Shepherd, J. E., 2004. Numerical solution methods for shock and detonation jump conditions. Tech. Rep. FM2006.006, GALCIT.
- [6] Pfahl, U., Schultz, E., and Shepherd, J., 1998. Detonation cell width measurements for H<sub>2</sub>-N<sub>2</sub>O-O<sub>2</sub>-CH<sub>4</sub>-NH<sub>3</sub> mixtures. Tech. Rep. FM98-5, GALCIT, April.
- [7] Meyers, M. A., 1994. *Dynamic behavior of materials*. John Wiley & Sons.
- [8] Inaba, K., and Shepherd, J. E., 2008. "Flexural waves in fluid-filled tubes subject to axial impact". In Proceedings of the ASME Pressure Vessels and Piping Conference. July 27-31, Chicago, IL USA. PVP2008-61672.
- [9] McGlaun, J., Thompson, S., Kmetyk, L., and Elrick, M., 1989. A brief description of the three-dimensional shock wave physics code CTH. Tech. Rep. SAND89-0607, Sandia National Laboratory.
- [10] McGlaun, J., Thompson, S., and Elrick, M., 1990. "CTH: A three-dimensional shock physics code". *International Journal of Impact Engineering*, **10**, pp. 351–360.
- [11] Beltman, W., and Shepherd, J., 2002. "Linear elastic response of tubes to internal detonation loading". *Journal of Sound and Vibration*, **252**(4).
- [12] Skalak, R., 1956. "An extension of the theory of water hammer". *Trans ASME*, **78**, pp. 105–116.

Table 4. Properties of CJ detonation in standard (0.3/0.7) H<sub>2</sub>-N<sub>2</sub>O mixture as computed with the Shock and Detonation Toolbox [5].

Initial conditions		
Pressure	100	(kPa)
Temperature	295	(K)
Density	1.2807	(kg/m <sup>3</sup> )
sound speed $a_1$ (frozen)	319.2198	(m/s)
$\gamma_1$ (frozen)	1.3051	(m/s)
CJ state		
Wave speed	2088.0993	(m/s)
Pressure	2.63	(MPa)
Temperature	3383.	(K)
Density	2.343	(kg/m <sup>3</sup> )
$w_2$ (wave frame)	1142.	(m/s)
$u_2$ (lab frame)	946.5	(m/s)
$a_2$ (frozen)	1187.0	(m/s)
$a_2$ (equilibrium)	1140.	(m/s)
$\gamma_2$ (frozen)	1.2542	(m/s)
$\gamma_2$ (equilibrium)	1.1566	(m/s)
Isentropic expansion to end of Taylor wave		
Pressure	0.958	(MPa)
Temperature	3005.	(K)
Volume	1.0218	(m <sup>3</sup> /kg)
Sound speed (frozen)	1107.2	(m/s)
Sound speed (equilibrium)	1065.4	(m/s)
$\gamma$ (frozen)	1.2519	(m/s)
$\gamma$ (equilibrium)	1.1593	(m/s)
Reflected Shock		
Speed	811.4	(m/s)
Pressure	6.529	(MPa)
Temperature	3784.	(K)